University of Alberta

Structure of Turbulent Flows around Bed-Mounted Cylinders in Open Channels

by

Muhammad Abdul Faheem Sadeque

A thesis submitted to the Faculty of Graduate Studies and Research
in partial fulfillment of the requirements for the degree of

Doctor of Philosophy
in
Water Resources Engineering

Department of Civil and Environmental Engineering

Edmonton, Alberta
Spring 2008

Library and
Archives Canada

Published Heritage
Branch

395 Wellington Street
Ottawa ON K1A 0N4
Canada

Bibliothèque et
Archives Canada

Direction du
Patrimoine de l'édition

395, rue Wellington
Ottawa ON K1A 0N4
Canada

Your file Votre référence
ISBN: 978-0-494-45590-6
Our file Notre référence
ISBN: 978-0-494-45590-6

NOTICE:
The author has granted a non-exclusive license allowing Library and Archives Canada to reproduce, publish, archive, preserve, conserve, communicate to the public by telecommunication or on the Internet, loan, distribute and sell theses worldwide, for commercial or non-commercial purposes, in microform, paper, electronic and/or any other formats.

The author retains copyright ownership and moral rights in this thesis. Neither the thesis nor substantial extracts from it may be printed or otherwise reproduced without the author's permission.

AVIS:
L'auteur a accordé une licence non exclusive permettant à la Bibliothèque et Archives Canada de reproduire, publier, archiver, sauvegarder, conserver, transmettre au public par télécommunication ou par l'Internet, prêter, distribuer et vendre des thèses partout dans le monde, à des fins commerciales ou autres, sur support microforme, papier, électronique et/ou autres formats.

L'auteur conserve la propriété du droit d'auteur et des droits moraux qui protège cette thèse. Ni la thèse ni des extraits substantiels de celle-ci ne doivent être imprimés ou autrement reproduits sans son autorisation.

In compliance with the Canadian Privacy Act some supporting forms may have been removed from this thesis.

While these forms may be included in the document page count, their removal does not represent any loss of content from the thesis.

Conformément à la loi canadienne sur la protection de la vie privée, quelques formulaires secondaires ont été enlevés de cette thèse.

Bien que ces formulaires aient inclus dans la pagination, il n'y aura aucun contenu manquant.

Canada

ABSTRACT

An experimental investigation of the characteristics of shallow turbulent wakes behind bed-mounted cylinders in an open channel was carried out. Cylindrical objects of equal diameter and four heights were tested under similar flow conditions on smooth and rough beds producing four different levels of submergence. As a part of the systematic approach followed in this study, properties of the undisturbed approach flow have been studied first. The altered flow patterns in the upstream region surrounding the cylinders are studied along with a study of the skewed turbulent boundary layer. In addition, flow visualization and detailed measurements of the bed shear stress around the cylinders are presented. The principal motivation for this study is to improve our understanding of the flows around simple fish habitat structures.

Analysis of the flow field around the cylinders in terms of the theories of three-dimensional turbulent boundary layers revealed that Perry and Joubert's model is sufficiently accurate to predict the deflected velocity magnitudes around the submerged and non-submerged cylinders.

The general flow patterns in the shallow near-wake region were explained using reliable velocity measurements. The mean velocity defect and wake turbulence were found to increase in the near-wake before decaying in the downstream direction. The rates of decay of the velocity defect and wake turbulence were related to the level of submergence of the cylinders and bed roughness.

Wall wake analyses demonstrated that the flows in the region away from the bed are quite similar and can be described with the well-known plane wake equation. Wall wake similarity was also observed for the turbulence properties, such as the turbulent kinetic energy and primary Reynolds stress for moderate to deeply submerged cylinders. Wake analyses on the horizontal plane showed that the mean velocity profiles were similar across the flow in the near-wake region at all elevations for slightly submerged and surface piercing cylinders; and at all elevations below the object height very close to the moderate to deeply submerged cylinders. Normalized mean velocity profiles across the wake in the horizontal plane for slightly submerged and surface piercing cylinders were in fair agreement with the well-known plane wake equation. However, the normalized mean velocity profiles were found to exhibit considerable similarity in all flow regimes when a slightly modified transverse length scale (i.e. half-width) was used.

Dedicated

to

my parents

ACKNOWLEDGEMENT

I would like to express my profound gratitude and respect to Dr. N. Rajaratnam for his constant supervision, encouragement, and keen interest throughout the work. His constructive views and comments helped me to develop a better understanding of the study. Dr. Raj always believed in my ability and tremendously inspired me whenever I met him. I also sincerely acknowledge the guidance and supervision provided by Dr. M. R. Loewen. His guidance was indispensable for conducting a systematic experimental study and data processing. Dr. Loewen always helped me to improve the quality of my research through his constructive remarks.

I am grateful to Dr. Pierre Julien, Professor, Colorado State University for reading the thesis in spite of his busy schedule. I am also thankful to all the respected members in my examination committee for their valuable suggestions.

My special appreciation goes to Mr. Perry Fedun for his laboratory assistance during the experiments. He has provided valuable assistance in building the experimental setup in Ellerslie River Engineering Laboratory, Edmonton, Alberta. I gratefully acknowledge the scholarship and research funds provided by the Faculty of Graduate Studies and Research (FGSR) at the University of Alberta and Natural Sciences and Engineering Research Council of Canada (NSERC).

I would like to extend my gratitude to my parents, family members and friends for their encouragement. I appreciate the technical assistance provided by my friend Shahnawaz. It was my privilege that my wife Shaheli could take part in technical discussions and actively support me during the experiments. Without her affection and support this study could not be completed.

Above all, I am grateful to the Almighty for the successful completion of the work.

TABLE OF CONTENTS

Chapter 1 Introduction 1
- 1.1 General 1
- 1.2 Fish Habitat Structures 1
- 1.3 Literature Review 2
- 1.4 Scope and Objectives of the Study 5
- 1.5 Organization of the Thesis 5
- 1.6 References 7

Chapter 2 Experimental Setup and Procedures 10
- 2.1 Open Channel Flume 10
- 2.2 Yaw Probe 11
- 2.3 Acoustic Doppler Velocimeter (ADV) 12
- 2.4 Design of Experiments 14
  - 2.4.1 The flow regimes 14
  - 2.4.2 Selection of flow and object dimensions 14
  - 2.4.3 Selection of sampling time and frequency 15
- 2.5 Data Processing Procedure 16
  - 2.5.1 Yaw probe data 16
  - 2.5.2 ADV data 17
- 2.6 Data Quality Investigation 20
  - 2.6.1 Repeatability and uncertainty of measurements 21
  - 2.6.2 Sources of error 23
- 2.7 References 43

Chapter 3 Turbulence in Narrow Open Channel Flows 45
- 3.1 Introduction 45
- 3.2 Experimental Setup and Procedure 47
- 3.3 Result Analysis and Discussions 49
  - 3.3.1 Bed shear stress and friction velocity 49

3.3.2 Turbulent intensities and kinetic energy 50
3.3.3 Primary Reynolds stress 52
3.3.4 Turbulence anisotropy 55
3.3.5 Production term for turbulence driven secondary current 56
3.3.6 Dissipation term for turbulence driven secondary current 57
3.3.7 Correlation of the primary Reynolds stress with turbulence 57
3.4 Conclusions 58
3.5 References 73

Chapter 4 Skewed Turbulent Boundary Layer around Cylinders 75
4.1 Introduction 75
4.2 Theories of Skewed Boundary Layer 78
4.2.1 Cross-flow models 79
4.2.2 Near-wall similarity models 81
4.3 Experimental Setup and Procedure 82
4.4 Part I: Smooth Bed Results and Discussions 83
4.4.1 Flow visualization test 83
4.4.2 Bed shear stress distribution 85
4.4.3 Analysis of deflected flow in terms of the theories of 3DTBL 87
4.4.4 General applicability of the models 91
4.4.5 Conclusions 92
4.5 Part II: Rough Bed Results and Discussions 113
4.5.1 Flow visualization test 113
4.5.2 Bed shear stress distribution 114
4.5.3 Analysis of deflected flow in terms of the theories of 3DTBL 116
4.5.4 General applicability of the models 119
4.5.5 Conclusions 120
4.6 References 140

Chapter 5 Turbulent Flow Field Upstream of Cylinders 143
5.1 Introduction 143
5.2 Experimental Setup and Procedure 144
5.3 Result Analysis and Discussions 145
5.3.1 Observations of mean velocity on upstream plane of symmetry 145
5.3.2 Observations of vorticity near the point of separation on upstream POS 147
5.3.3 Observations of logarithmic law, defect law and Clauser's scheme profiles 147
5.3.4 Observations of turbulence quantities on upstream POS 149
5.3.5 Upstream deflected flow: mean velocities and turbulence 150
5.3.6 Deflected flow at *x*=0 plane: mean velocities and turbulence 151
5.4 Conclusions 154
5.5 References 241

Chapter 6 Shallow Turbulent Near-Wakes behind Cylinders 242
6.1 Introduction 242
6.2 Literature Review 244
6.3 Experimental Setup and Procedure 249
6.4 Result Analysis and Discussions 250
6.4.1 Mean velocity on downstream plane of symmetry 250
6.4.2 Turbulence on downstream POS 254
6.4.3 Closed wake envelope and vorticity inside the recirculation zone 255
6.4.4 Wall wake analysis 257
6.4.5 Decay of longitudinal mean velocity defect on downstream POS 260
6.4.6 Decay of vertical mean velocity on downstream POS 262
6.4.7 Decay of increased turbulence on downstream POS 263
6.4.8 Wake analysis on horizontal plane 265

6.5 Conclusions 268
6.6 References 353

Chapter 7 Conclusions and Recommendations 355
7.1 Summary 355
7.2 Conclusions of the Study 355
7.3 Recommendations for Future Study 359

LIST OF TABLES

Table	Caption	Page
2.1	Primary Details of the Experiment Scenario	24
2.2	Repeatability of Yaw Probe Measured Bed Shear Stresses	25
2.3	Repeatability of Yaw Probe Measured Velocities	26
2.4(a)	Repeatability of ADV measurements at z = 15 cm	27
2.4(b)	Repeatability of ADV measurements at z = 7.5 cm	28
2.4(c)	Repeatability of ADV measurements at z = 0.5 cm	29
3.1	Friction Velocities and Bed Shear Stress Values	59
6.1	Power Function Parameters for the Decay of Mean Velocity Defect	272
6.2	Power Function Parameters for the Decay of Wake Turbulence	272
6.3	Power Function Parameters Obtained from Horizontal Wake Analysis	272

LIST OF FIGURES

Figure	Caption	Page
2.1	Schematic diagram showing the experimental setup	30
2.2	Measured grain size distribution of the 8/12 sand	30
2.3	Photograph of the traverse system with the ADV probe	31
2.4	Photograph of leveled and aligned yaw probe	31
2.5	Photograph of the setup for the yaw probe measurements	32
2.6	Photograph of the ADV probe mounted for smooth bed measurements	32
2.7	Photograph of leveled and aligned ADV probe	33
2.8	Definition sketch of flow regimes; (a) Regime-1: Deeply Submerged Object (Submergence ratio, $H/h \approx 4$), (b) Regime-2: Moderately Submerged Object ($H/h \approx 2$), (c) Regime-3: Slightly Submerged Object ($H/h \approx 1.1$), and (d) Regime-4: Non-Submerged Object ($h>H$)	33
2.9(a-f)	Sampling duration adequacy check using ADV data at $x=+4D$ and $y=0$ in Regime-4 on rough bed	34
2.10	A typical auto-spectral density function of the transverse velocity component (G_{vv}) showing the procedure of cut-off frequency selection	35
2.11	A segment of raw ADV data in the wake	35
2.12	High-pass filtered series obtained from raw ADV data	36
2.13	Low-frequency series obtained from raw ADV data	36
2.14	SNR and COR threshold filtered series obtained from high-pass filtered data	37
2.15	Clean ADV data in the wake	37
2.16(a-f)	Repeated ADV measurements at $x=-2D$ and $y=0$ in Regime-3 on rough bed	38
2.17(a-f)	Repeated ADV measurements at $x=0$ and $y=2.2D$ in Regime-3 on rough bed	39
2.18(a-f)	Repeated ADV measurements at $x=+2D$ and $y=0$ in Regime-3 on rough bed	40

2.19(a-c) Auto-spectral density functions plotted using repeated ADV measurements at x=+2D, y=0, z=13 cm in Regime-3 on rough bed; the dotted lines represent the 95% confidence limits based on Data-1 41

2.20(a-c) Auto-spectral density functions plotted using repeated ADV measurements at x=+2D, y=0, z=0.5 cm in Regime-3 on rough bed; the dotted lines represent the 95% confidence limits based on Data-1 42

2.21 Comparison of mean velocity profiles obtained from ADV and yaw probe measurements; (a) profile of U at x=+3D, y=1D; (b) profile of V at x=+3D, y=1D; (c) profile of U at x=+3D, y=0.5D; and (d) profile of V at x=+3D, y=0.5D in Regime-2 on smooth bed 43

3.1 Mean velocity profiles on smooth bed; at (a) y=0, (b) y=-0.3m, and (c) y=+0.3m 60

3.2 Mean velocity profiles on rough bed; at (a) y=0, (b) y=-0.3m, and (c) y=+0.3m 61

3.3 Mean velocity profiles at x=0; on (a) a smooth bed, and (b) a rough bed 62

3.4 Relative location of the velocity measurement stations 62

3.5 Logarithmic distribution of streamwise mean velocity on (a) a smooth bed; (b) a rough bed 63

3.6 The normalized root mean square velocities, u'/u_* versus the normalized depth, z/δ, at (a) station 1; (b) station 2 64

3.7 The normalized root mean square velocities, v'/u_* versus the normalized depth, z/δ, at (a) station 1; (b) station 2 65

3.8 The normalized root mean square velocities, w'/u_* versus the normalized depth, z/δ, at (a) station 1; (b) station 2 66

3.9 The non-dimensional turbulent kinetic energy, k/u_*^2 versus the normalized depth, z/δ, at (a) station 1; (b) station 2 67

3.10 The normalized primary Reynolds stress, $-\overline{uw}/\overline{u_*}^{2}$ versus the normalized depth, z/δ, at station 1 68

3.11	Ratios of turbulence anisotropy on (a) smooth bed; (b) rough bed at station 1	68
3.12	Ratios of turbulence anisotropy on (a) smooth bed; (b) rough bed at station 2	69
3.13	The normalized secondary current production term versus the normalized depth, z/H, at (a) station 1; (b) station 2	70
3.14	The normalized secondary current dissipation term versus the normalized depth, z/H, at (a) station 1; (b) station 2	71
3.15	Correlation coefficient, R_t versus the normalized depth, z/δ, at station 1	72
3.16	Correlation coefficient, R_k versus the normalized depth, z/δ, at station 1	72
4.1	Typical skewed turbulent boundary layer (Adapted from Ahmed and Rajaratnam 1997a)	94
4.2	Definition sketches of skewed turbulent boundary layer; (a) coordinate system and notations, (b) velocity components, (c) Johnston's polar plot, and (d) Perry and Joubert's model (Adapted from Ahmed and Rajaratnam 1997a)	95
4.3	Location of the velocity measuring stations relative to the object	95
4.4	Sketches of the horse-shoe vortex system and flow on the POS with respect to the cylinders in (a-b) Regime-1, (c-d) Regime-2, (e-f) Regime-3, and (g-h) Regime-4	96
4.5	Horse-shoe vortex in Regime-1	97
4.6	Wakes behind the cylinders	97
4.7	Normalized mean bed shear stress profiles on (a) the upstream, and (b) the downstream plane of symmetry	97
4.8(a-b)	Normalized mean bed shear stress (τ_0/τ_{00}) contours; (a) Regime-1, (b) Regime-2	98
4.8(c-d)	Normalized mean bed shear stress (τ_0/τ_{00}) contours; (c) Regime-3, (d) Regime-4	99
4.9	Transverse profile of normalized mean bed shear stress (a) magnitude and (b) angle on x=0 plane	100

4.10(a-b) Bed shear stress similarity profiles; (a) Regime-1, (b) Regime-2 100

4.10(c-d) Bed shear stress similarity profiles; (c) Regime-3, and (d) Regime-4 101

4.11 The normalized longitudinal velocities, U/U_e versus the normalized depth, z/δ; (a) Regime-1, (b) Regime-2, (c) Regime-3, and (d) Regime-4 102

4.12(a-b) Prandtl's functions G and gG versus the normalized depth, z/δ; (a) Regime-1, (b) Regime-2 103

4.12(c-d) Prandtl's functions G and gG versus the normalized depth, z/δ; (c) Regime-3, (d) Regime-4 104

4.13 Johnston's polar plots for Regime-1. The normalized velocity components along (U_s/q_e) and perpendicular (V_s/q_e) to the free streamline direction are plotted on horizontal and vertical axes. The arrow represents the direction of local bed shear stress (τ_0) 105

4.14 Johnston's polar plots for Regime-2. The normalized velocity components along (U_s/q_e) and perpendicular (V_s/q_e) to the free streamline direction are plotted on horizontal and vertical axes. The arrow represents the direction of local bed shear stress (τ_0) 106

4.15 Johnston's polar plots for Regime-3. The normalized velocity components along (U_s/q_e) and perpendicular (V_s/q_e) to the free streamline direction are plotted on horizontal and vertical axes. The arrow represents the direction of local bed shear stress (τ_0) 107

4.16 Johnston's polar plots for Regime-4. The normalized velocity components along (U_s/q_e) and perpendicular (V_s/q_e) to the free streamline direction are plotted on horizontal and vertical axes. The arrow represents the direction of local bed shear stress (τ_0) 108

4.17(a-b) Coles' wall and wake functions versus zu_*/ν and z/δ; (a) Regime-1, (b) Regime-2 109

4.17(c-d) Coles' wall and wake functions versus zu_*/ν and z/δ; (c) Regime-3, and (d) Regime-4 110

4.18(a-b) Perry and Joubert's defect function and $\Delta\beta$ versus the normalized depth, z/δ; (a) Regime-1, (b) Regime-2 111

4.18(c-d) Perry and Joubert's defect function and $\Delta\beta$ versus the normalized depth, z/δ; (c) Regime-3, (d) Regime-4 112

4.19 Sketches of the horse-shoe vortex system and flow on the POS with respect to the cylinders in (a-b) Regime-1, (c-d) Regime-2, (e-f) Regime-3, and (g-h) Regime-4 122

4.20 Horse-shoe vortex; (a) Regime-1, and (b) Regime-2 123

4.21 Wakes behind the cylinders; (a) Regime-2, (b) Regime-3, and (c) Regime-4 123

4.22 Normalized mean bed shear stress profiles on (a) the upstream, and (b) the downstream plane of symmetry 124

4.23(a-b) Normalized mean bed shear stress (τ_0/τ_{00}) contours; (a) Regime-1, (b) Regime-2 125

4.23(c-d) Normalized mean bed shear stress (τ_0/τ_{00}) contours; (c) Regime-3, (d) Regime-4 126

4.24 Transverse profile of normalized mean bed shear stress (a) magnitude and (b) angle on x=0 plane 127

4.25(a-b) Bed shear stress similarity profiles; (a) Regime-1, (b) Regime-2 127

4.25(c-d) Bed shear stress similarity profiles; (c) Regime-3, and (d) Regime-4 128

4.26 The normalized longitudinal velocities, U/U_e versus the normalized depth, z/δ; (a) Regime-1, (b) Regime-2, (c) Regime-3, and (d) Regime-4 129

4.27(a-b) Prandtl's functions G and gG versus the normalized depth, z/δ; (a) Regime-1, (b) Regime-2 130

4.27(c-d) Prandtl's functions G and gG versus the normalized depth, z/δ; (c) Regime-3, (d) Regime-4 131

4.28 Johnston's polar plots for Regime-1. The normalized velocity components along (U_s/q_e) and perpendicular (V_s/q_e) to the free streamline direction are plotted on horizontal and vertical axes. The arrow represents the direction of local bed shear stress (τ_0) 132
4.29 Johnston's polar plots for Regime-2. The normalized velocity components along (U_s/q_e) and perpendicular (V_s/q_e) to the free streamline direction are plotted on horizontal and vertical axes. The arrow represents the direction of local bed shear stress (τ_0) 133
4.30 Johnston's polar plots for Regime-3. The normalized velocity components along (U_s/q_e) and perpendicular (V_s/q_e) to the free streamline direction are plotted on horizontal and vertical axes. The arrow represents the direction of local bed shear stress (τ_0) 134
4.31 Johnston's polar plots for Regime-4. The normalized velocity components along (U_s/q_e) and perpendicular (V_s/q_e) to the free streamline direction are plotted on horizontal and vertical axes. The arrow represents the direction of local bed shear stress (τ_0) 135
4.32(a-b) Coles' wall and wake functions versus z/k_s and z/δ; (a) Regime-1, (b) Regime-2 136
4.32(c-d) Coles' wall and wake functions versus z/k_s and z/δ; (c) Regime-3, and (d) Regime-4 137
4.33(a-b) Perry and Joubert's defect function and $\Delta\beta$ versus the normalized depth, z/δ; (a) Regime-1, (b) Regime-2 138
4.33(c-d) Perry and Joubert's defect function and $\Delta\beta$ versus the normalized depth, z/δ; (c) Regime-3, (d) Regime-4 139
5.1 Typical velocity measuring stations relative to the object on a horizontal plane; small white circles are the stations used for velocity measurements 155
5.1(a) 2D velocity vectors on upstream POS: Smooth bed/Regime-1 156
5.2(b) 2D velocity vectors on upstream POS: Smooth bed/Regime-2 156
5.2(c) 2D velocity vectors on upstream POS: Smooth bed/Regime-3 157

5.2(d) 2D velocity vectors on upstream POS: Smooth bed/Regime-4 157

5.3(a) 2D velocity vectors on upstream POS: Rough bed/Regime-1 158

5.3(b) 2D velocity vectors on upstream POS: Rough bed/Regime-2 158

5.3(c) 2D velocity vectors on upstream POS: Rough bed/Regime-3 159

5.3(d) 2D velocity vectors on upstream POS: Rough bed/Regime-4 159

5.4 Normalized mean velocity profiles on upstream POS: Smooth bed/Regime-1; (a) longitudinal mean velocity (U/U_0), (b) speed up factor (U/U_z), and (c) vertical mean velocity (W/U_0) 160

5.5 Normalized mean velocity profiles on upstream POS: Smooth bed/Regime-2; (a) longitudinal mean velocity (U/U_0), (b) speed up factor (U/U_z), and (c) vertical mean velocity (W/U_0) 161

5.6 Normalized mean velocity profiles on upstream POS: Smooth bed/Regime-3; (a) longitudinal mean velocity (U/U_0), (b) speed up factor (U/U_z), and (c) vertical mean velocity (W/U_0) 162

5.7 Normalized mean velocity profiles on upstream POS: Smooth bed/Regime-4; (a) longitudinal mean velocity (U/U_0), (b) speed up factor (U/U_z), and (c) vertical mean velocity (W/U_0) 163

5.8 Normalized mean velocity profiles on upstream POS: Rough bed/Regime-1; (a) longitudinal mean velocity (U/U_0), (b) speed up factor (U/U_z), and (c) vertical mean velocity (W/U_0) 164

5.9 Normalized mean velocity profiles on upstream POS: Rough bed/Regime-2; (a) longitudinal mean velocity (U/U_0), (b) speed up factor (U/U_z), and (c) vertical mean velocity (W/U_0) 165

5.10 Normalized mean velocity profiles on upstream POS: Rough bed/Regime-3; (a) longitudinal mean velocity (U/U_0), (b) speed up factor (U/U_z), and (c) vertical mean velocity (W/U_0) 166

5.11 Normalized mean velocity profiles on upstream POS: Rough bed/Regime-4; (a) longitudinal mean velocity (U/U_0), (b) speed up factor (U/U_z), and (c) vertical mean velocity (W/U_0) 167

5.12 Vorticity (ω_y) profile at x=-1D on POS; (a) Smooth bed, and (b) Rough bed 168

5.13 (a) Logarithmic velocity, (b) defect velocity, and (c) Clauser's scheme profiles on upstream POS: Smooth bed/Regime-1 169

5.14 (a) Logarithmic velocity, (b) defect velocity, and (c) Clauser's scheme profiles on upstream POS: Smooth bed/Regime-2 170

5.15 (a) Logarithmic velocity, (b) defect velocity, and (c) Clauser's scheme profiles on upstream POS: Smooth bed/Regime-3 171

5.16 (a) Logarithmic velocity, (b) defect velocity, and (c) Clauser's scheme profiles on upstream POS: Smooth bed/Regime-4 172

5.17 (a) Logarithmic velocity, (b) defect velocity, and (c) Clauser's scheme profiles on upstream POS: Rough bed/Regime-1 173

5.18 (a) Logarithmic velocity, (b) defect velocity, and (c) Clauser's scheme profiles on upstream POS: Rough bed/Regime-2 174

5.19 (a) Logarithmic velocity, (b) defect velocity, and (c) Clauser's scheme profiles on upstream POS: Rough bed/Regime-3 175

5.20 (a) Logarithmic velocity, (b) defect velocity, and (c) Clauser's scheme profiles on upstream POS: Rough bed/Regime-4 176

5.21 (a) Logarithmic velocity, (b) defect velocity, and (c) Clauser's scheme profiles on upstream POS using local friction velocity: Smooth bed/Regime-1 177

5.22 (a) Logarithmic velocity, (b) defect velocity, and (c) Clauser's scheme profiles on upstream POS using local friction velocity: Smooth bed/Regime-2 178

5.23 (a) Logarithmic velocity, (b) defect velocity, and (c) Clauser's scheme profiles on upstream POS using local friction velocity: Smooth bed/Regime-3 179

5.24 (a) Logarithmic velocity, (b) defect velocity, and (c) Clauser's scheme profiles on upstream POS using local friction velocity: Smooth bed/Regime-4 180

5.25 (a) Logarithmic velocity, (b) defect velocity, and (c) Clauser's scheme profiles on upstream POS using local friction velocity: Rough bed/Regime-1 181

5.26 (a) Logarithmic velocity, (b) defect velocity, and (c) Clauser's scheme profiles on upstream POS using local friction velocity: Rough bed/Regime-2 182

5.27 (a) Logarithmic velocity, (b) defect velocity, and (c) Clauser's scheme profiles on upstream POS using local friction velocity: Rough bed/Regime-3 183

5.28 (a) Logarithmic velocity, (b) defect velocity, and (c) Clauser's scheme profiles on upstream POS using local friction velocity: Rough bed/Regime-4 184

5.29 Variation of Clauser's boundary layer parameter (a) δ^*_x, (b) Δ^* using undisturbed flow friction velocity u_*, and (c) Δ^* using local friction velocity u_*' with distance x/D 185

5.30 Normalized profiles of turbulence quantities (a) longitudinal r.m.s. velocity, (b) transverse r.m.s. velocity, (c) vertical r.m.s. velocity, (d) turbulent kinetic energy, and (e) primary Reynolds stress on upstream POS: Smooth bed/Regime-1 186

5.31 Normalized profiles of turbulence quantities (a) longitudinal r.m.s. velocity, (b) transverse r.m.s. velocity, (c) vertical r.m.s. velocity, (d) turbulent kinetic energy, and (e) primary Reynolds stress on upstream POS: Smooth bed/Regime-2 187

5.32 Normalized profiles of turbulence quantities (a) longitudinal r.m.s. velocity, (b) transverse r.m.s. velocity, (c) vertical r.m.s. velocity, (d) turbulent kinetic energy, and (e) primary Reynolds stress on upstream POS: Smooth bed/Regime-3 188

5.33 Normalized profiles of turbulence quantities (a) longitudinal r.m.s. velocity, (b) transverse r.m.s. velocity, (c) vertical r.m.s. velocity, (d) turbulent kinetic energy, and (e) primary Reynolds stress on upstream POS: Smooth bed/Regime-4 189

5.34 Normalized profiles of turbulence quantities (a) longitudinal r.m.s. velocity, (b) transverse r.m.s. velocity, (c) vertical r.m.s. velocity, (d) turbulent kinetic energy, and (e) primary Reynolds stress on upstream POS: Rough bed/Regime-1 190

5.35 Normalized profiles of turbulence quantities (a) longitudinal r.m.s. velocity, (b) transverse r.m.s. velocity, (c) vertical r.m.s. velocity, (d) turbulent kinetic energy, and (e) primary Reynolds stress on upstream POS: Rough bed/Regime-2 191

5.36 Normalized profiles of turbulence quantities (a) longitudinal r.m.s. velocity, (b) transverse r.m.s. velocity, (c) vertical r.m.s. velocity, (d) turbulent kinetic energy, and (e) primary Reynolds stress on upstream POS: Rough bed/Regime-3 192

5.37 Normalized profiles of turbulence quantities (a) longitudinal r.m.s. velocity, (b) transverse r.m.s. velocity, (c) vertical r.m.s. velocity, (d) turbulent kinetic energy, and (e) primary Reynolds stress on upstream POS: Rough bed/Regime-4 193

5.38 Normalized mean velocity profiles on $y=0.5D$ plane: Smooth bed/Regime-1; (a) longitudinal mean velocity (U/U_0), (b) speed up factor (U/U_z), (c) transverse mean velocity (V/U_0), and (d) vertical mean velocity (W/U_0) 194

5.39 Normalized mean velocity profiles on $y=0.8D$ plane: Smooth bed/Regime-1; (a) longitudinal mean velocity (U/U_0), (b) speed up factor (U/U_z), (c) transverse mean velocity (V/U_0), and (d) vertical mean velocity (W/U_0) 195

5.40 Normalized mean velocity profiles on $y=1D$ plane: Smooth bed/Regime-1; (a) longitudinal mean velocity (U/U_0), (b) speed up factor (U/U_z), (c) transverse mean velocity (V/U_0), and (d) vertical mean velocity (W/U_0) 196

5.41 Normalized mean velocity profiles on y=0.5D plane: Smooth bed/Regime-2; (a) longitudinal mean velocity (U/U_0), (b) speed up factor (U/U_z), (c) transverse mean velocity (V/U_0), and (d) vertical mean velocity (W/U_0) 197

5.42 Normalized mean velocity profiles on y=0.8D plane: Smooth bed/Regime-2; (a) longitudinal mean velocity (U/U_0), (b) speed up factor (U/U_z), (c) transverse mean velocity (V/U_0), and (d) vertical mean velocity (W/U_0) 198

5.43 Normalized mean velocity profiles on y=1D plane: Smooth bed/Regime-2; (a) longitudinal mean velocity (U/U_0), (b) speed up factor (U/U_z), (c) transverse mean velocity (V/U_0), and (d) vertical mean velocity (W/U_0) 199

5.44 Normalized mean velocity profiles on y=0.5D plane: Smooth bed/Regime-3; (a) longitudinal mean velocity (U/U_0), (b) speed up factor (U/U_z), (c) transverse mean velocity (V/U_0), and (d) vertical mean velocity (W/U_0) 200

5.45 Normalized mean velocity profiles on y=0.8D plane: Smooth bed/Regime-3; (a) longitudinal mean velocity (U/U_0), (b) speed up factor (U/U_z), (c) transverse mean velocity (V/U_0), and (d) vertical mean velocity (W/U_0) 201

5.46 Normalized mean velocity profiles on y=1D plane: Smooth bed/Regime-3; (a) longitudinal mean velocity (U/U_0), (b) speed up factor (U/U_z), (c) transverse mean velocity (V/U_0), and (d) vertical mean velocity (W/U_0) 202

5.47 Normalized mean velocity profiles on y=0.5D plane: Smooth bed/Regime-4; (a) longitudinal mean velocity (U/U_0), (b) speed up factor (U/U_z), (c) transverse mean velocity (V/U_0), and (d) vertical mean velocity (W/U_0) 203

5.48 Normalized mean velocity profiles on $y=0.8D$ plane: Smooth bed/Regime-4; (a) longitudinal mean velocity (U/U_0), (b) speed up factor (U/U_z), (c) transverse mean velocity (V/U_0), and (d) vertical mean velocity (W/U_0) 204

5.49 Normalized mean velocity profiles on $y=1D$ plane: Smooth bed/Regime-4; (a) longitudinal mean velocity (U/U_0), (b) speed up factor (U/U_z), (c) transverse mean velocity (V/U_0), and (d) vertical mean velocity (W/U_0) 205

5.50 Normalized mean velocity profiles on $y=0.5D$ plane: Rough bed/Regime-1; (a) longitudinal mean velocity (U/U_0), (b) speed up factor (U/U_z), (c) transverse mean velocity (V/U_0), and (d) vertical mean velocity (W/U_0) 206

5.51 Normalized mean velocity profiles on $y=0.8D$ plane: Rough bed/Regime-1; (a) longitudinal mean velocity (U/U_0), (b) speed up factor (U/U_z), (c) transverse mean velocity (V/U_0), and (d) vertical mean velocity (W/U_0) 207

5.52 Normalized mean velocity profiles on $y=1D$ plane: Rough bed/Regime-1; (a) longitudinal mean velocity (U/U_0), (b) speed up factor (U/U_z), (c) transverse mean velocity (V/U_0), and (d) vertical mean velocity (W/U_0) 208

5.53 Normalized mean velocity profiles on $y=0.5D$ plane: Rough bed/Regime-2; (a) longitudinal mean velocity (U/U_0), (b) speed up factor (U/U_z), (c) transverse mean velocity (V/U_0), and (d) vertical mean velocity (W/U_0) 209

5.54 Normalized mean velocity profiles on $y=0.8D$ plane: Rough bed/Regime-2; (a) longitudinal mean velocity (U/U_0), (b) speed up factor (U/U_z), (c) transverse mean velocity (V/U_0), and (d) vertical mean velocity (W/U_0) 210

5.55 Normalized mean velocity profiles on y=1D plane: Rough bed/Regime-2; (a) longitudinal mean velocity (U/U_0), (b) speed up factor (U/U_z), (c) transverse mean velocity (V/U_0), and (d) vertical mean velocity (W/U_0) 211

5.56 Normalized mean velocity profiles on y=0.5D plane: Rough bed/Regime-3; (a) longitudinal mean velocity (U/U_0), (b) speed up factor (U/U_z), (c) transverse mean velocity (V/U_0), and (d) vertical mean velocity (W/U_0) 212

5.57 Normalized mean velocity profiles on y=0.8D plane: Rough bed/Regime-3; (a) longitudinal mean velocity (U/U_0), (b) speed up factor (U/U_z), (c) transverse mean velocity (V/U_0), and (d) vertical mean velocity (W/U_0) 213

5.58 Normalized mean velocity profiles on y=1D plane: Rough bed/Regime-3; (a) longitudinal mean velocity (U/U_0), (b) speed up factor (U/U_z), (c) transverse mean velocity (V/U_0), and (d) vertical mean velocity (W/U_0) 214

5.59 Normalized mean velocity profiles on y=0.5D plane: Rough bed/Regime-4; (a) longitudinal mean velocity (U/U_0), (b) speed up factor (U/U_z), (c) transverse mean velocity (V/U_0), and (d) vertical mean velocity (W/U_0) 215

5.60 Normalized mean velocity profiles on y=0.8D plane: Rough bed/Regime-4; (a) longitudinal mean velocity (U/U_0), (b) speed up factor (U/U_z), (c) transverse mean velocity (V/U_0), and (d) vertical mean velocity (W/U_0) 216

5.61 Normalized mean velocity profiles on y=1D plane: Rough bed/Regime-4; (a) longitudinal mean velocity (U/U_0), (b) speed up factor (U/U_z), (c) transverse mean velocity (V/U_0), and (d) vertical mean velocity (W/U_0) 217

5.62 Normalized turbulent kinetic energy and primary Reynolds stress profiles on (a-b) y=0.5D plane, (c-d) y=0.8D plane, and (e-f) y=1D plane: Smooth bed/Regime-1 218

5.63 Normalized turbulent kinetic energy and primary Reynolds stress profiles on (a-b) y=0.5D plane, (c-d) y=0.8D plane, and (e-f) y=1D plane: Smooth bed/Regime-2 219

5.64 Normalized turbulent kinetic energy and primary Reynolds stress profiles on (a-b) y=0.5D plane, (c-d) y=0.8D plane, and (e-f) y=1D plane: Smooth bed/Regime-3 220

5.65 Normalized turbulent kinetic energy and primary Reynolds stress profiles on (a-b) y=0.5D plane, (c-d) y=0.8D plane, and (e-f) y=1D plane: Smooth bed/Regime-4 221

5.66 Normalized turbulent kinetic energy and primary Reynolds stress profiles on (a-b) y=0.5D plane, (c-d) y=0.8D plane, and (e-f) y=1D plane: Rough bed/Regime-1 222

5.67 Normalized turbulent kinetic energy and primary Reynolds stress profiles on (a-b) y=0.5D plane, (c-d) y=0.8D plane, and (e-f) y=1D plane: Rough bed/Regime-2 223

5.68 Normalized turbulent kinetic energy and primary Reynolds stress profiles on (a-b) y=0.5D plane, (c-d) y=0.8D plane, and (e-f) y=1D plane: Rough bed/Regime-3 224

5.69 Normalized turbulent kinetic energy and primary Reynolds stress profiles on (a-b) y=0.5D plane, (c-d) y=0.8D plane, and (e-f) y=1D plane: Rough bed/Regime-4 225

5.70 Transverse profiles of normalized mean velocity on x=0 plane: Smooth bed/Regime-1; (a) longitudinal mean velocity (U/U_0), (b) speed up factor (U/U_z), (c) transverse mean velocity (V/U_0), and (d) vertical mean velocity (W/U_0) 226

5.71 Transverse profiles of normalized mean velocity on x=0 plane: Smooth bed/Regime-2; (a) longitudinal mean velocity (U/U_0), (b) speed up factor (U/U_z), (c) transverse mean velocity (V/U_0), and (d) vertical mean velocity (W/U_0) 227

5.72 Transverse profiles of normalized mean velocity on x=0 plane: Smooth bed/Regime-3; (a) longitudinal mean velocity (U/U_0), (b) speed up factor (U/U_z), (c) transverse mean velocity (V/U_0), and (d) vertical mean velocity (W/U_0) 228

5.73 Transverse profiles of normalized mean velocity on x=0 plane: Smooth bed/Regime-4; (a) longitudinal mean velocity (U/U_0), (b) speed up factor (U/U_z), (c) transverse mean velocity (V/U_0), and (d) vertical mean velocity (W/U_0) 229

5.74 Transverse profiles of normalized mean velocity on x=0 plane: Rough bed/Regime-1; (a) longitudinal mean velocity (U/U_0), (b) speed up factor (U/U_z), (c) transverse mean velocity (V/U_0), and (d) vertical mean velocity (W/U_0) 230

5.75 Transverse profiles of normalized mean velocity on x=0 plane: Rough bed/Regime-2; (a) longitudinal mean velocity (U/U_0), (b) speed up factor (U/U_z), (c) transverse mean velocity (V/U_0), and (d) vertical mean velocity (W/U_0) 231

5.76 Transverse profiles of normalized mean velocity on x=0 plane: Rough bed/Regime-3; (a) longitudinal mean velocity (U/U_0), (b) speed up factor (U/U_z), (c) transverse mean velocity (V/U_0), and (d) vertical mean velocity (W/U_0) 232

5.77 Transverse profiles of normalized mean velocity on x=0 plane: Rough bed/Regime-4; (a) longitudinal mean velocity (U/U_0), (b) speed up factor (U/U_z), (c) transverse mean velocity (V/U_0), and (d) vertical mean velocity (W/U_0) 233

5.78(a) 2D velocity vectors on x=0 plane: Smooth bed/Regime-1 234

5.78(b) 2D velocity vectors on x=0 plane: Smooth bed/Regime-2 234

5.78(c) 2D velocity vectors on x=0 plane: Smooth bed/Regime-3 235

5.78(d) 2D velocity vectors on $x=0$ plane: Smooth bed/Regime-4 235
5.79(a) 2D velocity vectors on $x=0$ plane: Rough bed/Regime-1 236
5.79(b) 2D velocity vectors on $x=0$ plane: Rough bed/Regime-2 236
5.79(c) 2D velocity vectors on $x=0$ plane: Rough bed/Regime-3 237
5.79(d) 2D velocity vectors on $x=0$ plane: Rough bed/Regime-4 237
5.80 Streamwise vorticity profiles on $x=0$ plane: Smooth bed; (a) Regime-1, (b) Regime-2, (c) Regime-3, and (d) Regime-4 238
5.81 Streamwise vorticity profiles on $x=0$ plane: Rough bed; (a) Regime-1, (b) Regime-2, (c) Regime-3, and (d) Regime-4 239
5.82 Variation of normalized turbulent kinetic energy (k/U_0^2) with y/D at $z=0.02H$ on $x=0$ plane; (a) Smooth bed, and (b) Rough bed 240
5.83 Variation of normalized turbulent shear stress (τ_t/u_*^2) with y/D at $z=0.02H$ on $x=0$ plane; (a) Smooth bed, and (b) Rough bed 240
6.1 Definition sketch for plane turbulent wake 273
6.2 Definition sketch for plane wall wake in deep flow (Adapted from Rajaratnam and Rai 1979) 273
6.3 Schematic diagram of three-dimensional wall wake regions (Adapted from Sforza and Mons 1970) 274
6.4 Schematic diagram of the velocity profiles of a shallow three-dimensional wake (Adapted from Shamloo et al. 2001) 274
6.5 Typical velocity measuring stations relative to the object on a horizontal plane 275
6.6 Near-wake streamlines with velocity vectors on POS: Smooth bed/Regime-1 275
6.7 Near-wake streamlines with velocity vectors on POS: Smooth bed/Regime-2 276
6.8 Near-wake streamlines with velocity vectors on POS: Smooth bed/Regime-3 276
6.9 Near-wake streamlines with velocity vectors on POS: Smooth bed/Regime-4 277

6.10 Normalized mean velocity profiles on downstream POS: Smooth bed/Regime-1; (a) longitudinal mean velocity (U/U_0), (b) speed up factor (U/U_z), and (c) vertical mean velocity (W/U_0) 278
6.11 Normalized mean velocity profiles on downstream POS: Smooth bed/Regime-2; (a) longitudinal mean velocity (U/U_0), (b) speed up factor (U/U_z), and (c) vertical mean velocity (W/U_0) 279
6.12 Normalized mean velocity profiles on downstream POS: Smooth bed/Regime-3; (a) longitudinal mean velocity (U/U_0), (b) speed up factor (U/U_z), and (c) vertical mean velocity (W/U_0) 280
6.13 Normalized mean velocity profiles on downstream POS: Smooth bed/Regime-4; (a) longitudinal mean velocity (U/U_0), (b) speed up factor (U/U_z), and (c) vertical mean velocity (W/U_0) 281
6.14 Near-wake streamlines with velocity vectors on POS: Rough bed/Regime-1 282
6.15 Near-wake streamlines with velocity vectors on POS: Rough bed/Regime-2 282
6.16 Near-wake streamlines with velocity vectors on POS: Rough bed/Regime-3 283
6.17 Near-wake streamlines with velocity vectors on POS: Rough bed/Regime-4 283
6.18 Normalized mean velocity profiles on downstream POS: Rough bed/Regime-1; (a) longitudinal mean velocity (U/U_0), (b) speed up factor (U/U_z), and (c) vertical mean velocity (W/U_0) 284
6.19 Normalized mean velocity profiles on downstream POS: Rough bed/Regime-2; (a) longitudinal mean velocity (U/U_0), (b) speed up factor (U/U_z), and (c) vertical mean velocity (W/U_0) 285
6.20 Normalized mean velocity profiles on downstream POS: Rough bed/Regime-3; (a) longitudinal mean velocity (U/U_0), (b) speed up factor (U/U_z), and (c) vertical mean velocity (W/U_0) 286

6.21 Normalized mean velocity profiles on downstream POS: Rough bed/Regime-4; (a) longitudinal mean velocity (U/U_0), (b) speed up factor (U/U_z), and (c) vertical mean velocity (W/U_0) 287

6.22 Logarithmic velocity profiles on downstream POS: Smooth bed; (a) Regime-1, (b) Regime-2, (c) Regime-3, and (d) Regime-4 288

6.23 Logarithmic velocity profiles on downstream POS: Rough bed; (a) Regime-1, (b) Regime-2, (c) Regime-3, and (d) Regime-4 289

6.24 Normalized profiles of turbulence quantities (a) longitudinal r.m.s. velocity, (b) transverse r.m.s. velocity, (c) vertical r.m.s. velocity, (d) turbulent kinetic energy, and (e) primary Reynolds stress on downstream POS: Smooth bed/Regime-1 290

6.25 Normalized profiles of turbulence quantities (a) longitudinal r.m.s. velocity, (b) transverse r.m.s. velocity, (c) vertical r.m.s. velocity, (d) turbulent kinetic energy, and (e) primary Reynolds stress on downstream POS: Smooth bed/Regime-2 291

6.26 Normalized profiles of turbulence quantities (a) longitudinal r.m.s. velocity, (b) transverse r.m.s. velocity, (c) vertical r.m.s. velocity, (d) turbulent kinetic energy, and (e) primary Reynolds stress on downstream POS: Smooth bed/Regime-3 292

6.27 Normalized profiles of turbulence quantities (a) longitudinal r.m.s. velocity, (b) transverse r.m.s. velocity, (c) vertical r.m.s. velocity, (d) turbulent kinetic energy, and (e) primary Reynolds stress on downstream POS: Smooth bed/Regime-4 293

6.28(a) Longitudinal turbulent intensity contour on DPOS: Smooth bed/Regime-1 294

6.28(b) Transverse turbulent intensity contour on DPOS: Smooth bed/Regime-1 294

6.28(c) Vertical turbulent intensity contour on DPOS: Smooth bed/Regime-1 295

6.28(d) Normalized turbulent kinetic energy (k/U^2) contour on DPOS: Smooth bed/Regime-1 295

6.28(e) Normalized primary Reynolds stress ($-\overline{uw}/U^2$) contour on DPOS: Smooth bed/Regime-1 296

6.29(a) Longitudinal turbulent intensity contour on DPOS: Smooth bed/Regime-2 296

6.29(b) Transverse turbulent intensity contour on DPOS: Smooth bed/Regime-2 297

6.29(c) Vertical turbulent intensity contour on DPOS: Smooth bed/Regime-2 297

6.29(d) Normalized turbulent kinetic energy (k/U^2) contour on DPOS: Smooth bed/Regime-2 298

6.29(e) Normalized primary Reynolds stress ($-\overline{uw}/U^2$) contour on DPOS: Smooth bed/Regime-2 298

6.30(a) Longitudinal turbulent intensity contour on DPOS: Smooth bed/Regime-3 299

6.30(b) Transverse turbulent intensity contour on DPOS: Smooth bed/Regime-3 299

6.30(c) Vertical turbulent intensity contour on DPOS: Smooth bed/Regime-3 300

6.30(d) Normalized turbulent kinetic energy (k/U^2) contour on DPOS: Smooth bed/Regime-3 300

6.30(e) Normalized primary Reynolds stress ($-\overline{uw}/U^2$) contour on DPOS: Smooth bed/Regime-3 301

6.31(a) Longitudinal turbulent intensity contour on DPOS: Smooth bed/Regime-4 301

6.31(b) Transverse turbulent intensity contour on DPOS: Smooth bed/Regime-4 302

6.31(c) Vertical turbulent intensity contour on DPOS: Smooth bed/Regime-4 302

6.31(d) Normalized turbulent kinetic energy (k/U^2) contour on DPOS: Smooth bed/Regime-4 303

6.31(e) Normalized primary Reynolds stress ($-\overline{uw}/U^2$) contour on DPOS: Smooth bed/Regime-4 303

6.32 Normalized profiles of turbulence quantities (a) longitudinal r.m.s. velocity, (b) transverse r.m.s. velocity, (c) vertical r.m.s. velocity, (d) turbulent kinetic energy, and (e) primary Reynolds stress on downstream POS: Rough bed/Regime-1 304
6.33 Normalized profiles of turbulence quantities (a) longitudinal r.m.s. velocity, (b) transverse r.m.s. velocity, (c) vertical r.m.s. velocity, (d) turbulent kinetic energy, and (e) primary Reynolds stress on downstream POS: Rough bed/Regime-2 305
6.34 Normalized profiles of turbulence quantities (a) longitudinal r.m.s. velocity, (b) transverse r.m.s. velocity, (c) vertical r.m.s. velocity, (d) turbulent kinetic energy, and (e) primary Reynolds stress on downstream POS: Rough bed/Regime-3 306
6.35 Normalized profiles of turbulence quantities (a) longitudinal r.m.s. velocity, (b) transverse r.m.s. velocity, (c) vertical r.m.s. velocity, (d) turbulent kinetic energy, and (e) primary Reynolds stress on downstream POS: Rough bed/Regime-4 307
6.36(a) Longitudinal turbulent intensity contour on DPOS: Rough bed/Regime-1 308
6.36(b) Transverse turbulent intensity contour on DPOS: Rough bed/Regime-1 308
6.36(c) Vertical turbulent intensity contour on DPOS: Rough bed/Regime-1 309
6.36(d) Normalized turbulent kinetic energy (k/U^2) contour on DPOS: Rough bed/Regime-1 309
6.36(e) Normalized primary Reynolds stress ($-\overline{uw}/U^2$) contour on DPOS: Rough bed/Regime-1 310
6.37(a) Longitudinal turbulent intensity contour on DPOS: Rough bed/Regime-2 310
6.37(b) Transverse turbulent intensity contour on DPOS: Rough bed/Regime-2 311
6.37(c) Vertical turbulent intensity contour on DPOS: Rough bed/Regime-2 311
6.37(d) Normalized turbulent kinetic energy (k/U^2) contour on DPOS: Rough bed/Regime-2 312

6.37(e) Normalized primary Reynolds stress ($-\overline{uw}/U^2$) contour on DPOS: Rough bed/Regime-2 312
6.38(a) Longitudinal turbulent intensity contour on DPOS: Rough bed/Regime-3 313
6.38(b) Transverse turbulent intensity contour on DPOS: Rough bed/Regime-3 313
6.38(c) Vertical turbulent intensity contour on DPOS: Rough bed/Regime-3 314
6.38(d) Normalized turbulent kinetic energy (k/U^2) contour on DPOS: Rough bed/Regime-3 314
6.38(e) Normalized primary Reynolds stress ($-\overline{uw}/U^2$) contour on DPOS: Rough bed/Regime-3 315
6.39(a) Longitudinal turbulent intensity contour on DPOS: Rough bed/Regime-4 315
6.39(b) Transverse turbulent intensity contour on DPOS: Rough bed/Regime-4 316
6.39(c) Vertical turbulent intensity contour on DPOS: Rough bed/Regime-4 316
6.39(d) Normalized turbulent kinetic energy (k/U^2) contour on DPOS: Rough bed/Regime-4 317
6.39(e) Normalized primary Reynolds stress ($-\overline{uw}/U^2$) contour on DPOS: Rough bed/Regime-4 317
6.40(a) Zero velocity (i.e. U=0) envelope of the closed recirculating zone 318
6.40(b) Free shear (i.e. $\partial^2 U/\partial z^2$=0) envelope of the closed recirculating zone 318
6.41(a) Vorticity (ω_y) contour in the closed recirculating zone: Smooth bed/Regime-1 319
6.41(b) Vorticity (ω_y) contour in the closed recirculating zone: Smooth bed/Regime-2 319
6.41(c) Vorticity (ω_y) contour in the closed recirculating zone: Rough bed/Regime-1 320
6.41(d) Vorticity (ω_y) contour in the closed recirculating zone: Rough bed/Regime-2 320

6.42 Inner region similarity with logarithmic law in wall wake; (a) Smooth bed/Regime-1, (b) Smooth bed/Regime-2, (c) Rough bed/Regime-1, and (d) Rough bed/Regime-2 321
6.43 Wall wake similarity in the outer region with plane wake equation; (a) Smooth bed/Regime-1, (b) Smooth bed/Regime-2, (c) Rough bed/Regime-1, and (d) Rough bed/Regime-2 322
6.44 Variation of the velocity scale (U_{2m}/U_c) with distance x/h; (a) Smooth bed/Regime-1, (b) Smooth bed/Regime-2, (c) Rough bed/Regime-1, and (d) Rough bed/Regime-2 323
6.45 Variation of the length scale (b_2/h) with distance x/h 323
6.46 Similarity profiles for turbulent kinetic energy $(k-k_c)/k_m$ vs z/b_k; (a) Smooth bed/Regime-1, (b) Smooth bed/Regime-2, (c) Rough bed/Regime-1, and (d) Rough bed/Regime-2 324
6.47 Similarity profiles for turbulent shear stress $(\tau_t - \tau_{tc})/\tau_{tm}$ vs z/b_τ; (a) Smooth bed/Regime-1, (b) Smooth bed/Regime-2, (c) Rough bed/Regime-1, and (d) Rough bed/Regime-2 325
6.48 Variation of (a) turbulent kinetic energy scale (k_m/U_0^2), and (b) turbulent shear stress scale (τ_{tm}/u_*^2) with distance x/h 326
6.49 Variation of the length scale of (a) turbulent kinetic energy (b_k/h), and (b) turbulent shear stress (b_τ/h) with distance x/h 326
6.50 Variation of maximum defect in mean velocity ($-\Delta U_{max}/U_H$) with distance x/D; (a) Smooth bed, and (b) Rough bed 327
6.51 Variation of maximum defect in mean velocity ($-\Delta U_{max}/U_H$) in logarithmic scale with distance x/D; (a) Smooth bed, and (b) Rough bed 327
6.52 Variation of the height of maximum velocity defect z_{max}/H with distance x/D; (a) Smooth bed, and (b) Rough bed 327
6.53 Normalized vertical mean velocity magnitudes profile on downstream POS on Smooth bed; (a) Regime-1, (b) Regime-2, (c) Regime-3, and (d) Regime-4 328

6.54 Normalized vertical mean velocity magnitudes profile on downstream POS on Rough bed; (a) Regime-1, (b) Regime-2, (c) Regime-3, and (d) Regime-4 329

6.55 Variation of the maximum normalized vertical mean velocity with distance *x/D*; (a) Smooth bed, and (b) Rough bed 330

6.56 Variation of the maximum normalized vertical mean velocity with distance *x/D* in logarithmic scale; (a) Smooth bed, and (b) Rough bed 330

6.57 Variation of the maximum values of normalized (a) turbulent kinetic energy $(k/u_*^2)_{max}$, and (b) turbulent shear stress $(-\overline{uw}/u_*^2)_{max}$ with distance *x/D* on Smooth bed 331

6.58 Variation of the maximum values of normalized (a) turbulent kinetic energy $(k/u_*^2)_{max}$, and (b) turbulent shear stress $(-\overline{uw}/u_*^2)_{max}$ with distance *x/D* on Rough bed 331

6.59 Variation of the maximum values of normalized (a) turbulent kinetic energy $(k/u_*^2)_{max}$, and (b) turbulent shear stress $(-\overline{uw}/u_*^2)_{max}$ with distance *x/D* in logarithmic scale on Smooth bed 332

6.60 Variation of the maximum values of normalized (a) turbulent kinetic energy $(k/u_*^2)_{max}$, and (b) turbulent shear stress $(-\overline{uw}/u_*^2)_{max}$ with distance *x/D* in logarithmic scale on Rough bed 332

6.61 Normalized mean velocity profile across the wake at (a) *x/D*=+0.7, (b) *x/D*=+1, (c) *x/D*=+1.5, (d) *x/D*=+2, and (e) *x/D*=+3: Smooth bed/Regime-1 333

6.62 Normalized mean velocity profile across the wake at (a) *x/D*=+0.8, (b) *x/D*=+1, (c) *x/D*=+1.5, (d) *x/D*=+2, and (e) *x/D*=+3: Smooth bed/Regime-2 334

6.63 Normalized mean velocity profile across the wake at (a) *x/D*=+0.7, (b) *x/D*=+1, (c) *x/D*=+1.5, (d) *x/D*=+2, and (e) *x/D*=+3: Smooth bed/Regime-3 335

6.64 Normalized mean velocity profile across the wake at (a) x/D=+0.8, (b) x/D=+1, (c) x/D=+1.5, (d) x/D=+2, and (e) x/D=+3: Smooth bed/Regime-4 336

6.65 Normalized mean velocity profile across the wake at (a) x/D=+0.7, (b) x/D=+1, (c) x/D=+1.5, (d) x/D=+2, and (e) x/D=+3: Rough bed/Regime-1 337

6.66 Normalized mean velocity profile across the wake at (a) x/D=+0.8, (b) x/D=+1, (c) x/D=+1.5, (d) x/D=+2, and (e) x/D=+3: Rough bed/Regime-2 338

6.67 Normalized mean velocity profile across the wake at (a) x/D=+0.8, (b) x/D=+1, (c) x/D=+1.5, (d) x/D=+2, and (e) x/D=+3: Rough bed/Regime-3 339

6.68 Normalized mean velocity profile across the wake at (a) x/D=+0.8, (b) x/D=+1, (c) x/D=+1.5, (d) x/D=+2, and (e) x/D=+3: Rough bed/Regime-4 340

6.69 Normalized mean velocity profile at z=h/2 across the wake on Smooth bed; (a) x/D=+0.7 or +0.8, (b) x/D=+1, (c) x/D=+1.5, (d) x/D=+2, and (e) x/D=+3 341

6.70 Normalized mean velocity profile at z=h/2 across the wake on Rough bed; (a) x/D=+0.7 or +0.8, (b) x/D=+1, (c) x/D=+1.5, (d) x/D=+2, and (e) x/D=+3 342

6.71(a-b) Wake similarity profile at z=h/2 on Smooth bed; (a) Regime-1, and (b) Regime-2 343

6.71(c-d) Wake similarity profile at z=h/2 on Smooth bed; (c) Regime-3, and (d) Regime-4 344

6.72(a-b) Wake similarity profile at z=h/2 on Rough bed; (a) Regime-1, and (b) Regime-2 345

6.72(c-d) Wake similarity profile at z=h/2 on Rough bed; (c) Regime-3, and (d) Regime-4 346

6.73 Variation of the velocity scale ($U_{1m}/U_{h/2}$) with distance x/D on Smooth bed; (a) Regime-1, and (b) Regime-2, (c) Regime-3, and (d) Regime-4 347

6.74 Variation of the velocity scale ($U_{1m}/U_{h/2}$) with distance x/D on Rough bed; (a) Regime-1, and (b) Regime-2, (c) Regime-3, and (d) Regime-4 348

6.75 Variation of the length scale (b_1/D and b/D) with distance x/D on (a) Smooth bed, and (b) Rough bed 349

6.76 Normalized turbulent kinetic energy profile across the wake at $z=h/2$ on Smooth bed; (a) Regime-1, (b) Regime-2, (c) Regime-3, and (d) Regime-4 350

6.77 Normalized turbulent kinetic energy profile across the wake at $z=h/2$ on Rough bed; (a) Regime-1, (b) Regime-2, (c) Regime-3, and (d) Regime-4 351

6.78 Normalized turbulent shear stress profile across the wake at $z=h/2$ on Smooth bed; (a) Regime-1, and (b) Regime-2 352

6.79 Normalized turbulent shear stress profile across the wake at $z=h/2$ on Rough bed; (a) Regime-1, and (b) Regime-2 352

LIST OF SYMBOLS

B = channel width;
b_k = length scale for turbulent kinetic energy similarity in wall wake;
b_τ = length scale for turbulent shear stress similarity in wall wake;
b_1 = half-width, or length scale in plane wake;
b_2 = half-width, or length scale in wall wake;
C_D = drag coefficient;
C_f = skin friction coefficient;
C_k = coefficients of the turbulent kinetic energy decay power function;
C_τ = coefficients of the turbulent shear stress decay power function;
D = diameter of cylinder;
D_{50} = median size of the sand particles;
F = Froude number;
f = frequency;
G_uu = auto-spectral density function of longitudinal velocity component;
G_vv = auto-spectral density functions of transverse velocity component;
G_ww = auto-spectral density functions of vertical velocity component;
g = gravitational acceleration;
H = total depth of water;
h = cylinder height;
k = turbulent kinetic energy;
k_e = turbulent kinetic energy in the upper layer where $\partial U/\partial z=0$;
k_m = maximum value of k_1;
k_s = Nikuradse's sand roughness height;
k_z = turbulent kinetic energy of undisturbed flow at any elevation z;
k_1 = increased turbulent kinetic energy in the wake, i.e. $k_1 = k - k_e$;
n = exponent of power function for the rate of decay of velocity defect;
$p1$ = exponents of the turbulent kinetic energy decay power function;
q = deflected mean velocity;
$q1$ = exponents of the turbulent shear stress decay power function;

q_e = deflected mean velocity at the free stream;
q_* = friction velocity;
R = Reynolds number;
R_k = coefficient of correlation between the primary Reynolds stress and turbulent kinetic energy;
R_t = coefficient of correlation between the primary Reynolds stress and turbulent velocities;
S = Strouhal number;
S_f = energy gradient;
S_w = shallow wake stability parameter;
T = sampling duration;
U = time-averaged longitudinal velocity;
U_e = time-averaged longitudinal velocity at free stream;
U_H = undisturbed mean longitudinal velocity at the free stream;
$U_{h/2}$ = undisturbed mean longitudinal velocity at $z=h/2$;
U_s = time-averaged velocity at any elevation z along the streamline at the free surface;
U_{se} = the value of U_s at the free stream;
U_z = undisturbed mean longitudinal velocity at any elevation z;
U_0 = cross-sectional mean velocity;
U_1 = velocity defect, U_∞-U;
U_2 = velocity defect, U_e-U;
U_{1m} = maximum value of U_1, or velocity scale of plane wake;
U_{2m} = maximum value of U_2, or velocity scale of wall wake;
U_∞ = undisturbed uniform ambient velocity;
u' = random fluctuation or, root mean square velocity in longitudinal direction;
$\widetilde{u}$ = periodic fluctuation in longitudinal direction;
u_* = friction velocity;
u_*' = local friction velocity computed from direct measurements;
$\overline{u_*}$ = mean friction velocity across the channel bed;

$\overline{u^2}$ = turbulent normal stress in longitudinal direction;

V = time-averaged spanwise velocity,

V_m = time-averaged velocity magnitude;

V_s = time-averaged velocity orthogonal to the free streamline;

v' = random fluctuation or, root mean square velocity in spanwise direction;

$\widetilde{v}$ = periodic fluctuation in spanwise direction;

$\overline{v^2}$ = turbulent normal stress in spanwise direction;

W = time-averaged vertical velocity;

W_{mag} = magnitudes of vertical mean velocity;

w' = random fluctuation or, root mean square velocity in vertical direction;

$\widetilde{w}$ = periodic fluctuation in vertical direction;

$\overline{w^2}$ = turbulent normal stress in vertical direction;

$\overline{uv}$ = Reynolds shear stress on x-y plane;

$\overline{uw}$ = Reynolds shear stress on x-z plane;

$-\overline{uw}_{max}$ = maximum Reynolds shear stress on x-z plane;

$\overline{vw}$ = Reynolds shear stress on y-z plane;

x = longitudinal direction, or distance from the center of the cylinder;

y = spanwise direction, or distance from the center of the channel cross-section;

z = vertical direction, or distance from the channel bed;

z_{max} = elevation z where the velocity defect is maximum;

α = free stream deflection angle;

β = angle between the vectors $\boldsymbol{q}_e$ and $(\boldsymbol{q}_e\text{-}\boldsymbol{q})$;

Δ^* = Clauser's integral parameter;

$-\Delta U$ = velocity defect, U_z-U;

$-\Delta U_{max}$ = maximum velocity defect;

δ = boundary layer thickness;

δ^*_x = Clauser's boundary layer thickness;

γ = unit weight of water;

γ_w = skewing of the bottom streamline from the free stream;

ν = kinematic viscosity of water;

Ω = streamwise vorticity;

ρ = density of water;

θ = yaw angle;

τ_0 = bed shear stress;

$\overline{\tau_0}$ = mean shear stress across the channel bed;

τ_{00} = bed shear stress of the approach flow;

$\tau_{0\,\max}$ = maximum shear stress across the channel bed;

τ_t = turbulent shear stress ($-\overline{uw}$);

τ_{te} = Reynolds stress in the upper layer where $\partial U/\partial z = 0$;

τ_{tm} = maximum value of τ_{t1};

τ_{tz} = turbulent shear stress of undisturbed flow at any elevation z;

τ_{t1} = increased turbulent shear stress in the wake, i.e. $\tau_{t1} = \tau_t - \tau_{te}$

τ_{uv} = turbulent shear stress on x-y plane;

τ_{uw} = turbulent shear stress on x-z plane;

ω_x = streamwise vorticity;

ω_y = spanwise vorticity;

ω_z = vorticity in z direction;

Chapter 1: Introduction

1.1 General

Shallow turbulent wakes created by bluff bodies are often found in environmental and geophysical flow systems. Simple fish habitat structures (e.g. boulders), water intake or outfall structures, or coastal islands in shallow water may generate wakes of three-dimensional nature especially in the near-wake region. The objects that generate shallow wakes in natural flow systems could be submerged or surface piercing. Previous studies have shown that the near-wake regions immediately downstream of the wake generator are more complex than the far wake. Therefore, an experimental investigation of the characteristics of shallow turbulent wakes behind bed-mounted cylinders of different levels of submergence in open channel flows on smooth and rough beds was carried out. As a part of the systematic approach followed in this study, properties of mean and turbulent undisturbed approach flow were studied first so that the changes in the flow pattern caused by the cylindrical objects can be precisely determined. The altered flow patterns in the upstream region surrounding the cylinders are studied along with a study of skewed turbulent boundary layer. In addition, detailed measurements of the bed shear stress around the cylinders are also presented. The principal motivation for this study is to improve our understanding of the flows around simple fish habitat structures.

1.2 Fish Habitat Structures

In the last few decades, there has been an increasing awareness and concern regarding human impact on stream and riverine ecosystems (Bockelmann et al. 2004). This increasing awareness about the value of natural ecosystems has resulted in a movement toward manipulation and control of river restoration and conservation. Natural habitats of instream fish species are often destroyed by the altered flow patterns caused by upstream hydraulic structures (Shamloo et al. 2001). Provision for fish habitat structures for the downstream shallow flows is therefore, an integral part of major hydraulic structure projects. There are a variety of fish habitat structures in use; such as groins, V-weirs, pools, single rock or cluster of rocks. However, in the absence of reliable knowledge regarding the hydraulics, local structures for habitat improvement are currently designed on the basis of engineering judgment. Alberta Environmental Protection published guideline sketches for fish habitat enhancement design (Lowe 1992). These typical sketches can only provide a rough idea about the size, shape and other construction features of the habitat structures in use.

Ecological studies (e.g. Bockelmann et al. 2004, Kemp et al. 2000) revealed that different in-stream species can tolerate different ranges of flow velocities, water depths, bed substrates and water quality properties. Secondary currents, turbulence and variation in local velocity and water depth are essential habitat conditions for both the diversity of river benthos and fishes (Bockelmann et al. 2004). Statzner and Higler (1986) and Kemp et al. (2000) found that stream hydraulics is the most important determinant of the in-stream habitat quality. Lamouroux et al. (1992) found that the shear stress prevailing at the channel bed is of major importance for erosion of bed material, and thus channel form and the presence of organisms. Therefore, they claimed that the local stream bed shear stress provides the link for collaboration between the hydraulic engineers and the ecologists. Ecological studies (e.g. Maddock 1999, Bockelmann et al. 2004) have shown the demand for hydraulic structures that create morphological features and encourage a physical environment, which is enriched by longitudinal and lateral variations in water depth, velocity, turbulence and bed shear stress. Natural rocks offer a simple solution to provide shelter and food for fish in adverse flow situations by creating an altered flow pattern, nutrient accumulation and biological activity in the wake region. Therefore, the study of hydraulics of the flow around rock-like obstacles in open channel would provide quantitative knowledge for the design of fish habitat structures.

1.3 Literature Review

A shallow wake is defined as the situation where the horizontal length scale of a typical eddy is significant compared to the vertical scale or, the depth of flow (Balachandar et al. 2000). Flow past a vertical cylinder in shallow water gives rise to a wake that has distinctive characteristics compared to a deep wake (Akilli and Rockwell 2002). It is well known that in a deep uniform flow incident on a two-dimensional (2D) cylinder with its axis vertical, vortex shedding occurs with strong three-dimensional (3D) components

(Lloyd and Stansby 1997a). In the case of shallow wakes, the incident velocity has boundary layer profile. Ingram and Chu (1987) observed that bed friction effects become important in shallow wakes. Chen and Jirka (1995) urged that an improved understanding of the shallow wakes is needed for a number of reasons, such as the tendency for pollutant trapping in the lee of islands or headlands, the optimal siting of discharge facilities, patterns of sedimentation, and nutrient accumulation and biological activity for the species of aquatic environment (e.g. fish habitat).

Study of shallow wakes has received considerable attention in recent years (e.g. Chen and Jirka 1995, Lloyd and Stansby 1997a and 1997b). However, only a few studies have been conducted on flows around submerged bluff bodies. Shamloo (1997) was one of the first to conduct an experimental study on the hydraulics of fish habitat structures, which was published later by Shamloo et al. (2001). He studied the mean flow field around hemispherical habitat structures. After a series of flow visualization tests he proposed four flow regimes for habitat structures based on the relative submergence i.e. the ratio of flow depth to object height. Flows around deeply submerged, moderately submerged and slightly submerged objects were studied in addition to one, where the object height was greater than the flow depth. Shamloo (1997) also studied bed shear stress and the scour pattern around a single hemispherical habitat structure. The scour patterns obtained for different submergence levels also indicated the distinctions between the proposed flow regimes. Concurrently, Albers (1997) studied the behavior of a cluster of hemispheres modeled as a habitat structure. He experimentally determined the relative spacing at which the cluster behaves like a single hemisphere. Recently, Burrows and Steffler (2005) examined the depth-averaged velocities around individual boulders in a numerical study. In another numerical study, Smith and Foster (2007) studied the wake created by short submerged horizontal cylinders as a model of submerged pipelines in rivers. They evaluated the time-dependant bed shear stress and used the mean and peak Shields parameters to highlight the processes relevant to scour. Chen and Jirka (1995) classified the instabilities observed in the near-wake region of shallow flows around a surface piercing cylinder. They held the depth constant and used different diameters of the cylinders to investigate wake instability. Lloyd and Stansby (1997a, 1997b) carried out extensive experimental and numerical investigations on instabilities in shallow wakes behind surface piercing and submerged conical model islands with gentle slopes. Rajaratnam and Rai (1979) proposed a two-layer model for two-dimensional wall wake similarity in the far wake region. They found that the simple wake equation given by Schlichting (1968) can describe the velocity distribution in the outer region, whereas in the inner region the Prandtl-Karman's law-of-wall equations perform satisfactorily. Tachie and Balachandar (2001) proposed slightly modified length scale compared to the one used for wake equation given by Schlichting (1968) for similarity of velocity profiles across the wake in the near-wake region of surface piercing cylinder. In a geophysical study, Ingram and Chu (1987) observed the effect of bottom friction on the wake behind islands in Rupert bay in northern Canada. Arya and Gadiyaram (1986) studied the atmospheric flow and dispersion in the wakes downstream of three-dimensional models of low hills. Pingree and Maddock (1979) studied the general flow field and sediment processes around sand mounds and tidal banks including the dynamics of their own formation and erosion.

In addition to these studies of wakes, different flow elements around bluff bodies have been investigated as a part of fundamental studies of fluid mechanics; but mostly in deep flow situations. For example, the approach flow upstream of a cylinder has been studied in order to elucidate the nature of flow around bridge piers and its relation to local scour (e.g., Ahmed and Rajaratnam 1998, Dey and Raikar 2007). Baker (1979, 1980) studied the system of horse-shoe vortices developed in laminar and turbulent boundary layers around submerged cylinders in wind and smoke tunnels. Ahmed and Rajaratnam (1997) studied the skewed three-dimensional turbulent boundary layer (3DTBL), where both the magnitude and direction of the velocity vectors change with the distance from the bed under the influence of a lateral pressure gradient, around bridge pier-like cylinders in open channels.

Menna and Pierce (1988) claimed that there is a severe shortage of comprehensive experimental data of turbulent and complex flows around bluff bodies that can serve for an unbiased test of the predictive capabilities of computational models. Moreover, there are only a few recent studies on flow around submerged models (e.g., Shamloo et al. 2001, Lloyd and Stansby 1997b) in open channel flows that can be used in computational modeling. In these circumstances, the scope and demand for the study of flow around cylinders modeled as simple fish habitat structure can be considered to be enormous.

1.4 Scope and Objectives of the Study

A systematic approach has been adopted to study the structure of flows around bed-mounted cylinders in open channels. The mean and turbulence properties of the undisturbed approach flow were studied first so that the flow disturbances caused by the cylinders on smooth and rough beds can be determined. The flow structures around the cylinders have been studied for similar flow conditions on smooth and rough beds. The objectives of the study can be listed as follows:

1. Experimental investigation of the undisturbed flow.
2. Flow visualization study around the cylinders.
3. Measurements of bed shear stress around the cylinders.
4. Analysis of the flow field around the cylinders in terms of the theories of three-dimensional turbulent boundary layers.
5. Investigation of the changes in the flow structure on the upstream plane of symmetry, and the region surrounding the cylinders.
6. Investigation of the turbulent flow structure in the downstream plane of symmetry.
7. Study of the decay of turbulence and velocity defect in the cylinder wakes.
8. Application of the wake similarity concept for both mean and turbulent flow structures.

1.5 Organization of the Thesis

This thesis presents the results of an experimental study of the turbulent flow structure around bed-mounted cylinders in open channels. Following is a brief introduction to each chapter.

In chapter 2, the experimental setup and procedures are explained. The open channel flume system and the instrumentation are described in detail. The design of experiments, data acquisition and processing procedures are described. Finally, the results of data quality investigations are also provided in this chapter.

Results of experimental investigation on the mean and turbulent flow structures of the undisturbed approach flow are presented in chapter 3. The differences between the 3D flow structure in a narrow open channel and the 2D flow structure in wide channels are described.

The results of 3D boundary layer analyses are presented in chapter 4. This chapter also presents the flow visualization test results and direct measurements of bed shear stress.

Turbulent flow structures in the upstream region surrounding the cylinders are presented in chapter 4. 3D turbulent velocity measurements at upstream stations close to the cylinders, and on the transverse plane at the shoulder of the cylinders are presented in this chapter. This chapter also presents the changes in the flow structure on the upstream plane of symmetry.

Results of experimental investigation on shallow turbulent near-wakes are presented in chapter 6. The turbulent flow field on the downstream plane of symmetry is presented in this chapter. The rates of decay of increased turbulence and velocity defect; wall wake similarity analysis for moderate to deeply submerged cylinders; and wake similarity analysis in the transverse direction for cylinders of different submergence levels are also presented in this chapter.

Finally, the conclusions of the entire study are summarized in chapter 7. Recommendations for future studies are also presented in this chapter.

1.6 References

Ahmed, F., and Rajaratnam, N. (1997). "The three-dimensional turbulent boundary layer flow around bridge piers." *Journal of Hydraulic Research*, 35(2), 209-224.

Ahmed, F., and Rajaratnam, N. (1998). "Flow around bridge piers." *Journal of Hydraulic Engineering*, 124(3), 288-300.

Akilli, H., and Rockwell, D. (2002). "Vortex formation from a cylinder in shallow water." *Physics of Fluids*, 14(9), 2957-2967.

Albers, C. D. (1997). *Hydraulics of a three obstacle cluster in open channels*, M. Sc. thesis, University of Alberta, Edmonton, AB, Canada.

Arya, S. P. S. and Gadiyaram, P. S. (1986). "An experimental study of flow and dispersion in the wakes of three-dimensional low hills." *Atmospheric Environment*, 20(4), 729-740.

Baker, C. J. (1979). "The laminar horseshoe vortex." *Journal of Fluid Mechanics*, 95, 347-367.

Baker, C. J. (1980). "The turbulent horseshoe vortex." *Journal of Wind Engineering and Industrial Aerodynamics*, 6, 9-23.

Balachandar, R., Ramachandran, S., and Tachie, M. F. (2000). "Characteristics of shallow turbulent near wakes at low Reynolds numbers." *Journal of Fluids Engineering*, 122, 302-308.

Bockelmann, B. N., Fenrich, E. K., Lin, B. and Falconer, R. A. (2004). "Development of an ecohydraulics model for stream and river restoration." *Ecological Engineering*, 22, 227-235.

Burrows, A. D. and Steffler, P. M. (2005). "Depth averaged modeling of flow around individual boulders." *Proc., 17th Canadian Hydrotechnical Conf.*, CSCE, Edmonton, Alberta, 395-404.

Chen, D., and Jirka, G. H. (1995). "Experimental study of plane turbulent wakes in a shallow water layer." *Fluid Dynamics Research*, 16, 11-41.

Dey, S., and Raikar, R. V. (2007). "Characteristics of horseshoe vortex in developing scour holes at piers." *Journal of Hydraulic Engineering*, 133(4), 399-413.

Ingram, R. G., and Chu, V. H. (1987). "Flow around islands in Rupert bay: An investigation of the bottom friction effect." *Journal of Geophysical Research*, 92(C13), 14521-14533.

Kemp, J. L., Harper, D. M., and Crosa, D. A. (2000). "The habitat-scale ecohydraulics of rivers." *Ecological Engineering*, 16, 17-29.

Lamouroux, N., Statzner, B., Fuchs, U., Kohmann, F., and Schmedtje, U. (1992). "An unconventional approach to modeling spatial and temporal variability of local shear stress in stream segments." *Water Resources Research*, 28(12), 3251-3258.

Lloyd, P. M., and Stansby, P. K. (1997a). "Shallow-water flow around model conical islands of small side slope. I: Surface piercing." *Journal of Hydraulic Engineering*, 123(12), 1057-1067.

Lloyd, P. M., and Stansby, P. K. (1997b). "Shallow-water flow around model conical islands of small side slope. II: Submerged." *Journal of Hydraulic Engineering*, 123(12), 1068-1077.

Lowe, S. (1992). *Fish habitat enhancement designs*, Alberta Environmental Protection, Water Resources Management Services, Technical Services and Monitoring Division, River Engineering Branch, Alberta, Canada.

Maddock, I. (1999). "The importance of physical habitat assessment for evaluating river health." *Freshwater Biology*, 41, 373-391.

Menna, J. D., and Pierce, F. J. (1988). "The mean flow structure around and within a turbulent junction or horseshoe vortex-Part I: The upstream and surrounding three-dimensional boundary layer." *Journal of Fluids Engineering*, 110, 406-414.

Pingree, R. D., and Maddock, L. (1979). "The tidal physics of headland flows and offshore tidal bank formation." *Marine Geology*, 32, 269-289.

Rajaratnam, N., and Rai, S. P. (1979). "Plane turbulent wall wakes." *Journal of the Engineering Mechanics Division*, 105(EM5), 779-794.

Schlichting, H. (1968). *Boundary-layer theory*, 6th Edition, McGraw-Hill Book Company, NY, USA.

Shamloo, H. (1997). *Hydraulics of simple habitat structures*, Ph. D. thesis, University of Alberta, Edmonton, AB, Canada.

Shamloo, H., Rajaratnam, N., and Katopodis, C. (2001). "Hydraulics of simple habitat structures." *Journal of Hydraulic Research*, 39(4), 351-366.

Smith, H. D., and Foster, D. L. (2007). "Three-dimensional flow around a bottom-mounted short cylinder." *Journal of Hydraulic Engineering*, 133(5), 534-544.

Statzner, B. and Higler, B. (1986). "Stream hydraulics as a major determinant of benthic invertebrate zonation patterns." *Freshwater Biology*, 16, 127-139.

Tachie, M. F., and Balachandar, R. (2001). "Shallow wakes generated on smooth and rough surfaces." *Experiments in Fluids*, 30, 467-474.

Chapter 2: Experimental Setup and Procedures

2.1 Open Channel Flume

Experiments were conducted in Ellerslie River Engineering Laboratory in Edmonton, Alberta. A schematic diagram showing the experimental setup is presented in Figure 2.1. The coordinate system considered for the experiments is also shown in Figure 2.1. The direction of flow defines the positive *x*-axis, while *y* and *z* axes are in the transverse and vertical directions respectively according to the right-hand rule. The channel system has a straight, rectangular, horizontal flume, 18 m long, 1.22 m wide (B) and 0.65 m deep. A 0.2 m high smooth painted plywood false bed was installed above the original aluminum bed. The recirculating flume has a pump (maximum discharge of 105 L/s) that draws water from a 2 m deep underground sump. The pump delivers water to a head tank (2.44 m long and 1.8 m wide) through a circular polyvinyl chloride (PVC) pipe of 25.4 cm diameter. The PVC pipe enters the head tank vertically from top and releases water from a horizontal diffuser. The diffuser is an end-capped PVC pipe with holes around the surface. The holes on the horizontal diffuser were kept relatively large and closely spaced at the far end compared to the near end of the outlet so that water can be released uniformly throughout the outlet. In addition, a vertical screen was placed inside the head tank to damp the turbulence and straighten the flow. The water then flowed over the false bed through a gradual converging section followed by a ramp. The water depth was controlled by a hinged tail gate located at the downstream end of the aluminum bed of the flume. For the rough bed experiments, coarse-uniform 8/12 sand (D_{50}=2.68 mm) was carefully glued on the plywood surface using a thin coating of paint, so that a densely packed sand layer with a thickness of a single grain was achieved. The grain size distributions are presented in Figure 2.2.

A Foxboro electromagnetic flow meter (Model No. 2800) was attached to the PVC pipe that delivers water inside the head tank. The flow meter was calibrated for accurate measurements of discharge. A digital voltmeter connected to the electromagnetic flow meter through a transmitter (Model No. E96R-VA) enables to read the discharge in the unit of electric voltage (volt).

A 2D motorized traverse from Velmex Inc. (Unislide traverse, Model No. B4015W1J, Serial No. 786) was used to position the yaw probe and Acoustic Doppler Velocimeter (ADV) probe for point measurements. This traverse was attached to a three-wheeled carriage that runs on rails. In order to position a probe at a measuring point (x, y, z) the carriage was moved in the x-direction and the traverse was moved in the spanwise and vertical directions. The accuracy of positioning a probe at a measuring point was approximately 1 mm. A photograph showing the traverse system with the ADV mounted over a rough bed is presented in Figure 2.3.

A vertical point gauge, mounted on the carriage was used for water depth measurement. Precise measurement of water depth was enabled by the attached Vernier scale of 0.1 mm accuracy. For smooth bed experiments the datum for water depth (H) and elevation (z) of any point measurement was the smooth surface of plywood. However, for rough bed experiments the datum was adjusted to $0.2D_{50}$ below the top of the sand grains based on earlier studies (Einstein and El-Samni 1949, and Hollingshead 1972).

At the beginning of any experiment the sump and the head tank were filled with water from an external source. Then the pump was used to supply water towards the channel. Once the flow was established the water depth and the discharge was controlled to achieve the desired flow conditions.

2.2 Yaw Probe

A thin yaw-type Preston probe was used for two-dimensional mean velocity and bed shear stress (τ_0) measurements. A photograph showing the yaw probe mounted on the traverse for rough bed measurements is presented in Figure 2.4. The yaw probe has three tubes of 1.2 mm external diameter. The nose of the probe was milled so that the face of the central tube is perfectly flat and the side tubes are chamfered at an angle of 45°. The total head differences between the central tube and each of the side tubes were measured. Thus the probe can measure the 2D velocity at a point. If the probe is placed on the bed it can measure bed shear stress. A detail description of the configuration and calibration of this yaw-type Preston probe are available in Rajaratnam and Muralidhar (1968). For the purpose of data acquisition the probe was connected to two differential pressure transducers (Validyne Engineering Corp., Model No. DP45) by plastic tubing. For real-time data observation a battery operated digital transducer indicator (Validyne Engineering Corp., Model No. CD379) was used.

For yaw probe measurements, the probe was carefully mounted on the traverse system. The probe was leveled and aligned through careful visual observation using a bubble level and a 2 m long string stretched along the channel center [see Fig. 2.4]. Before any measurement the pressure transducers were calibrated as 1 inch pressure difference equivalent to 1 volt at the beginning of any measurement. However, calibrations were repeated at regular intervals (approximately every 2-3 hours) during long hours of measurement. The accuracy of the calibration was of the order of 0.001 volt.

Figure 2.5 shows a photograph of the entire setup for yaw probe measurement. There was a digital data acquisition system for the yaw-type Preston probe. Pressure transducers connected to the yaw-type Preston probe transfer analog data to an analog to digital converter (AD board). The computer was equipped for digital recording by a Lab-view data acquisition card (National Instruments, Model No. AT-MIO-16XE-50). A Lab-view program allowed continuous data recording at high frequency.

2.3 Acoustic Doppler Velocimeter (ADV)

A 10 MHz 3D down looking flexible head ADV probe (Model No. 1349) from SonTek Inc. was used for velocity measurements. ADV is a sensor system based on Acoustic Doppler principle and suitable for high resolution measurements of three-dimensional velocities at a rate of 25 Hz. It is a semi-intrusive velocity measuring device that sends sound pulse from the transmitting probe and receives its reflection from the seeding material in water by three receiving probes. The transmitting probe transmits pulses downward along the vertical axis, while the receiving probes are positioned around the transmitting probe slanted at an angle of 30° from the vertical transmitting axis. The receivers are rotated at 120° relative azimuth angles and are focused on a sampling volume located 5 cm below the transmitter (SonTek 1997a). Therefore, the down looking

3D ADV probe cannot be used to make measurements closer than 5 cm from the free surface. Moreover, the whole assembly of the probes with a transmitter and three receivers need to be immersed in water. Thus near-surface velocity measurements are restricted to approximately 7 cm below the free water surface. Using the correlations between the transmitting and receiving signals and probe geometry ADV can compute the Doppler shift from the segments of echo. The echo is Doppler shifted in proportion to the seeding particle velocity. Thus ADV can measure three-dimensional velocity at the center of sampling volume. ADV does not need repeated calibration as it is calibrated only once by the manufacturer. Figure 2.6 shows a photograph of the ADV probe mounted for smooth bed measurements. Details about the configuration, working principles and operation of ADV probe are available in ADV operation manual (SonTek 1997a) and ADV principles of operation (SonTek 2001) published by SonTek Inc.

For ADV measurements, the probe was carefully mounted on the traverse system. The probe was leveled and aligned through careful visual observation using a bubble level and a 2 m long string stretched along the channel center as shown in the photograph presented in Figure 2.7.

For good scattering of sound pulse SonTek recommends for using seeding materials in the flowing water. Particles that have a density close to that of water and a mean diameter of 10-20 μm are recommended to use in a concentration of 10-50 mg/L (SonTek 1997a). For the present study adequate fine spherical hollow glass particles (mean diameter of 11 μm; density of 1,100 kg/m^3, Potters Industries, Valley Forge, PA) were added in the flowing water and allowed to mix thoroughly before any measurement.

ADV data were recorded in digital mode in a computer equipped with an ADV card supplied by SonTek for the 10 MHz ADV. The experimental conditions (e.g. water temperature, salinity) and total number of samples according to sampling duration (T) and frequency in burst mode were entered manually in an ADV execution file while recording. For this purpose water temperature was measured by a digital thermometer at regular intervals (at every 15 minutes) during ADV measurements.

2.4 Design of Experiments

2.4.1 *The flow regimes*

In order to satisfy the principal focus of the research objectives the present study adopts the flow regime definitions given by Shamloo et al. (2001). The flow regimes are illustrated in Figure 2.8. Shamloo et al. (2001) tried many different levels of submergence while studying the mean flow hydraulics in the wake around hemispherical habitat structures in shallow flows. They observed some distinct differences in the flow as well as in the scour patterns for certain ranges of submergence ratio. Thus Shamloo et al. (2001) proposed a set of flow regimes as shown in Figure 2.8. Similar regime definitions were also used by Albers (1997) and Burrows and Steffler (2005) for studies related to fish habitat structures.

2.4.2 *Selection of flow and object dimensions*

Several limitations of the available experimental facilities were considered when setting the experimental flow conditions. A channel aspect ratio (B/H) of at least 10 is required for a wide channel consideration (Nezu and Nakagawa 1993). Therefore, for the available channel width (B=122 cm) the water depth should not exceed 12 cm. However, a considerable water depth (say, at least 10 cm below the sampling volume) is required for an ideal experimental condition while using ADV (SonTek 1997b). In order to facilitate for measuring velocity profile over a major portion (up to $z \approx 0.7H$) of the water depth, H=22 cm is required. This results in a channel aspect ratio of 5.5; but for the physical limitations of ADV, a 22 cm water depth was accepted for the present study.

The experiments should be carried out with a discharge that can produce a turbulent subcritical flow commonly observed in natural streams. Therefore, a discharge of 50 L/s with 22 cm water depth (H) was chosen. This flow produced a cross-sectional mean velocity, U_0=18.63 cm/s for which the Reynolds number ($R_H \equiv U_0 H/\nu$) was 40,000 and the Froude number ($F \equiv U_0/(gH)^{0.5}$) was 0.13. The experimental flow conditions are summarized in Table 2.1.

The object heights (*h*) were determined to be 5.5, 12, 20 and 30 cm for Regime-1, 2, 3 and 4 respectively on the basis of submergence ratio (*h*/*H*). Ideally when studying flow around an object the width of the object should not be greater than 10% of the total channel width (*B*=122 cm) to avoid the influence of the side wall. Hemispherical object was a primary choice as it was used in the previous studies (e.g. Shamloo et al. 2001) of fish habitat structures. However, for the present study hemispherical objects would obstruct the flow as high as half of the total width. The possible 3D objects are, therefore, a cylinder or a cone. For the present study, cylindrical objects of four heights with equal diameter (*D*=11.4 cm) were selected for the convenience of construction. This object diameter satisfied the physical limit regarding flow obstruction, as $D/B<0.1$. In addition, this object size ensured the development of shallow wake, as the water depth (*H*) was not very large ($H/D{\sim}2<10$) compared to the size of the wake generator (*D*) (Chen and Jirka 1995). Hollow PVC cylinders with caps fitting smoothly on top were mounted on 25 mm thick discs screwed to the false bed. In order to produce a symmetric flow, the cylinders were located along the centerline of the channel cross-section. To allow for flow development the cylinders were placed at a distance of 8.5 m downstream from the head tank.

2.4.3 *Selection of sampling time and frequency*

ADV data were sampled at the highest possible frequency of 25 Hz for the 10 MHz ADV probe. The sampling frequency was chosen to be 250 Hz for the yaw-type Preston probe. For the purpose of selection of an adequate sampling duration for ADV and yaw-type Preston probe several measurements were repeated at the same point for similar flow conditions with different sampling durations. Mean estimates of the bed shear stress and the two-dimensional velocity obtained from the yaw-type Preston probe were compared to observe the consistency of measurements. Thus an acceptable sampling duration was selected. Similarly, repeated ADV measurements at many different points were compared for mean and turbulent velocity estimates, along with frequency spectra. These comparisons indicate that a 2 minutes sampling duration is adequate for mean estimates of velocity and shear stress obtained from yaw probe. For the ADV a minimum duration of 2-3 minutes is required to capture the highly turbulent 3D velocity field around the cylinders.

Figure 2.9(a-f) present the results of mean and turbulent velocity estimates obtained from ADV using different sampling durations ranging from 1-10 minutes. It can be observed that the results of 1 minute sampling duration are often away from the other results in a profile. This indicates that 1 minute sampling duration is inadequate, and hence a minimum sampling duration of 2 minutes is required for ADV measurements. However, a sampling duration of 3 minutes was chosen for the ADV measurements close to the cylinders on the downstream plane of symmetry, as the turbulence was very high in this region.

2.5 Data Processing Procedure

There were three kinds of data gathered in the present study; a) bed shear stress, b) 2D velocity data measured by the yaw probe, and c) 3D velocity data measured by the ADV. The detailed procedures used to process this data are described in the following sections. The data processing programs are provided in the attached diskette.

2.5.1 *Yaw probe data*

Shear stress and 2D velocity data were recorded as two sets of pressure differences. Shear stress data were processed by Matlab programs named 'Smooth Shear.m' and 'Rough Shear.m' for smooth and rough bed conditions respectively. These programs first convert the unit of measurements according to the calibration factor. Then following the yaw probe calibration given by Rajaratnam and Muralidhar (1968) yaw angle (θ) of the mean bed shear stress are computed. The yaw angles are taken positive if the stress vector points outward or away from the cylinder. Subsequently the mean bed shear stress magnitudes (τ_0) are determined using the calibration curves provided by Patel (1965) and Hollingshead and Rajaratnam (1980) for smooth and rough bed conditions respectively. 2D velocity data were processed by a Matlab program named 'Yaw Velocity.m'. This program first converts the unit of measurements according to the calibration factor, and then using the yaw probe calibration relationships given by Rajaratnam and Muralidhar

(1968) yaw angle (θ) and the magnitude of mean velocity are determined. Thus two mean velocity components (*U* and *V*) are obtained.

2.5.2 *ADV data*

3D velocity data sampled at 25 Hz were recorded in three different time series for duration of 2-3 minutes. WinADV32-Version 1.83, public domain software developed for ADV data processing by the USBR (Wahl 2000), was used to convert the raw ADV data recorded in binary format to ASCII format.

These data were then further processed to eliminate noise (spikes) and poor signal. Usually higher scores of signal to noise ratio (SNR) and correlation (COR) between the transmitting and receiving signal indicate reliable measurements. SonTek recommends that the SNR and COR should be greater than 15 and 70, respectively, for reliable turbulence measurements (SonTek 2001). However, such thresholds can be considered suitable for favorable flow conditions (e.g. approximately 10 cm away from the bed, relatively less turbulent flow), because bed interference and flow turbulence may affect the SNR and COR (Wahl 2000, SonTek 2001). Therefore, the thresholds of SNR and COR for obtaining reliable measurements in this study were determined by a systematic study with trial combinations of SNR and COR. At first ADV stations were grouped on the basis of percentage of good data that satisfy the recommended thresholds (i.e. SNR≥15 and COR≥70). Then a set of samples from each group were filtered with a different combination of SNR and COR thresholds (e.g. SNR≥10 and COR≥60) and the percentage of data that satisfy these thresholds were noted. This filtered data set was used for computing mean and turbulent velocities. The results were compared with the same obtained from the data filtered with recommended thresholds. The probability density functions were also compared to see if the data filtered with a combination of SNR and COR thresholds (e.g. SNR≥10 and COR≥60) form a cluster of similar kinds with the data filtered with recommended thresholds. The combination of SNR and COR that was found to produce satisfactory results in the comparisons of mean and turbulent velocity estimates, and probability density functions for all the ADV data was chosen for data filtering procedure in the present study. It was found from the trial observations that SNR and COR scores of 10 and 60 can serve as satisfactory filtering thresholds. If any instantaneous signal of any of the three components of velocity fails to satisfy either of these thresholds that velocity data point was eliminated from the time series without any replacement. In addition to SNR and COR thresholds, the despiking method (Phase-Space Thresholding Method) proposed by Goring and Nikora (2002) was adopted to eliminate poor signals. The concepts of despiking method are: (1) differentiation enhances the high frequency portion of a signal, (2) expected maximum of a random series is given by the Universal threshold, and (3) good data cluster in a dense cloud in phase space or Poincaré maps. Using these three concepts a three-dimensional ellipsoid was constructed in phase space and points lying outside the ellipsoid were considered as spikes, and hence eliminated without any replacement.

Once the ADV data of undisturbed flow and flow in the upstream region surrounding the cylinders were filtered to eliminate spikes (by Phase-Space Thresholding Method) and poor signal (with $\mathrm{SNR}\geq 10$ and $\mathrm{COR}\geq 60$ thresholds), mean and turbulence properties (time-averaged and root mean square velocities, turbulent kinetic energy and Reynolds shear stresses) are computed. A Matlab program named 'Filter ADV.m' was used for these processing.

Usually an instantaneous velocity at any time t can be expressed as, $u(t)=U+u'(t)$ where U is the mean velocity and u' is the fluctuating velocity. Downstream of the cylinders the velocity data captured periodic signals due to the physical process of vortex shedding. Therefore, downstream velocity data can be considered to possess three components of velocity in each direction; namely a mean component (U, V and W), a periodic fluctuation or coherent component ($\widetilde{u}$, $\widetilde{v}$ and $\widetilde{w}$) and a random fluctuation or pure turbulence (u', v' and w'). Thus an instantaneous velocity at any time t can be expressed as, $u(\mathrm{t})=U+\widetilde{u}(t)+u'(t)$. In order to avoid ambiguity with downstream periodic data in despiking procedure (e.g. a minor fluctuation may appear as spike if it occurs at the crest/trough of the periodic signal), raw ADV data needs to be first processed by a high-pass filter. The selection of high-pass cut-off frequency (f_c) is explained below.

Velocity data with nearly periodic nature due to shedding vortices allow the definition of phase and the calculation of phase averaged quantities. For such instances, the phase averaging procedure introduced by Reynolds and Hussain (1972) was adopted by many researchers (e.g. Perrin et al. 2006) in cylinder wake studies. However, for the present study periodic vortex shedding was observed only in Regime-3 and Regime-4 (see Chapter 4). A closed recirculating 3D wake was observed in Regime-1 and Regime-2 (see Chapter 4), where the periodic nature is absent in the velocity data. Moreover, in addition to the primary vortex shedding frequency a second significant frequency consistently appeared in the auto-spectral density functions of the transverse velocity component (G_{vv}) in Regime-3 and Regime-4. In these circumstances the phase averaging technique of Reynolds and Hussain (1972) is inappropriate. To facilitate comparison of the results from different regimes, application of the same data processing algorithm to all flow regimes was considered essential. A typical auto-spectral density functions of transverse velocity component (G_{vv}) is shown in Figure 2.10. It can be observed from the figure that there are two peaks approximately at 0.4 Hz and 1.2 Hz. The spectral distribution for the second peak spreads up to 1.5 Hz, and above that no significant frequency can be noticed in the higher frequency region. Similarly the spectral functions (auto-spectral density functions, cross-spectral density functions and coherence functions) were examined at different measuring points at randomly chosen downstream stations of all the flow regimes on smooth and rough beds. It was found from these observations that no significant frequency exists in spectral distributions above 1.5 Hz. Therefore, all signals below 1.5 Hz are considered to be resulting from large-scale motions, and all signals above 1.5 Hz are considered to be turbulence. Thus a single cut-off frequency (f_c=1.5 Hz) was determined to separate the large scale motions from pure turbulence for all flow regimes.

Once the downstream ADV data were processed by a high-pass filter with a cut-off frequency (f_c) of 1.5 Hz, the high-pass filtered data were further processed using SNR and COR thresholds of 10 and 60 respectively, as explained previously. These data were then finally processed using the despiking algorithm (as explained previously) prior to computing turbulence estimates (root mean square velocities, turbulent kinetic energy and Reynolds shear stresses). All these processing of ADV data for the downstream region were accomplished by a Matlab program named 'Wake ADV.m'.

A typical set of velocity time series are presented in Figure 2.11 to 2.15. Figure 2.11 shows the raw ADV data in the downstream region of a cylinder for a sampling period of 20 seconds (i.e. 500 samples at 25 Hz). Figure 2.12 shows the high-pass filtered data of the same record as presented in Figure 2.11. Similarly Figure 2.13 shows the low-frequency (f<1.5 Hz) data corresponding to large-scale motions. The processed (using SNR and COR thresholds and despiking algorithm) data obtained from high-pass filtered series (as presented in Fig. 2.12) is shown in Figure 2.14. The final processed ADV data of the same record as shown in Figure 2.11 is presented in Figure 2.15. It can be noticed from Figure 2.14 and 2.15 that the processing removed three samples, approximately at sample number 50, 120 and 180. These processed data are then used for the computation of mean and turbulence properties (time-averaged and root mean square velocities, turbulent kinetic energy and Reynolds shear stresses). However, for spectral analysis, such as auto spectral density function, cross-spectral density function or coherence function computations the unfiltered data are used to avoid discontinuities in the time series.

2.6 Data Quality Investigation

2.6.1 *Repeatability and uncertainty of measurements*

Repeatability and uncertainty of each experimental measurement (velocity and shear stress) were investigated by comparison of repeated measurements made at 12-15 different times at the same measuring point/station for similar flow conditions. Every measurement made for this investigation was collected on a different day after resuming the experiments so that the bias and random error of the experimental setup and procedure could be detected. For velocity measurements repeatability and uncertainty have been investigated at three different elevations to explore the influence of the distance from the bed on the measurements.

Table 2.2 shows the repeatability of bed shear stress measured using yaw-type Preston probe in 15 different occasions. The standard deviation of the bed shear stress measurements was found to be 0.036 N/m^2 in magnitude and 2.6° in yaw angle. These repeated measurements were conducted on rough bed. Minor irregularities on the channel bed have been found to affect the bed shear stress measurements by yaw-type Preston probe, as the probe itself is very thin (only 1.2 mm). The mean size of the sand grain (D_{50}) is 2.68 mm. Therefore, relatively large uncertainties are involved in the measurements of rough bed shear stress.

Table 2.3 shows the repeatability of 2D velocity measured using yaw probe at three different elevations in 15 different occasions. The standard deviation of mean velocity magnitude was 0.96 cm/s, 1.02 cm/s and 1.05 cm/s at three different elevations (z=20.35 cm, 6.94 cm and 0.11 cm) above the bed. The respective standard deviations in yaw angle were 0.6993°, 1.3562° and 2.5759°. These results show that the uncertainties in near-bed measurements are relatively greater than the measurements away from the bed.

Repeatability of the ADV measurements is presented in Table 2.4(a-c) using 12 sets of data sampled at three elevations (z=15 cm, 7.5 cm and 0.5 cm). These results indicate that the reliability of ADV measurements is excellent, as the standard deviations of mean and turbulent estimates are minor.

In order to investigate further on the repeatability of ADV measurements close to the cylinders and especially in the wake the measurements were repeated at three stations for entire profile (i.e. 15 point measurement at each station) in Regime-3 on rough bed. Figure 2.16(a-f) to 2.18(a-f) show the results of repeated measurements at 1) x=-2D, y=0; 2) x=0, y=2.2D; and 3) x=+2D, y=0. At station x=-2D, y=0 the transverse and vertical mean velocities are expected to be very small. Therefore, the variations of the profiles obtained from two different data sets agree well in Figure 2.16(a-f). At station x=0, y=2.2D the transverse mean velocities are expected to have positive values showing deflection away from the cylinder. The variations observed in the profiles of transverse velocities in Figure 2.17(b) are minor when considered with respect to the corresponding longitudinal velocities. A variation of 1 cm/s in the transverse direction with respect to 20 cm/s longitudinal velocity indicates an error of ADV probe alignment of only 2.8°. Therefore, the variations of the profiles obtained from two different data sets agree well in Figure 2.17(a-f). At station x=+2D, y=0 in Regime-3 on rough bed the flow is extremely turbulent, as the station is located at the end of the recirculation wake-bubble. Figure 2.18(a) shows that the mean velocities in the longitudinal direction do not produce a smooth profile (even when sampled for 10 minute duration, as shown by the second data set). However, if we consider a mean profile through these data, the deviation of each data point is no more than 1 cm/s. The transverse mean velocities are expected to be zero at station x=+2D, y=0. The variations observed in the profiles of transverse velocities in Figure 2.18(b) can be considered minor, as they vary in a range of ±0.8 cm/s. Therefore, the variations of the profiles obtained from two different data sets agree well in Figure 2.18(a-f).

Several auto-spectral density functions at different elevations of the same stations were also plotted with 95% confidence band based on first set of measurement. Two typical set of auto-spectral density functions at z=13 cm and z=0.5 cm elevations for the station at x=+2D, y=0 in Regime-3 on rough bed are presented in Figure 2.19 and 2.20. It can be noticed from these spectral distributions that the spectral distributions are similar for two sets of data. These results further establish the reliability of ADV measurements of the present study.

Lastly, mean velocity profiles (i.e. U and V) measured using the ADV and the yaw probe at five different stations around the cylinder on a smooth bed were compared. Two typical comparisons at 1) x=+3D, y=1D; and 2) x=+3D, y=0.5D in Regime-2 are shown in Figure 2.21(a-d). These comparisons show that the mean velocities measured using the ADV and the yaw probe agree very well.

2.6.2 *Sources of error*

In spite of minor uncertainty in measurements for most cases, a few measurements were found to be affected by some unavoidable circumstances; e.g. an unusually large sand grain in front of or below the yaw probe or, coincident receiving signals from the sampling volume and the bed reflection in ADV. Minor irregularities on the channel bed have been found to affect the bed shear stress measurements by yaw-type Preston probe, as the probe itself is very thin (only 1.2 mm). Care has been taken during measurements so that any unwanted irregularity can be avoided. During ADV measurements adequate seeding materials were mixed in the flowing water for better reflection from the sampling volume. However, it is realized that sometimes the hazy appearance of water mislead in adding appropriate amount of seeding materials. More importantly, the velocity range setting and corresponding bed reflection interference have been found to affect some ADV measurements. There are several options for velocity range setting in ADV data acquisition software ranging from ±3 cm/s to ±250 cm/s. SonTek recommends (SonTek 2001) the selection of the lowest velocity range setting that will cover the maximum velocity expected in a given experiment, as higher velocity ranges have higher noise levels. However, they also state that when operating in highly turbulent flows the noise level may be reduced by increasing the velocity range. SonTek (2001) suggested that if the turbulent fluctuations are 5% or more of the velocity range setting (i.e. greater than 5 cm/s when using the ±100 cm/s velocity range), performance may be improved by changing to the next higher velocity range. Moreover, trial measurements showed that bed reflections interfere with ADV measurements at certain ranges of elevations for different velocity range settings. From the above considerations a velocity range of ±30 cm/s was used for near-bed measurements, while a range of ±100 cm/s was used for measurements away from the bed to minimize error and discontinuity in measurements. In spite of all these awareness, some measurements were found to be affected by either bed reflection or inadequate seeding materials. However, the data points with suspect of error are eliminated from analyses in the subsequent chapters.

Table 2.1 Primary Details of the Experiment Scenario

Experiment		Object Height, h (mm)	Water Depth, H (mm)	Discharge, Q (L/s)	Cross-Sectional Mean Velocity, U_0 (m/s)	Object Reynolds No., Re_D
Smooth bed	Regime-1	55	220	50	0.186	21000
	Regime-2	120	220	50	0.186	21000
	Regime-3	200	220	50	0.186	21000
	Regime-4	300	220	50	0.186	21000
Rough bed	Regime-1	55	220	50	0.186	21000
	Regime-2	120	220	50	0.186	21000
	Regime-3	200	220	50	0.186	21000
	Regime-4	300	220	50	0.186	21000

Table 2.2 Repeatability of Yaw Probe Measured Bed Shear Stresses

Day	Yaw angle θ (deg)	Shear stress τ (N/m^2)	Friction velocity u_* (m/s)
1	-1.82	0.09	0.0095
2	-5.83	0.06	0.0076
3	2.10	0.11	0.0106
4	2.81	0.12	0.0107
5	-5.10	0.12	0.0107
6	-1.37	0.17	0.0129
7	-2.99	0.11	0.0104
8	1.37	0.17	0.0129
9	-4.86	0.17	0.0130
10	-1.56	0.14	0.0119
11	0.48	0.10	0.0098
12	-1.58	0.14	0.0119
13	0.01	0.08	0.0088
14	-0.12	0.09	0.0093
15	-1.38	0.16	0.0127
Mean	-1.32	0.120	0.0108
Standard deviation	2.5759	0.0358	0.0017

Table 2.3 Repeatability of Yaw Probe Measured Velocities

Day	z=20.35 cm		z=6.94 cm		z=0.11 cm	
	Velocity (cm/s)	Yaw angle θ (deg)	Velocity (cm/s)	Yaw angle θ (deg)	Velocity (cm/s)	Yaw angle θ (deg)
1	23.28	1.29	21.56	4.37	6.53	-1.82
2	21.96	-0.01	21.11	-1.16	5.28	-5.83
3	23.96	-0.47	23.44	-1.12	7.22	2.10
4	23.70	0.09	22.73	0.67	7.33	2.81
5	22.61	-0.36	22.55	-0.86	7.26	-5.10
6	22.65	0.75	22.33	0.47	8.68	-1.37
7	22.70	-0.10	22.43	-0.86	7.13	-2.99
8	22.33	1.74	21.90	1.38	8.63	1.37
9	22.73	-0.64	22.45	0.21	8.65	-4.86
10	21.95	1.36	21.60	1.10	8.01	-1.56
11	21.45	0.17	20.45	0.24	6.73	0.48
12	21.21	-0.08	20.00	-0.13	8.07	-1.58
13	21.50	0.14	20.96	0.16	6.08	0.01
14	20.76	0.24	20.49	0.20	6.37	-0.12
15	21.02	0.00	20.45	-0.06	8.52	-1.38
Mean	22.26	0.27	21.63	0.31	7.37	-1.32
Std. dev.	0.96	0.6993	1.02	1.3562	1.05	2.5759

Table 2.4(a) Repeatability of ADV measurements at z = 15 cm

Day	U (cm/s)	V (cm/s)	W (cm/s)	u' (cm/s)	v' (cm/s)	w' (cm/s)	k $(\mathrm{cm}^2/\mathrm{s}^2)$	$\overline{uw}$ $(\mathrm{cm}^2/\mathrm{s}^2)$
1	21.35	0.17	-0.16	1.73	1.58	0.89	3.14	0.02
2	20.31	0.32	-0.20	1.56	1.54	0.82	2.75	0.08
3	20.41	0.38	-0.30	1.37	1.46	0.78	2.31	0.02
4	20.47	0.26	-0.18	1.44	1.49	0.80	2.46	0.05
5	20.24	-0.02	-0.25	1.56	1.51	0.72	2.62	0.06
6	20.87	0.10	-0.31	1.60	1.59	0.83	2.89	-0.02
7	21.07	0.14	-0.26	1.65	1.62	0.83	3.01	0.01
8	21.06	0.09	-0.23	1.69	1.59	0.85	3.06	-0.09
9	20.96	0.06	-0.38	1.66	1.73	0.81	3.19	-0.05
10	20.88	0.20	-0.30	1.55	1.50	0.79	2.64	-0.08
11	20.90	0.06	-0.48	1.65	1.63	0.81	3.01	-0.01
12	20.01	0.08	-0.38	1.55	1.44	0.81	2.56	0.02
Mean	21.71	0.15	-0.29	1.58	1.56	0.81	2.80	0.00
Std. dev.	0.4073	0.1191	0.0930	0.1024	0.0822	0.0427	0.2873	0.0533

Table 2.4(b) Repeatability of ADV measurements at z = 7.5 cm

Day	U (cm/s)	V (cm/s)	W (cm/s)	u' (cm/s)	v' (cm/s)	w' (cm/s)	k (cm^2/s^2)	$\overline{uw}$ (cm^2/s^2)
1	21.19	0.46	0.03	1.90	1.62	0.88	3.50	-0.17
2	20.15	0.26	0.06	1.50	1.23	0.82	2.22	-0.31
3	20.26	0.28	-0.07	1.45	1.14	0.82	2.03	-0.25
4	20.78	0.30	0.01	1.32	1.16	0.73	1.82	-0.17
5	20.17	-0.25	-0.19	1.67	1.25	0.74	2.45	-0.41
6	21.12	-0.33	-0.57	1.48	1.27	0.80	2.22	-0.23
7	20.99	-0.41	-0.47	1.57	1.27	0.78	2.34	-0.29
8	20.80	-0.31	-0.37	1.80	1.30	0.81	2.79	-0.42
9	20.92	-0.40	-0.55	1.46	1.28	0.74	2.16	-0.12
10	20.62	-0.42	-0.45	1.57	1.26	0.78	2.33	-0.26
11	20.94	-0.29	-0.47	1.78	1.32	0.83	2.79	-0.43
12	20.17	-0.42	-0.45	1.47	1.20	0.76	2.09	-0.33
Mean	20.68	-0.13	-0.29	1.58	1.27	0.79	2.39	-0.28
Std. dev.	0.3917	0.3423	0.2421	0.1721	0.1195	0.0438	0.4486	0.1023

Table 2.4(c) Repeatability of ADV measurements at $z = 0.5$ cm

Day	U (cm/s)	V (cm/s)	W (cm/s)	u' (cm/s)	v' (cm/s)	w' (cm/s)	k (cm^2/s^2)	$\overline{uw}$ (cm^2/s^2)
1	14.26	0.21	0.13	2.29	1.70	0.87	4.44	-0.78
2	14.45	0.08	0.24	2.29	1.58	0.78	4.17	-0.69
3	14.05	0.14	0.06	2.39	1.61	0.84	4.51	-0.90
4	14.36	0.16	0.06	2.42	1.61	0.84	4.57	-0.84
5	14.41	-0.24	0.12	2.40	1.91	0.82	5.04	-0.63
6	14.29	-0.43	-0.28	2.49	1.80	0.80	5.05	-0.86
7	14.44	-55	-0.13	2.48	1.74	0.82	4.93	-0.84
8	14.40	-0.60	-0.05	2.48	1.77	0.83	4.99	-0.72
9	14.00	-0.90	-0.23	2.50	1.88	0.80	5.21	-0.66
10	14.50	-0.63	-0.12	2.47	1.81	0.82	5.04	-0.86
11	14.48	-0.30	-0.24	2.50	1.86	0.83	5.21	-0.75
12	14.60	-0.65	-0.17	2.19	1.75	0.82	4.26	-0.70
Mean	14.35	-0.31	-0.05	2.41	1.75	0.82	4.79	-0.77
Std. dev.	0.1777	0.3778	0.1694	0.1035	0.1104	0.0226	0.3728	0.0893

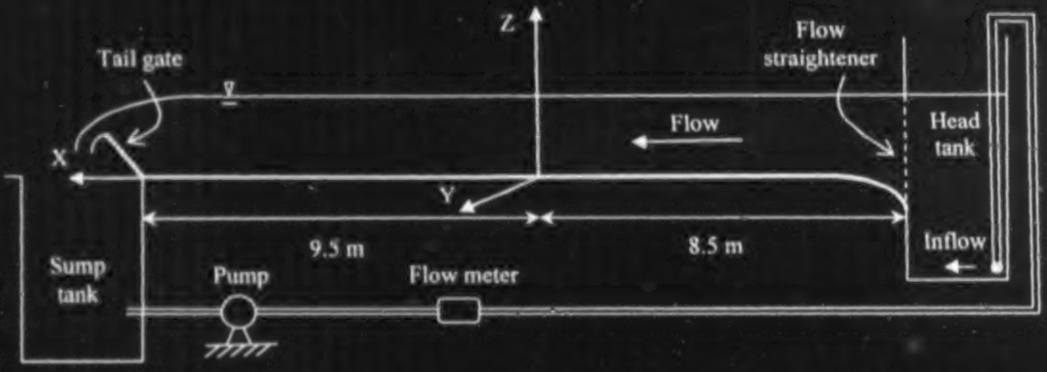
Z
Tail gate
∇
Flow
straightener
Flow
Head
tank
X
Y
9.5 m
8.5 m
Inflow
Sump
tank
Pump
Flow meter

Fig. 2.1 Schematic diagram showing the experimental setup

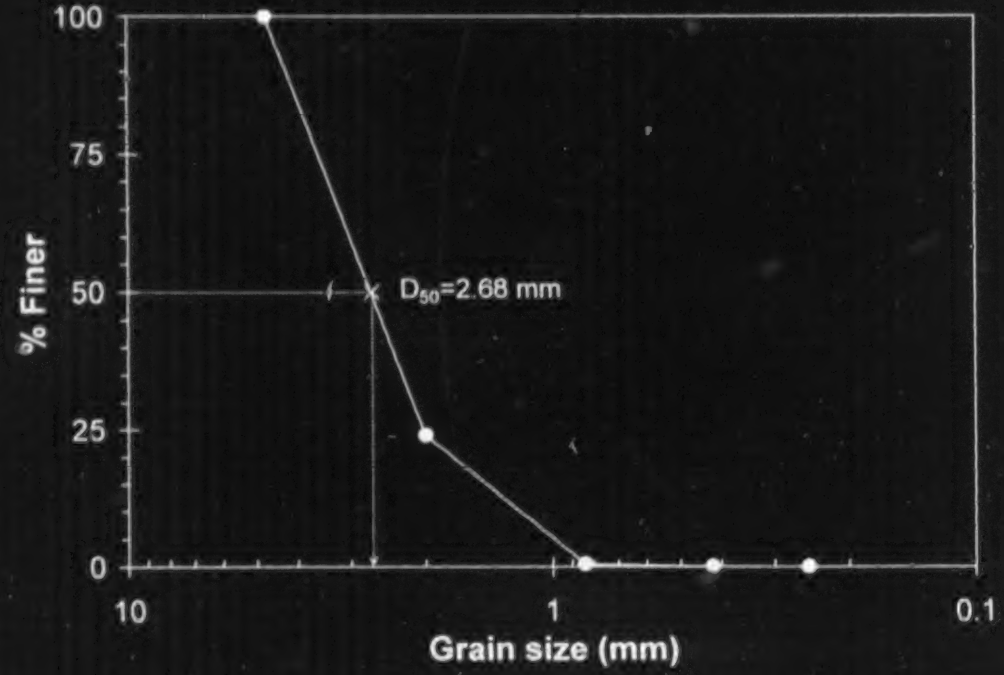

Fig. 2.2 Measured grain size distribution of the 8/12 sand

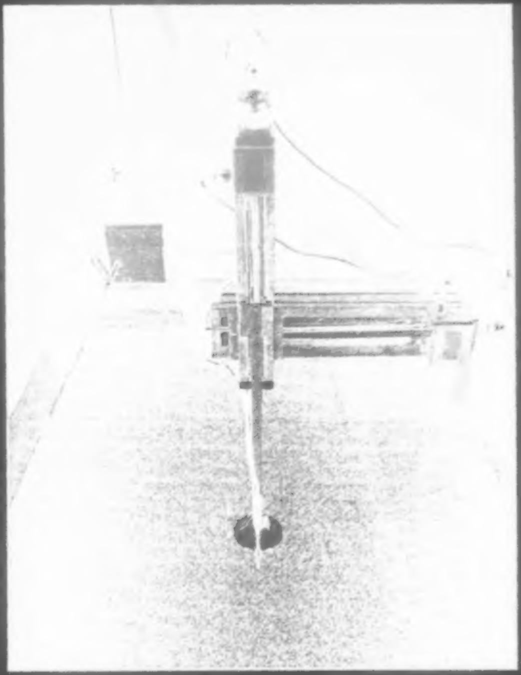

Fig. 2.3 Photograph of the traverse system with the ADV probe

Fig. 2.4 Photograph of leveled and aligned yaw probe

Fig. 2.5 Photograph of the setup for the yaw probe measurements

Fig. 2.6 Photograph of the ADV probe mounted for smooth bed measurements

Fig. 2.7 Photograph of leveled and aligned ADV probe

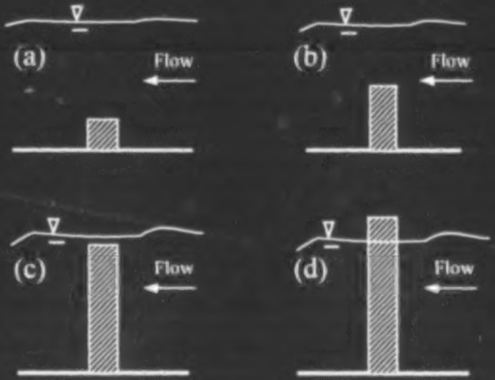

Fig. 2.8 Definition sketch of flow regimes; (a) Regime-1: Deeply Submerged Object (Submergence ratio, $H/h\approx4$), (b) Regime-2: Moderately Submerged Object ($H/h\approx2$), (c) Regime-3: Slightly Submerged Object ($H/h\approx1.1$), and (d) Regime-4: Non-Submerged Object (h>H)

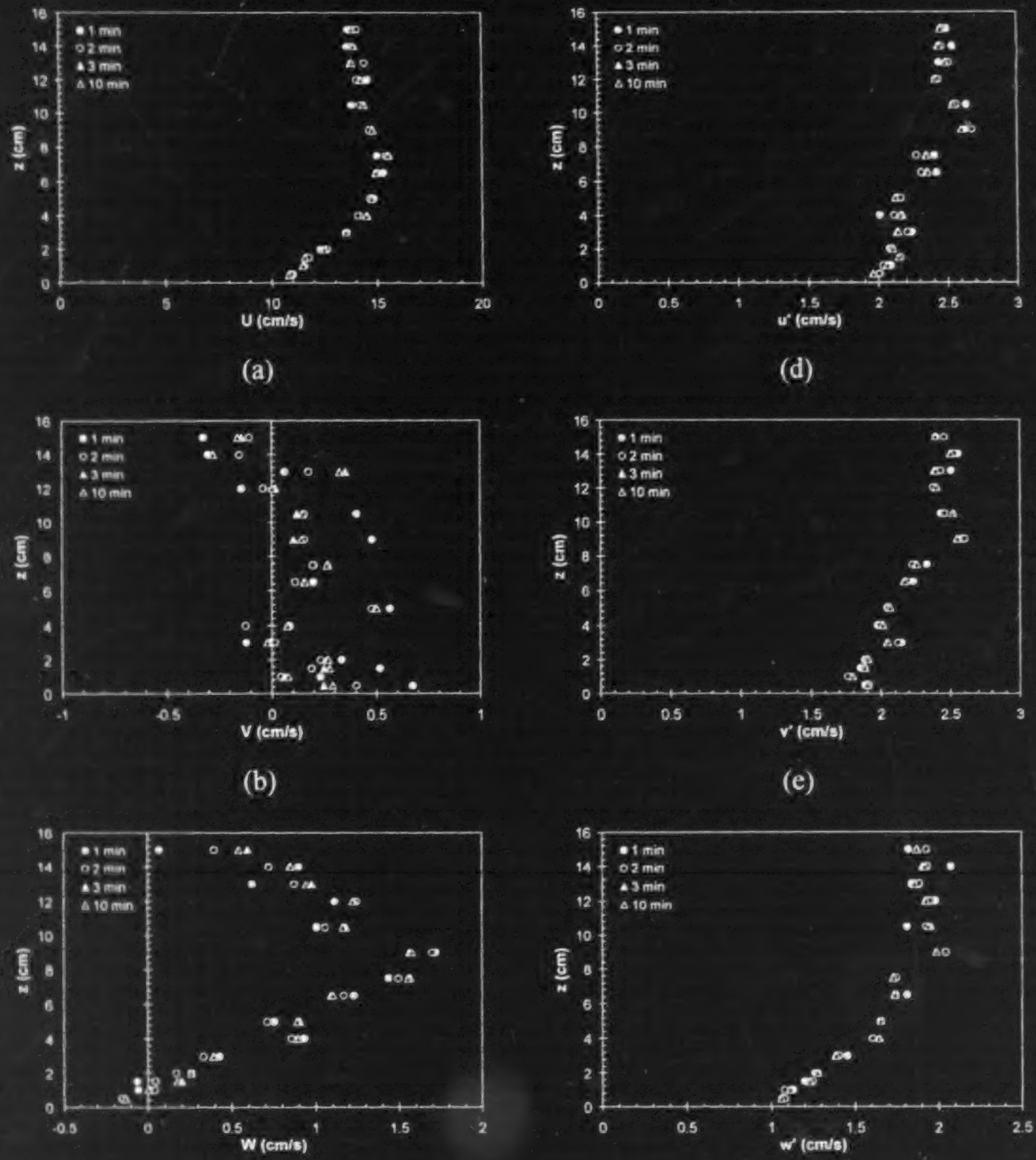

(a) (d)

(b) (e)

(c) (f)

Fig. 2.9(a-f) Sampling duration adequacy check using ADV data at *x*=+4*D* and *y*=0 in Regime-4 on rough bed

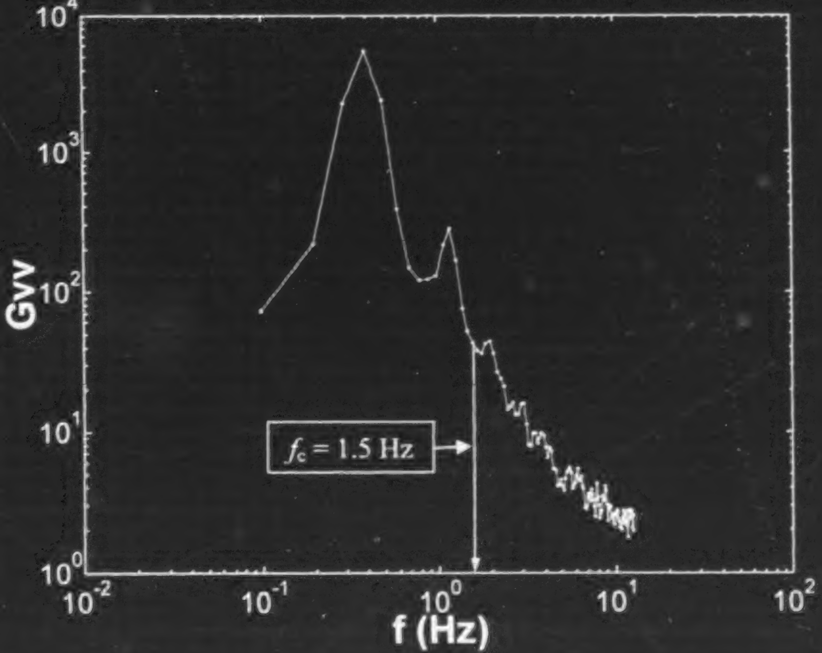

Fig. 2.10 A typical auto-spectral density function of the transverse velocity component (G_{vv}) showing the procedure of cut-off frequency selection

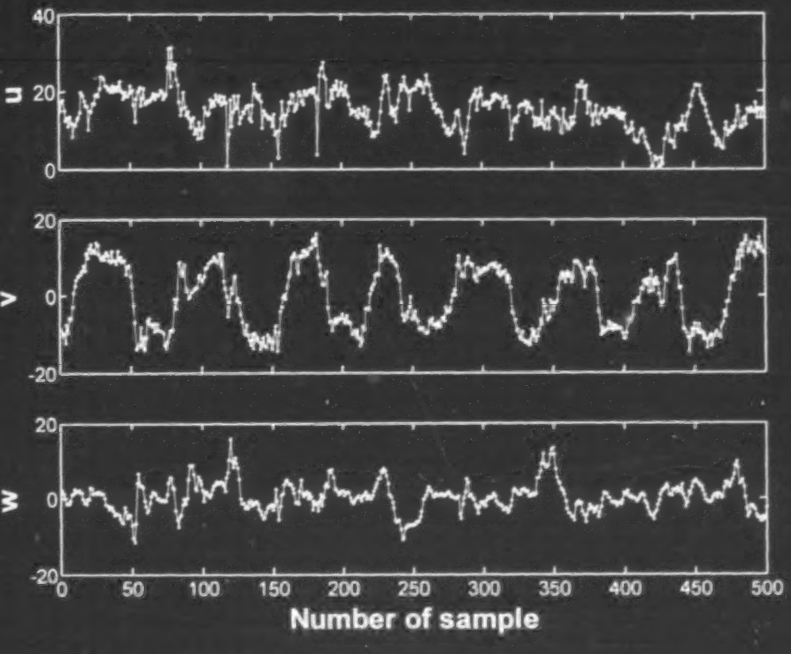

Fig. 2.11 A segment of raw ADV data in the wake

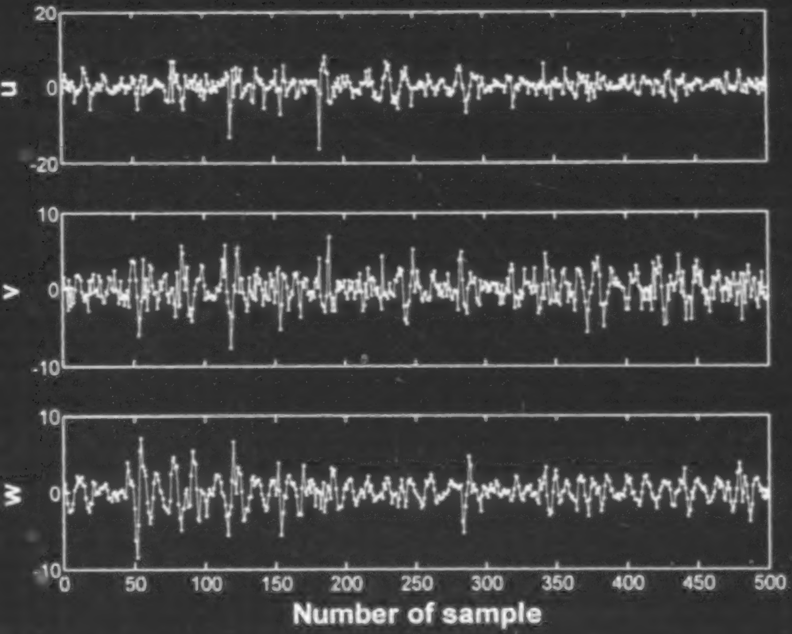

Fig. 2.12 High-pass filtered series obtained from raw ADV data

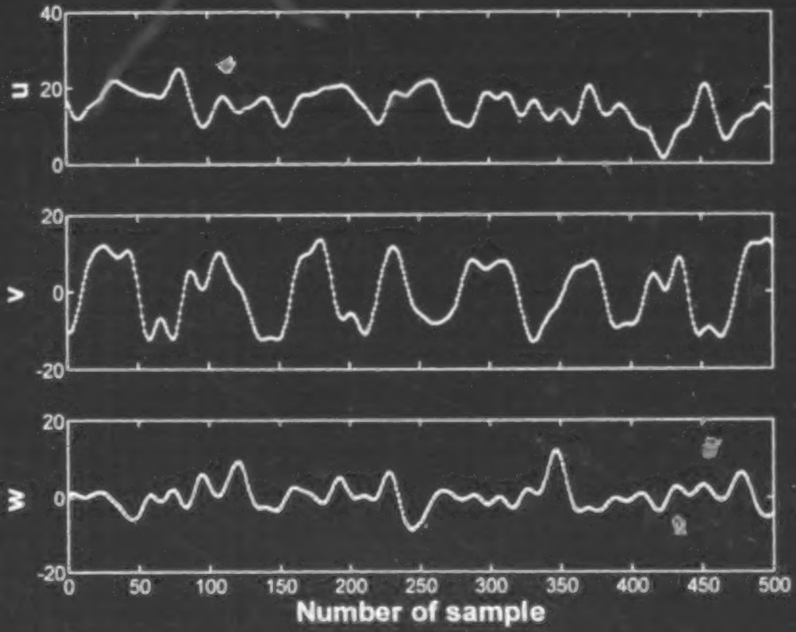

Fig. 2.13 Low-frequency series obtained from raw ADV data

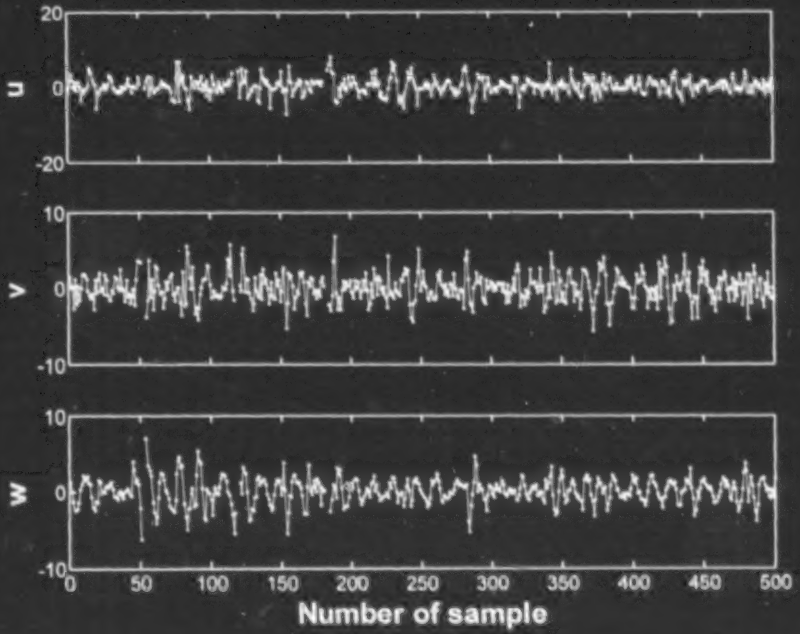

Fig. 2.14 SNR and COR threshold filtered series obtained from high-pass filtered data

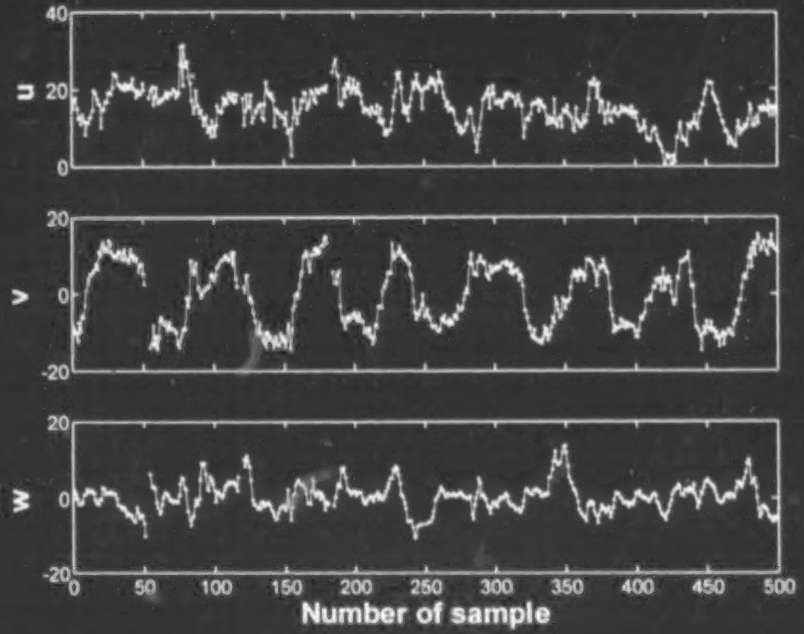

Fig. 2.15 Clean ADV data in the wake

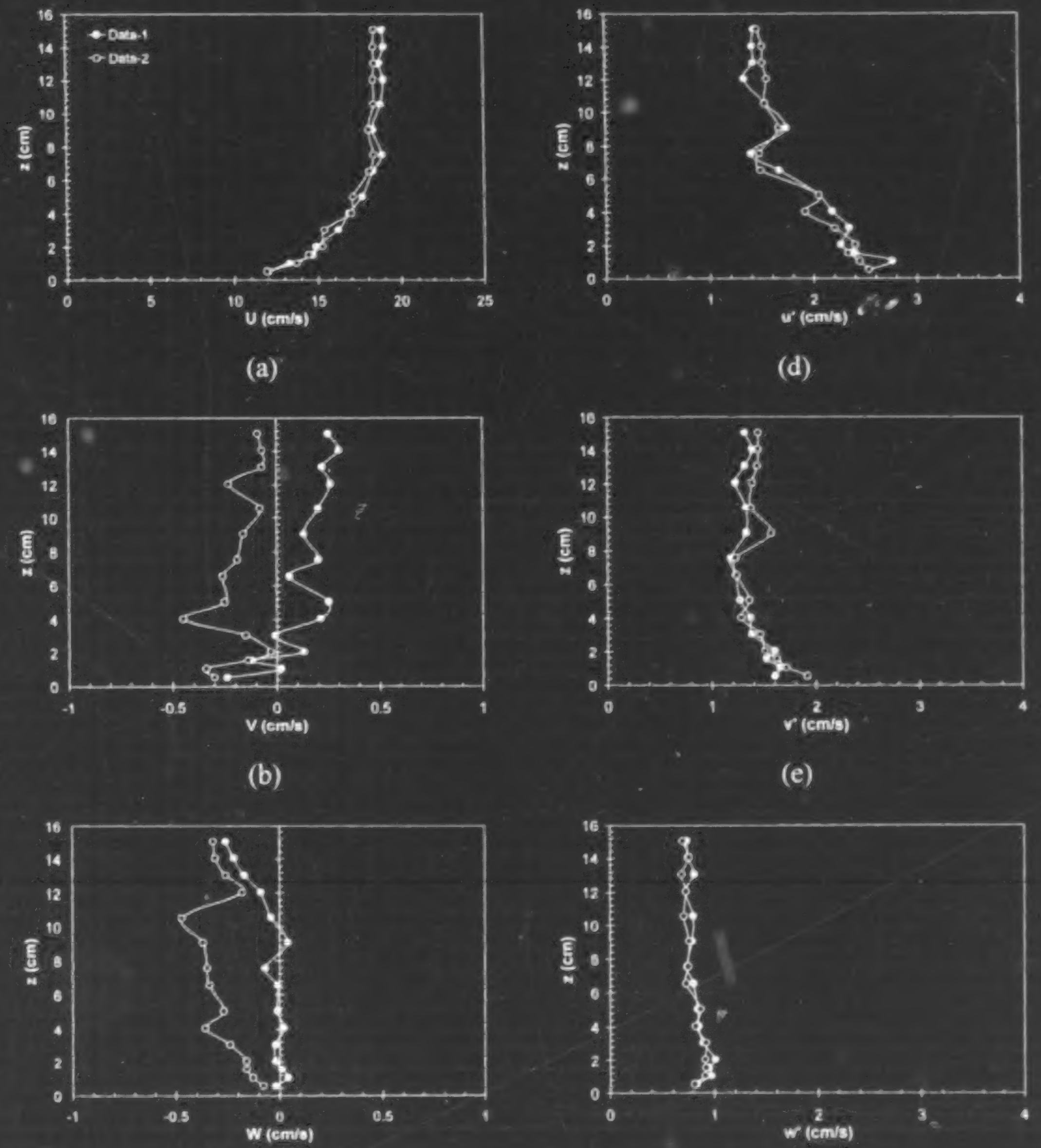

(a) (d)

(b) (e)

(c) (f)

Fig. 2.16(a-f) Repeated ADV measurements at *x*=-2*D* and *y*=0 in Regime-3 on rough bed

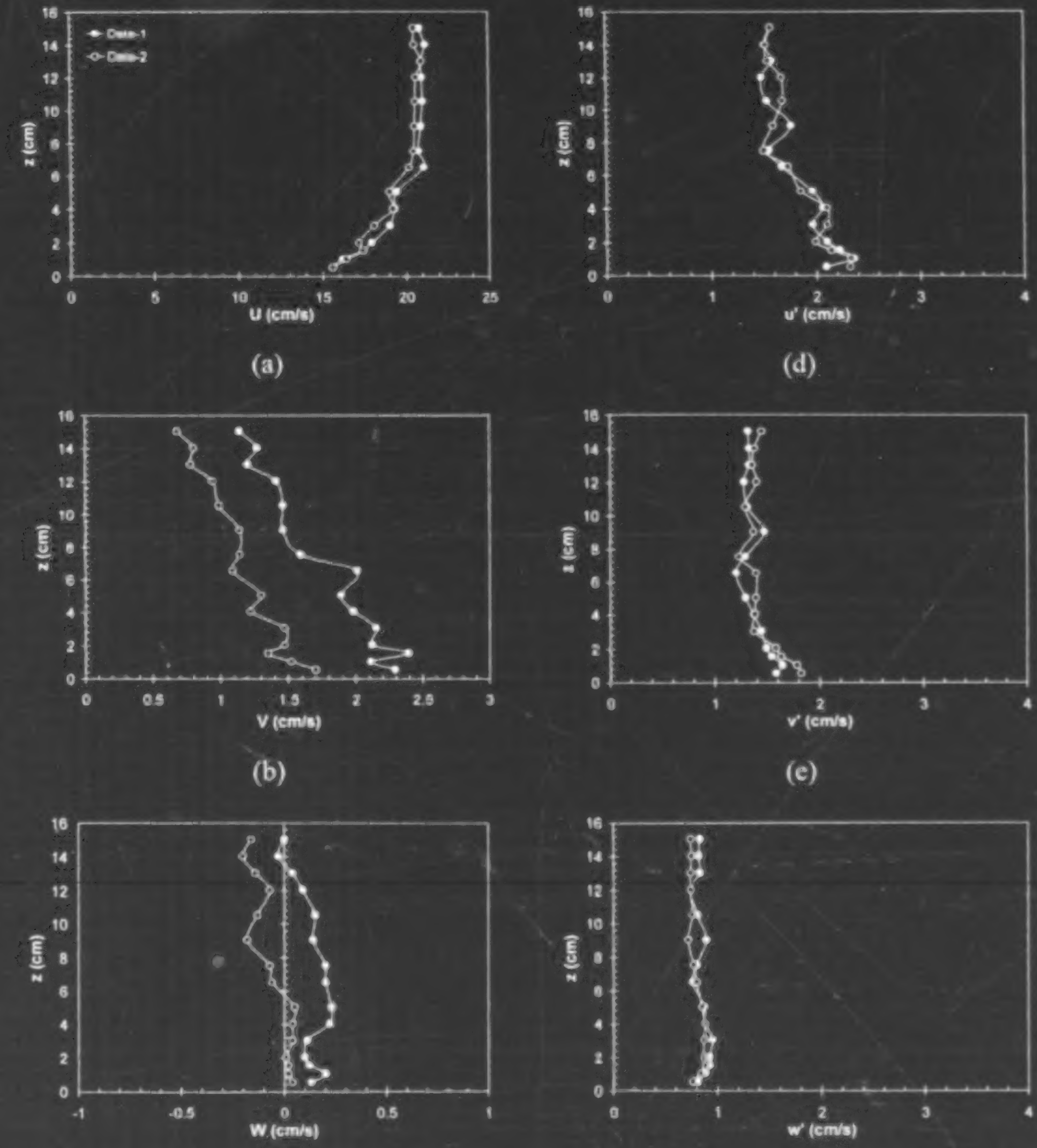

(a) (d)

(b) (e)

(c) (f)

Fig. 2.17(a-f) Repeated ADV measurements at *x*=0 and *y*=2.2*D* in Regime-3 on rough bed

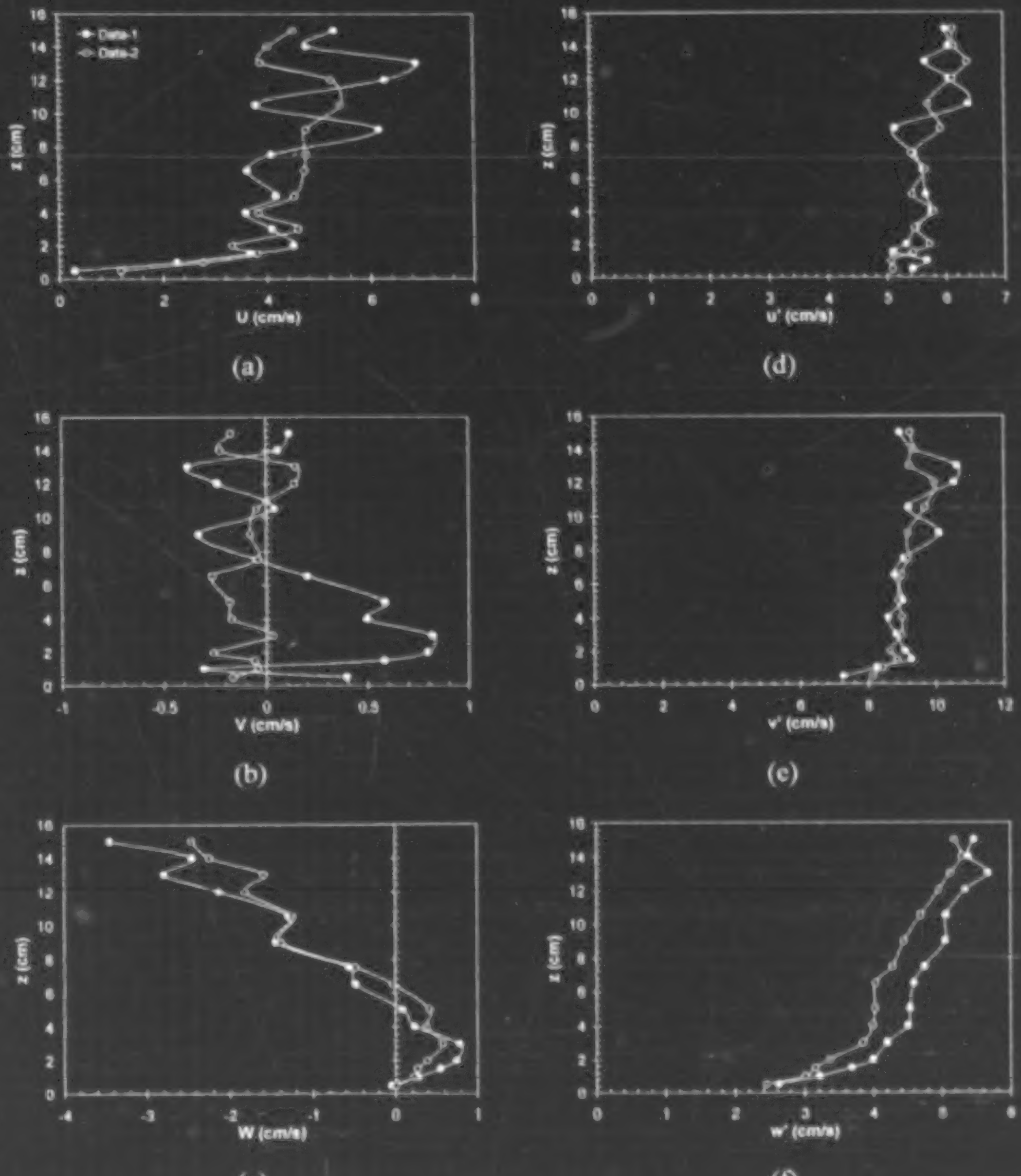

(a) (d)

(b) (e)

(c) (f)

Fig. 2.18(a-f) Repeated ADV measurements at x=+2D and y=0 in Regime-3 on rough bed

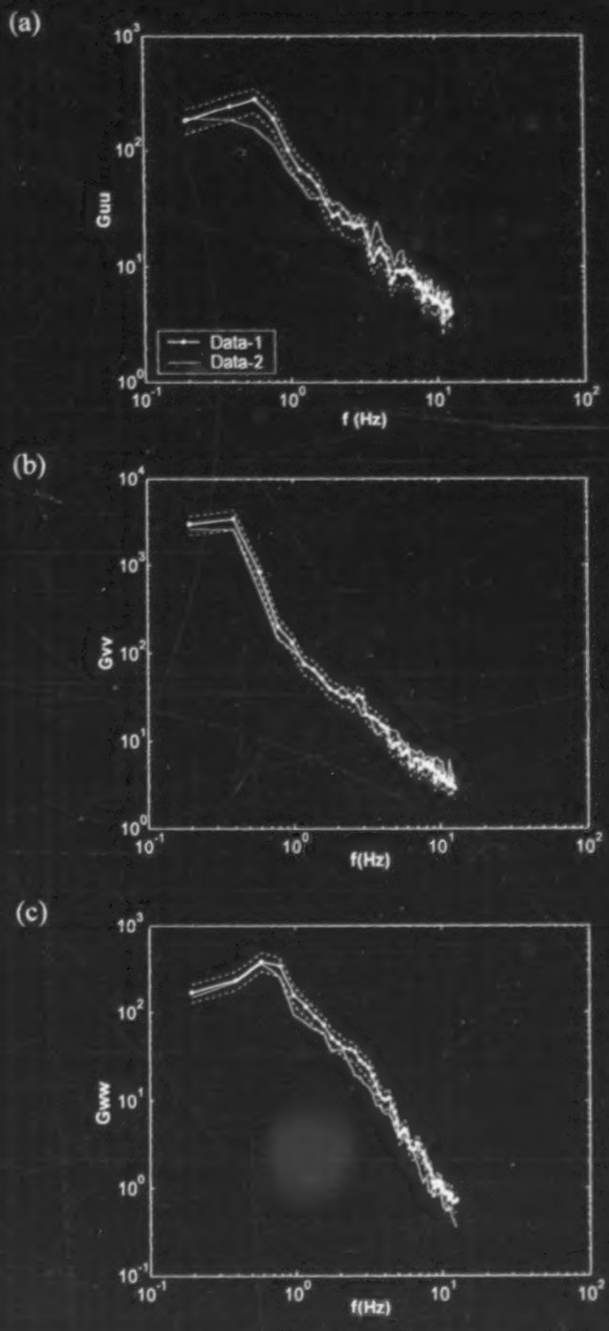

Fig. 2.19(a-c) Auto-spectral density functions plotted using repeated ADV measurements at $x=+2D$, $y=0$, $z=13$ cm in Regime-3 on rough bed; the dotted lines represent the 95% confidence limits based on Data-1

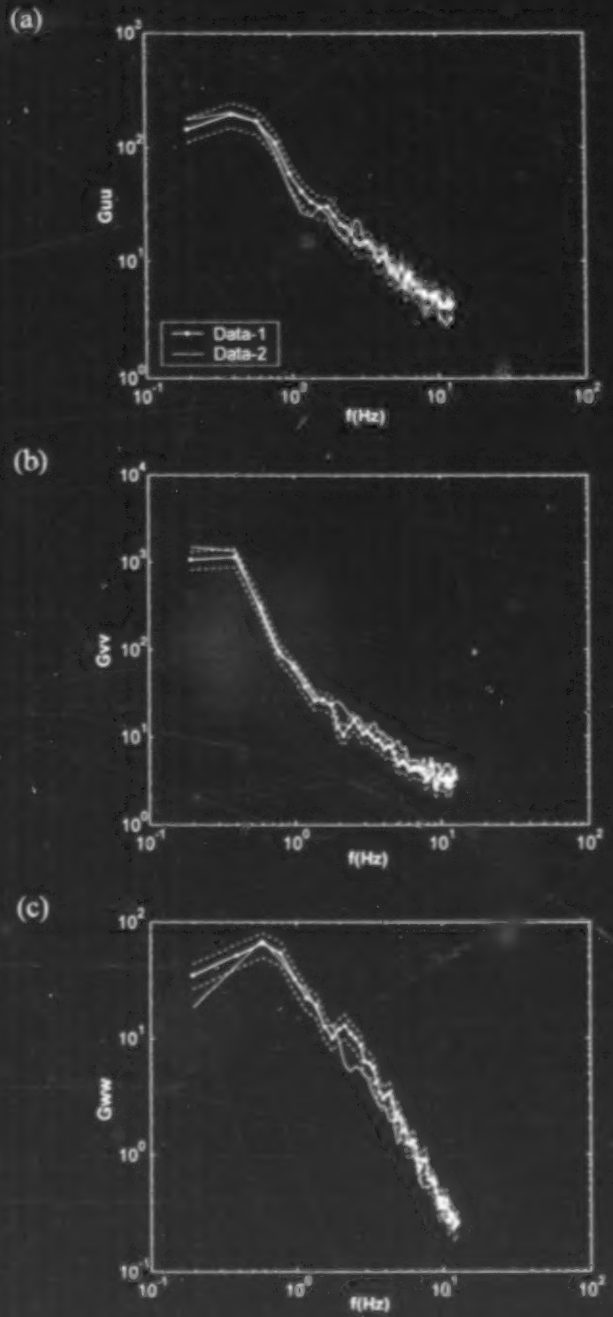

Fig. 2.20(a-c) Auto-spectral density functions plotted using repeated ADV measurements at x=+2D, y=0, z=0.5 cm in Regime-3 on rough bed; the dotted lines represent the 95% confidence limits based on Data-1

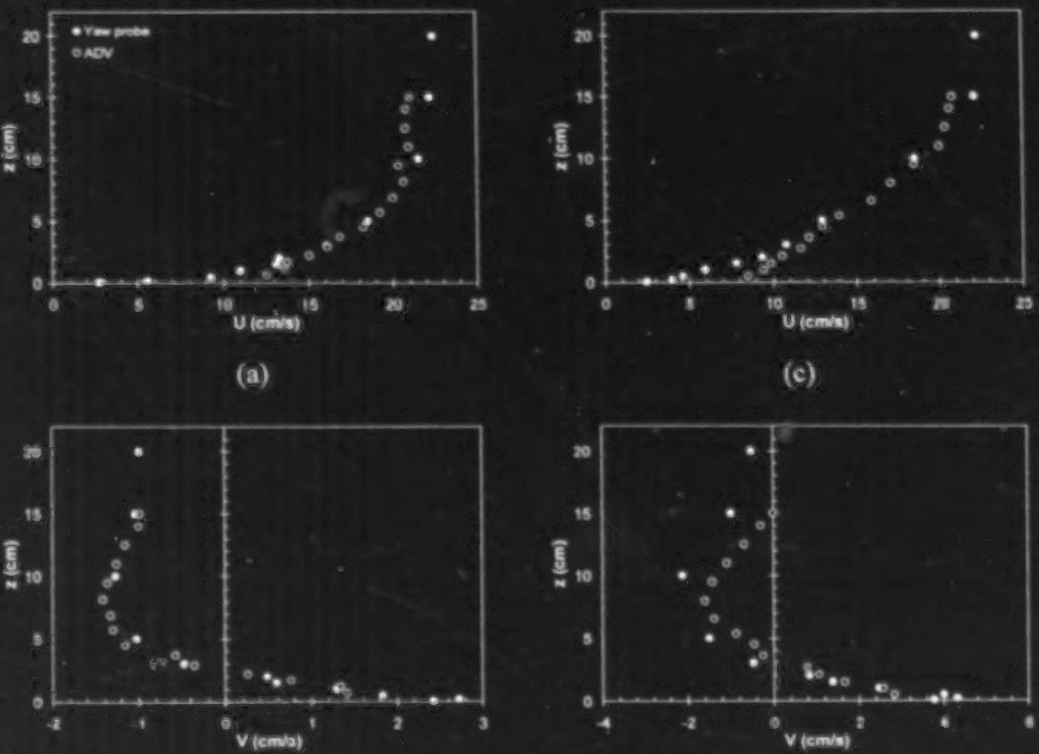

(a) (c)

(b) (d)

Fig. 2.21 Comparison of mean velocity profiles obtained from ADV and yaw probe measurements; (a) profile of U at $x=+3D$, $y=1D$; (b) profile of V at $x=+3D$, $y=1D$; (c) profile of U at $x=+3D$, $y=0.5D$; and (d) profile of V at $x=+3D$, $y=0.5D$ in Regime-2 on smooth bed

2.7 References

Albers, C. D. (1997). *Hydraulics of a three obstacle cluster in open channels*, M. Sc. thesis, University of Alberta, Edmonton, AB, Canada.

Burrows, A. D. and Steffler, P. M. (2005). "Depth averaged modeling of flow around individual boulders." *Proc., 17th Canadian Hydrotechnical Conf.*, CSCE, Edmonton, AB, 395-404.

Chen, D., and Jirka, G. H. (1995). "Experimental study of plane turbulent wakes in a shallow water layer." *Fluid Dynamics Research*, 16, 11-41.

Einstein, H. A., and El-Samni, E. S. A. (1949). "Hydrodynamic forces on a rough wall." *Review of Modern Physics*, 21(3), 520-524.

Goring, D. G., and Nikora, V. I. (2002). "Despiking acoustic Doppler Velocimeter data." *Journal of Hydraulic Engineering*, 128(1), 117-126.

Hollingshead, A. B. (1972). *Boundary shear distribution in open channel flow*, Ph. D. thesis, University of Alberta, Edmonton, AB, Canada.

Hollingshead, A. B., and Rajaratnam, N. (1980). "A calibration chart for the Preston tube." *Journal of Hydraulic Research*, 18(4), 313-326.

Nezu, I., and Nakagawa, H. (1993). *Turbulence in open-channels*, IAHR-monograph, Balkema, Rotterdam, The Netherlands.

Patel, V. C. (1965). "Calibrations of the Preston tube and limitations on its use in pressure gradients." *Journal of Fluid Mechanics*, 23, 185-208.

Perrin, R., Braza, M., Cid, E., Cazin, S., Moradei, F., Barthet, A., Sevrain, A., and Hoarau, Y. (2006). "Near-wake turbulence properties in the high Reynolds number incompressible flow around a circular cylinder measured by two and three component PIV." *Flow Turbulence Combust*, 77, 185-204.

Rajaratnam, N. and Muralidhar, D. (1968). "Yaw probe used as Preston tube." *The Aeronautical Journal of the Royal Aeronautical Society*, 72, 1059-1060.

Reynolds, W. C. and Hussain, A. K. M. F. (1972). "The mechanics of an organized wave in turbulent shear flow, Part 3, Theoretical models and comparisons with experiments." *Journal of Fluid Mechanics*, 54, 263-288.

Shamloo, H., Rajaratnam, N., and Katopodis, C. (2001). "Hydraulics of simple habitat structures." *Journal of Hydraulic Research*, 39(4), 351-366.

SonTek. (1997a). *ADV operation manual*, Firmware Version 4.0, San Diego. CA.

SonTek. (1997b). *ADV software reference manual*, Version 4.0, San Diego. CA.

SonTek. (2001). *Acoustic Doppler Velocimeter principles of operation*, San Diego. CA.

Wahl, T. L. (2000). "Analyzing ADV data using WinADV." *Proc., 2000 Joint Conference on Water Resources Engineering and Water Resources Planning and Management*, ASCE, Minneapolis, MN.

Chapter 3: Turbulence in Narrow Open Channel Flows

3.1 Introduction

Experimental studies on open channel turbulence have attracted much interest in the last few decades. Experimental results for two-dimensional open channel turbulence have been available since mid 1970s (Nezu and Nakagawa 1993). The advent of laser anemometry in the early 1980s opened up the prospect of experimental research on turbulence, permitting detailed investigations of not only basic two-dimensional uniform flows, but also unsteady and three-dimensional open channel flows (Nezu 2005). More recently, Acoustic Doppler Velocimeter (ADV) and Particle Image Velocimetry (PIV) have expanded the scope of turbulence research in open channels. However, most researchers have focused on the turbulence characteristics of two-dimensional wide open channel flows. Nakagawa et al. (1975) were the first to measure all three components of turbulence intensities for open channel flows (Nezu and Nakagawa 1993). Subsequently, Steffler et al. (1985) and Nezu and Rodi (1986) conducted detailed studies of turbulence in two-dimensional straight open channel flow. It had been a long time since river engineers noticed the existence of secondary current in straight open channel flows where the channels were not very wide (Nezu and Nakagawa 1993). In particular, they noticed that the maximum velocity occurs well below the free surface, when the channel is not very wide. This phenomenon is commonly known as ‘velocity dip’. However, the complexity of turbulence in straight open channels with secondary currents was essentially ignored until the study of Nezu and Nakagawa (1984).

Nezu and Rodi (1985) classified open channels as narrow and wide on the basis of the velocity dip phenomenon. They found that the velocity dip occurs when the channel aspect ratio (B/H) falls below 5, where B is the channel width and H is the flow depth. However, the influence of secondary currents on the turbulence and bed shear stress was observed in the study of Tominaga et al. (1989) for aspect ratios as high as 8. Therefore, a channel with aspect ratio less than 10 cannot be considered wide and in this case the turbulent flow characteristics will differ significantly from those in a 2D channel.

If the flow is not uniform in the streamwise direction, streamwise vorticity is generated by vortex stretching. Secondary currents generated by this mechanism are known as 'secondary current of Prandtl's first kind'. This type of secondary current is driven by the centrifugal force and it is commonly found in a channel bend. This type of secondary current can be about 20-30% of the main stream velocity (Nezu and Nakagawa 1993). However, the other kind of secondary current develops in straight uniform open channel flows. Einstein and Li (1958, after Nezu and Nakagawa 1993) first ascribed the origin of secondary currents in straight open channels to gradients in the Reynolds stresses, on the basis of the streamwise vorticity (Ω) equation as follows:

$$[3.1] \quad \underbrace{W\left(\frac{\partial\Omega}{\partial y}\right)+V\left(\frac{\partial\Omega}{\partial z}\right)}_{A}=\underbrace{\frac{\partial^2}{\partial y\partial z}\left(\overline{w^2}-\overline{v^2}\right)}_{B}+\underbrace{\left(\frac{\partial^2}{\partial y^2}-\frac{\partial^2}{\partial z^2}\right)\overline{vw}}_{C}+\underbrace{\nu\nabla^2\Omega}_{D}$$

where, $\Omega=\partial V/\partial y-\partial W/\partial z$, V and W are the time-averaged velocities, $\overline{v^2}$ and $\overline{w^2}$ are the normal stresses in the transverse (y) and vertical (z) directions, $-\overline{vw}$ is the Reynolds shear stress in y-z plane and ν is the kinematic viscosity of water.

Non-homogenous and anisotropic turbulence is responsible for the gradients in the Reynolds stresses in straight open channel flow. Therefore, this type of secondary current is called 'turbulence driven secondary current' or 'secondary current of Prandtl's second kind'. Secondary currents in straight channel will have magnitudes of about 5% of the maximum streamwise velocity (Nezu and Nakagawa 1993).

In a straight channel, terms B and C contribute most to generating secondary currents; i.e. non-homogeneity and anisotropy of turbulence. Viscous term D is negligible except for regions near the bed. Term A represents the advection of vorticity, i.e. the existence of secondary current. Term B promotes and term C suppresses the secondary current. It had been verified by experimental (Nezu and Nakagawa 1984) and numerical studies (Demuren and Rodi 1984) that terms B and C are the dominant ones; they have opposite signs and are much larger than the advection term A. Therefore, the difference between the terms B and C drives the secondary current in straight channels.

Most of the studies of turbulence driven secondary currents in open channel flow have differentiated between the secondary current structure in straight open channel flow and that in closed conduit (e.g. Nezu et al. 1989). However, knowledge about the differences in the structure of 2D and 3D turbulent flows in straight open channels is limited. Nezu and Nakagawa (1993) summarized the research on turbulence in 2D and 3D open channel flows up to 1993. In a concurrent field study, Nezu et al. (1993) investigated the turbulence characteristics and bed shear stress distribution in a river and an irrigation canal where the aspect ratio was 8 and 2.5 respectively. Nezu (2005), in a very recent forum article, described the latest developments including the major contributions from the past in the field of open channel turbulence research. After a detailed review of literature, it has been recognized that the effect of turbulence driven secondary currents on the over all flow structure is mostly unknown. Therefore, the objective of the present study is to examine the differences between the 3D turbulence structure in a narrow open channel and the 2D flow structure in wide channels. The effect of roughness on this complex 3D flow structure is also studied.

3.2 Experimental Setup and Procedure

General description of the experimental setup and procedure is given in Chapter 2. For the present study, a discharge of 50 L/s with 22 cm water depth (H) was tested on smooth and rough beds in a 122 cm wide (B) open channel. This has produced a turbulent ($R_H \equiv U_0 H/\nu=40000$) subcritical flow ($F$=0.13) and a relatively narrow channel aspect ratio, B/H=5.5. Development of approach flow was tested by comparing the mean velocity profiles at x=0 [see Fig. 2.1] with the profiles at two other stations at a distance of 1 m upstream (i.e. at x=-1m) and downstream (i.e. at x=+1m) from the central test station. Figure 3.1(a-c) and Figure 3.2(a-c) show the comparison of mean velocity profiles along three longitudinal planes at y=-0.3m, 0 and +0.3m on smooth and rough beds respectively. In all cases the velocity profiles are found to collapse in a narrow band representing fully developed flow. Similarly the symmetry of flow across the channel was confirmed by comparing the mean velocity profiles (at y=-0.3m, 0 and +0.3m) at x=0 in Fig. 3.3(a-b). For both smooth and rough beds velocity profiles at y=-0.3m and +0.3m collapse together with a small offset from the profile at y=0. This is due to relatively less channel aspect ratio. However, the mean velocity at y=-0.3m and +0.3m (i.e. at y/B=±0.25) compared to the velocity at y=0 are only 8-12% less. Such a variation in mean velocity across the channel is not uncommon in natural rivers. For example, Nezu et al. (1993) found 7-10% deviation of mean velocity at y/B=±0.25 compared to channel center (i.e. at y=0) in field measurement at Biwako Soui River in Kyoto, Japan where the channel aspect ratio (B/H) was 8. It is also observed in the present study that the transverse velocity component at y/B=±0.25 do not exceed 3-5% of the velocity in the main stream direction.

Thickness of the turbulent boundary layer (δ) in the fully developed flow region is observed. By definition (Schlichting 1968), δ is the elevation above the bed where the longitudinal component of velocity (U) equals 99% of the free stream velocity. It can be observed from the mean longitudinal velocity profiles (Fig. 3.1 and Fig. 3.2) that there is no appreciable change in velocity gradient at z>0.05 m and z>0.1 m at the channel center (i.e. at y=0) for smooth and rough beds, respectively. However, the change in velocity gradient considerably diminishes only at z=0.15 m for both smooth and rough beds away from the channel center (i.e. at y=±0.3 m). Therefore, from the overall observations of the fully developed velocity profiles δ can be taken approximately equal to 15 cm.

For the purpose of studying the differences in turbulence structure and its significance in developing turbulence driven secondary current in a narrow open channel compared to the 2D flow structure in wide channels velocities are measured at two stations across the channel at x=0. The stations chosen for this study are located at 1) the centerline (i.e., at y=0) and 2) at y=B/4 (i.e., the quarter width of the channel). Figure 3.4 shows the position of velocity measuring stations 1 and 2 with respect to the channel cross-section. The 3D turbulent velocity was measured using a 10 MHz Acoustic Doppler Velocimeter (ADV) at a sampling rate of 25 Hz for durations of at least 2 min. In addition, a thin yaw-type

Preston probe was used for direct measurements of bed shear stress (τ_0). Details about the application of ADV and yaw probe are presented in Chapter 2.

3.3 Result Analysis and Discussions

3.3.1 *Bed shear stress and friction velocity*

Friction velocity can be considered to be the most fundamental parameter for normalizing the turbulence properties. Therefore, accurate evaluation of the friction velocity (u_*) is a prime requirement for detailed investigation of turbulent structures in open channel flow (Nezu and Nakagawa 1993). Friction velocities at station 1 and 2 are computed from the logarithmic profiles of streamwise mean velocities (U) near the bed. Direct measurements of bed shear stress (τ_0) using yaw-type Preston probe are also available at the center of the cross-section for both smooth and rough beds. Friction velocities (u_*) obtained from these two methods agree within a maximum deviation of 7%. Nikuradse's sand roughness height (k_s) is computed from logarithmic profiles of U on the rough bed. Normalized logarithmic profiles of streamwise mean velocities along the channel center (i.e. y=0) at x=-1m, 0, and +1m are plotted along with law of wall on smooth and rough beds in Figure 3.5(a) and 3.5(b).

Many investigators in the past have reported that the bed shear stress varies in the spanwise direction in open channel flow (e.g. Rajaratnam and Muralidhar 1969). Knight and Patel (1985) reported that the spanwise variation of bed shear stress is dependant on the number and spacing of secondary current cells. However, several researchers have reported more or less similar spanwise variation of bed shear stress for channel aspect ratios 2-8 (Nezu and Nakagawa 1984, Steffler et al. 1985, Nezu et al. 1989, Tominaga et al. 1989 etc.). Their results show that the τ_0 distribution across the smooth bed from y=0 to B/2 has two maxima, one at the centre of the channel (i.e. y/B=0) and the other at approximately y/B=0.35. The maximum shear stress $\tau_{0max} \approx 1.1\text{-}1.2\,\overline{\tau_0}$, where $\overline{\tau_0}$ is the average τ_0 across the channel bed, occurs at the centre of the channel. The second maxima has a value $\tau_0 \approx 1.05\,\overline{\tau_0}$. However, at approximately the quarter width (i.e. y/B=0.25), the bed shear stress is very close to $\overline{\tau_0}$ and near the side-wall it is very small compared to $\overline{\tau_0}$. Nezu et al. (1989) and Tominaga et al. (1989) had also presented the spanwise distribution of τ_0 on rough bed. They found that the maximum shear stress (τ_{0max}) increased with increasing roughness height, but the second maxima gradually disappeared to produce a wide open channel like parabolic distribution of τ_0 with τ_{0max} at the centre. However, it was interesting to note that, similar to the smooth bed result, $\tau_0 \approx \overline{\tau_0}$ at the quarter width ($y/B \approx 0.25$) of the channel. Nezu et al. (1993) observed a similar distribution of τ_0 in field measurements in a prismatic irrigation canal ($B/H=2.5$), though the distribution of τ_0 in a river ($B/H=8$) had three maxima. However, τ_{0max} values in both occasions were around $1.2\overline{\tau_0}$, similar to other studies on a rough bed.

Knight et al. (1984) published a set of empirically derived equations for the shear stress distribution on a smooth open channel boundary as a function of aspect ratio (B/H). They used a wide range of experimental data with $B/H=0.31\text{-}19.12$. According to their empirical relationships, the mean bed shear stress, $\overline{\tau_0}=0.768\,\gamma HS_f$, and the maximum bed shear stress at the center, $\tau_{0max}=0.83\gamma HS_f$ for $B/H=5.5$, where γ is the unit weight of water and S_f is the energy slope. Thus we get a relationship between the mean and the maximum bed shear stress on smooth bed of a rectangular channel with $B/H=5.5$ as, $\tau_{0max}=1.1\overline{\tau_0}$.

The values of u_* and τ_0 for the present experiments are presented in Table 3.1. It is found that the τ_0 values for smooth and rough beds at station 1 (at $y/B=0$) are about 1.1 and 1.4 times the magnitude of τ_0 at station 2 (at $y/B=0.25$). Therefore, on the basis of previous arguments regarding the relationship of mean bed shear stress with τ_{0max} at the channel center, the bed shear stresses at station 2 are considered approximately equal to the mean bed shear stresses for the present experiments.

3.3.2 *Turbulence intensities and kinetic energy*

Nezu (1977) proposed a set of semi-theoretical relationships for turbulence intensities and turbulent kinetic energy for 2D turbulent open channel flow regardless of Reynolds and Froude numbers. The equations are valid in the outer region, where the effect of viscosity is negligible. Nezu (1977) noted that bed roughness has no effect on turbulence intensities except near the bed, where turbulence intensities in rough open channel are somewhat less when $z/\delta<0.3$. The proposed relationships were verified by data obtained from numerous experimental investigations (Nezu and Nakagawa 1993).

$$[3.2] \quad \frac{u'}{u_*} = 2.3\exp\left(\frac{-z}{\delta}\right)$$

$$[3.3] \quad \frac{v'}{u_*} = 1.63\exp\left(\frac{-z}{\delta}\right)$$

$$[3.4] \quad \frac{w'}{u_*} = 1.27\exp\left(\frac{-z}{\delta}\right)$$

$$[3.5] \quad \frac{k}{u_*^2} = 4.78\exp\left(\frac{-2z}{\delta}\right)$$

In Figure 3.6(a) and 3.6(b) profiles of the normalized root mean square velocities u'/u_* in the streamwise direction versus the normalized water depth z/δ are plotted for stations 1 and 2, respectively. Relationships for 2D flow are also plotted for the comparison of turbulence intensities in smooth and rough narrow open channel flow with 2D plane flow. It has been observed from Figure 3.6(a) that at station 1 the data agrees with Equation [3.2] up to $z/\delta=0.4$ on smooth and rough beds, respectively. However, at greater heights the streamwise turbulence intensities on smooth and rough beds are larger than the values from Equation [3.2]. At station 2 [Fig. 3.6(b)], turbulence intensities u'/u_* for both smooth and rough beds are found to be 20-25% higher than the intensities at station 1, and the profiles of turbulence intensities do not follow Equation [3.2].

Vertical profiles of the spanwise turbulence intensities v'/u_* at stations 1 and 2 are presented in Figure 3.7(a) and 3.7(b) respectively and compared with Equation [3.3]. For $z/\delta<0.5$ smooth bed v'/u_* are approximately 20-25% higher, while rough bed v'/u_* are in good agreement compared to those of 2D flows [Fig. 3.7(a)]. However, the spanwise intensities (v'/u_*) are 2-3 times higher than expected for two-dimensional flow at $z/\delta>0.5$.

Spanwise turbulence intensities for smooth bed at station 2 [Fig. 3.7(b)] are similar to the values at station 1, but rough bed v'/u_* are relatively higher.

Figure 3.8(a) and 3.8(b) show profiles of the vertical turbulence intensities w'/u_* at stations 1 and 2, respectively. Smooth and rough bed profiles are compared to the profile of w'/u_* in two-dimensional flow given by Equation [3.4]. For $z/\delta<0.6$ the vertical turbulence intensities are much smaller than predicted by Equation [3.4]. The vertical turbulence intensities are almost constant over the depth at the stations, though it is relatively higher at station 2 compared to station 1. It is also interesting to note that the effect of bed roughness is negligible on w'/u_*.

Figure 3.9(a) and 3.9(b) show the profiles of the non-dimensional turbulent kinetic energy k/u_*^2 at stations 1 and 2, respectively. Smooth and rough bed profiles of k/u_*^2 are compared to Equation [3.5]. The values of k/u_*^2 at $z/\delta<0.4$ are 5-10% higher on the smooth bed, while these are 5-10% smaller on the rough bed than Equation [3.5] predicts. However, for $z/\delta>0.4$ the turbulent kinetic energy on both smooth and rough beds is much higher than predicted by Equation [3.5]. The magnitudes of k/u_*^2 at station 2 are higher than those at station 1.

3.3.3 *Primary Reynolds stress*

Profiles of normalized Reynolds stresses $-\overline{uw}/\overline{u_*}^2$ at station 1 are plotted versus the normalized water depth z/δ in Figure 3.10, where $\overline{u_*}$ is the mean friction velocity across the channel bed. The linear stress profile expected for a wide open channel is also plotted for comparison. The maximum values of the normalized Reynolds stresses occur near the bed, whereas the magnitudes of $-\overline{uw}/\overline{u_*}^2$ are very small negative for $z/\delta>0.6$ (i.e. $z/H>0.4$). Similar results were presented by Nezu and Nakagawa (1993) for a smooth narrow open channel ($B/H=2$), where the maximum $-\overline{uw}$ occurred near the bed in the central part of the channel and $-\overline{uw}_{\max}=1.1\,\overline{u_*}^2$, zero at $z/H=0.65$ and negative above. Tominaga et al. (1989), stated that the negative region of $-\overline{uw}$ appears near the free surface and near side wall in narrow rectangular channel. They argued that the negative region corresponds well with the region of negative velocity gradient of $\partial U/\partial z$ near the surface due to velocity dip. However, the mean longitudinal velocity profiles of the present study (Fig. 3.1 and 3.2) do not exhibit velocity dip.

For the present experiments with B/H=5.5, the maximum $-\overline{uw}$ is equal to $0.5\overline{u_*}^2$ on the smooth bed and $0.96\overline{u_*}^2$ on the rough bed (Fig. 3.10). If we compare the bed shear stresses at the center of the channel with the corresponding Reynolds stress profile, a huge difference between τ_0/ρ and $-\overline{uw}_{max}$ can be observed. For smooth bed τ_0/ρ at the channel center is about 2 times of $-\overline{uw}_{max}$ and for rough bed it is about 1.5 times of $-\overline{uw}_{max}$. This discrepancy can be attributed to the turbulence driven secondary currents.

The observations of Steffler et al. (1985) for B/H=5-12.3 do not agree with the above observations. They reported that the values of u_* computed from velocity profiles and stress profiles agree within ±5% for the entire range of aspect ratio. They also reported that for B/H=5 the distribution of Reynolds stress over the depth in the central region was linear except very close to bed, but that the distribution was complicated away from the centerline.

A theoretical explanation in favor of a non-linear stress profile for narrow open channel can be obtained from Nezu and Nakagawa (1993). It is well known that the primary Reynolds stress in plane 2D flows follows a linear relationship except very close to the bed. If we consider that the boundary layer intersects the water surface, i.e. $\delta=H$ the linear relationship for turbulent shear stress can be expressed as:

[3.6] $$\frac{\tau_{uw}}{\rho} = gS_f(H-z) = u_*^2\left(1-\frac{z}{H}\right)$$

However, for the flows with secondary currents the primary Reynolds stress deviates from this linear relationship. For such cases, Nezu and Nakagawa (1993) derived the following relationship by integrating the streamwise momentum equation in both the vertical and spanwise directions:

$$[3.7]\quad \frac{\tau_{uw}}{\rho} \equiv -\overline{uw} + \upsilon\frac{\partial U}{\partial z} = \underbrace{gS_f(H-z)}_{\text{G}} + \underbrace{\int_H^z W\frac{\partial U}{\partial z}dz}_{\text{SC1}} + \underbrace{\int_H^z V\frac{\partial U}{\partial y}dz}_{\text{SC2}} + \underbrace{\int_H^z \frac{\partial}{\partial y}\left(\frac{-\tau_{uv}}{\rho}\right)dz}_{\text{SUV}}$$

In regions where the transverse velocity is almost zero (i.e., $V \approx 0$) except near the channel bed Equation [3.7] can be reduced to Equation [3.8].

$$[3.8]\quad -\overline{uw} = \underbrace{gS_f(H-z)}_{\text{G}} - \underbrace{\int_z^H W\frac{\partial U}{\partial z}dz}_{\text{SC1}} - \underbrace{\int_z^H \frac{\partial \overline{uv}}{\partial y}dz}_{\text{SUV}}$$

From experimental observations Gessner (1973) and Nezu and Nakagawa (1981) found that the transverse gradient of $\overline{uv}$ is negative for upward flow and vice versa. Using these experimental observations Nezu and Nakagawa (1993) did an analysis of magnitude of the terms in Equation [3.8]. They found that the primary Reynolds stress $-\overline{uw}$ deviates appreciably from G depending on the vertical motion of the flow. For an upward flow SC1 is positive and SUV is negative. Therefore, SUV has an additive and SC1 has a subtractive effect on the magnitude of the right hand side of Equation [3.8] for an upward flow. Nezu and Nakagawa (1993) found that $-\overline{uw}$ becomes greater than G in the upward flow and smaller in the downward flow region. Thus they recognized that SUV plays more important role on the magnitude of the primary Reynolds stress $-\overline{uw}$ than the secondary current term SC1.

The bed shear stress τ_0 can be obtained from Equation [3.7] for z=0 and for the boundary condition that W=0 at z=0 and z=H, as follows:

$$[3.9]\quad \frac{\tau_0}{\rho} = \underbrace{gS_f H}_{\text{G}} + \underbrace{\int_0^H \frac{\partial}{\partial y}(-UV)dz}_{\text{SC2}} - \underbrace{\int_0^H \frac{\partial \overline{uv}}{\partial y}dz}_{\text{SUV}}$$

Nezu and Nakagawa (1993) conducted an analysis of magnitude of the terms in Equation [3.9] similar to Equation [3.8]. They found that in an upward flow region τ_0/ρ is less than G, where SC2 and SUV are negative. This indicates that SC2 plays a more important role than does the Reynolds stress term SUV in determining the bed shear stress. Therefore, the contributions of secondary currents to the Reynolds stress $-\overline{uw}$ and to the bed shear stress τ_0/ρ differ significantly from each other.

3.3.4 *Turbulence anisotropy*

Profiles of the ratios of the root mean square turbulent velocities (u'/v', u'/w' and v'/w') at station 1 are presented in Figures 3.11(a) and 3.11(b) for smooth and rough bed, respectively. These ratios are the indicators of turbulence anisotropy. Except for $z/H < 0.4$, the ratio of u'/v' is very close to unity. This indicates that the turbulence in the streamwise and spanwise directions are almost isotropic, especially on rough bed. However, the vertical component of turbulence is 2-3 times smaller than the streamwise and spanwise components on smooth bed. This significant anisotropy is responsible for causing turbulence driven secondary current (see Eqn. [3.1]). The anisotropy of spanwise and vertical turbulence on the rough bed is relatively less significant, although the streamwise turbulent velocity remains 2-3 times larger than the vertical turbulent velocity. According to Equations [3.2] to [3.4] the ratios of the root mean square velocities for 2D turbulent flows in wide open channel are $u'/v'=1.4$, $u'/w'=1.8$ and $v'/w'=1.28$. This indicates that the turbulence anisotropy in a narrow open channel flow is quite different from that in wide open channel flows.

In Figures 3.12(a) and 3.12(b) profiles of the root mean square turbulent velocities at station 2 are plotted for smooth and rough bed, respectively. If we compare the respective profiles of Figure 3.11 and 3.12, it can be observed that there is almost no considerable difference in turbulence anisotropy at station 2 as observed at station 1.

3.3.5 *Production term for turbulence driven secondary current*

Several researchers explained with the help of Equation [3.1] that the gradients of $(\overline{v^2} - \overline{w^2})$ in the vertical and spanwise directions are responsible for the production of secondary current in a straight channel (e.g. Nezu and Nakagawa 1984). Figure 3.13(a) shows vertical profiles of the normalized secondary current production term $(\overline{v^2} - \overline{w^2})/\overline{u_*}^2$ at station 1 for flows on smooth and rough bed. Figure 3.13(b) shows the vertical profiles of $(\overline{v^2} - \overline{w^2})/\overline{u_*}^2$ at station 2. It can be noticed from Figure 3.13(a) and 3.13(b) that the vertical gradients of normal stresses $(\overline{v^2} - \overline{w^2})$ are large near the bed and towards the free surface. This is because of higher values of spanwise turbulence v'/u_* and smaller values of vertical turbulence w'/u_* near the bed and the free surface [see Fig. 3.7 and 3.8]. If we compare the profiles in Figure 3.13(a) and 3.13(b) for $z/H>0.4$, it can be observed that the effect of the free surface on the vertical gradients of turbulent normal stress reduces away from the channel center for both smooth and rough bed. Tominaga et al. (1989) also reported similar observations for rectangular and trapezoidal open channels. It can be observed from Figure 3.13(a) and 3.13(b) that the magnitudes of $(\overline{v^2} - \overline{w^2})/\overline{u_*}^2$ for similar flows on smooth and rough beds are significantly different, but the gradients of $(\overline{v^2} - \overline{w^2})/\overline{u_*}^2$ in spanwise direction are greater near the free surface compared to near-bed region for both smooth and rough beds. However, greater differences in magnitudes of $(\overline{v^2} - \overline{w^2})/\overline{u_*}^2$ near the free surface across the channel on smooth bed cause higher gradient. It is interesting to note that the vertical gradients of $(\overline{v^2} - \overline{w^2})$ are strong but of opposite sign towards the bed and the free surface from the central region of the channel for both smooth and rough beds [Fig. 3.13(a)], but such change in gradient diminishes at station 2 especially for smooth bed [Fig. 3.13(b)]. Consequently the overall significance of the gradients of $(\overline{v^2} - \overline{w^2})$ is found to be stronger on smooth bed. Therefore, bed roughness can be considered to have a preventive effect on the turbulence driven secondary current. Thus the streamwise vorticity or in other words, the cellular current is stronger on smooth bed for similar flow in a narrow open channel.

3.3.6 *Dissipation term for turbulence driven secondary current*

In Figure 3.14(a) and 3.14(b) profiles of the normalized secondary current dissipation term $-\overline{vw}/\overline{u_*}^2$ are plotted for smooth and rough bed flows at station 1 and 2, respectively. For both stations on smooth and rough beds $-\overline{vw}/\overline{u_*}^2$ values are negative or close to zero. Figure 3.14(a) shows a gradual decrease in $-\overline{vw}/\overline{u_*}^2$ from a value of zero near the bed with increasing z/H for the smooth bed. However, the trend is opposite for the rough bed, with a sharp increase in $-\overline{vw}/\overline{u_*}^2$ with increasing z/H from a high negative value near the bed. The data in Figure 3.14(b) for the rough bed at station 2 are more scattered, although the smooth bed results are quite similar to those at station 1.

3.3.7 *Correlation of the primary Reynolds stress with turbulence*

There are two correlation coefficients that indicate the degree of similarity of the primary Reynolds stress with turbulent velocities and kinetic energy (Nezu and Nakagawa 1993), which can be defined as: $R_t \equiv -\overline{uw}/u'w'$ and $R_k \equiv -\overline{uw}/2k$. Figure 3.15 shows profiles of R_t for smooth and rough beds at station 1. For 2D flow the value of R_t near the bed ($z/\delta<0.1$) is 0.3-0.4, then it remains constant at about 0.4-0.5 in the intermediate region ($0.1<z/\delta<0.7$) and finally it decreases in the free surface region (Nezu and Nakagawa 1993). From the present experimental results, the variation of R_t is quite different for both smooth and rough beds, except the magnitudes near the bed. The value of R_t near the smooth bed is about 0.3 which decreases to zero at $z/\delta=0.5$. On the other hand, the values of R_t on rough bed increases from 0.35 to 0.4 near the bed, then decreases to zero at $z/\delta=0.7$.

Figure 3.16 shows profiles of R_k for smooth and rough bed at station 1. It can be observed from Figure 3.15 and 3.16 that the variations of the two correlations (R_t and R_k) are similar. For 2D flow the value of R_k at $z/\delta<0.1$ is 0.08-0.12, remains constant at about 0.12-0.16 at the intermediate depths ($0.1<z/\delta<0.7$) and finally decreases sharply in the free surface region (Nezu and Nakagawa 1993). However, the present experimental results show that the turbulence driven secondary current reduces the correlation between the primary Reynolds stress and the turbulent kinetic energy, especially on smooth bed.

The maximum value of R_k is about 0.05 for smooth bed, and 0.1 for rough bed. However, this correlation reduces to zero for z/δ=0.6-0.7.

3.4 Conclusions

Turbulent flow characteristics in a straight rectangular open channel with small aspect ratio (B/H=5.5) are compared with those of a wide rectangular open channel. The present experimental results show that the turbulence driven secondary currents can alter the turbulent flow structure in a straight rectangular open channel. The mean velocity profile at the channel center follows the law of the wall up to the intermediate flow region on both smooth and rough beds. However, non-homogenous and anisotropic turbulent flow is observed in the channel that results secondary currents. In the present experiments the longitudinal and spanwise turbulence intensities at the channel center are found higher than those in 2D flows in the upper flow region (z/δ>0.5). However, the near bed (z/δ<0.3) turbulence intensity of the vertical component is much smaller when compared to that in a 2D flow. Ratio of streamwise and spanwise turbulent velocity components to the vertical component on the center plane remains 2-3 for flow on smooth bed. The bed roughness is found to suppress this anisotropy by 20-25%.

The turbulent kinetic energy at the channel center is found to vary similar to the flow in wide open channel up to mid-depth of flow. The upper flow region (z/δ>0.5) is found to contain considerably higher (2-3 times) turbulent kinetic energy compared to 2D flows. The bed roughness is found to reduce the turbulent kinetic energy as observed for similar flow on smooth bed.

The primary Reynolds stress is the turbulence parameter that has been found most different from its counterpart in wide open channel flow. The conventional theory of a linear variation of primary Reynolds stress in plane 2D flows does not apply for a narrow channel. The magnitude of turbulent shear stress near the bed is not comparable to the magnitude of bed shear stress in narrow open channel flow. In the present study, τ_0/ρ at the channel center is about 2 times of $-\overline{uw}_{max}$ on a smooth bed and it is about 1.5 times

$-\overline{uw}_{\max}$ on a rough bed. However, the maximum turbulent shear stress is equal to $0.5\overline{u_*}^2$ on smooth bed and $0.96\overline{u_*}^2$ on rough bed. As a result, the correlations of turbulent shear stress with turbulence itself are quite different from those of two-dimensional open channel flow.

The vertical variation of the production term of turbulence driven secondary current reveals that production is prominent near the bed and the free surface. However, the magnitudes of the secondary current production term are found to be significantly less on a rough bed. The vertical variation of the dissipation term of turbulence driven secondary current also indicates that bed roughness tends to suppress the development of secondary currents.

Table 3.1 Friction Velocities and Bed Shear Stress Values

Experiment	Station 1 (Center plane)				Station 2 (Quarter plane)		Mean shear properties of the flow	
	From logarithmic profile		From yaw-type Preston tube		From logarithmic profile			
	u_* (mm/s)	τ_0 (N/m^2)	u_* (mm/s)	τ_0 (N/m^2)	u_* (mm/s)	τ_0 (N/m^2)	$\overline{u_*}$ (mm/s)	$\overline{\tau_0}$ (N/m^2)
Smooth bed	10.01	0.100	10.74	0.1155	9.48	0.0898	9.48	0.0898
Rough bed	12.00	0.144	11.98	0.1435	10.14	0.1029	10.14	0.1029

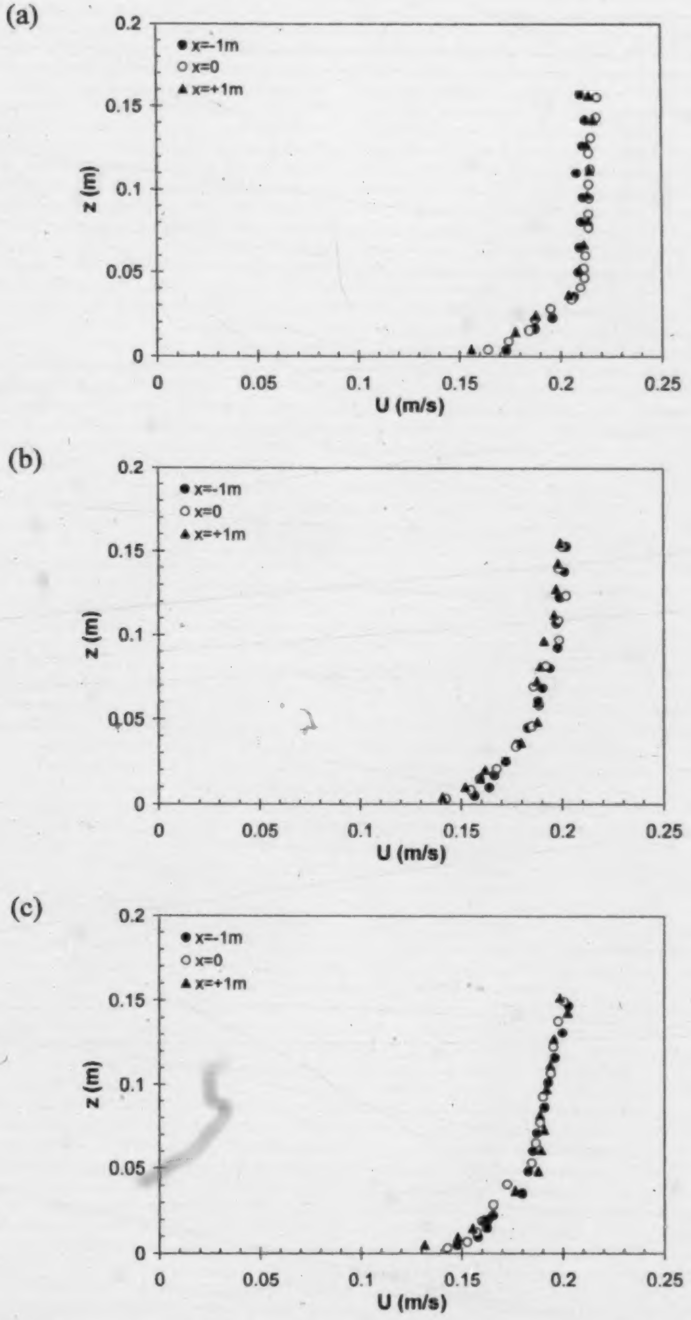

Fig. 3.1 Mean velocity profiles on smooth bed; at (a) *y*=0, (b) *y*=-0.3m, and (c) *y*=+0.3m

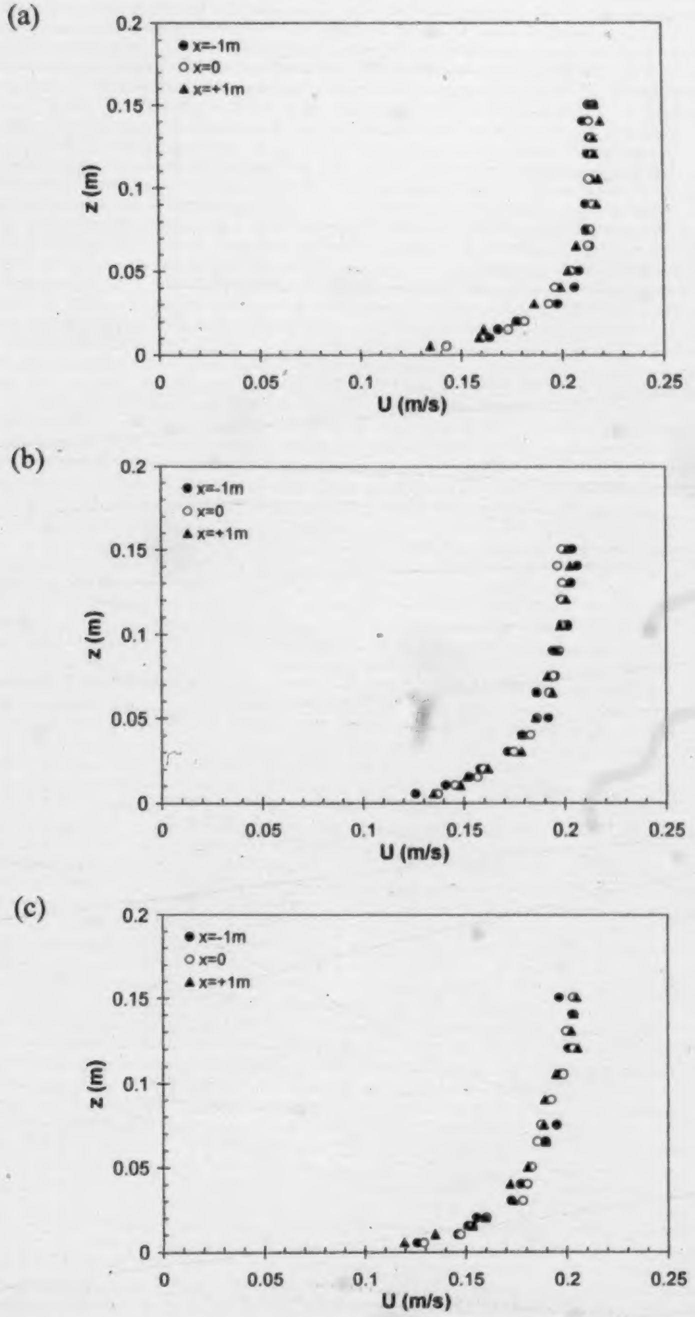

Fig. 3.2 Mean velocity profiles on rough bed; at (a) *y*=0, (b) *y*=-0.3m, and (c) *y*=+0.3m

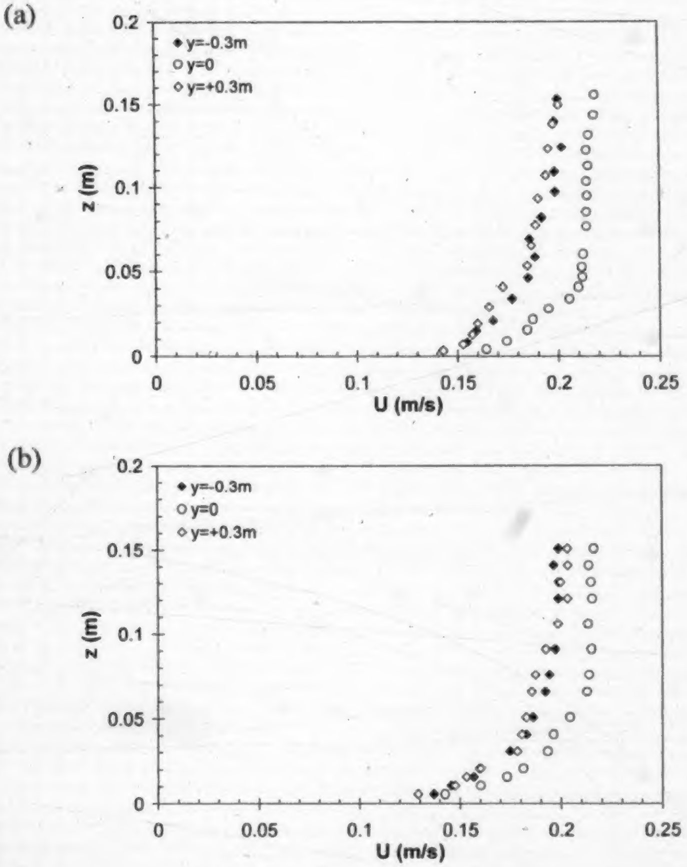

Fig. 3.3 Mean velocity profiles at x=0; on (a) a smooth bed, and (b) a rough bed

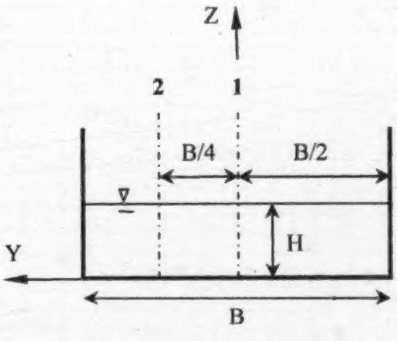

Fig. 3.4 Relative location of the velocity measurement stations

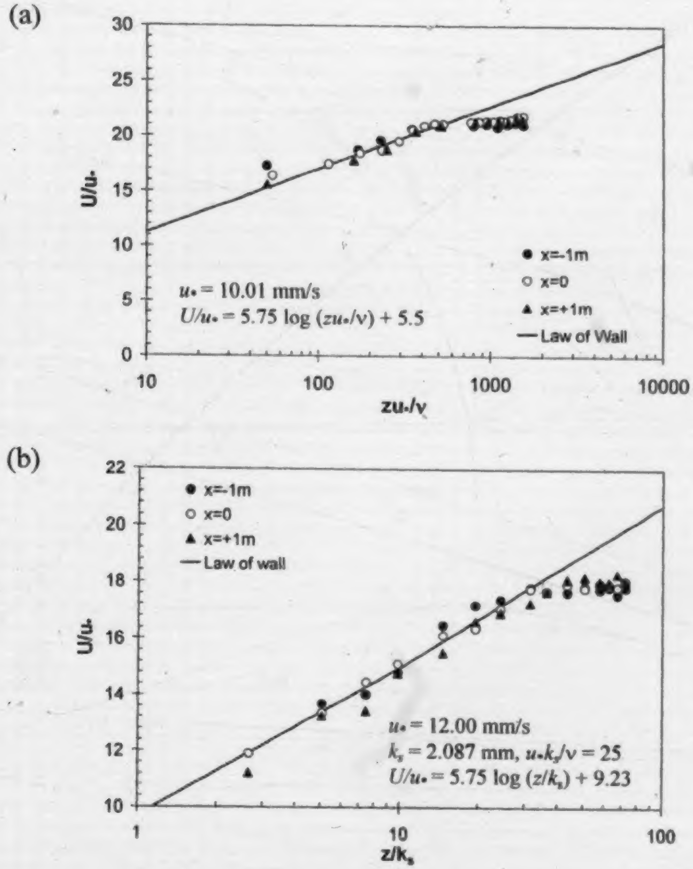

Fig. 3.5 Logarithmic distribution of streamwise mean velocity on (a) a smooth bed; (b) a rough bed

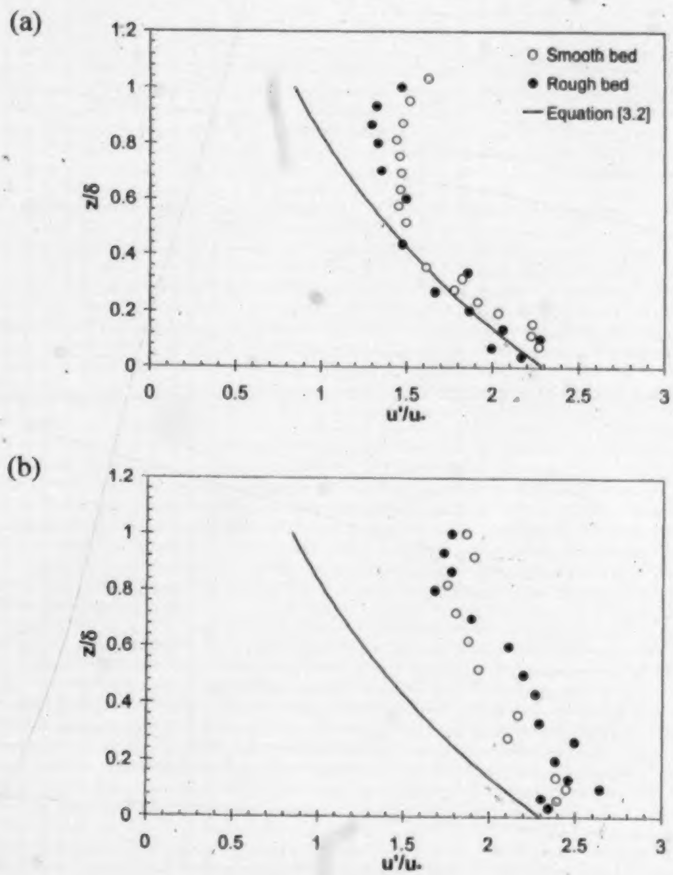

Fig. 3.6 The normalized root mean square velocities, *u'/u** versus the normalized depth, *z/δ*, at (a) station 1; (b) station 2

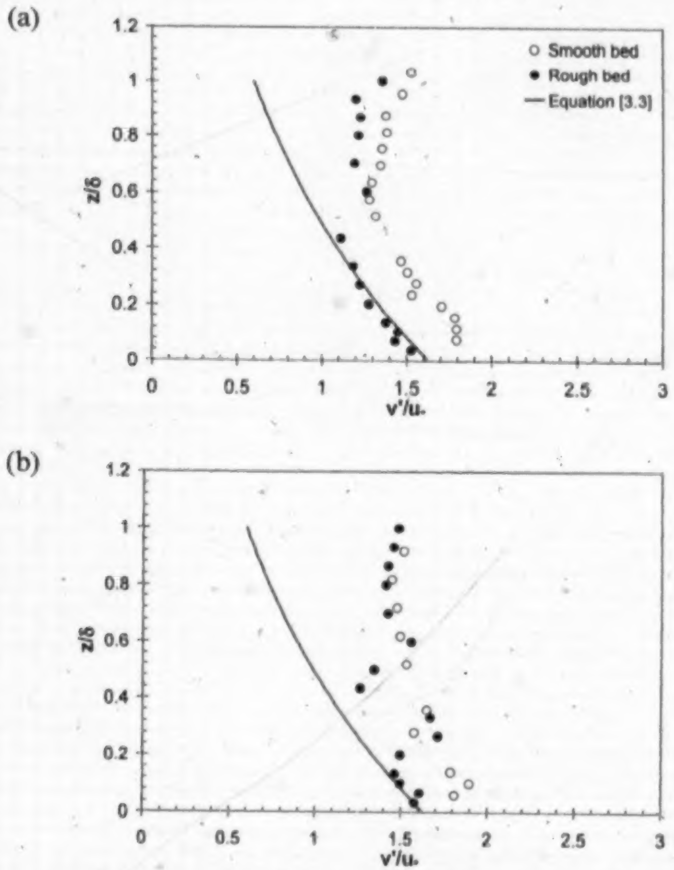

Fig. 3.7 The normalized root mean square velocities, v'/u_* versus the normalized depth, z/δ, at (a) station 1; (b) station 2

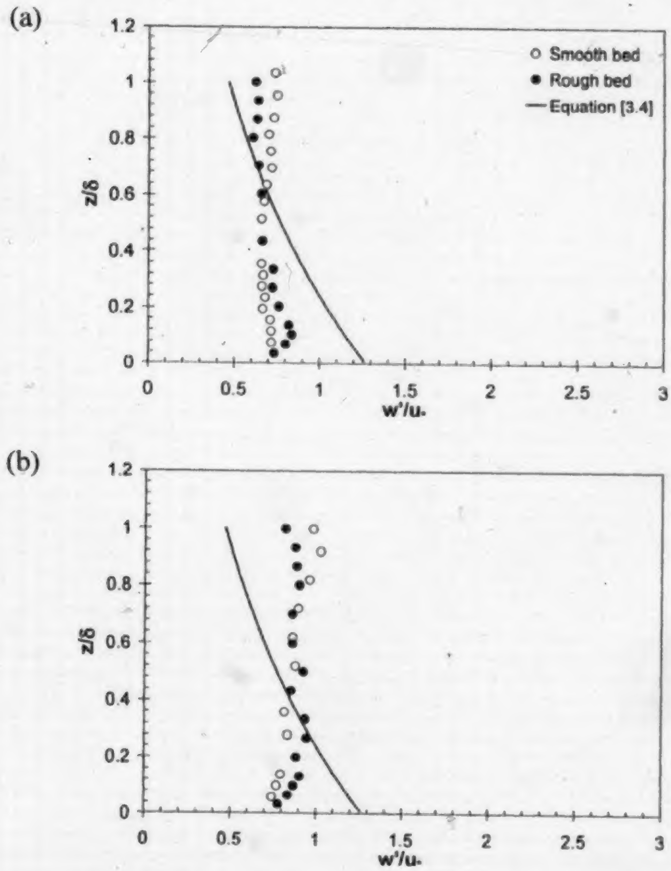

Fig. 3.8 The normalized root mean square velocities, w'/u_* versus the normalized depth, z/δ, at (a) station 1; (b) station 2

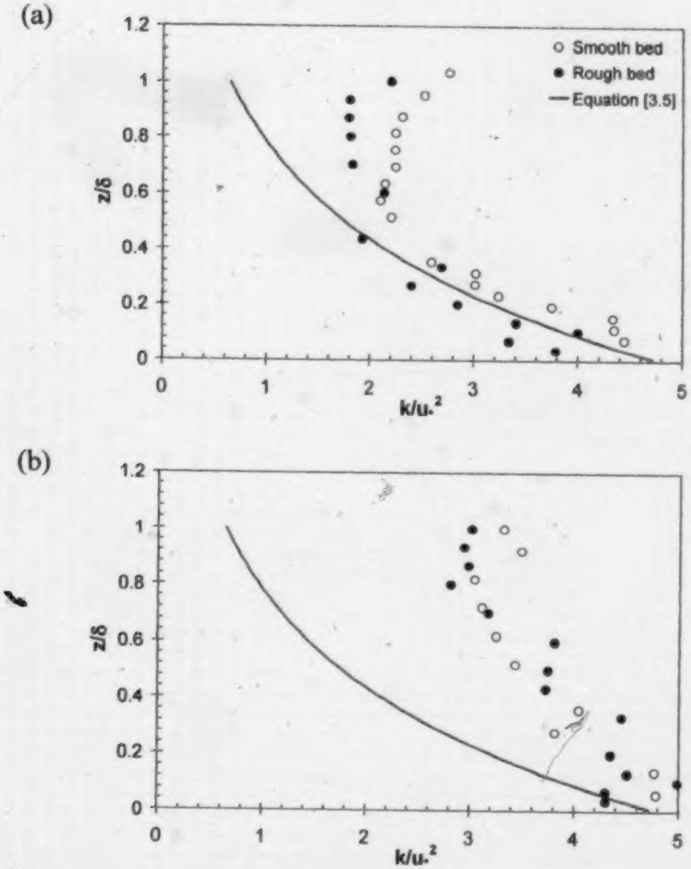

Fig. 3.9 The non-dimensional turbulent kinetic energy, k/u_*^2 versus the normalized depth, z/δ, at (a) station 1; (b) station 2

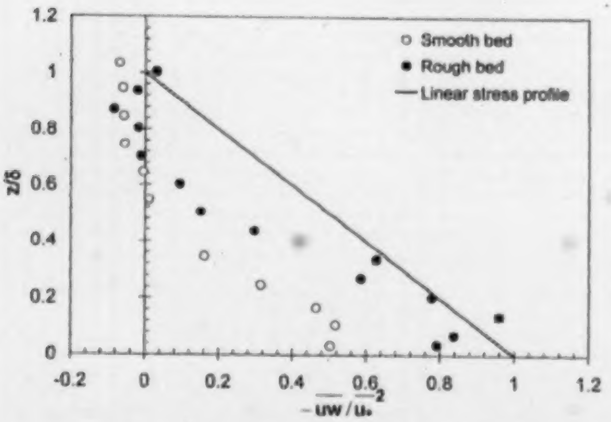

Fig. 3.10 The normalized primary Reynolds stress, $-\overline{uw}/\overline{u_*}^2$ versus the normalized depth, z/δ, at station 1

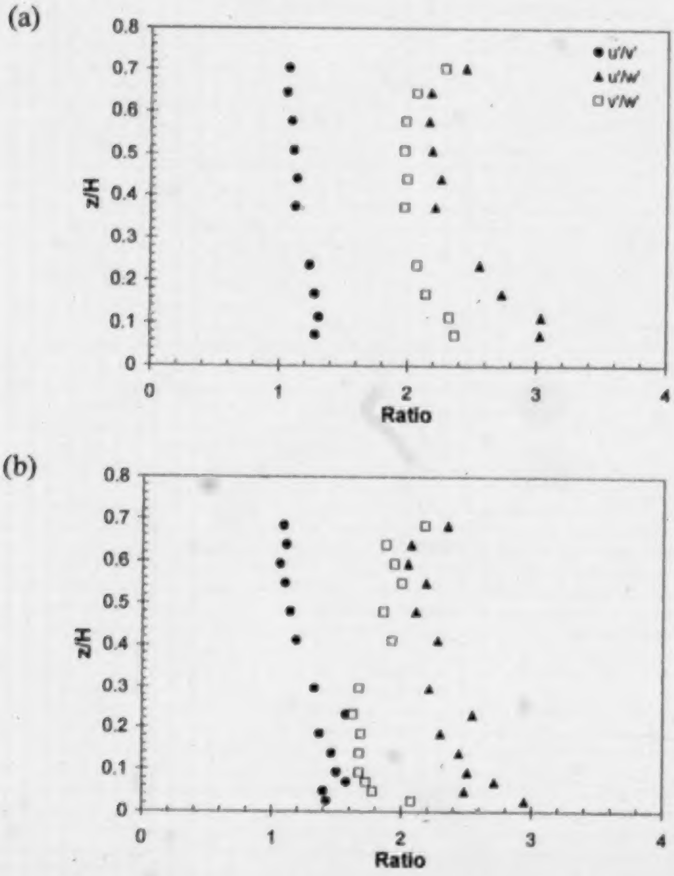

Fig. 3.11 Ratios of turbulence anisotropy on (a) smooth bed; (b) rough bed at station 1

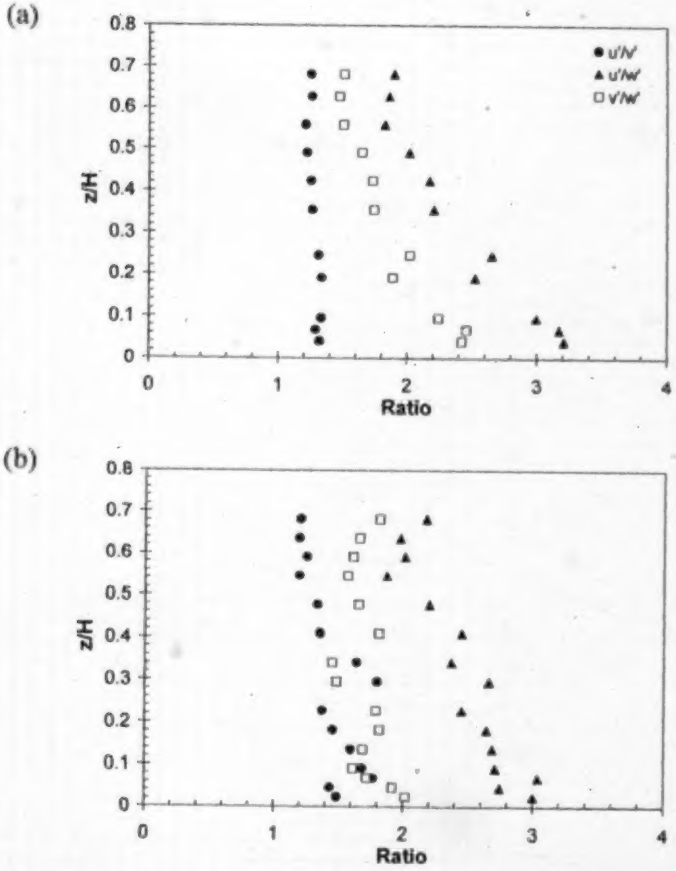

Fig. 3.12 Ratios of turbulence anisotropy on (a) smooth bed; (b) rough bed at station 2

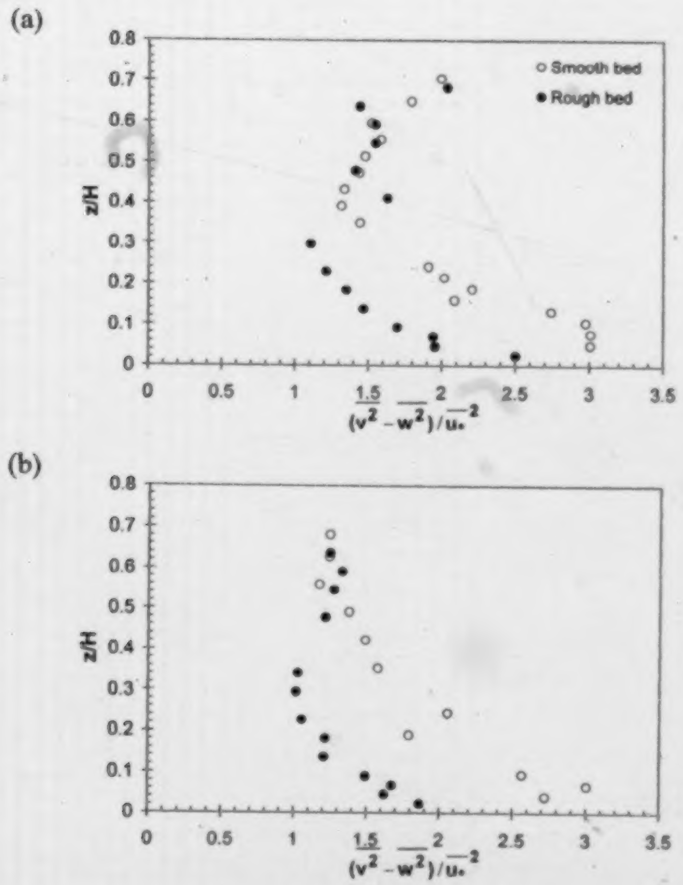

Fig. 3.13 The normalized secondary current production term versus the normalized depth, *z*/*H*, at (a) station 1; (b) station 2

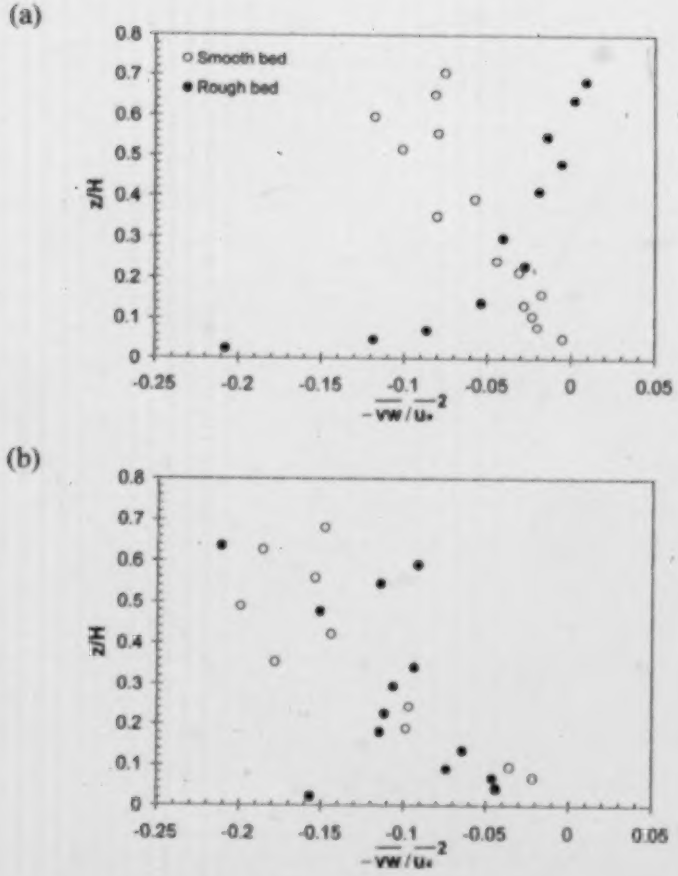

Fig. 3.14 The normalized secondary current dissipation term versus the normalized depth, *z*/*H*, at (a) station 1; (b) station 2

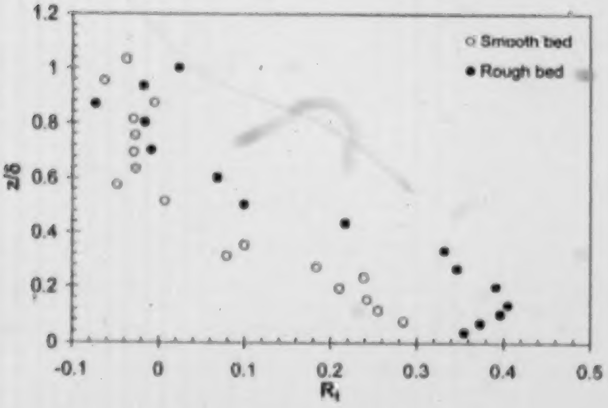

Fig. 3.15 Correlation coefficient, R_t versus the normalized depth, z/δ, at station 1

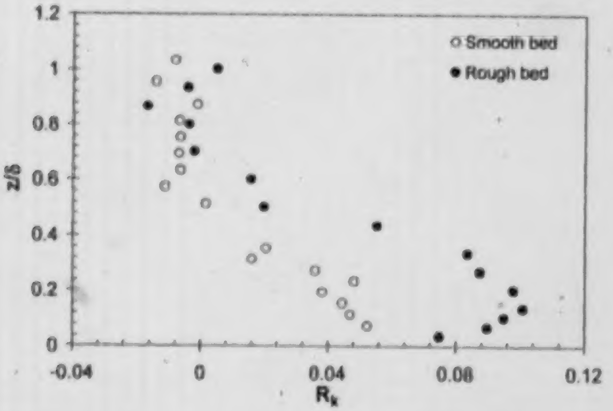

Fig. 3.16 Correlation coefficient, R_k versus the normalized depth, z/δ, at station 1

3.5 References

Demuren, A. O., and Rodi, W. (1984). "Calculation of turbulence-driven secondary motion in non-circular ducts." Journal of Fluid Mechanics, 140, 189-222.

Einstein, H. A., and Li, H. (1958). "Secondary currents in straight channels." Trans. American Geophysical Union, 39, 1085-1088.

Gessner, F. B. (1973). "The origin of secondary flow in turbulent flow along a corner." Journal of Fluid Mechanics, 58, 1-25.

Knight, D. W., Demetriou, J. D., and Hamed, M. E. (1984). "Boundary shear in smooth rectangular channels." Journal of Hydraulic Engineering, 110(4), 405-422.

Knight, D. W., and Patel, H. S. (1985). "Boundary shear in smooth rectangular ducts." Journal of Hydraulic Engineering, 111(1), 29-47.

Nakagawa, H., Nezu, I., and Ueda, H. (1975). "Turbulence of open channel flow over smooth and rough beds." Journal of JSCE, 241, 155-168.

Nezu, I. (1977). "Turbulent structures in open-channel flows." PhD thesis, Kyoto University, Japan.

Nezu, I. (2005). "Open-channel flow turbulence and its research prospect in the 21st century." Journal of Hydraulic Engineering, 131(4), 229-246.

Nezu, I., and Nakagawa, H. (1981). "Coherent structures in turbulent open-channel flows." *Proc.. of 2nd Symposium on Geophysical Turbulent Flows*, National Institute for Environmental Studies, Japan, 1-68.

Nezu, I., and Nakagawa, H. (1984). "Cellular secondary currents in straight conduit." Journal of Hydraulic Engineering, 110(2), 173-193.

Nezu, I., and Nakagawa, H. (1993). *Turbulence in open-channels*, IAHR-monograph, Balkema, Rotterdam, The Netherlands.

Nezu, I., Nakagawa, H., and Rodi, W. (1989). "Significant difference between secondary currents in closed channels and narrow open channels." *Proc. of 23rd IAHR Congress*, Vol. A, Ottawa, Canada, 125-132.

Nezu, I., and Rodi, W. (1985). "Experimental study on secondary currents in open channel flow." *Proc. of 21st IAHR Congress*, Vol. 2, Melbourne, Australia, 115-119.

Nezu, I., and Rodi, W. (1986). "Open-channel flow measurements with a Laser Doppler Anemometer." Journal of Hydraulic Engineering, 112(5), 335-355.

Nezu, I., Tominaga, A., and Nakagawa, H. (1993). "Field measurements of secondary currents in straight rivers." Journal of Hydraulic Engineering, 119(5), 598-614.

Rajaratnam, N. and Muralidhar, D. (1969). "Boundary shear stress distribution in rectangular open channel." La Houille Blanche, 6, 603-609.

Schlichting, H. (1968). *Boundary-layer theory*, 6th Edition, McGraw-Hill Book Company, NY, USA.

Steffler, P. M., Rajaratnam, N., and Peterson, A. W. (1985). "LDA measurements in open channel." Journal of Hydraulic Engineering, 111(1), 119-130.

Tominaga, A., Nezu, I., Ezaki, K., and Nakagawa, H. (1989). "Three-dimensional turbulent structure in straight open channel flows." Journal of Hydraulic Research, 27(1), 149-173.

Chapter 4: Skewed Turbulent Boundary Layer around Cylinders

4.1 Introduction

The study of flow around bluff bodies in open channels has been of interest for many decades. For example, knowledge of the flow generated around surface piercing cylinders in open channel is essential in bridge design. In spite of the considerable number of studies of flow around bridge-pier-like objects, our knowledge of flow around submerged bluff bodies remains limited. Flow around submerged bluff bodies in open channels is of interest to engineers because it will lead to improved design of submerged structures such as fish habitat structures and water intakes. Flows around submerged islands are of interest to geophysicists. The principal motivation for this study is to improve our understanding of the flows around simple fish habitat structures.

In the last few decades, there has been an increasing awareness and concern regarding the human impact on stream and riverine ecosystems (Bockelmann et al. 2004). Natural habitats of instream fish species are often destroyed by the altered flow patterns caused by upstream hydraulic structures (Shamloo et al. 2001). Ecological studies (e.g. Statzner and Higler 1986, Kemp et al. 2000) revealed that different instream species can tolerate different ranges of flow velocities, water depths, bed substrates and water quality properties. Secondary currents, turbulence and variation in local velocity and water depth are essential habitat conditions for both the diversity of river benthos and fish species (Bockelmann et al. 2004). Statzner and Higler (1986) and Kemp et al. (2000) found that stream hydraulics is the most important determinant of the instream habitat quality. Therefore, ecological studies (e.g. Maddock 1999, Bockelmann et al. 2004) indicate the need for hydraulic structures that create morphological features and improve fish habitat by creating longitudinal and lateral variations in water depth, velocity, turbulence and bed shear stress. Provision for fish habitat structures in downstream shallow flows is therefore, an integral part of major hydraulic structure projects. There are a variety of fish habitat structures in use; such as groins, V-weirs, pools, single rocks or cluster of rocks. However, at the present there are only rough guidelines available for the design of these structures (e.g. Lowe 1992).

Natural rocks offer a simple solution to provide shelter and food for fish in adverse flow situations by creating an altered flow pattern, nutrient accumulation and biological activity in the wake region. Flow deflection, local scour and the wake created downstream of natural rocks provide refuge for fish. Fish habitat structures are usually built in shallow flows. Therefore, bed roughness and the location of the free surface can influence the flow around habitat structures to a great extent. However, the lack of knowledge of flow hydraulics means that current assessment tools for designing habitat improvement projects cannot include such hydraulic components. The physical habitat simulation program (PHABSIM) developed by the U. S. Geological Survey is a world-wide accepted tool for the prediction of micro-habitat (depth, velocities and channel substrate) conditions in rivers as a function of stream flow, and the relative suitability of those conditions to aquatic life (Waddle 2001). This program uses a one-dimensional hydraulic model to predict water depths and velocities at different cross-sections in a river. Using empirical sets of velocity observations as templates, the velocity distributions are calculated at different cells in a cross-section. Detailed measurements of flow deflection patterns and bed shear stress distributions around objects at different levels of submergence can be used to improve habitat simulation programs, such as PHABSIM.

Study of shallow wakes has received a lot of attention in recent years (e.g. Chen and Jirka 1995, Lloyd and Stansby 1997a and 1997b). In shallow flows, bed friction effects become important and are quantified in terms of a friction length scale, which is usually defined as the ratio of the depth of flow (H) to the skin friction coefficient (C_f). Ingram and Chu (1987) proposed a stability parameter for shallow wakes ($S_w=C_fD/H$, where D is the characteristic length of the wake generator across the flow) as a relative measure of stabilizing effect of bed friction and destabilizing effect of transverse shear. However, there are only a few studies on shallow flows around submerged bluff bodies. Shamloo et al. (2001) studied the mean flow hydraulics in the wake around hemispherical habitat structures in shallow flows, and measured shear stress distributions and scour patterns. They tried many different levels of submergence and finally proposed a set of flow regimes based on flow visualization experiments, as they observed some distinct differences in the flow for certain ranges of submergence ratio. However, Shamloo et al. (2001) did not study the deflected flow around the hemispheres. They varied the depth and discharge for different flow regimes and this made their results difficult to generalize. Albers (1997) studied the scour pattern around a group of hemispheres, and the flow regimes were defined similar to Shamloo et al. (2001) on the basis of submergence ratios. Recently, Burrows and Steffler (2005) also adopted the definitions of flow regimes given by Shamloo et al. (2001) in a numerical study. They used the experimental data of Shamloo et al. (2001) to examine the depth-averaged velocities around individual boulders. In another numerical study, Smith and Foster (2007) studied the wake created by short submerged horizontal cylinders to model submerged pipelines in rivers. They evaluated the time-dependant bed shear stress and used the mean and peak Shields parameters to highlight the processes relevant to scour. Chen and Jirka (1995) classified the instabilities observed in the near-wake region of shallow flows around a surface piercing cylinder. They held the depth constant and used different diameters of the cylinders to investigate wake instability, and finally proposed critical values of the shallow wake stability parameter for different instabilities. Lloyd and Stansby (1997a, 1997b) carried out extensive experimental and numerical investigations on instabilities in shallow wakes behind surface piercing and submerged conical model islands with gentle slopes. In a geophysical study, Ingram and Chu (1987) observed the effect of bottom friction on the wake behind islands in Rupert bay in northern Canada. Arya and Gadiyaram (1986) studied the atmospheric flow and dispersion in the wakes downstream of three-dimensional models of low hills.

Previous experimental studies showed that the analysis of deflected flow in terms of the theories of three-dimensional turbulent boundary layer (3DTBL) could provide valuable understanding of the complex flows around bluff bodies e.g., bridge pier (Ahmed and Rajaratnam 1997b), abutment (Ahmed and Rajaratnam 2000) and groins (Rajaratnam and Nwachukwu 1983). Unfortunately none of these previous studies attempted to analyze the nature of the deflected approach flow around submerged bluff bodies. The deflected approach flow develops a skewed boundary layer (3DTBL) around the object, where both the magnitude and direction of velocity vectors change with the distance from the bed as shown in Figure 4.1. The outer flow (near the free surface) establishes the pressure gradient that controls the behavior of the inner flow (near the bed). The flow approaching a circular cylinder turns under the influence of a lateral pressure gradient which is determined by the potential flow outside the boundary layer or by the outer region of the boundary layer when such potential flow is absent. This causes a skewing of the velocity vectors over the depth and creates streamwise vorticity. Since large variations of velocity usually occur near the bed, all these effects are most pronounced in that region. The slower-moving inner fluid (near bed) with less momentum turns more than the faster moving outer fluid (Ahmed and Rajaratnam 1997a).

The purpose of this study is, therefore, to analyze the deflected mean flow in terms of the theories of 3DTBL to identify and explore the characteristics of flow when the flow deflecting object is submerged. Unlike Shamloo et al. (2001) this study has been conducted using a constant approach flow depth and discharge for different regimes, so that the flow elements can be precisely studied. Flow visualization and direct measurements of bed shear stress around the cylinders were used to investigate the flow separation and scouring potential of the flow around cylindrical objects with different levels of submergence. This chapter presents the study in two parts; Part I shows the results obtained from smooth bed, and Part II shows the results obtained from rough bed. Results of Part I of this chapter are already published by Sadeque et al. (2008) in Journal of Engineering Mechanics, ASCE. The purpose of study in Part II is to investigate the effect of bed roughness in similar flow conditions used in Part I. This study will enhance the knowledge of flow hydraulics around simple habitat structures in natural streams and rivers.

4.2 Theories of Skewed Boundary Layer

Nash and Patel (1972) summarized numerous theories of skewed turbulent boundary layers (3DTBL). The theoretical analysis of skewed boundary layers has not been as successful as that of plane turbulent boundary layers. Our present knowledge of 3DTBL has come largely from experimental observations (Ahmed 2000). Several competing theories of 3DTBL are available in the literature, but due to limitations in application, none of them has yet been accepted as universal (Ahmed 1995). A brief review of the competing theories can be obtained from Ahmed and Rajaratnam (1997a). Definition sketches used for skewed boundary layers (3DTBL) are given in Figure 4.2. The vertical velocity component is assumed to be negligible in 3DTBL; therefore, the theory of 3DTBL is only applicable relatively far away from the object. The wake, the separated flow, the down-flow immediately upstream of cylinder and the up-flow immediately downstream of cylinder cannot be described by the equations of 3DTBL (Ahmed and Rajaratnam 1997a). A brief introduction to several cross-flow and near-wall similarity models is presented herein to facilitate an appreciation of the results of the present study.

4.2.1 *Cross-flow models*

Cross-flow is produced by a lateral pressure gradient and the curvature of streamlines is caused by deflection of the flow. Four different models for describing the cross-flow profiles in 3DTBL are presented below:

a) Prandtl's model

Prandtl (1946) proposed the following equations for the mean streamwise and mean cross flows respectively:

$$[4.1] \quad \frac{U_s}{U_{se}} = G\left(\frac{z}{\delta}\right)$$

$$[4.2] \quad \frac{V_s}{U_{se}} = eG\left(\frac{z}{\delta}\right)g\left(\frac{z}{\delta}\right)$$

where, U_s is the mean velocity at any elevation z along the streamline at the free surface, V_s is the corresponding orthogonal mean velocity, U_{se} is the value of U_s at the free stream, δ is the boundary layer thickness and $e \equiv tan(y_w)$ [see Fig. 4.2(a)]. Prandtl assumed that G and g are universal functions of z/δ.

b) Coles' model

Coles (1956) extended his 2D boundary layer model to the vector form to account for 3DTBL. The mathematical expression of this model is given by,

[4.3] $$\boldsymbol{q} = \boldsymbol{q}_{wall} + \boldsymbol{q}_{wake}$$

where, $\boldsymbol{q}$ is the deflected mean velocity at any elevation z, $\boldsymbol{q}_{wall}$ is the wall component of $\boldsymbol{q}$ along the direction of bed shear stress and $\boldsymbol{q}_{wake}$ is the wake component in the orthogonal direction. Their magnitudes are given by Equation [4.4] and [4.5], respectively,

[4.4] $$\frac{q_{wall}}{q_*} = f\left(\frac{zq_*}{\upsilon}\right)$$

[4.5] $$\frac{q_{wake}}{q_*} = \frac{1}{\kappa}\Pi(x,y)\omega\left(\frac{z}{\delta}\right)$$

where, q_* is the shear velocity, f is the wall function, κ is von Karman's constant, Π is a profile parameter dependent on the outer flow and $\omega(z/\delta)$ is Coles' universal wake function.

c) Johnston's model

Johnston (1960) proposed a model which takes into account the deflection of the main flow (a) as well as the relative skewing of the bottom streamline (γ_w). Johnston's model uses a polar plot as shown in Figure 4.2(c). This model divides the boundary layer into collateral (Region I) and skewed (Region II) zones. The cross-flow is defined by Equation [4.6] and [4.7] in Region I and II, respectively,

[4.6] $$\frac{V_s}{q_e} = e\frac{U_s}{q_e}$$

[4.7] $$\frac{V_s}{q_e} = A\left(1 - \frac{U_s}{q_e}\right)$$

where the parameter A is related to the outer potential flow by,

$$[4.8] \quad A = -2q_e^{\,2} \int_0^{\alpha} \frac{d\alpha}{q_e^{\,2}}$$

For a constant q_e along a streamline, Equation [8] reduces to A=-2α.

d) Perry and Joubert's model

Perry and Joubert (1965) introduced a model which may be described as the three-dimensional counterpart of the velocity defect law for plane turbulent boundary layers. This model can be mathematically expressed as,

$$[4.9] \quad \frac{\mathbf{q_e} - \mathbf{q}}{q_*} = \mathbf{\Pi}'(x, y)\varphi\left(\frac{z}{\delta}\right)$$

where, $\mathbf{q_e}$ is $\mathbf{q}$ at the free stream, $\varphi(z/\delta)$ is the velocity defect function of the undisturbed upstream flow and $\mathbf{\Pi'}$ is a factor similar to Coles' Π and is determined by the outer flow. The magnitude of $\mathbf{\Pi'}$ (i.e. Π') provides the necessary stretching to fit the defect function and its direction gives the direction of ($\mathbf{q_e}$-$\mathbf{q}$). The angle between the vectors $\mathbf{q_e}$ and ($\mathbf{q_e}$-$\mathbf{q}$) is defined as β. Similar to Johnston's (1960) model, Perry and Joubert assumed that the tips of each velocity vector $\mathbf{q}$, will form a triangle with $\mathbf{q_e}$ as shown in Figure 4.2(d).

4.2.2 *Near-wall similarity models*

There are several scalar and complex near-wall similarity models for 3DTBL on a smooth bed. Equation [4.10] shows the general form of the near-wall similarity models, where $\hat{q}$ is the velocity component. It is either only the streamwise component for scalar models or both the streamwise and cross-flow components for complex models.

$$[4.10] \quad q^+ = \frac{\hat{q}}{\hat{q}_*} = \frac{1}{\kappa}\ln\left(\frac{z\hat{q}_*}{\upsilon}\right) + C$$

In Equation [4.10], the velocity component $\hat{q}$ is normalized by an equivalent shear velocity $\hat{q}_*$ and C is a constant. Only one complex model (Chandrashekhar and Swamy 1976) has been used in this study. The equivalent quantities for different models are presented by Ahmed and Rajaratnam (1997a).

4.3 Experimental Setup and Procedure

Cylindrical objects of equal diameter (D = 11.4 cm) and four heights (h) were tested under similar approach flow conditions (discharge 50 L/s) and water depths (H = 22 cm) to create different levels of submergence in an open channel. Submergence levels were selected such that four flow regimes, as defined by Shamloo et al. (2001), can be produced. Definition sketches for four flow regimes are given in Figure 2.8. The experimental flow conditions are summarized in Table 2.1. Smooth painted plywood surface was used as the channel bed for smooth bed experiments. Again, for the rough bed experiments, coarse-uniform 8/12 sand (D_{50}=2.68 mm) was carefully glued on the plywood surface using a thin coating of paint, so that a densely packed sand layer with a thickness of a single grain was achieved. General description of the experimental setup and procedure is given in Chapter 2. The undisturbed flow was first established without the cylinder and the approach flow velocity and bed shear stress were measured [see Chapter 3]. Fully developed undisturbed approach flow was confirmed by comparing the velocity profile at the location of the cylinder with the profiles at two other stations at a distance of 1 m upstream and downstream from the object.

Flow visualization tests were conducted prior to the detailed measurements of velocity and bed shear stress on smooth and rough beds. Red dye (food color) was injected at different points in the water around the cylindrical objects to identify the size and location of different flow elements. Digital images of the flow features were gathered.

A thin yaw-type Preston probe was used for two-dimensional mean velocity and bed shear stress (τ_0) measurements. The yaw probe has three tubes of 1.2 mm external diameter. The nose of the probe is milled so that the face of the central tube is perfectly flat and the side tubes are chamfered at an angle of 45^0. The total head differences between the central tube and each of the side tubes are measured. Thus the probe can measure the 2D velocity at a point. If the probe is placed on the bed it can measure bed shear stress. Details about the configuration and calibration of yaw-type Preston probe are available in Rajaratnam and Muralidhar (1968). The probe was connected to two differential pressure transducers by plastic tubing. Digital recording of the pressure transducer data was accomplished using a Labview (National Instruments) program at a sampling rate of 250 Hz for 2 minutes. Finally, the raw data (i.e. pressure differences) were processed to obtain velocity and bed shear stress using the calibration provided by Rajaratnam and Muralidhar (1968), Patel (1965) and Hollingshead and Rajaratnam (1980).

The 2D velocity measuring stations were chosen close to the objects where the skewed nature of the turbulent boundary layer can be observed, but at same time the stations were far enough from the object such that the vertical component of velocity can be ignored. The velocity measuring stations around the cylindrical objects are shown in Figure 4.3.

4.4 Part I: Smooth Bed Results and Discussions

4.4.1 *Flow visualization test*

The major observations of the flow visualization tests are illustrated by a set of sketches in Figure 4.4. The key variations of the horse-shoe vortex system and the downstream wake can be realized from these sketches. Figure 4.5 is a typical image showing the zone occupied by the horse-shoe vortex around the cylindrical object in Regime-1. Due to the adverse pressure gradient in front of the objects, the flow decelerates before the separation line. The point of separation on the plane of symmetry was detected by injecting dye at several points along the centerline upstream of the object. The point where the dye plume was found to roll up without any axial translation and was eventually swept around the object was considered to be the point of separation or in other words the location of the horse-shoe vortex. This location was not a steady point on the bed; rather it oscillated over a small distance. The mean position of the boundary layer separation, that forms the horse-shoe vortex, occurred in a region from 0.9 to 1 diameter upstream of the object in Regimes 1, 2 and 3. However, the separation occurred further upstream, at about 1.5 to 1.7 diameters from the cylinder in Regime-4. The reason behind this difference in the location of horse-shoe vortex was investigated by injecting dye plumes at different depths upstream of the object. It was observed that the upper fluid particles accelerate and the streamlines pass over the objects when the objects are submerged. On the other hand, there was no such escape route for the streamlines in Regime-4, where the object height was greater than the water depth. Significant downward flow from the upper flow zone on the upstream face of the cylinder in Regime-4 results in a strong backward flow close to the bed, and hence the horse-shoe vortex system moves upstream.

For moderate to deeply submerged cylinders a closed wake downstream of the cylinder was found to be a distinguishable feature of the flow. Dye injected behind the shallow objects was observed to stay confined in a zone with recirculating water. When dye was injected near the top surface of moderate or deeply submerged cylinders, most of the dye was entrained in the zone immediately behind the object where it tended to accumulate in the closed recirculating zone and then gradually diffuse into the outer fluid. Faster moving shear layers create a three dimensional envelope behind the shallow objects in water. Diffusion of dye from the recirculating zone made it difficult to estimate the length of the recirculating wake. It was therefore estimated from the measurements of bed shear stress downstream of the shallow objects. Similar observations were made for Regime-2, but Regimes 3 and 4 did not produce any recirculating wake behind the objects.

For non-submerged and slightly submerged cylinders the vortex street was found to be a characteristic feature of the flow. However, the accelerated shear flow over the top of moderate to deeply submerged cylinders prevented the alternate shedding of the wake vortices. The slightly submerged object in Regime-3 also had a thin layer of accelerated overflow that interfered with the formation of wake vortices and as a result the strength of the vortex system appeared to be weak. The wake bubble in Regime-3 was relatively longer than that of Regime-4. Further the vortex street was relatively wide when compared to that of Regime-4. Strouhal numbers (S), computed on the basis of visual observation of the number of vortices passing a given station for a period of time, were approximately 0.2 for both Regime-3 and Regime-4. Figure 4.6 shows images of the wake in (a) Regime-2, (b) Regime-3, and (c) Regime-4, where alternate vortex shedding can be observed in Regime-3 and Regime-4.

The presence of standing waves immediately upstream of the cylinder was a unique feature of the slightly submerged object in Regime-3. These surface waves are indicators of the surface disturbance caused by the presence of the object in flowing water. Moderate or deeply submerged objects produced much smaller surface disturbances.

4.4.2 *Bed shear stress distribution*

Observations made from the flow visualization tests can be verified from the results of bed shear stress measurements. Inception of reverse flow and zero shear stress at the bed can be used to identify the point of flow separation for two dimensional and axisymmetric flows (Chang 1970). Figure 4.7(a) shows the variation of the normalized mean bed shear stress upstream of the objects on the plane of symmetry. Negative shear stresses indicate flow reversal and the transition from positive to negative shear indicates the point of separation or the upstream edge of the horse-shoe vortex. The boundary layer separation that forms the horse-shoe vortex takes place in a region from 0.9 to 1 diameter upstream of the object in Regime-1, 2 and 3. However, the separation occurs farther upstream, at about 1.5 to 1.7 diameters upstream of the cylinder, in Regime-4.

Figure 4.7(b) shows the variation of the normalized mean bed shear stress downstream of the cylinder in Regime-1 and Regime-2 on the plane of symmetry. Negative shear stresses indicate flow reversal inside the closed wake. Transition from negative to positive shear indicates the point of reattachment of the separated stream impinging on the bed which encloses the recirculating wake. It is evident from Figure 4.7(b) that the length of closed wake in Regime-1 (~2.2D) is considerably larger than that in Regime-2 (~1.4D). The complex interaction between the separated streams from the top and the lateral faces of the cylinder shortens the recirculating wake envelope downstream of moderately submerged objects.

Contours of the normalized mean bed shear stress (τ_0/τ_{00}) around the cylindrical objects in four different regimes subjected to similar flow conditions are plotted in Figure 4.8(a-d), where τ_{00} is the bed shear stress of the approach flow. Bed shear stress (τ_0) increases in the vicinity of the lateral face of the cylinder in all flow regimes. The maximum bed shear stress (τ_{0max}) for Regime-4 is approximately 5.5 times larger than τ_{00}. On the other hand, τ_{0max} is only 3.5 times larger than τ_{00} for Regime-1. Regime-2 and Regime-3 had maximum bed shear stresses of 4.5 to 5 times τ_{00}, respectively. It was observed from flow visualization that the upper fluid particles accelerate and the streamlines pass over the submerged cylinders, while there was no such escape route for the streamlines in Regime-4. As a result the mass flux in the vicinity of the shoulder of the cylinders increases with decreasing level of submergence and consequently the drag on the bed (i.e. bed shear stress) in the vicinity of the shoulder is a maximum in Regime-4. The lateral expanse of increased shear stress is the smallest for Regime-1 and Regime-3. In these two regimes τ_0 falls below 1.5 times τ_{00} at a distance of $1D$ away from the plane of symmetry. Regime-2 has a larger area of increased shear stress and τ_0 falls below 1.5 times τ_{00} at a distance of $1.5D$ in the transverse direction. The largest lateral expanse of increased shear stress ($1.5\tau_0/\tau_{00}$) occurs in Regime-4, where it extends up to a distance of $2D$.

In Figure 4.9, one can observe that the maximum shear and the maximum deflection occur in different flow regimes. The maximum intensity of bed shear stress was observed in Regime-4, but the maximum deflection close to the object occurred in Regime-1. Flow over the entire depth near the lateral face of the object changes direction in Regime-4. It causes an increase in velocity magnitude (V_m) over the entire depth. On the other hand, a considerable portion of flow does not change direction in Regime-1. Therefore, the difference in velocity magnitude between the inner flow (close to bed) and the outer flow (near the free surface) is higher in Regime-1. The profiles of V_m (not shown here) at a station located at $x=-0.5D$ and $y=0.5D$ showed that the difference in velocity magnitude in Regime-1 between the inner and outer streams is about $0.4U_o$, where U_o is the cross-sectional mean velocity, and in Regime-4 it is only $0.2U_o$. In a skewed three-dimensional boundary layer, low velocity layers near the bed turn under the influence of the outer flow. Therefore, the smaller near-bed velocities in Regime-1 experienced greater turning.

For the same reason, the extent of the increased bed shear stress is larger in the transverse direction in Regime-2 as compared to Regime-3.

A similarity analysis has been conducted for the longitudinal profiles of the normalized bed shear stress (τ_0/τ_{00}) for all flow regimes. The results of the similarity analysis are presented in Figure 4.10. The longitudinal (x) and transverse (y) distances are normalized by the diameter (D) of the cylinders. For each flow regime, the variations of $\Delta\tau_0/\Delta\tau_{0m}$ are plotted against X'/D in Figure 4.10(a-1 to d-1), where $\Delta\tau_0 = \tau_0 - \tau_{00}$, $\Delta\tau_{0m} = \tau_{0m} - \tau_{00}$, $X' = x - x_m$, and x_m is the location of maximum bed shear stress (τ_{0m}) along each profile. The data shows scatter in Regime-1 and 2, but upstream of x_m in Regime-3 and 4 there is good similarity, and a mean curve could be drawn to approximately describe the data. The scatter increases downstream of x_m for Regime-3, but it is minimal for Regime-4. The similarity profiles of $\Delta\tau_0/\Delta\tau_{0m}$ are replotted in Figure 4.10(a-2 to d-2) against $\eta_\tau = (X'/D)/[(X'/D)_{1/2}]$, where $(X'/D)_{1/2} = X'/D$ at $\Delta\tau_0/\Delta\tau_{0m} = 0.5$. This improved the similarity of the profiles in the downstream side of x_m for all flow regimes. It is observed from the similarity analyses that the longitudinal profiles of bed shear stress are most similar for Regime-4 since the data collapsed best in this case.

4.4.3 *Analysis of deflected flow in terms of the theories of 3DTBL*

It is essential to know the thickness of the turbulent boundary layer (δ) before any analysis can be completed. By definition (Schlichting 1968), δ is the elevation above the bed where the longitudinal component of velocity (U) equals 99% of the free stream velocity (U_e). The normalized longitudinal velocities (U/U_e) are plotted over the normalized depth z/δ in Figure 4.11(a-d). It has been observed from the experimental results of all the stations in all flow regimes that the magnitudes of U at $z = 15$ cm are almost equal to U_e. Therefore, δ is taken to be 15 cm for the analysis. However, the coarse resolution (5 cm) of the point measurements of velocity away from the bed can result in an uncertainty of ±2.5 cm at different stations. It can be observed from Figure 4.11 that the profiles of U/U_e vs z/δ collapse on each other for most of the stations in all flow regimes, where the exceptions (e.g. stations in the wake) could be the result of relatively strong velocity components in other directions.

Prandtl's Model

The variations of the functions of G and gG (i.e. U_s/U_{se} and $V_s/(U_{se}\tan\gamma_w)$) with z/δ are presented in Figure 4.12. It can be observed from Figure 4.12(a-1) that the velocities in the free stream direction (U_s) are increased or decreased in similar proportion to their respective free stream velocities (U_{se}) at all stations in Regime-1, except stations 6 and 7. The ratio of U_s/U_{se} for $z/\delta \leq 0.3$ (i.e. $z<h$), at stations 6 and 7, could not recover from the effect of the backward flow as these two stations are immediately behind the closed recirculating zone. Figure 4.12(a-2) shows that the outward deflection reaches a maximum at station 4, where $gG\sim1$. Then the flow turns back toward the cylinder at stations 5, 6 and 7. The change in direction of the transverse component of velocity between station 4 and 5 indicates the existence of a vortex about z-axis. However, the flow gradually straightens in the downstream direction.

Similar to Regime-1, in Regime-2 stations 6 and 7 were close to the closed recirculating zone, and hence U_s was smaller relative to U_{se} for $z/\delta \leq 0.7$ (i.e. $z<h$), as observed in Figure 4.12(b-1). However, at station 4 U_s/U_{se} values for $z \leq h$ were relatively higher. The flow was deflected away from the cylinder up to station 3 (Fig. 4.12(b-2)) in Regime-2, but then it turned sharply inward at station 4 with $gG\sim-2$. This represents a relatively strong vortex, compared to Regime-1, about the z-axis between station 3 and 4. The data at subsequent stations indicates that the flow straightened out downstream of the vortex.

Figure 4.12(c-1) shows that the profiles of G (i.e. U_s/U_{se}) vs z/δ collapse together, except for station 7. The flow passing over the top of the object caused the free stream velocities (U_{se}) at station 7 to remain virtually unchanged for $z>h$, but the velocities behind the object at $z \leq h$ were decelerated. The most interesting observation comes from Figure 4.12(c-2). Flow was deflected outward up to station 3, and then the direction changed sharply inward at station 4 and then outward at station 5. The magnitudes of gG reached -1.2 and 4 at stations 4 and 5, respectively. This indicates the existence of a pair of strong alternating vortices about the z-axis. Flow visualization pictures of alternate vortex shedding in Regime-3 also support this observation. In Figure 4.12(c-2) the data for stations 6 and 7 show that the transverse velocity components were approximately zero at these locations (i.e. gG~0). This is because; these two stations fell inside the wake formed by the alternate vortex shedding and this nullified the transverse components.

In Figure 4.12(d-1) the profiles of G vs z/δ at all stations of Regime-4 collapsed together. This indicates that the velocities in the free stream direction (U_s) are increased or decreased in similar proportion to their respective free stream velocities (U_{se}) at all stations in Regime-4. Outward deflection increased to a maximum at station 3 with gG~3.5 (Fig. 4.12(d-2)), and then the flow turned inward at station 4. At downstream stations the flow deflection was decreased. This indicates that there is a vortex between station 3 and 4, but unlike Regime-3 an alternating pair of vortices did not exist between station 4 and 5. This is because the width of the wake is narrower in Regime-4 compared to Regime-3. However, stations 6 and 7 still fell inside the wake and their transverse components were nullified by alternate shedding vortices similar to Regime-3 (Fig. 4.12(d-2)).

Johnston's Model

Johnston's polar plots for all the stations in different flow regimes are produced in Figure 4.13 to 4.16. The properties of a polar plot are illustrated in Figure 4.2(c). The polar plots show the relative deviations of the velocity vectors with respect to the directions of corresponding free stream velocity vector ($\boldsymbol{q_e}$). The direction of local bed shear stress (τ_0) is shown by an arrow in each polar plot. The outward deflected flow has positive V_s/q_e.

In Regime-1 (stations 1 to 4) (Fig. 4.13), the near-bed velocities were deflected more than the free stream velocity in the outward direction, but the upper velocity vectors gradually turned towards the free stream direction. However, at station 5 the near-bed velocity vectors turned towards the cylinder while the upper velocity vectors turned away from the cylinder. This observation indicates that the low pressure in the closed recirculating wake was strong enough to overcome the outward flow caused by the lateral pressure gradient. It is interesting to note that downstream of the closed recirculating wake (stations 6 and 7), near-bed velocities were directed outward, but velocities near the free surface tended to straighten out and were aligned along the channel.

In Regime-2 (stations 1 to 3) (Fig. 4.14), the outward deflections of near-bed velocities were more pronounced compared to the observations in Regime-1. The existence of the collateral and skewed zones in the boundary layer was clearly observed at station 3. Similar to Regime-1, at stations 4 and 5 in Regime-2 the near-bed velocities were directed towards the closed recirculating zone, while the upper flow velocities were directed outward from the cylinder. Observations downstream of the closed recirculating wake (stations 6 and 7) were similar to those of Regime-1, where the near-bed velocities were outward, but the velocities near the free surface tended to straighten out along the channel.

The existence of collateral and skewed zones in the boundary layer can be observed at stations 1 to 3 (Fig. 4.15) in Regime-3. The outward deflections of the near-bed velocities with respect to the free stream velocities were significant at these three stations. However, at stations 4 and 5 the inward near-bed flows were not as strong as those observed in Regime-2. Figure 4.15(f-g) shows that the relative directions of the near-bed velocities with respect to the free stream velocities are quite different at stations 6 and 7. The near-bed velocities were turned outward at station 6 and inward at station 7. This observation suggests that the structure of the wake vortex was not vertical, but inclined. In a study of the instability of the shear layer separating from a cylindrical bluff body, Prasad and Williamson (1997) showed that the end conditions can trigger oblique or parallel shedding of wake vortices. Williamson (1996) reported typical oblique angles to the axis of cylinder of 15-20°.

In Regime-4 (Fig. 4.16), the existence of collateral and skewed zone in the boundary layer was observed at stations 1 and 2. The outward deflections of the near-bed velocities with respect to the free stream velocities were less significant at stations 1 to 3 compared to Regime-2 and Regime-3. However, the inward near-bed flows, at stations 4 and 5, were stronger compared to the other regimes. Similar to Regime-3, at stations 6 and 7 in Regime-4 there were significant differences in the directions of near-bed velocities with respect to free stream velocities, but the velocities were turned inward. This observation suggests that the structure of the wake vortex is still inclined as observed in Regime-3.

4.4.4 *General applicability of the models*

Cross-flow models do not account for S-shaped velocity profiles (Ahmed and Rajaratnam 1997a). Moreover, the 3DTBL models are not capable of describing the flow in the wake of a cylinder. Therefore, the velocity profiles at stations downstream of the cylinders may not satisfy the models. Any evaluation of the models' performance for general applicability should consider this fact.

Prandtl's model is not found satisfactory. Though the profiles of function G collapsed together for most of the stations in all flow regimes, the profiles of the combined function gG do not produce any encouraging results. Johnston's model has only limited applicability to generalize the nature of flow, as only a few stations in Regime-2, 3 and 4 exhibited the expected triangular form with the collateral and skewed zone in the turbulent boundary layer. Coles' wall and wake functions were plotted for all of the stations in the different regimes in Figure 4.17(a-d). It was observed that except for a few downstream stations (e.g. stations 6 and 7), the wall functions were in reasonably good agreement with the theoretical line, for $zq_*/\nu>30$. However, the wake function data do not agree with the theoretical curve. Interestingly, the wake functions at most of the stations have a general trend, which indicates a different form of wake function might be appropriate. Six similarity models were also tested in this study. The tested scalar models include Cole's (1956) model, Johnston's (1960) model, Hornung and Joubert's (1963) model, Pierce and Krommenhoek's (1968) model and Prahlad's (1968) model. The only complex model tested in this study is Chandrashekhar and Swamy's (1976) model. None of the theoretical profiles provided by these models agreed with the experimental profiles (figures are not presented here). Similarly, the complex model performed poorly. The predictions of U were similar to that of the scalar models, and the measured values of V fell far away from the theoretical curves.

Perry and Joubert's model performed better than any other models available for 3DTBL. There are two functions to evaluate the performance of Perry and Joubert's model. These are the defect function and the angular difference $\Delta\beta$ between the vectors $\boldsymbol{q}_e$-$\boldsymbol{q}$ and $(\boldsymbol{q}_e-\boldsymbol{q})_{max}$ in the skewed zone. The defect function can test the validity of the model for predicting the velocity magnitude, while Δβ tests the validity of their assumption of a triangular polar plot (see Fig. 4.2(d)) in 3DTBL. The maximum deflection, compared to the free stream vector, usually occurred for the velocity vector nearest to the bed. Moving upwards the vectors gradually turned towards the free stream direction. As observed in previous studies (e.g. Rajaratnam and Nwachukwu 1983, Ahmed and Rajaratnam 1997b), the tips of the velocity vectors in the skewed zone do not always fall along a straight line. Instead, the tips of the velocity vectors follow a curve. Therefore, when the vectors are more or less skewed, Δβ would be positive and negative respectively. Moreover, in a boundary layer the upper velocities are almost equal in magnitude to the free stream velocity, and therefore a small experimental uncertainty can lead to a large angular deviation (Δβ). For the above reasons, larger values of Δβ along with significant fluctuations can occur in the outer region (usually at $z/\delta>0.5$) of the boundary layer (Ahmed and Rajaratnam 1997b). However, as per Perry and Joubert's model, Δβ should ideally be zero in the outer layer (i.e. the skewed zone).

Defect functions and the variations of Δβ with the normalized depth, z/δ for different flow regimes are plotted in Figure 4.18(a-d). At most stations, except for stations 6 and 7, the experimentally computed defect functions agree reasonably well with the theoretical curve. Submergence of the flow deflecting object did not appear to limit the applicability of the model. The corresponding variations of Δβ for all the measuring stations were also examined. The magnitudes of Δβ were small near the bed, but at $z/\delta>0.2$ they ranged as high as ±20° to 100°. This indicates that the experimental data could not satisfy Perry and Joubert's assumption of triangular polar plot, but as mentioned earlier such high values of Δβ do not necessarily mean poor performance of the model. It was already noted that Johnston's polar plots [see Fig. 4.13 to 4.16] are satisfactory at most upstream stations. Therefore, Perry and Joubert's model performance can be considered reasonably satisfactory for generalizing the nature of the deflected flow.

4.4.5 *Conclusions*

Experimental observations made from flow visualizations, bed shear stress measurements, and velocity measurements were consistent and complementary. Flow visualizations revealed that when the cylinders become more deeply submerged the upstream boundary layer separation point moves closer to the object, and as a result the size of the horse-shoe vortex system becomes smaller. Wake vortices were found to shed in alternate fashion with S~0.2 for the slightly submerged and non-submerged cylinders. The width of the wake, however, was less for the non-submerged cylinder. A closed recirculating wake was found to be a characteristic feature of the flows around moderate to deeply submerged objects. Bed shear stress amplification near the shoulder of the cylinders was common in all flow regimes. However, the relative increase in bed shear stress is found to be inversely related to the level of submergence of the cylinders. Bed shear stress results presented in this paper provide qualitative information on the scour potential of the flow around submerged cylinders. Similar measurements on a rough bed that will be presented in the future will provide additional information on scour potential.

Prandtl and Johnston's cross-flow models were found to be helpful for describing the skewed 3D flow around the cylindrical objects in all four regimes. Except for the stations downstream of the closed recirculating wake, the longitudinal velocities (U) at all depths were found to accelerate or decelerate in similar proportion to their respective free stream velocities (U_e) in all flow regimes. In a test of the general applicability of 3DTBL models to the flow around cylinders in the four flow regimes, Perry and Joubert's velocity defect function performed the best. The experimentally computed defect functions agreed reasonably well with the model except in the wake.

It is evident from this study that a cylindrical object or a natural rock can alter the approach flow in different ways depending on the relative height of the object compared to the flow depth. The observed flow deflection patterns and bed shear stress distributions measured around objects at different levels of submergence will enhance the quality of hydraulic modeling required for river health assessment. This study showed that Perry and Joubert's velocity defect function can be a useful tool for predicting the deflected flow around submerged objects. Specifically the theory can be used to predict the magnitudes of velocity in the deflected flow around fish habitat structures, water intake or outfall structures and submerged islands. As well the present experimental results can serve as a hydraulic data base for future computational modeling of similar flows.

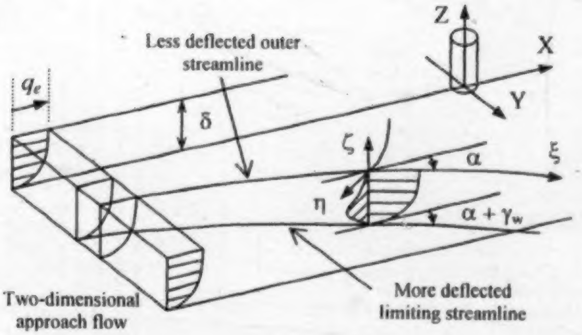
Less deflected outer streamline
Z
X
Y
q_e
δ
ζ
α
ξ
η
α + γ_w
Two-dimensional approach flow
More deflected limiting streamline

Fig. 4.1 Typical skewed turbulent boundary layer (Adapted from Ahmed and Rajaratnam 1997a)

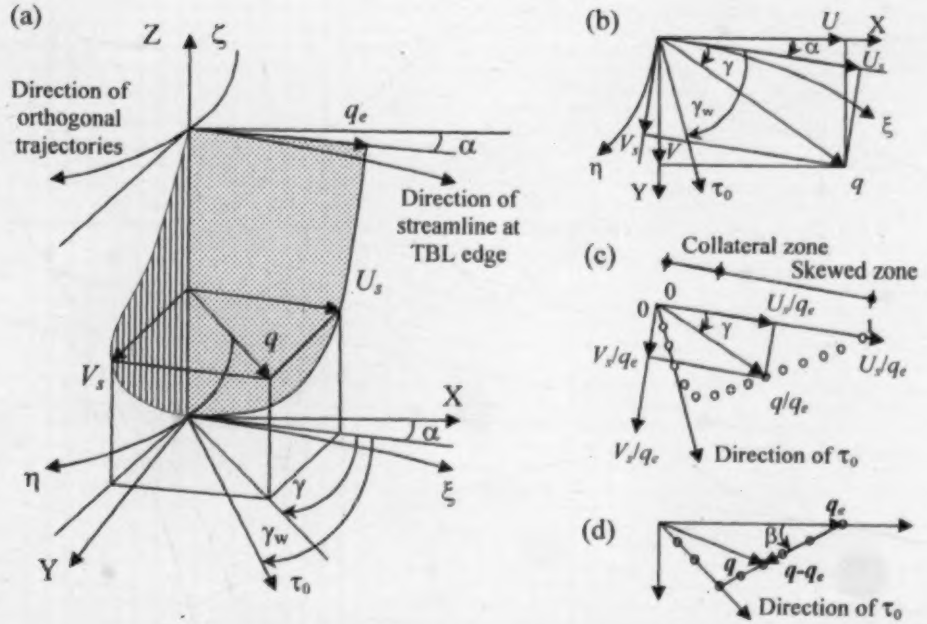
(a)
Z
ζ
Direction of orthogonal trajectories
q_e
α
Direction of streamline at TBL edge
U_s
q
V_s
X
α
η
ξ
γ
γ_w
Y
τ_0
(b)
U
X
α
U_s
γ
γ_w
ξ
V_s
V
η
Y
τ_0
q
(c)
Collateral zone
Skewed zone
0
0
U_s/q_e
γ
V_s/q_e
U_s/q_e
q/q_e
V_s/q_e
Direction of τ_0
(d)
q_e
β
q
q-q_e
Direction of τ_0

Fig. 4.2 Definition sketches of skewed turbulent boundary layer; (a) coordinate system and notations, (b) velocity components, (c) Johnston's polar plot, and (d) Perry and Joubert's model

(Adapted from Ahmed and Rajaratnam 1997a)

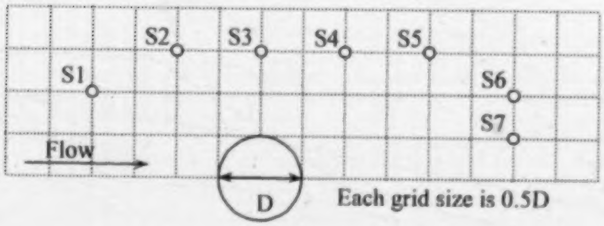
S1
S2
S3
S4
S5
S6
S7
Flow
D
Each grid size is 0.5D

Fig. 4.3 Location of the velocity measuring stations relative to the object

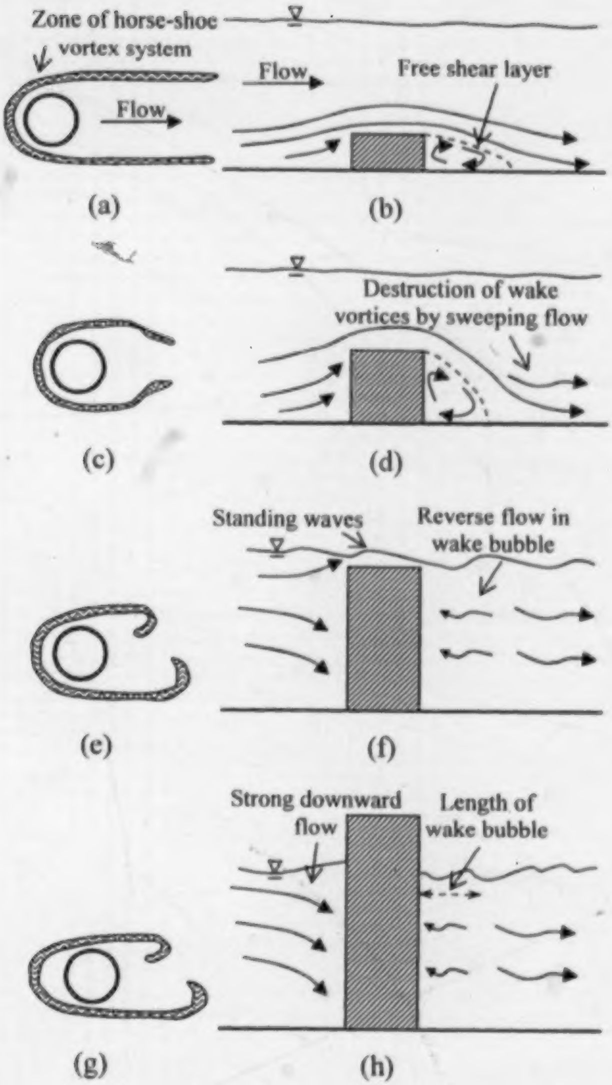
Zone of horse-shoe vortex system
Flow
Flow
Free shear layer
(a)
(b)
Destruction of wake vortices by sweeping flow
(c)
(d)
Standing waves
Reverse flow in wake bubble
(e)
(f)
Strong downward flow
Length of wake bubble
(g)
(h)

Fig. 4.4 Sketches of the horse-shoe vortex system and flow on the POS with respect to the cylinders in (a-b) Regime-1, (c-d) Regime-2, (e-f) Regime-3, and (g-h) Regime-4

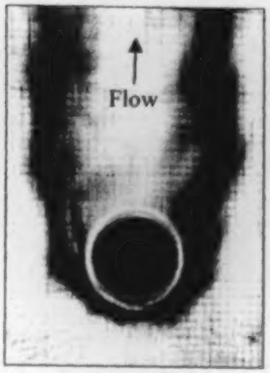

Fig. 4.5 Horse-shoe vortex in Regime-1

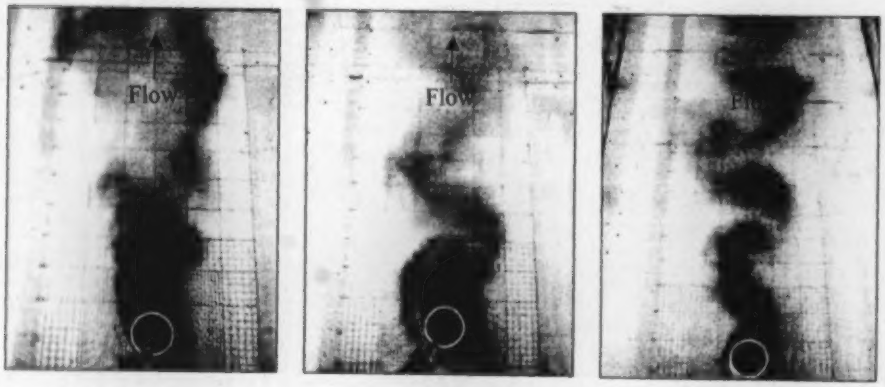

(a) Regime-2 (b) Regime-3 (c) Regime-4

Fig. 4.6 Wakes behind the cylinders

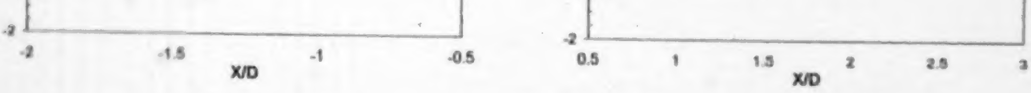

(a) (b)

Fig. 4.7 Normalized mean bed shear stress profiles on (a) the upstream, and (b) the downstream plane of symmetry

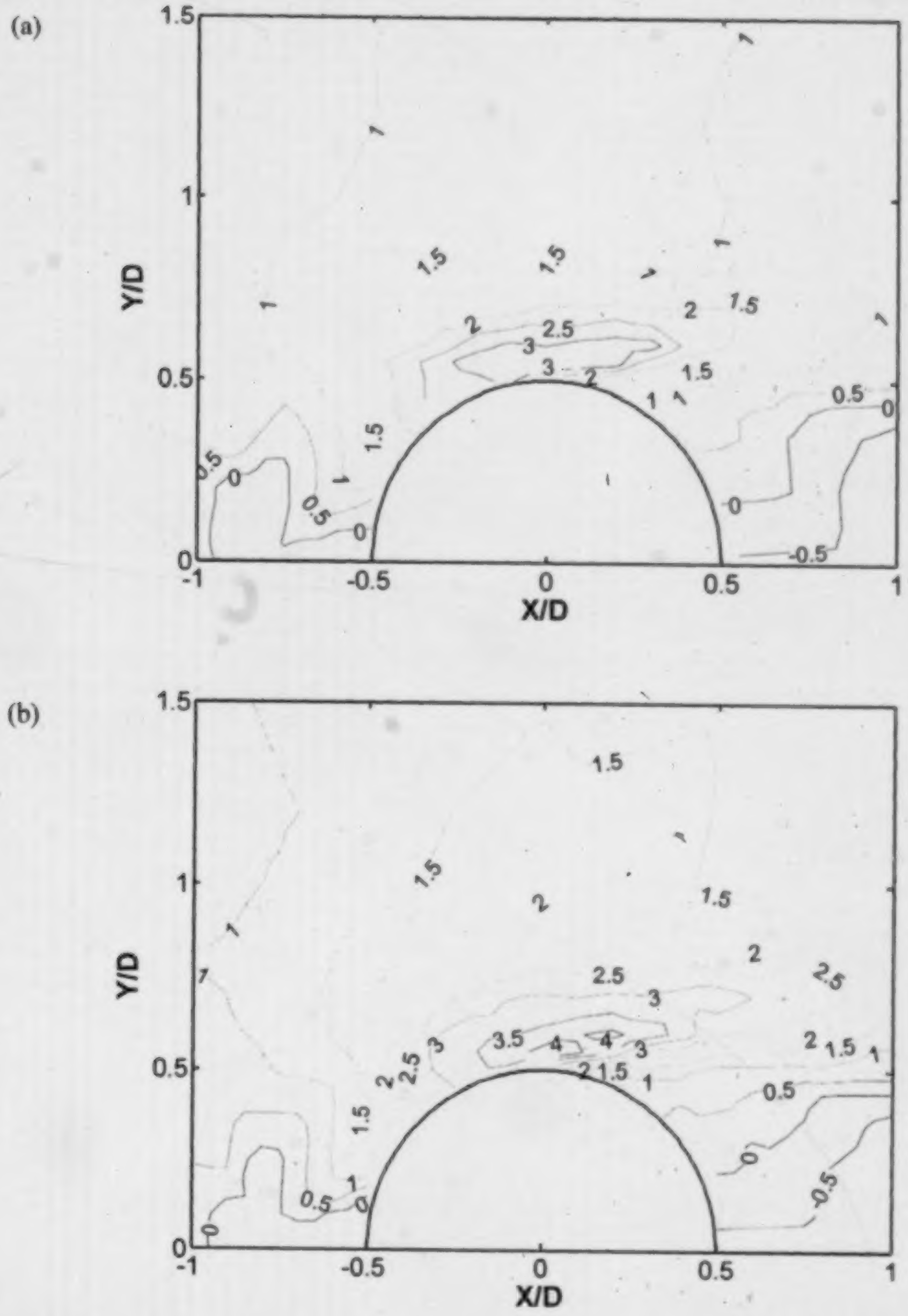

Fig. 4.8 Normalized mean bed shear stress (τ_0/τ_{00}) contours; (a) Regime-1, (b) Regime-2

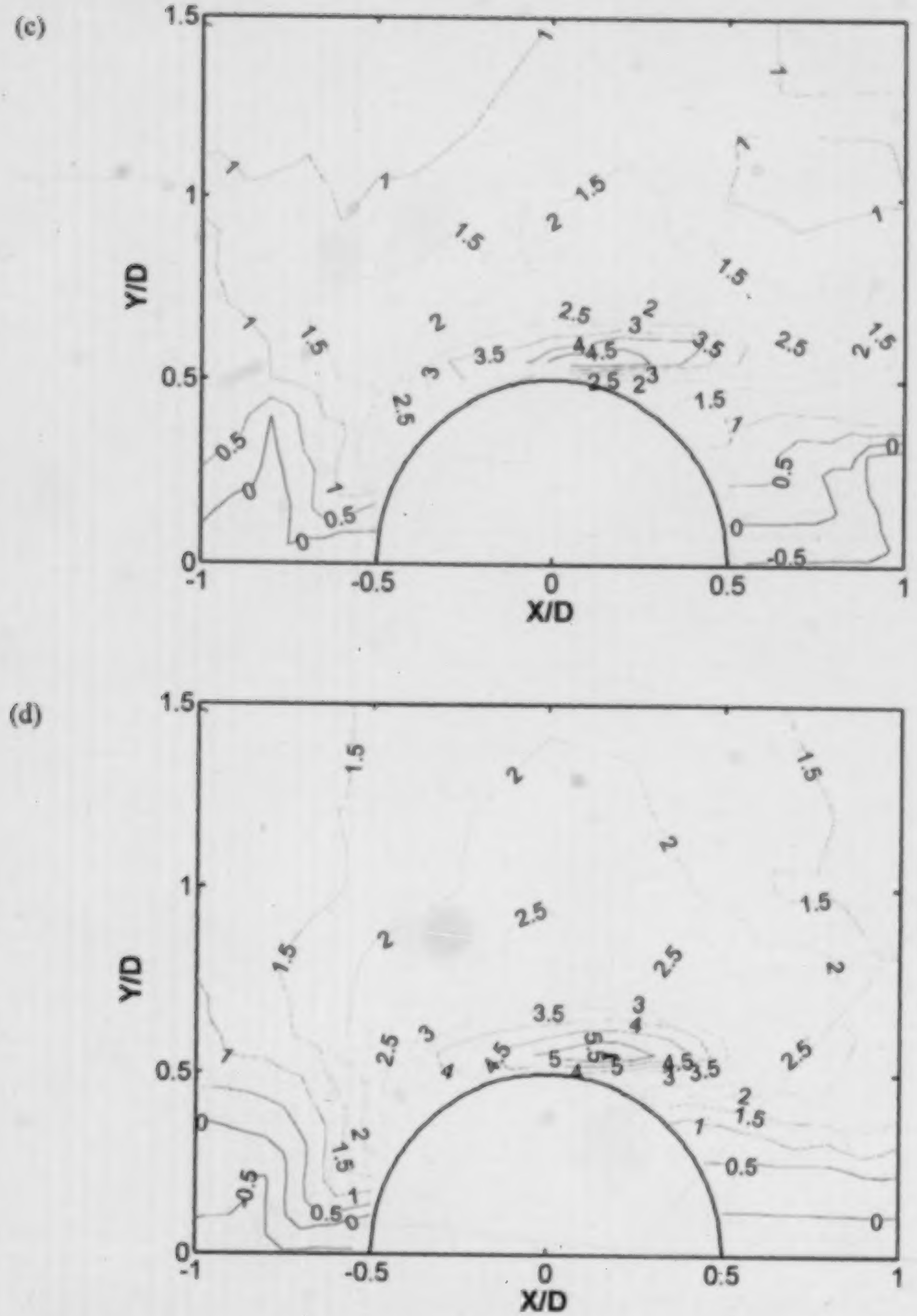

Fig. 4.8 (contd.) Normalized mean bed shear stress (τ_0/τ_{00}) contours; (c) Regime-3, (d) Regime-4

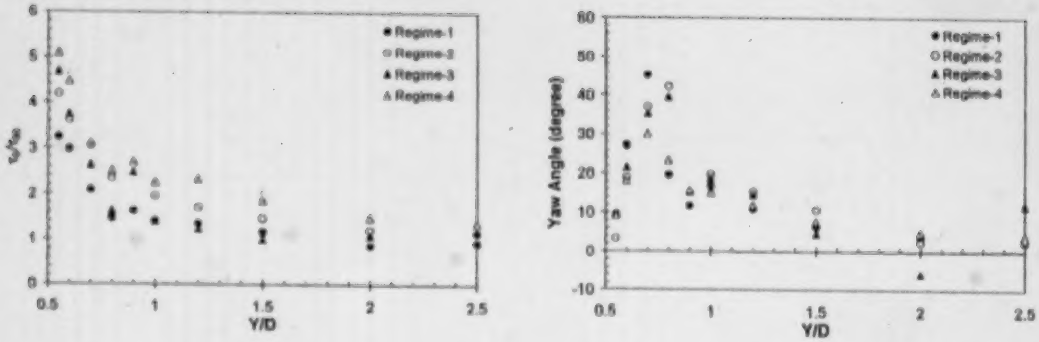

(a)

(b)

Fig. 4.9 Transverse profile of normalized mean bed shear stress (a) magnitude and (b) angle on x=0 plane

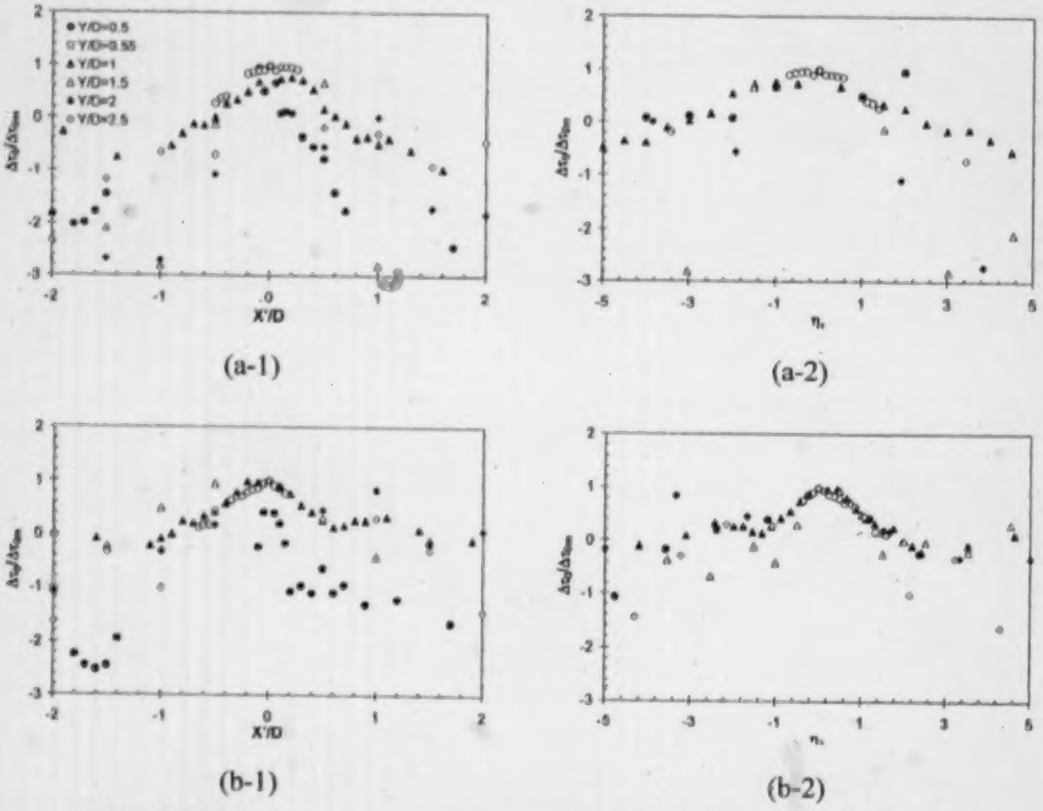

(a-1)

(a-2)

(b-1)

(b-2)

Fig. 4.10 Bed shear stress similarity profiles; (a) Regime-1, (b) Regime-2

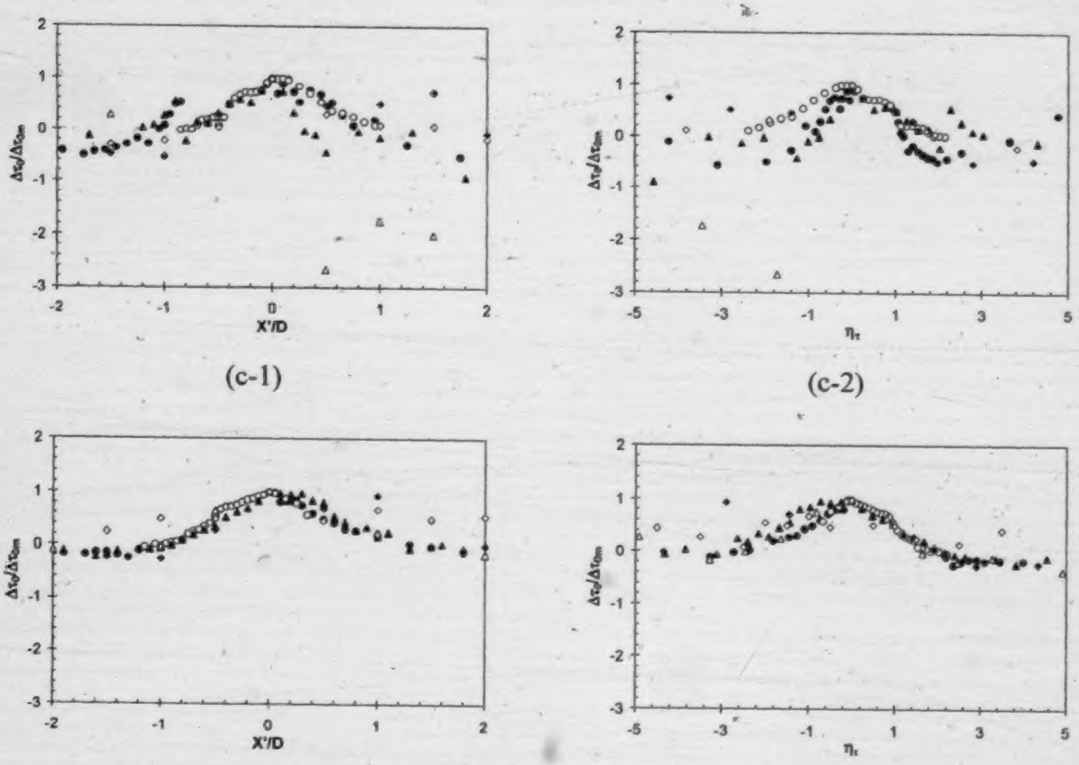

(c-1)

(c-2)

(d-1)

(d-2)

Fig. 4.10 (contd.) Bed shear stress similarity profiles; (c) Regime-3, and (d) Regime-4

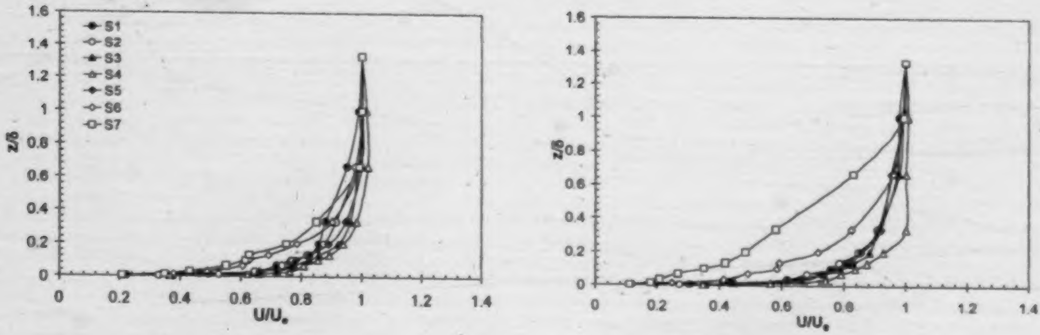

(a) Regime-1

(b) Regime-2

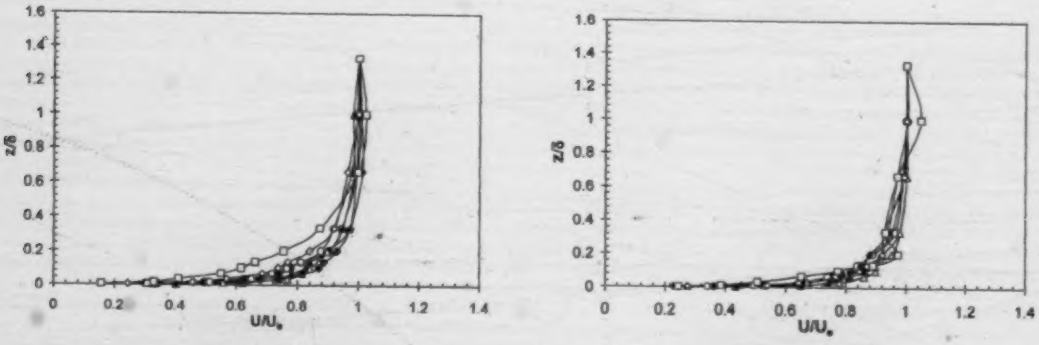

(c) Regime-3

(d) Regime-4

Fig. 4.11 The normalized longitudinal velocities, U/U_e versus the normalized depth, z/δ; (a) Regime-1, (b) Regime-2, (c) Regime-3, and (d) Regime-4

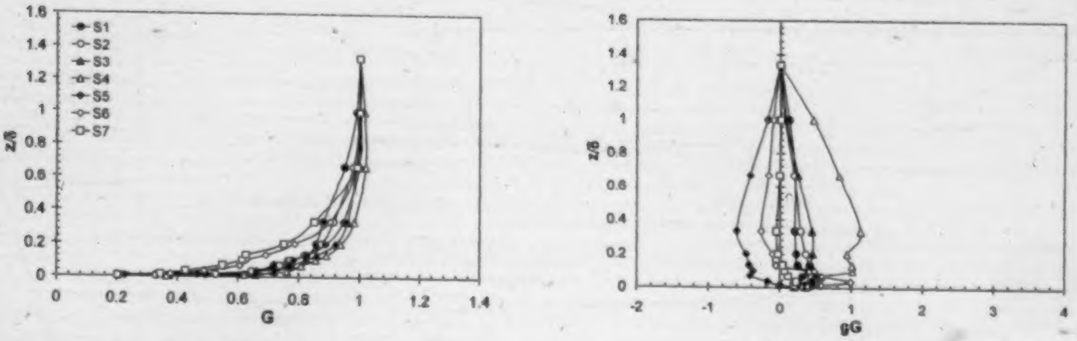

(a-1) Regime-1

(a-2) Regime-1

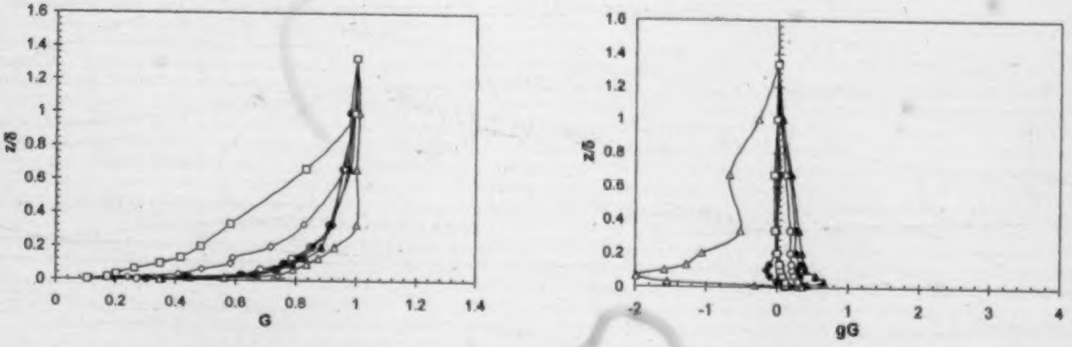

(b-1) Regime-2

(b-2) Regime-2

Fig. 4.12 Prandtl's functions *G* and *gG* versus the normalized depth, *z*/δ; (a) Regime-1, (b) Regime-2

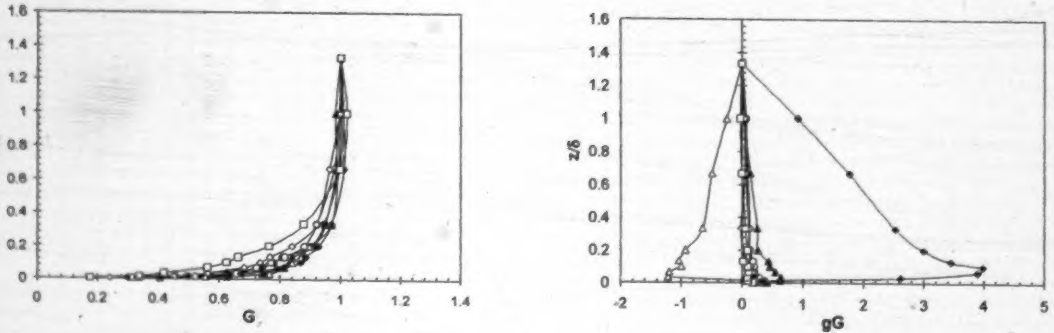

(c-1) Regime-3

(c-2) Regime-3

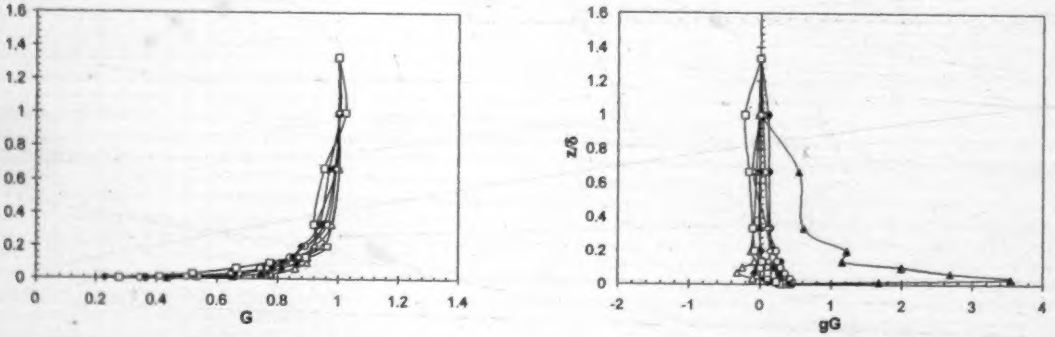

(d-1) Regime-4

(d-2) Regime-4

Fig. 4.12 (contd.) Prandtl's functions *G* and *gG* versus the normalized depth, *z*/δ; (c) Regime-3, (d) Regime-4

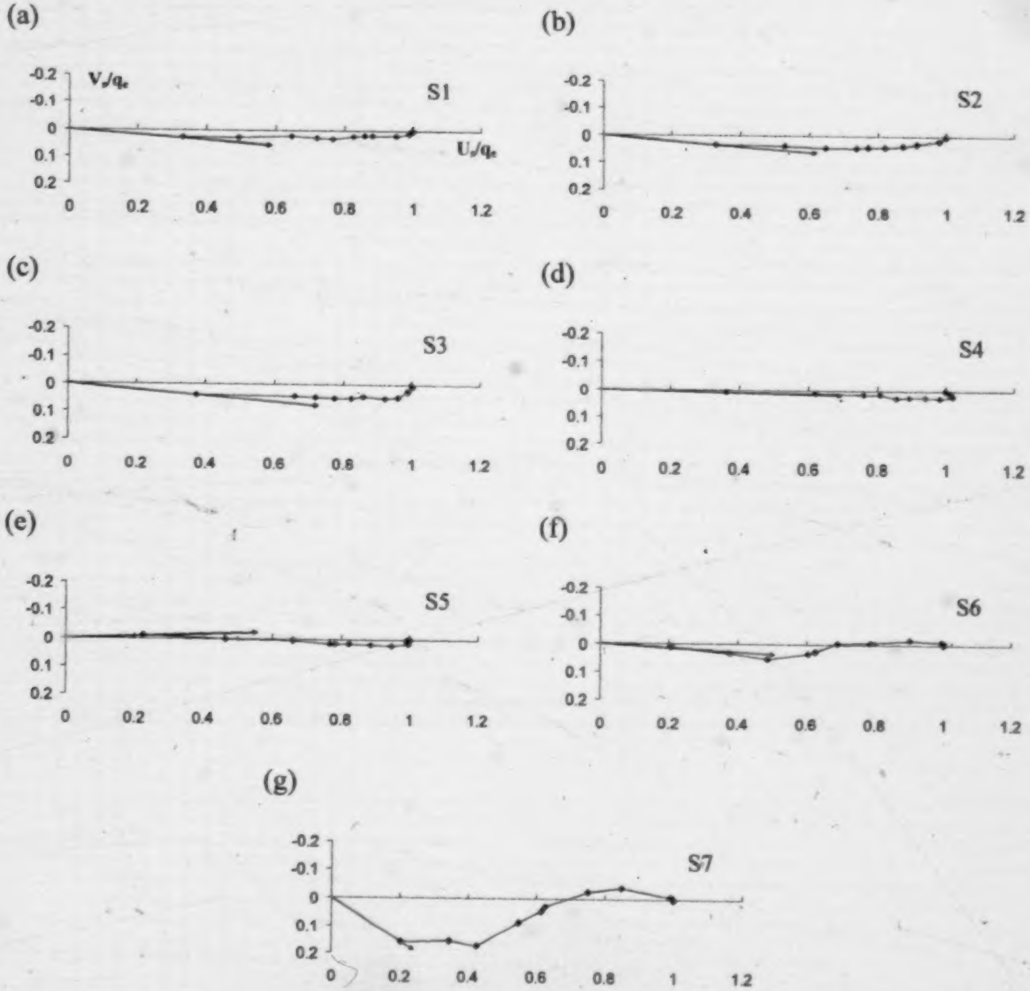

Fig. 4.13 Johnston's polar plots for Regime-1.

The normalized velocity components along (U_s/q_e) and perpendicular (V_s/q_e) to the free streamline direction are plotted on horizontal and vertical axes. The arrow represents the direction of local bed shear stress (τ_0).

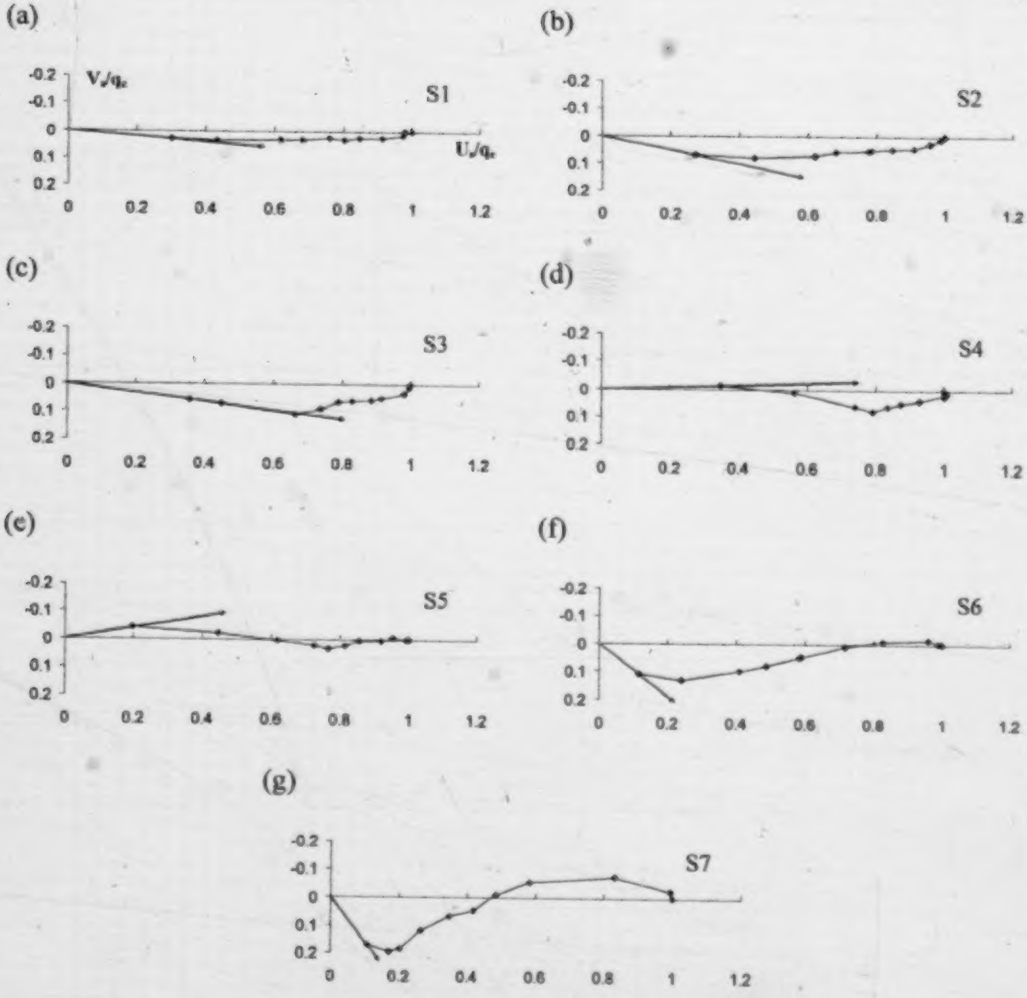

Fig. 4.14 Johnston's polar plots for Regime-2.

The normalized velocity components along (U_s/q_e) and perpendicular (V_s/q_e) to the free streamline direction are plotted on horizontal and vertical axes. The arrow represents the direction of local bed shear stress (τ_0).

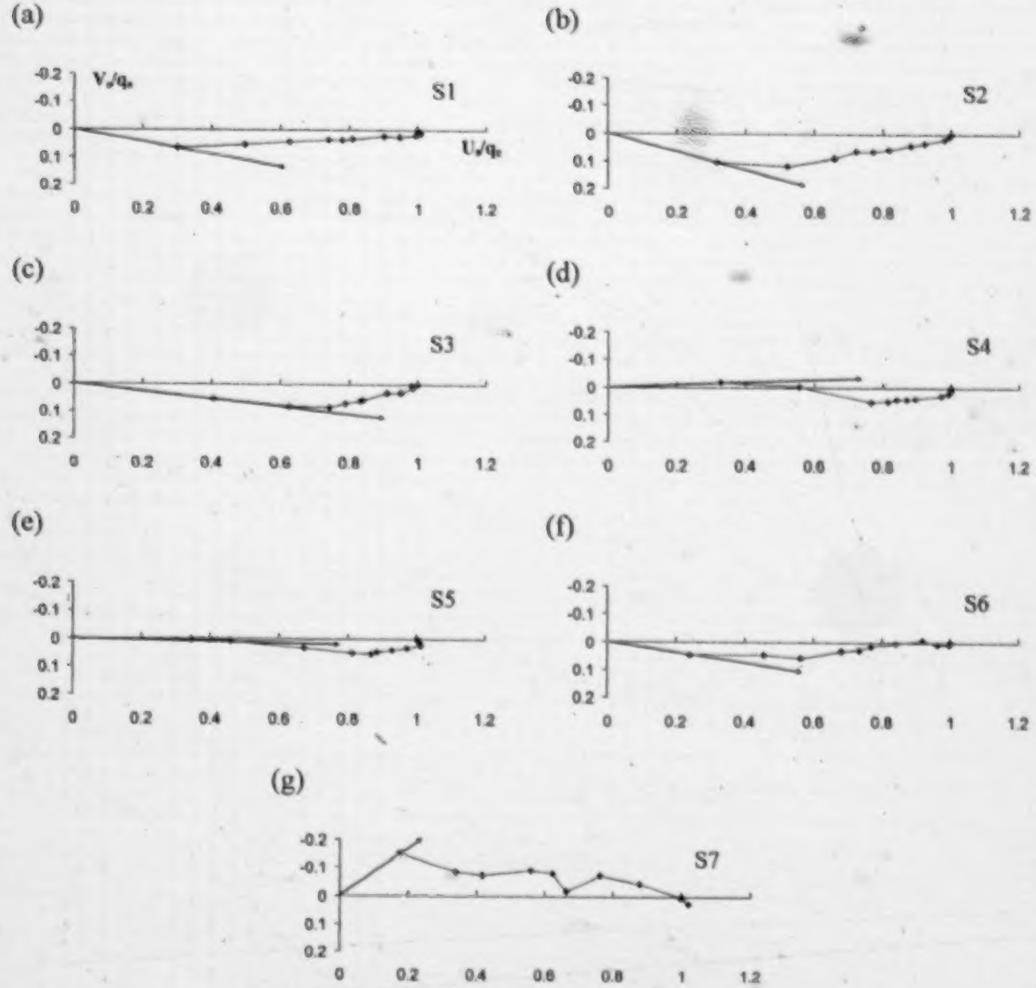

Fig. 4.15 Johnston's polar plots for Regime-3.

The normalized velocity components along (U_s/q_e) and perpendicular (V_s/q_e) to the free streamline direction are plotted on horizontal and vertical axes. The arrow represents the direction of local bed shear stress (τ_0).

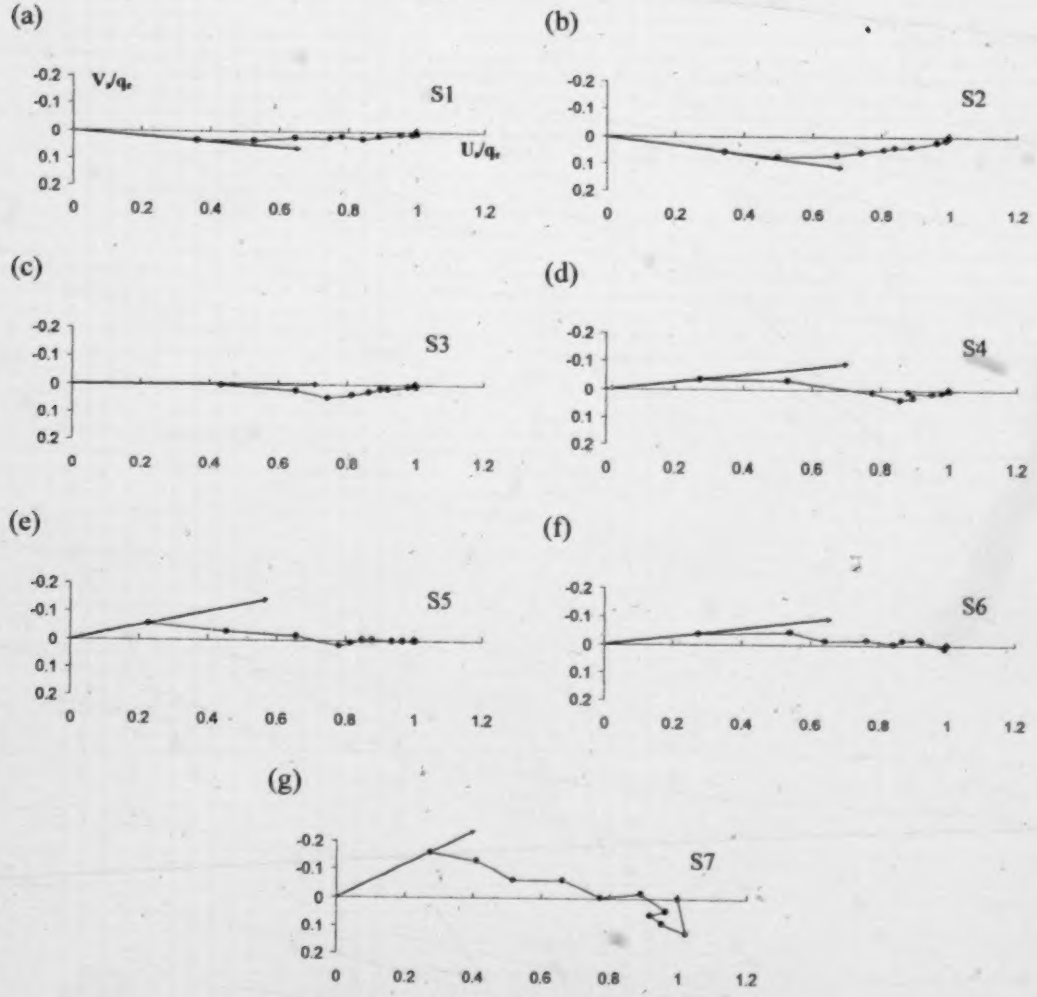

Fig. 4.16 Johnston's polar plots for Regime-4.

The normalized velocity components along (U_s/q_e) and perpendicular (V_s/q_e) to the free streamline direction are plotted on horizontal and vertical axes. The arrow represents the direction of local bed shear stress (τ_0).

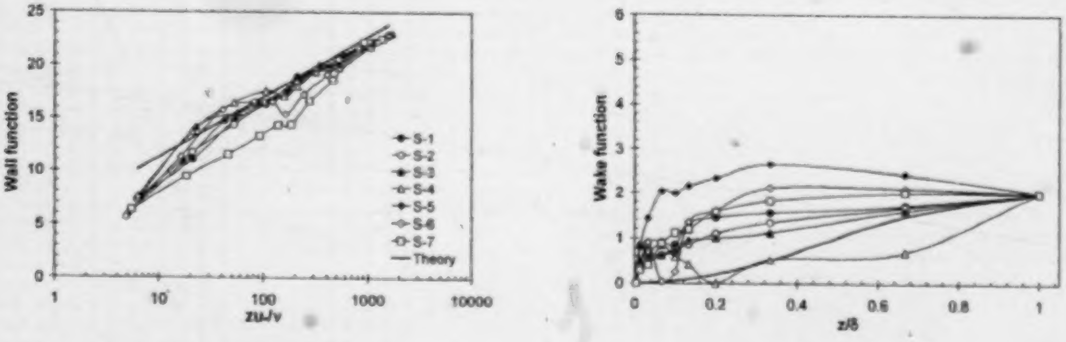

(a-1) Regime-1

(a-2) Regime-1

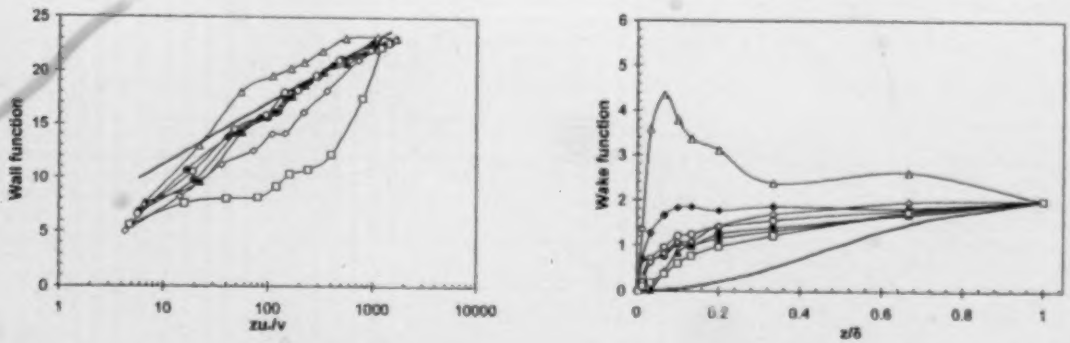

(b-1) Regime-2

(b-2) Regime-2

Fig. 4.17 Coles' wall and wake functions versus zu_*/ν and z/δ;

(a) Regime-1, (b) Regime-2

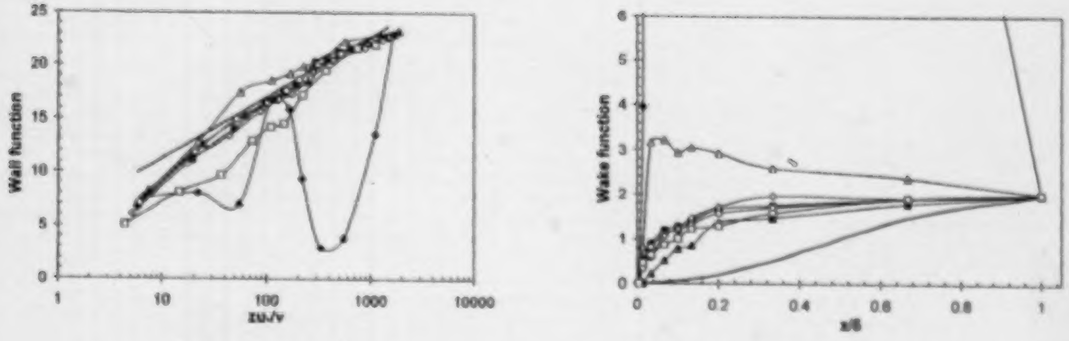

(c-1) Regime-3

(c-2) Regime-3

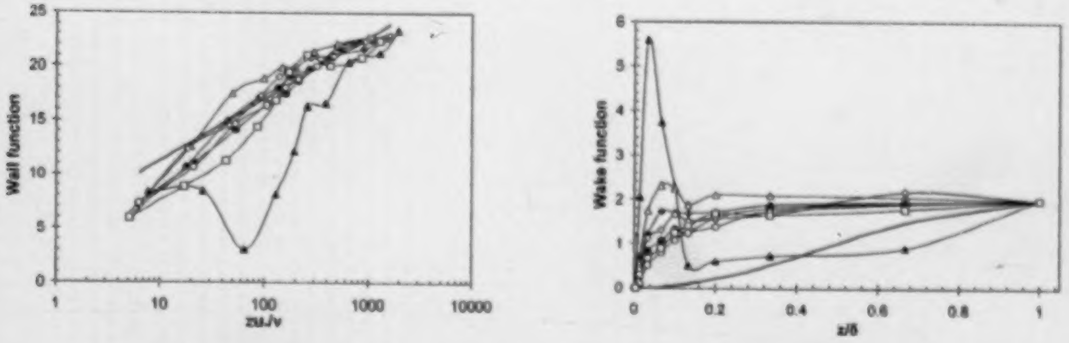

(d-1) Regime-4

(d-2) Regime-4

Fig. 4.17 (contd.) Coles' wall and wake functions versus zu_*/ν and z/δ;

(c) Regime-3, and (d) Regime-4

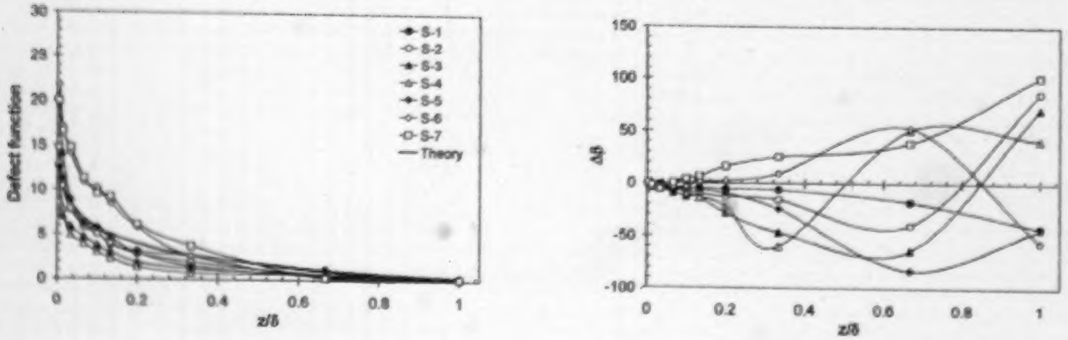

(a-1) Regime-1

(a-2) Regime-1

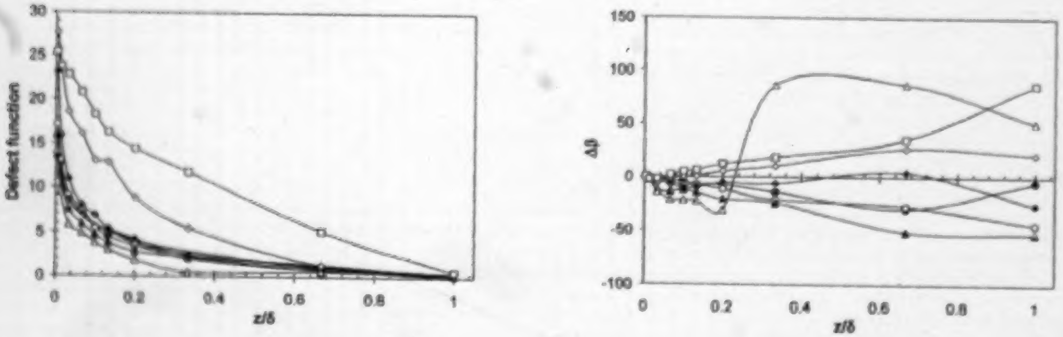

(b-1) Regime-2

(b-2) Regime-2

Fig. 4.18 Perry and Joubert's defect function and Δβ versus the normalized depth, *z*/δ; (a) Regime-1, (b) Regime-2

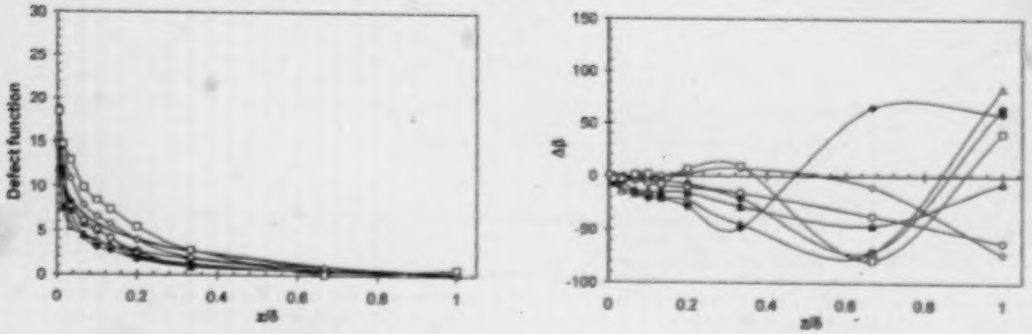

(c-1) Regime-3

(c-2) Regime-3

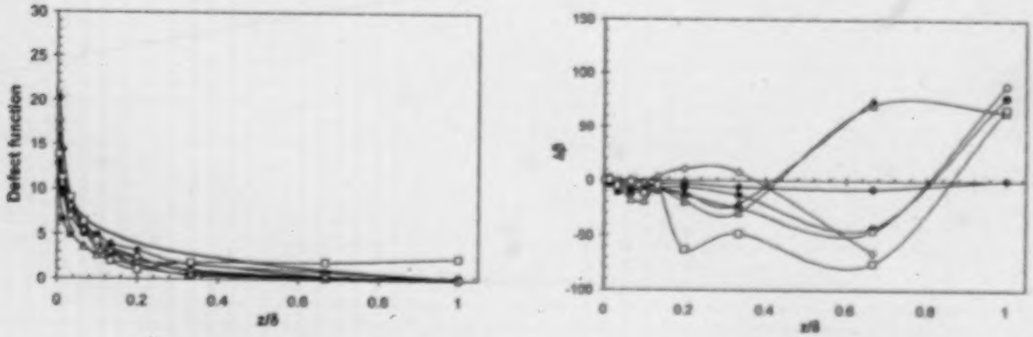

(d-1) Regime-4

(d-2) Regime-4

Fig. 4.18 (contd.) Perry and Joubert's defect function and Δβ versus the normalized depth, z/δ; (c) Regime-3, (d) Regime-4

4.5 Part II: Rough Bed Results and Discussions

4.5.1 *Flow visualization test*

The major observations of the flow visualization tests are illustrated by a set of sketches in Figure 4.19. Most of the observations were similar to smooth bed except for the zone occupied by the horse-shoe vortex system around the cylindrical objects. Figure 4.20(a-b) show images of the zone occupied by the horse-shoe vortex around the cylindrical objects in Regime-1 and Regime-2 on rough bed. The point of separation on the plane of symmetry was detected by injecting dye at several points along the centerline upstream of the object. The point where the dye plume was found to roll up without any axial translation and was eventually swept around the object was considered to be the point of separation or in other words the location of the horse-shoe vortex. This location was not a steady point on the bed; rather it oscillated over a small distance. The mean position of the boundary layer separation, that forms the horse-shoe vortex, occurred at about -1*D* for Regime-1; and -1.2*D* in Regimes 2, 3 and 4 on rough bed. The major difference in the observation of upstream separation point on smooth and rough beds occurred in Regime-4. The separation occurred significantly upstream, at about -1.5 to -1.7*D* from the cylinder, in Regime-4 on smooth bed [see Part I]. It was observed from smooth bed experiments that a significant downward flow from the upper flow zone on the upstream face of the cylinder in Regime-4 results in a strong backward flow close to the bed, and hence the horse-shoe vortex system moves upstream. However, the rough bed experiments showed that the bed resistance to the backward flow is strong enough to hold the separation point in a short region of -1*D* to -1.2*D* irrespective of the level of submergence.

It was also observed from flow visualization tests that the horse-shoe vortex trails were relatively wider (~0.4*D*) and further away from the cylinder surface on a rough bed. Again the high velocity flow separation from the cylinder surface that leads to wake vortices was interrupted near the bed. Dye plume was found to spread away from the cylinder near the bed (at $z<0.2H$) without forming wake vortices. However, the wake vortices were found to freely interact with the horse-shoe vortex system on smooth bed to turn the trail of the system towards the wake [see Part I]. These observations indicate that the bed roughness tends to inhibit the interaction of wake vortices with horse-shoe vortex system.

Similar to smooth bed [Part I], a closed recirculating wake for moderate to deeply submerged cylinders (i.e. in Regime-1 and 2); and alternately shedding vortices for non-submerged and slightly submerged cylinders (i.e. Regime-3 and 4) were found to be the characteristic features of the flow. Strouhal numbers (S), computed on the basis of visual observation of the number of vortices passing a given station for a period of time, were approximately 0.2 for both Regime-3 and Regime-4 on smooth and rough beds. Figure 4.21 shows images of the wake in (a) Regime-2, (b) Regime-3, and (c) Regime-4, where alternate vortex shedding can be observed in Regime-3 and Regime-4.

4.5.2 *Bed shear stress distribution*

Figure 4.22(a) shows the variation of the normalized mean bed shear stress upstream of the objects on the plane of symmetry. Similar to smooth bed observations [Part I], the point of separation or the upstream edge of the horse-shoe vortex was identified from the transition of shear stress from positive to negative. For the present study on rough bed the points of separation in different flow regimes are not far apart. It occurred approximately at -0.85D in Regime-1 and at -1.1 to 1.2D in Regime-2, 3 and 4. These observations agreed well with flow visualization.

Figure 4.22(b) shows the variation of the normalized mean bed shear stress downstream of the cylinder in Regime-1 and Regime-2 on the plane of symmetry. The zone of recirculating closed wake behind the cylinders had negative shear due to flow reversal. Therefore, the transition from negative to positive shear indicates the approximate location of the point of reattachment of the separated stream impinging on the bed. According to Figure 4.22(b) the length of closed wake in Regime-1 (~1.5D) is considerably smaller than that in Regime-2 (~2.8D). However, smooth bed results [Part I] showed a longer closed wake in Regime-1. It appeared that the separated streams from the lateral face of the cylinder shortened the recirculating wake in Regime-2 on smooth bed. It was observed from flow visualization on rough bed that there is an interference of bed roughness to the formation of wake vortices from the lateral faces of the cylinders. This might be the reason that allowed the reverse flow to continue longer in Regime-2 on rough bed.

Contours of the normalized mean bed shear stress (τ_0/τ_{00}) around the cylindrical objects in four different regimes subjected to similar flow conditions were plotted in Figure 4.23(a-d), where τ_{00} is the bed shear stress of the approach flow. Similar to smooth bed observations [Part I], bed shear stress (τ_0) increases in the vicinity of the lateral face of the cylinder in all flow regimes. The maximum bed shear stress (τ_{0max}) in Regime-4 is approximately 12 times larger than τ_{00} on rough bed, whereas τ_{0max} is only 6 times larger than τ_{00} in Regime-1. Regime-2 and Regime-3 had maximum bed shear stresses of $9\tau_{00}$ and $11\tau_{00}$, respectively. These ratios are approximately twice bigger than those observed on smooth bed for similar flow conditions [see Part I]. Ahmed and Rajaratnam (1998) also observed 2-2.5 times increase in maximum bed shear stress ratio (τ_{0max}/τ_{00}) on rough bed compared to smooth bed for similar flow around surface piercing cylinder. These increased shear stresses indicate the potential for local scour of different flow regimes in natural rough beds.

Figure 4.24(a) shows the variation of τ_0/τ_{00} in the transverse direction from the shoulder of the cylinders at x=0. It was observed that the increased shear stress drops significantly within a short distance (~0.8D) from the cylinder. However, the lateral expanses of increased shear (i.e. the region where $\tau_0/\tau_{00} \geq 1.5$) were relatively greater on rough bed as compared to smooth bed [see Part I]. For similar flow on rough bed τ_0 reached or fell below 1.5 times τ_{00} at y=1.5 to 2D. Figure 4.24(b) shows the variation of the direction (i.e. angle) of τ_0 in the transverse direction at x=0. A negative angle represents a shear stress vector pointing inward (i.e. towards the cylinder). As the horse-shoe vortex system spread outward on rough bed (an observation made from flow visualization), a region close to the cylinder surface near the bed fell in negative pressure zone. This had forced the shear stress vectors to turn inward in all flow regimes. However, the shear stress vectors were found to deflect significantly outward from the edge of the horse-shoe vortex system at $x=0$; and τ_0 vectors are very random in direction inside the zone occupied by the trailing vortex system.

A similarity analysis has been conducted for the longitudinal profiles of the normalized bed shear stress (τ_0/τ_{00}) for all flow regimes. The results of the similarity analysis are presented in Figure 4.25(a-d). The longitudinal (x) and transverse (y) distances are normalized by the diameter (D) of the cylinders. For each flow regime, the variations of $\Delta\tau_0/\Delta\tau_{0m}$ are plotted against X'/D in Figure 4.25(a-1 to d-1), where $\Delta\tau_0 = \tau_0 - \tau_{00}$, $\Delta\tau_{0m} = \tau_{0m} - \tau_{00}$, $X' = x - x_m$, and x_m is the location of maximum bed shear stress (τ_{0m}) along each profile. The data shows scatter in Regime-1, 2 and 3, but the scatter is minimal in Regime-4. A good similarity of bed shear stress was also observed in Regime-3 and Regime-4 on smooth bed for similar flow condition [see Part I]. The similarity profiles of $\Delta\tau_0/\Delta\tau_{0m}$ were replotted in Figure 4.25(a-2 to d-2) against $\eta_\tau = (X'/D)/[(X'/D)_{1/2}]$, where $(X'/D)_{1/2} = X'/D$ at $\Delta\tau_0/\Delta\tau_{0m} = 0.5$. This improved the similarity of the profiles in the downstream side of x_m for all flow regimes. The observations of present and previous [Part I] similarity study for bed shear stress showed that similarity exists the best for Regime-4 on both smooth and rough beds.

4.5.3 *Analysis of deflected flow in terms of the theories of 3DTBL*

Similar to smooth bed studies, the definition of the thickness of the turbulent boundary layer (δ) is taken from Schlichting (1968). Figure 4.26(a-d) shows the normalized longitudinal velocity (U/U_e) profiles over z/δ at different stations for all flow regimes. The experimental results of velocity (U) profiles on rough bed showed that except for stations in the wake (i.e. Station 6 and 7) $U/U_e \geq 0.96$ at $z=15$ cm. Moreover, it is known form the undisturbed velocity profile (Fig. 3.1 and 3.2) that δ is approximately 15 cm. Therefore, δ was taken to be 15 cm, similar to smooth bed experiments [Part I]. For a resolution of 30 mm for the point measurements of velocity away from the bed an uncertainty of ±15 mm can be considered in the selection of δ. It can be observed from Figure 4.26 that the profiles of U/U_e vs z/δ collapse in a narrow band for most of the stations in all flow regimes, with the exceptions of stations in the wake.

Prandtl's (1946) Model

The variations of the functions of G and gG (i.e. U_s/U_{se} and $V_s/(U_{se} \tan\gamma_w)$) with z/δ are plotted in Figure 4.27(a-d). Figure 4.27(a-1 to d-1) show that, similar to smooth bed observations [Part I], the velocities (U_s) along the free stream are increased or decreased approximately in similar proportion to their respective free stream velocities (U_{se}), except at stations 6 and 7. The velocity deficit in the wake of Regime-1 and 2 were significant, and as a result U_s/U_{se} values were relatively small at $z \leq h$ for stations 6 and 7. However, unlike smooth bed the profiles of U_s/U_{se} did not collapse in a narrow band at all stations in Regime-3 and 4. Similar to Regime-1 and Regime-2, higher surface velocity over the cylinder compared to lower velocity on rough bed resulted in a smaller U_s/U_{se} in Regime-3 at stations 6 and 7. On the contrary, Regime-4 on rough bed showed $U_s/U_{se} \geq 1$ at stations 6 and 7. This might be the result of increased upward flow [see Chapter 6] immediately behind the cylinder on rough bed, which finally contributed to the longitudinal velocity.

Figure 4.27(a-2 to d-2) show that the effect of negative pressure zone developed behind the cylinders is significant on rough bed at $x=0$, as the flow turns inward (i.e. towards the cylinder), at least near the bed, at station 3. Similar to smooth bed [Part I], the change in direction of the transverse component of velocity was alternate and significant between stations 3 and 5 in Regime-3 and 4 to indicate the existence of a vortex about z-axis. However, it was not significant between stations 3 and 4 in Regime-1 and 2.

Johnston's (1960) Model

Johnston's polar plots for all the stations in different flow regimes are presented in Figure 4.28 to 4.31. The properties of a polar plot are illustrated in Figure 4.2(c). The polar plots show the relative deviations of the velocity vectors with respect to the directions of corresponding free stream velocity vector (q_e). The direction of local bed shear stress (τ_0) is shown by an arrow in each polar plot. The outward deflected flow has positive V_s/q_e.

The overall observation of the polar plots on rough bed (Fig. 4.28 to 4.31) is that the near-bed velocities were less deflected as compared to smooth bed [Part I]. Velocities at station-1 experienced minimal deflection. The outward deflections were most pronounced at station-2. The nature of velocity deflections at station-2 for all four regimes could approximately be considered to follow the theory. That is the near-bed velocities were deflected more than the free stream velocity in the outward direction, and the upper velocity vectors gradually turned towards the free stream direction so that the polar plots assume a triangular shape. For similar flow condition on smooth bed [Part I], almost all the upstream stations in each flow regime demonstrated gradual turning and hence approximately triangular polar plot. Station-1 in Regime-3 and 4 [Fig. 4.30(a) and 4.31(a)] could also roughly be considered to follow the theory, except with relatively less turning of the near-bed velocities.

The most surprising observation was at station-3 [Fig. 4.28(c) to 4.31(c)], where the near bed velocities were turned towards the negative pressure zone immediately behind the cylinders. However, relatively upper velocities were turned outward and they were turned back towards the free stream direction at higher elevations, as observed on smooth bed for similar flow conditions [see Part I]. The effect of negative pressure was more prominent at stations 4 and 5 [Fig. 4.28(d-e) to 4.31(d-e)], where the deflection patterns were mostly opposite; i.e. inward over the entire depth. Smooth bed results [Part I] also showed some influence of the leeward low pressure zone on the flow deflection pattern, but it appeared more pronounced on rough bed. The observations at stations 6 and 7 on rough bed in all flow regimes were very similar to smooth bed [Part I]. Velocities were straightening towards the free stream, except for near-bed outward deflections downstream of the closed recirculating wake in Regime-1 and 2.

The above observations indicate that the bed roughness acts to nullify the effect of lateral pressure gradient that causes cross flow in skewed turbulent boundary layer. This allows the negative pressure of the leeward face to dominate in greater region of the flow around the cylinders. Though the effect of bed roughness is confined very close to the bed, this interrupts the general deflection pattern and some theoretical estimates (e.g. γ_w). As a result the theoretical computations do not agree very well in most part of the flow around cylinders on rough bed.

4.5.4 *General applicability of the models*

There are some limitations in general applicability of the cross-flow models as described in Part I. Cross-flow models are not applicable for S-shaped velocity profiles and for flows in the wake. Therefore, the velocity profiles at stations downstream of the cylinders may not satisfy the models. Performance evaluation of the models' general applicability should consider this fact.

The performance of Prandtl's (1946) model on rough bed is similar to smooth bed [Part I] and unsatisfactory. The profiles of function G collapsed together for most of the stations, but the combined function gG did not produce any encouraging results. Johnston's (1960) model was found satisfactory only at station-2. Therefore, it is unable to generalize the flow deflection around the cylinders of different levels of submergence. Coles' (1956) wall and wake functions were plotted for different regimes in Figure 4.32(a-d). It was observed that except for a few stations (mostly in the downstream side) the wall functions were in reasonably good agreement with the theoretical line, but the wake functions did not agree with the theoretical curve. However, the wake functions at most of the stations have a general trend, which is similar to smooth bed observations [see Part I]. Similarity models (e.g. Hornung and Joubert (1963)) could not be tested in this study as they were proposed for smooth bed only.

Interestingly Perry and Joubert's (1965) model performed very well on rough bed. This model was also very good for smooth bed results [see Part I]. There are two functions to evaluate the performance of Perry and Joubert's model. These are the defect function and the angular difference $\Delta\beta$ between the vectors $\boldsymbol{q}_e\text{-}\boldsymbol{q}$ and $(\boldsymbol{q}_e\text{-}\boldsymbol{q})_{max}$ in the skewed zone. The defect function tests the validity of the model for predicting the velocity magnitude, while $\Delta\beta$ tests the validity of their assumption of a triangular polar plot (see Fig. 4.2(d)) in 3DTBL. Defect functions and corresponding variations of $\Delta\beta$ for different flow regimes on rough bed are plotted in Figure 4.33(a-d). The experimentally computed defect functions agree reasonably well with the theoretical curve at most stations. Bed roughness and the submergence of the flow deflecting object did not appear to limit the applicability of the model. The magnitudes of $\Delta\beta$ were small near the bed (except for stations 6 and 7 in Regime-4), but at $z/\delta>0.3$ they ranged as high as ±20° to 75°. This observation is however; better than the observation on smooth bed [see Part I]. Though such angular variations indicate that the experimental data could not satisfy Perry and Joubert's assumption of triangular polar plot, high values of $\Delta\beta$ do not necessarily mean poor performance of the model. Therefore, Perry and Joubert's (1965) model performance can be considered reasonably satisfactory for predicting magnitudes of the deflected flow.

4.5.5 *Conclusions*

Experimental observations of the present study complement the results of similar study on smooth bed in Part I. The present results clearly identify the effects of bed roughness on the overall deflection of flow around cylinders of different levels of submergence. Similar to smooth bed study, flow visualizations, bed shear stress measurements, and velocity measurements on rough bed were consistent and complementary.

Flow visualizations revealed that the bed resistance to the backward flow upstream of the cylinders is strong enough to hold the separation point in a short region of $-1D$ to $-1.2D$ irrespective of the level of submergence. It was observed that the horse-shoe vortex trails were relatively wider (~0.4D) and away from the cylinder surface on rough bed. Bed roughness was also found to interrupt wake vortices and their interaction with the horse-shoe vortex system near the bed.

Similar to smooth bed [Part I], bed shear stresses were found significantly high near the shoulder of the cylinders in all flow regimes. However, the ratios of τ_{0max}/τ_{00} are approximately twice bigger than those observed on smooth bed for similar flow conditions. Bed shear stress results presented in this paper would provide qualitative information on the scour potential of the flow around submerged cylinders in natural rough bed streams.

Skewed 3D flow around the cylindrical objects on rough bed was explained with the help of Prandtl and Johnston's cross-flow models. The existence of the collateral and skewed zones in the boundary layer was clearly observed only at station 2. Bed roughness was found to inhibit the effect of lateral pressure gradient that causes skewing in the boundary layer. As a result the near-bed velocities did not turn much compared to the free stream as they are expected according to 3DTBL theories. However, Perry and Joubert's (1965) velocity defect function performed very well to predict experimental deflected velocity magnitudes on rough bed.

It is evident from this study that the bed roughness significantly alters the deflection pattern of flow around cylinders. The observed bed shear stress distributions and velocity deflections around cylinders of different levels of submergence will enhance the quality of hydraulic modeling required for natural river health assessment. This study showed that Perry and Joubert's velocity defect function can be a useful tool for predicting the deflected flow magnitudes around submerged objects like fish habitat structures, water intake or outfall structures and submerged islands on natural stream bed. The present experimental results can also serve as a hydraulic data base for future computational modeling of similar flows.

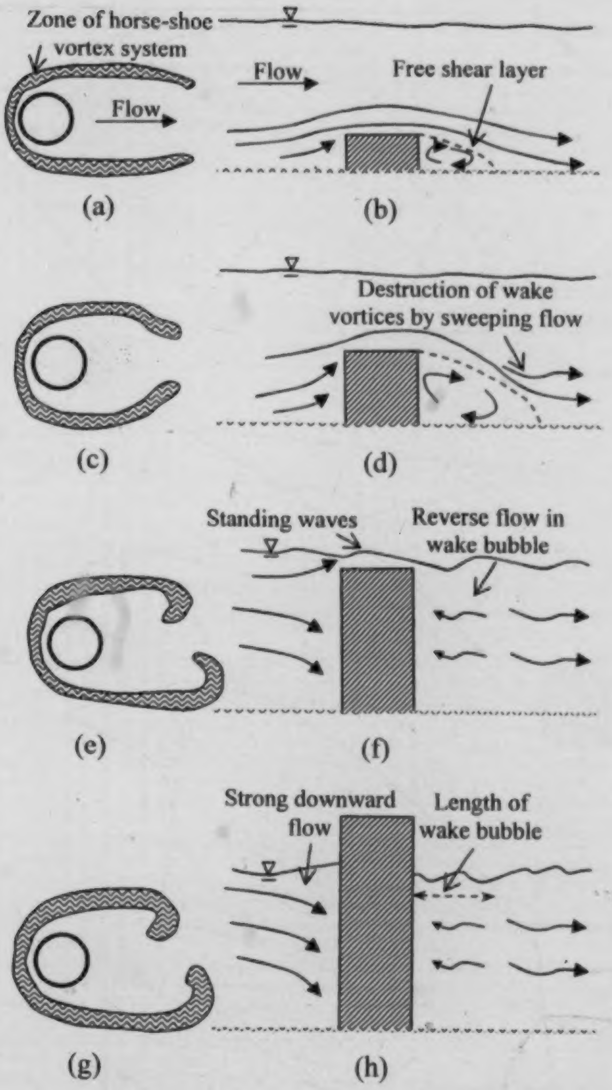
Zone of horse-shoe vortex system
Flow
Flow
Free shear layer
(a)
(b)
Destruction of wake vortices by sweeping flow
(c)
(d)
Standing waves
Reverse flow in wake bubble
(e)
(f)
Strong downward flow
Length of wake bubble
(g)
(h)

Fig. 4.19. Sketches of the horse-shoe vortex system and flow on the POS with respect to the cylinders in (a-b) Regime-1, (c-d) Regime-2, (e-f) Regime-3, and (g-h) Regime-4

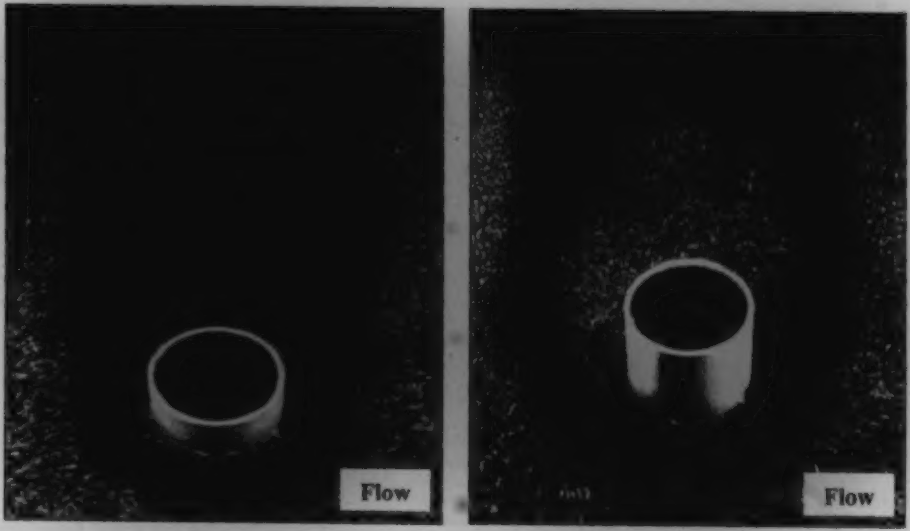

(a) Regime-1 (b) Regime-2

Fig. 4.20 Horse-shoe vortex; (a) Regime-1, and (b) Regime-2

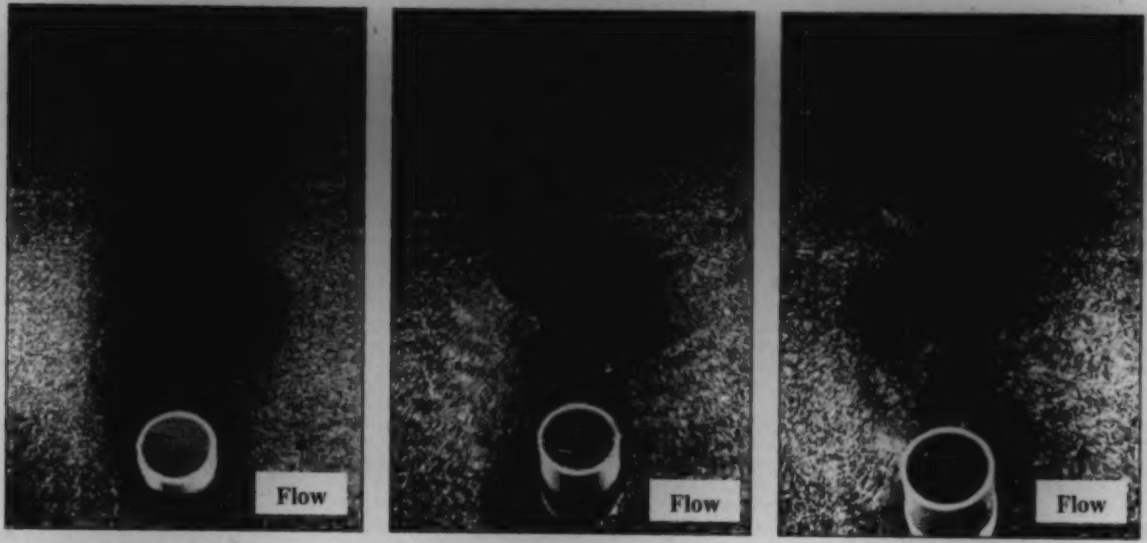
Flow
Flow
Flow

(a) Regime-2 (b) Regime-3 (c) Regime-4

Fig. 4.21 Wakes behind the cylinders; (a) Regime-2, (b) Regime-3, and (c) Regime-4

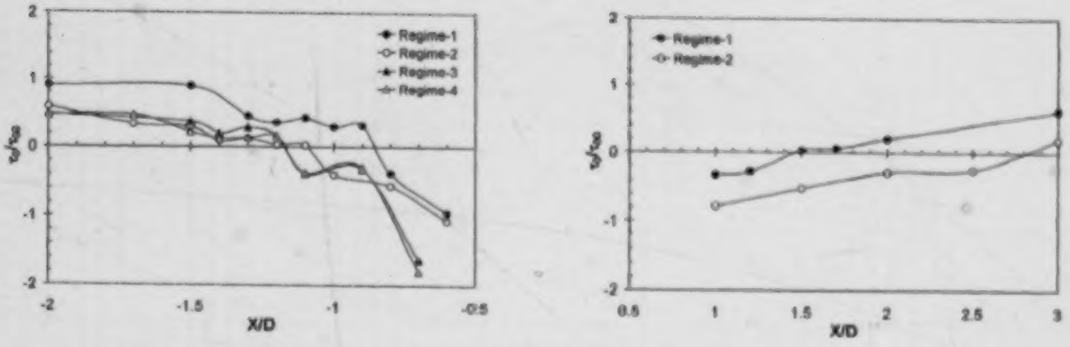

(a)

(b)

Fig. 4.22 Normalized mean bed shear stress profiles on (a) the upstream, and (b) the downstream plane of symmetry

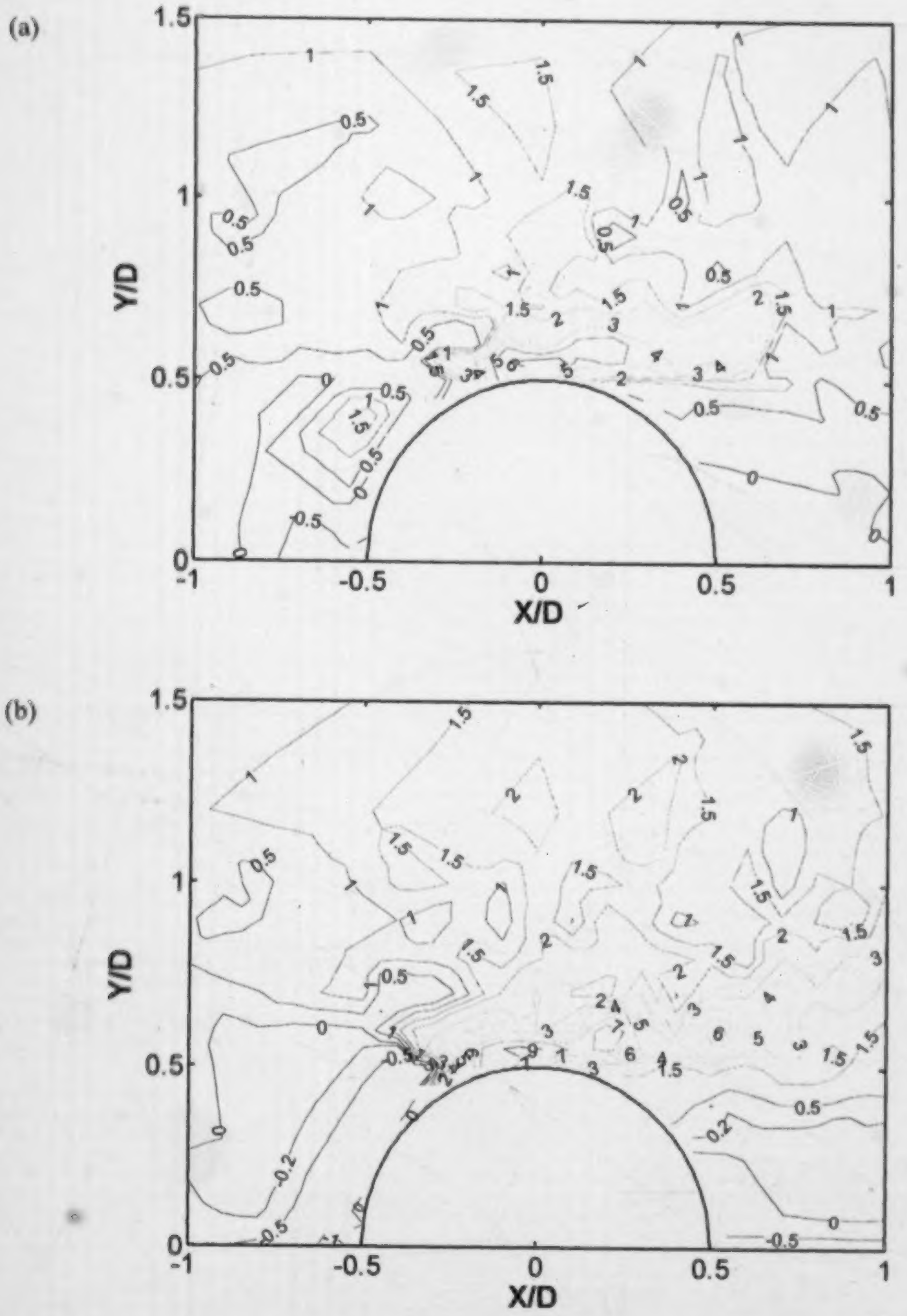

Fig. 4.23 Normalized mean bed shear stress (τ_0/τ_{00}) contours;

(a) Regime-1, (b) Regime-2

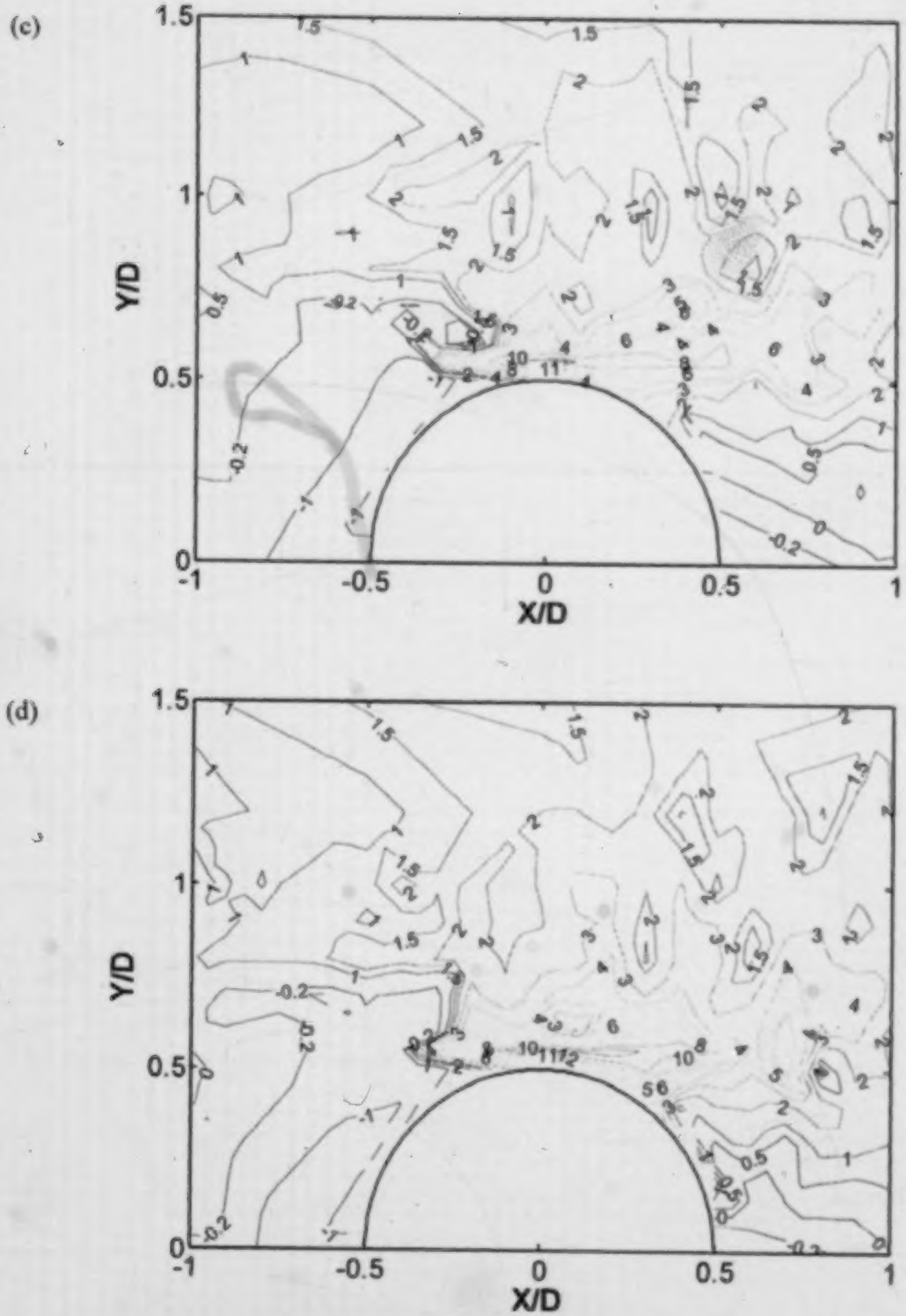

Fig. 4.23 (contd.). Normalized mean bed shear stress (τ_0/τ_{00}) contours; (c) Regime-3, (d) Regime-4

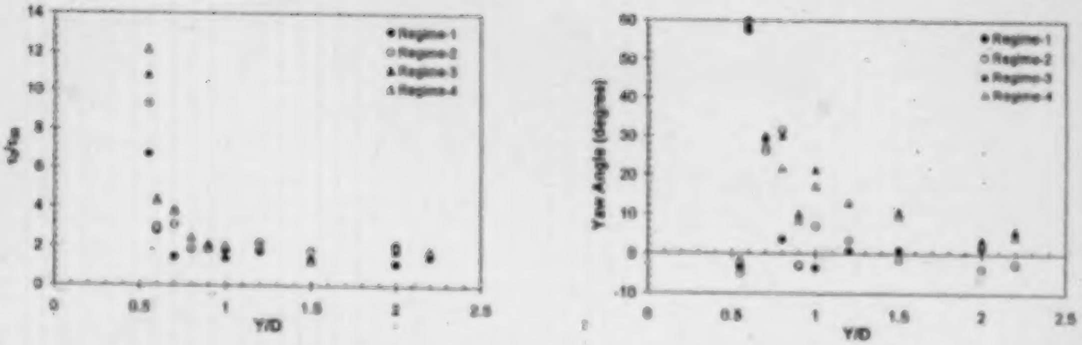

(a) (b)

Fig. 4.24 Transverse profile of normalized mean bed shear stress (a) magnitude and (b) angle on x=0 plane

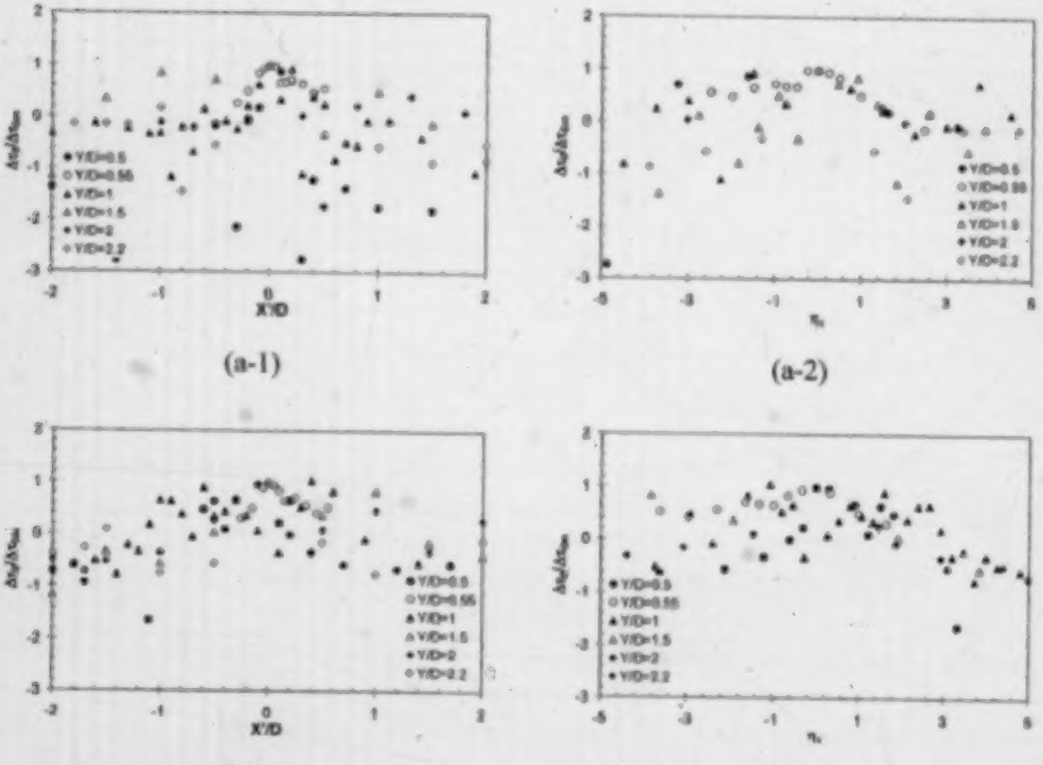

(a-1) (a-2)

(b-1) (b-2)

Fig. 4.25 Bed shear stress similarity profiles; (a) Regime-1, (b) Regime-2

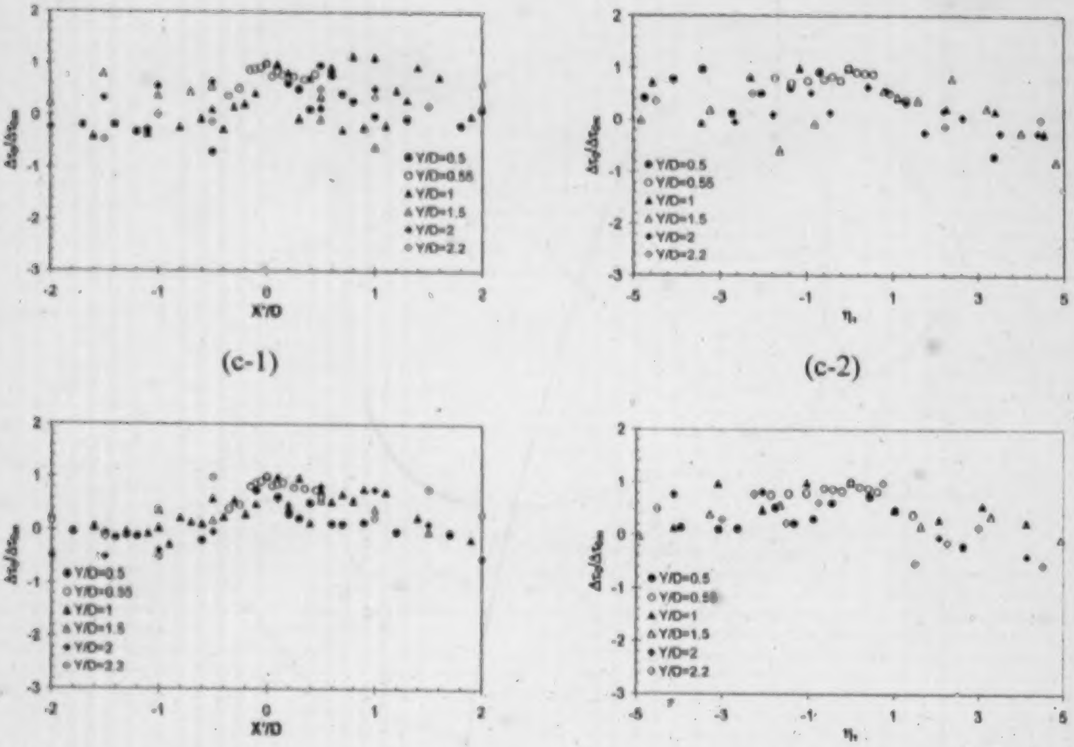

(c-1)

(c-2)

(d-1)

(d-2)

Fig. 4.25 (contd.) Bed shear stress similarity profiles; (c) Regime-3, and (d) Regime-4

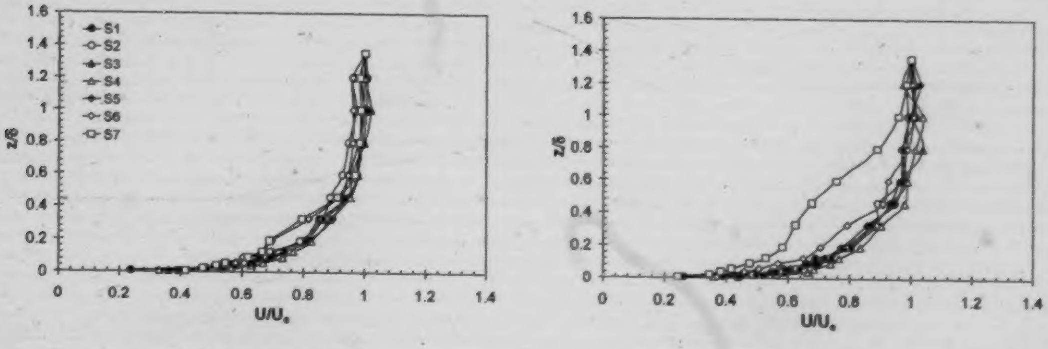

(a) Regime-1

(b) Regime-2

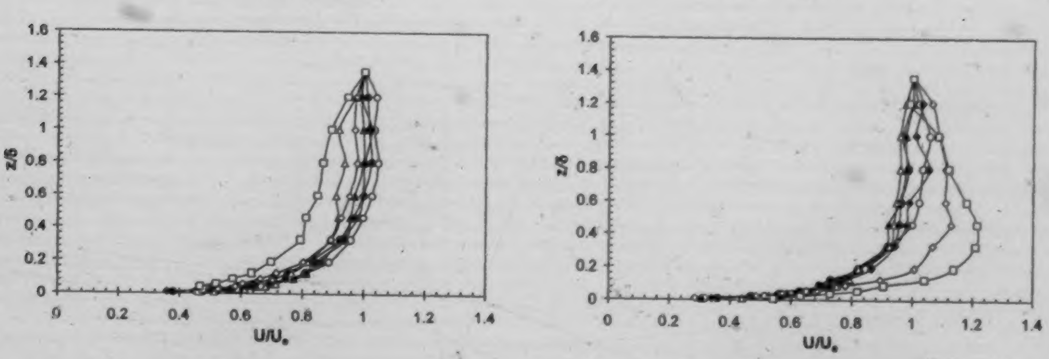

(c) Regime-3

(d) Regime-4

Fig. 4.26 The normalized longitudinal velocities, U/U_e versus the normalized depth, z/δ; (a) Regime-1, (b) Regime-2, (c) Regime-3, and (d) Regime-4

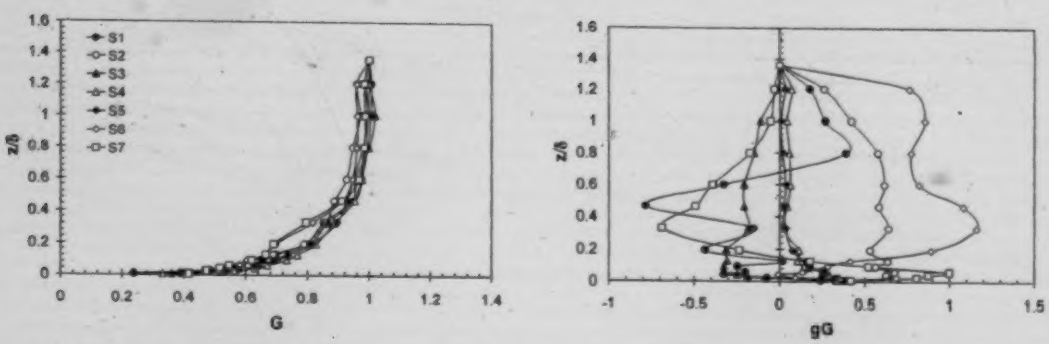

(a-1) Regime-1

(a-2) Regime-1

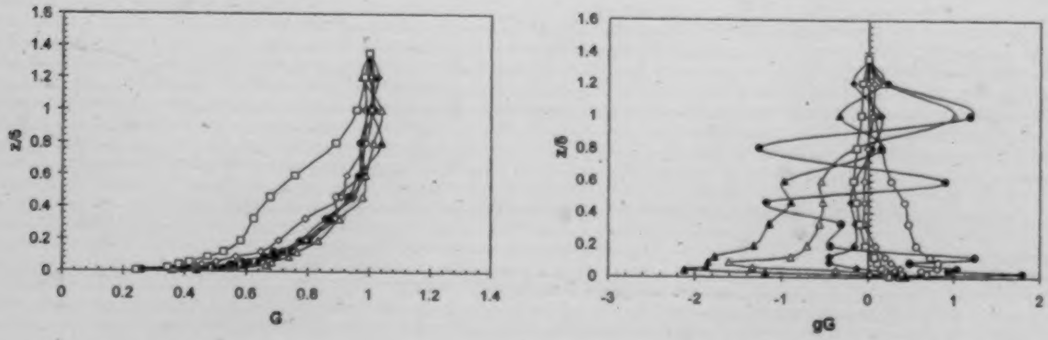

(b-1) Regime-2

(b-2) Regime-2

Fig. 4.27 Prandtl's functions *G* and *gG* versus the normalized depth, *z*/δ;

(a) Regime-1, (b) Regime-2

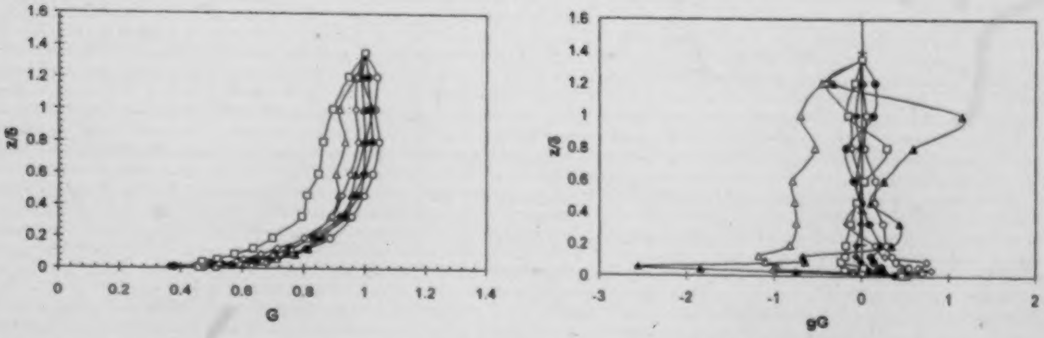

(c-1) Regime-3

(c-2) Regime-3

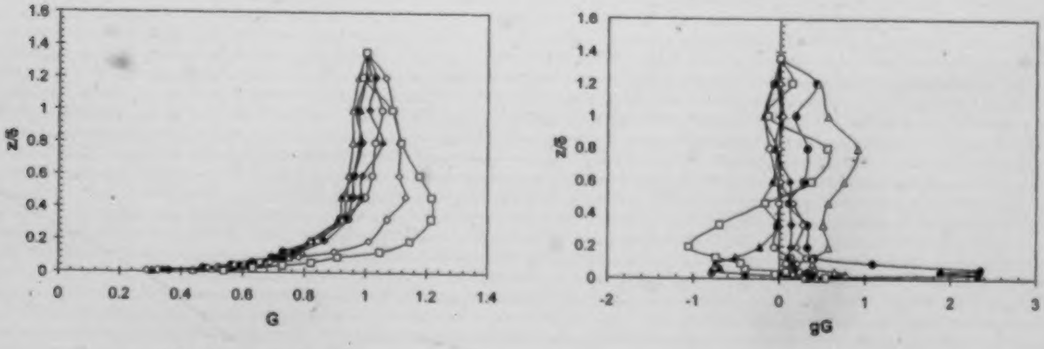

(d-1) Regime-4

(d-2) Regime-4

Fig. 4.27 (contd.) Prandtl's functions *G* and *gG* versus the normalized depth, *z*/δ; (c) Regime-3, (d) Regime-4

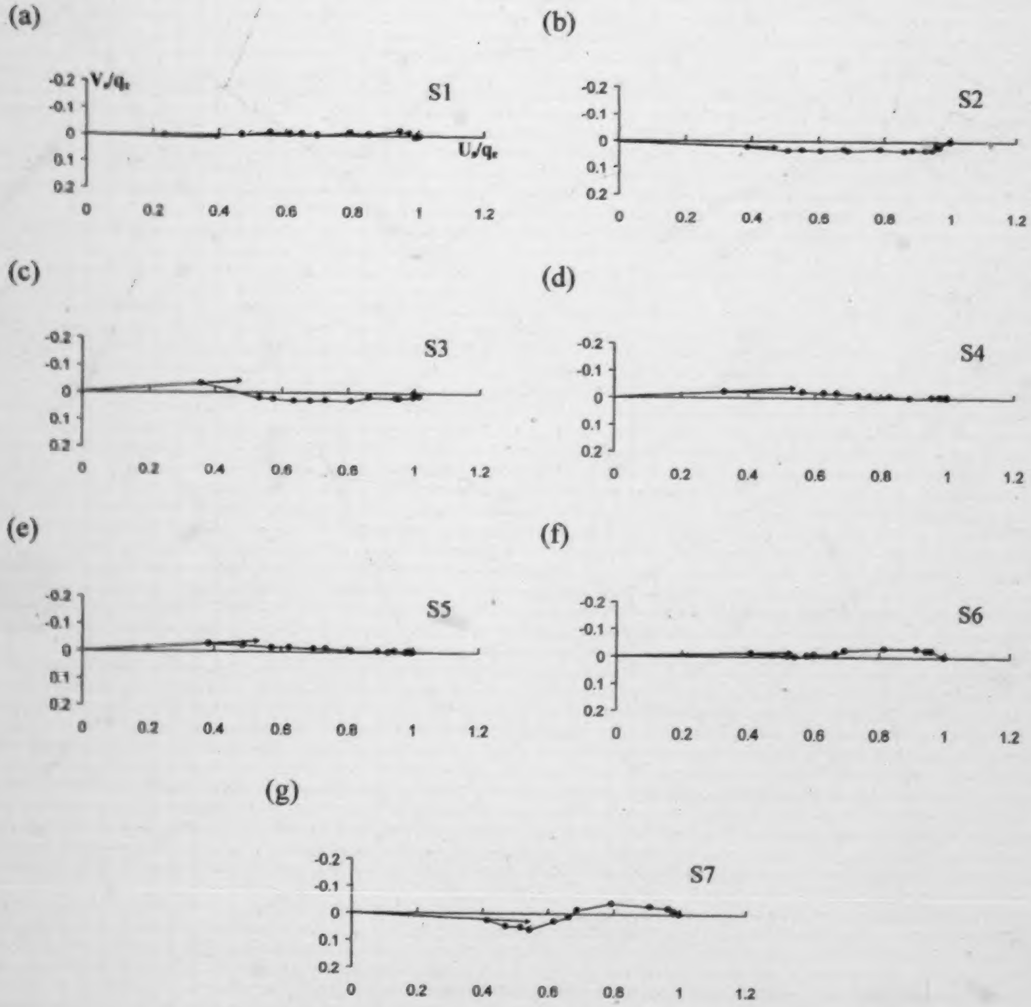

Fig. 4.28 Johnston's polar plots for Regime-1.

The normalized velocity components along (U_s/q_e) and perpendicular (V_s/q_e) to the free streamline direction are plotted on horizontal and vertical axes. The arrow represents the direction of local bed shear stress (τ_0).

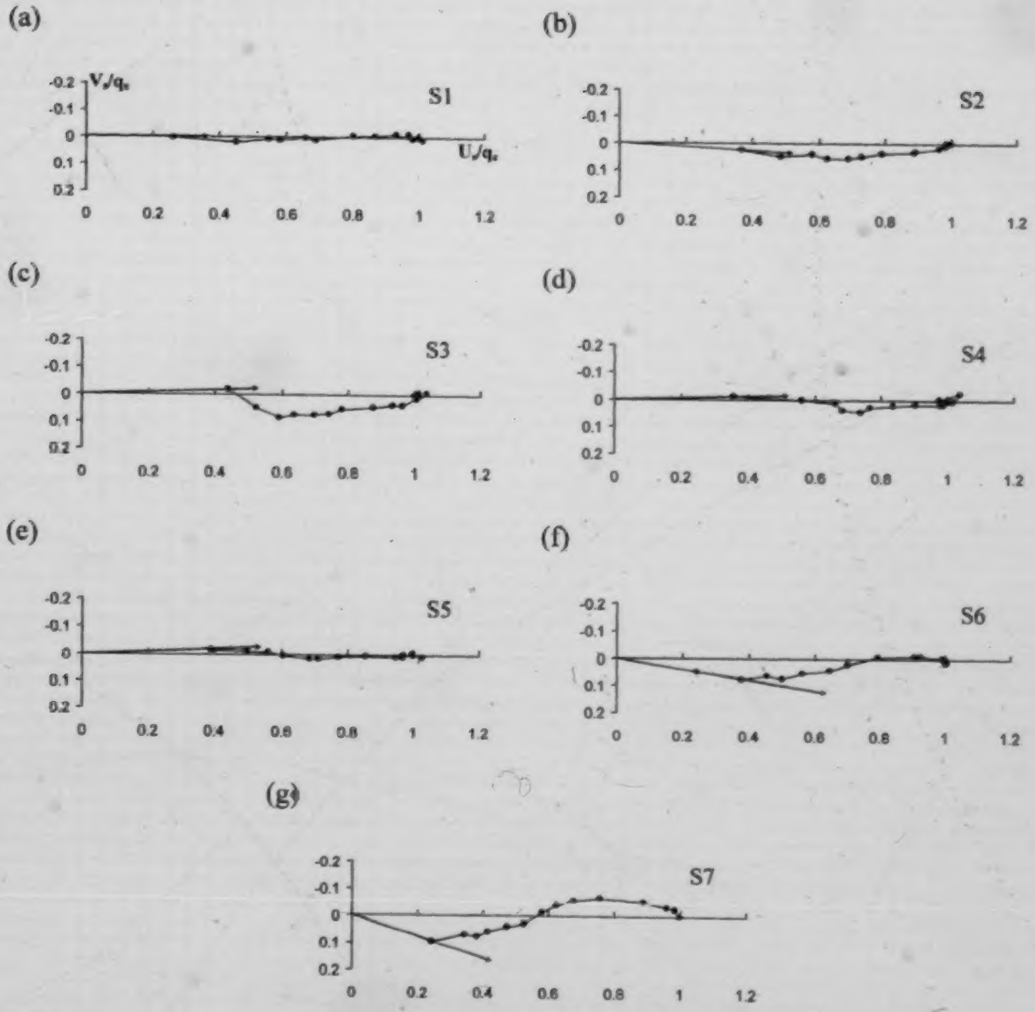

Fig. 4.29 Johnston's polar plots for Regime-2.

The normalized velocity components along (U_s/q_e) and perpendicular (V_s/q_e) to the free streamline direction are plotted on horizontal and vertical axes. The arrow represents the direction of local bed shear stress (τ_0).

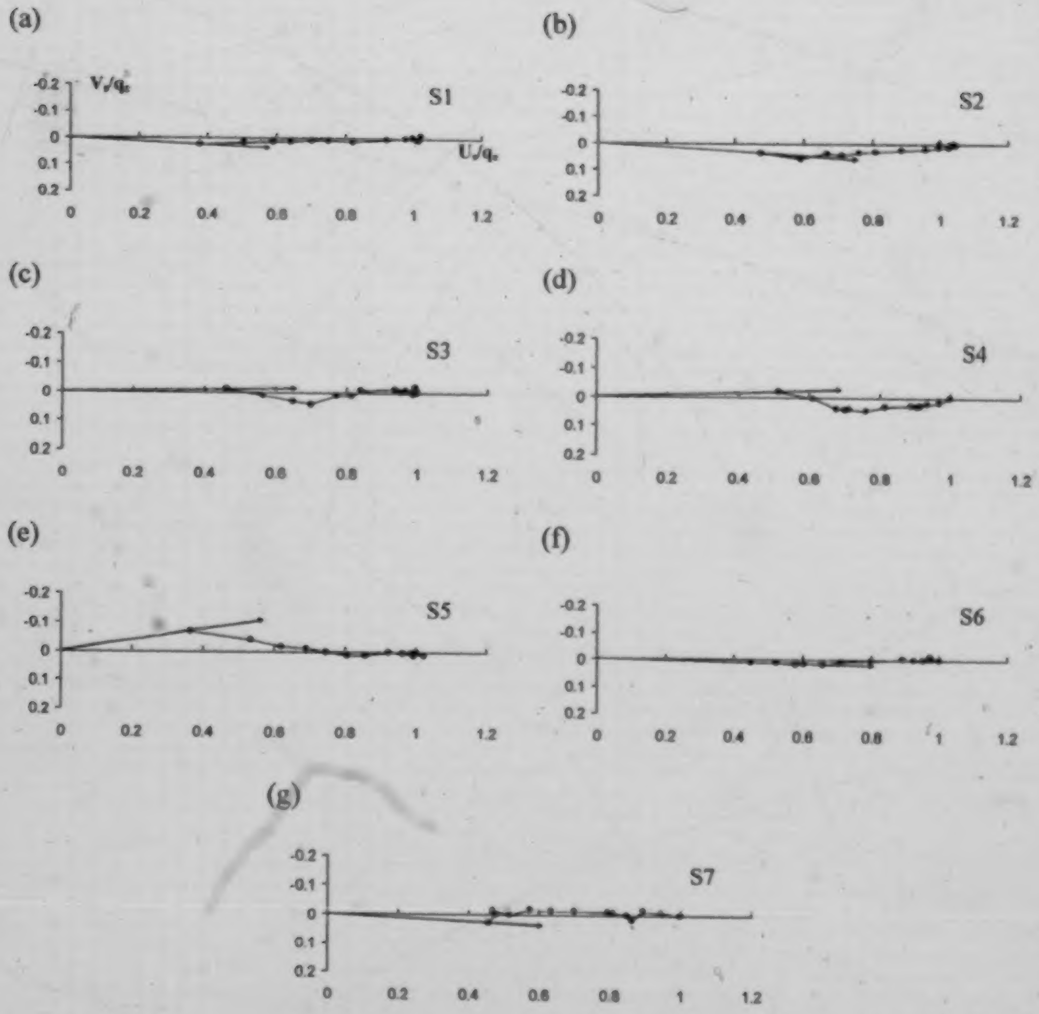

Fig. 4.30 Johnston's polar plots for Regime-3.

The normalized velocity components along (U_s/q_e) and perpendicular (V_s/q_e) to the free streamline direction are plotted on horizontal and vertical axes. The arrow represents the direction of local bed shear stress (τ_0).

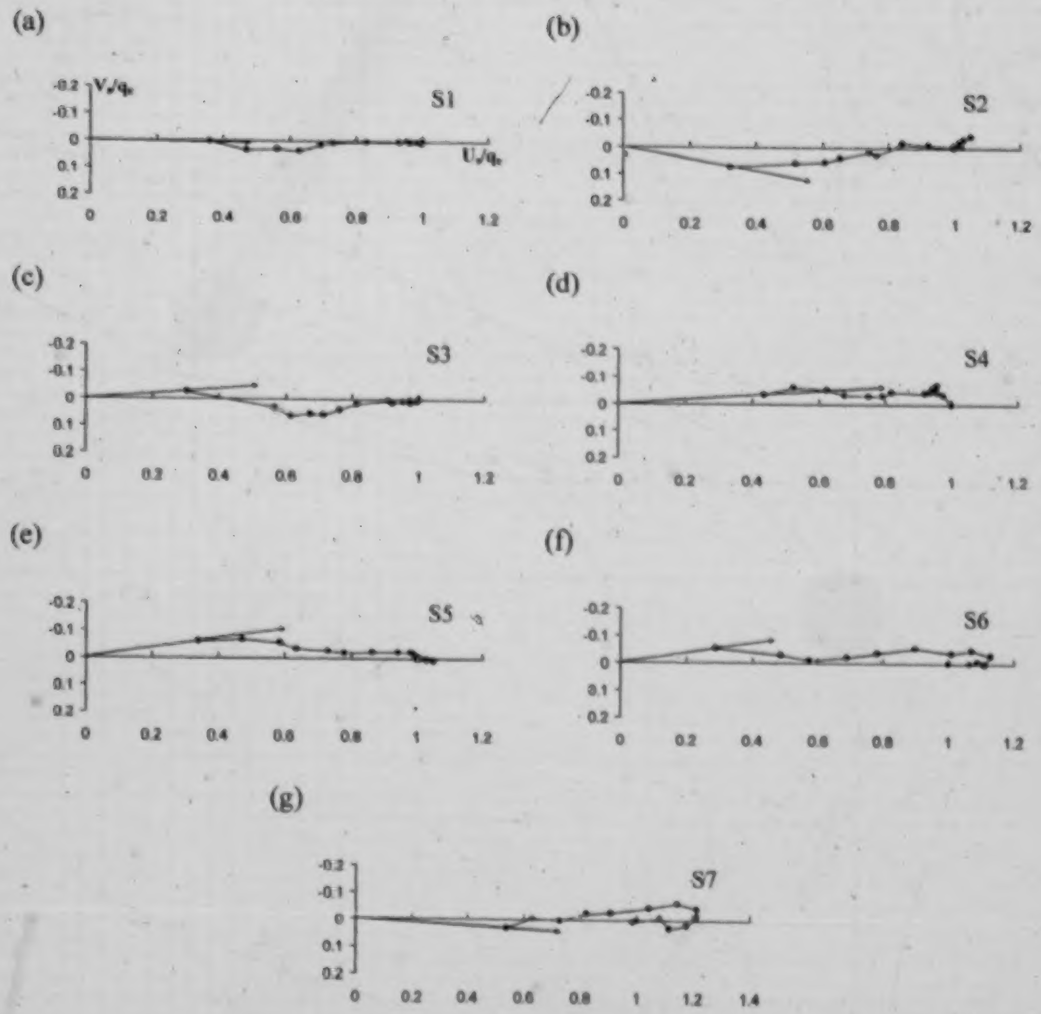

Fig. 4.31 Johnston's polar plots for Regime-4.

The normalized velocity components along (U_s/q_e) and perpendicular (V_s/q_e) to the free streamline direction are plotted on horizontal and vertical axes. The arrow represents the direction of local bed shear stress (τ_0).

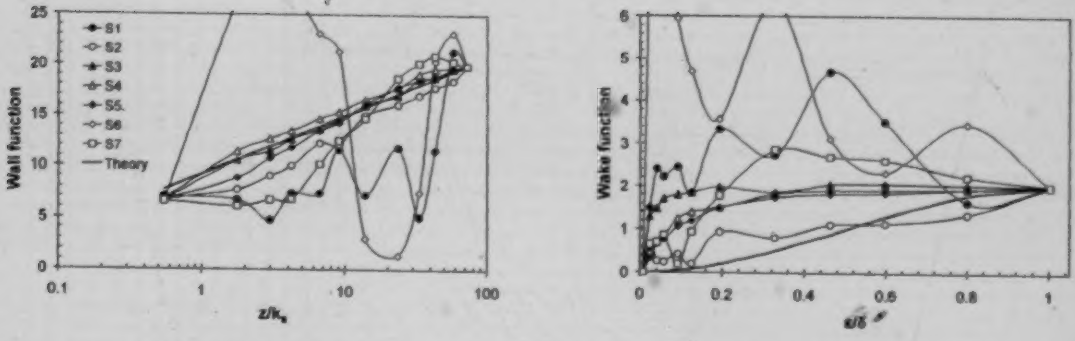

(a-1) Regime-1

(a-2) Regime-1

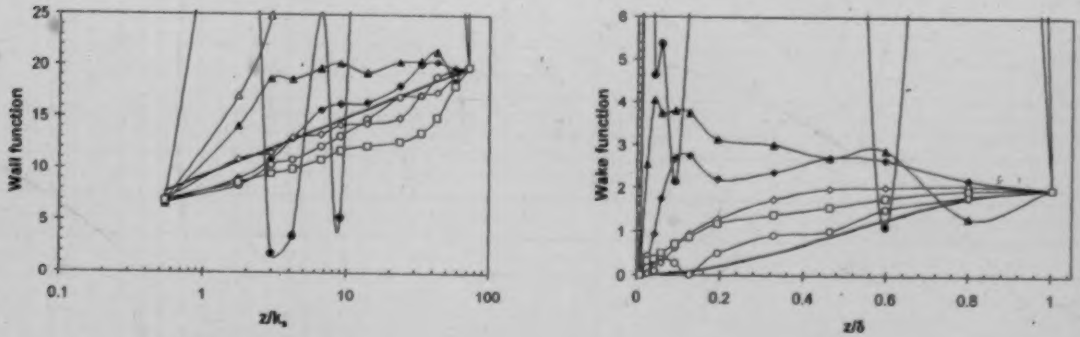

(b-1) Regime-2

(b-2) Regime-2

Fig. 4.32 Coles' wall and wake functions versus z/k_s and z/δ;

(a) Regime-1, (b) Regime-2

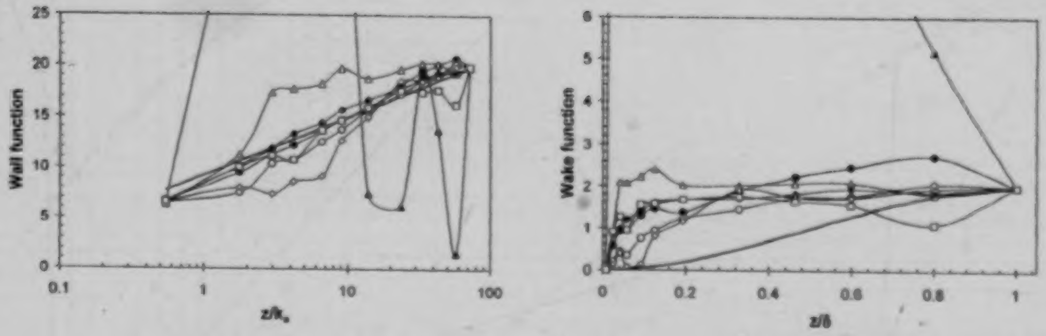

(c-1) Regime-3

(c-2) Regime-3

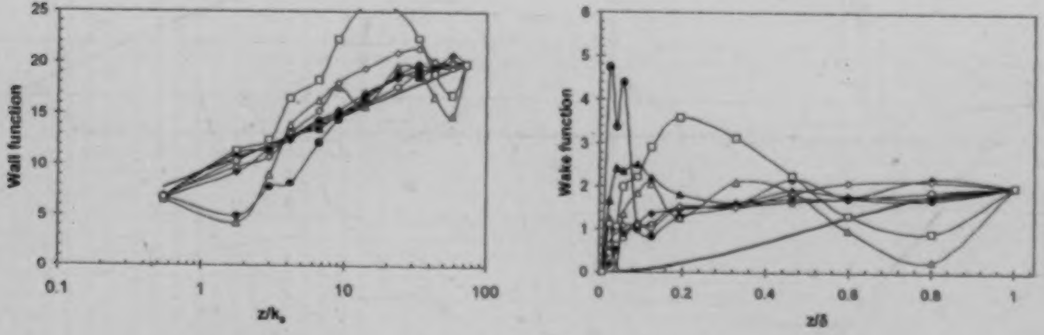

(d-1) Regime-4

(d-2) Regime-4

Fig. 4.32 (contd.) Coles' wall and wake functions versus z/k_s and z/δ; (c) Regime-3, and (d) Regime-4

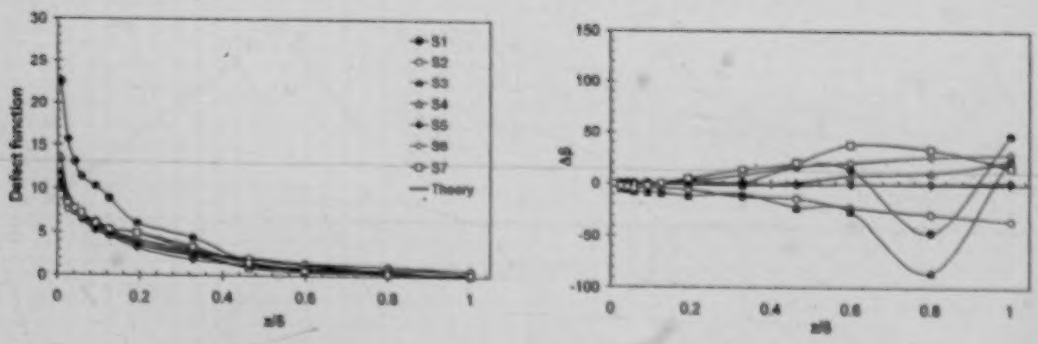

(a-1) Regime-1 (a-2) Regime-1

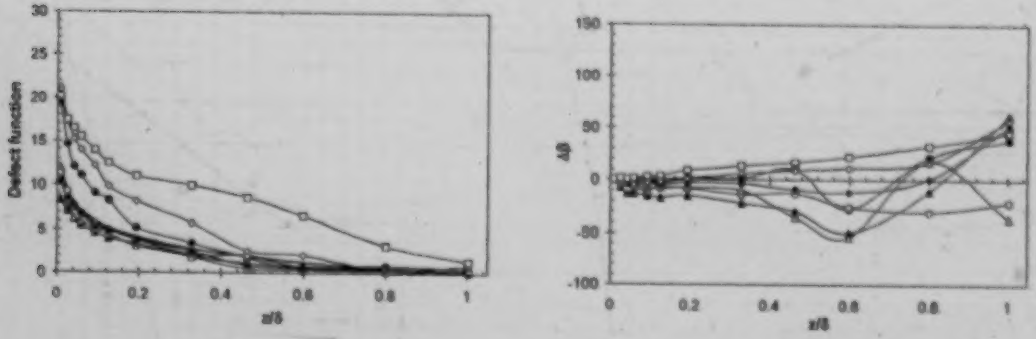

(b-1) Regime-2 (b-2) Regime-2

Fig. 4.33 Perry and Joubert's defect function and Δβ versus the normalized depth, z/δ; (a) Regime-1, (b) Regime-2

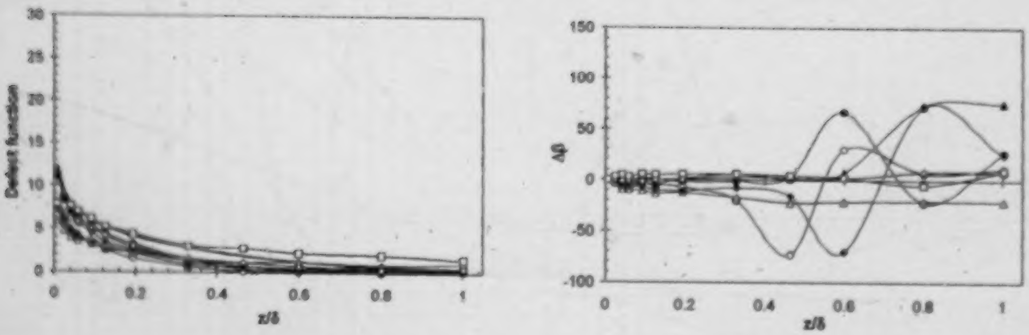

(c-1) Regime-3 (c-2) Regime-3

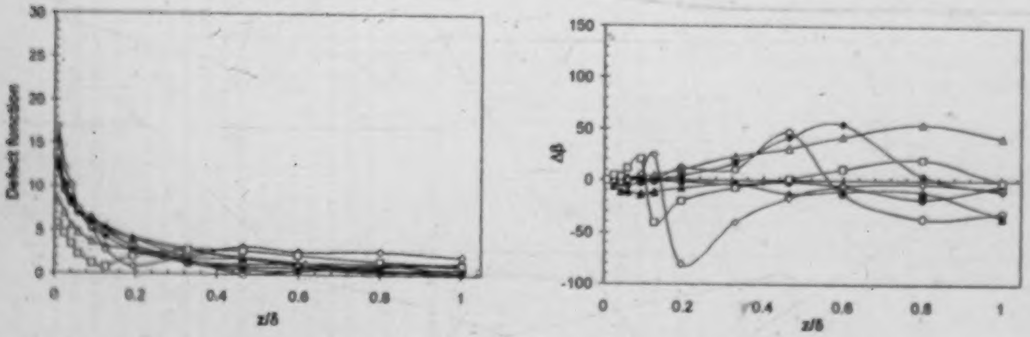

(d-1) Regime-4 (d-2) Regime-4

Fig. 4.33 (contd.) Perry and Joubert's defect function and Δβ versus the normalized depth, *z*/δ; (c) Regime-3, (d) Regime-4

4.6 References

Ahmed, F. (1995). *Flow and erosion around bridge piers*, Ph. D. thesis, University of Alberta, Edmonton, AB, Canada.

Ahmed, F. (2000). "Three-dimensional mean velocity analysis of a 30 degree bend flow." *Journal of Engineering Mechanics*, 126(12), 1262-1272.

Ahmed, F., and Rajaratnam, N. (1997a). "Three-dimensional turbulent boundary layers: A review." *Journal of Hydraulic Research*, 35(1), 81-98.

Ahmed, F., and Rajaratnam, N. (1997b). "The three-dimensional turbulent boundary layer flow around bridge piers." *Journal of Hydraulic Research*, 35(2), 209-224.

Ahmed, F., and Rajaratnam, N. (1998). "Flow around bridge piers." *Journal of Hydraulic Engineering*, 124(3), 288-300.

Ahmed, F., and Rajaratnam, N. (2000). "Observations of flow around bridge abutment." *Journal of Engineering Mechanics*, 126(1), 51-59.

Albers, C. D. (1997). *Hydraulics of a three obstacle cluster in open channels*, M. Sc. thesis, Department of Civil and Environmental Engineering, University of Alberta, Edmonton, AB, Canada.

Arya, S. P. S. and Gadiyaram, P. S. (1986). "An experimental study of flow and dispersion in the wakes of three-dimensional low hills." *Atmospheric Environment*, 20(4), 729-740.

Bockelmann, B. N., Fenrich, E. K., Lin, B. and Falconer, R. A. (2004). "Development of an ecohydraulics model for stream and river restoration." *Ecological Engineering*, 22, 227-235.

Burrows, A. D. and Steffler, P. M. (2005). "Depth averaged modeling of flow around individual boulders." *Proc., 17th Canadian Hydrotechnical Conference*, CSCE, Edmonton, Alberta, 395-404.

Chandrashekhar, N., and Swamy, N. V. C. (1976). "Wall shear stress inference for three-dimensional turbulent boundary layer velocity profiles." *Journal of Applied Mechanics*, 43, 20-27.

Chang, P. K. (1970). *Separation of flow*, Pergamon Press, New York, NY, USA.

Chen, D., and Jirka, G. H. (1995). "Experimental study of plane turbulent wakes in a shallow water layer." *Fluid Dynamics Research*, 16, 11-41.

Coles, D. (1956). "The law of the wake in the turbulent boundary layer." *Journal of Fluid Mechanics*, 1, 191-226.

Hollingshead, A. B., and Rajaratnam, N. (1980). "A calibration chart for the Preston tube." *Journal of Hydraulic Research*, 18(4), 313-326.

Hornung, H. G., and Joubert, P. N. (1963). "The mean velocity profile in three-dimensional turbulent boundary layers." *Journal of Fluid Mechanics*, 15, 368-384.

Ingram, R. G., and Chu, V. H. (1987). "Flow around islands in Rupert bay: An investigation of the bottom friction effect." *Journal of Geophysical Research*, 92(C13), 14521-14533.

Johnston, J. P. (1960). "On the three-dimensional turbulent boundary layer generated by secondary flow." *Journal of Basic Engineering*, 233-248.

Kemp, J. L., Harper, D. M., and Crosa, D. A. (2000). "The habitat-scale ecohydraulics of rivers." *Ecological Engineering*, 16, 17-29.

Lloyd, P. M., and Stansby, P. K. (1997a). "Shallow-water flow around model conical islands of small side slope. I: Surface piercing." *Journal of Hydraulic Engineering*, 123(12), 1057-1067.

Lloyd, P. M., and Stansby, P. K. (1997b). "Shallow-water flow around model conical islands of small side slope. II: Submerged." *Journal of Hydraulic Engineering*, 123(12), 1068-1077.

Lowe, S. (1992). *Fish habitat enhancement designs*, Alberta Environmental Protection, Water Resources Management Services, Technical Services and Monitoring Division, River Engineering Branch, Alberta, Canada.

Maddock, I. (1999). "The importance of physical habitat assessment for evaluating river health." *Freshwater Biology*, 41, 373-391.

Nash, J. F., and Patel, V. C. (1972). *Three-dimensional turbulent boundary layers*, SBC Technical Books, Scientific and Business Consultants, Inc., Atlanta, USA.

Patel, V. C. (1965). "Calibrations of the Preston tube and limitations on its use in pressure gradients." *Journal of Fluid Mechanics*, 23, 185-208.

Perry, A. E., and Joubert, P. N. (1965). "A three-dimensional turbulent boundary layer." *Journal of Fluid Mechanics*, 22, 285-304.

Pierce, F. J., and Krommenhoek, D. H. (1968). *Wall shear stress diagnostics in three-dimensional turbulent boundary layers*, Interim Technical Report No. 2, Project 6858E U. S. Army Research Office-Durham, Virginia Polytechnic Institute and State University, USA.

Prahlad, T. S. (1968). "Wall similarity in three-dimensional turbulent boundary layers." *American Institute of Aeronautics and Astronautics Journal*, 6, 1772-1774.

Prandtl, L. (1946). *On boundary layers in three-dimensional flow*, Reports and Transactions No. 64, British Ministry of Aircraft Production, Volkenrode.

Prasad, A., and Williamson, C. H. K. (1997). "The instability of the shear layer separating from a bluff body." *Journal of Fluid Mechanics*, 333, 375-402.

Rajaratnam, N., and Muralidhar, D. (1968). "Yaw probe used as Preston tube." *The Aeronautical Journal of the Royal Aeronautical Society*, 72, 1059-1060.

Rajaratnam, N., and Nwachukwu, B. A. (1983). "Flow near groin-like structures." *Journal of Hydraulic Engineering*, 109(3), 463-480.

Sadeque, M. A. F., Rajaratnam, N., and Loewen, M. R. (2008). "Flow around cylinders in open channels." In press, *Journal of Engineering Mechanics*.

Schlichting, H. (1968). *Boundary-layer theory*, 6th Edition, McGraw-Hill Book Company, NY, USA.

Shamloo, H., Rajaratnam, N., and Katopodis, C. (2001). "Hydraulics of simple habitat structures." *Journal of Hydraulic Research*, 39(4), 351-366.

Smith, H. D., and Foster, D. L. (2007). "Three-dimensional flow around a bottom-mounted short cylinder." *Journal of Hydraulic Engineering*, 133(5), 534-544.

Statzner, B. and Higler, B. (1986). "Stream hydraulics as a major determinant of benthic invertebrate zonation patterns." *Freshwater Biology*, 16, 127-139.

Waddle, T. J., ed., (2001). *PHABSIM for windows: user's manual and exercises*, Open-File Report 01-340, U.S. Geological Survey, Fort Collins, CO.

Williamson, C. H. K. (1996). "Vortex dynamics in the cylinder wake." *Annual Review of Fluid Mechanics*, 28, 477-539.

Chapter 5: Turbulent Flow Field Upstream of Cylinders

5.1 Introduction

Studies of flow around submerged and surface piercing bluff bodies in open channels are of interest to engineers because it will lead to improved understanding of the flow and its consequences; e.g. scour. Bridge pier is probably the best example of surface piercing object in open channel flows. Thousands of hydraulic studies had been conducted for better understanding of the nature of flow around bridge piers and its relation to local scour (e.g., Ahmed and Rajaratnam 1998, Dey and Raikar 2007). Submerged structures are relatively uncommon to hydraulic engineers, except for a few structures like submerged intake or outfall. However, flows around submerged bluff bodies have a lot of relevance to many environmental and geophysical flow systems; e.g. flow around simple fish habitat structures, effluent discharge in a braided river, flow around emerging islands in shallow coastal estuaries etc. Similar to bridge pier submerged hydraulic structures can experience local scour problem. On the other hand, local scour is essential for useful fish habitat structures, like fish rocks. In coastal region sand mounds, tidal banks and coral reefs are naturally developed bodies which could be submerged or surface piercing. The general flow field and sediment processes around these natural bodies or man-made structures are of interests to engineers, ecologists and geophysicists. For example, Shamloo et al. (2001) studied the flow and erosion around hemispherical objects modeled as simple fish habitat structures; Pingree and Maddock (1979) studied the general flow field and sediment processes around sand mounds and tidal banks including the dynamics of their own formation and erosion; Wolanski et al. (1984) studied the flow around coral reefs in the coral-rich coast of north-eastern Australia. In spite of extensive studies of flow around bridge-pier-like objects, our knowledge of flow around bluff bodies in open channel remains limited. Menna and Pierce (1988) claimed that there is a severe shortage of comprehensive experimental data of turbulent and complex flows around bluff bodies that can serve for an unbiased test of the predictive capabilities of computational models. They documented a detailed experimental database on the upstream and surrounding three-dimensional boundary layer flows around a stream-lined surface piercing cylinder. Ahmed and Rajaratnam (1998), Dargahi (1987), Melville (1975) and many other researchers provided excellent experimental results on flow around bridge-piers that enabled computational modelers (e.g., Salaheldin et al. 2004) to examine the predictive capabilities and shortcomings of their models. However, there are only a few recent studies on flow around submerged models (e.g., Shamloo et al. 2001, Lloyd and Stansby 1997) in open channel flows that can serve for computational modeling. Recently, Burrows and Steffler (2005) used the experimental data of Shamloo et al. (2001) for depth-averaged modeling of velocities around individual boulders. Sadeque et al. (2008) [Note that this study is presented in Chapter 4: Part I] measured two-dimensional velocities around submerged and surface piercing cylinders on smooth bed in an open channel to examine the applicability of three-dimensional boundary layer theories. They observed that only Perry and Joubert's (1965) model can reasonably predict the deflected velocity magnitudes around the cylinders. However, Sadeque et al. (2008) had to measure the velocities relatively far from the cylinders so that vertical components could be ignored, as the theories were not developed for the boundary layer close to the cylinder. In these circumstances, the study of flow around submerged cylinders can be considered to be in a primitive state. Therefore, the scope and demand for the study of flow around submerged and surface piercing cylinders in open channels can be considered to be enormous.

Therefore, as a part of detailed study of flow around submerged and surface piercing cylinders, the present study has been designed to experimentally observe the mean and turbulent flow fields in the upstream region surrounding the cylinders.

5.2 Experimental Setup and Procedure

Cylindrical objects of equal diameter (D = 11.4 cm) and four heights (h) were tested under similar approach flow conditions (discharge 50 L/s) and water depths (H = 22 cm) to create different levels of submergence in an open channel. Submergence levels were selected such that four flow regimes, as defined by Shamloo et al. (2001), can be produced. Definition sketches for four flow regimes are given in Figure 2.8. Experiments were conducted on smooth and rough beds to study the effect of bed roughness on the upstream flow. Three components of velocities were measured using a 10 MHz Acoustic

Doppler Velocimeter (ADV) at stations close to the cylinders so that nature of three-dimensional flow can be observed in finer details. Typical measuring stations upstream of the cylinders are shown in Figure 5.1. The experimental flow conditions are summarized in Table 2.1. General description of the experimental setup and procedure is given in Chapter 2. At first the flow development was studied on smooth and rough beds without any cylinder and the approach flow velocity and bed shear stress were measured at the channel center [see Chapter 3]. A set of flow visualization tests was also conducted prior to the detailed measurements of velocity. Flow visualization test results are presented in Chapter 4.

5.3 Result Analysis and Discussions

5.3.1 *Observations of mean velocity on upstream plane of symmetry*

The 2D velocity vectors plotted in Figure 5.2(a-d) and 5.3(a-d) show the general flow pattern upstream of the cylinders on the plane of symmetry (POS). These vectors are normalized by the cross-sectional mean velocity U_0. In all flow regimes, the upstream flow velocities on the POS experience appreciable deceleration when approach very close to the object (~1D). In Regime-1 (Fig. 5.2(a) and 5.3(a)) and Regime-2 (Fig. 5.2(b) and 5.3(b)) the deceleration of the upstream flow velocities are observed only near the bed, i.e., for $z \leq 0.5h$ in Regime-1 and $z \leq 0.67h$ in Regime-2. However, the flows over an elevation move upward to pass over the submerged objects. In Regime-3 (Fig. 5.2(c) and 5.3(c)) and Regime-4 (Fig. 5.2(d) and 5.3(d)) the deceleration of the upstream flow velocities are observed over the entire depth of measurements ($z \sim 0.7H$). Moreover, the upstream flow in Regime-3 and Regime-4 has downward movement in front of the cylinders. Overall the bed roughness causes greater deceleration to the near-bed velocities as compared to the smooth bed flow in all flow regimes. The resolution of the point measurements made in this study could not trace any point/line of separation upstream of the object in any flow regime.

U/U_0 vs z/H, U/U_z vs z/H, and W/U_0 vs z/H profiles for Regime-1 on smooth bed are plotted in Figure 5.4(a-c). Similar set of profiles are plotted for other flow regimes on smooth and rough beds in Figure 5.5(a-c) to 5.11(a-c). Here, U_z is the mean velocity U at any elevation z in undisturbed flow on the respective bed condition. U/U_0 vs z/H profiles show the relative speed of the flow at different elevation of different station in different flow regimes on smooth and rough beds. U/U_z vs z/H profiles show the relative speed of the disturbed approach flow compared to the undisturbed flow in different flow situations. Variations in the upward and downward flow intensities can be studied from the W/U_0 vs z/H profiles.

It can be observed from Figure 5.4 and 5.5 that, in Regime-1 and Regime-2 on smooth bed, the approach flow started to slow down considerably from x=-1D, but the extent of retardation is somewhat greater in Regime-2. The upward flow velocities are found maximum at the level of object height for both the regimes, though it was relatively stronger in Regime-2. This might be the reason of observing a distinct change in curvature of the U/U_0 vs z/H profiles from x=-1D in Regime-2. Regime-3 and Regime-4 on smooth bed have some similarity as well (Figure 5.6 and Figure 5.7). The intensities of approach flow retardation very close to the object are almost similar over the depth. However, the approach flow starts to slow down abruptly after passing the station at x=-3D in Regime-4, which is relatively gradual in Regime-3. The downward flow near the object is prominent in both Regime-3 and Regime-4, but there is some upward flow at z>0.5H in Regime-3.

Flow visualization tests and bed shear stress measurements revealed that flow separation points on the upstream POS are within x=-1.7D to -0.9D for different regimes depending on the bed conditions (see Chapter 4). However, the reverse flow due to horse-shoe vortex system could not be traced by velocity measurements near the object, though the lowest point of measurement was only 5 mm away from the bed. However, it is interesting to note that the flow within bottom 10% of the water depth experience the greatest deceleration when approach very close to the object in any flow regime. This might be the region affected by the thin layer of horse-shoe vortex system developed at the toe of the cylinders. The rough bed profiles (Figure 5.8 to 5.11) are very similar to those of smooth bed profiles, except for relatively greater deceleration of the near-bed (z<0.1H) velocities.

5.3.2 *Observations of vorticity near the point of separation on upstream POS*

In order to investigate the strength of vorticity near the separation point at the toe of the cylinders the profiles of ω_y vs z/H on the upstream POS at $x/D = -1$ in all flow regimes on smooth and rough beds are plotted in Figure 5.12(a-b). The profile of ω_y vs z/H in undisturbed approach flow is also presented on the same figure to facilitate the observation of change in vorticity near the separation point. Figure 5.12(a) shows that there is significant increase in vorticity near the bed as compared to the undisturbed flow condition. However, the results shown in Figure 5.12(b) do not indicate any significant increase in vorticity. This is due to the fact that the separation point is yet to arrive. Flow visualization and bed shear stress results shown in Chapter 4 support this observation, as the point of separation is observed relatively closer to the cylinder (at less or equal to 1D upstream) on rough bed.

5.3.3 *Observations of logarithmic law, defect law and Clauser's scheme profiles*

Logarithmic [U/u_* vs zu_*/ν], defect function [$(U_e-U)/u_*$ vs z/δ] and Clauser's scheme profiles are plotted for Regime-1 on smooth bed in Figure 5.13(a-c). Similar set of profiles are plotted for other flow regimes on smooth and rough beds in Figure 5.14(a-c) to 5.20(a-c). Here, u_* is the friction velocity of the undisturbed approach flow, k_s is the Nikuradse's equivalent sand thickness, U_e is the local free stream mean velocity in disturbed flow, δ is the boundary layer thickness (δ=15 cm as observed in Chapter 3 and 4), and Δ^* is the Clauser's integral parameter. For the present study, U_e is taken to be the mean velocity U at the highest measuring point at each station (i.e. at z=15 cm) and Δ^* is computed by numerical integration. Theoretical lines showing the law-of-the-wall and the theoretical curves showing the velocity defect law are also plotted in relevant figures. The measurements in undisturbed approach flow provided the parameters (u_*, k_s etc.) required for producing the theoretical line of the law-of-the-wall on rough bed.

It can be observed from the logarithmic profiles [Fig. 5.13(a), 5.14(a), 5.15(a), 5.16(a), 5.17(a), 5.18(a), 5.19(a), and 5.20(a)] that the bottom portion of the measured profiles of all flow regimes on smooth and rough beds fall close to the theoretical line of the law-of-the-wall when the measuring stations are far away from the cylinders. As the flow approach closer the measured profiles gradually move away from the theoretical line indicating increased level of flow disturbance. Velocities measured sufficiently above the cylinder height in Regime-1 and Regime-2 do not experience any disturbance, and hence the data points corresponding to upper elevations from all the upstream stations collapse in a narrow band. However, the logarithmic profiles in Regime-3 and Regime-4 shift downward from the theoretical line, but parallel to most of the upstream profiles. This indicates that gradually increasing flow disturbance take place over the entire depth of measurements as the flow approaches near the cylinder.

The profiles of the velocity defect function in Regime-1 and Regime-2 [Fig. 5.13(b), 5.14(b), 5.17(b), and 5.18(b)] collapse in a narrow band, when the measuring stations are far away from the cylinders. Since the velocity above the top surface of the cylinders in Regime-1 and Regime-2 are not disturbed enough, the defect functions do not perform well. However, the profiles are not very far from the theoretical curves of velocity defect law. Regime-3 and Regime-4 [Fig. 5.15(b), 5.16(b), 5.19(b), and 5.20(b)] produce very good agreement among the upstream profiles, though they have a little different shape compared to the theoretical curves. However, the rough bed profiles are closer to the theoretical curves. The profiles obtained from Clauser's scheme [Fig. 5.13(c), 5.14(c), 5.15(c), 5.16(c), 5.17(c), 5.18(c), 5.19(c), and 5.20(c)] are found to collapse in a narrow band in all flow regimes on both smooth and rough beds. These results indicate that an approximate relationship can be determined to describe the approach flow profiles subjected to an adverse pressure gradient on smooth and rough beds.

Using the magnitudes of local friction velocities (u_*') computed from direct measurements of bed shear stress (τ_0), logarithmic [U/u_*' vs zu_*'/ν], defect function [$(U_e-U)/u_*'$ vs z/δ] and Clauser's scheme profiles are replotted for Regime-1 on smooth bed in Figure 5.21(a-c). Similar set of profiles are plotted for other flow regimes on smooth and rough beds in Figure 5.22(a-c) to 5.28(a-c). Here, the velocity profiles are plotted only for the stations where τ_0 is positive; i.e. for the stations upstream of the separation point. It can be observed from the logarithmic profiles [Fig. 5.21(a), 5.22(a), 5.23(a), 5.24(a), 5.25(a), 5.26(a), 5.27(a) and 5.28(a)] that the bottom portion of the measured profiles of all flow regimes on smooth and rough beds fall close to the theoretical line of the law-of-the-wall when the measuring stations are far away from the cylinders. As the flow approach closer the measured profiles gradually move away from the theoretical line indicating reduced longitudinal velocity (U) and smaller friction velocity (u_*') due to increased level of flow disturbance. The logarithmic profiles with local friction velocity (u_*') show two changes; reduction in bed shear stress along with flow retardation. The measured profiles of the velocity defect function and Clauser's scheme using local friction velocities (u_*') are found similar to those observed using approach flow friction velocity (u_*).

The variations of δ^*_x with distance (i.e. x/D) on the upstream POS in all flow regimes on both smooth and rough beds are plotted in Figure 5.29(a). The figure shows that Regime-1 and Regime-2 have similar trends of δ^*_x vs x/D. However, Regime-3 and Regime-4 have similar trends until the flow reach very close to the cylinders. Similar is the observation from Figure 5.29(b), where the variations of Δ^* with x/D on the upstream POS in all flow regimes on both smooth and rough beds are plotted. In Figure 5.29(b), the magnitudes of Δ^* are computed using the undisturbed flow friction velocity (u_*). Similar to Figure 5.29(b), the variations of Δ^* with x/D on the upstream POS for smooth and rough bed results are replotted in Figure 5.29(c), where the magnitudes of Δ^* are computed using the magnitudes of local friction velocity (u_*'). However, the results are similar to Figure 5.29(b).

5.3.4 *Observations of turbulence quantities on upstream POS*

Profiles of the turbulence quantities on smooth and rough bed flows are plotted in Figure 5.30 to 5.37. The normalized profiles of three components of r.m.s. velocities (u'/u_*, v'/u_* and w'/u_*), turbulent kinetic energy (k/u_*^2), and the primary Reynolds stress ($-\overline{uw}/\overline{u_*}^2$) for Regime-1 on smooth bed are plotted in Figure 5.30(a-e). Similar set of profiles are plotted for other flow regimes on smooth and rough beds in Figure 5.31(a-e) to 5.37(a-e). Here, u_* is the friction velocity of the undisturbed approach flow at the channel center, and $\overline{u_*}$ is the cross-sectional average of the friction velocities of the approach flow.

Upstream measurements on smooth bed have produced a lot of scatter in turbulence quantities due to bed reflection noise received by ADV. Rough bed measurements are, however, free from these noise as the reflections are scattered away from the ADV probe by irregular surface of the sand grains. However, the data points near the bed ($z<0.2H$) on smooth bed are reliable and consistent. The rough bed results, on the other hand, are very consistent over the entire depth of measurements.

It is interesting to note that all the upstream profiles on the POS are found comparable to those obtained for undisturbed flow on smooth and rough beds at the center plane of the channel [see Chapter 3]. There are no significant differences in near bed turbulence quantities at upstream measuring stations for different flow regimes on smooth bed (Fig. 5.30 to 5.33), except for a little higher turbulence at stations (x=-1 to -0.85D) closer to the cylinders. The horse-shoe vortex system at the toe of the cylinders could be the reason for such increased turbulence near the bed at closer stations. Similarly, all the upstream profiles of turbulence quantities on rough bed in different flow regimes (Fig. 5.34 to 5.37) collapse in a narrow band, with slightly higher turbulence near the bed at x=-1 to -0.85D. However, the rough bed turbulence quantities are somewhat higher than those on smooth bed for similar flow conditions. These observations indicate that unlike the mean flow the turbulence properties of the upstream approach flow on the POS do not change in any regime for a given bed condition until the flow reaches very close to the object.

5.3.5 *Upstream deflected flow: mean velocities and turbulence*

Normalized mean velocity (U/U_0, U/U_z, V/U_0 and W/U_0) profiles at x=-1D, -0.85D, -0.5D and 0 on three different longitudinal planes (at y=0.5D, 0.8D and 1D) on smooth and rough beds are plotted in Figure 5.38(a-d) to 5.61(a-d). These figures indicate that the longitudinal mean velocity (U) slows down (i.e., $U/U_z<1$) in the longitudinal direction along the plane at y=0.5D, but it speeds up (i.e., $U/U_z>1$) considerably at y=0.8D and 1D. The change in U is the least in the upstream region surrounding the cylinder in Regime-1, though the deflection is strong in transverse ($V\approx0.1\text{-}0.3U_0$) as well as in vertical ($W\approx0.05\text{-}0.15U_0$) direction. Flow deflection is much stronger in Regime-2 ($V\approx0.1\text{-}0.45U_0$ and $W\approx0.05\text{-}0.2U_0$) than in Regime-1. However, the deflected transverse velocity (V)

gradually diminishes away from the bed. On the other hand, Regime-3 and Regime-4 produce very strong transverse velocity (V), as high as 0.5-$0.6U_0$ near the cylinders, and its distribution is also uniform over the entire depth except very close to the bed (at $z/H \leq 0.1$). Vertical flow (W) in the upstream region surrounding the cylinder goes only upward in Regime-1 and mostly downward in Regime-4. But the vertical component of velocity (W) has different trend at very close stations (e.g. at x=-0.5D) in Regime-2 and Regime-3, where the flow goes upward in the upper zone and downward in the lower zone. Overall the maximum intensity of vertical flow (W) is as high as 0.1-$0.2U_0$ near the cylinders, but it falls to 0.02-$0.08U_0$ away from cylinders at y=1D. Mean velocity deflection patterns in the transverse and vertical directions in the upstream region surrounding the cylinders are, therefore, different for different regimes, but the effect of bed roughness on the deflection pattern is minimal for the stations close to the cylinders.

The profiles of normalized turbulence quantities (k/u_*^2, $-\overline{uw}/\overline{u_*}^2$) at x=-1D, -0.85D, -0.5D and 0 on three different longitudinal planes (at y=0.5D, 0.8D and 1D) on smooth and rough beds are plotted in Figure 5.62(a-f) to 5.69(a-f). These figures indicate that the near-bed turbulence increases considerably when the flow approaches very close to the cylinders. Near-bed turbulent kinetic energy and turbulent shear stress increase as high as 2-3 times compared to those observed relatively far away from the cylinders. However, there is very little change in turbulence away from the bed at $z>0.1H$ if compared to the profiles at relatively far away from the cylinders. The effect of bed roughness on turbulence has been found to be insignificant.

5.3.6 *Deflected flow at x=0 plane: mean velocities and turbulence*

It is known that the flow speeds up while passing the shoulder of a cylinder. According to the potential flow solution for flow around free ended circular cylinder longitudinal velocity at the shoulder could be twice of the uniform ambient velocity. However, for an open channel boundary layer of a real fluid approaching a bed-mounted vertical cylinder this velocity amplification at the shoulder is expected to be different from potential flow solution. Ahmed and Rajaratnam (1998) observed that the velocity magnitude could be as high as 1.8 times of the undisturbed velocity (U_z) at z/H=0.2 for surface piercing cylinders. However, they observed that the velocity amplifications had been less when measured away from the bed. Present study investigates the variation of longitudinal velocity amplification for submerged and surface piercing cylinders in shallow water on smooth and rough beds for similar flows. The profiles of U/U_0, U/U_z, V/U_0 and $W/U_0$with y/D are plotted for all flow regimes on smooth and rough beds at different elevations (i.e. z/H) on the x=0 plane in Figure 5.70(a-d) to 5.77(a-d). The profiles of U/U_0 with y/D indicate that the major portion of the water depth have similar flow intensity except near the bed. Though the near-bed flow intensities (U/U_0) are relatively less compared to the upper velocities, the amplification with respect to the undisturbed flow condition (U/U_z) is greater near the bed. Such velocity amplifications can be considered partly responsible for local scour initiation on mobile bed. The maximum amplification (at y=0.8D) of near-bed longitudinal velocity (U) with respect to undisturbed flow condition (U_z) on smooth bed has been found to be 1.06, 1.18, 1.3, and 1.42 for Regime-1, 2, 3 and 4 respectively; whereas for rough bed these amplifications are 1.08, 1.26, 1.38 and 1.4. Therefore, it seems like bed roughness tends to increase the near-bed velocity amplifications for submerged flow regimes. Transverse deflection intensities are studied from the profiles of V/U_0 with y/D [Fig. 5.70(c) to 5.77(c)]. It can be clearly observed that the measurements at the bottom-most elevation show the greatest deflection in all flow regimes. This observation supports the theories of three-dimensional turbulent boundary layer, where the lateral pressure gradient is held responsible for greatest outward deflection of slowly moving fluid particles near the bed. The maximum transverse velocities (V) are approximately 0.23U_0 in Regime-1, 0.34U_0 in Regime-2, 0.37U_0 in Regime-3, and 0.36U_0 in Regime-4. Bed roughness has been found to increase the magnitudes of near-bed transverse velocity for submerged flow regimes at y=0.8-0.9D by some extent; where V is approximately 0.27U_0 in Regime-1, 0.39U_0 in Regime-2, 0.39U_0 in Regime-3, and 0.35U_0 in Regime-4. Regime-3 and Regime-4 produce uniform deflection over the entire depth except very close to the bed (at $z/H \leq 0.1$). However, the deflected transverse velocity (V) gradually diminishes away from the cylinders. The lateral spread (y) of significant deflection ($V \geq 0.1U_0$) on smooth bed can be considered to be 1.5D for Regime-1, 2D for Regime-2, and 2.5D for Regime-3, and Regime-4. It can be noticed from the rough bed results that the bed roughness tends to arrest the lateral spread of flow deflection. The profiles of W/U_0 with y/D help to examine the characteristics of deflection in the vertical direction. The magnitudes of W/U_0 near the cylinders indicate that the flows passing the shoulder of the cylinders are strongly three-dimensional in all flow regimes. However, the directions of vertical flow are found to vary depending on flow regimes and bed roughness condition. The maximum intensity of vertical flow (W/U_0) on smooth bed has been found to be $0.12U_0$ in Regime-1, $0.16U_0$ in Regime-2, $0.08U_0$ in Regime-3, and $0.05U_0$ in Regime-4; whereas for rough bed it becomes $0.09U_0$, $0.11U_0$, $0.08U_0$ and $0.11U_0$ respectively. In general large cell of secondary current can be visualized from the deflection patterns on x=0 plane as shown in Figure 5.78(a-d) to 5.79(a-d) by 2D vector plots. These vectors are plotted using y and z components of velocity (i.e. V and W). The profiles of streamwise vorticity (ω_x) on the x=0 plane plotted in Figure 5.80(a-d) to 5.81(a-d) for all flow regimes on smooth and rough beds confirm unidirectional streamwise vorticity. However, the strength of streamwise vorticity is significant only near the bed; and these are probably due to the horse-shoe vortex systems passing the cylinders.

The variations of normalized turbulent kinetic energy (k/k_z) and turbulent shear stress (τ_t/τ_{tz}) with y/D are observed (Figures are not presented) for all flow regimes on smooth and rough beds at different elevations (i.e. z/H). The profiles near the bed have shown considerable deviations from undisturbed conditions (k_z and τ_{tz}); and these can be qualitative indicators of potential scour on erodible bed. Therefore, the bottom-most (at z=0.02H) profiles of turbulent kinetic energy and turbulent shear stress on x=0 plane are plotted in scales of k/U_0^2 and τ_t/u_*^2 with y/D in Figure 5.82(a-b) and 5.83(a-b), where U_0 is the cross-sectional mean velocity and u_* is the undisturbed flow friction velocity. Increased turbulence has been observed close to the cylinder on x=0 plane for all the flow regimes on smooth and rough beds. The maximum k/U_0^2 and τ_t/u_*^2 on smooth and rough beds are found to be in a range of 0.025-0.027and 1.25-1.62. The spread of increased turbulence is found up to y=1.2D on both smooth and rough beds. Surprisingly the variations of turbulent kinetic energy and shear stress have similar patterns to the bed shear stress (τ_0/τ_{00}) profiles at x=0 as presented in Chapter 4 [see Fig. 4.9(a) and 4.24(a)].

Future scour measurements on erodible bed in similar flow condition can indicate the correlation of local scour with the increased near-bed turbulence and bed shear stress.

5.4 Conclusions

The mean and turbulent flow structure in the upstream region surrounding the cylinders in open channel with different levels of submergence are presented in this study. Three-dimensional velocity measuring stations are positioned close to the cylinder surface so that the complex flow patterns can be adequately explained. The effect of bed roughness is also reported from the observations of the similar flow on rough bed.

This study shows that in spite of deceleration of the approach flow on the plane of symmetry, the mean longitudinal velocity profiles plotted in terms of Clauser's scheme collapse in a narrow band in all flow regimes on both smooth and rough beds. These results indicate that an approximate relationship can be determined to describe the approach flow profiles (up to x=-0.85D) subjected to an adverse pressure gradient. Flow deflections in transverse as well as in vertical direction in the upstream region surrounding the cylinders are enormous irrespective of the level of submergence. The influence of bed roughness on the flow deflection patterns and the lateral spread of increased turbulence are nominal for different flow regimes. Increased turbulence region on x=0 plane spreads up to y=1.2D. In the upstream region surrounding the cylinders, near-bed turbulent kinetic energy and turbulent shear stress increase as high as 2-3 times compared to those observed relatively far away from the cylinders. Near-bed turbulent kinetic energy at x=0 has been found to be approximately 2.5% of the mean kinetic energy for all flow regimes on smooth and rough beds.

The present experimental study, thus provide an extremely valuable database for computational modeling of similar flows in hydraulic, environmental and geophysical flow systems. Near-bed observations of increased turbulence surrounding the cylinders and velocity amplification at x=0 could be indicators of local scour. Future studies of similar flows on erodible beds can enhance our knowledge regarding the influence of flow structure on local scour.

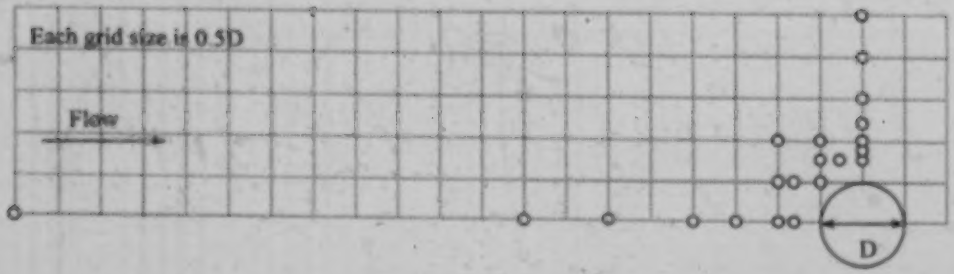
Each grid size is 0.5D
Flow
D

Fig. 5.1 Typical velocity measuring stations relative to the object on a horizontal plane; small white circles are the stations used for velocity measurements

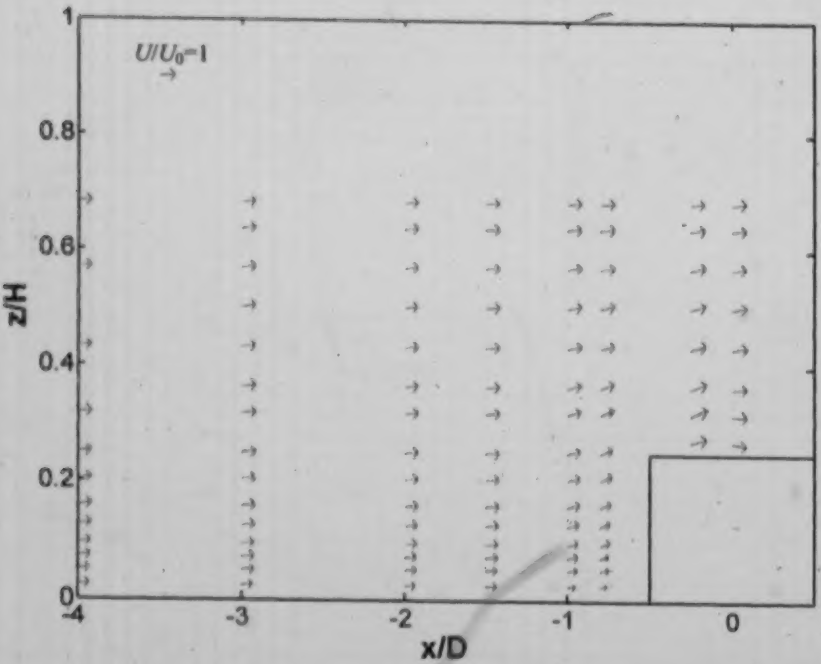

Fig. 5.2(a) 2D velocity vectors on upstream POS: Smooth bed/Regime-1

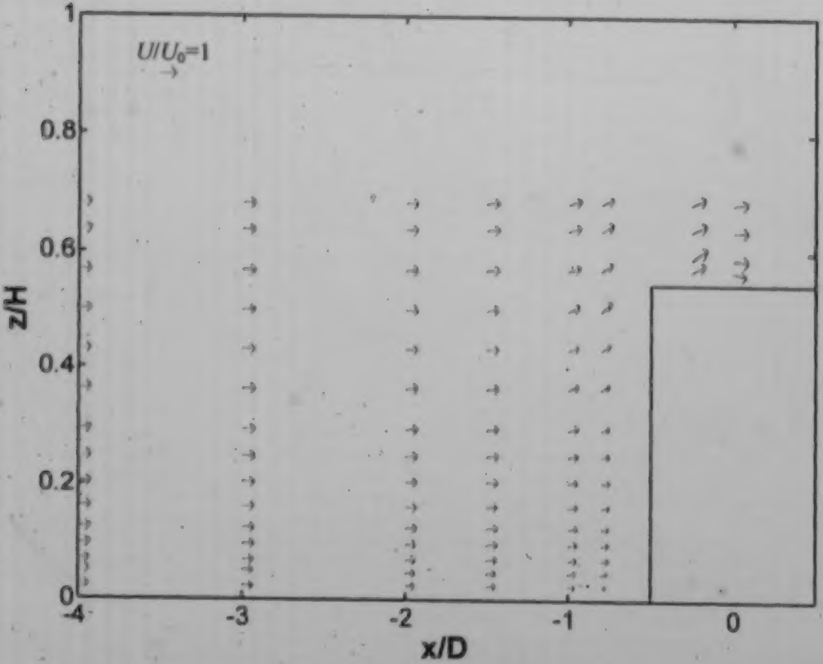

Fig. 5.2(b) 2D velocity vectors on upstream POS: Smooth bed/Regime-2

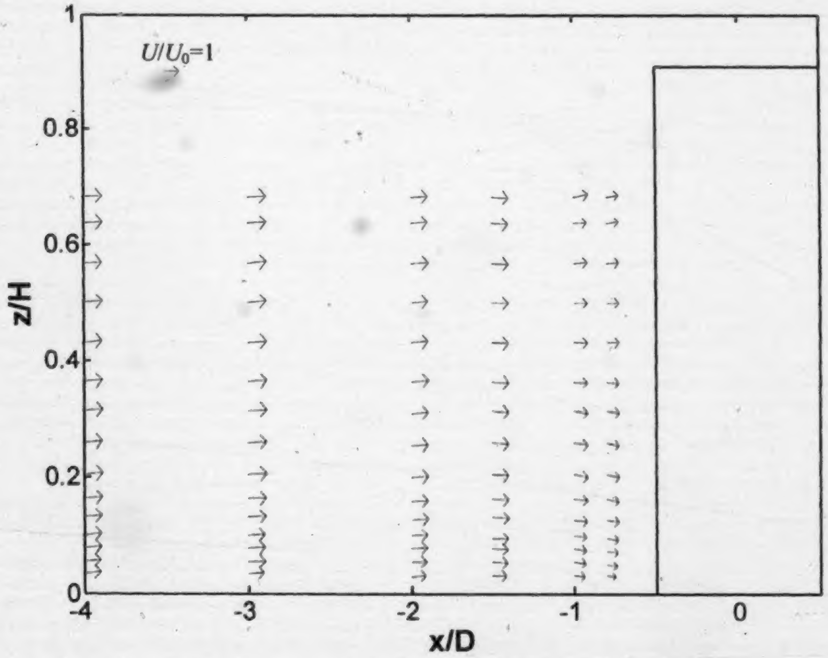

Fig. 5.2(c) 2D velocity vectors on upstream POS: Smooth bed/Regime-3

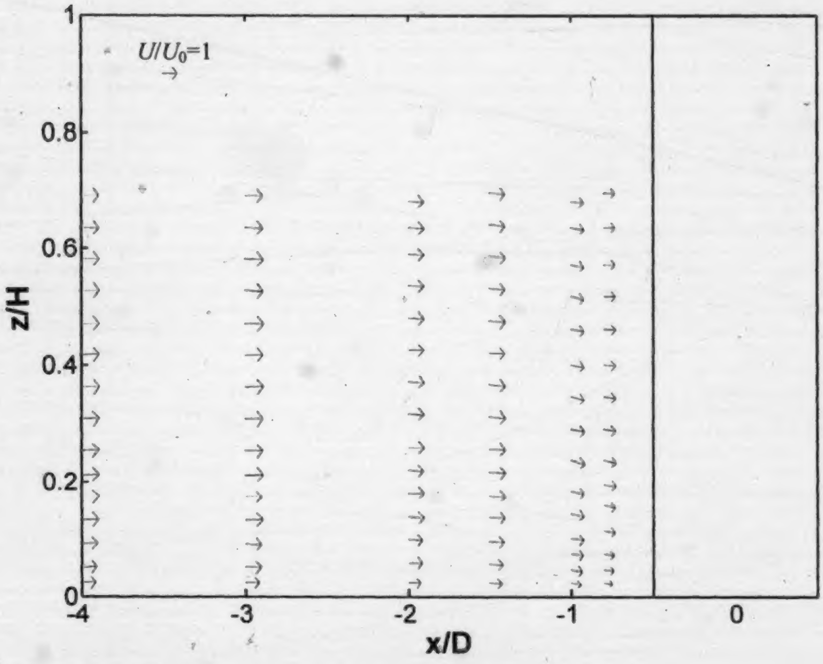

Fig. 5.2(d) 2D velocity vectors on upstream POS: Smooth bed/Regime-4

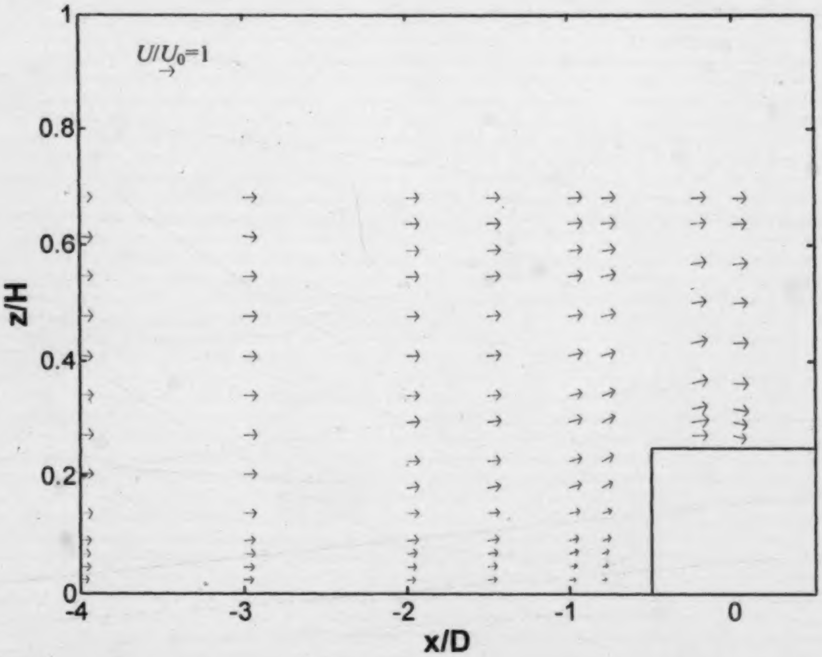

Fig. 5.3(a) 2D velocity vectors on upstream POS: Rough bed/Regime-1

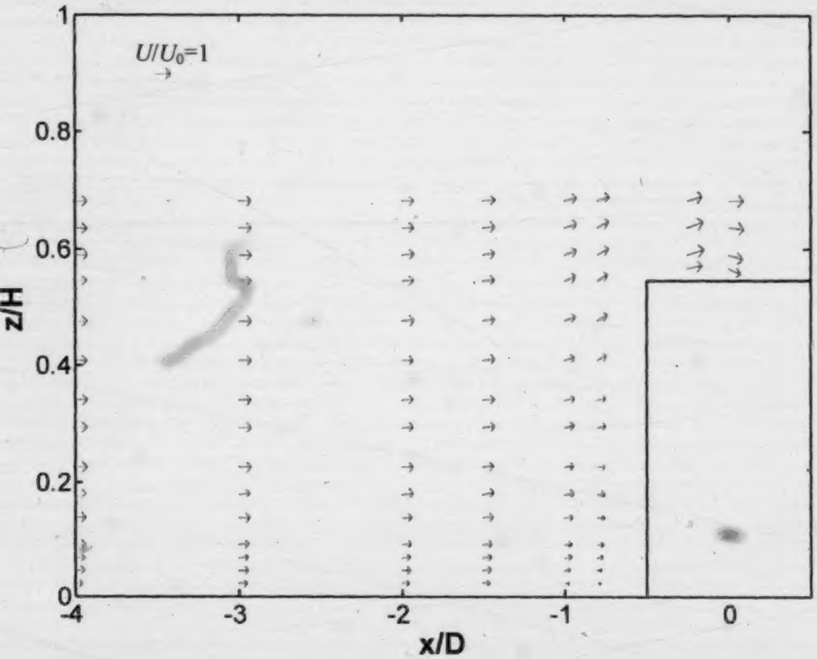

Fig. 5.3(b) 2D velocity vectors on upstream POS: Rough bed/Regime-2

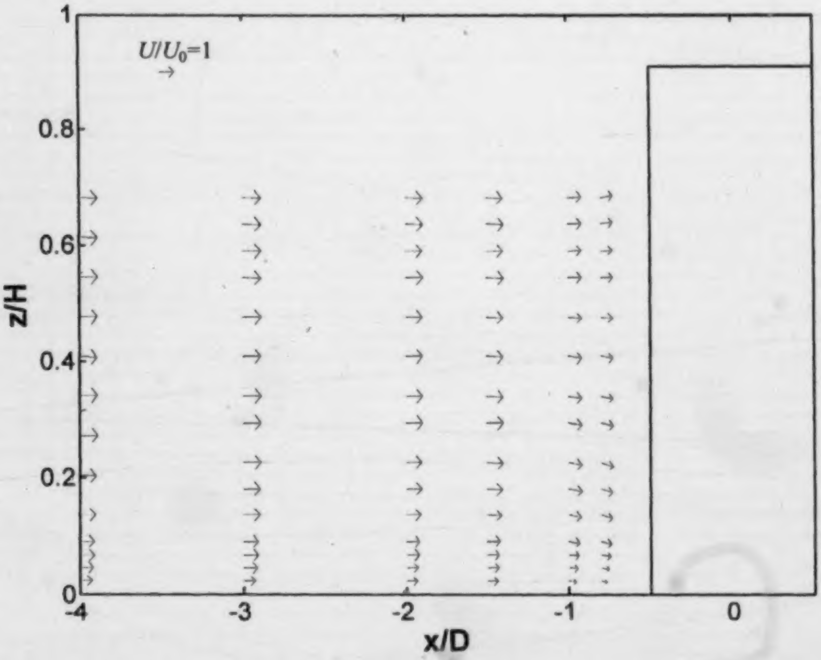

Fig. 5.3(c) 2D velocity vectors on upstream POS: Rough bed/Regime-3

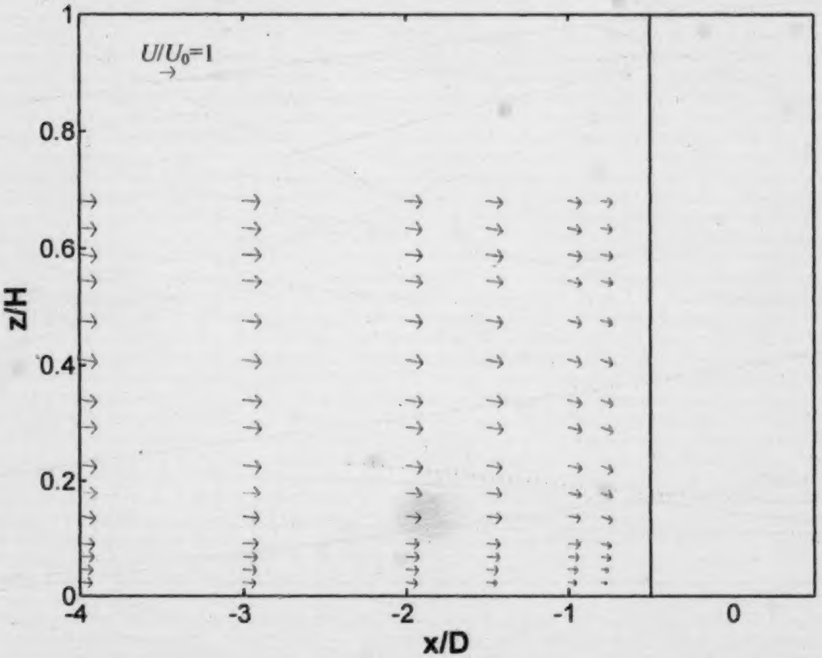

Fig. 5.3(d) 2D velocity vectors on upstream POS: Rough bed/Regime-4

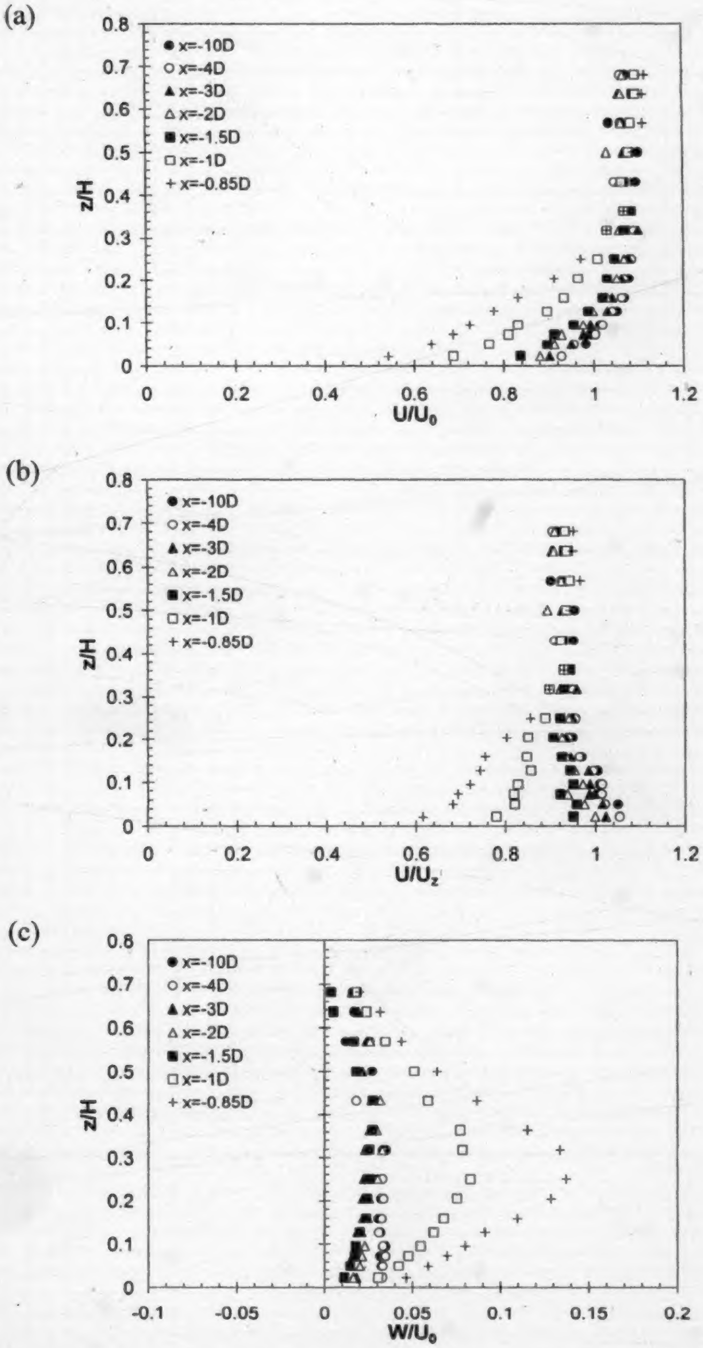

Fig. 5.4 Normalized mean velocity profiles on upstream POS: Smooth bed/Regime-1; (a) longitudinal mean velocity (U/U_0), (b) speed up factor (U/U_z), and (c) vertical mean velocity (W/U_0)

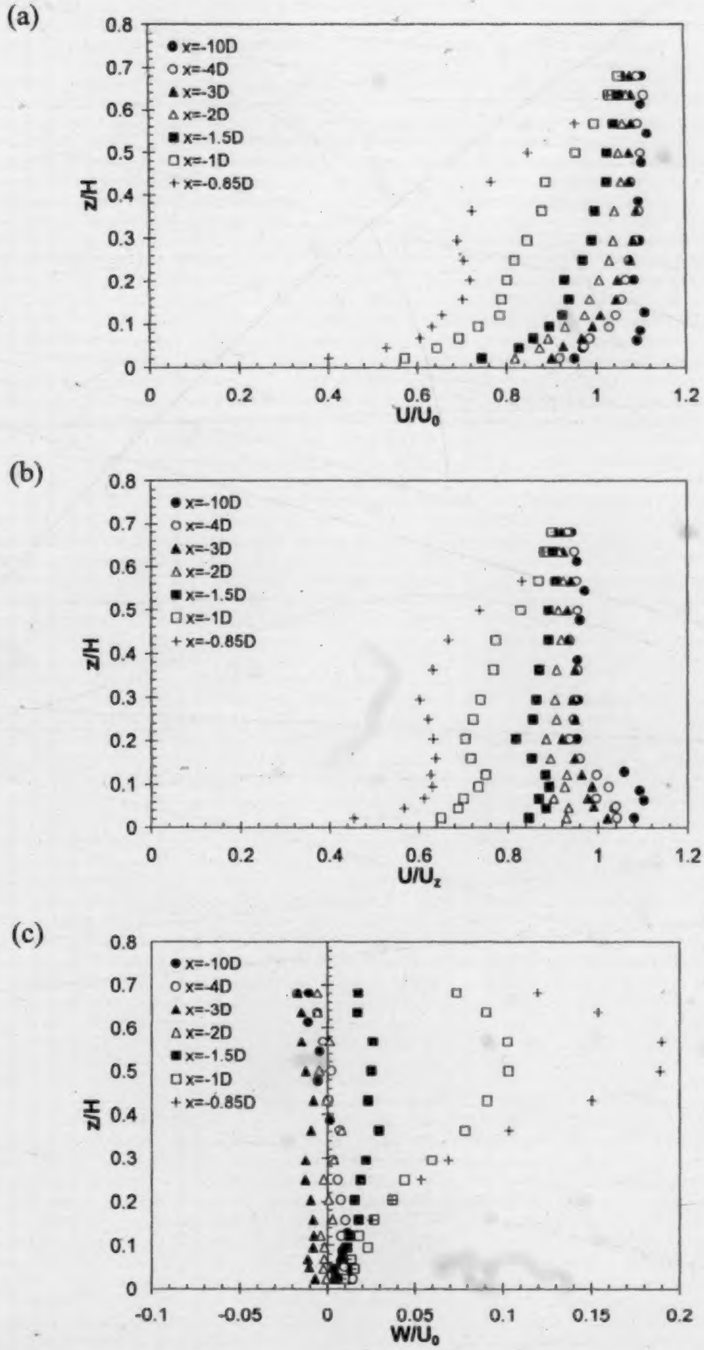

Fig. 5.5 Normalized mean velocity profiles on upstream POS: Smooth bed/Regime-2; (a) longitudinal mean velocity (U/U_0), (b) speed up factor (U/U_z), and (c) vertical mean velocity (W/U_0)

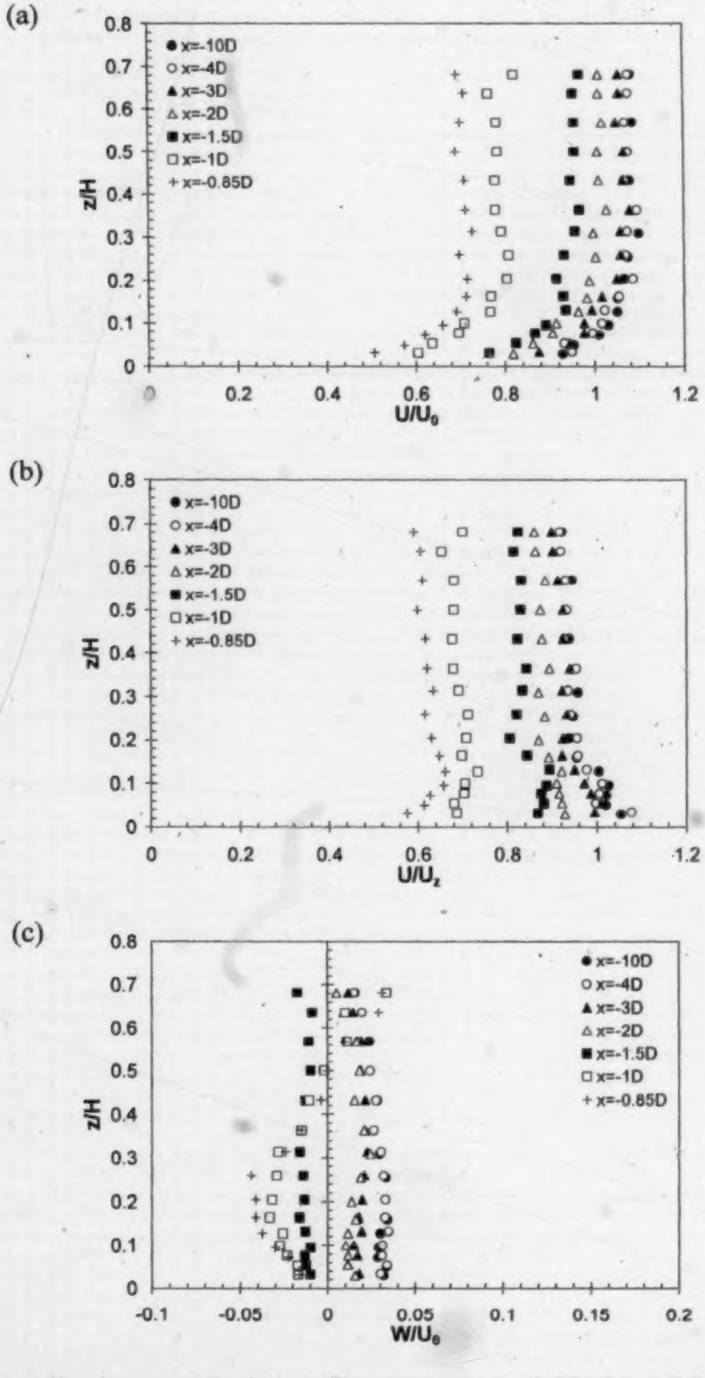

Fig. 5.6 Normalized mean velocity profiles on upstream POS: Smooth bed/Regime-3; (a) longitudinal mean velocity (U/U_0), (b) speed up factor (U/U_z), and (c) vertical mean velocity (W/U_0)

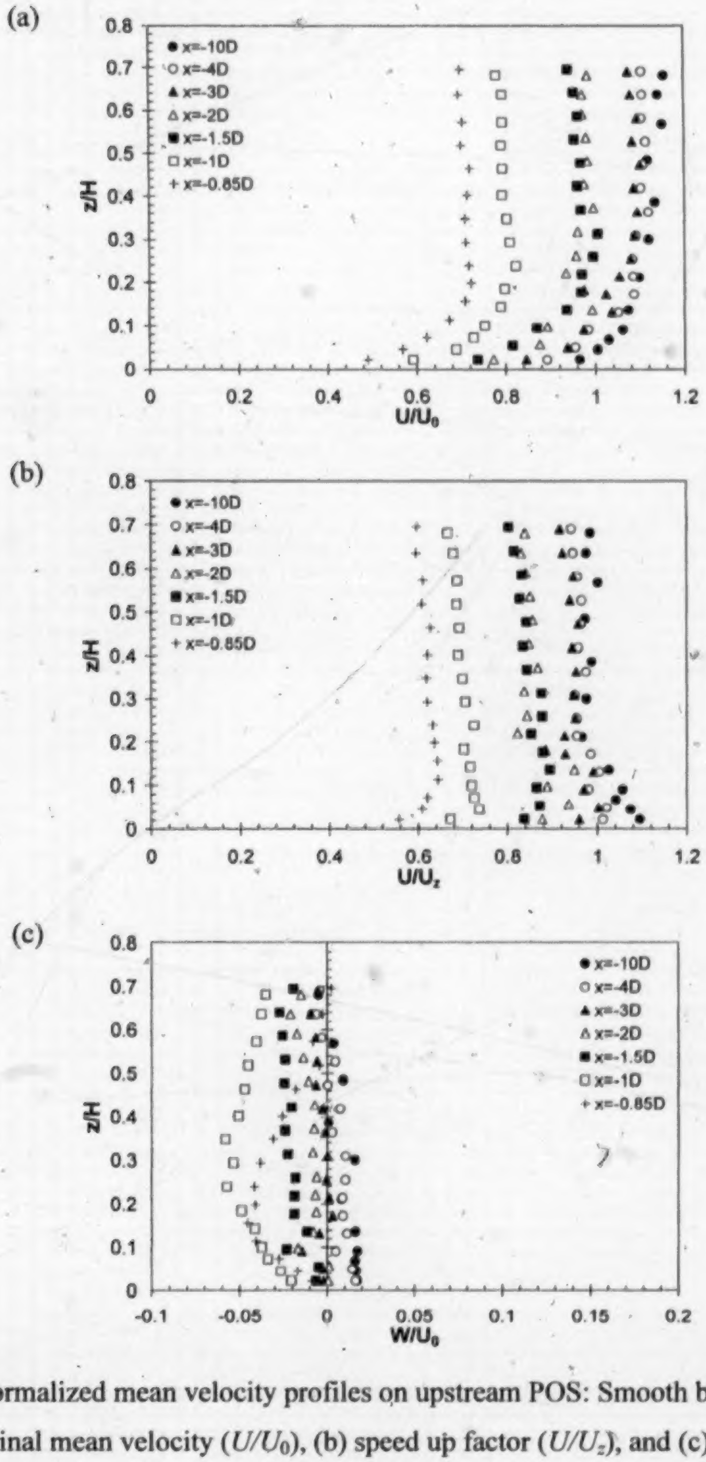

Fig. 5.7 Normalized mean velocity profiles on upstream POS: Smooth bed/Regime-4; (a) longitudinal mean velocity (U/U_0), (b) speed up factor (U/U_z), and (c) vertical mean velocity (W/U_0)

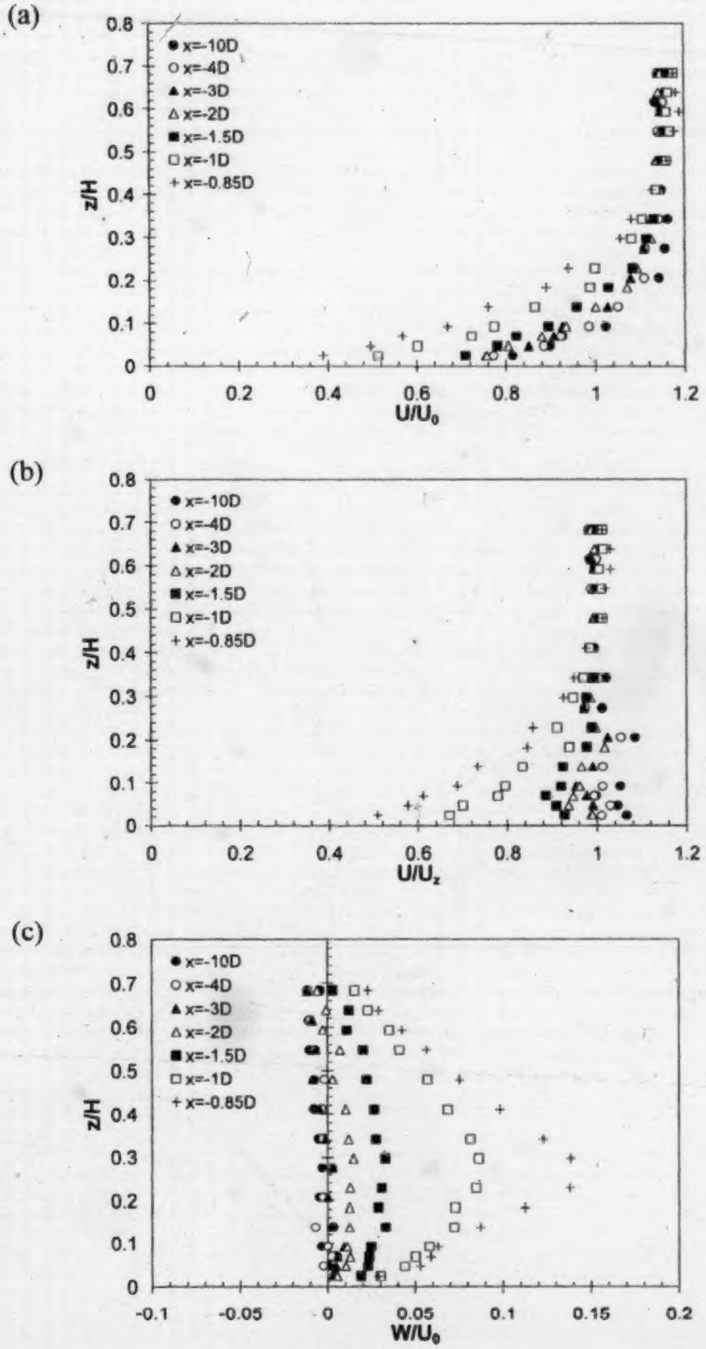

Fig. 5.8 Normalized mean velocity profiles on upstream POS: Rough bed/Regime-1; (a) longitudinal mean velocity (*U*/*U*$_0$), (b) speed up factor (*U*/*U*$_z$), and (c) vertical mean velocity (*W*/*U*$_0$)

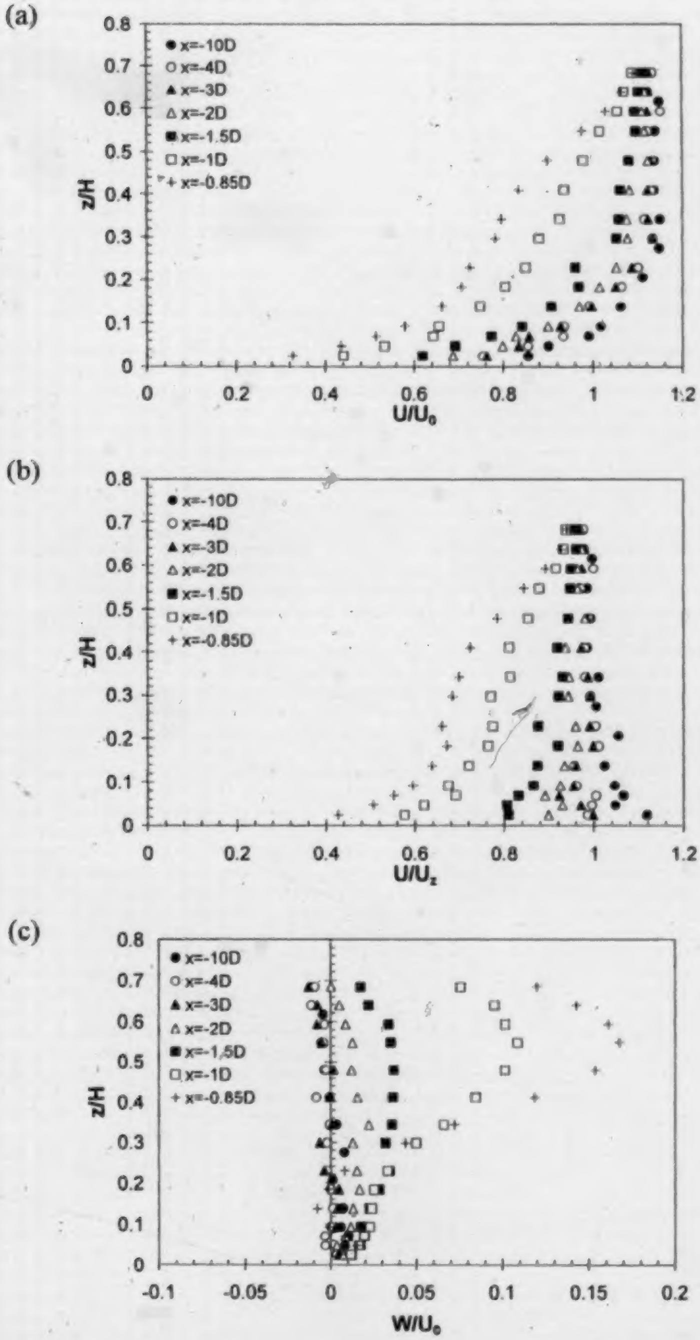

Fig. 5.9 Normalized mean velocity profiles on upstream POS: Rough bed/Regime-2; (a) longitudinal mean velocity (U/U_0), (b) speed up factor (U/U_z), and (c) vertical mean velocity (W/U_0)

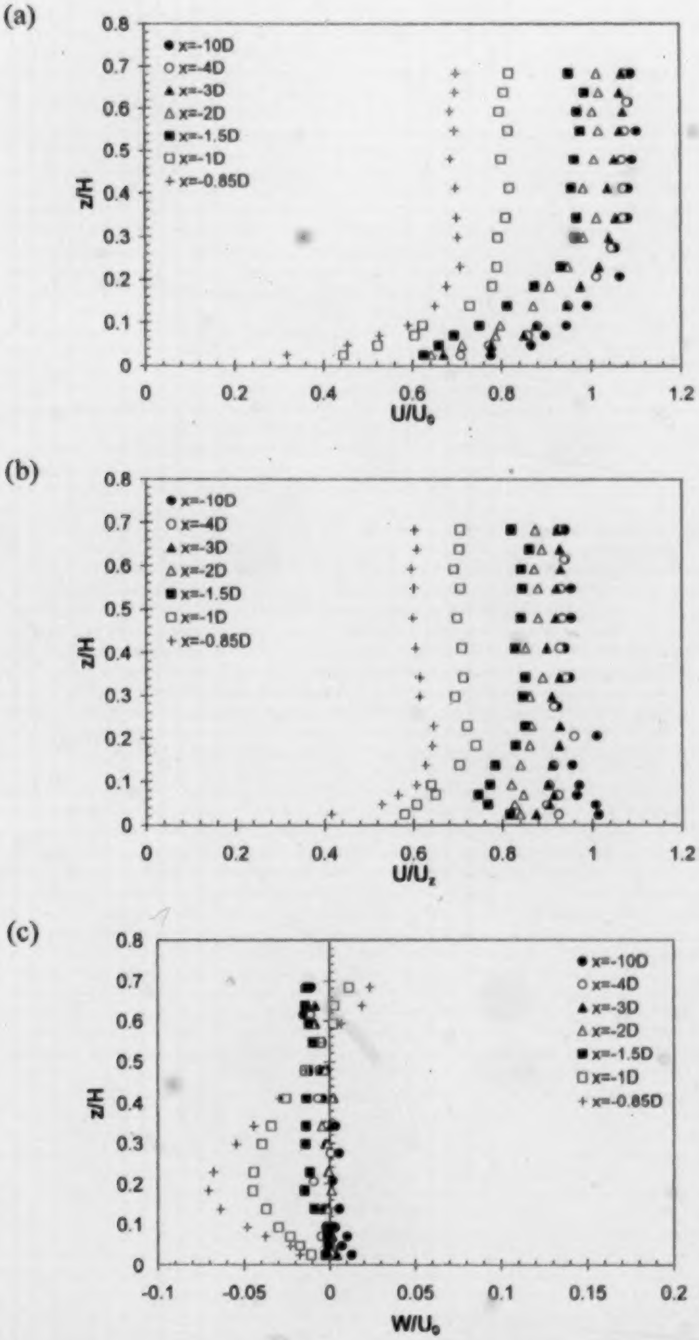

Fig. 5.10 Normalized mean velocity profiles on upstream POS: Rough bed/Regime-3; (a) longitudinal mean velocity (U/U_0), (b) speed up factor (U/U_z), and (c) vertical mean velocity (W/U_0)

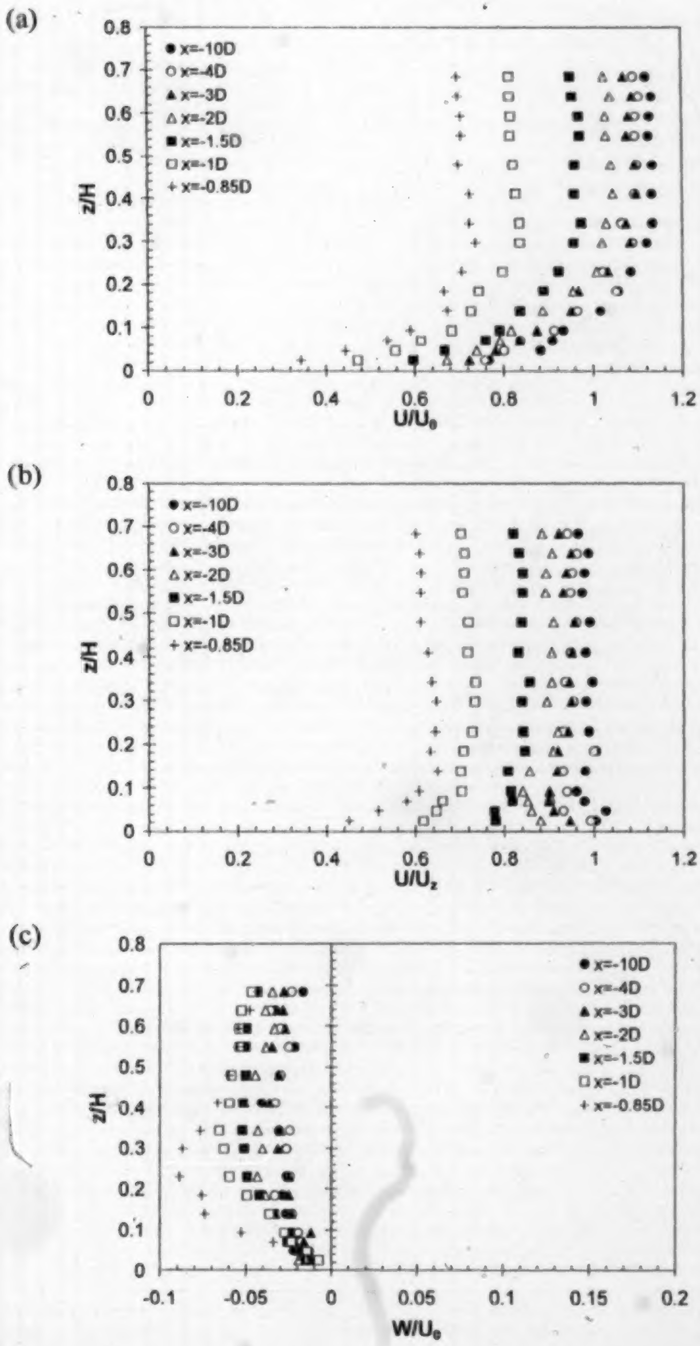

Fig. 5.11 Normalized mean velocity profiles on upstream POS: Rough bed/Regime-4; (a) longitudinal mean velocity (U/U_0), (b) speed up factor (U/U_z), and (c) vertical mean velocity (W/U_0)

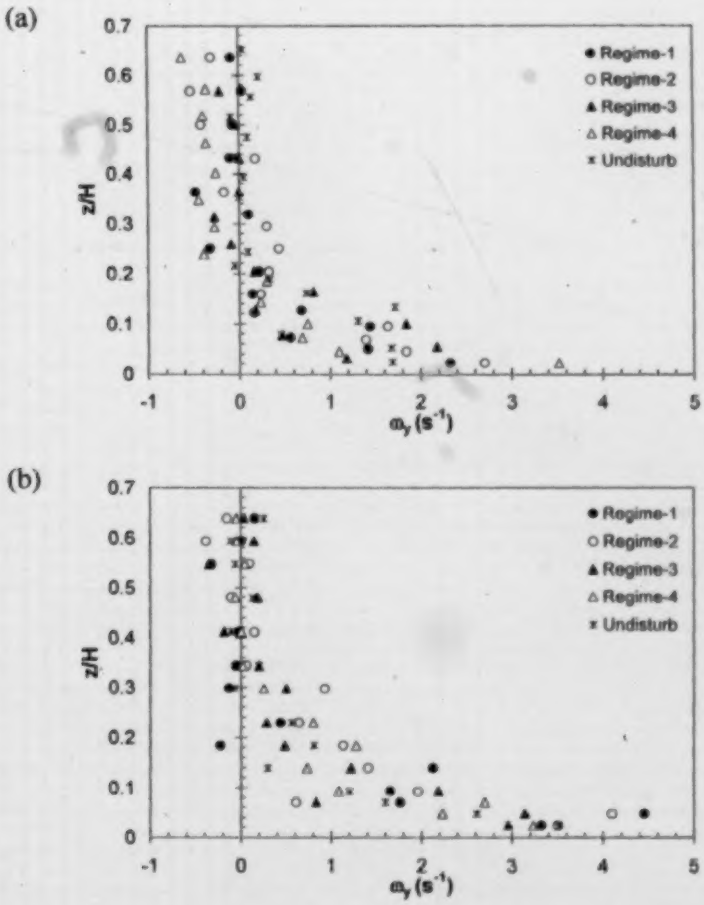

Fig. 5.12 Vorticity (ω_y) profile at x=-1D on POS; (a) Smooth bed, and (b) Rough bed

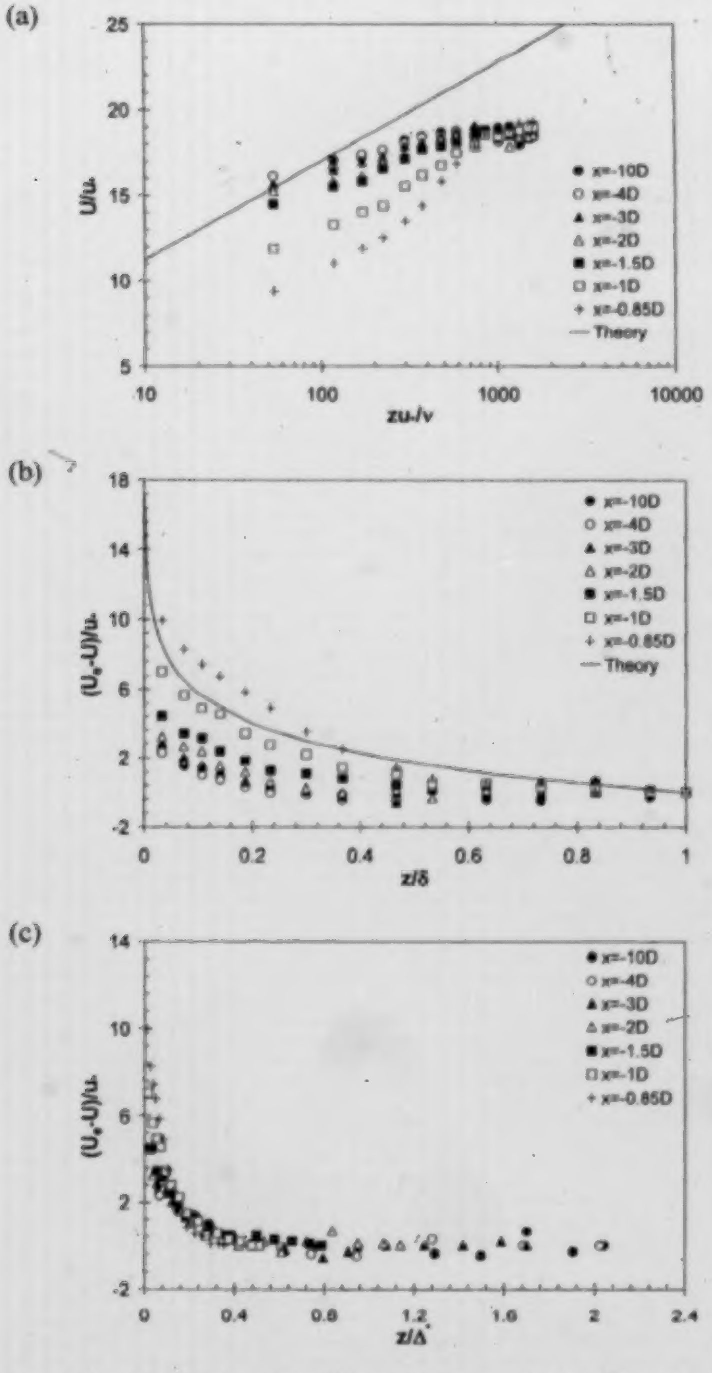

Fig. 5.13 (a) Logarithmic velocity, (b) defect velocity, and (c) Clauser's scheme profiles on upstream POS: Smooth bed/Regime-1

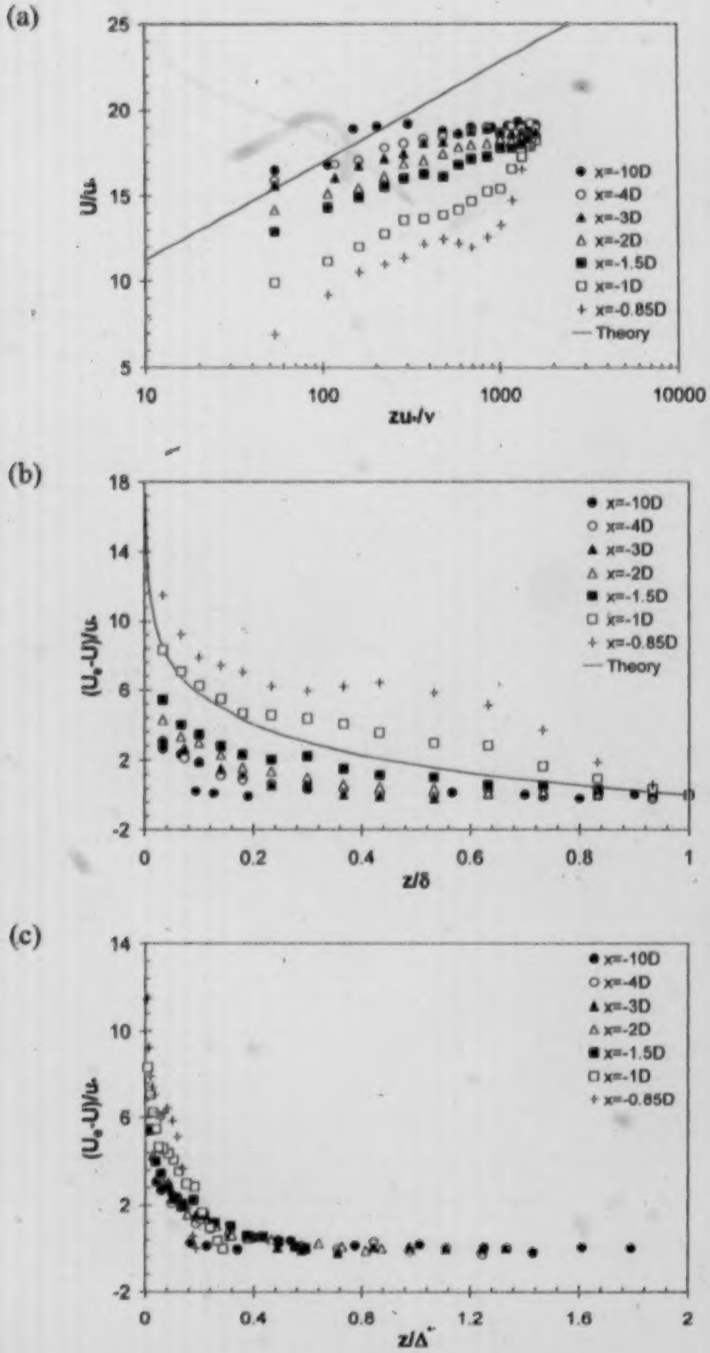

Fig. 5.14 (a) Logarithmic velocity, (b) defect velocity, and (c) Clauser's scheme profiles on upstream POS: Smooth bed/Regime-2

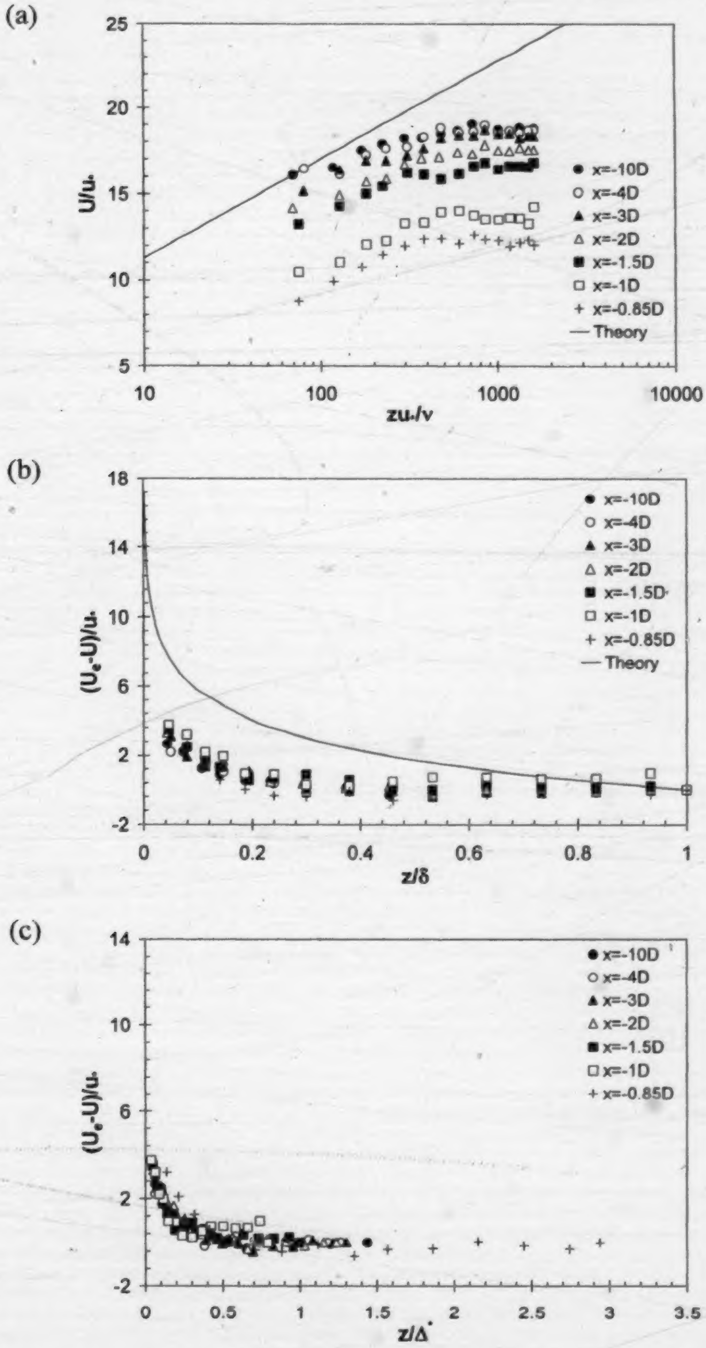

Fig. 5.15 (a) Logarithmic velocity, (b) defect velocity, and (c) Clauser's scheme profiles on upstream POS: Smooth bed/Regime-3

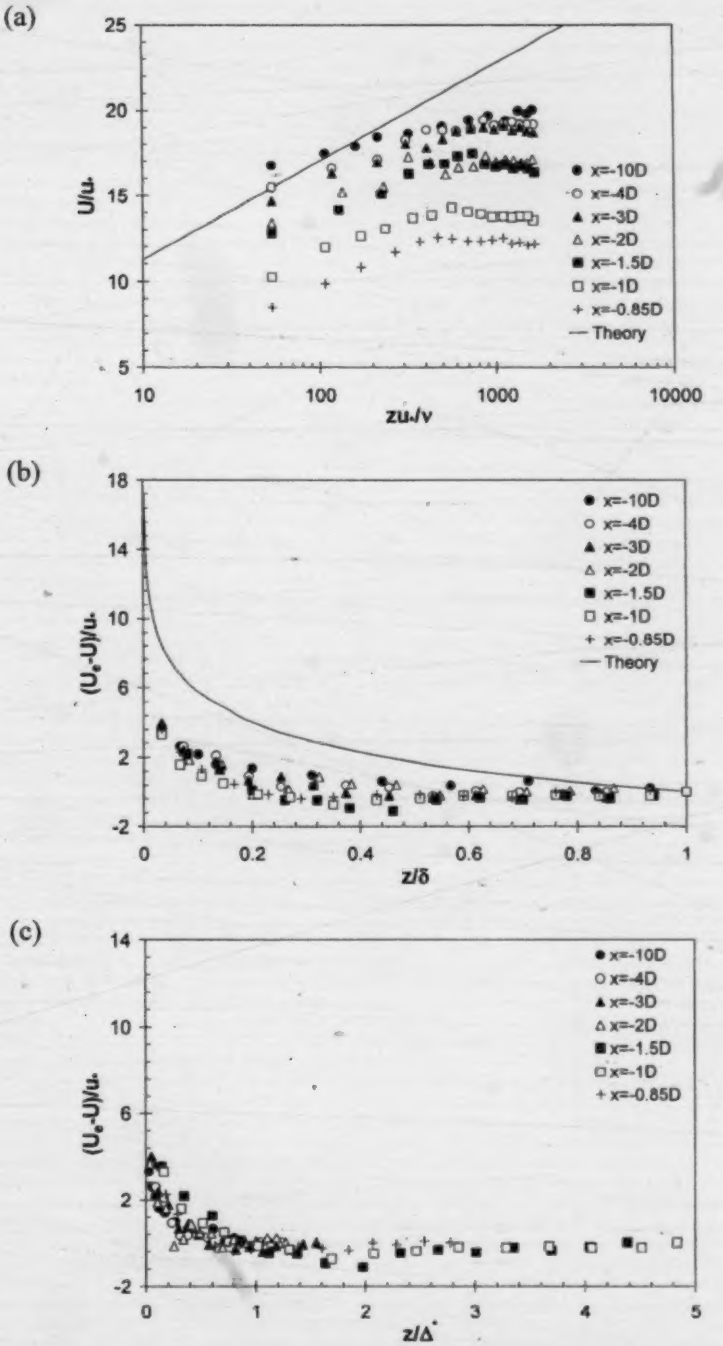

Fig. 5.16 (a) Logarithmic velocity, (b) defect velocity, and (c) Clauser's scheme profiles on upstream POS: Smooth bed/Regime-4

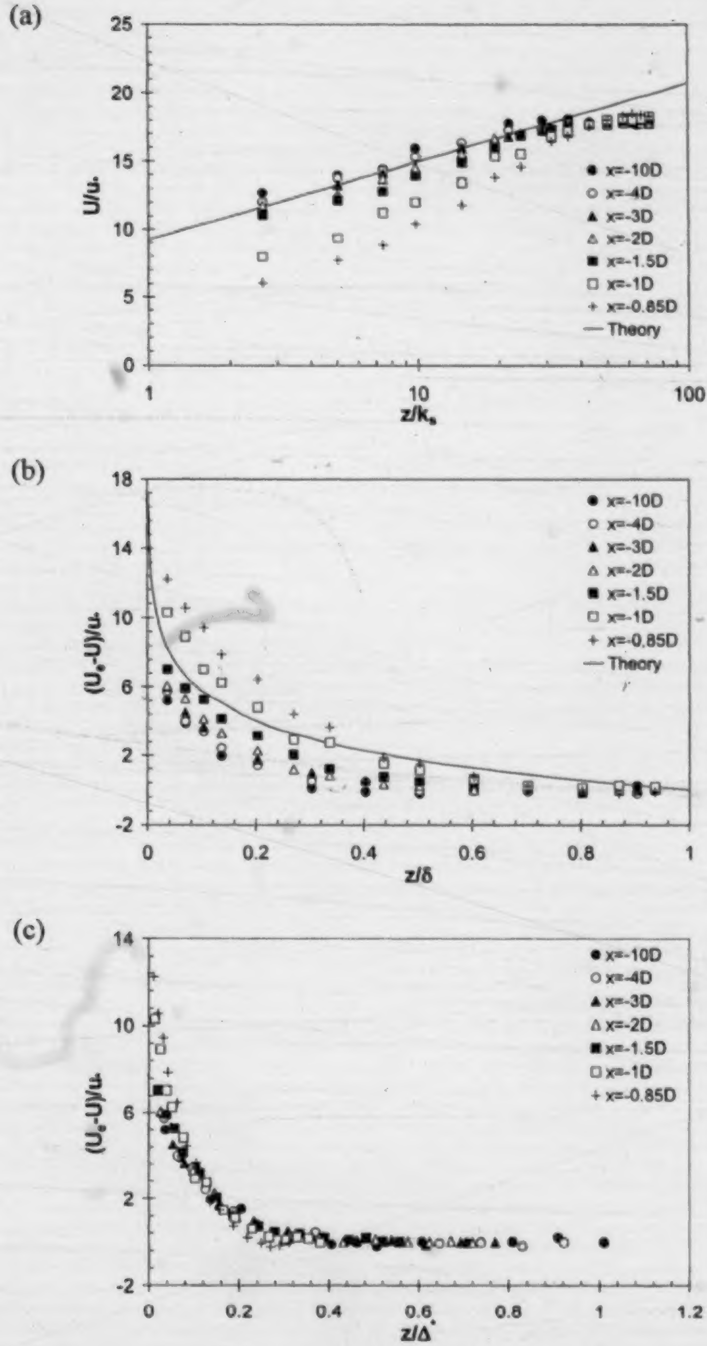

Fig. 5.17 (a) Logarithmic velocity, (b) defect velocity, and (c) Clauser's scheme profiles on upstream POS: Rough bed/Regime-1

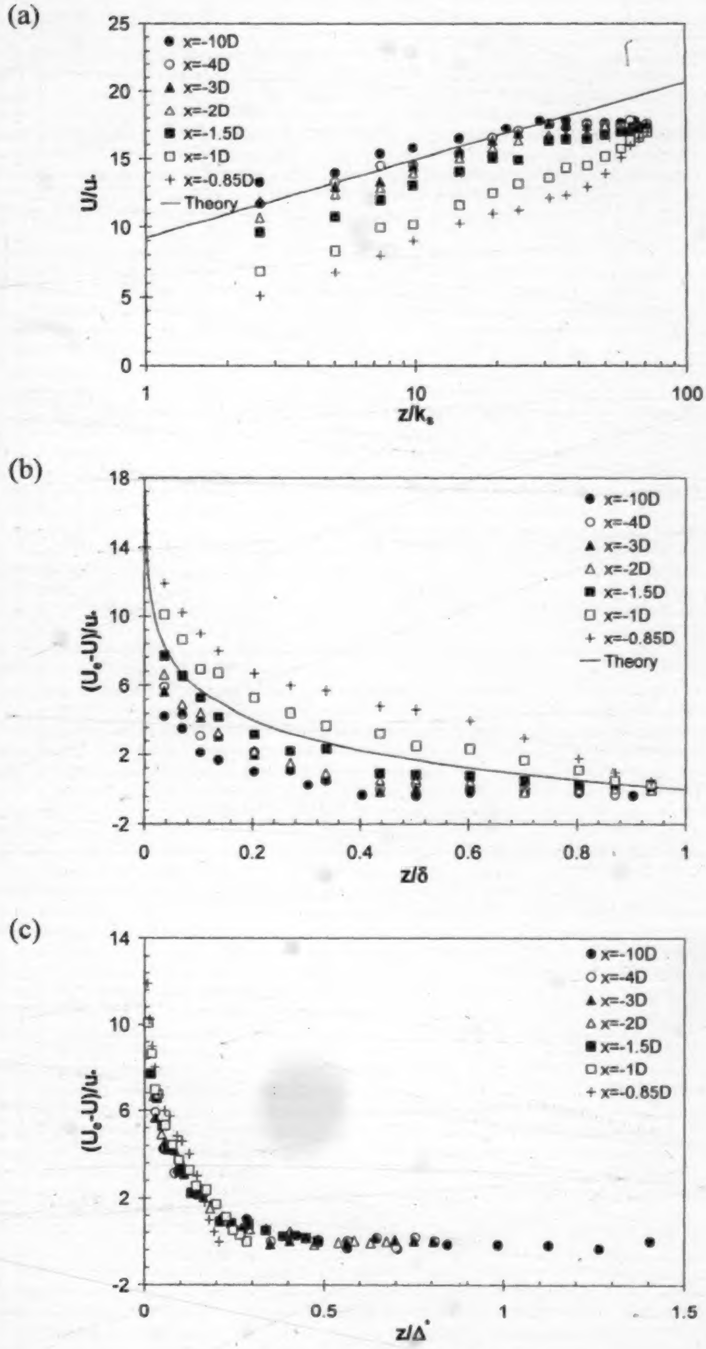

Fig. 5.18 (a) Logarithmic velocity, (b) defect velocity, and (c) Clauser's scheme profiles on upstream POS: Rough bed/Regime-2

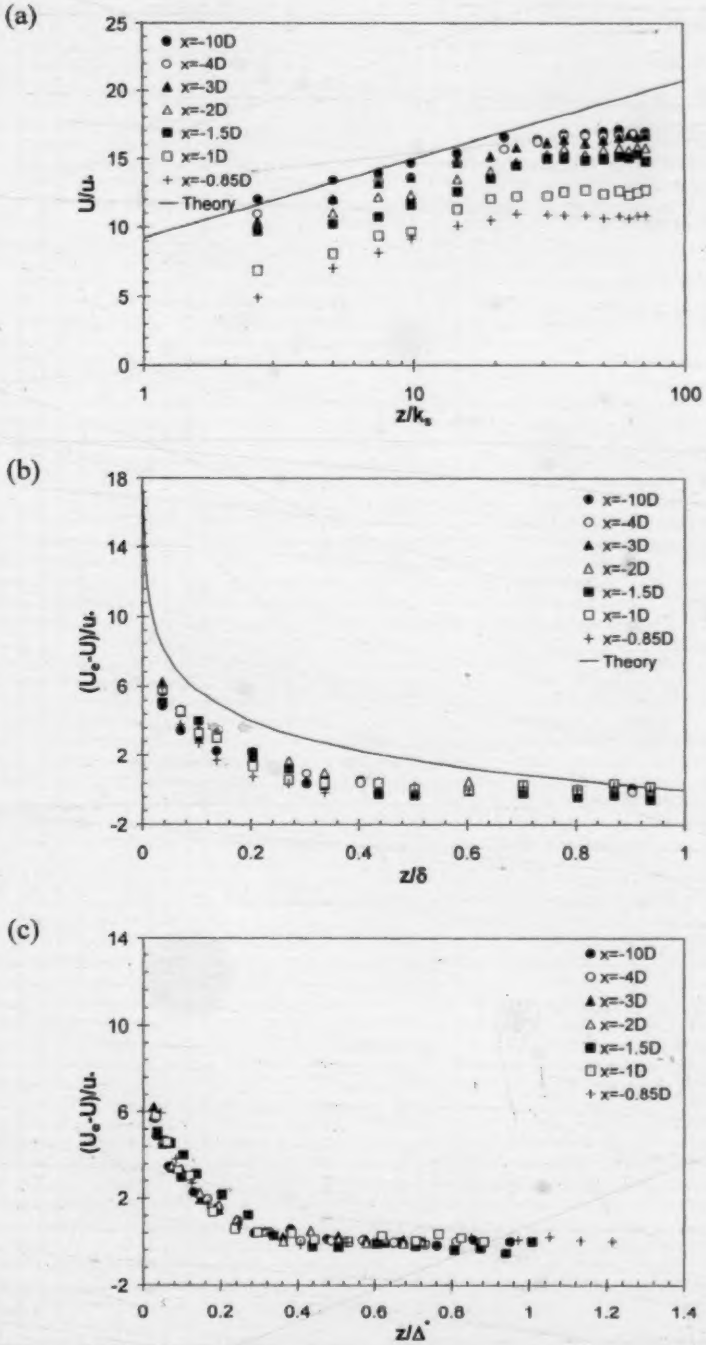

Fig. 5.19 (a) Logarithmic velocity, (b) defect velocity, and (c) Clauser's scheme profiles on upstream POS: Rough bed/Regime-3

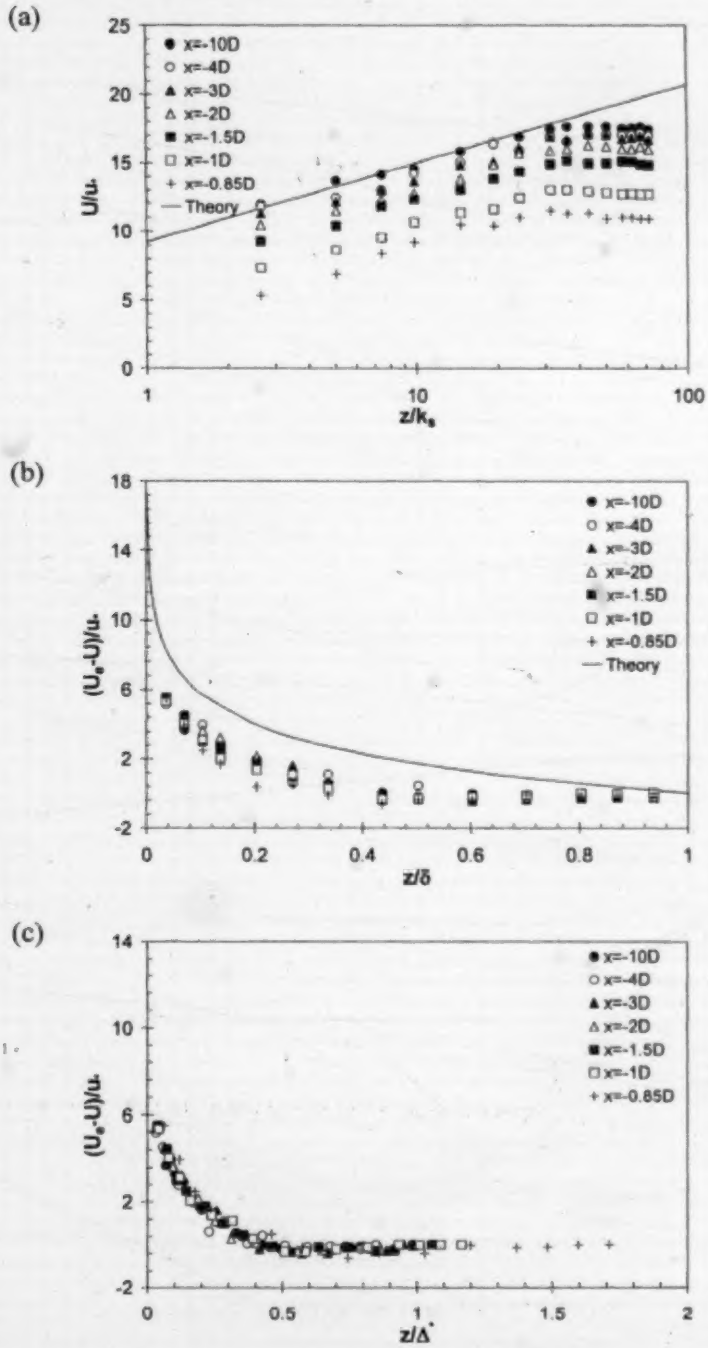

Fig. 5.20 (a) Logarithmic velocity, (b) defect velocity, and (c) Clauser's scheme profiles on upstream POS: Rough bed/Regime-4

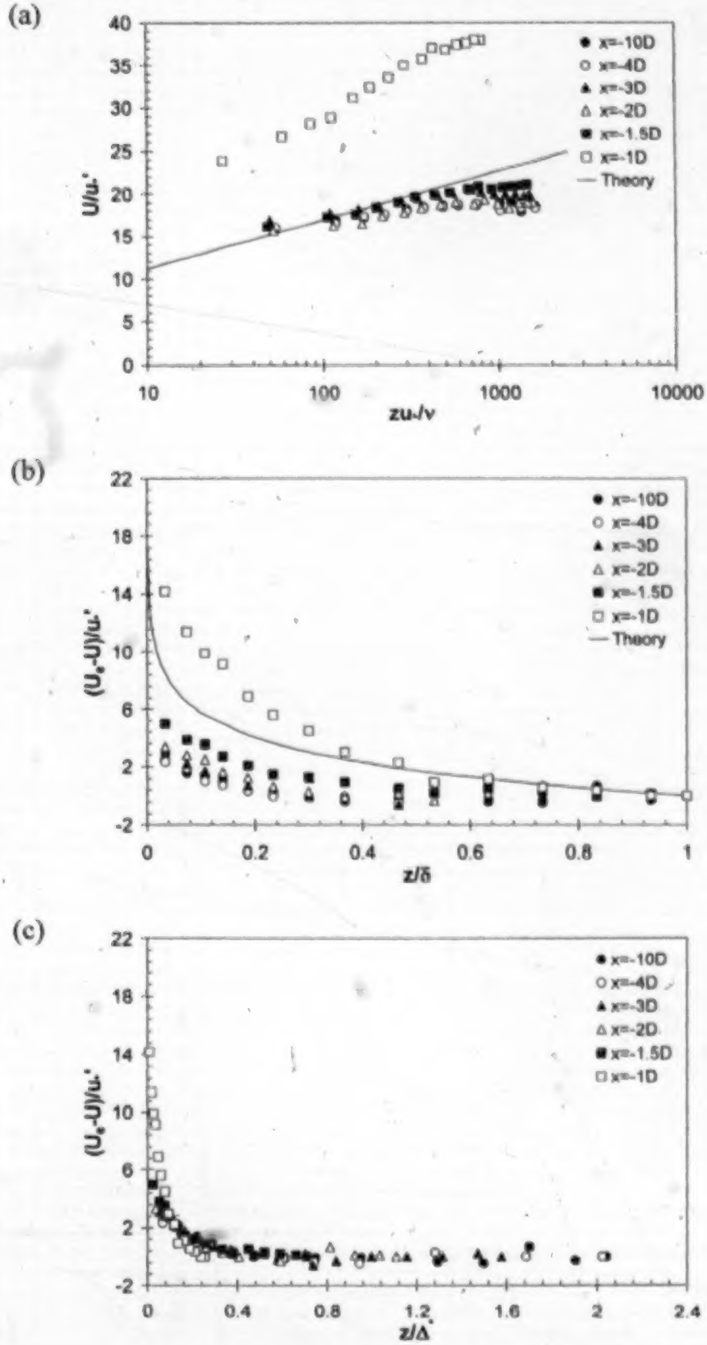

Fig. 5.21 (a) Logarithmic velocity, (b) defect velocity, and (c) Clauser's scheme profiles on upstream POS using local friction velocity: Smooth bed/Regime-1

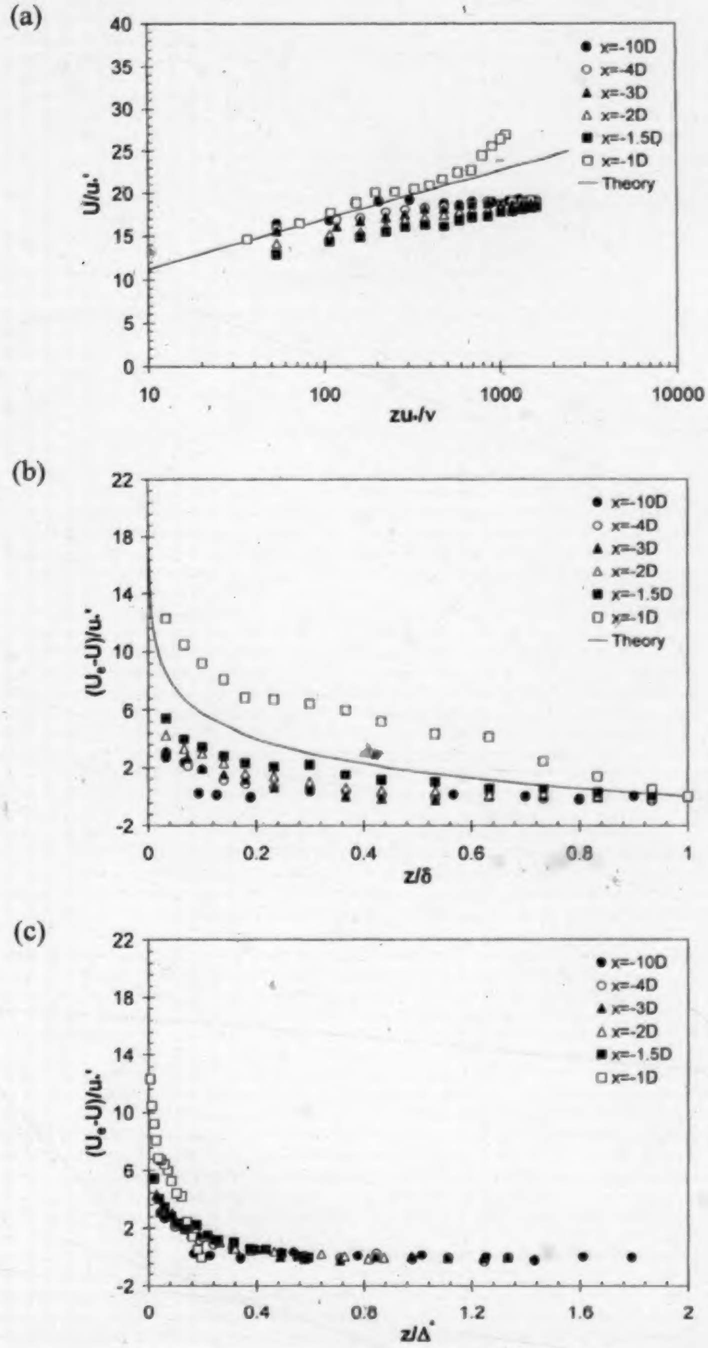

Fig. 5.22 (a) Logarithmic velocity, (b) defect velocity, and (c) Clauser's scheme profiles on upstream POS using local friction velocity: Smooth bed/Regime-2

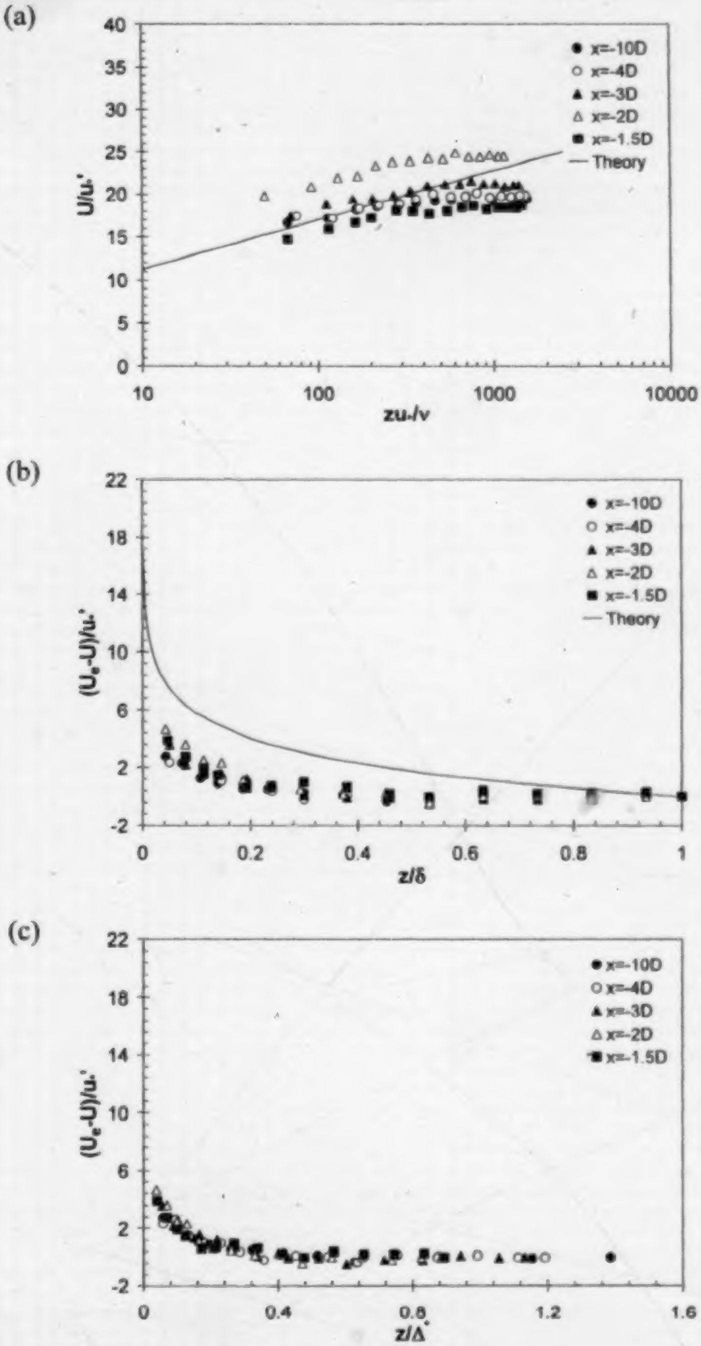

Fig. 5.23 (a) Logarithmic velocity, (b) defect velocity, and (c) Clauser's scheme profiles on upstream POS using local friction velocity: Smooth bed/Regime-3

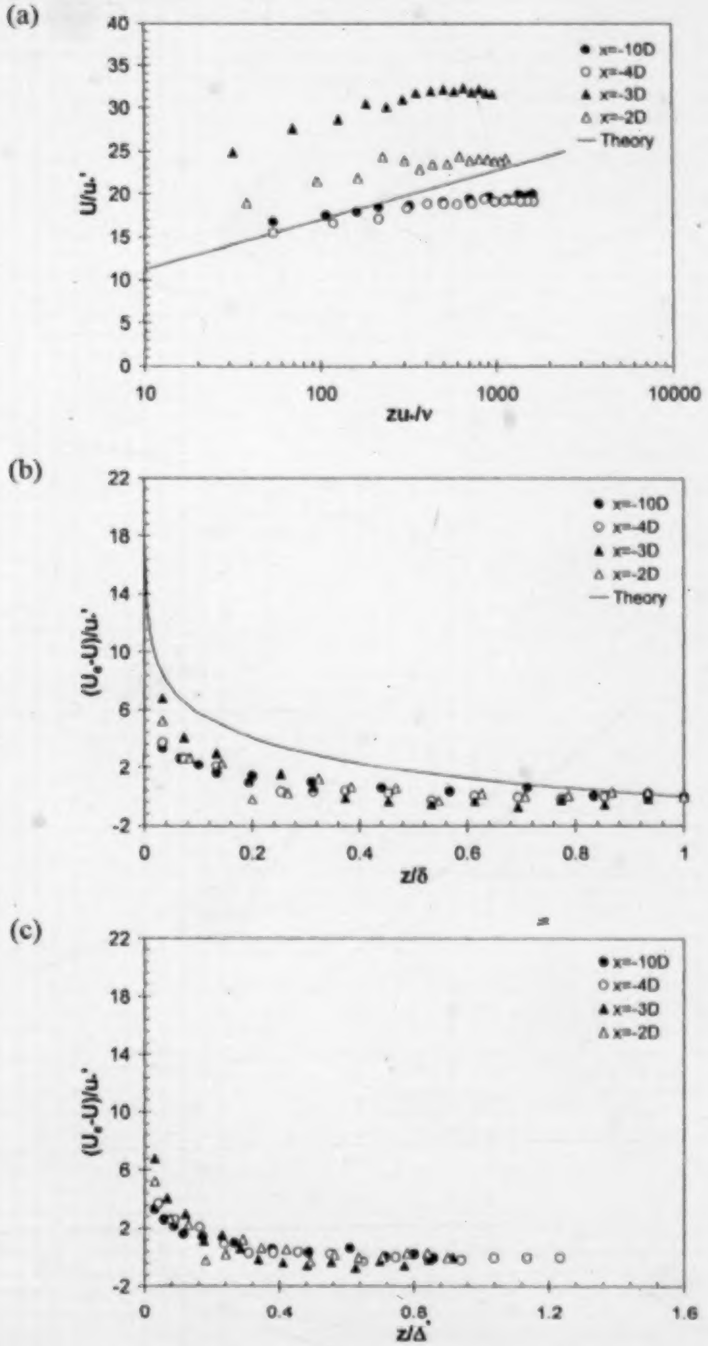

Fig. 5.24 (a) Logarithmic velocity, (b) defect velocity, and (c) Clauser's scheme profiles on upstream POS using local friction velocity: Smooth bed/Regime-4

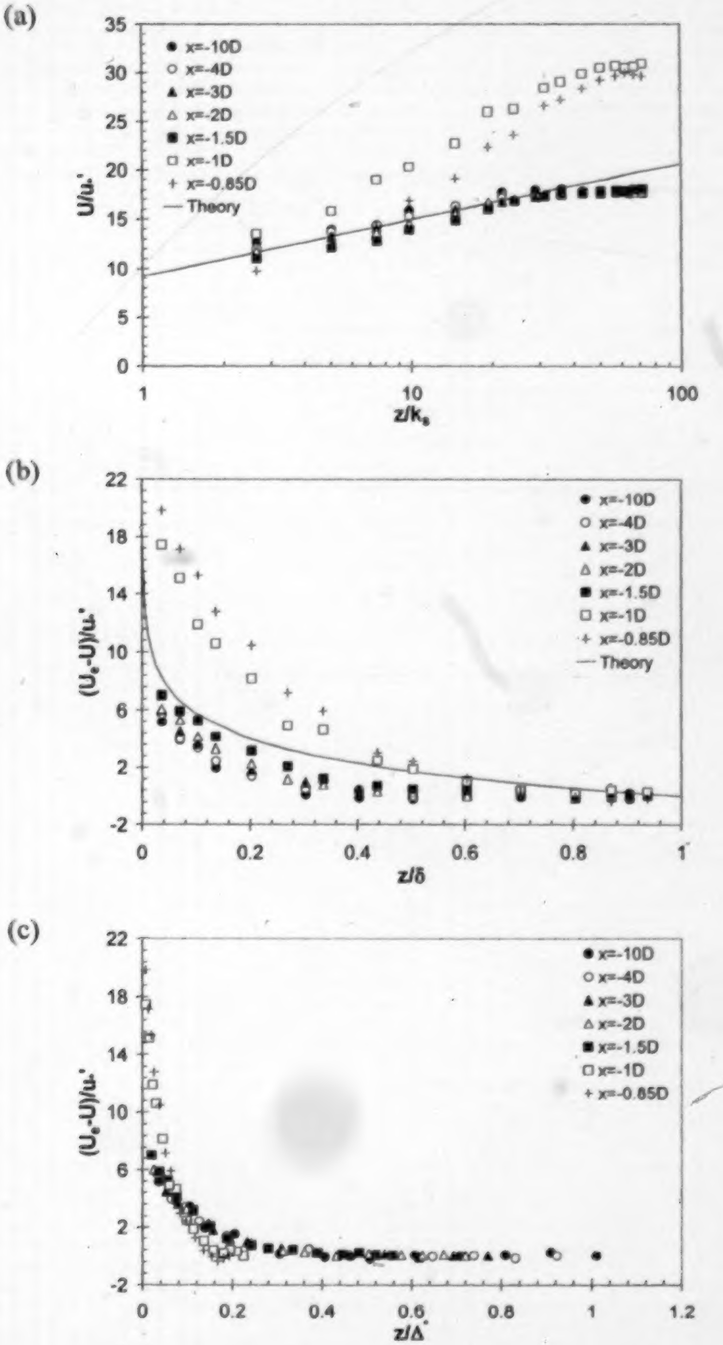

Fig. 5.25 (a) Logarithmic velocity, (b) defect velocity, and (c) Clauser's scheme profiles on upstream POS using local friction velocity: Rough bed/Regime-1

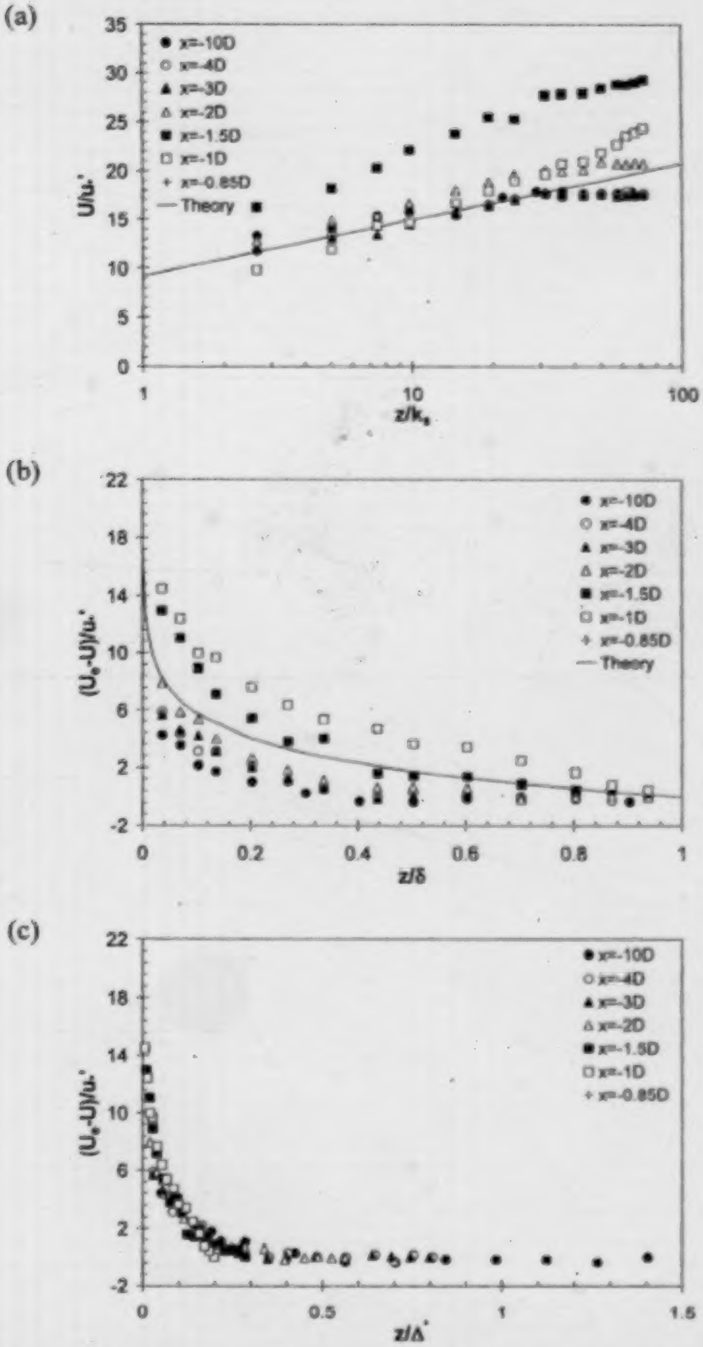

Fig. 5.26 (a) Logarithmic velocity, (b) defect velocity, and (c) Clauser's scheme profiles on upstream POS using local friction velocity: Rough bed/Regime-2

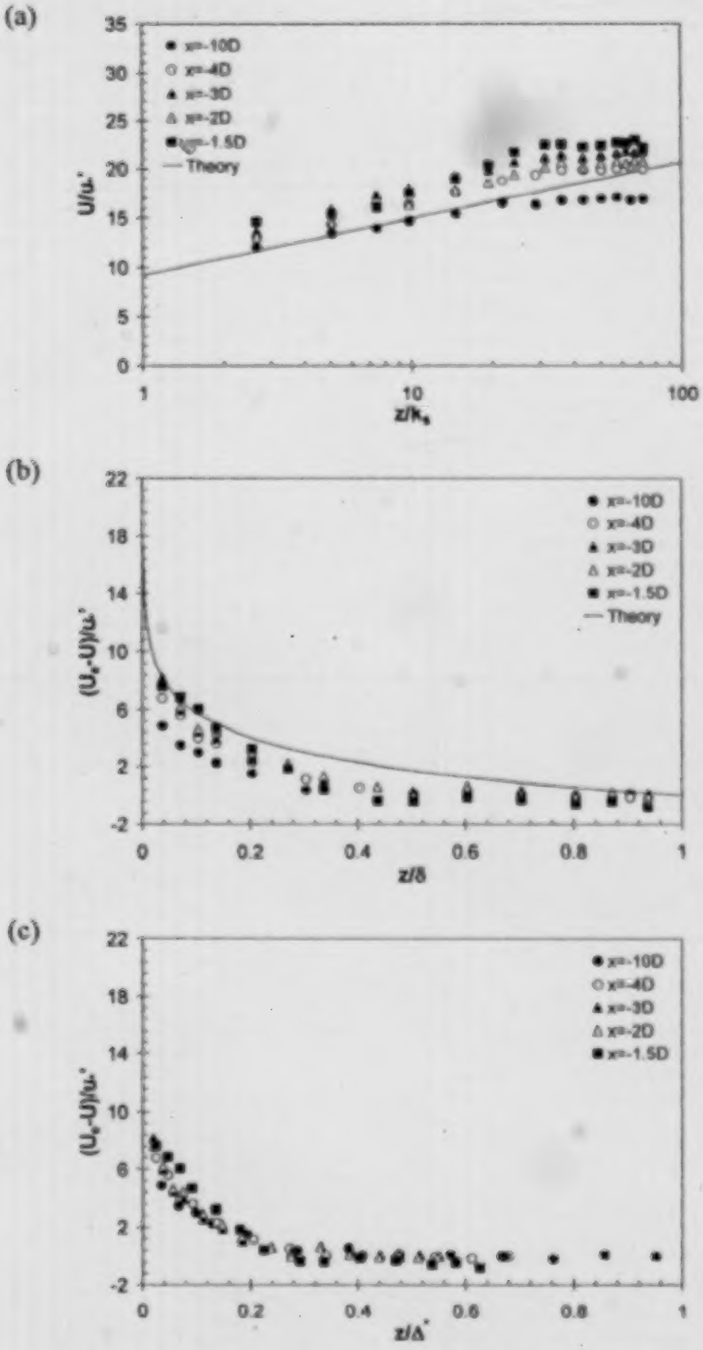

Fig. 5.27 (a) Logarithmic velocity, (b) defect velocity, and (c) Clauser's scheme profiles on upstream POS using local friction velocity: Rough bed/Regime-3

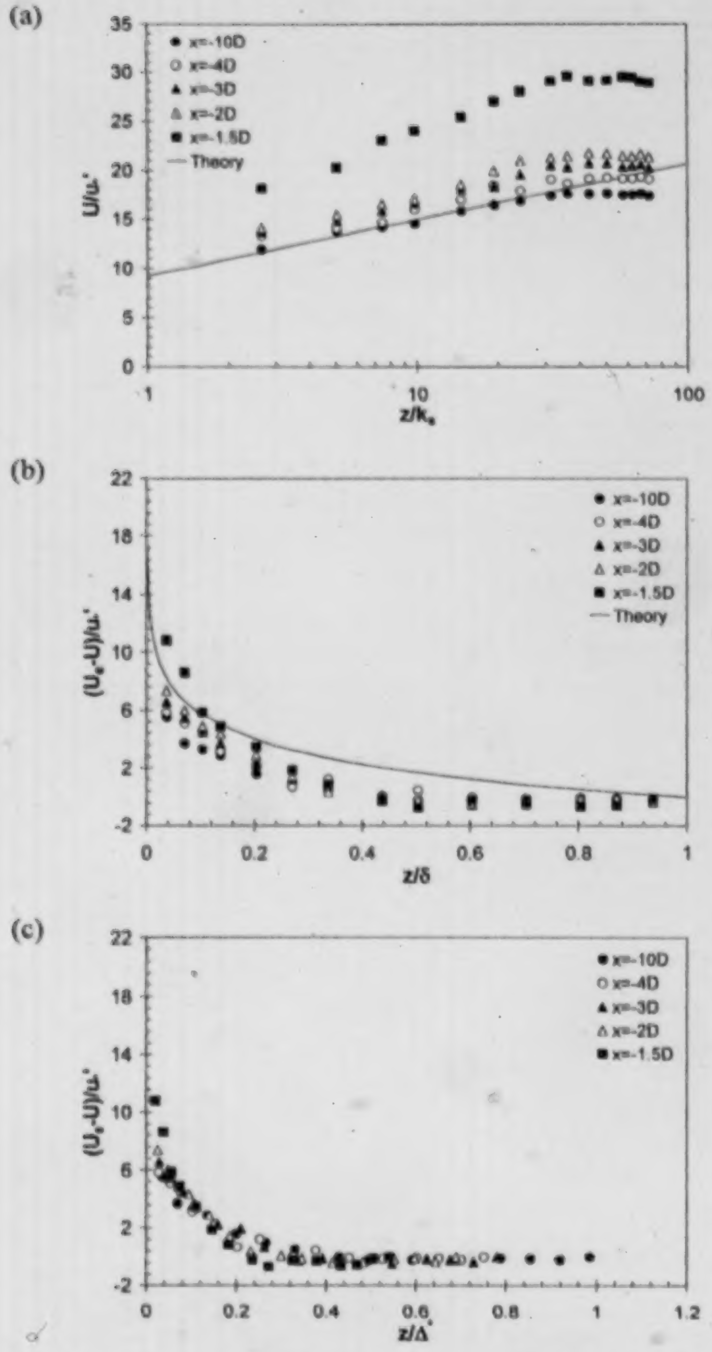

Fig. 5.28 (a) Logarithmic velocity, (b) defect velocity, and (c) Clauser's scheme profiles on upstream POS using local friction velocity: Rough bed/Regime-4

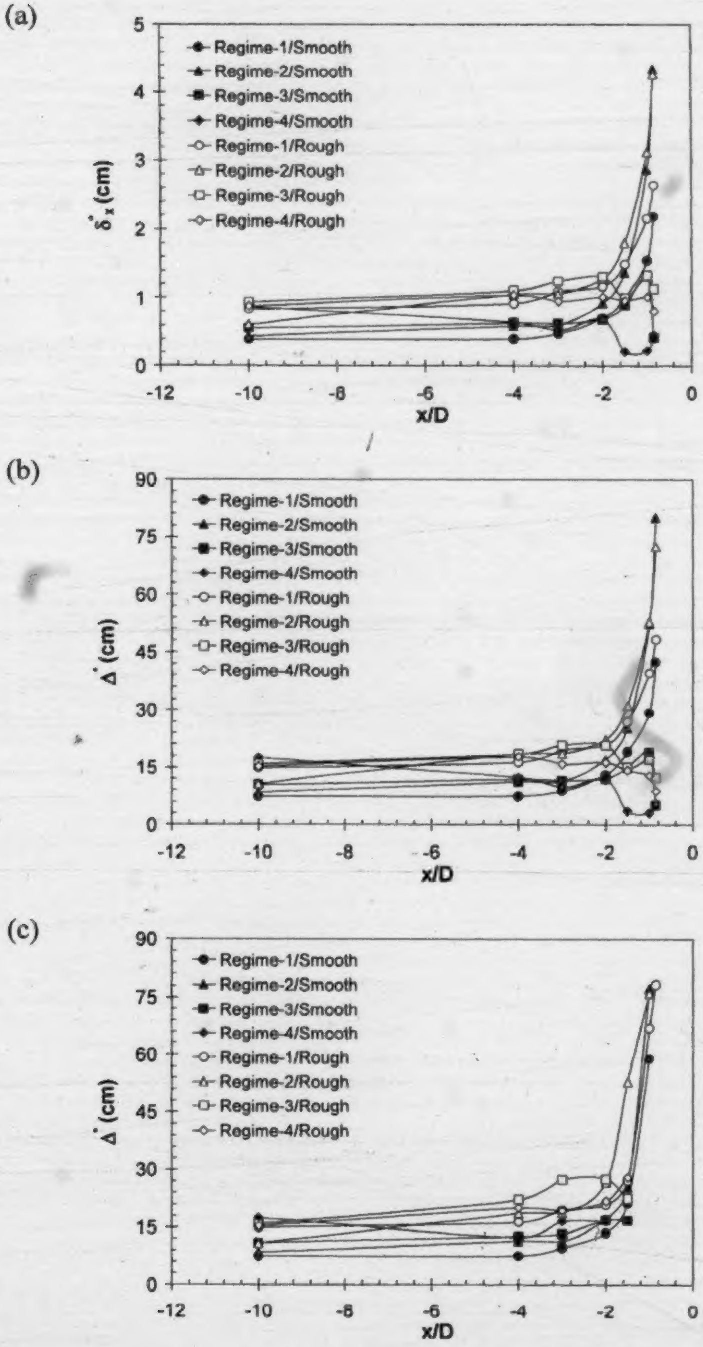

Fig. 5.29 Variation of Clauser's boundary layer parameter (a) δ^*_x, (b) Δ^* using undisturbed flow friction velocity u_*, and (c) Δ^* using local friction velocity u_*' with distance *x/D*

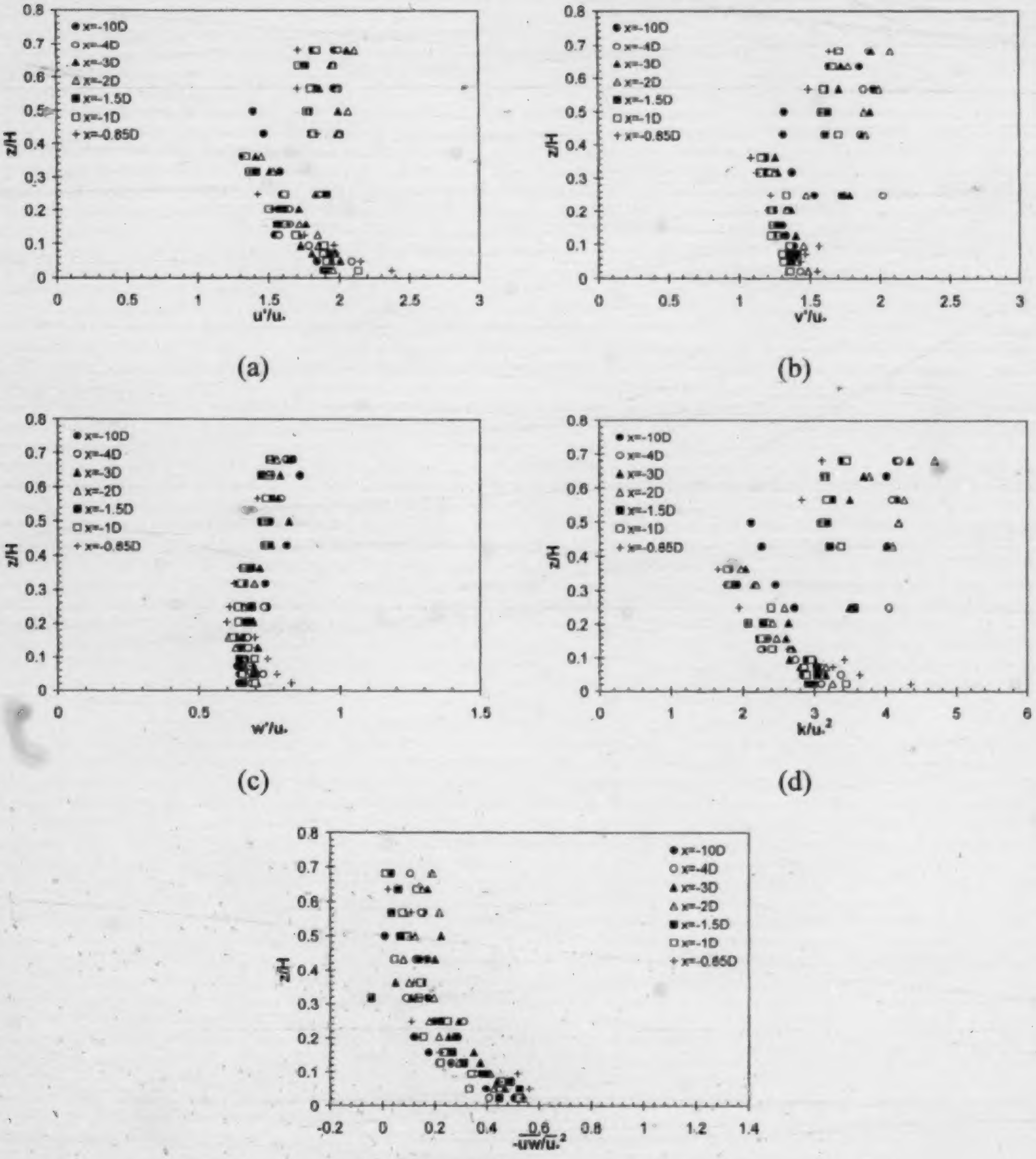

(a) (b)

(c) (d)

(e)

Fig. 5.30 Normalized profiles of turbulence quantities (a) longitudinal r.m.s. velocity, (b) transverse r.m.s. velocity, (c) vertical r.m.s. velocity, (d) turbulent kinetic energy, and (e) primary Reynolds stress on upstream POS: Smooth bed/Regime-1

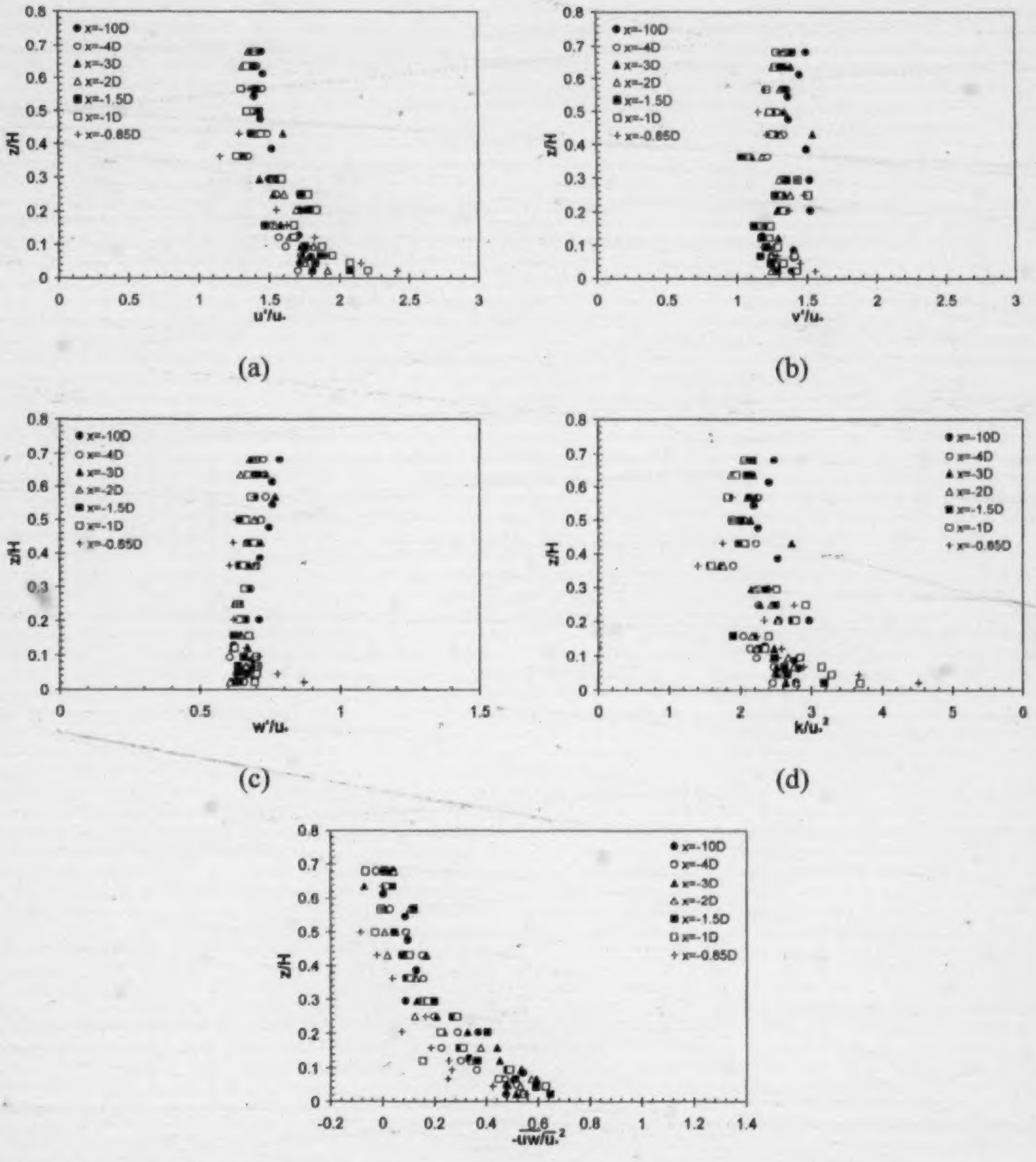

(a) (b) (c) (d) (e)

Fig. 5.31 Normalized profiles of turbulence quantities (a) longitudinal r.m.s. velocity, (b) transverse r.m.s. velocity, (c) vertical r.m.s. velocity, (d) turbulent kinetic energy, and (e) primary Reynolds stress on upstream POS: Smooth bed/Regime-2

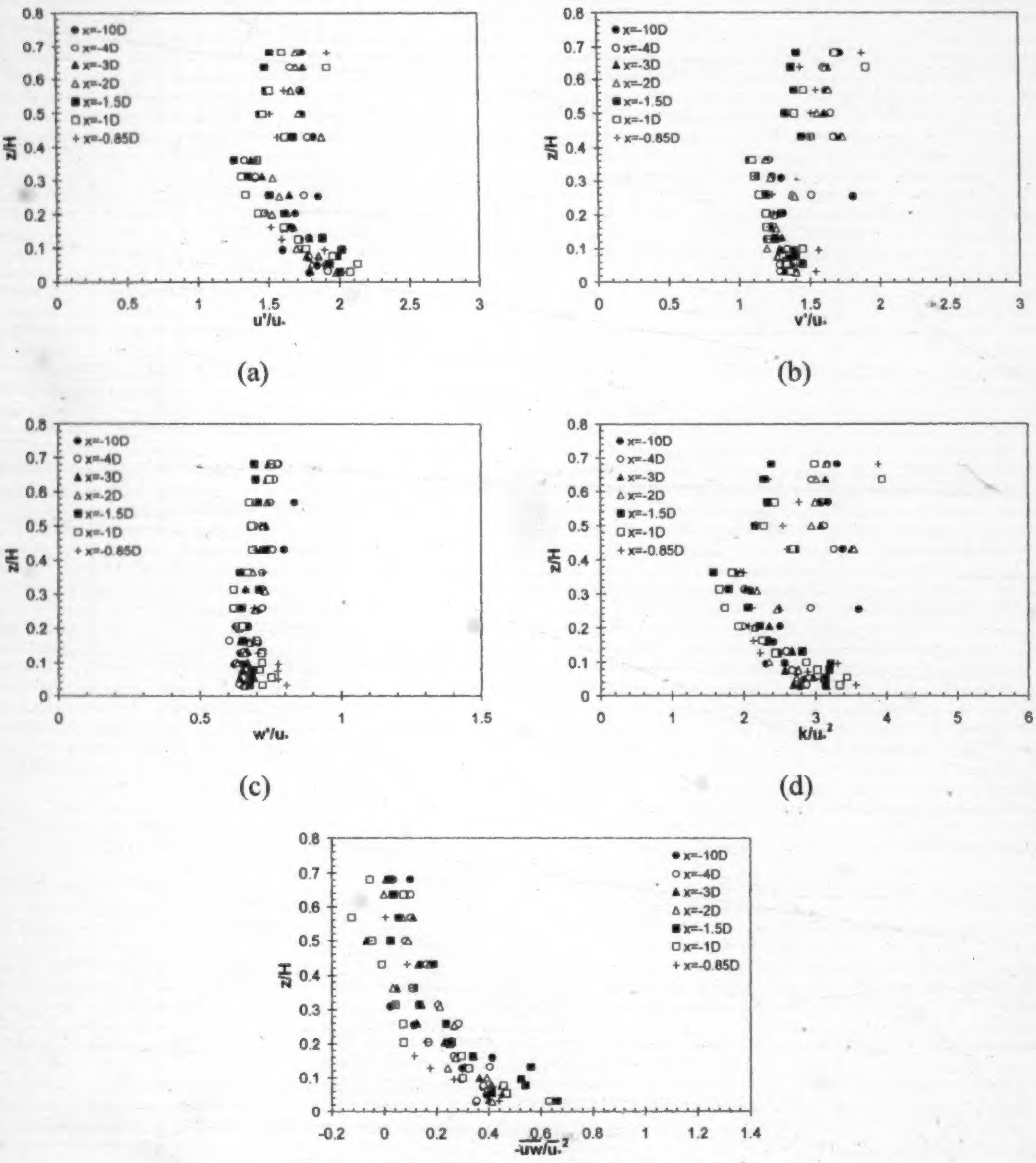

(a) (b)

(c) (d)

(e)

Fig. 5.32 Normalized profiles of turbulence quantities (a) longitudinal r.m.s. velocity, (b) transverse r.m.s. velocity, (c) vertical r.m.s. velocity, (d) turbulent kinetic energy, and (e) primary Reynolds stress on upstream POS: Smooth bed/Regime-3

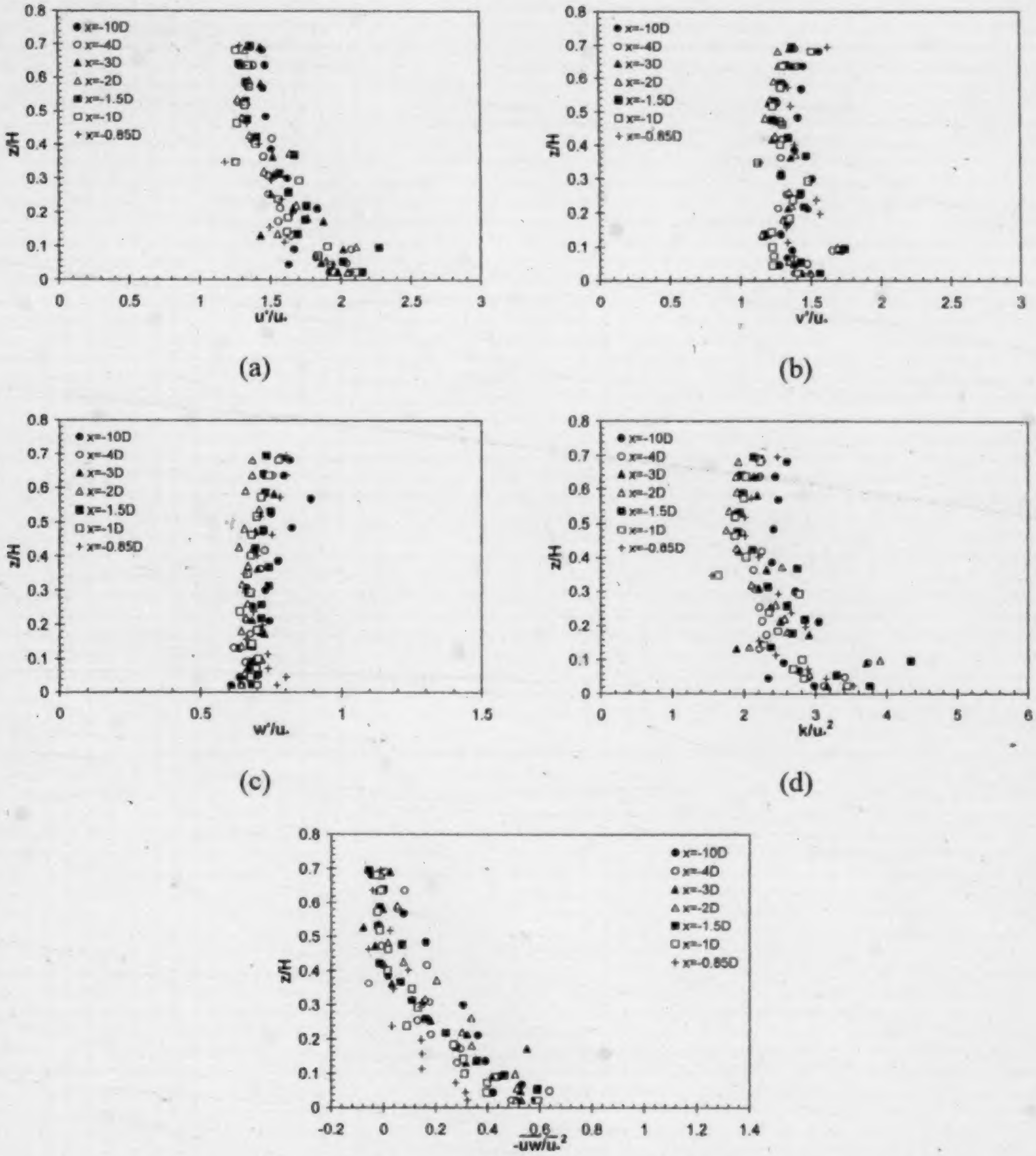

(a) (b) (c) (d) (e)

Fig. 5.33 Normalized profiles of turbulence quantities (a) longitudinal r.m.s. velocity, (b) transverse r.m.s. velocity, (c) vertical r.m.s. velocity, (d) turbulent kinetic energy, and (e) primary Reynolds stress on upstream POS: Smooth bed/Regime-4

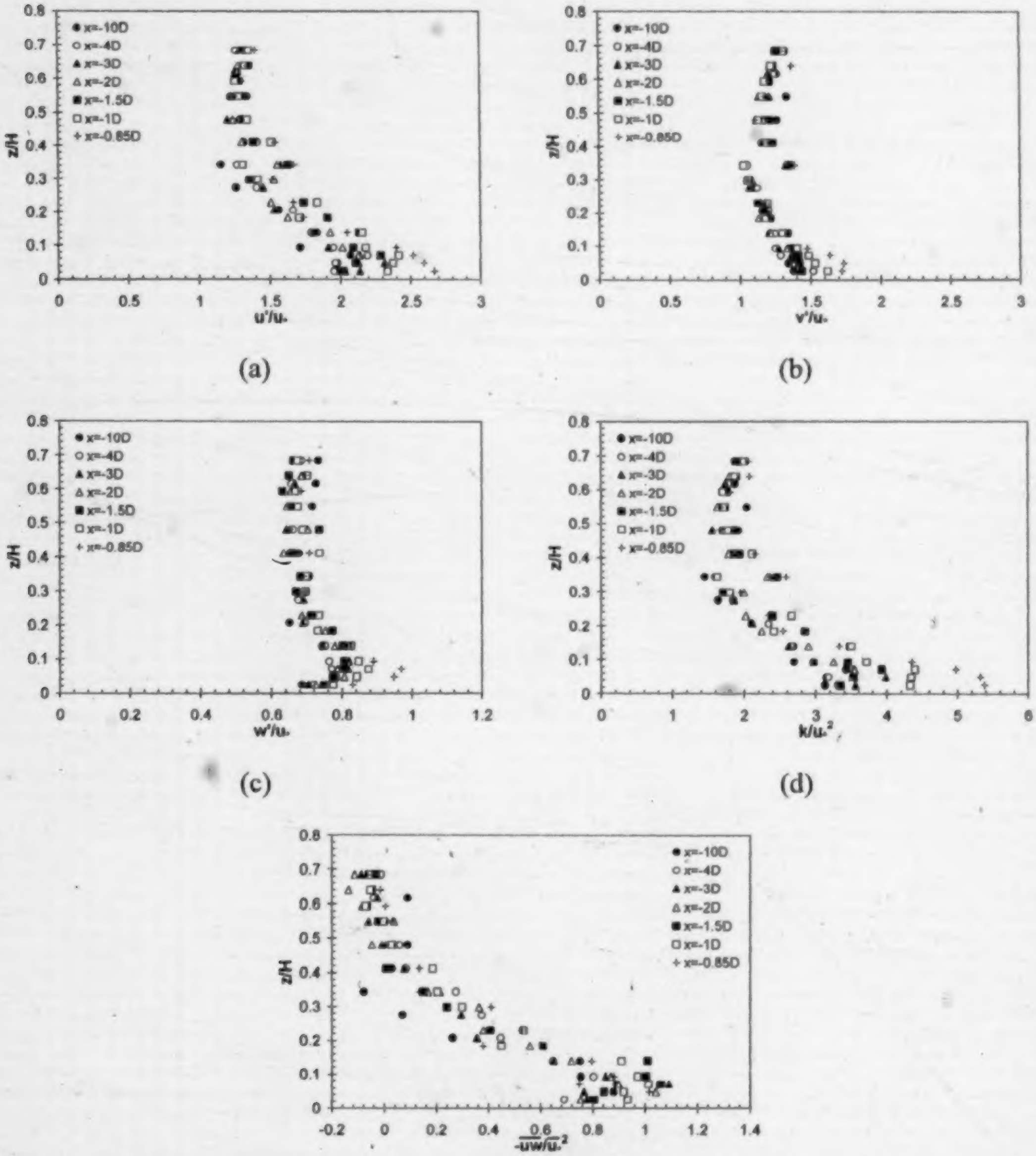

(a) (b)

(c) (d)

(e)

Fig. 5.34 Normalized profiles of turbulence quantities (a) longitudinal r.m.s. velocity, (b) transverse r.m.s. velocity, (c) vertical r.m.s. velocity, (d) turbulent kinetic energy, and (e) primary Reynolds stress on upstream POS: Rough bed/Regime-1

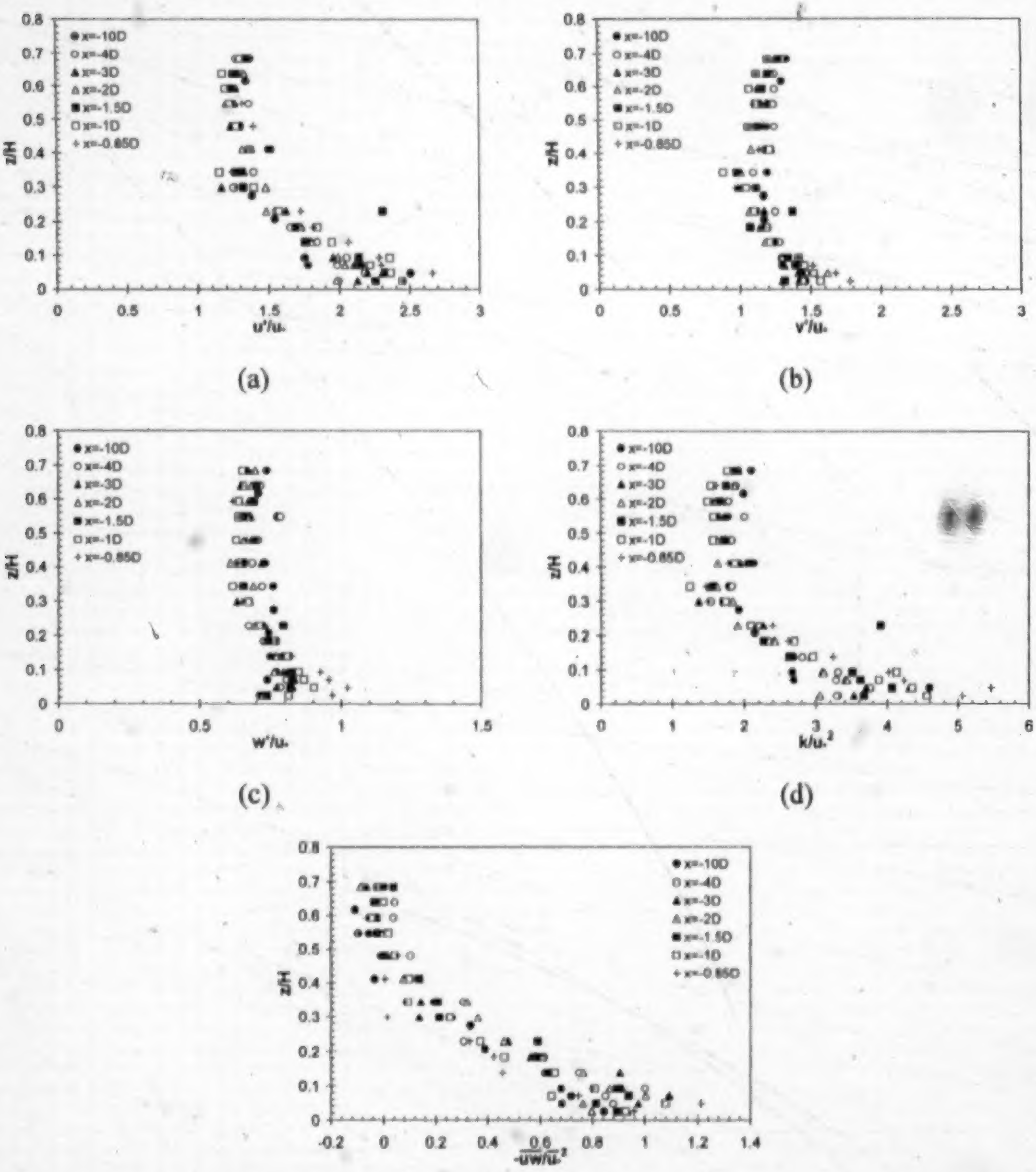

(a) (b)

(c) (d)

(e)

Fig. 5.35 Normalized profiles of turbulence quantities (a) longitudinal r.m.s. velocity, (b) transverse r.m.s. velocity, (c) vertical r.m.s. velocity, (d) turbulent kinetic energy, and (e) primary Reynolds stress on upstream POS: Rough bed/Regime-2

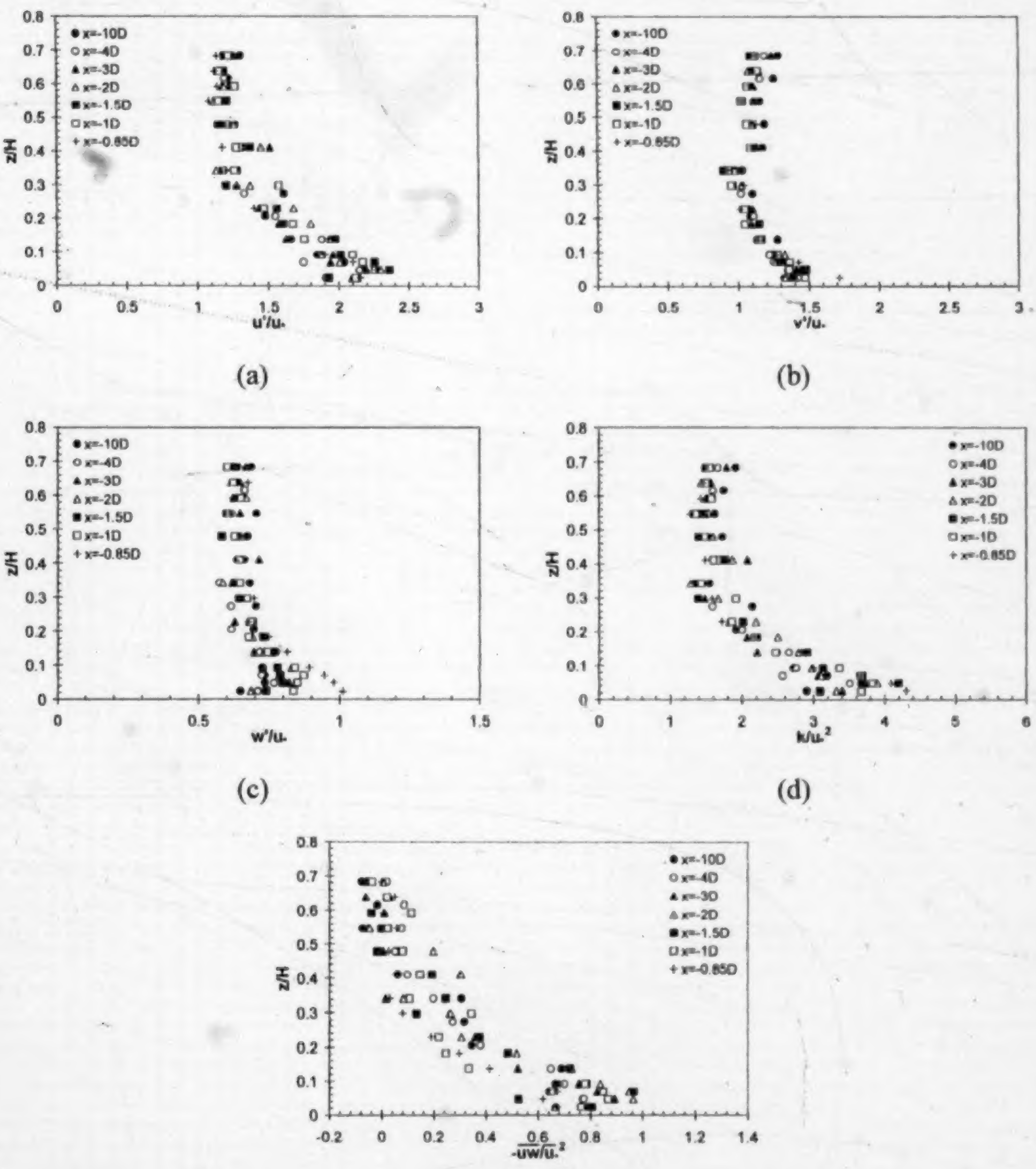

(a) (b)

(c) (d)

(e)

Fig. 5.36 Normalized profiles of turbulence quantities (a) longitudinal r.m.s. velocity, (b) transverse r.m.s. velocity, (c) vertical r.m.s. velocity, (d) turbulent kinetic energy, and (e) primary Reynolds stress on upstream POS: Rough bed/Regime-3

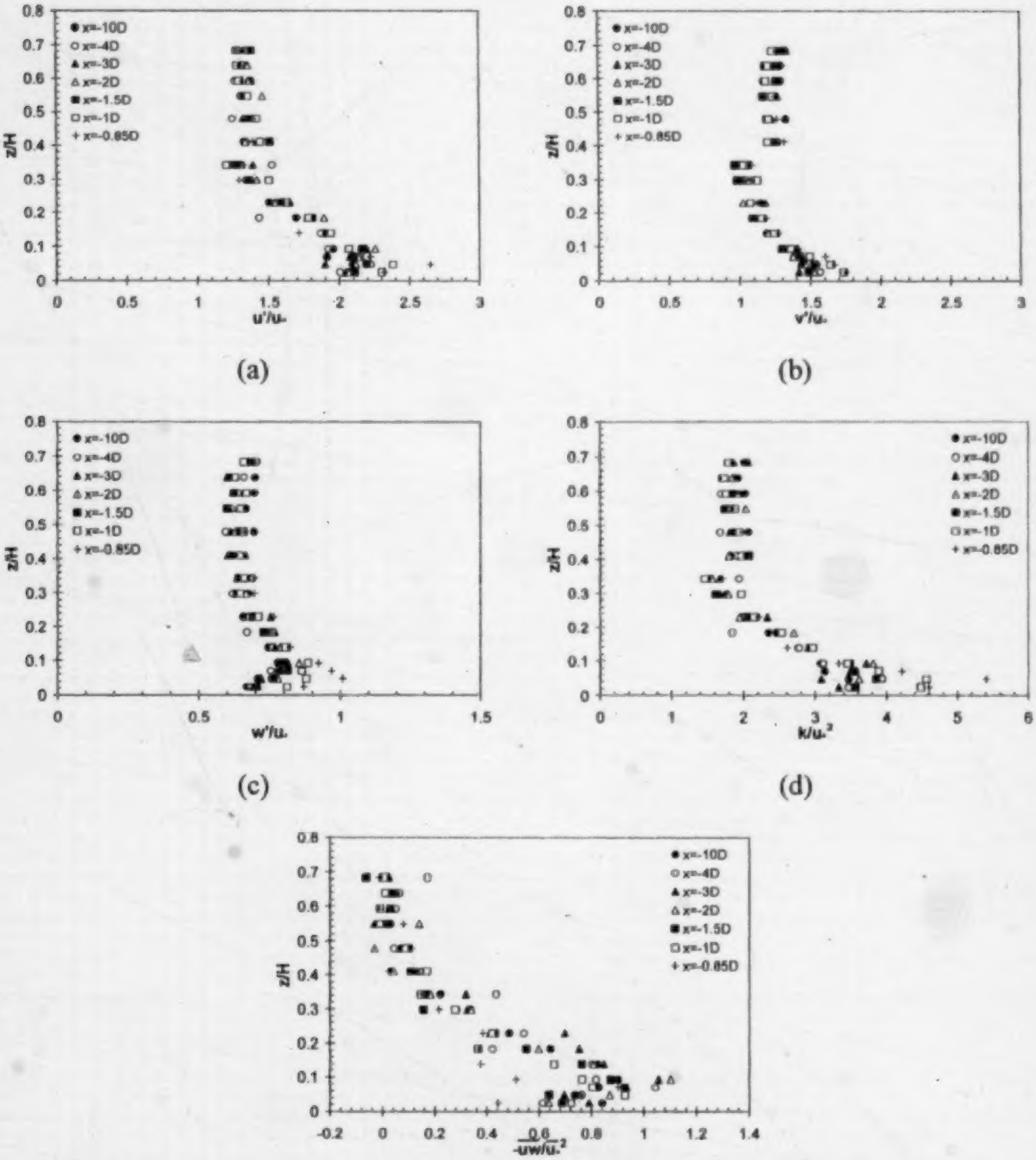

(a) (b)

(c) (d)

(e)

Fig. 5.37 Normalized profiles of turbulence quantities (a) longitudinal r.m.s. velocity, (b) transverse r.m.s. velocity, (c) vertical r.m.s. velocity, (d) turbulent kinetic energy, and (e) primary Reynolds stress on upstream POS: Rough bed/Regime-4

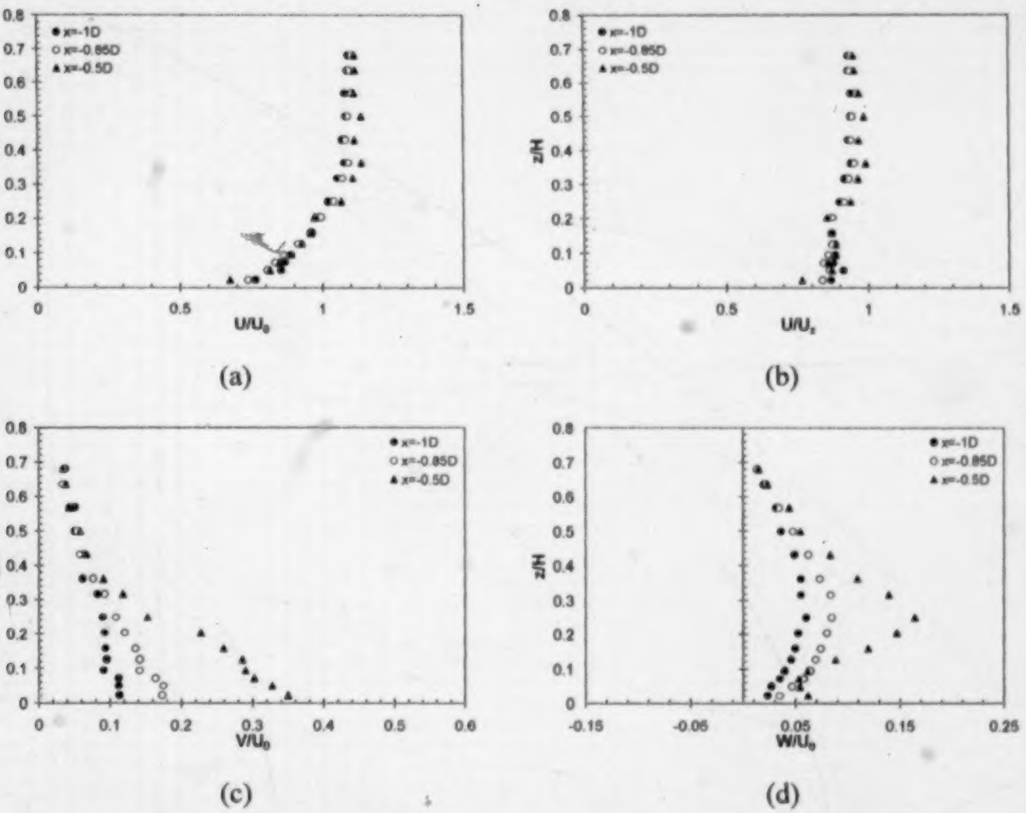

Fig. 5.38 Normalized mean velocity profiles on y=0.5D plane: Smooth bed/Regime-1; (a) longitudinal mean velocity (U/U_0), (b) speed up factor (U/U_z), (c) transverse mean velocity (V/U_0), and (d) vertical mean velocity (W/U_0)

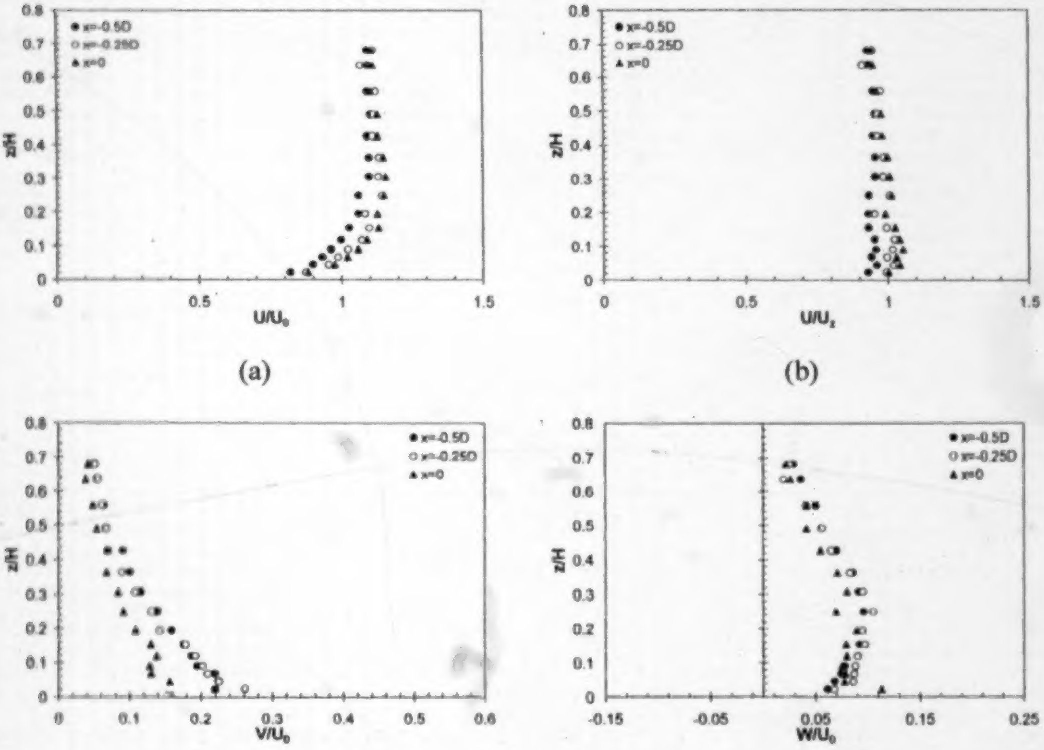

(a) (b)

(c) (d)

Fig. 5.39 Normalized mean velocity profiles on y=0.8D plane: Smooth bed/Regime-1; (a) longitudinal mean velocity (U/U_0), (b) speed up factor (U/U_z), (c) transverse mean velocity (V/U_0), and (d) vertical mean velocity (W/U_0)

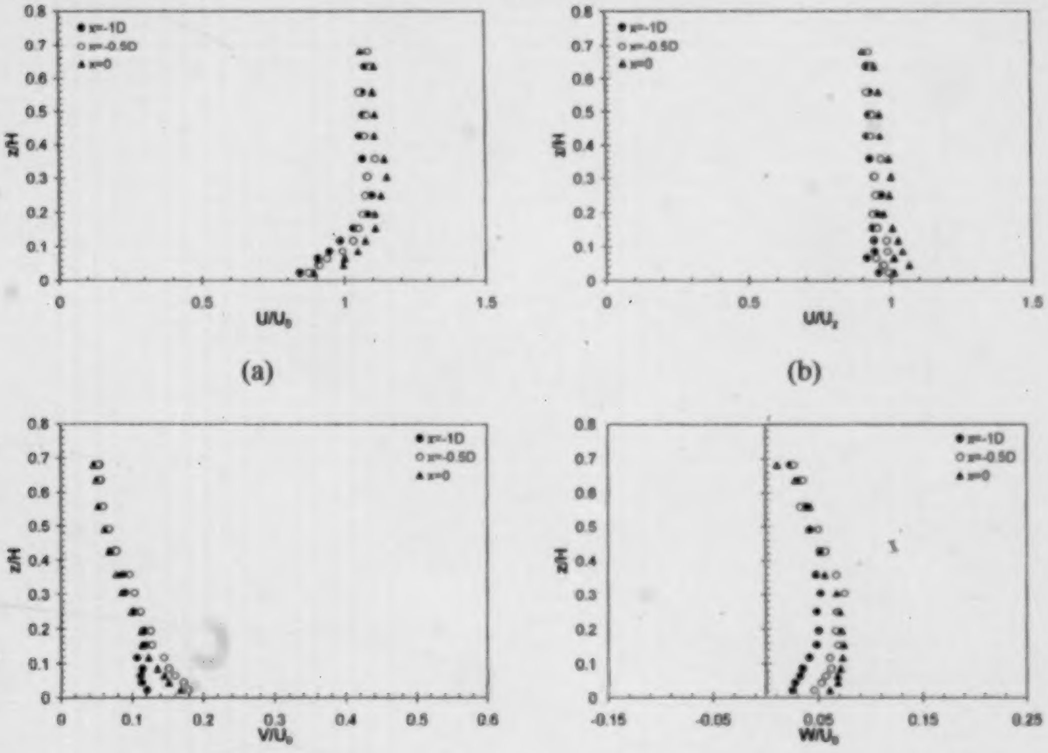

(a) (b)

(c) (d)

Fig. 5.40 Normalized mean velocity profiles on y=1D plane: Smooth bed/Regime-1; (a) longitudinal mean velocity (U/U_0), (b) speed up factor (U/U_z), (c) transverse mean velocity (V/U_0), and (d) vertical mean velocity (W/U_0)

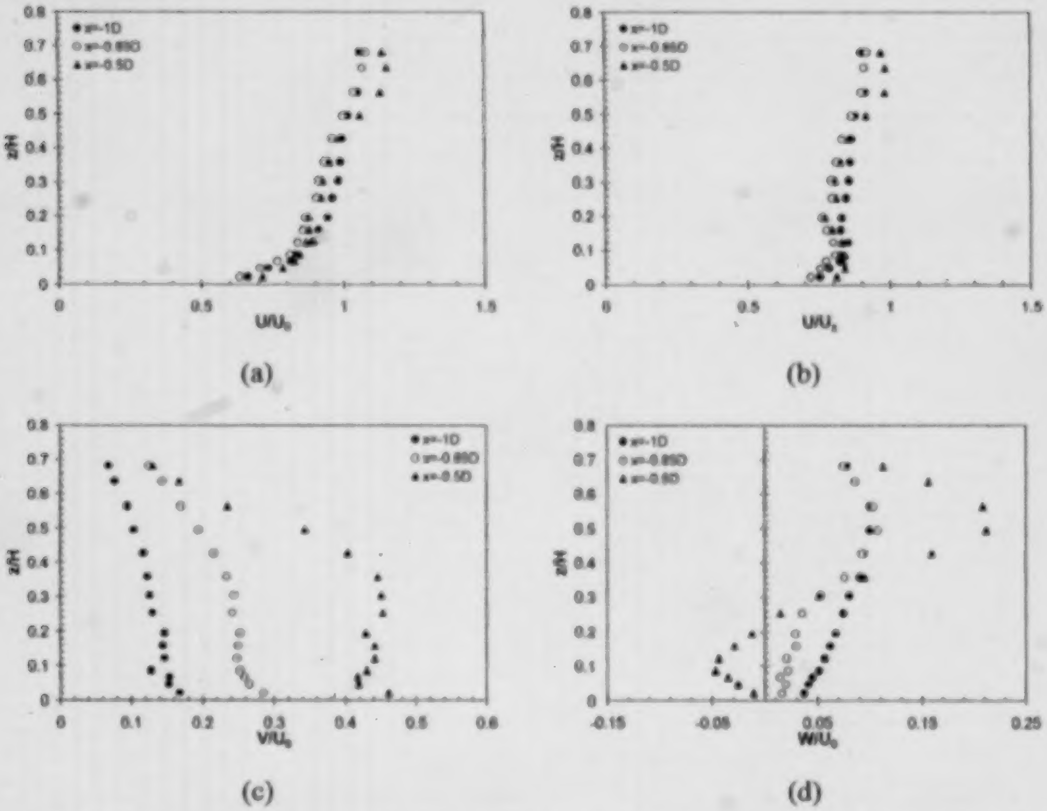

(a) (b)

(c) (d)

Fig. 5.41 Normalized mean velocity profiles on $y=0.5D$ plane: Smooth bed/Regime-2; (a) longitudinal mean velocity (U/U_0), (b) speed up factor (U/U_z), (c) transverse mean velocity (V/U_0), and (d) vertical mean velocity (W/U_0)

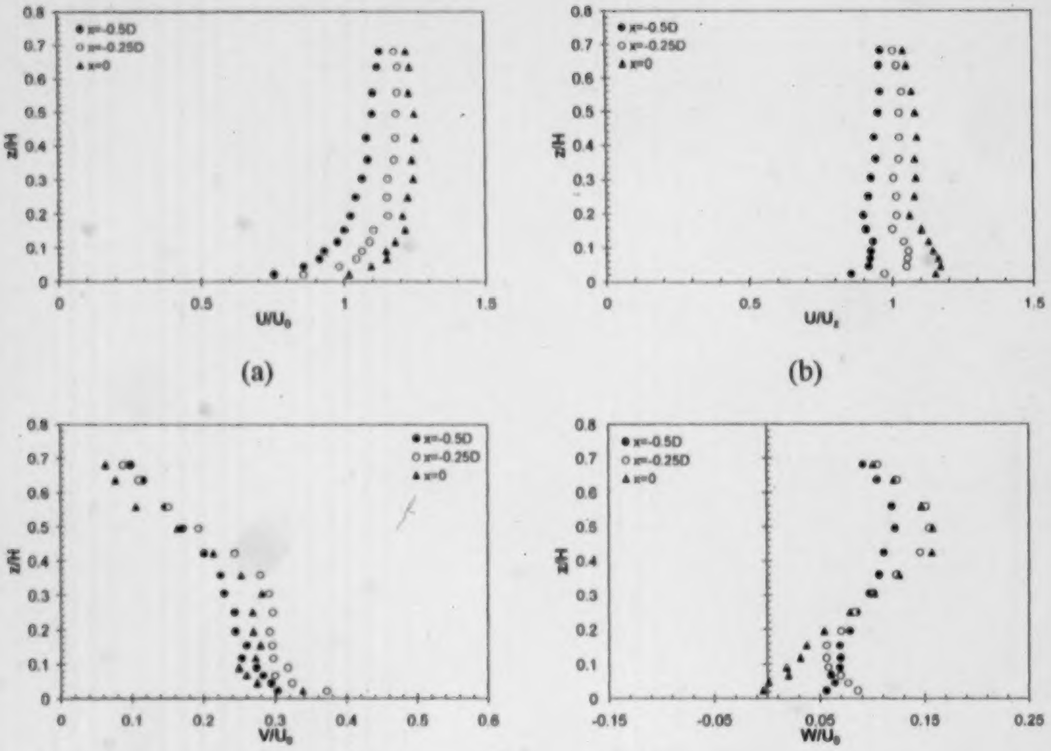

(a) (b)

(c) (d)

Fig. 5.42 Normalized mean velocity profiles on *y*=0.8*D* plane: Smooth bed/Regime-2; (a) longitudinal mean velocity (U/U_0), (b) speed up factor (U/U_z), (c) transverse mean velocity (V/U_0), and (d) vertical mean velocity (W/U_0)

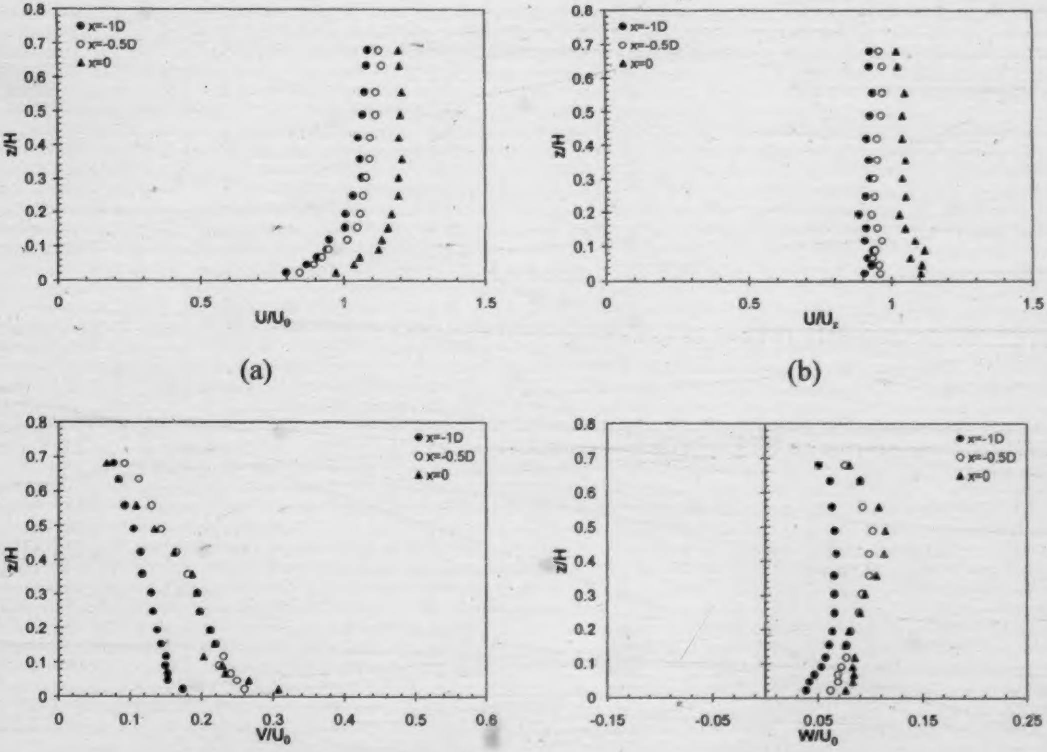

(a) (b)

(c) (d)

Fig. 5.43 Normalized mean velocity profiles on *y*=1*D* plane: Smooth bed/Regime-2; (a) longitudinal mean velocity (U/U_0), (b) speed up factor (U/U_z), (c) transverse mean velocity (V/U_0), and (d) vertical mean velocity (W/U_0)

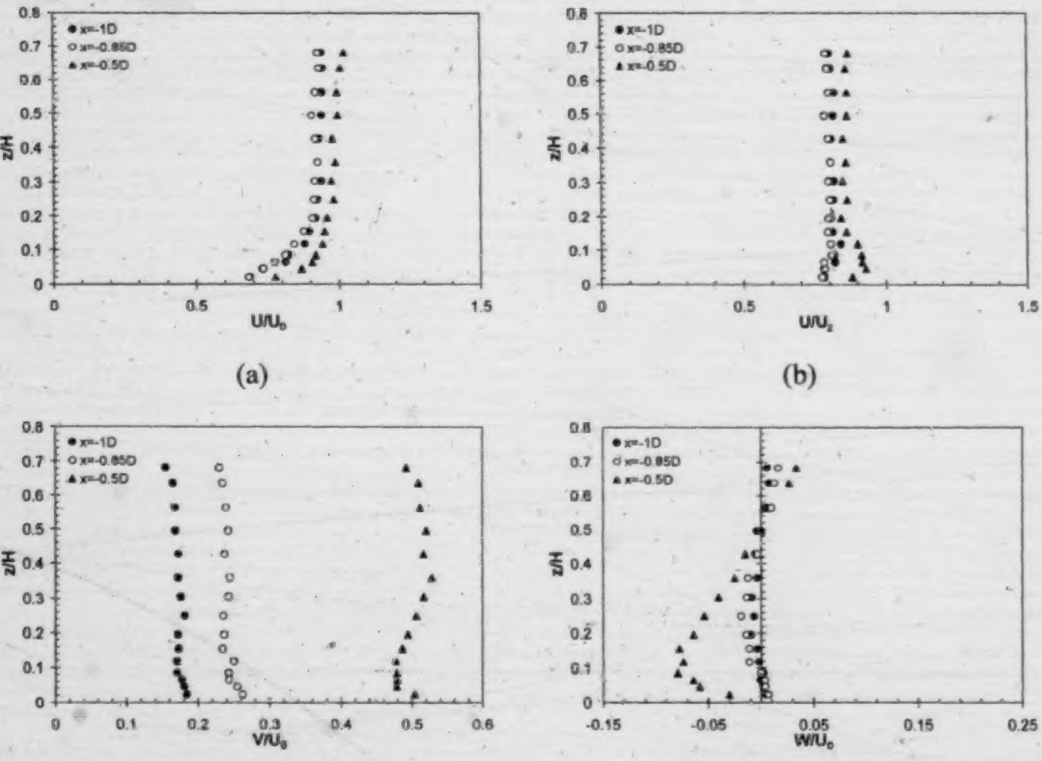

(a) (b)

(c) (d)

Fig. 5.44 Normalized mean velocity profiles on y=0.5D plane: Smooth bed/Regime-3; (a) longitudinal mean velocity (U/U_0), (b) speed up factor (U/U_z), (c) transverse mean velocity (V/U_0), and (d) vertical mean velocity (W/U_0)

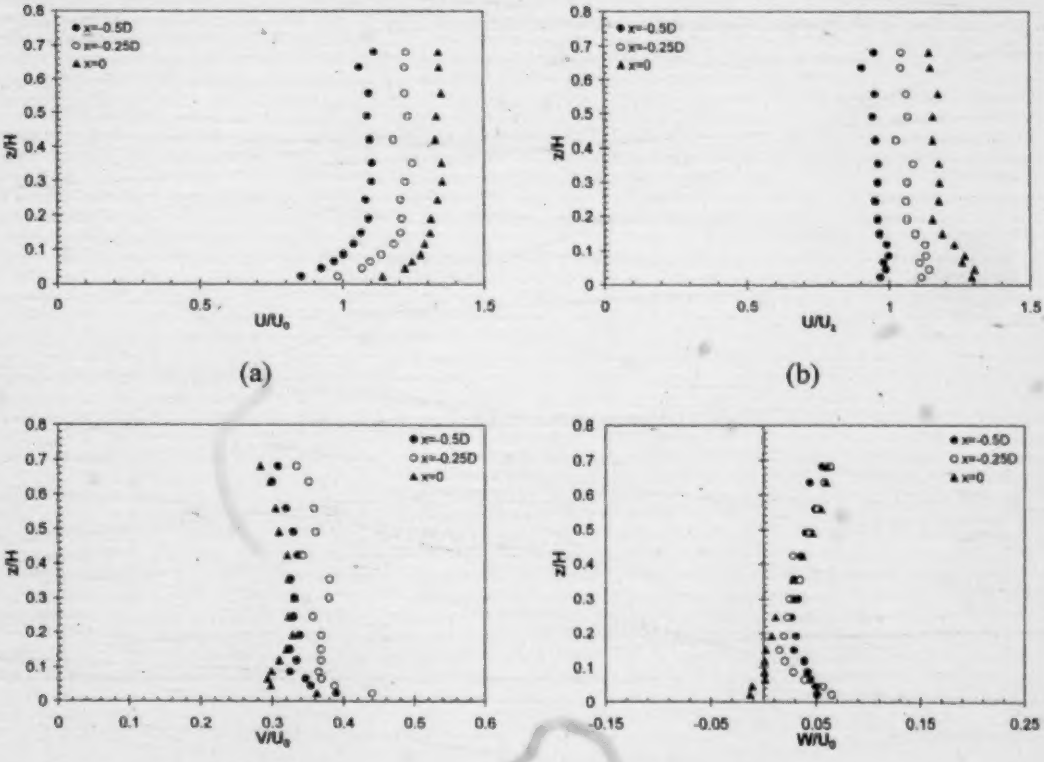

(a) (b)

(c) (d)

Fig. 5.45 Normalized mean velocity profiles on y=0.8D plane: Smooth bed/Regime-3; (a) longitudinal mean velocity (U/U_0), (b) speed up factor (U/U_z), (c) transverse mean velocity (V/U_0), and (d) vertical mean velocity (W/U_0)

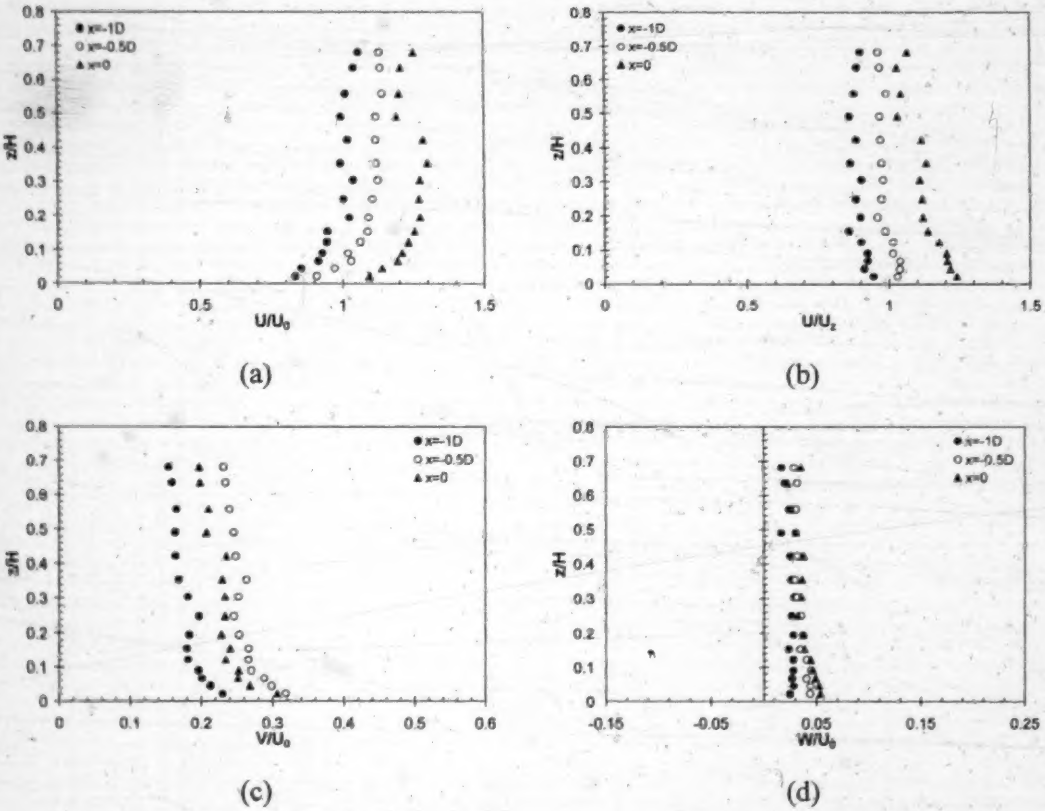

(a) (b)

(c) (d)

Fig. 5.46 Normalized mean velocity profiles on $y=1D$ plane: Smooth bed/Regime-3; (a) longitudinal mean velocity (U/U_0), (b) speed up factor (U/U_z), (c) transverse mean velocity (V/U_0), and (d) vertical mean velocity (W/U_0)

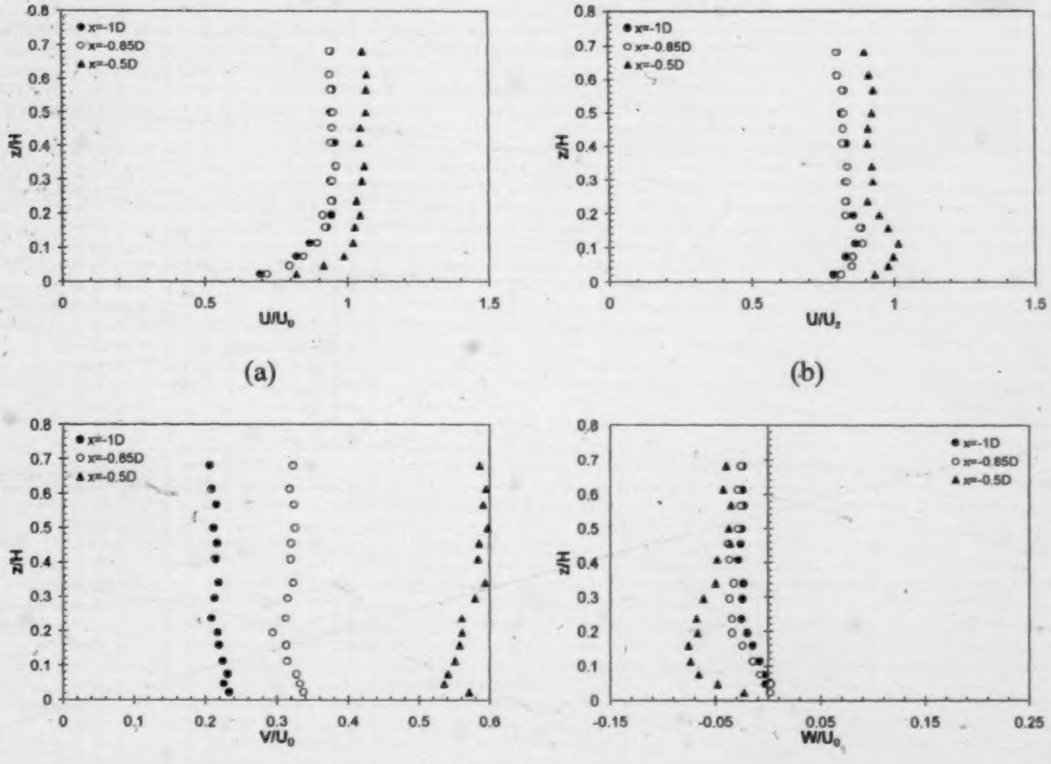

(a) (b)

(c) (d)

Fig. 5.47 Normalized mean velocity profiles on *y*=0.5*D* plane: Smooth bed/Regime-4; (a) longitudinal mean velocity (U/U_0), (b) speed up factor (U/U_z), (c) transverse mean velocity (V/U_0), and (d) vertical mean velocity (W/U_0)

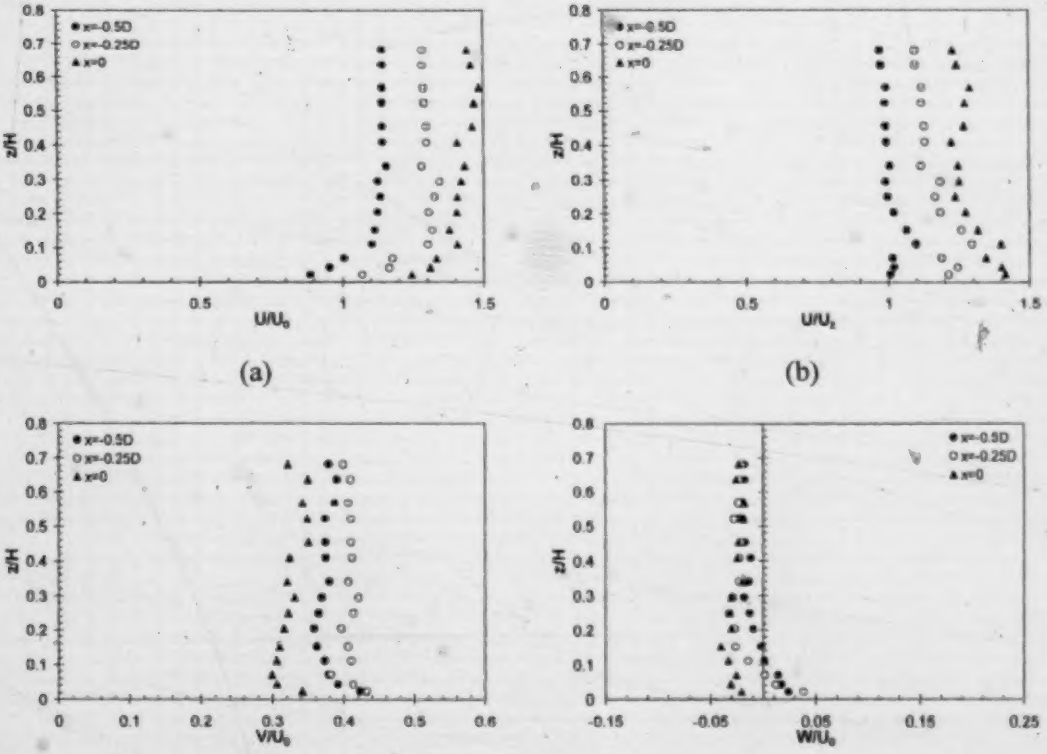

(a) (b)

(c) (d)

Fig. 5.48 Normalized mean velocity profiles on y=0.8D plane: Smooth bed/Regime-4; (a) longitudinal mean velocity (U/U_0), (b) speed up factor (U/U_z), (c) transverse mean velocity (V/U_0), and (d) vertical mean velocity (W/U_0)

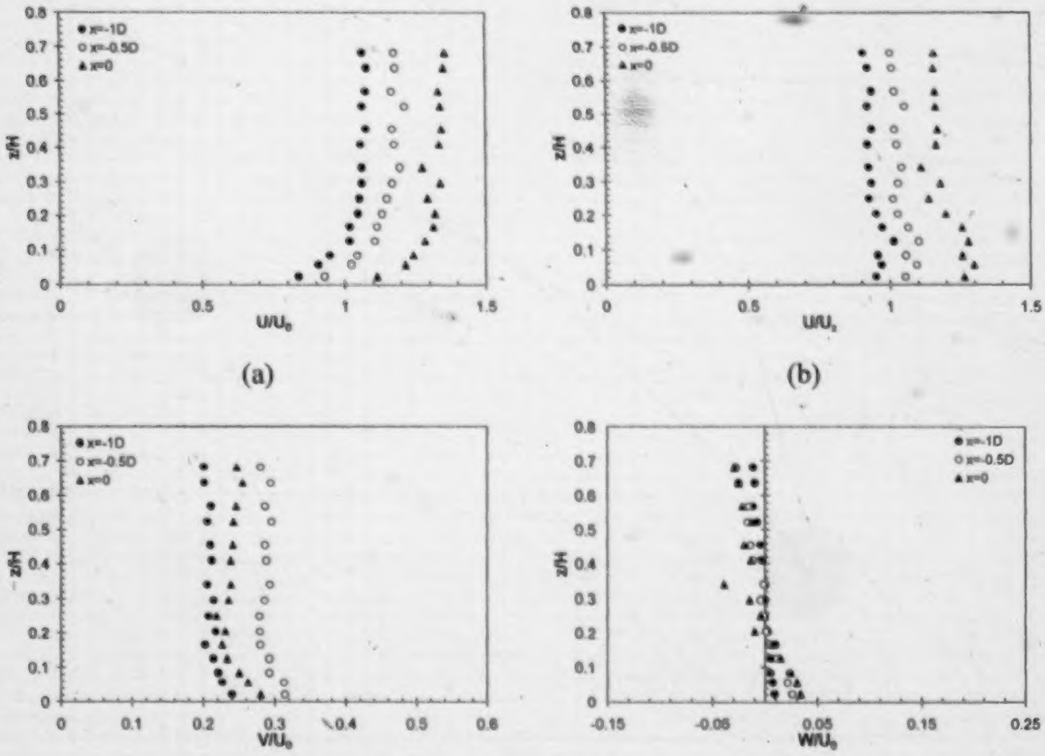

(a) (b)

(c) (d)

Fig. 5.49 Normalized mean velocity profiles on y=1D plane: Smooth bed/Regime-4; (a) longitudinal mean velocity (U/U_0), (b) speed up factor (U/U_z), (c) transverse mean velocity (V/U_0), and (d) vertical mean velocity (W/U_0)

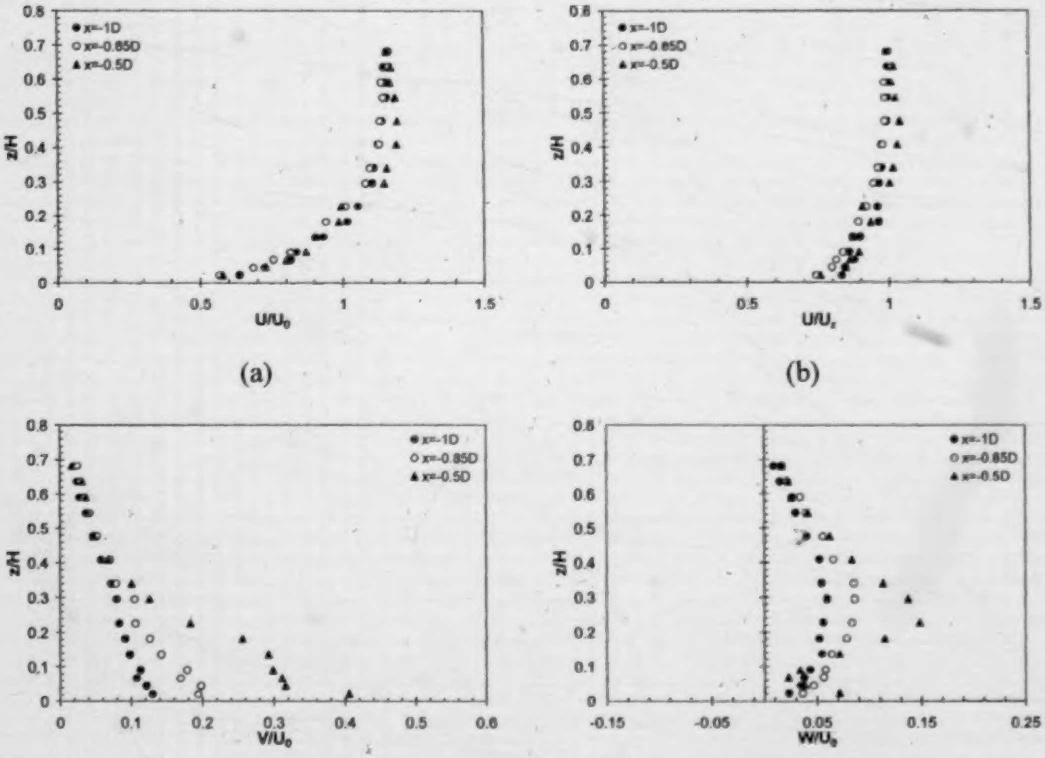

(a) (b)

(c) (d)

Fig. 5.50 Normalized mean velocity profiles on *y*=0.5*D* plane: Rough bed/Regime-1; (a) longitudinal mean velocity (U/U_0), (b) speed up factor (U/U_z), (c) transverse mean velocity (V/U_0), and (d) vertical mean velocity (W/U_0)

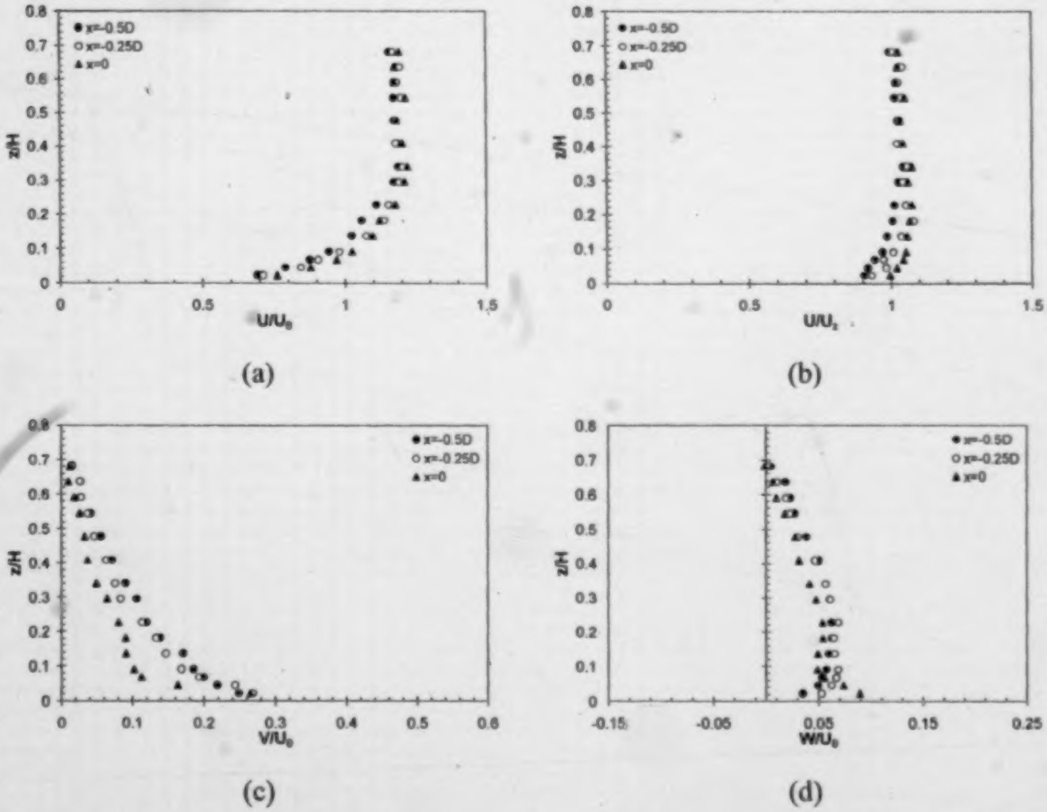

Fig. 5.51 Normalized mean velocity profiles on y=0.8D plane: Rough bed/Regime-1; (a) longitudinal mean velocity (U/U_0), (b) speed up factor (U/U_z), (c) transverse mean velocity (V/U_0), and (d) vertical mean velocity (W/U_0)

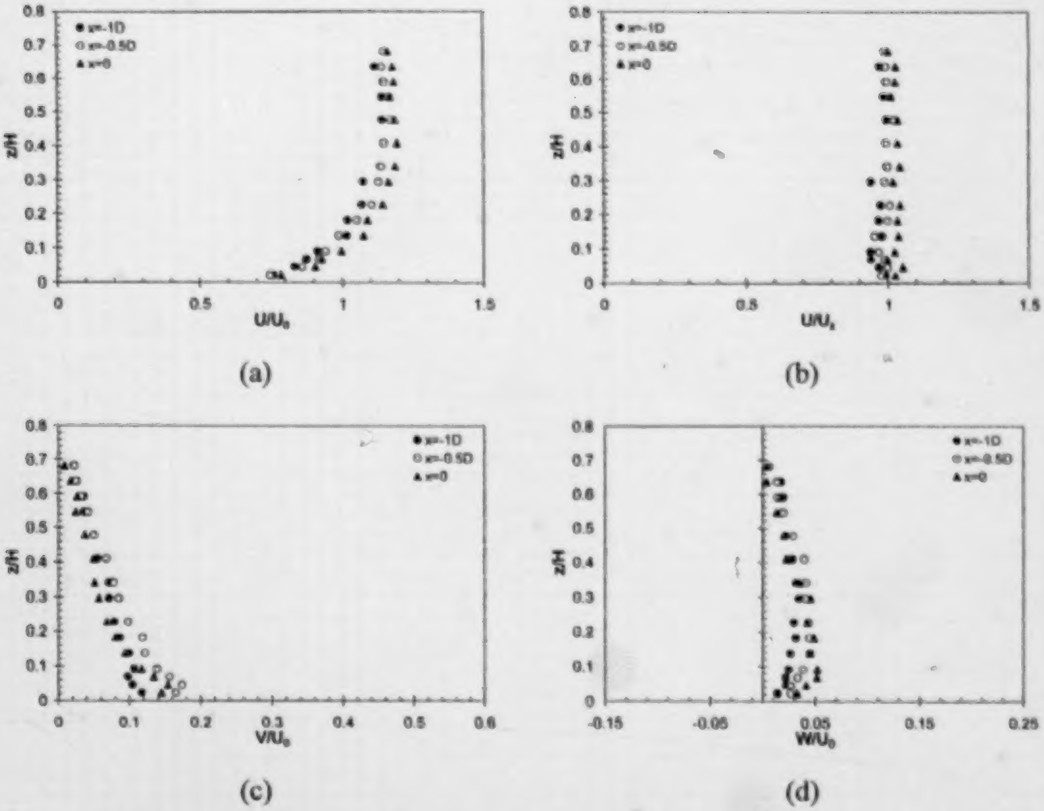

Fig. 5.52 Normalized mean velocity profiles on y=1D plane: Rough bed/Regime-1; (a) longitudinal mean velocity (U/U_0), (b) speed up factor (U/U_z), (c) transverse mean velocity (V/U_0), and (d) vertical mean velocity (W/U_0)

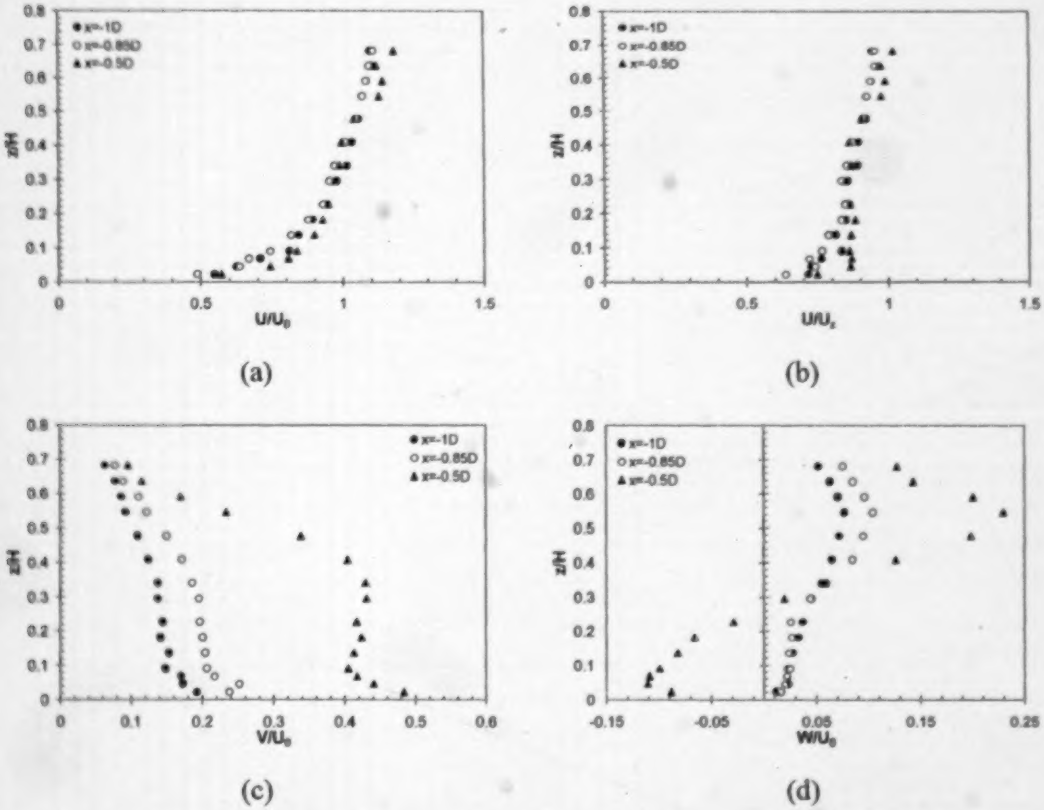

Fig. 5.53 Normalized mean velocity profiles on y=0.5D plane: Rough bed/Regime-2; (a) longitudinal mean velocity (U/U_0), (b) speed up factor (U/U_z), (c) transverse mean velocity (V/U_0), and (d) vertical mean velocity (W/U_0)

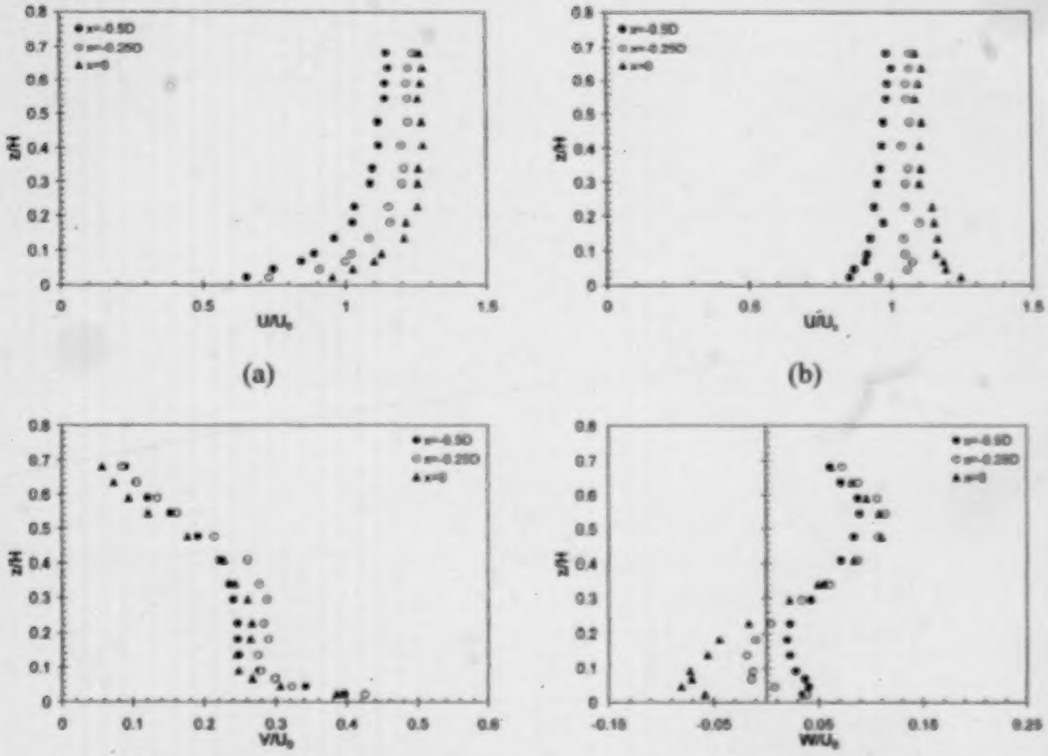

(a) (b)

(c) (d)

Fig. 5.54 Normalized mean velocity profiles on y=0.8D plane: Rough bed/Regime-2; (a) longitudinal mean velocity (U/U_0), (b) speed up factor (U/U_z), (c) transverse mean velocity (V/U_0), and (d) vertical mean velocity (W/U_0)

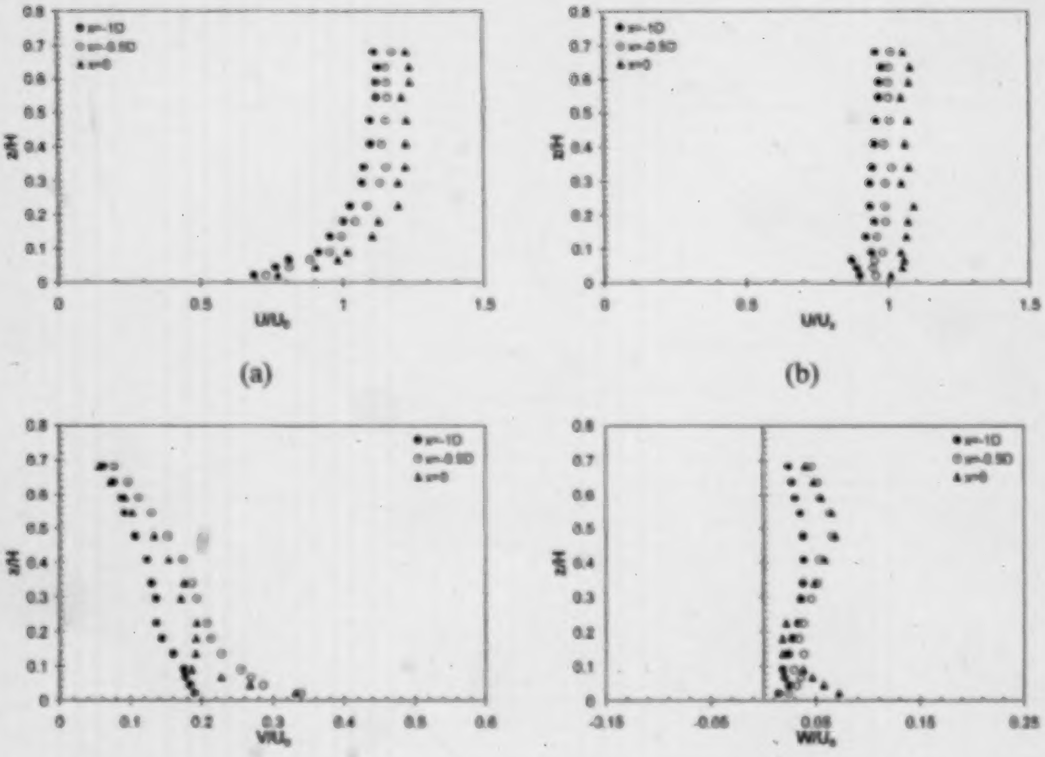

(a) (b)

(c) (d)

Fig. 5.55 Normalized mean velocity profiles on $y=1D$ plane: Rough bed/Regime-2; (a) longitudinal mean velocity (U/U_0), (b) speed up factor (U/U_z), (c) transverse mean velocity (V/U_0), and (d) vertical mean velocity (W/U_0)

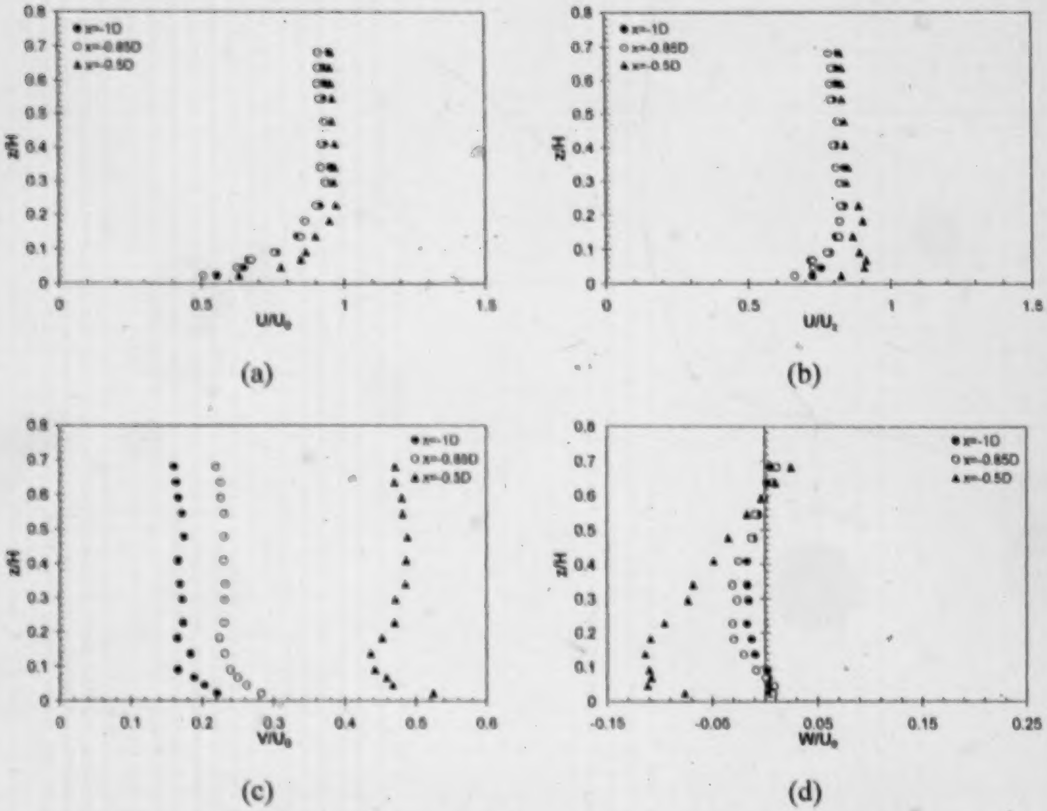

Fig. 5.56 Normalized mean velocity profiles on y=0.5D plane: Rough bed/Regime-3; (a) longitudinal mean velocity (U/U_0), (b) speed up factor (U/U_z), (c) transverse mean velocity (V/U_0), and (d) vertical mean velocity (W/U_0)

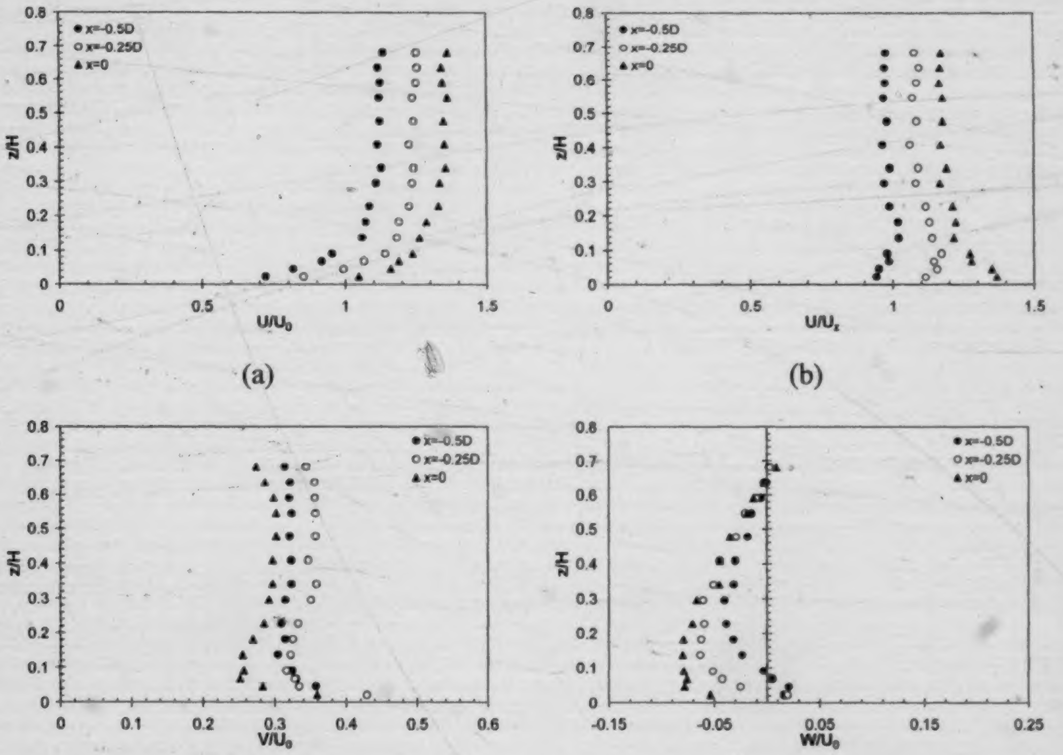

(a) (b)

(c) (d)

Fig. 5.57 Normalized mean velocity profiles on y=0.8D plane: Rough bed/Regime-3; (a) longitudinal mean velocity (U/U_0), (b) speed up factor (U/U_z), (c) transverse mean velocity (V/U_0), and (d) vertical mean velocity (W/U_0)

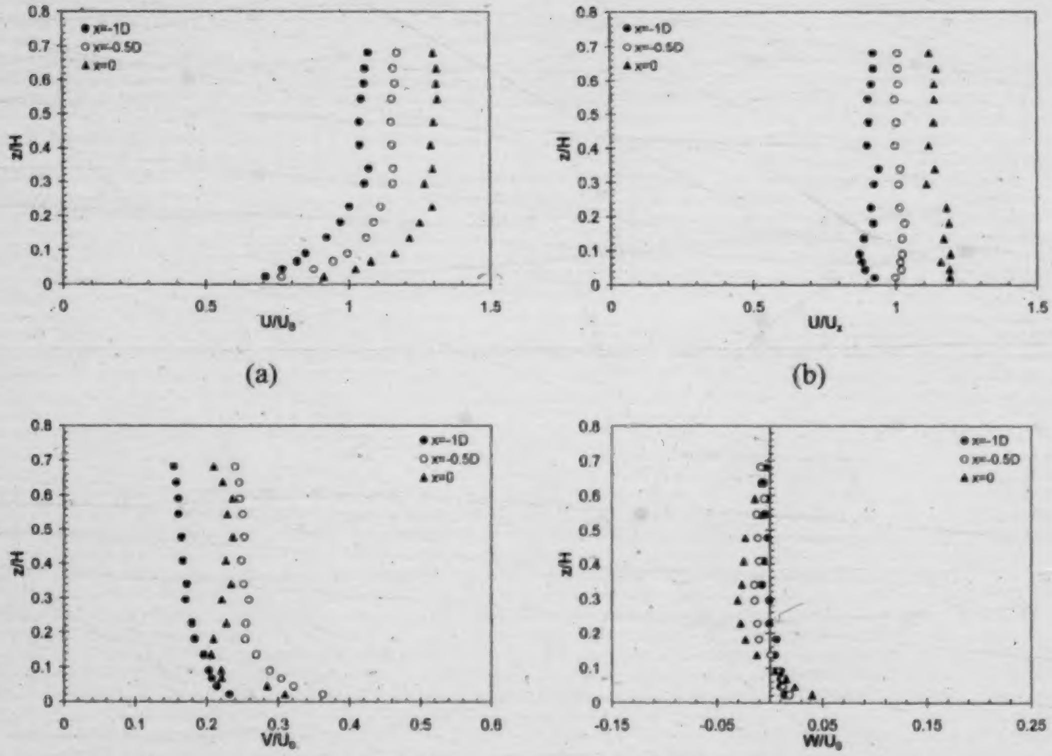

(a) (b)

(c) (d)

Fig. 5.58 Normalized mean velocity profiles on *y*=1*D* plane: Rough bed/Regime-3; (a) longitudinal mean velocity (U/U_0), (b) speed up factor (U/U_z), (c) transverse mean velocity (V/U_0), and (d) vertical mean velocity (W/U_0)

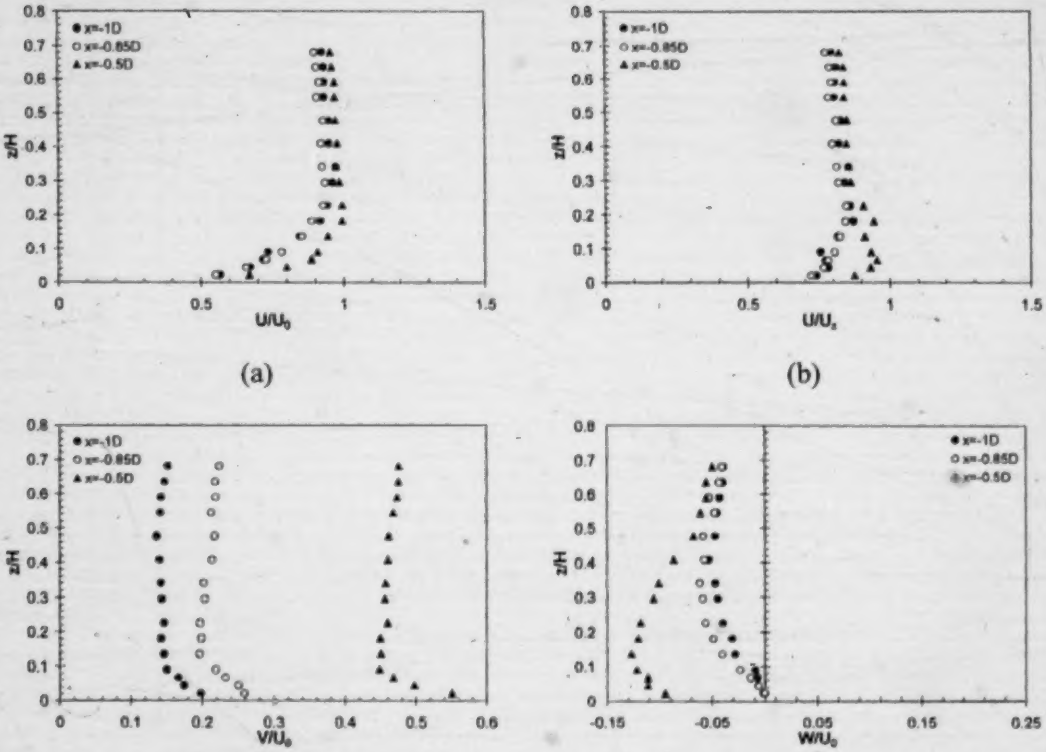

(a) (b)

(c) (d)

Fig. 5.59 Normalized mean velocity profiles on y=0.5D plane: Rough bed/Regime-4; (a) longitudinal mean velocity (U/U_0), (b) speed up factor (U/U_z), (c) transverse mean velocity (V/U_0), and (d) vertical mean velocity (W/U_0)

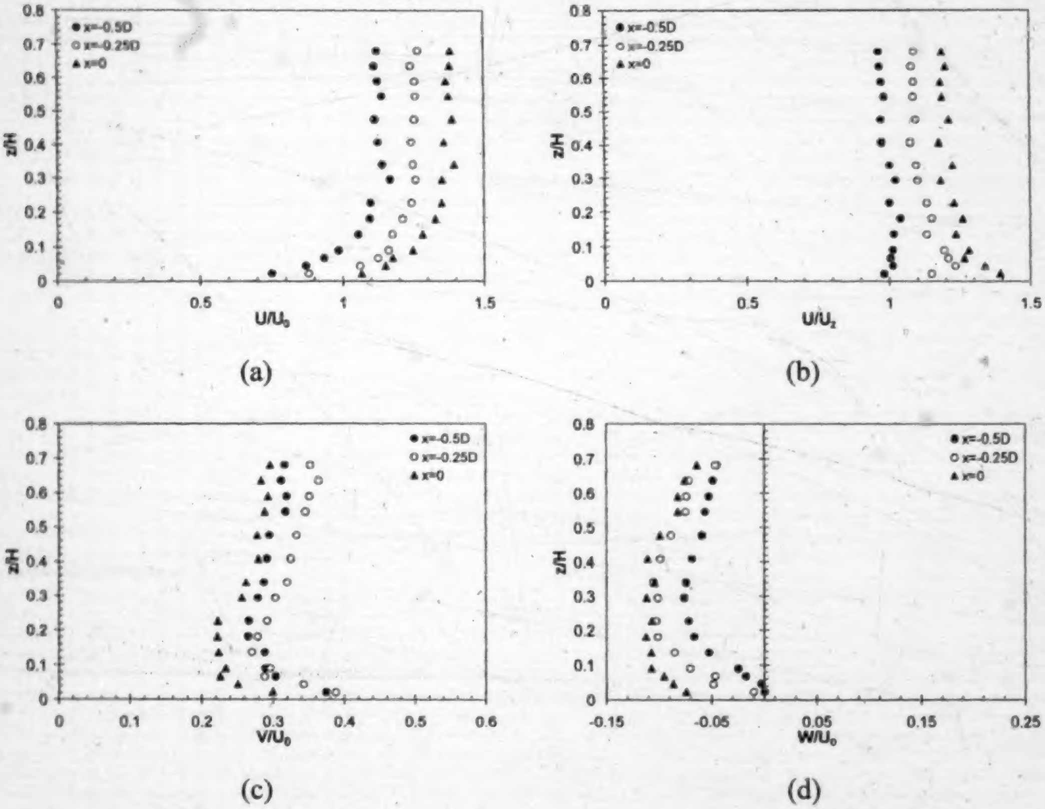

(a) (b)

(c) (d)

Fig. 5.60 Normalized mean velocity profiles on *y*=0.8*D* plane: Rough bed/Regime-4; (a) longitudinal mean velocity (U/U_0), (b) speed up factor (U/U_z), (c) transverse mean velocity (V/U_0), and (d) vertical mean velocity (W/U_0)

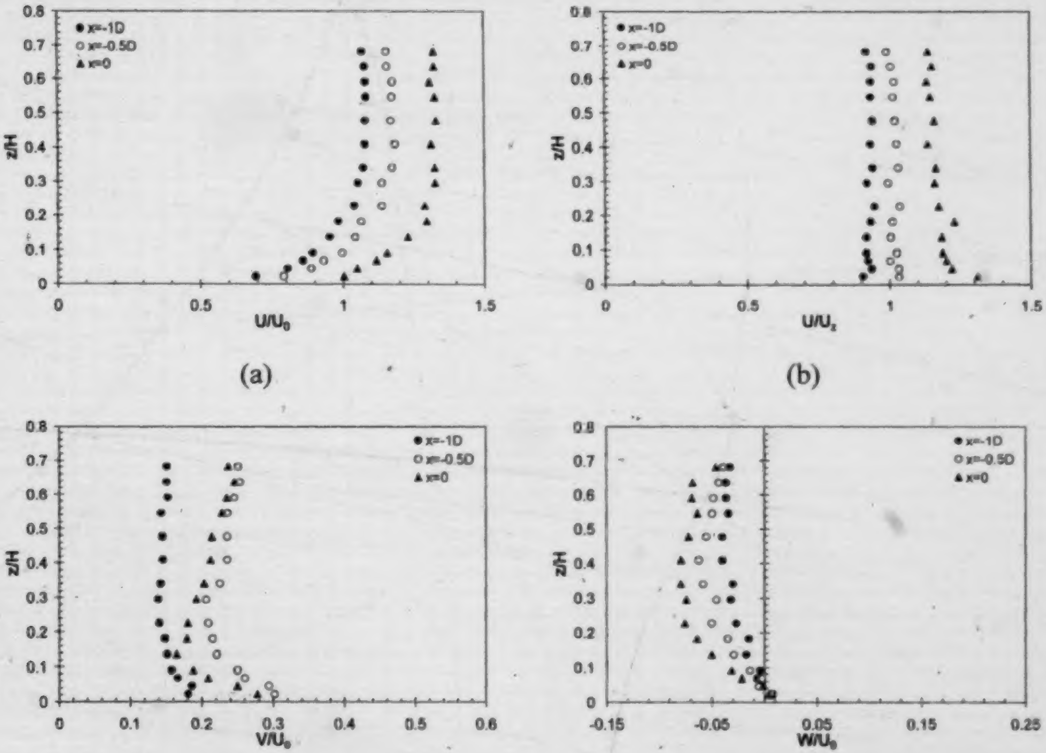

(a) (b)

(c) (d)

Fig. 5.61 Normalized mean velocity profiles on $y=1D$ plane: Rough bed/Regime-4; (a) longitudinal mean velocity (U/U_0), (b) speed up factor (U/U_z), (c) transverse mean velocity (V/U_0), and (d) vertical mean velocity (W/U_0)

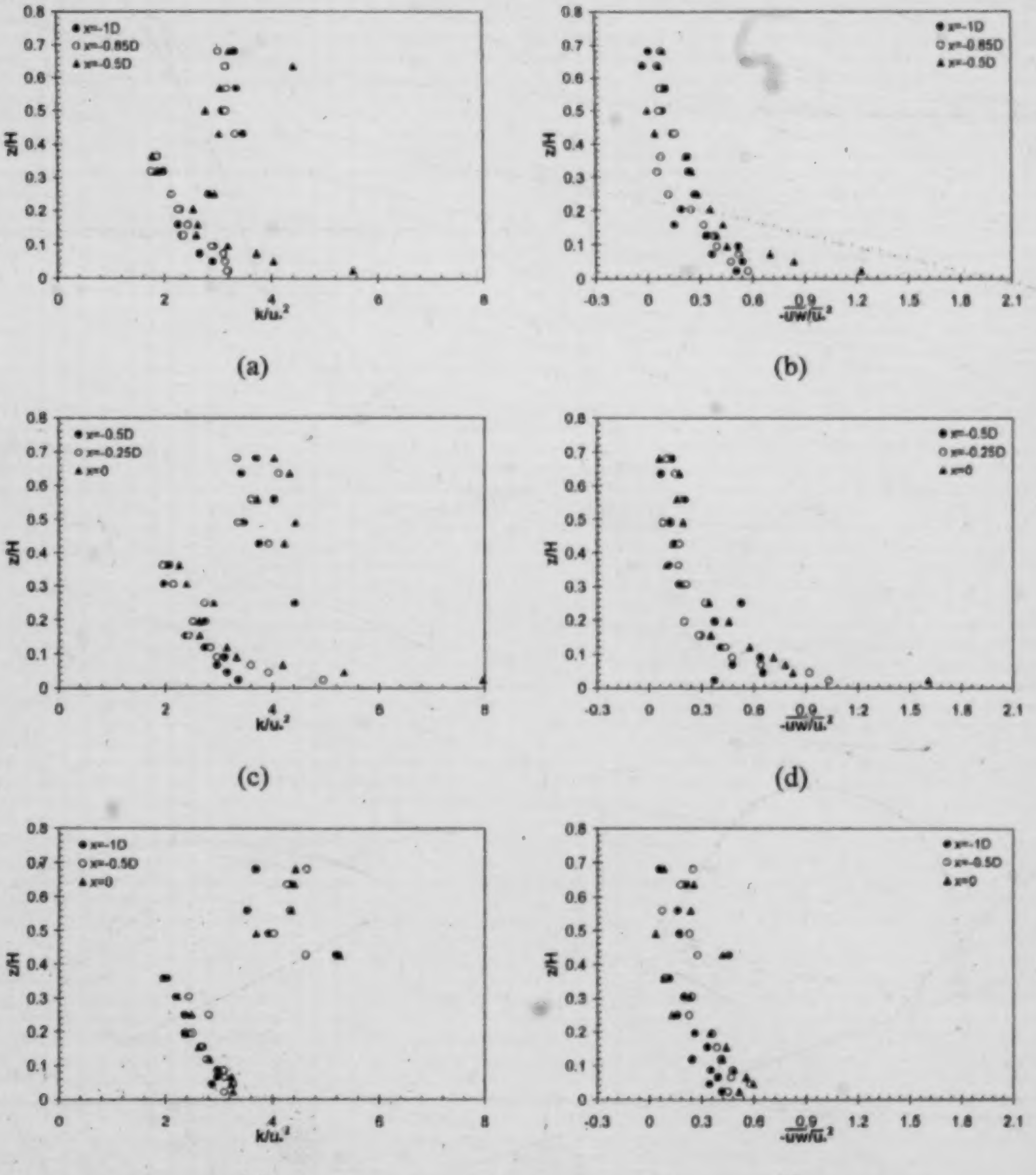

(a) (b)

(c) (d)

(e) (f)

Fig. 5.62 Normalized turbulent kinetic energy and primary Reynolds stress profiles on (a-b) y=0.5D plane, (c-d) y=0.8D plane, and (e-f) y=1D plane: Smooth bed/Regime-1

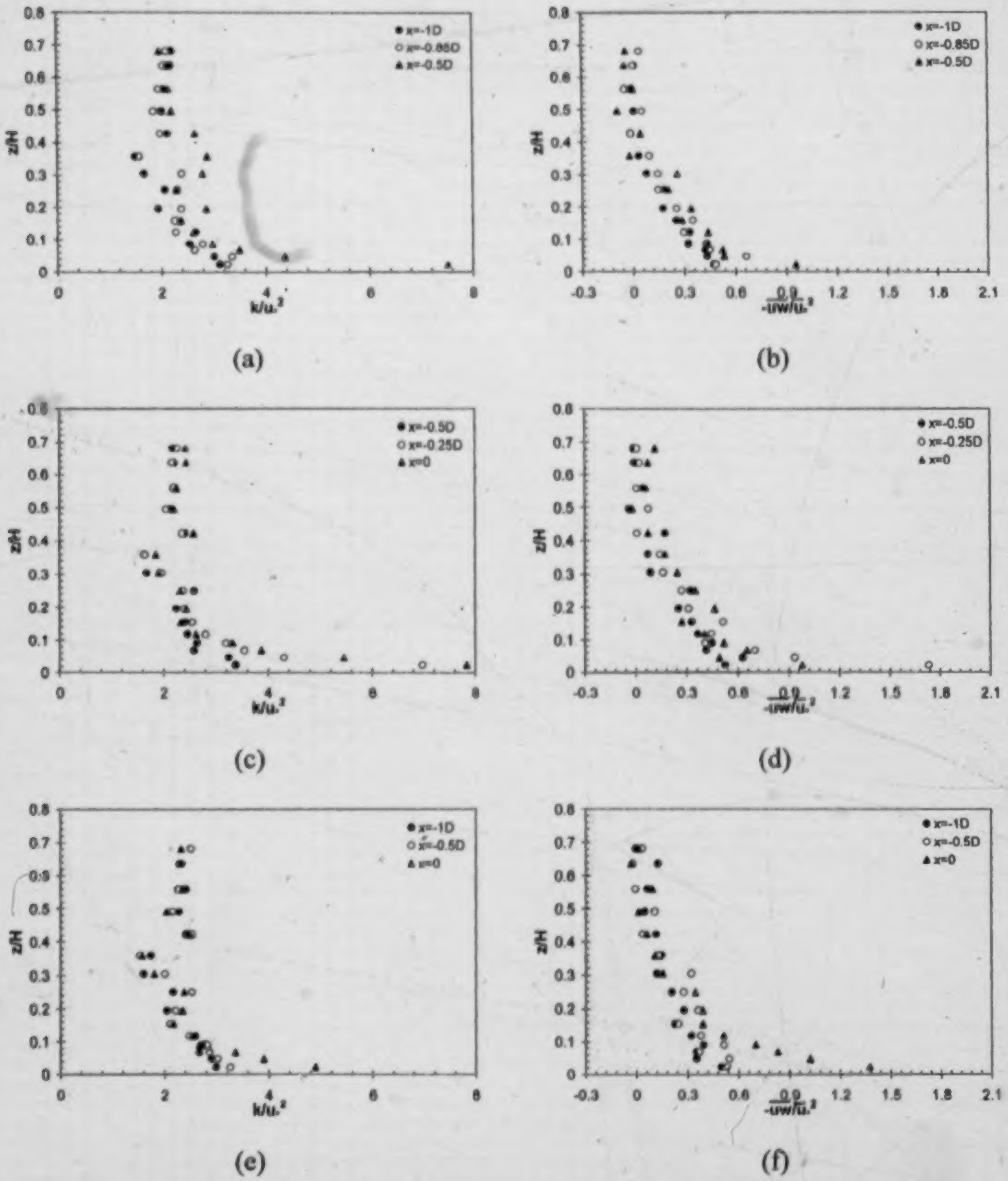

Fig. 5.63 Normalized turbulent kinetic energy and primary Reynolds stress profiles on (a-b) y=0.5D plane, (c-d) y=0.8D plane, and (e-f) y=1D plane: Smooth bed/Regime-2

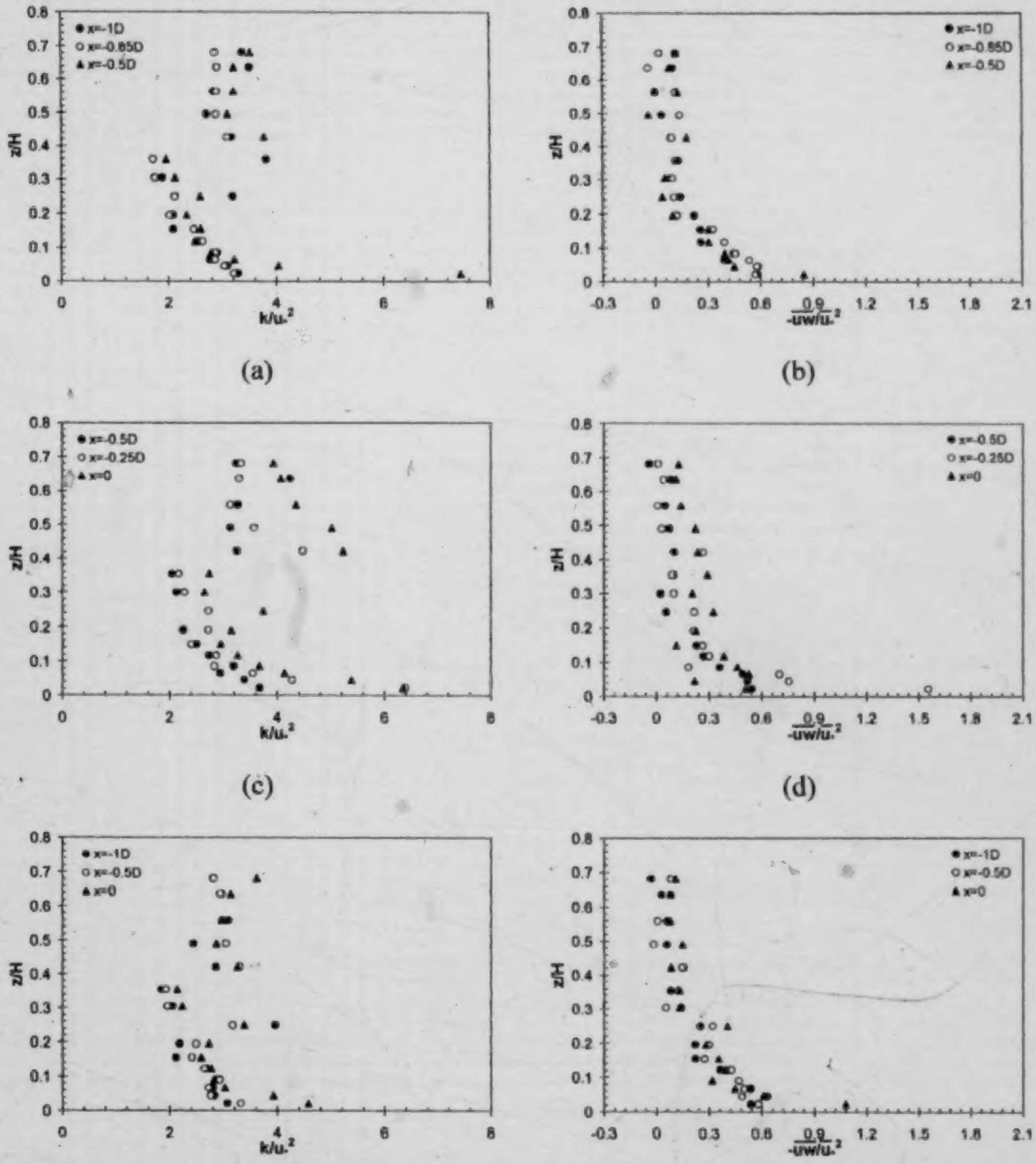

(a) (b)

(c) (d)

(e) (f)

Fig. 5.64 Normalized turbulent kinetic energy and primary Reynolds stress profiles on (a-b) $y=0.5D$ plane, (c-d) $y=0.8D$ plane, and (e-f) $y=1D$ plane: Smooth bed/Regime-3

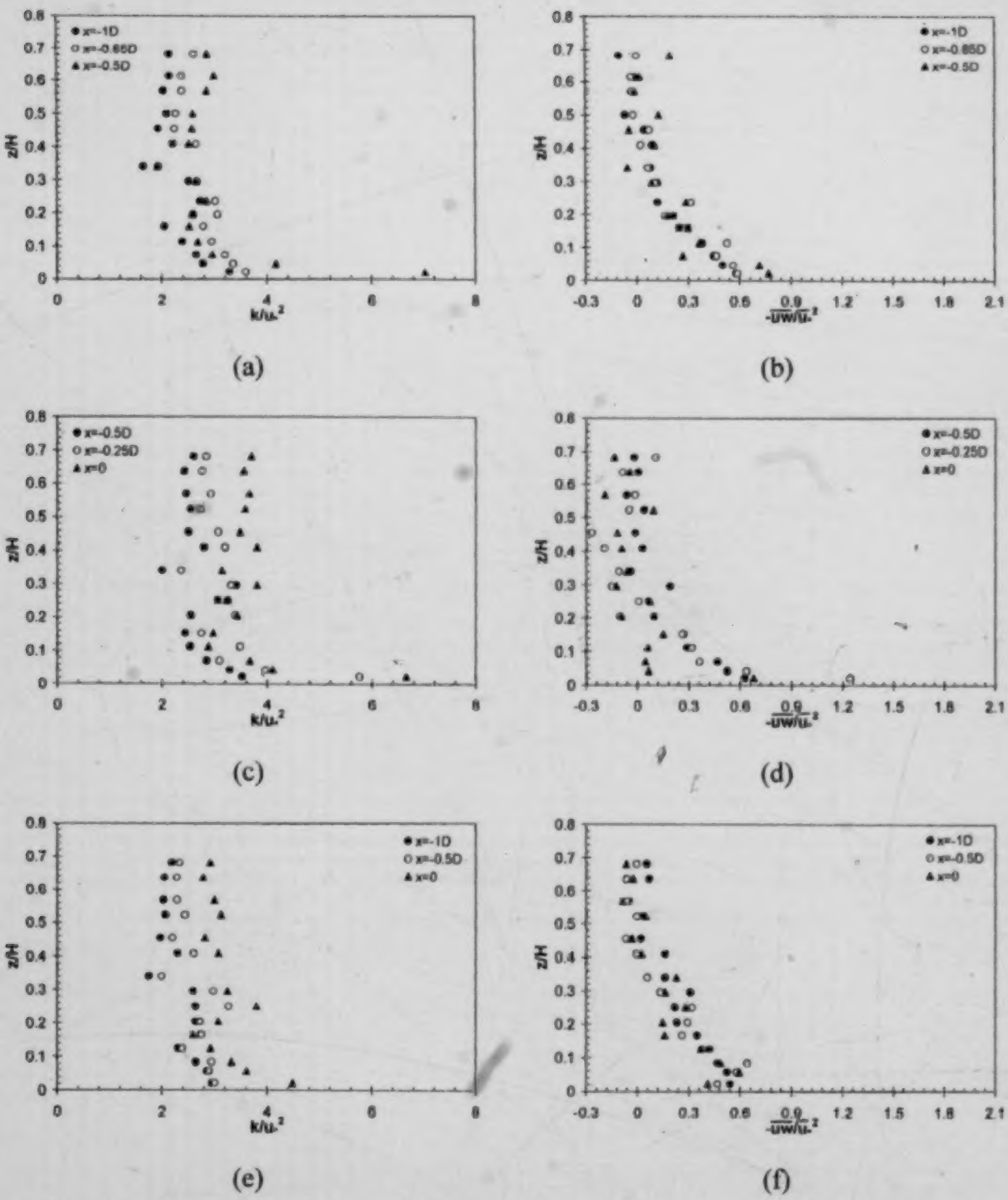

(a) (b)

(c) (d)

(e) (f)

Fig. 5.65 Normalized turbulent kinetic energy and primary Reynolds stress profiles on (a-b) y=0.5D plane, (c-d) y=0.8D plane, and (e-f) y=1D plane: Smooth bed/Regime-4

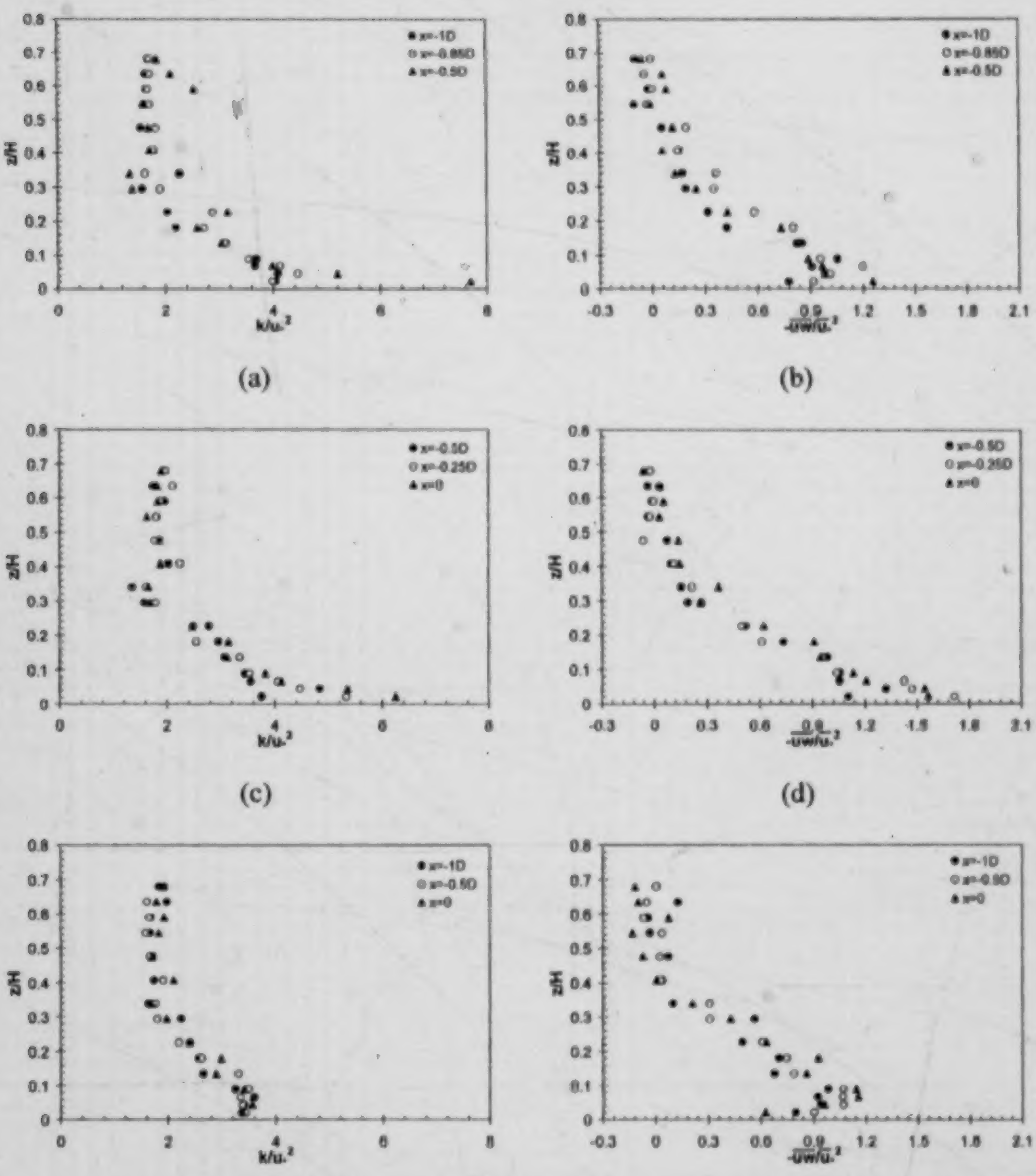

(a) (b)

(c) (d)

(e) (f)

Fig. 5.66 Normalized turbulent kinetic energy and primary Reynolds stress profiles on (a-b) y=0.5D plane, (c-d) y=0.8D plane, and (e-f) y=1D plane: Rough bed/Regime-1

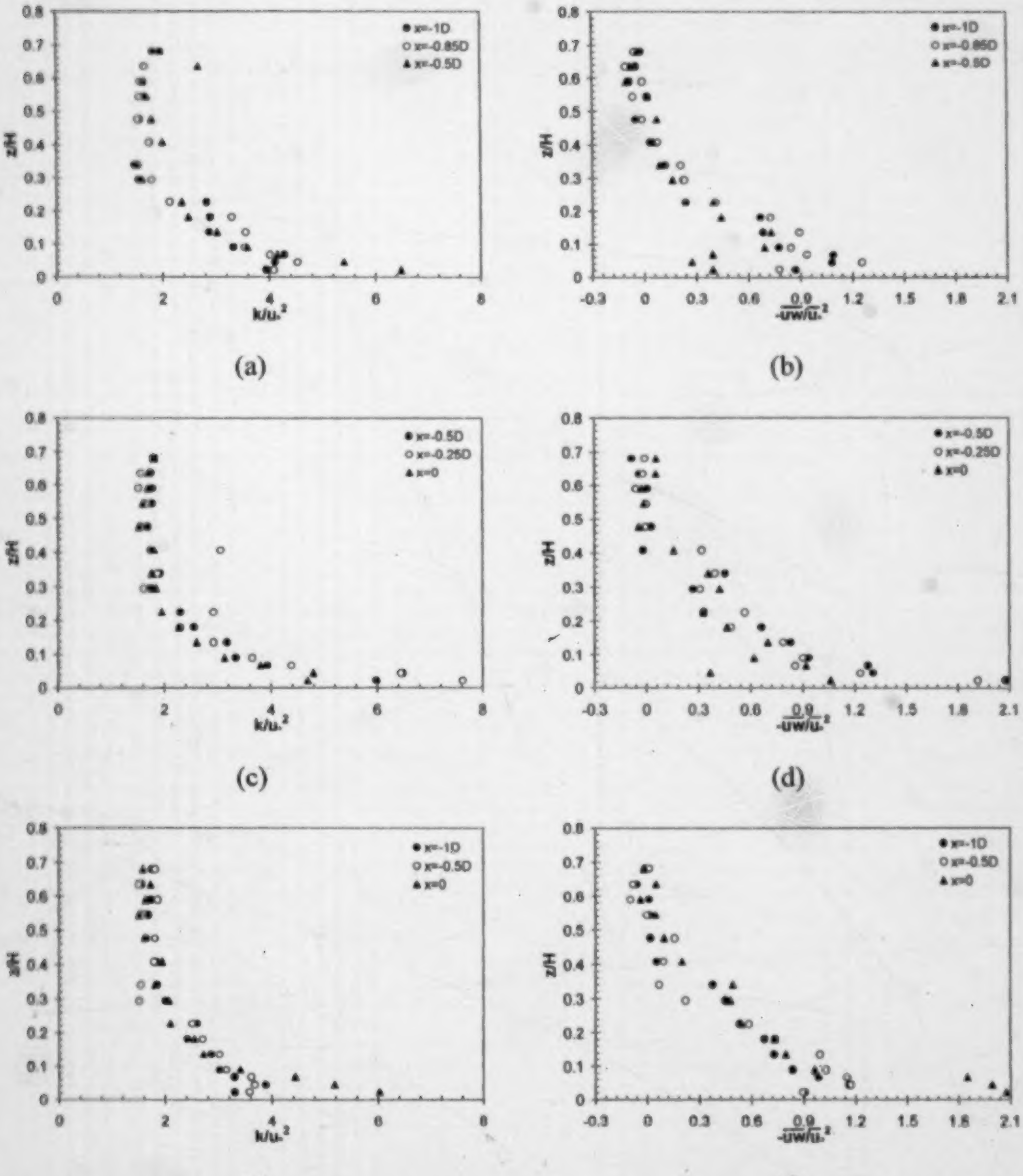

(a) (b)

(c) (d)

(e) (f)

Fig. 5.67 Normalized turbulent kinetic energy and primary Reynolds stress profiles on (a-b) y=0.5D plane, (c-d) y=0.8D plane, and (e-f) y=1D plane: Rough bed/Regime-2

9

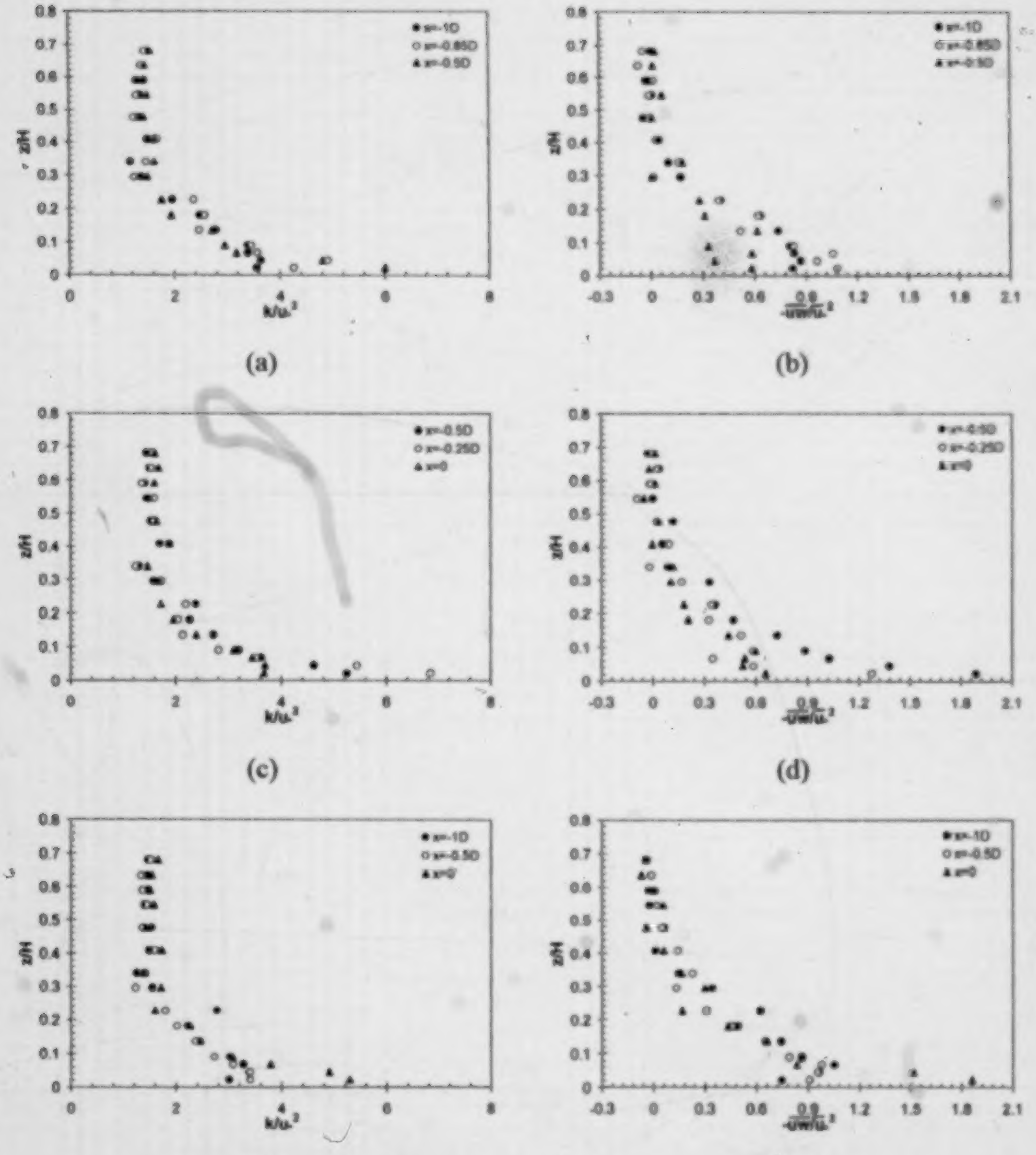

(a) (b)

(c) (d)

(e) (f)

Fig. 5.68 Normalized turbulent kinetic energy and primary Reynolds stress profiles on (a-b) y=0.5D plane, (c-d) y=0.8D plane, and (e-f) y=1D plane: Rough bed/Regime-3

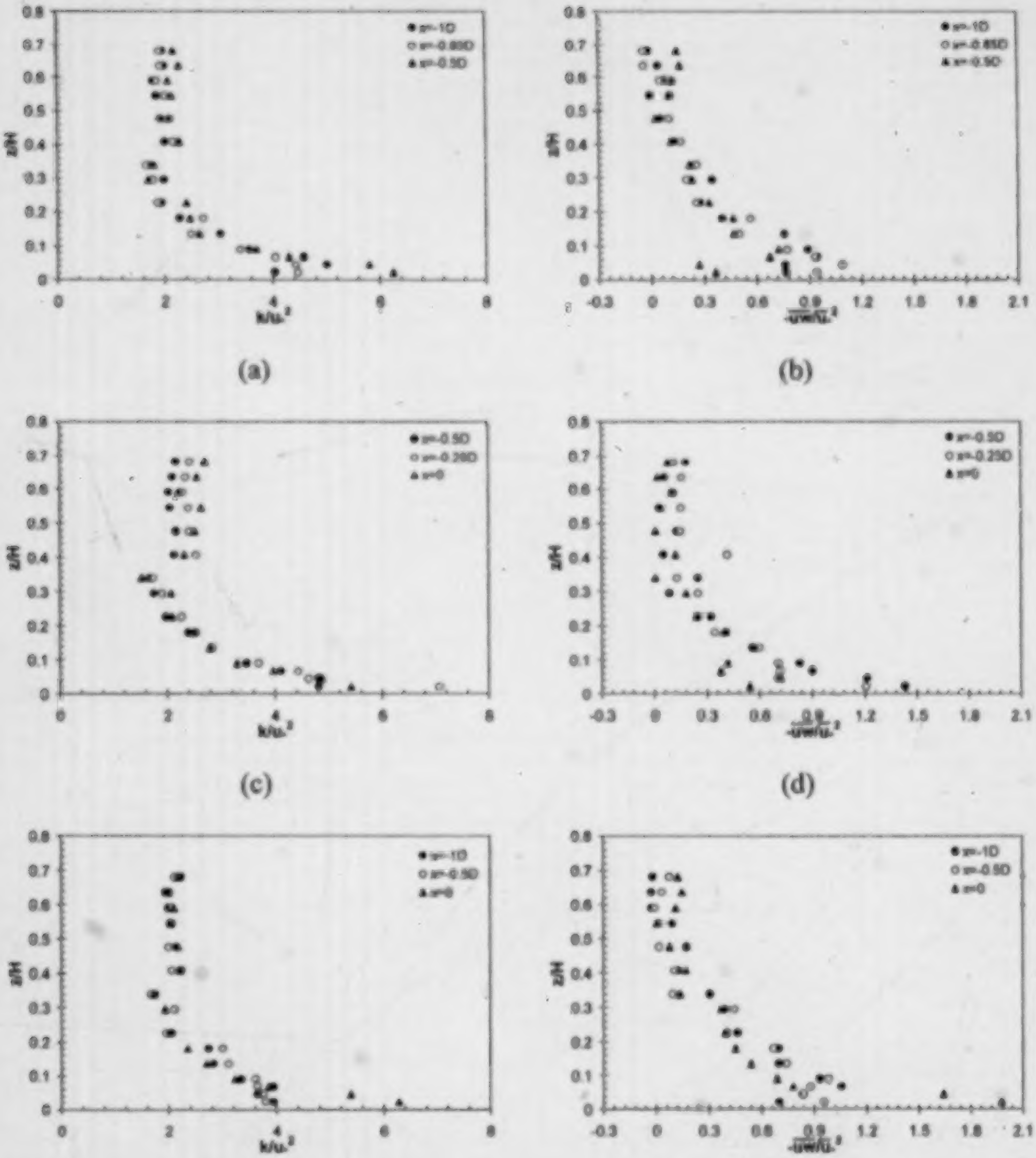

(a) (b)

(c) (d)

(c) (f)

Fig. 5.69 Normalized turbulent kinetic energy and primary Reynolds stress profiles on (a-b) y=0.5D plane, (c-d) y=0.8D plane, and (e-f) y=1D plane: Rough bed/Regime-4

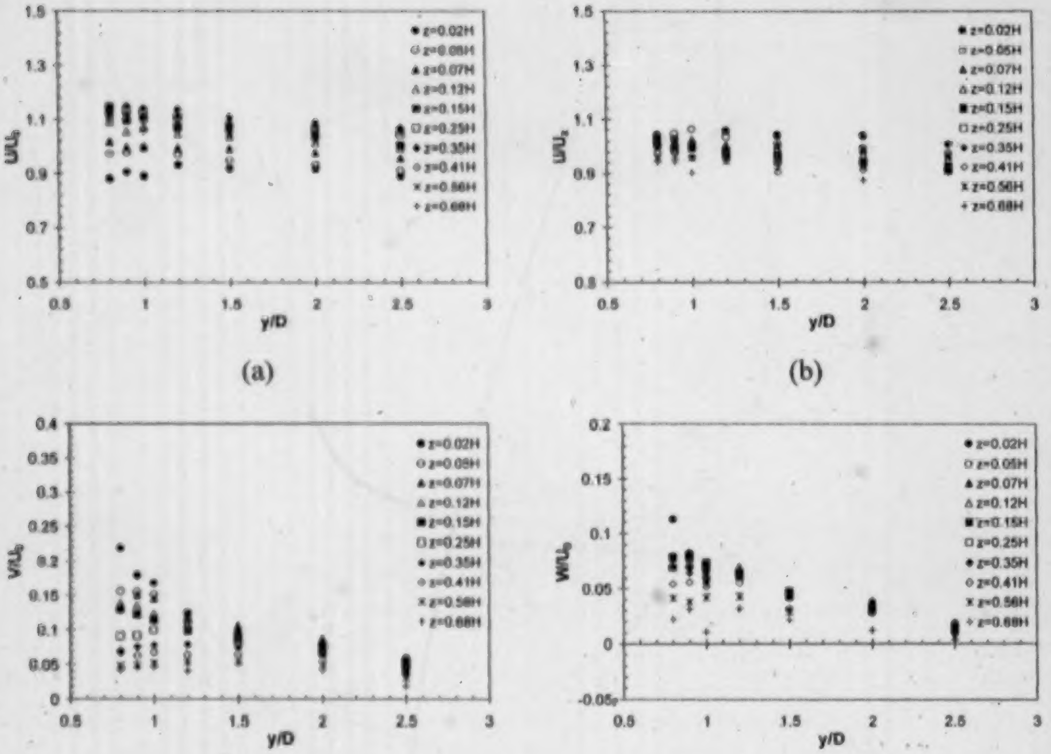

(a) (b)

(c) (d)

Fig. 5.70 Transverse profiles of normalized mean velocity on x=0 plane: Smooth bed/Regime-1; (a) longitudinal mean velocity (U/U_0), (b) speed up factor (U/U_z), (c) transverse mean velocity (V/U_0), and (d) vertical mean velocity (W/U_0)

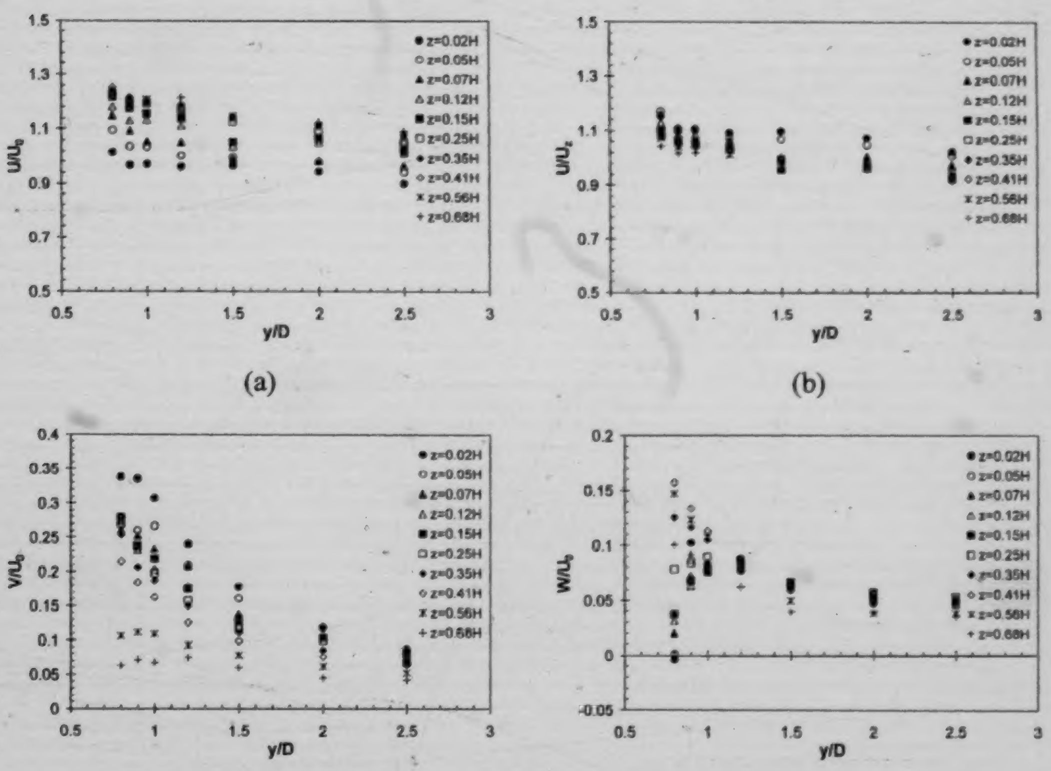

(a) (b)

(c) (d)

Fig. 5.71 Transverse profiles of normalized mean velocity on x=0 plane: Smooth bed/Regime-2; (a) longitudinal mean velocity (U/U_0), (b) speed up factor (U/U_z), (c) transverse mean velocity (V/U_0), and (d) vertical mean velocity (W/U_0)

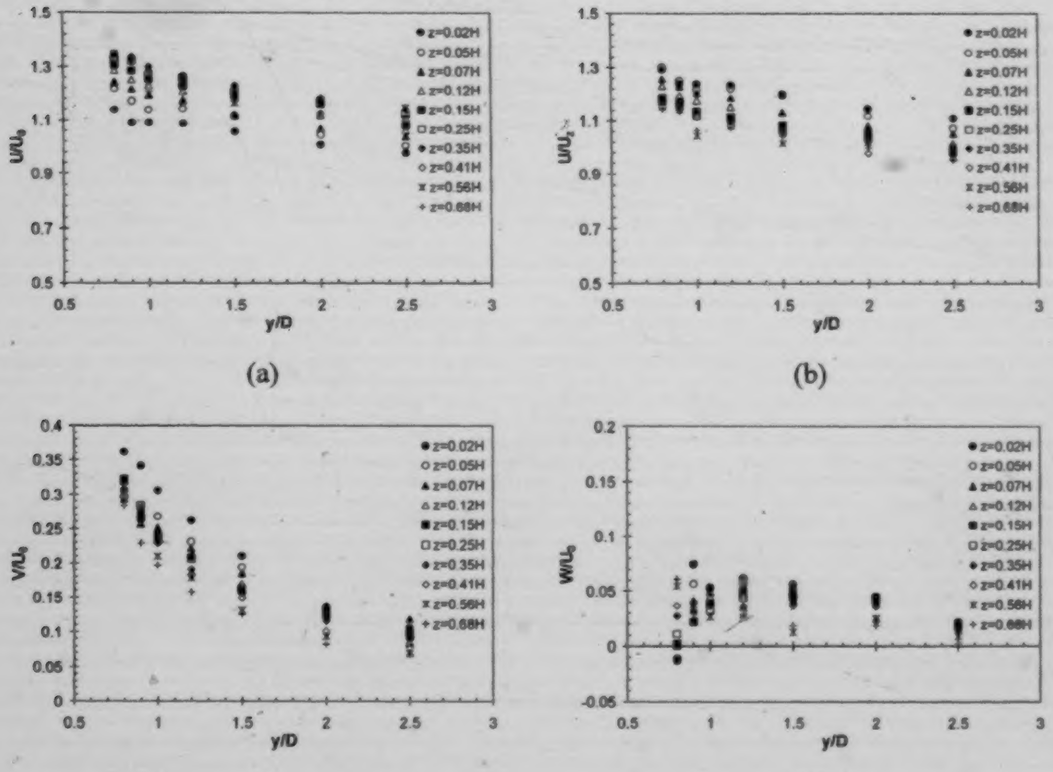

(a) (b)

(c) (d)

Fig. 5.72 Transverse profiles of normalized mean velocity on x=0 plane: Smooth bed/Regime-3; (a) longitudinal mean velocity (U/U_0), (b) speed up factor (U/U_z), (c) transverse mean velocity (V/U_0), and (d) vertical mean velocity (W/U_0)

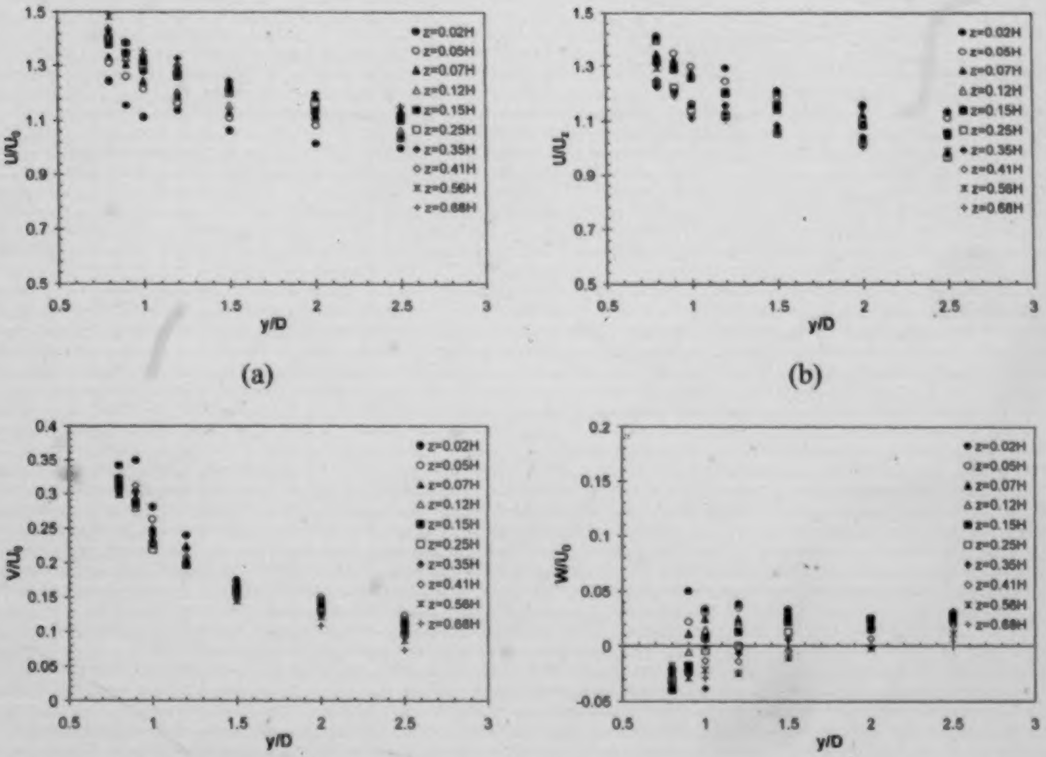

(a) (b)

(c) (d)

Fig. 5.73 Transverse profiles of normalized mean velocity on x=0 plane: Smooth bed/Regime-4; (a) longitudinal mean velocity (U/U_0), (b) speed up factor (U/U_z), (c) transverse mean velocity (V/U_0), and (d) vertical mean velocity (W/U_0)

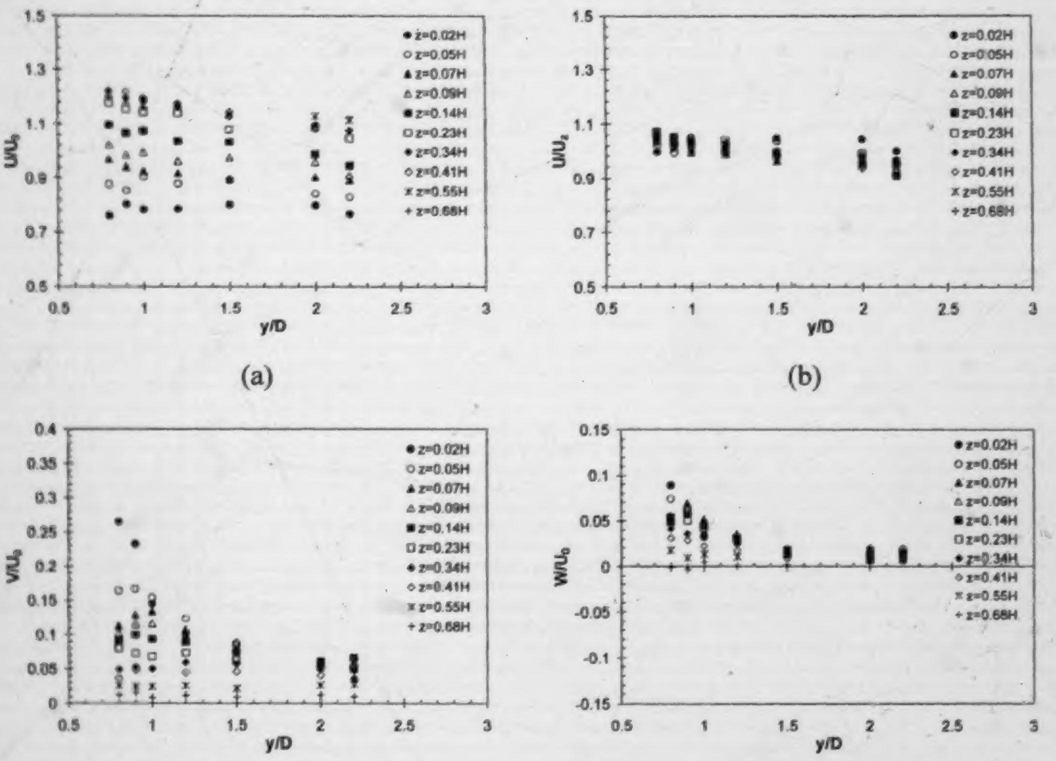

(a) (b)

(c) (d)

Fig. 5.74 Transverse profiles of normalized mean velocity on x=0 plane: Rough bed/Regime-1; (a) longitudinal mean velocity (U/U_0), (b) speed up factor (U/U_z), (c) transverse mean velocity (V/U_0), and (d) vertical mean velocity (W/U_0)

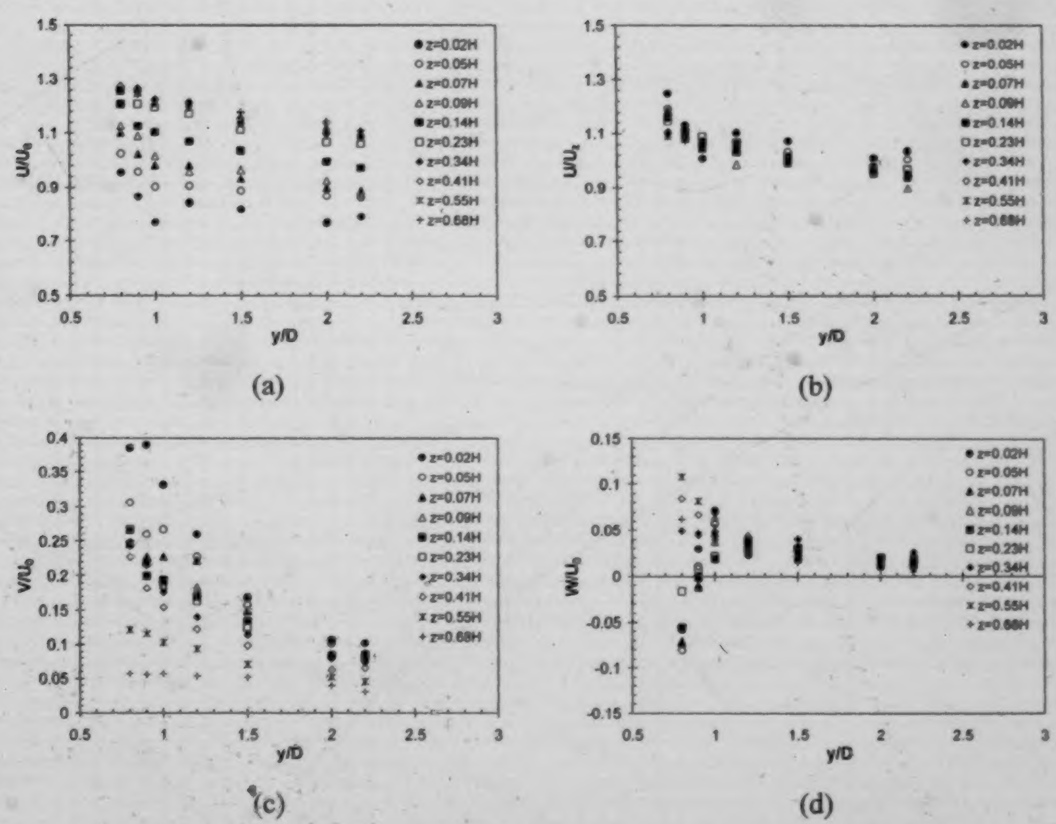

Fig. 5.75 Transverse profiles of normalized mean velocity on x=0 plane: Rough bed/Regime-2; (a) longitudinal mean velocity (U/U_0), (b) speed up factor (U/U_z), (c) transverse mean velocity (V/U_0), and (d) vertical mean velocity (W/U_0)

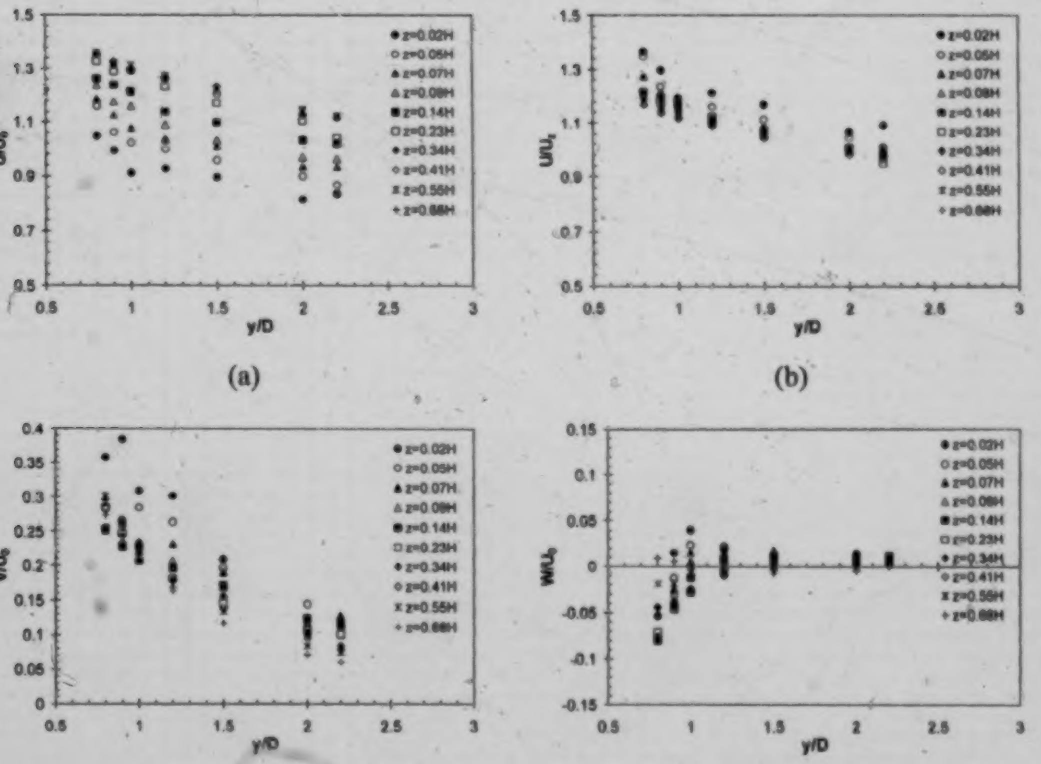

(a) (b)

(c) (d)

Fig. 5.76 Transverse profiles of normalized mean velocity on x=0 plane: Rough bed/Regime-3; (a) longitudinal mean velocity (U/U_0), (b) speed up factor (U/U_z), (c) transverse mean velocity (V/U_0), and (d) vertical mean velocity (W/U_0)

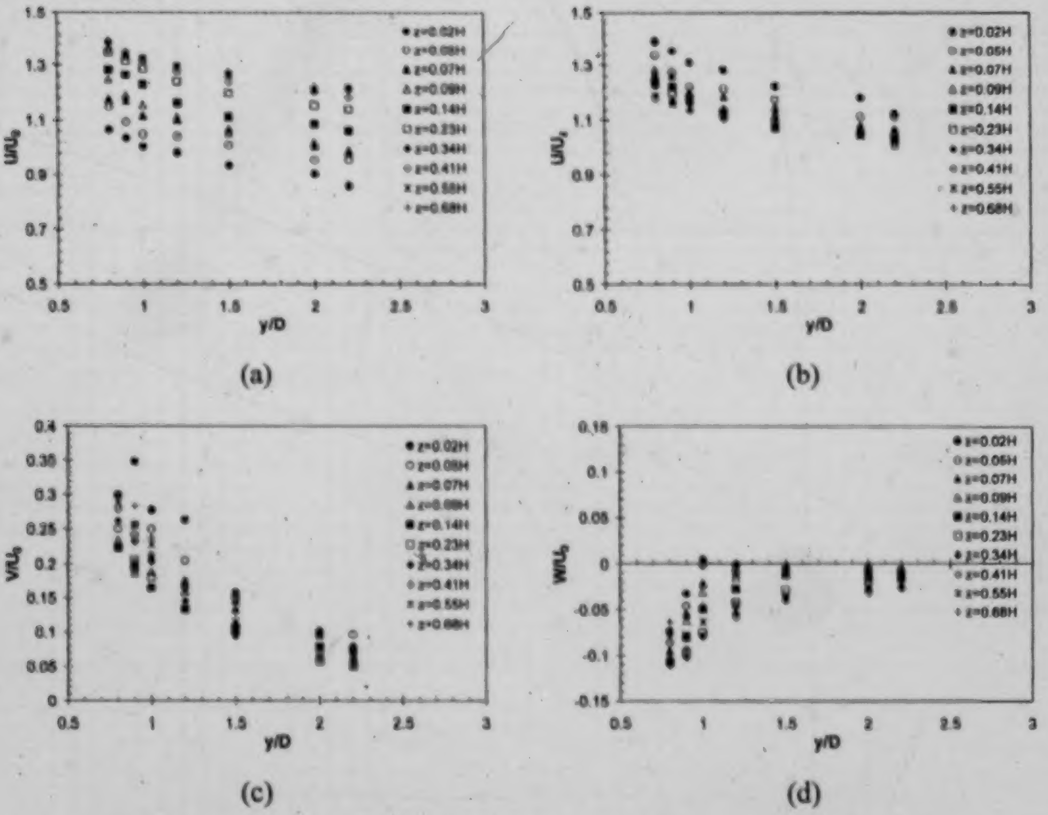

Fig. 5.77 Transverse profiles of normalized mean velocity on x=0 plane: Rough bed/Regime-4; (a) longitudinal mean velocity (U/U_0), (b) speed up factor (U/U_z), (c) transverse mean velocity (V/U_0), and (d) vertical mean velocity (W/U_0)

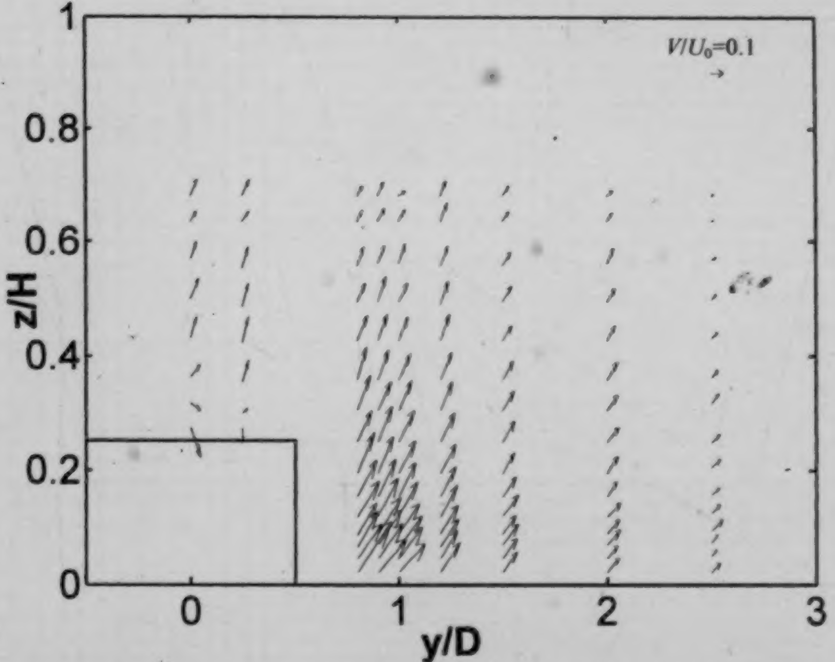

Fig. 5.78(a) 2D velocity vectors on x=0 plane: Smooth bed/Regime-1

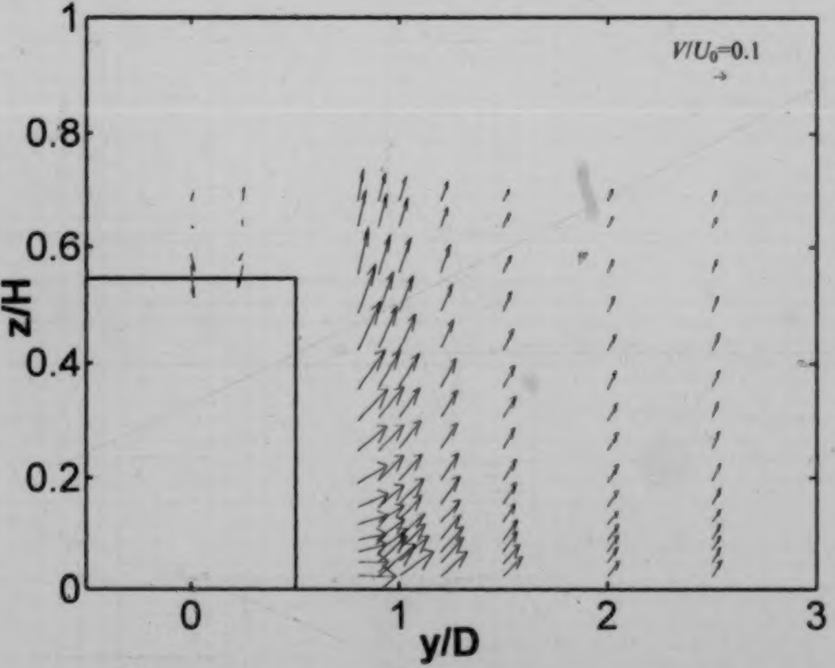

Fig. 5.78(b) 2D velocity vectors on x=0 plane: Smooth bed/Regime-2

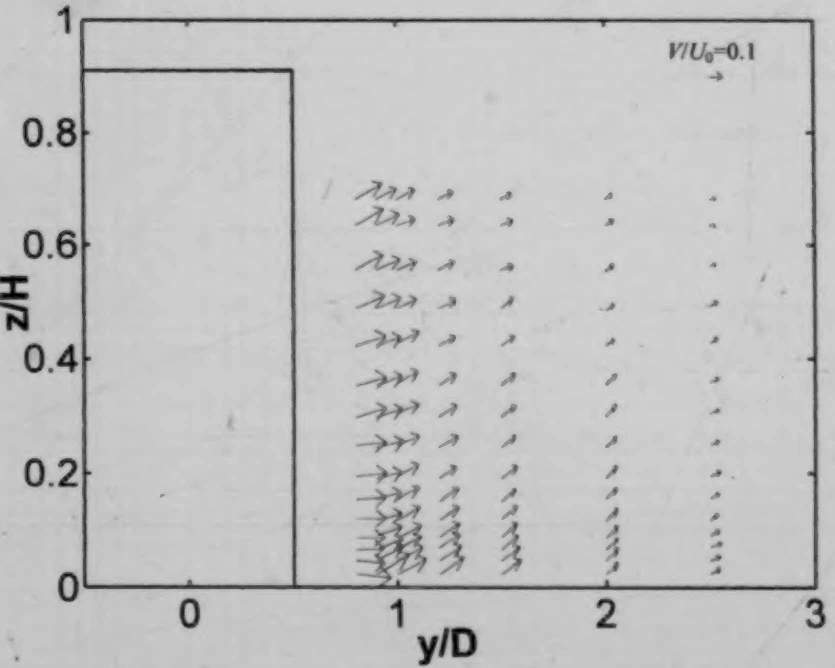

Fig. 5.78(c) 2D velocity vectors on *x*=0 plane: Smooth bed/Regime-3

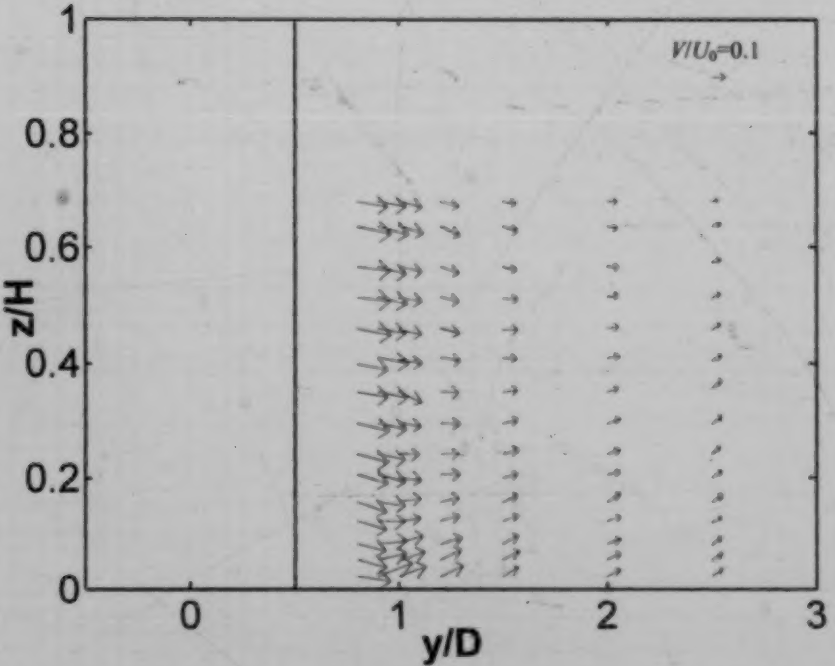

Fig. 5.78(d) 2D velocity vectors on *x*=0 plane: Smooth bed/Regime-4

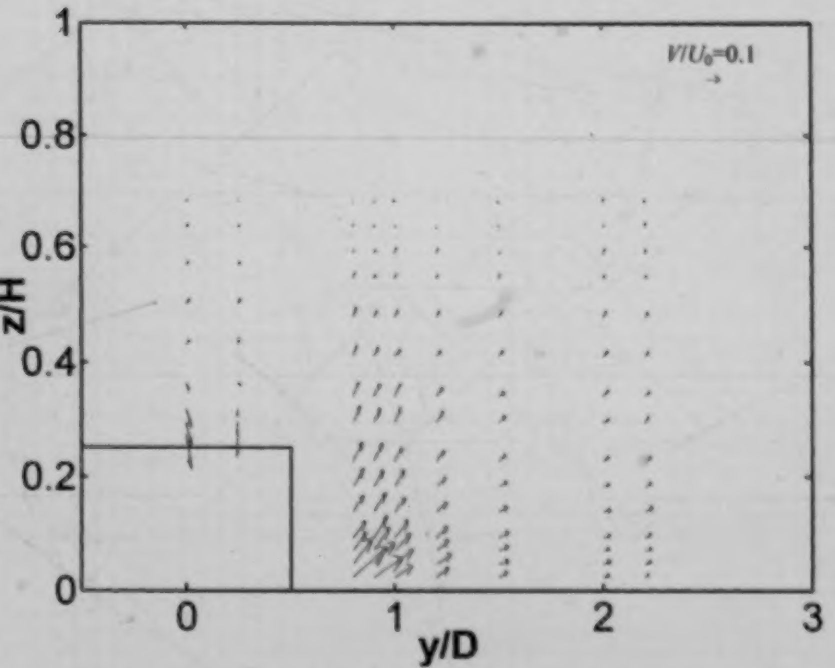

Fig. 5.79(a) 2D velocity vectors on x=0 plane: Rough bed/Regime-1

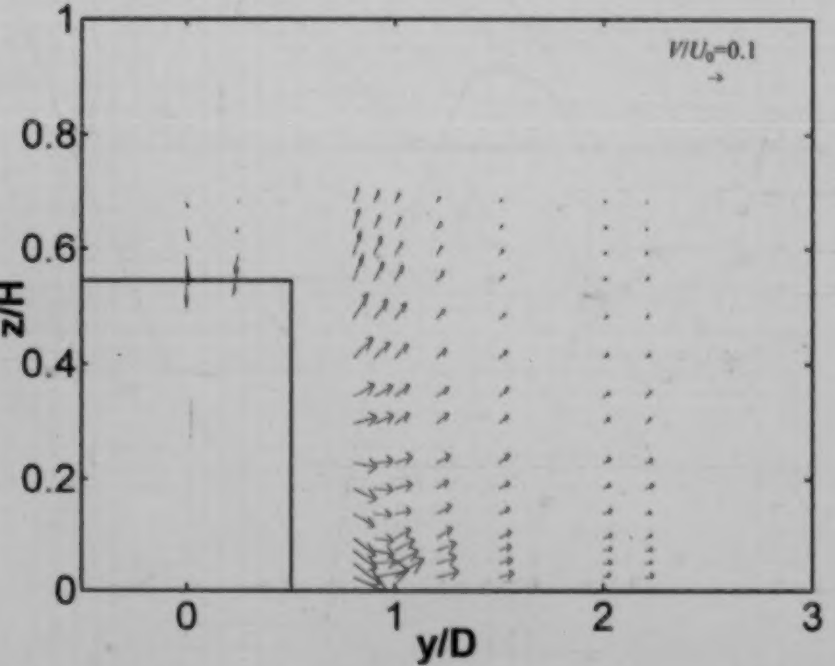

Fig. 5.79(b) 2D velocity vectors on x=0 plane: Rough bed/Regime-2

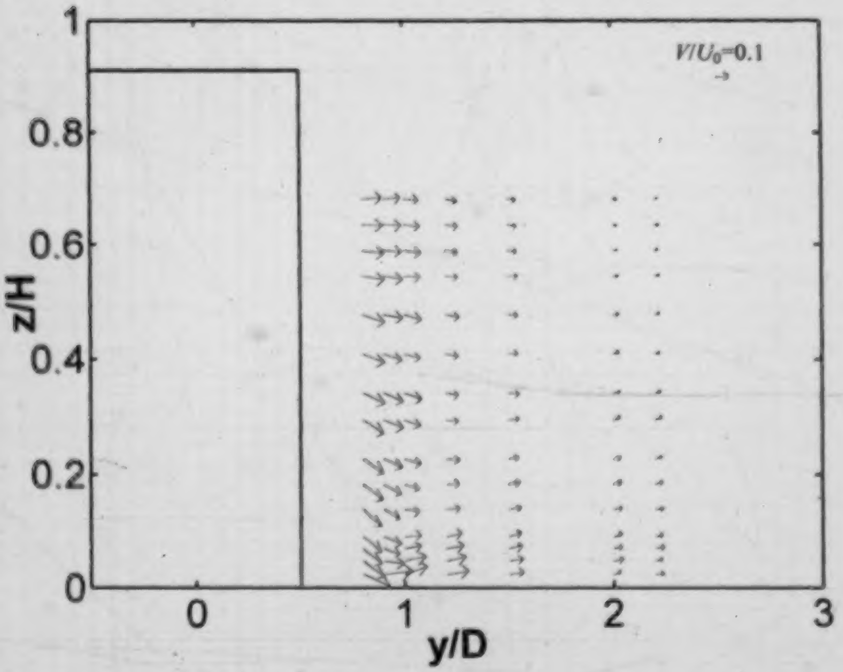

Fig. 5.79(c) 2D velocity vectors on x=0 plane: Rough bed/Regime-3

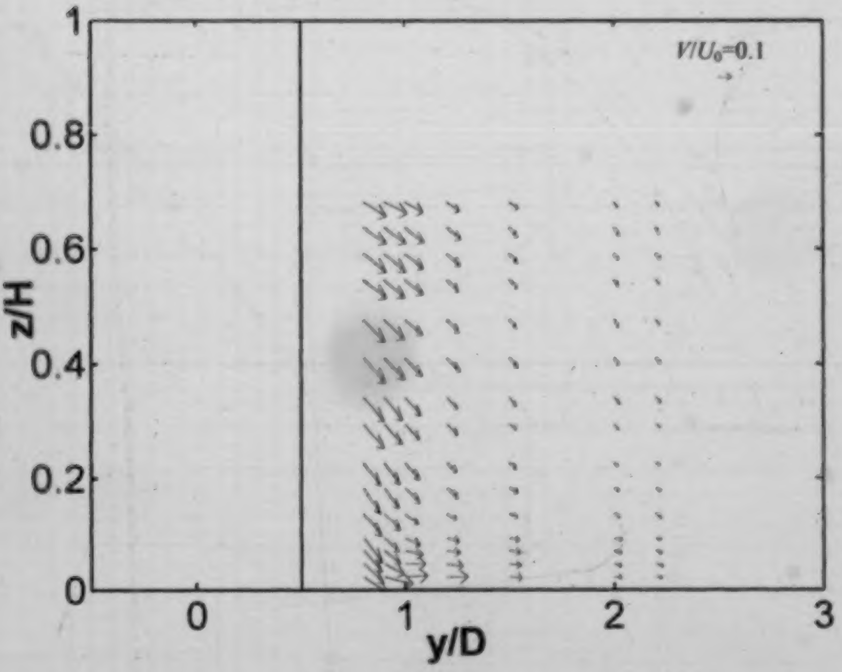

Fig. 5.79(d) 2D velocity vectors on x=0 plane: Rough bed/Regime-4

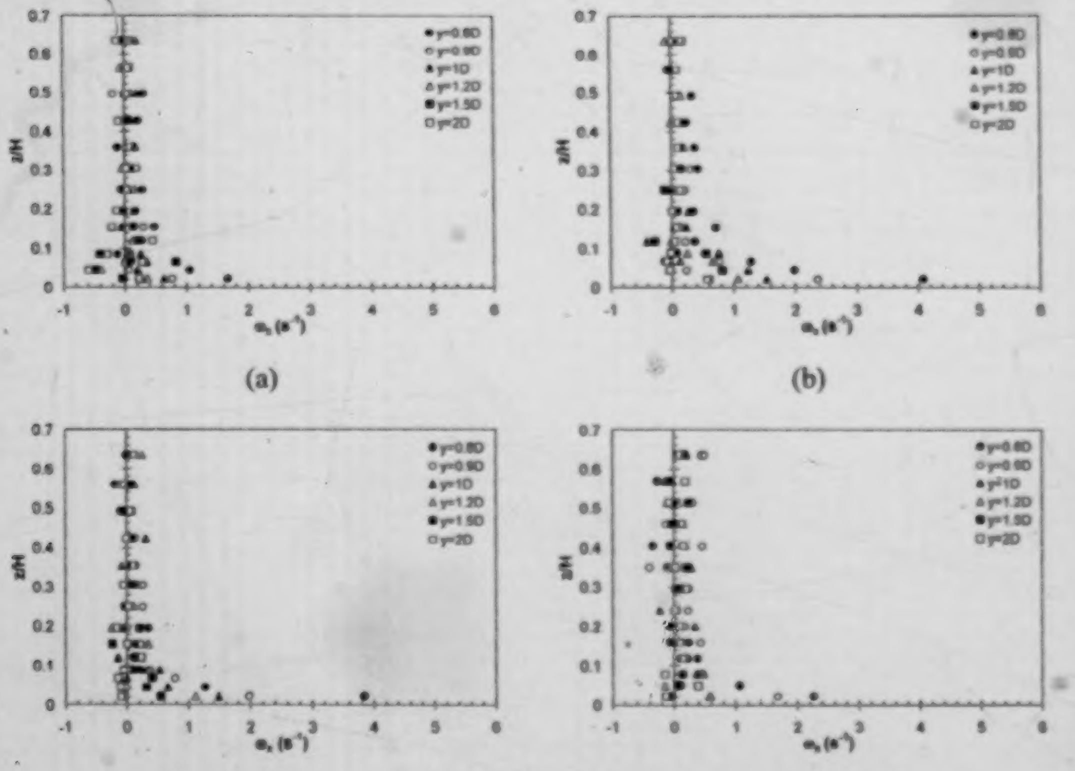

(a) (b)

(c) (d)

Fig. 5.80 Streamwise vorticity profiles on x=0 plane: Smooth bed; (a) Regime-1, (b) Regime-2, (c) Regime-3, and (d) Regime-4

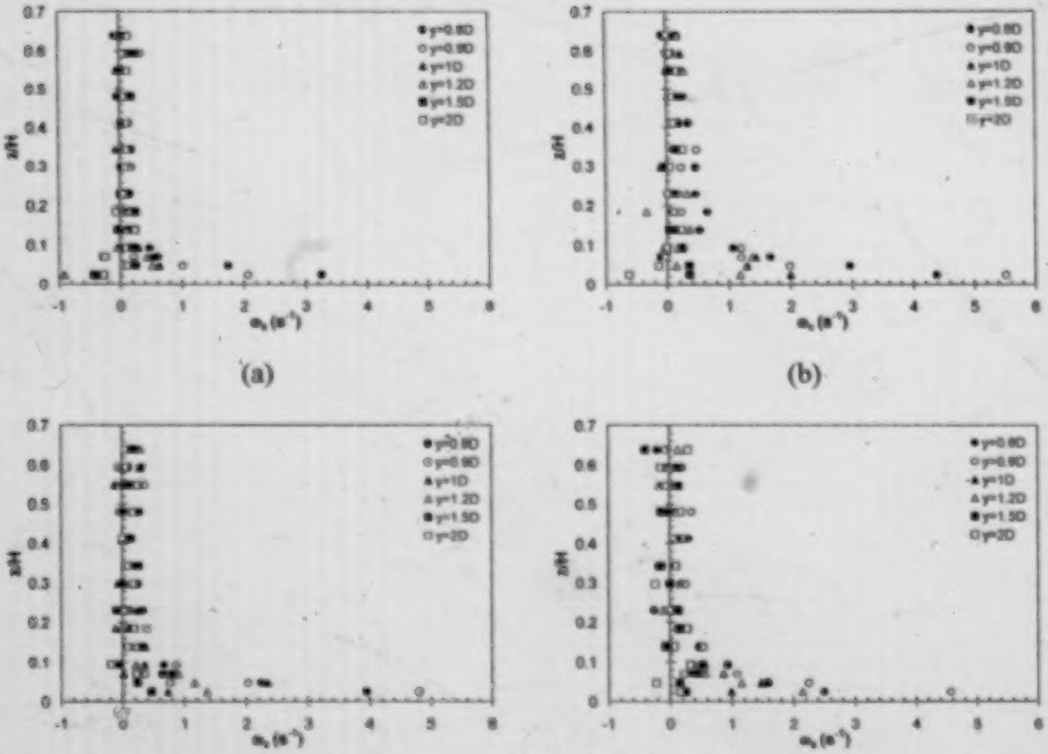

(a) (b)

(c) (d)

Fig. 5.81 Streamwise vorticity profiles on *x*=0 plane: Rough bed;

(a) Regime-1, (b) Regime-2, (c) Regime-3, and (d) Regime-4

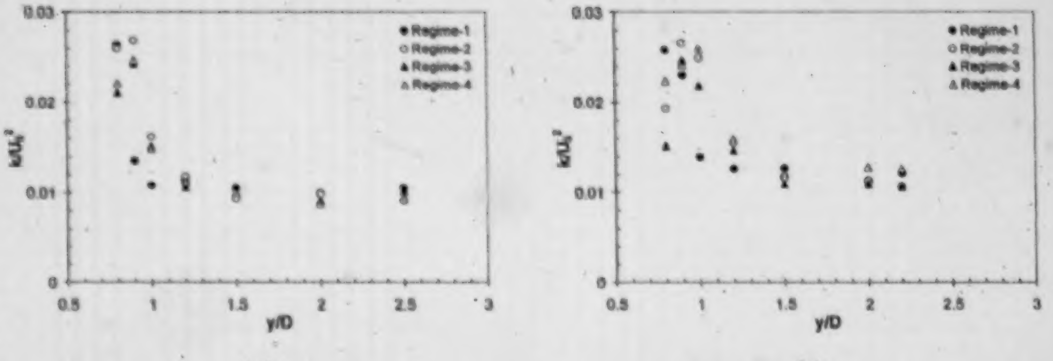

(a) (b)

Fig. 5.82 Variation of normalized turbulent kinetic energy (k/U_0^2) with y/D at z=0.02H on x=0 plane; (a) Smooth bed, and (b) Rough bed

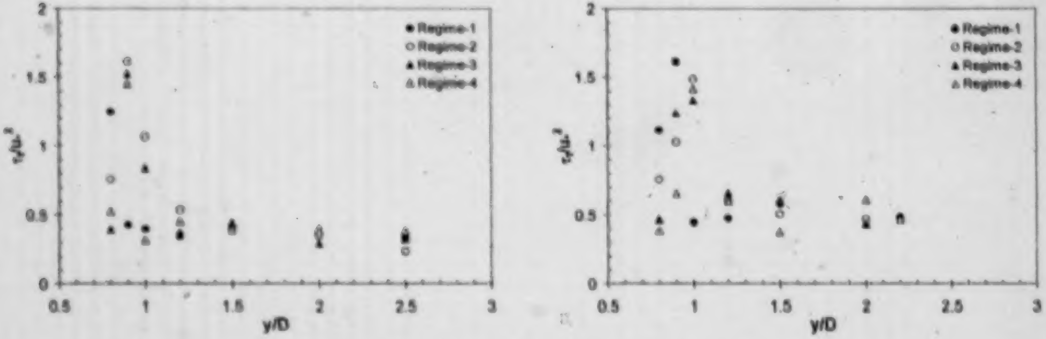

(a) (b)

Fig. 5.83 Variation of normalized turbulent shear stress (τ_t/u_*^2) with y/D at z=0.02H on x=0 plane; (a) Smooth bed, and (b) Rough bed

5.5 References

Ahmed, F., and Rajaratnam, N. (1998). "Flow around bridge piers." *Journal of Hydraulic Engineering*, 124(3), 288-300.

Burrows, A. D. and Steffler, P. M. (2005). "Depth averaged modeling of flow around individual boulders." *Proc., 17th Canadian Hydrotechnical Conference*, CSCE, Edmonton, Alberta, 395-404.

Dargahi, B. (1987). "Flow field and local scouring around a pier." *Bulletin No. TRITA-VBI-137*, Hydraulic Laboratory, Royal Institute of Technology, Stockholm, Sweden.

Dey, S., and Raikar, R. V. (2007). "Characteristics of horseshoe vortex in developing scour holes at piers." *Journal of Hydraulic Engineering*, 133(4), 399-413.

Lloyd, P. M., and Stansby, P. K. (1997). "Shallow-water flow around model conical islands of small side slope. II: Submerged." *J. of Hydraulic Eng.*, 123(12), 1068-1077.

Melville, B. W. (1975). "Local scour at bridge sites." *Report No. 117*, School of Engineering, University of Auckland, New Zealand.

Menna, J. D., and Pierce, F. J. (1988). "The mean flow structure around and within a turbulent junction or horseshoe vortex-Part I: The upstream and surrounding three-dimensional boundary layer." *Journal of Fluids Engineering*, 110, 406-414.

Perry, A. E., and Joubert, P. N. (1965). "A three-dimensional turbulent boundary layer." *Journal of Fluid Mechanics*, 22, 285-304.

Pingree, R. D., and Maddock, L. (1979). "The tidal physics of headland flows and offshore tidal bank formation." *Marine Geology*, 32, 269-289.

Sadeque, M. A. F., Rajaratnam, N., and Loewen, M. R. (2008). "Flow around cylinders in open channels." *Journal of Engineering Mechanics*, 134(1), 60-71.

Salaheldin, T. M., Imran, J., and Chaudhry, M. H. (2004). "Numerical modeling of three-dimensional flow field around circular piers." *J. of Hydraulic Eng.*, 130(2), 91-100.

Shamloo, H., Rajaratnam, N., and Katopodis, C. (2001). "Hydraulics of simple habitat structures." *Journal of Hydraulic Research*, 39(4), 351-366.

Wolanski, E., Imberger, J., and Heron, M. L. (1984). "Island wakes in shallow coastal waters." *Journal of Geophysical Research*, 89(C6), 10553-10569.

Chapter 6: Shallow Turbulent Near-Wakes behind Cylinders

6.1 Introduction

Wakes behind bluff body has been a major research interest in fluid mechanics for several decades. This is mainly due to immense practical applications and the usefulness of these flows to validate computational fluid dynamic (CFD) models. Most research in the past focused on wakes behind circular cylinders in wind tunnels, where the flow was considerably deep and the aspect ratio (flow depth, H compared to cylinder diameter, D) was high (e.g. Roshko 1961, Antonia 1991). A shallow wake is defined as the situation where the horizontal length scale of a typical eddy is significant compared to the vertical scale or, the depth of flow (Balachandar et al. 2000). Flow past a vertical cylinder in shallow water gives rise to a wake that has distinctive characteristics compared to a deep wake (Akilli and Rockwell 2002). It is well known that in a deep uniform flow incident on a two-dimensional (2D) cylinder with its axis vertical, vortex shedding occurs with strong three-dimensional (3D) components (Lloyd and Stansby 1997a). On the other hand, shallow wakes are generated behind obstacles where the incident velocity has boundary layer profile. Ingram and Chu (1987) observed that bed friction effects become important in shallow wakes. Therefore, they proposed a stability parameter for shallow wakes ($S_w=C_fD/H$, where C_f is the skin friction coefficient, D is the characteristic length of the wake generator across the flow and H is the depth of flow) as a relative measure of stabilizing effect of bed friction and destabilizing effect of transverse shear. Chen and Jirka (1995) provided the distinctions between the vortex shedding observed in deep wake and shallow wake. They experimentally observed in shallow flows around a surface piercing cylinder that vortex street kind of instabilities occur when the shallow wake parameter (S_w) remains less than 0.2; and beyond this limit the vortex shedding is annihilated. Chen and Jirka (1995) argued that vortex street type instabilities in shallow wakes are like Karman vortex street but there are differences between these two. Karman vortex street occurs for a Reynolds number (R_D) range of 100 to 200 in deep wake, where the height of cylinder, $h\geq10D$. Overall it occurs in laminar unbounded plane wake. On the other hand, vortex street occurs at high Reynolds number (R_D~10^4-10^5) in shallow wake, where the free water surface is not far (i.e. bounded wall wake). Chen and Jirka

(1995) also attributed that Karman vortex street has well defined streak line, whereas vortex street in shallow wakes has fuzzy and streaky wakes due to turbulent diffusion instead of molecular diffusion. Reynolds number ($R_D=U_0D/\nu$) plays a significant role in the characteristics of deep wake (Chang 1970). The location of the separation points, drag coefficient and the Strouhal number (S) are dependent on the flow Reynolds number. Therefore, there are thousands of studies of cylinder wake in deep flow for a range of Reynolds number starting from the order of 1 to 10^6 or infinity. Zdravkovich (1997) provided a comprehensive guide through flow phenomena, experiments, applications, mathematical models, and computer simulations on flow around circular cylinders from creeping flow to extremely turbulent flow conditions. However, the gravity force is more important compared to viscous force for an open channel flow, and hence Froude number (F) plays more important role compared to Reynolds number. The critical Reynolds number ($R_H=U_0H/\nu$) for ambient open channel flows to be turbulent is only 500 and when $R_H>1500$ shallow wake instabilities are uniquely dependent on shallow wake parameter, S_w (Chen and Jirka 1995). Natural open channel flows are always turbulent and therefore, the studies of wakes in open channels are confined to turbulent regime ($R_D \sim 10^3$-10^5).

The wake of a bluff body in shallow water has relevance to a number of environmental and geophysical flow systems (Kahraman et al. 2002). In a study of shallow wake Shamloo et al. (2001) used hemispherical objects of different levels of submergence to model simple fish habitat structures. Smith and Foster (2007) studied the wake created by short submerged horizontal cylinders to model submerged pipelines in rivers. Lloyd and Stansby (1997a, 1997b) studied instabilities in shallow wakes behind surface piercing and submerged conical model islands. In a geophysical study, Ingram and Chu (1987) observed the effect of bottom friction on the wake behind islands in Rupert bay in northern Canada. Arya and Gadiyaram (1986) studied the atmospheric flow and dispersion in the wakes downstream of three-dimensional models of low hills. Chen and Jirka (1995) urged that an improved understanding of the shallow wakes is needed for a number of reasons, such as the tendency for pollutant trapping in the lee of islands or headlands, the optimal siting of discharge facilities, and patterns of sedimentation, nutrient accumulation, or biological activity for the species of aquatic environment (e.g. fish habitat). For all the above situations the object that generates shallow wake could be submerged or surface piercing. Therefore, it is essential to study the hydraulics of shallow wakes behind objects of different levels of submergence. Moreover, the near-wake regions immediately downstream of the wake generator appear more important than the far wake. Far wake studies received a lot of attention from the past, where the velocity defect is very small compared to the undisturbed or ambient free stream velocity, and the flow is dynamically similar and self-preserving; i.e. the transverse distributions of mean velocity and other mean quantities change with distance downstream, but their distributions retain same functional forms, merely changing their transverse length-scale and the scales of the mean value quantities (Townsend 1976). On the other hand, near-wake flows can be characterized by a region of strong vorticity followed by a region of turbulent diffusion (Sforza and Mons 1970). The purpose of this study is, therefore, to experimentally investigate the characteristics of shallow turbulent near-wake behind bed-mounted cylinders of different levels of submergence in open channel flows on smooth and rough beds.

6.2 Literature Review

There are numerous studies of wakes in literature. Experimental and numerical studies of plane wakes behind cylinder, wall wakes behind 2D and 3D objects, turbulent mixing, wake instabilities, vortex dynamics, perturbation or velocity defect etc. occupy the large portion of literature. However, the subject of interest in wake studies varied among the researchers from different disciplines; e.g. fluid mechanics, environmental, geophysical or atmospheric science. Some of the literatures are found relevant for theoretical considerations and subsequent discussions in the context of the present study.

It is well-known that the velocity distributions in the far wake region of plane turbulent wakes are similar. Velocity distribution equation (Equation [6.1]) given by Schlichting (1968) is well-accepted among the researchers.

[6.1] $$\frac{U_1}{U_{1m}} = \left(1 - 0.293\lambda^{3/2}\right)^2$$

In Equation [6.1] velocity defect, $U_1 = U_\infty - U$ where U_∞ is the undisturbed ambient velocity, U_{1m} is the maximum value of U_1, $\lambda = y/b_1$, and $b_1 = y$ where $U_1 = 0.5U_{1m}$. U_{1m} and b_1 are considered velocity and length scales for plane wake. Figure 6.1 shows the definition sketch for plane wake parameters. Using the continuity and Navier-Stokes equation for 2D flow with zero pressure gradient the rates of growth of wake (i.e. the transverse length scale, b_1) and decay of velocity defect (U_{1m}) for plane turbulent wake were deduced by Schlichting (1968) as power functions of the distance in the downstream direction as Equation [6.2] and [6.3].

[6.2] $$\frac{U_{1m}}{U_\infty} = C_1\left(\frac{x}{C_D D}\right)^{-0.5}$$

[6.3] $$\frac{b_1}{DC_D} = C_2\left(\frac{x}{C_D D}\right)^{0.5}$$

In Equation [6.2] and [6.3] C_D is the drag coefficient, D is the cylinder diameter, $C_1=1$ and $C_2=0.25$.

When a uniform approach flow separates at the top edge of a 2D obstacle forming a recirculation region behind it and becomes reattached to the wall after a certain distance, the disturbed flow in the far downstream appears to possess the characteristics of a wake in the outer region while the inner region is affected by the wall. Such a wake can be called a plane wall wake (Rajaratnam and Rai 1979). In a wind tunnel study Rajaratnam and Rai (1979) observed that a two-layer model perform adequately in the far wake region for 2D turbulent wall wakes. They found that the simple wake equation (Equation [6.1]) given by Schlichting (1968) can describe the velocity distribution in the outer region, whereas in the inner region the Prandtl-Karman's law-of-wall equations perform satisfactorily. Rajaratnam and Rai (1979) also provided equations for plane wall wake scales similar to plane wake equations (i.e. Equation [6.2] and [6.3]) given by Schlichting (1968). The power function equations for plane wall wake are similar to Equation [6.2] and [6.3], except the values of the coefficients. For plane wall wake C_1=1.3 and C_2=0.46; and the length scale is in the vertical direction. The exponents representing the rates of decay of velocity defect and growth of wake were similar (i.e. -1/2 and 1/2 for velocity and length scales respectively). Figure 6.2 shows the definition sketch of a plane wall wake. For clarity in future discussions a different set of notations for the velocity and length scales U_{2m} and b_2 are considered.

Sforza and Mons (1970) studied 2D and 3D turbulent wall wakes. They found that the bulk properties of the flow and the applicability of theoretical models are highly dependant on obstacle geometry. Sforza and Mons (1970) defined the velocity defect to be $(U_\infty - U)$, where U_∞ is the mean velocity U at $z=\infty$. For their models being deeply submerged the mean velocity U at $z=\infty$ were unchanged in disturbed flow compared to undisturbed flow condition. Sforza and Mons (1970) observed that the decay of mean velocity defect in the wake is dramatically rapid in 3D wake compared to 2D wake. They considered a different form of power function, as given in Equation [6.4], and found the exponent (n) of power function for the rate of decay of velocity defect to be -2.55 for 3D obstacle, compared to -1 for a 2D obstacle. However, the length scales were found to grow almost at the same rate (with exponents~0.4) for both 2D and 3D obstacles in the far wake region, though there were almost no change in length scale in the near-wake region up to 10 characteristic length x/h, where h is the height of object.

$$[6.4] \qquad \frac{(U_\infty - U)_{\max}}{U_\infty} \propto \left(\frac{x}{h}\right)^n$$

Sforza and Mons (1970) characterized the wake behind three-dimensional obstacle on a flat plate by three sequential regions as shown in Figure 6.3. 1) Recirculation region, where the effects of the vorticity induced by the obstacle dominate over the effects of viscous diffusion. The velocity profiles were characterized by zero and slightly negative velocities (i.e. reverse flow) directly behind the obstacle changing to considerably greater than free stream velocity near the exposed edges of the obstacle. 2) Characteristic decay region, where the mixing effects due to the obstacle permeate the flow field and the flow field is highly sensitive to the obstacle geometry. 3) Asymptotic decay region, where the viscous effects dominate the flow field and the flow asymptotes to the undisturbed boundary layer, i.e. the boundary layer becomes oblivious to the initial perturbation.

Studies of the near-wake regions are relatively new. The advent of sophisticated measuring techniques; such as laser anemometry, Acoustic Doppler Velocimeter (ADV) and Particle Image Velocimetry (PIV) opened up the prospect of experimental research on near-wake turbulent region. Recently, Balachandar et al. (2000), Tachie and Balachandar (2001), Balachandar et al. (1999), Akilli and Rockwell (2002), Perrin et al. (2006) studied the near-wake flow of surface piercing objects. Balachandar et al. (2000), and Tachie and Balachandar (2001) used sharp-edged 2D plates as wake generator to demonstrate similarity of mean velocity profiles across the wake away from the channel boundary with slightly modified length scale (b) in the transverse direction. They considered that the length scale $b=y$ where $(U-U_{\min})/(U_{\max}-U_{\min})=0.5$; however the velocity scale $(U_{\max}-U_{\min})$ was equivalent to U_{1m}. Balachandar et al. (1999) provided theoretical models for the prediction of the growth of deep and shallow wake behind surface-piercing objects. According to their model, a deep wake can grow indefinitely, however a shallow wake spread assumes an asymptotic value when the dimensionless bed friction number $S_f=C_f x/H$ reaches a critical value S_{fc} ($S_f=S_{fc}$ when the development of vortex street is annihilated), where C_f is the skin friction coefficient, x is the longitudinal distance in the downstream direction from the center of the wake generator and H is the depth of flow. Akilli and Rockwell (2002) and Perrin et al. (2006) studied the topology of vortex field in the near-wake region of circular cylinder. Akilli and Rockwell (2002) also studied the vortex formation and their interactions with the channel bed in shallow flows. Both of these studies could nicely demonstrate the instantaneous and mean properties of the flow, wake vortices and the streamlines on the plane across the cylinder. Akilli and Rockwell (2002) observed that the formation of large-scale Karman-type vortex involves upward ejection of fluids through its center, which eventually leads to a horizontal vortex that includes significant distortion of the free surface. They also observed that the streamline topology that shows the structure of wake vortices changes with elevation. Bed roughness has been found to be very important in stabilizing the shallow wake instabilities (Chen and Jirka 1995, Ingram and Chu 1987 etc.). Tachie and Balachandar (2001) observed that the ratio of transverse shear parameter (computed as a non-dimensional transverse slope of the velocity defect profile) to bed friction coefficient is relatively smaller for rough bed than smooth bed. Interestingly Kahraman et al. (2002) found that the influence of localized roughness elements, placed immediately downstream of the base of the cylinder, to alter the streamline topology and Reynolds stress is not only near the bed but also global extending up to the plane at mid-height of the cylinder. They observed from the patterns of instantaneous velocity and vorticity that the consistent formation of large-scale vortices in the near-wake region is attenuated with very small surface roughness on the bed.

Only a few studies are there in literature on shallow wakes in open channels behind submerged obstacles (e.g. Shamloo et al. 2001). Shamloo et al. (2001) studied the shallow wakes behind hemispherical objects with different levels of submergence in open channels. They resolved the complexity of studying 3D wake produced by submerged objects by considering a wall wake on the vertical plane and a horizontal wake similar to plane turbulent wake as shown in Figure 6.4. Shamloo et al. (2001) analyzed velocity profiles on the downstream plane of symmetry for moderate to deeply submerged hemispheres using the concept of two-layer model for plane wall wake as given by Rajaratnam and Rai (1979). They could demonstrate good wall wake similarity in the outer region at $z/b_2 \geq 1$, but the inner region profiles produced similarity with logarithmic profile only in the far-wake region at $x/D \geq 10$. Shamloo et al. (2001) could also demonstrate similarity of velocity profiles across the wake on the horizontal plane at different elevations for slightly submerged and surface piercing hemispheres with the plane wake equation given by Schlichting (1968) in region relatively far from the hemispheres at $x/D \geq 4$. However, moderate to deeply submerged hemispheres did not produce good similarity with plane wake equation as the data were random. Shamloo et al. (2001) expressed a general power function from a group of relatively random data for the decay of velocity defect (U_{1m}/U_0, where U_0 is the cross-sectional mean velocity) in the downstream direction of the shallow wakes of hemispheres with an exponent of -0.792. However, they did not explain the variation of wake length scales with downstream direction. For all these analyses of wake and velocity defect, Shamloo et al. (2001) used only smooth bed measurements. Research into the flow around bodies submerged in a fluid is more common in atmospheric and geophysical sciences (e.g. Arya and Gadiyaram 1986, Arya and Shipman 1981, Castro and Snyder 1982, Pingree and Maddock 1979, Wolanski et al. 1984). Arya and Gadiyaram (1986), Arya and Shipman (1981) and Castro and Snyder (1982) experimentally studied the perturbation of flow and dispersion in the wakes of two and three-dimensional low hills in a wind tunnel. They observed that the mean velocity defect, and the increased Reynolds stress and variances of velocity fluctuations in the wake at $x/h>4$ decay with x/h according to some power laws. The hill slope had significant effect on the rate of decay of mean flow defect. The mean flow perturbation decayed faster in the wake of gentler hill. However, the rates of decay of turbulence were more or less constant with hill slope. Unlike Sforza and Mons (1970) the perturbation studies conducted by the researchers from atmospheric sciences considered an unusual velocity scale U_h (i.e. U at $z=h$ in undisturbed flow, where h is the height of the model) for normalizing velocity defects defined as $(U_\infty - U)$. Arya and Gadiyaram (1986) found the exponent of power function relating $(U_\infty - U)/U_h$ and x/h to be -1.1 and -1.5 for steeper (26.5° side-slope) and gentler (17.5° side-slope) conical hills with bed and model surface roughness in a deeply submerged flow condition. The exponents of power functions representing decay of turbulence perturbations were -1.5 to -1.7 (on average -1.6). Pingree and Maddock (1979) and Wolanski et al. (1984) studied the shallow wake in coastal water to investigate the effect of sand mounds, tidal banks and coral reefs on the general flow field, vertical mixing, sediment processes, including the dynamics of their own formation and erosion.

6.3 Experimental Setup and Procedure

General description of the experimental setup and procedure is given in Chapter 2. The experiments were carried out with a discharge of 50 L/s with 22 cm water depth (H) on smooth and rough beds to produce a turbulent ($R_H \equiv U_0 H/\upsilon=40000$) subcritical flow ($F=0.13$). For the purpose of studying shallow turbulent wakes in the immediate downstream of bed-mounted cylinders [see Fig. 2.8], the aspect ratio (*H*/*D*) was kept low (~2). The experimental flow conditions are summarized in Table 2.1.

At first the flow development was studied on smooth and rough beds without any cylinder and the approach flow velocity and bed shear stress were measured at the channel center [see Chapter 3]. A set of flow visualization tests was conducted prior to the detailed measurements of velocity. Flow visualization test results are presented in Chapter 4. The 3D turbulent velocity was measured using a 10 MHz Acoustic Doppler Velocimeter (ADV) at a sampling rate of 25 Hz for durations of 2-3 min. A typical diagram showing the velocity measuring stations in the wake of a cylinder is shown in Figure 6.5. Details about the application of ADV and data processing procedure are explained in Chapter 2.

6.4 Result Analysis and Discussions

6.4.1 *Mean velocity on downstream plane of symmetry*

The general flow patterns in the near-wake plane of symmetry (POS) on smooth bed in different flow regimes can be realized from Figure 6.6-6.9. In these figures near-wake streamlines are plotted along with the measured 2D velocity vectors on the downstream POS. In order to present the results in the same relative scale of magnitudes, the velocity vectors are normalized by the cross-sectional mean velocity U_0. The size of closed recirculation zone and the point of reattachment on the bed in Regime-1 (x~+3D) and Regime-2 (x~+3.5D) are noticeable from Figure 6.6 and 6.7. The vertical flows tend to diminish quickly after the closed recirculation zone in Regime-1. However, it takes longer (x>+4D) in Regime-2 to overcome the strong vertical flow in the downstream direction.

On the horizontal plane the streamlines in the back of the surface piercing cylinders form shapes of bubble or owl-face due to reverse flow (Akilli and Rockwell 2002 and Perrin et al. 2006). The length of wake-bubble or recirculation zone can be identified from the line of farthest points of reverse flow on the vertical plane in near-wake region. Figure 6.8 and Figure 6.9 show the size of wake-bubble immediately behind the cylinders, which is

~1.5D near the surface and ~1.8D near the bed in Regime-3 and ~1.1D over the entire depth in Regime-4. There are distinct differences in Regime-3 and Regime-4 in the vertical flow patterns inside the wake-bubble. Strong upward flow in a short length of wake-bubble can be observed in Regime-4 (Fig. 6.9), whereas strong downward flow with small extent (only up to $z<0.2H$) of upward flow can be observed in relatively longer (1.5D-1.8D) wake-bubble in Regime-3 (Fig. 6.8). In Regime-3 the downward and upward vertical flows tend to converge at z~0.15D and quickly straighten in the downstream direction. However, such vertical flow convergence is apparent at z~0.6H in Regime-4 and near-bed upward flow does not cease considerably even at x=+4D.

U/U_0 vs z/H, U/U_z vs z/H and W/U_0 vs z/H profiles for Regime-1 on smooth bed are plotted in Figure 6.10(a-c). Similar set of profiles are plotted for other flow regimes on smooth bed in Figure 6.11(a-c) to 6.13(a-c). Here, U_z is the mean velocity U at any elevation z in undisturbed flow on smooth bed. U/U_0 vs z/H profiles show the relative speed of the flow at different elevation of different station as the flow moves away from the cylinders in different flow regimes on smooth bed. U/U_z vs z/H profiles show the relative speed of the disturbed flow compared to the undisturbed flow. Vertical flow intensities can be studied from the W/U_0 vs z/H profiles.

It can be observed in Regime-1 and Regime-2 (Figure 6.10(a) and 6.11(a)) that there are small zone of jet-like flow above the cylinders. However, this jet-like high velocity profile can persist only up to x~+2D. The profiles of U/U_0 vs z/H in Regime-1 and Regime-2 have two opposite curvatures in the near-wake zone. The profiles at stations outside the recirculating zone show a gradual retrieval towards flow development. The profiles of U/U_z vs z/H in Regime-1 and Regime-2 (Fig. 6.10(b) and 6.11(b)) show that the flows in the wake gradually overcome the disturbance caused by the cylinders, though there are some extent of speed up near the bed due to impinging flow downstream of the closed recirculating zone. As a result, Figure 6.10(b) and 6.11(b) show some acceleration (i.e. $U/U_z>1$) in the zones of jet-like flow above the height of cylinders and near the bed relatively far downstream. However, in general the velocity defects in the wake of Regime-1 and Regime-2 compared to undisturbed flow can be observed from Figure

6.10(b) and 6.11(b). Velocity defect in the wake is found to be stronger in Regime-2 compared to Regime-1. Significant upward and downward flow can be observed in the wake of Regime-1 and Regime-2 (Fig. 6.10(c) and 6.11(c)). The maximum intensities of vertical flow can be observed at $z=0.1H$ to $0.25H$ (i.e. $0.4h$ to $1h$) in Regime-1 and at $z=0.25H$ to $0.45H$ (i.e. $0.45h$ to $0.8h$) in Regime-2.

The profiles of U/U_0 vs z/H in Regime-3 and Regime-4 (Fig. 6.12(a) and 6.13(a)) show the intensity of reverse flow in the zone of wake-bubble. It is interesting to note that in spite of longer wake bubble the reverse flow intensity is higher in Regime-3 as compared to Regime-4. Flow tends to develop quickly immediately after the zone of wake bubble in both Regime-3 and Regime-4, but the process slows down in far wake. The profiles of U/U_z vs z/H (Fig. 6.12(b) and 6.13(b)) show that the disturbance caused by the cylinders cannot be recovered even at $x=+20D$, though the near-bed magnitudes of U/U_z approach the unity. This gives indication that the near bed velocities can overcome the cylinder induced disturbance faster than the upper velocities. The impinging vertical flows in Regime-3 diminish within the top half-height of the cylinder (Fig. 6.12(c)). In general the intensity of vertical flow in Regime-4 (Fig. 6.13(c)) is insignificant compared to Regime-1, Regime-2 and Regime-3 (Fig. 6.10(c), 6.11(c) and 6.12(c)). However, the near-bed ($z<0.25H$) upward flow in Regime-4 after the wake-bubble (i.e. at $x>1.1D$) could have considerable effect on local scour for similar flows on erodible bed.

Similar to the smooth bed, the rough bed results are presented in Figure 6.14 to 6.21. Near-wake streamlines and 2D velocity vectors in Regime-1 and Regime-2 on rough bed (Fig. 6.14 and 6.15) are similar to those on smooth bed. However, the streamlines in Regime-3 and Regime-4 on rough bed (Fig. 6.16 and 6.17) are found to be significantly influenced by bed roughness. Regime-3 on rough bed has relatively thicker upflow zone (up to $z=0.25H$), but the length of wake-bubble ($x\sim1.75D$) are more or less similar to that of smooth bed. Surprisingly Regime-4 on rough bed has almost equal length of wake bubble as that of Regime-3 on rough bed. Moreover, the length of wake-bubble is more or less uniform over the entire depth in both Regime-3 and Regime-4. This indicates that bed roughness tends to stabilize the near-wake flow behind the cylinders in Regime-3 and

Regime-4. The nature of the profiles of U/U_0 vs z/H, U/U_z vs z/H and W/U_0 vs z/H on rough bed (Figure 6.18 to 6.21) in all four flow regimes are more or less similar to those on smooth bed. However, the near-bed velocities in Regime-4 have some distinctions; longitudinal mean velocities (U) in the wake-bubble are almost zero, while the upward flow at $z<0.25H$ has increased considerably as compared to smooth bed. The maximum upward velocity on rough bed occurs at $x=1.5D$ and it is more than two times bigger than that on smooth bed. This indicates that the bed roughness enhances local scour potential downstream of the cylinders in Regime-4.

Logarithmic [U/u_* vs zu_*/ν] profiles for all flow regimes on a smooth bed are plotted in Figure 6.22(a-d). Similarly logarithmic [U/u_* vs z/k_s] profiles for all flow regimes on a rough bed are plotted in Figure 6.23(a-d). Here, u_* is the friction velocity of the undisturbed approach flow, k_s is the Nikuradse's equivalent sand thickness Theoretical lines showing the law-of-the-wall are also plotted in Figure 6.22(a-d) and Figure 6.23(a-d). It can be observed from these figures that the bottom portion of the measured profiles of all flow regimes on smooth and rough beds fall close to the theoretical line of the law-of-the-wall when the measuring stations are far away from the cylinders. For stations closer to the objects the measured profiles are away from the theoretical line indicating significant flow disturbance. Velocities measured sufficiently above the cylinder height in Regime-1 and Regime-2 do not experience much disturbance, and hence the data points corresponding to upper elevations from all the downstream stations collapse in a narrow band and remain closer to the theoretical line. However, the measured logarithmic profiles in Regime-3 and Regime-4 are found way below the theoretical line, but parallel to the most downstream profiles. This indicates that the entire profiles at all stations are subjected to disturbances which are gradually released in the downstream direction. However, it is interesting to note that the measured logarithmic profiles in all flow regimes approach towards the theoretical line faster than those on smooth bed. Therefore, bed roughness seems to remove the defect in mean velocity profile and helps the development of flow in the wake behind cylinders.

6.4.2 *Turbulence on downstream POS*

For a turbulent wake, the self-preserving flow far downstream of a long cylinder is better known than the apparently non-preserving flow immediately behind the body (Chang 1970). In the immediate downstream region of cylinders (i.e. at small values of x/D), the variations of turbulence intensities are much larger than those at greater x/D, i.e. far behind the body where these values are small and vary slightly with x/D, indicating that self-preserving flow prevails.

The normalized profiles of three components of r.m.s. velocities (u'/u_*, v'/u_* and w'/u_*), turbulent kinetic energy (k/u_*^2), and the primary Reynolds stress ($-\overline{uw}/\overline{u_*}^2$) for Regime-1 on smooth bed are plotted in Figure 6.24(a-e). Similar set of profiles are plotted for other flow regimes on smooth bed in Figure 6.25(a-e) to 6.27(a-e). Here, u_* is the friction velocity of the undisturbed approach flow at the channel center, and $\overline{u_*}$ is the cross-sectional average of the friction velocities of the approach flow. Longitudinal, transverse and vertical turbulent intensities (i.e. u'/U, v'/U and w'/U), normalized turbulent kinetic energy (k/U^2) and normalized primary Reynolds stress ($-\overline{uw}/U^2$) contours in the near-wake region of Regime-1 on smooth bed are plotted in Figure 6.28(a-e). Similar contours in other flow regimes on smooth bed are plotted in Figure 6.29(a-e) to 6.31(a-e). Results of similar turbulence estimates of different flow regimes on rough bed are presented in Figure 6.32 to 6.39 in similar sequence of smooth bed results.

Increased turbulence in the near-wake region is the common observation in all flow regimes on both smooth and rough beds. However, increase in turbulence inside the closed wake envelope in Regime-1 and Regime-2 is significant. It is also common to observe that the turbulence estimates gradually decay in the downstream direction in all flow regimes. Profiles of the turbulent quantities may often be appeared to be scattered or random, but the contours clearly represent the pattern of variations in turbulence in the near-wake region. It can be observed from the contours that bed roughness damped near-wake turbulence in general and also interfere with its structure. It is interesting to note that the leading edges from the center of the closed recirculating wake of both Regime-1 and Regime-2 are associated with extreme turbulent intensities, kinetic energy and stress (Fig. 6.28(a-e), 6.29(a-e), 6.36(a-e) and 6.37(a-e)). However, Regime-1 on smooth bed has been found to create greater turbulence compared to Regime-2 on smooth bed at the closed wake leading edge. Bed roughness has been found to push the turbulence core away from the bed to a relatively higher elevation, especially in Regime-2. Moreover, Regime-1 has no longer been found to create greater turbulence compared to Regime-2 on rough bed. Regime-3 on both smooth and rough beds is found to create an intense turbulent zone where the high velocity over flowing water impinge behind the slightly submerged cylinders at $z{\sim}0.7H$ (Fig. 6.30(a-e) and 6.38(a-e)). Surprisingly, this intense turbulent zone in Regime-3, despite being extremely away from bed, has been found to be damped by the change in flow structure caused by bed roughness. This observation is in accordance with Kahraman et al. (2002) who found that even localized bed roughness could influence the gross turbulent structure in shallow wake. However, near-bed turbulence at the edge of wake-bubble in Regime-3 has been increased significantly on rough bed as compared to smooth bed. Similar to Regime-3, Regime-4 has created intense turbulence at the edge of wake-bubble, but not near the bed on smooth bed (Fig. 6.31(a-e)). However, bed roughness has made all the difference in creating significant turbulent core near the bed at the edge of wake-bubble in Regime-4 (Fig. 6.39(a-e)). These observations of turbulence behind cylinders of four flow regimes indicate that the turbulence related local scour potential on natural stream is significant in the near-wake region.

6.4.3 *Closed wake envelope and vorticity inside the recirculation zone*

Flow visualization tests reveal that there are closed recirculation wake in Regime-1 and Regime-2, whereas alternate vortex shedding is observed in Regime-3 and Regime-4 [see Chapter 4]. The primary vorticity is observed on the downstream vertical plane in Regime-1 and Regime-2, whereas Regime-3 and Regime-4 have primary vorticity on the horizontal plane. Therefore, ω_y and ω_z are the primary vorticity in the near-wake regions of moderate to deeply submerged regimes (Regime-1 and 2) and slightly submerged to non-submerged flow regimes (Regime-3 and 4) respectively. Many investigators (e.g. Akilli and Rockwell 2002 and Perrin et al. 2006) had already studied the topology of vortex field in the near-wake region of circular surface piercing cylinder. Yakhot et al. (2006) conducted a direct numerical simulation of turbulent flow around bed-mounted cube, without any comparison to the experimental observations. The present study shows experimental observations of closed recirculating wake in moderate to deeply submerged flow regimes (Regime-1 and Regime-2).

Chang (1970) stated that according to the classical concept of two-dimensional and axisymmetric flow zero incidence identifies separation of flow by the inception of reverse flow, the separation point being the forward boundary of a vortex sheet embedded within a separated region. However, on a three-dimensional body the separated region consists of a vortex embedded between the body surface and a stream surface attached to the body in a closed curve.

Tracing the locus of zero velocity (i.e. U=0) and $\partial^2 U/\partial z^2=0$ on the plane of symmetry downstream of the cylinders two set of envelopes are drawn in Figure 6.40(a-b) for Regime-1 and Regime-2 on both smooth and rough beds. Zero velocity envelopes represent the boundary of forward and reverse flow region. On the other hand, $\partial^2 U/\partial z^2=0$ envelopes indicate the dividing streamline emanating from the top edge of the cylinders. The envelopes are very similar for Regime-1 on smooth and rough beds. It is, however, slightly different in Regime-2. Rough bed envelopes are a little shorter than those on smooth bed. It can be noticed from Figure 6.40(a-b) that the reverse flow zone covers most of the height enveloped by the dividing streamline on the plane of symmetry. This observation is consistent with Chang (1970), who found that for a backward facing step back flow covers a considerable height from the bottom surface and extends almost the total length of the region of free shear layer.

Chang (1970) also stated that sheets of vorticity leave the surface when flow separation occurs. Immediately after separation, most of the vorticity in the separated flow is perpendicular to the direction of free stream velocity and parallel to the separated surface streamline sheet. Besides this primary vorticity, a secondary vorticity can be created by the turning of flow before or after separation. This secondary vorticity causes the separated surface streamline to roll up into a vortex and this secondary vorticity is parallel to the direction of the main flow bounding the separated surface streamline skeleton.

The primary vorticity (ω_y) inside the zone bounded by the line of separation are computed as Equation [6.5].

$$[6.5] \quad \omega_y = \frac{\partial U}{\partial z} - \frac{\partial W}{\partial x}$$

The results of primary vorticity (ω_y) inside the closed recirculating wake in Regime-1 and Regime-2 on smooth and rough beds are presented in Figure 6.41(a-d). It is interesting to note that the strength of vorticity is relatively greater in Regime-1 as compared to that of Regime-2 on both smooth and rough beds. It can also be noticed from Figure 6.41(a-d) that the strengths of vorticity in Regime-1 and Regime-2 are relatively higher on rough bed as compared to smooth bed.

6.4.4 *Wall wake analysis*

The mean velocity (U) distributions on the downstream POS in Regime-1 and Regime-2 on smooth and rough beds (Fig. 6.10(a), 6.11(a), 6.18(a) and 6.19(a)) show that the profiles outside the closed recirculation region (i.e. where $U>0$) are very similar to the profile of wall wake (see Fig. 6.2). The velocity profiles in Regime-3 and Regime-4 (Fig. 6.12(a), 6.13(a), 6.20(a) and 6.21(a)) are not similar to plane wall wake profile at all. Therefore, a wall wake analysis is conducted for the velocity profiles of Regime-1 and Regime-2 on the downstream POS. In addition a similarity analysis for the turbulence properties (turbulent kinetic energy and primary Reynolds stress) of the near-wake flow in Regime-1 and Regime-2 has been conducted.

Only the stations (i.e. x/D) where the entire profile shows positive velocity (i.e. $U>0$) are considered for the purpose of wall wake similarity analysis. Similar to Rajaratnam and Rai (1979) the velocity profiles are first plotted in logarithmic scales (i.e. U/u_*' vs zu_*'/ν

or z/k_s) in Figure 6.42(a-d). The local magnitudes of friction velocity u_*', measured previously [see Chapter 4], is used for this purpose. Yaw probe measured bed shear stresses were negative at few stations downstream of the cylinders. For the purpose of wake analysis in this study only the stations having positive shear stresses are considered for plotting in logarithmic scales in Figure 6.42(a-d). Unlike the far-wake velocity profiles of 2D wall wake of Rajaratnam and Rai (1979), the near-wake profiles of the present study are away from the theoretical line representing the law-of-wall. The logarithmic profiles (Fig. 6.42(a-d)) indicate that the inner layer is still developing in the near-wake region. Wall wake similarity in the outer region is, however, achieved for Regime-1 and Regime-2 on both smooth and rough beds. Fig. 6.43(a-d) show the similarity profiles for the mean velocity (U). For the present shallow wake study U_e replaces U_∞ (ambient velocity), where U_e is the free stream velocity (assumed to be equal to the velocity in the upper layer where there is almost no gradient) at each individual measuring station. U_{2m} and b_2 are the velocity and length scales for wall wake computed as Rajaratnam and Rai (1979), where the velocity defect, $U_2 = U_e - U$, U_{2m} is the maximum value of U_2, and $b_2 = z$ where $U_2 = 0.5U_{2m}$ (see Fig. 6.2). The variations of the velocity and length scales (U_{2m} and b_2) in the downstream direction are plotted in non-dimensional terms in Figure 6.44(a-d) and 6.45. The results (Fig. 6.44(a-d)) show that U_{2m}/U_e has good correlation with x/h in all cases with regression coefficients ~0.99. The rate of decay of U_{2m}/U_e is faster on smooth bed (as the exponent$\approx$-2) compared to rough bed (as the exponent$\approx$-1.3). However, the rate of decay of U_{2m}/U_e observed in the present study of 3D wall wake on both smooth and rough beds is very fast compared 2D wall wake as observed by Rajaratnam and Rai (1979), as the exponent was only -0.5. Sforza and Mons (1970), however, indicated that the rate of decay of velocity defect is faster in 3D wall wakes compared to 2D wall wakes, though they used a different scale other than U_{2m} (see Equation [6.4]). On the other hand, the length scale is found to be more or less constant, except far downstream on rough bed (Fig. 6.45). Interestingly, b_2/h values remain similar for smooth and rough beds in a given flow regime. It is approximately 0.6 for Regime-1 and 0.5 for Regime-2 on smooth and rough beds. This indicates that though there is distinct evidence of wall wake similarity in the outer region (i.e. away from the bed), the wall wake does not grow in the shallow near-wake region bounded by channel bed and free water surface. Wind tunnel experimental data of Sforza and Mons (1970) also showed similar results in the near-wake region up to x/h=10, though the length scale grew (with exponent~0.4) for both 2D and 3D obstacles in the far-wake region.

Similar to mean velocity turbulence profile similarity is investigated in the near-wake region of Regime-1 and Regime-2. The profiles of turbulent kinetic energy (k) and primary Reynolds stress ($-\overline{uw}$) are examined for similarity. The similarity profiles for turbulent kinetic energy are plotted in Figure 6.46(a-d) considering $k_1 = k - k_e$, where k_e is the turbulent kinetic energy in the upper layer where there is almost no velocity gradient (i.e. $\partial U/\partial z$=0) at each individual measuring station, and k_m = maximum value of k_1, and b_k=z where k_1=0.5k_m. Again, the similarity profiles for primary Reynolds stress (τ_t=$-\overline{uw}$) are plotted in Figure 6.47(a-d) considering $\tau_{t1} = \tau_t - \tau_{te}$, where τ_{te} is the Reynolds stress in the upper layer (which is approximately zero) where there is almost no velocity gradient (i.e. $\partial U/\partial z$=0) at each individual measuring station, and τ_{tm} = maximum value of τ_{t1}, and b_τ=z where τ_{t1}=0.5 τ_{tm}. The results [Fig. 6.46(a-d) and 6.47(a-d)] show that the turbulent kinetic energy and primary Reynolds stress profiles are considerably similar in the near-wake region of Regime-1 and Regime-2 on smooth and rough beds for some distance downstream (up to x=+4D) of the cylinders, as the data points collapse in a narrow band. The characteristic profiles of similarity in turbulent structure of shallow near-wake region would be very useful for future applications (e.g. numerical simulations). The variations of the turbulence scales (k_m and τ_{tm}) in the downstream direction are plotted in non-dimensional terms (k_m/U_0^2 and τ_{tm}/u_*^2 vs x/h) in Figure 6.48(a-b). Here, U_0 is the cross-sectional mean velocity and u_* is the approach flow friction velocity. The results show that the scales decay faster in Regime-1 compared to Regime-2 in the downstream direction , and the effect of bed roughness is negligible in the decay of turbulence scales (k_m/U_0^2 and τ_{tm}/u_*^2) as smooth and rough bed data grouped together for Regime-1 and Regime-2. The length scales b_k and b_τ are also plotted in Figure 6.49(a-b) in non-dimensional terms. It can be observed from Figure 6.45 and 6.49(a-b) that the turbulent length scales (b_k and b_τ) are smaller than the mean velocity length scale (b_2) in the wall wake. Most data from Regime-1 and Regime-2 on smooth and rough beds in Figure 6.49(a-b) collapse in bands of 0.3-0.4 and 0.2-0.3 for b_k/h and b_τ/h respectively in regions close to the cylinders, indicating non-growing wake as observed from the variation of length scale (b_2) related to mean velocity [see Fig. 6.45].

6.4.5 *Decay of longitudinal mean velocity defect on downstream POS*

For the purpose of this analysis the velocity defect is defined as the deviation from undisturbed velocity profile; i.e. the deviation of mean velocity (U) at any elevation z with respect to the undisturbed velocity at the same elevation U_z is considered as the defect. Therefore, velocity defect, $-\Delta U=U_z-U$. Sforza and Mons (1970), Arya and Gadiyaram (1986) or any other studies of atmospheric sciences defined the velocity defect as $(U_\infty - U)$, where U_∞ is the mean velocity U at $z=\infty$. However, the present open channel flow study put significance on the approach flow boundary layer. Moreover, for atmospheric studies the models are always deeply submerged and the mean velocity U at $z=\infty$ is unchanged in disturbed flow compared to undisturbed flow condition. But for the present study the disturbance reaches the water surface, especially in Regime-3 and Regime-4. Therefore, a different definition of velocity defect has been adopted for the present study of decay of mean velocity defect.

In order to observe the relative variation of speed of the disturbed flow compared to the undisturbed approach flow the profiles of U/U_z vs z/H (Fig. 6.10(b), 6.11(b), 6.12(b), 6.13(b), 6.18(b), 6.19(b), 6.20(b) and 6.21(b)), presented earlier, are first examined to know the pattern of velocity defect in different flow regimes with distance (i.e. x/D). Then the maximum defect ($-\Delta U_{max}$) at each station (i.e. x/D) are computed for all the flow regimes on smooth and rough beds. The variations of $-\Delta U_{max}/U_H$ with x/D are presented in Figure 6.50(a-b) for four flow regimes on smooth and rough beds, respectively, in normal scale. Here, U_H is the undisturbed mean longitudinal velocity at the free surface (i.e. at $z=H$, where H is the water depth). Figure 6.50(a-b) show that the near-wake regions have significant velocity defect. The velocity defects are found to increase in the near-wake before decaying in the downstream direction. The maximum defects in mean longitudinal velocity (U) are observed at the center of the closed recirculating wake in Regime-1 (at $x=+0.75D$ to $+0.8D$) and Regime-2 (at $x=+0.9D$ to $+1D$) on both smooth and rough beds. Similarly, these are observed at or near the center of the wake-bubble in Regime-3 (at x=+1D) and Regime-4 (at x=+0.75D and +1D) on smooth and rough beds. However, the velocity defect decays monotonically in the downstream direction. In order to study the rate of decay of velocity defect, the variations of $-\Delta U_{max}/U_H$ with x/D are plotted in logarithmic scales in Figure 6.51(a-b) for smooth and rough beds respectively. Figure 6.51(a-b) show that power function relationships can be established between $-\Delta U_{max}/U_H$ and x/D for different flow regimes as Equation [6.6].

$$[6.6] \quad \frac{-\Delta U_{\max}}{U_H} = \alpha 1 \left(\frac{x}{D} \right)^{\beta 1}$$

The coefficients and the exponents of the above function for different flow regimes on smooth and rough beds can be computed from the logarithmic distributions shown in Figure 6.51(a-b). Table 6.1 shows the computed magnitudes of the coefficients and exponents of Equation [6.6]. The exponents of the power functions (i.e. slope of the profiles in logarithmic scale) represent the rate of decay. The rates of decay immediately downstream of the station of maximum defect and far downstream (e.g. $x \geq 10D$) from the cylinders are observed to be considerably less compared to those observed in the intermediate region (e.g. x~1D-10D). Therefore, the power functions are fitted with good agreement for the region where the rate of decay is dominant and also consistent for a considerable distance along the plane of symmetry.

The above results (Table 6.1) show that the rate of decay of velocity defect ($-\Delta U_{max}$) is related to the level of submergence of the cylinders (i.e. flow regimes) and bed roughness. Regime-1 with deeply submerged cylinder releases mean velocity defect very quick on both smooth and rough beds. With the increase in object height relative to the water depth the rate of decay is found to reduce. Thus Regime-4 is found to preserve mean velocity deficit in the wake longer than any other regime. However, bed roughness has been found to promote the rate of decay of mean velocity defect in all flow regimes.

Figure 6.52(a-b) show the variations of z_{max}/H vs x/D for all the flow regimes on smooth and rough beds respectively. Here, z_{max} is the elevation z where the defect is maximum (i.e. $-\Delta U_{max}$). Unlike wind tunnel studies (e.g. Arya and Gadiyaram 1986) growth and relaxation of the wake is complicated in open channel. It can be observed from these figures (Fig. 6.52(a-b)) that there is no definite trend in the variations of z_{max}/H with x/D in the shallow near-wake region of open channel flow.

6.4.6 *Decay of vertical mean velocity on downstream POS*

The vertical mean velocity (W) in the approach flow is negligible compared to the longitudinal mean velocity (U). However, the disturbance caused by the cylinders produce 3D velocity field in the near-wake region. The pattern and intensity of vertical flow on the downstream POS can be observed from the streamlines and W/U_0 vs z/H profiles presented in Fig. 6.6-6.21. The significant vertical flow could be upward or downward depending on the flow regimes. Therefore, only the magnitudes of vertical mean velocities (W_{mag}) are considered for the study of decay of vertical flow in the wake. W_{mag}/U_H vs z/H profiles for Regime-1, 2, 3 and 4 on smooth and rough beds are plotted in Figure 6.53(a-d) and 6.54(a-d). These figures show the relative intensity of vertical flow and their location in the wake of cylinders. The maximum values of W_{mag}/U_H for all the regimes on smooth and rough beds are then plotted against x/D in Figure 6.55(a-b) and 6.56(a-b) in normal and logarithmic scales respectively. It can be observed from (Fig. 6.53(a-d) and 6.54(a-d)) that the intensity of vertical flow in the near-wake region for a given regime remains similar in trend on both smooth and rough beds. However, Regime-2 has been found to produce most intense vertical flow compared to other flow regimes. It is also observed from Fig. 6.55 and Fig. 6.56 that Regime-2 takes longer distance than any other regimes to suppress the vertical flow in the wake on both smooth and rough beds, though the logarithmic profiles of $(W_{mag}/U_H)_{max}$ vs x/D (Fig. 6.56(a-b)) show that Regime-1 and Regime-2 have similar rate of decay of vertical flow. Regime-3 and Regime-4 can gradually eliminate vertical flow in the downstream direction, but the rates increase significantly on rough bed.

6.4.7 *Decay of increased turbulence on downstream POS*

In order to study the decay of increased turbulence in the wake, the maximum values of the normalized turbulence quantities (i.e. k/u_*^2 and $-\overline{uw}/u_*^2$) are plotted with the distance (x/D) in the downstream direction behind the cylinders for all flow regimes on smooth and rough beds in Figure 6.57(a-b) and 6.58(a-b). Here, u_* is the friction velocity of the undisturbed approach flow. All the profiles of maximum non-dimensional turbulence are first plotted in normal scale (Fig. 6.57(a-b) and 6.58(a-b)), and then in logarithmic scale (Fig. 6.59(a-b) and 6.60(a-b)) to investigate the pattern of variation in turbulence and the rate of decay in different regimes.

It can be observed from the figures (Fig. 6.57 to 6.60) that the wake turbulence increases up to a certain distance in the near-wake, and then starts to decay in the downstream direction in all flow regimes on smooth and rough beds. Similar to mean velocity defect, turbulence attains maximum values at or near the center of circulation inside the closed wake of Regime-1 and Regime-2. On the other hand, unlike mean velocity defect Regime-3 and Regime-4 attain maximum turbulence at the edge of the wake-bubble. The above observations of location of maximum turbulence hold true for both smooth and rough beds. These observations are similar to those of Castro and Snyder (1982), who studied the near-wake dispersion with a deeply submerged 3D model in wind tunnel and found that turbulent kinetic energy increases in the near-wake region reaching maximum at $x \sim 2h$ (Here, h is the object height) and thereafter decays with distance. It is interesting to note from Figure 6.57 to 6.60 that most of the wake turbulence decays within $x=+4D$ in Regime-1, and at $x=+10D$ in Regime-3, but it continues to decay up to $x=+10D$ in Regime-2 and $x=+20D$ in Regime-4 on smooth bed. These observations are similar on rough bed, except in Regime-2 where most of the wake turbulence decays in $x=+7D$. Unavailability of data at $x=+7D$ in Regime-2 on smooth bed might be the reason of such variation of observations on smooth and rough beds. Another important observation in Regime-2 (Fig. 6.57 to 6.60) is that there is hardly any decay of turbulence up to approximately $x=+2.5D$, whereas in the subsequent downstream stations the rate is very high on both smooth and rough beds. This indicates that the closed recirculating wake preserves the flow turbulence generated by flow separation and vortices due to flow around cylinders in Regime-2. Similar observations can be found in Regime-1 on smooth bed (Fig. 6.57 and 6.59), but not on rough bed (Fig. 6.58 and 6.60).

For the purpose of studying wake turbulence decay the variations of turbulence quantities are expressed by power functions as Equation [6.7] and Equation [6.8].

$$[6.7] \quad \frac{k}{u_*^2} = C_k \left(\frac{x}{D} \right)^{p1}$$

$$[6.8] \quad \frac{-\overline{uw}}{u_*^2} = C_\tau \left(\frac{x}{D} \right)^{q1}$$

Then the coefficients and the exponents of the above functions are computed from the logarithmic distributions shown in Figure 6.59 and 6.60. Table 6.2 shows the computed magnitudes of the coefficients and exponents of Equation [6.7] and [6.8]. As the rate of decay (i.e. slope of the profiles) can be observed to be considerably receded far downstream of the cylinders, these power functions are fitted with good agreement for the region where the rate of decay is dominant and also consistent for a considerable distance along the POS.

Overall the decay of turbulence in Regime-1 and Regime-2 is rapid on both smooth and rough beds, and bed roughness makes the rate of decay faster in Regime-2 than on smooth bed. However, Regime-1 has relatively reduced rate of turbulence decay on rough bed. Level of submergence of the cylinders has significant effect on the decay of increased turbulence. Regime-4 can release the increased wake turbulence very slowly compared to other flow regimes. However, the increased turbulent kinetic energy decays much quicker on rough bed in Regime-4, though turbulent stress decays very slowly. The rates of turbulence decay in Regime-3 are quite high as compared to Regime-4 on smooth bed, but the rough bed results for these two regimes are very similar, except for the decay of turbulent stress.

6.4.8 *Wake analysis on horizontal plane*

In previous studies of deep unbounded flows around cylinders wake analyses were conducted for mean velocity (U) on the horizontal plane in the far-wake regions considering the wake to be two-dimensional. Velocity distribution equation (i.e. Equation [6.1]) given by Schlichting (1968) could define the similarity of the profiles for deep and far-wake flows. However, the effect of bed and free surface on the wake similarity could be enormous in flows around surface piercing cylinders on open channels. Moreover, the near-wake unsteady flow could make the flow more complicated to obtain similarity. When the cylinders are subjected to submergence the wake is completely three-dimensional and even more complicated. For the purpose of analysis 3D wake behind submerged cylinders (e.g. in Regime-1 and Regime-2) could be resolved into two separate wakes on vertical and horizontal plane (Shamloo et al. 2001). The vertical plane wake analyses for Regime-1 and Regime-2 are already presented as wall wake analysis earlier in this chapter. Now, the wake analysis is performed on the horizontal plane for all four regimes on smooth and rough beds.

First of all, the mean velocity profiles U/U_z vs y/D for all flow regimes on smooth and rough beds are plotted across the channel for different elevations (i.e. z/H) at $x=+0.7D$ or $+0.8D$ to $+3D$ in Figure 6.61(a-e) to 6.68(a-e). These figures show that the profiles U/U_z vs y/D for Regime-3 and Regime-4 are similar at all elevations on smooth and rough beds, as the profiles collapse in a narrow band. However, the profiles U/U_z vs y/D for Regime-1 and Regime-2 can be considered similar at all elevations below the object height (i.e. at $z<h$) only very close to the objects (i.e. at $x=+0.7D$ to $+1D$). The upper (i.e. at $z>h$) velocity profiles across the wake are least disturbed and hence remain close to $U/U_z\sim1$. Gradually the profiles of U/U_z vs y/D at $z<h$ approach towards $U/U_z\sim1$ in the downstream direction (at $x/D>1$), indicating the release of velocity defect ($-\Delta U=U_z-U$) for Regime-1 and Regime-2. Bed roughness has been found to produce relatively increased defect, as the values of U/U_z on rough bed are less compared to smooth bed.

The variation of the mid-height (i.e. at $z=h/2$) wake profiles (U/U_z vs y/D) for different regimes on smooth and rough beds at different downstream distances can be observed from Figure 6.69(a-e) and 6.70(a-e). The profiles are very similar for all flow regimes immediately behind the cylinders. However, the wake profiles of Regime-1 move away from those of the other regimes at $x \geq +1D$. It is interesting to note that though Regime-2 apparently produces wake (e.g. closed recirculating wake) similar to Regime-1, the wake profiles at $x \leq +3D$ on the horizontal plane are similar to Regime-3 and Regime-4. Bed roughness has minor effect on the wake profiles of Regime-2 to move away from those of Regime-3 and Regime-4.

In order to compare the shallow near-wake flows with deep far-wake flow the plane wake similarity equation (i.e. Equation [6.1] given by Schlichting (1968)) has been adopted with a simple modification. According to Schlichting (1968) velocity defect, $U_1 = U_\infty - U$ where U_∞ is the undisturbed and uniform ambient velocity. In present study the approach flow has a boundary layer profile; therefore the term U_∞ in the wake similarity equation needs a modification. Since the wake similarity investigation has been carried out only at the mid-height (i.e. at $z=h/2$) of the cylinders, the undisturbed approach velocity at $z=h/2$ ($U_{h/2}$) is considered as U_∞, i.e. U_∞ is replaced by $U_{h/2}$. The other parameters (e.g. velocity scale U_{1m}, length scale b_1 etc.) are defined similar to the description given by Schlichting (1968) for plane turbulent wake. The near-wake similarity profile [$(U\text{-}U_{min})/U_{1m}$ vs y/b], as suggested by Balachandar et al. (2000), is also tried to obtain similarity on wakes on the horizontal plane. A fourth-order polynomial equation (Equation [6.9]) for near-wake similarity profile is derived in the present study for the purpose of comparison using the conditions: a) $(U\text{-}U_{min})/U_{1m}=0$ at $y/b=0$, b) gradient of $(U\text{-}U_{min})/U_{1m}=0$ at $y/b=0$, c) $(U\text{-}U_{min})/U_{1m}=0.5$ at $y/b=1$, d) $(U\text{-}U_{min})/U_{1m}=1$ at $y/b=2.25$, and e) gradient of $(U\text{-}U_{min})/U_{1m}=0$ at $y/b \geq 2.25$.

$$[6.9] \quad \frac{U-U_{min}}{U_{1m}} = 0.8616\left(\frac{y}{b}\right)^2 - 0.4148\left(\frac{y}{b}\right)^3 + 0.0532\left(\frac{y}{b}\right)^4$$

The wake similarity profiles at mid-height of the cylinders in four flow regimes on smooth and rough beds are presented in Figure 6.71(a-d) and 6.72(a-d). Plane wake similarity equation (i.e. Equation [6.1]) and near-wake similarity equation (i.e. Equation [6.9]) are also plotted in these figures for comparison. It can be observed that there are fair agreement between the shallow near-wake data of Regime-3 and Regime-4 with plane wake similarity equation, but the Regime-1 and Regime-2 data are relatively scattered and away from the theoretical line. However, the wake profiles are found to be considerably similar when plotted in terms of the near-wake similarity equation. The variations of the velocity and length scales (U_{1m}, b_1 and b) with downstream distance (x/D) are also studied from Figure 6.73(a-d), 6.74(a-d) and 6.75(a-b). The exponents of the power functions [$U_{1m}/U_{h/2}=C_{1h}(x/D)^{n1}$] representing the trend line of the experimental data in Figure 6.73(a-d) and 6.74(a-d) indicate the rate of decay of $U_{1m}/U_{h/2}$. The effect of submergence has been found to be significant on the rate of decay of $U_{1m}/U_{h/2}$, while the effect of bed roughness is apparently insignificant except in Regime-1. Except for Regime-4 on smooth bed, there is no definite trend of variations of length scale (b_1/D and b/D) with x/D (Fig. 6.75(a-b)). Moreover, the growth rate (exponent of the power functions [$b_1/D=C_{2h}(x/D)^{n2}$]) observed in Regime-4 on smooth bed (with an exponent of 0.503) agrees very well with the theoretical growth rate of plane turbulent wake (exponent=0.5) around cylinders in unbounded flow. Table 4 shows the coefficients and exponents of the power functions obtained from horizontal wake analysis at mid-height of the cylinders.

Finally, the turbulence similarity has been investigated across the wake on horizontal plane. Only turbulent kinetic energy (k) and primary Reynolds stress ($\tau_t=-\overline{uw}$) are considered for turbulence similarity investigation. The profiles of k/k_z vs y/D and τ_t/τ_{tz} vs y/D for all flow regimes on smooth and rough beds are plotted (not shown here) across the channel for different elevations (i.e. z/H) at $x=+0.7D$ or $+0.8D$ to $+3D$. Only the profiles of k/k_z vs y/D at $z=h/2$ for all flow regimes on smooth and rough beds (Fig. 76 and 77) and the profiles of τ_t/τ_{tz} vs y/D at $z=h/2$ for Regime-1 and 2 on smooth and rough beds (Fig. 78 and 79) are presented.

It can be observed from the distribution of turbulent kinetic energy across the wake (Fig. 76 and 77) that there is a pattern. Though the experimental data points fall in a band with some scatter depending on the distances (i.e. x/D), a general distribution can be approximated for different regimes. These distributions are found to be dependant on channel bed roughness and flow regimes (i.e. submergence of the cylinders), as the magnitudes of k/k_z vary with bed roughness conditions and flow regimes. However, the profiles of k/k_z vs y/D at different elevations z/H (not shown here) suggest that for $z \leq h$, the patterns are similar but the magnitudes of k/k_z are relatively smaller at $z<h/2$ and greater at $z>h/2$. Therefore, a general similarity profile for turbulent kinetic energy could not be established.

The profiles of τ_t/τ_{tz} vs y/D at different elevations z/H for different downstream stations (not shown here) cannot produce a general pattern. This is mainly because of change in direction of mean flow in the near-wake measuring stations. Another reason for this discrepancy could be the smaller channel aspect ratio that has produced considerably smaller turbulent shear stress in the undisturbed flow (τ_{tz}) compared to linear stress profile [see Chapter 3]. The magnitudes of turbulent shear stress were very small or small negative at $z \leq 0.34H$ [see Fig. 3.10]. Therefore, the profiles of τ_t/τ_{tz} vs y/D at $z=h/2$ are plotted only for Regime-1 and 2 on smooth and rough beds in Figure 78 and 79. The velocity measuring stations at $x/D \geq 1.5$, where the mean longitudinal velocities are positive, are considered for these figures. These results show a pattern of turbulent shear stress distribution in the near-wake region, at least for Regime-1 and Regime-2.

6.5 Conclusions

The present study provides a good understanding of the three-dimensional shallow turbulent near-wake flows behind bed-mounted cylinders with different levels of submergence in an open channel. Mean and turbulent flow fields in the near-wake region are explained with reliable ADV measurements. Two sets of measurements in similar flow conditions on smooth and rough beds are consistent; and thus provide valuable knowledge on the effect of bed roughness on shallow near-wake flows and the reliability of the measurements as well.

The general near-wake flow patterns on the POS are demonstrated by streamlines accompanied by 2D vectors. The complex three-dimensional flow in the near-wake region with significant variations in the vertical flow components can be realized with distinctions for different regimes on smooth and rough beds from this study. The size of closed recirculation zone and the point of reattachment in Regime-1 and Regime-2; and the length of wake-bubble or recirculation zone in Regime-3 and Regime-4 can easily be noticed from the presentations.

Two sets of closed wake envelopes are drawn for Regime-1 and Regime-2 tracing the locus of zero velocity and zero shear on the plane of symmetry downstream of the cylinders. Zero velocity envelopes represent the boundary of forward and reverse flow region, while the zero shear envelopes indicate the line of flow separation emanating from the top edge of the submerged cylinders. The primary vorticity (ω_y) in the near-wake region of moderate to deeply submerged regimes (Regime-1 and 2) are also presented. It has been found that the deeply submerged object creates stronger vorticity compared to moderately submerged object; and bed roughness enhances the strength of the vorticity in the closed wake region.

Wall wake analyses conducted for the velocity profiles of Regime-1 and Regime-2 on the downstream POS reveal that the inner layer remains in a developing stage in the near-wake region; however the outer region produces great similarity with the well-known plane wake equation. Moreover, the non-dimensional velocity scale U_{2m}/U_e has produced good correlation with x/h, indicating the rate of decay of U_{2m}/U_e for different regimes on smooth and rough beds. It has been found that the rate of decay of U_{2m}/U_e is faster on smooth bed (power function exponent$\approx$-2) compared to rough bed (exponent$\approx$-1.3); and these rates are significantly faster than 2D wall wake (exponent$\approx$-0.5) as known from previous study. On the other hand, the length scale (b_2) is found to be more or less constant; 0.6 for Regime-1 and 0.5 for Regime-2 on smooth and rough beds, indicating non-growing wake. Surprisingly similarity has been observed for the turbulence properties (turbulent kinetic energy and primary Reynolds stress) in the wall wake profiles of Regime-1 and Regime-2. Results show that the profiles of turbulent kinetic energy and primary Reynolds stress collapse in a narrow band, indicating considerable similarity for some distance downstream (up to x=+4D) of the cylinders.

The study of mean velocity defect compared to the undisturbed velocity reveals that the near-wake regions of all flow regimes are associated with significant defects. The mean velocity defects are found to increase in the near-wake before decaying in the downstream direction. The maximum defects in mean longitudinal velocity (U) are observed at the center of the closed recirculating wake in Regime-1 and Regime-2. Similarly, the defects reach maximum at or near the center of the wake-bubble in Regime-3 and Regime-4. The power function relationships established between $-\Delta U_{max}/U_H$ and x/D show that the rate of decay of velocity defect ($-\Delta U_{max}$) is related to the level of submergence of the cylinders (i.e. flow regimes) and bed roughness. With the increase in object height relative to the water depth the rate of decay is found to reduce. Thus Regime-4 is found to preserve mean velocity defect in the wake longer than any other regime. However, bed roughness has been found to promote the rate of decay of mean velocity defect in all flow regimes. Three-dimensional velocity field in the near-wake region has significant vertical flow depending on the flow regimes; however the three-dimensionality of the wake is most pronounced and longest persistent in Regime-2 than any other regimes.

It was known from previous studies that the level of turbulence increases in the near-wake region. The present study extends the knowledge to demonstrate the variations of magnitude, location and the rate of decay of increased turbulence in different flow regimes on smooth and rough beds. Similar to mean velocity defect, the center of the closed recirculating wake of both Regime-1 and Regime-2 are associated with extreme turbulent intensities, kinetic energy and stress. On the other hand, unlike mean velocity defect Regime-3 and Regime-4 attain maximum turbulence at the edge of the wake-bubble. Bed roughness is found to have a general dampening effect on near-wake turbulence. Similar to mean velocity defect, wake turbulence starts to decay in the downstream direction after the peak. The rate of decay of increased turbulence in the wake has been studied using power function relationship between the normalized turbulence quantities (i.e. k/u_*^2 and $-\overline{uw}/u_*^2$) and the distance (x/D). Level of submergence of the cylinders has significant effect on the rate of decay of increased turbulence. Most of the wake turbulence decays within $x=+4D$ in Regime-1, $+7D$ to $+10D$ in Regime-2, and $+10D$ in Regime-3; but it continues to decay up to $x=+20D$ in Regime-4. Overall the rate of decay of turbulence in Regime-1 and Regime-2 is rapid on both smooth and rough beds, and bed roughness promotes the rate of decay. The rates of turbulence decay in Regime-3 are quite high as compared to Regime-4 on smooth bed, but the rough bed results for these two regimes are very similar, except for the decay of turbulent stress.

Wake analyses on the horizontal plane reveal that similarity of mean velocity profiles (U/U_z vs y/D) exist in the near-wake region for Regime-3 and Regime-4 at all elevations on smooth and rough beds; and at all elevations below the object height (i.e. at $z<h$) only very close to the objects (i.e. at $x=+0.7D$ to $+1D$) for Regime-1 and Regime-2. The upper (i.e. at $z>h$) velocity profiles across the wake in Regime-1 and Regime-2 are least disturbed and hence remain close to $U/U_z \sim 1$. It is interesting to note that though Regime-2 apparently produces wake (e.g. closed recirculating wake) similar to Regime-1, the mid-height wake profiles at $x \leq +3D$ on the horizontal plane are similar to Regime-3 and Regime-4. In an attempt to investigate wake similarity with well-known plane wake equation fair agreement has been found for Regime-3 and Regime-4; but the profiles of $(U-U_{\min})/U_{1m}$ with y/b for all flow regimes have been found to exhibit considerable similarity with near-wake similarity equation as given by Equation [6.9]. The effect of submergence has been found to be significant on the rate of decay of velocity scale ($U_{1m}/U_{h/2}$), while the effect of bed roughness is apparently insignificant except in Regime-1. Finally, the turbulence similarity has also been investigated across the wake on the horizontal plane. The present study shows that the turbulence similarity does not exist among the profiles at different elevations; but the pattern of turbulent kinetic energy distribution (k/k_z vs y/D) across the wake are similar for different regimes on smooth and rough beds.

It is, therefore, evident that the results of the present study will provide a database for use in computational fluid dynamic (CFD) modeling, and overall significant advancements of the knowledge of flow hydraulics in shallow turbulent near-wake of bed-mounted objects. This study will improve our understanding of the complex three-dimensional wake, and facilitate in practical engineering applications in environmental and geophysical flow systems.

Table 6.1 Power Function Parameters for the Decay of Mean Velocity Defect

Parameter	Smooth Bed				Rough Bed			
	R-1	R-2	R-3	R-4	R-1	R-2	R-3	R-4
$\alpha 1$	1.40	2.56	2.05	1.26	1.23	2.90	2.32	2.44
$\beta 1$	-2.15	-1.71	-1.31	-1.14	-2.31	-1.99	-1.52	-1.39

Table 6.2 Power Function Parameters for the Decay of Wake Turbulence

Parameter	Smooth Bed				Rough Bed			
	R-1	R-2	R-3	R-4	R-1	R-2	R-3	R-4
C_k	13.17	20.00	24.36	15.50	9.00	24.36	18.03	18.28
C_τ	4.33	5.00	2.61	1.69	4.21	4.00	1.57	0.50
$p1$	-1.17	-0.98	-0.79	-0.55	-0.94	-1.28	-0.85	-0.85
$q1$	-1.72	-1.40	-1.12	-0.94	-1.64	-1.54	-0.94	-0.47

Table 6.3 Power Function Parameters Obtained from Horizontal Wake Analysis

Parameter	Smooth Bed				Rough Bed			
	R-1	R-2	R-3	R-4	R-1	R-2	R-3	R-4
C_{1h}	0.810	1.180	1.175	1.020	0.890	1.200	1.320	1.268
C_{2h}	0.417	0.799	0.502	0.383	0.355	0.824	0.540	0.706
$n1$	-1.890	-1.080	-0.902	-0.882	-1.357	-1.170	-0.980	-0.750
$n2$	0.760	0.089	0.172	0.503	0.172	-0.230	0.395	0.102

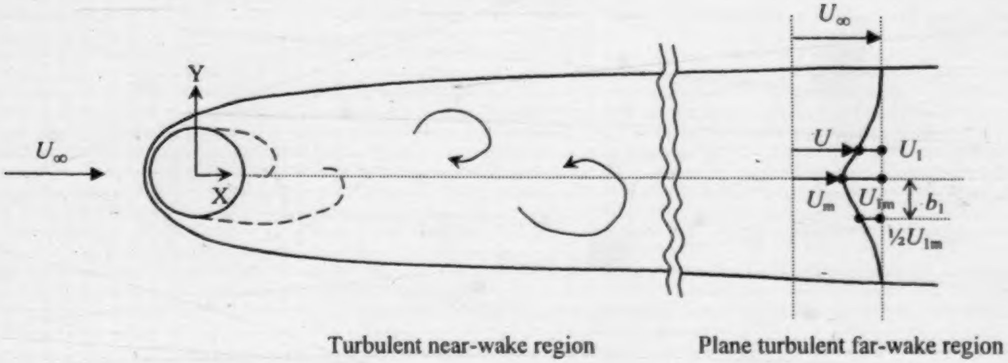
U∞
Y
U∞
X
U
U1
Um
U1m
b1
½U1m
Turbulent near-wake region
Plane turbulent far-wake region

Fig. 6.1 Definition sketch for plane turbulent wake

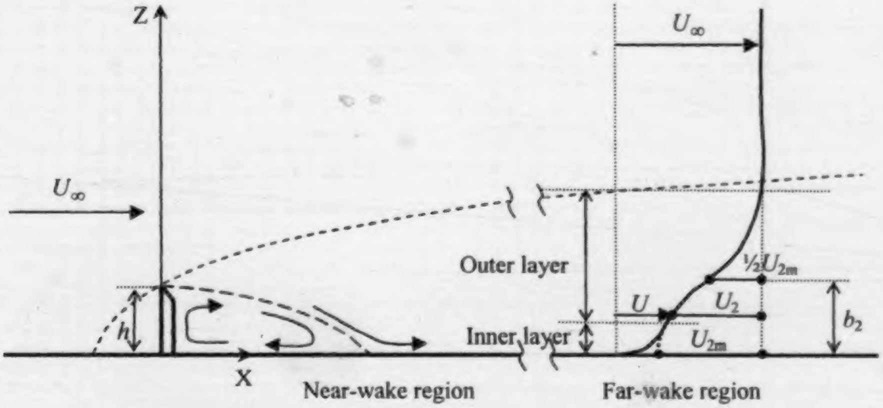
Z
U∞
U∞
Outer layer
½U2m
U
U2
b2
h
Inner layer
U2m
X
Near-wake region
Far-wake region

Fig. 6.2 Definition sketch for plane wall wake in deep flow

(Adapted from Rajaratnam and Rai 1979)

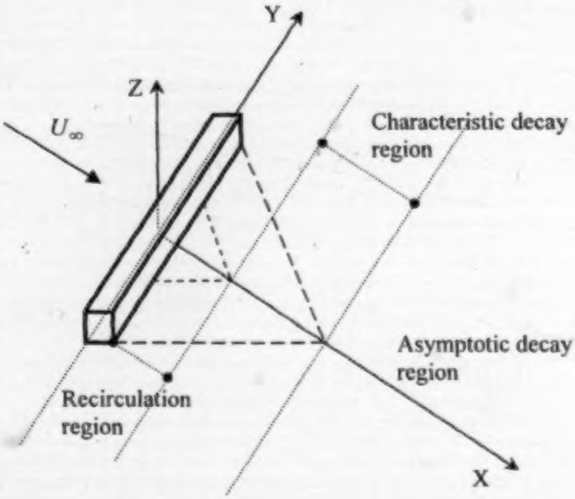
Y
Z
U_∞
Characteristic decay region
Asymptotic decay region
Recirculation region
X

Fig. 6.3 Schematic diagram of three-dimensional wall wake regions (Adapted from Sforza and Mons 1970)

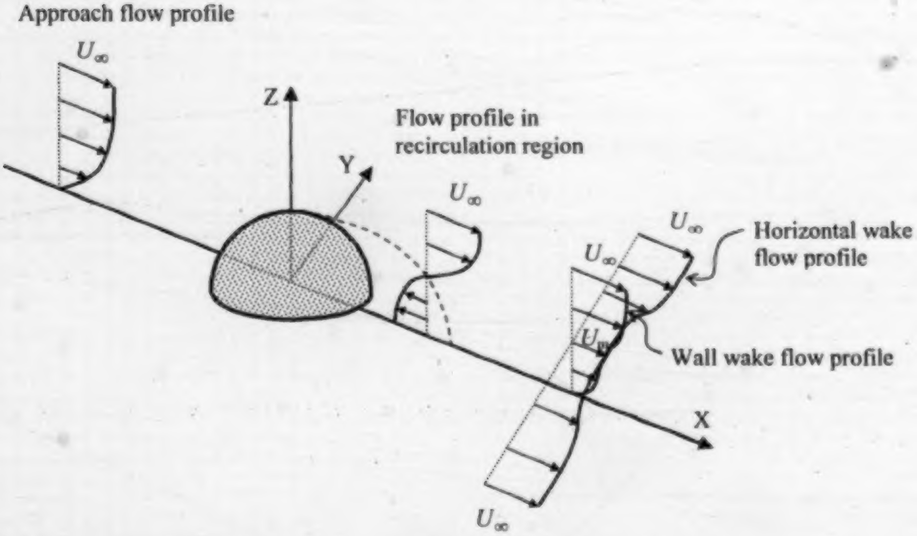
Approach flow profile
U_∞
Z
Y
Flow profile in recirculation region
U_∞
U_∞
U_∞
Horizontal wake flow profile
U_m
Wall wake flow profile
X
U_∞

Fig. 6.4 Schematic diagram of the velocity profiles of a shallow three-dimensional wake (Adapted from Shamloo et al. 2001)

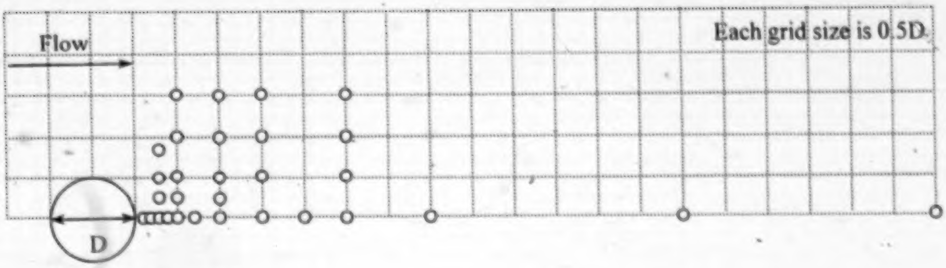
Flow
Each grid size is 0.5D.
D

Fig. 6.5 Typical velocity measuring stations relative to the object on a horizontal plane

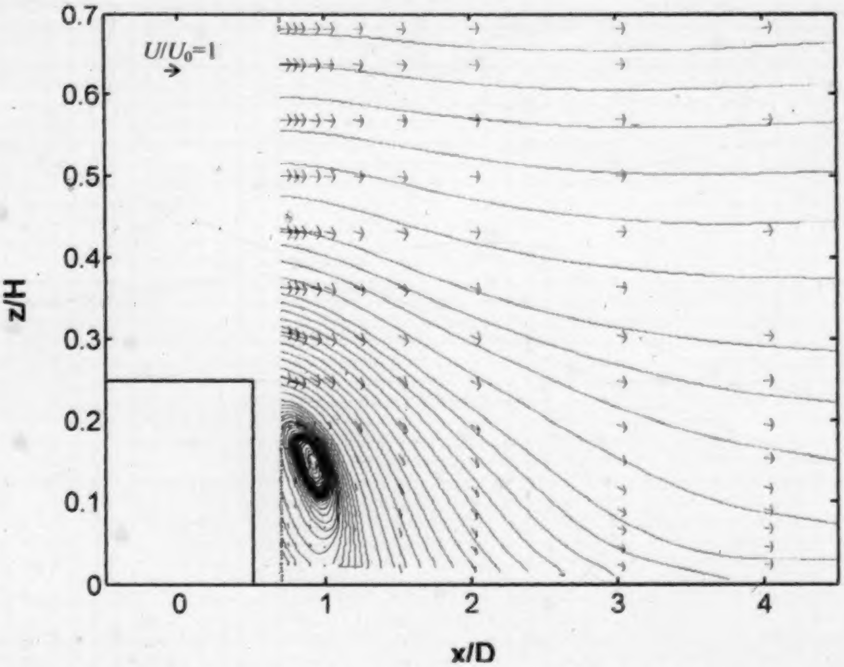

Fig. 6.6 Near-wake streamlines with velocity vectors on POS: Smooth bed/Regime-1

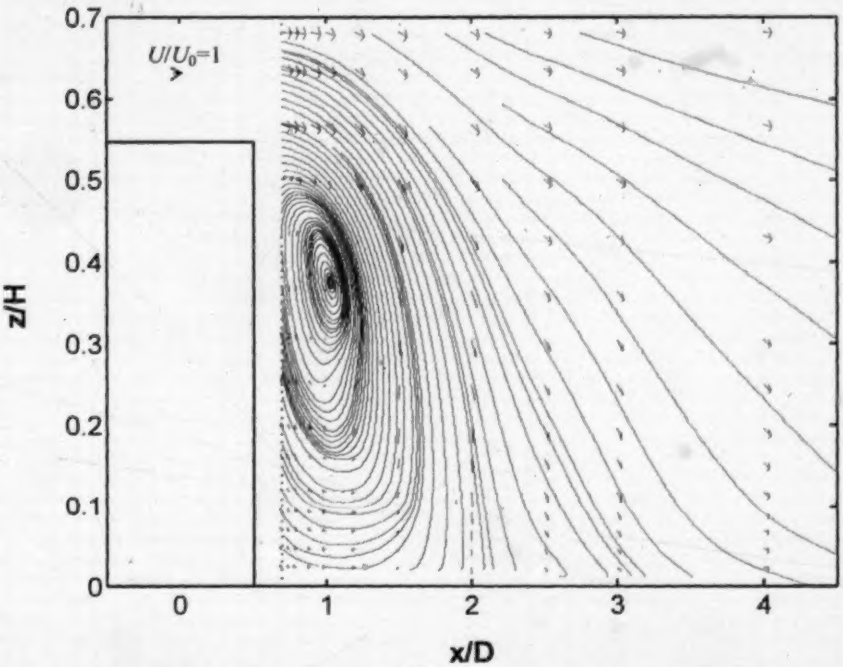

Fig. 6.7 Near-wake streamlines with velocity vectors on POS: Smooth bed/Regime-2

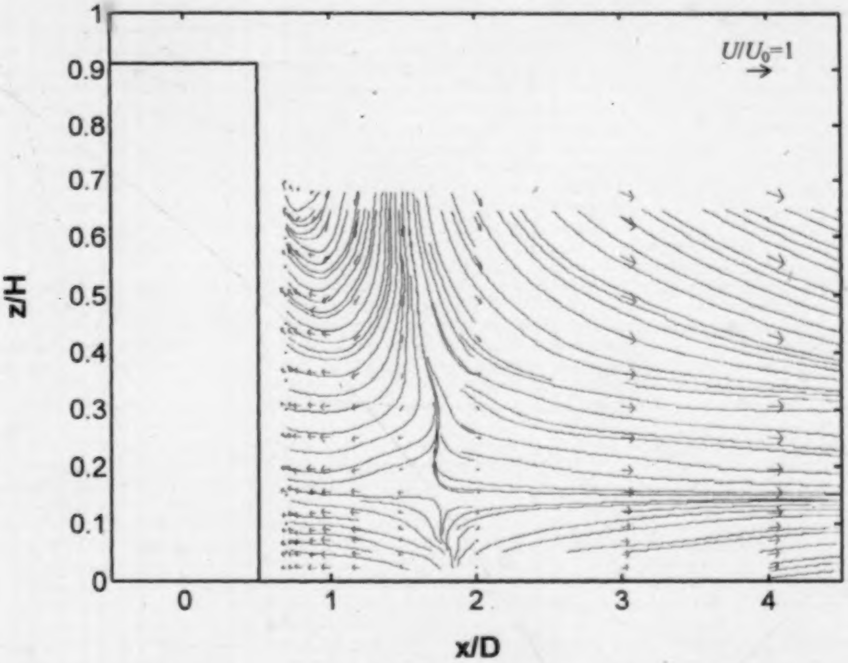

Fig. 6.8 Near-wake streamlines with velocity vectors on POS: Smooth bed/Regime-3

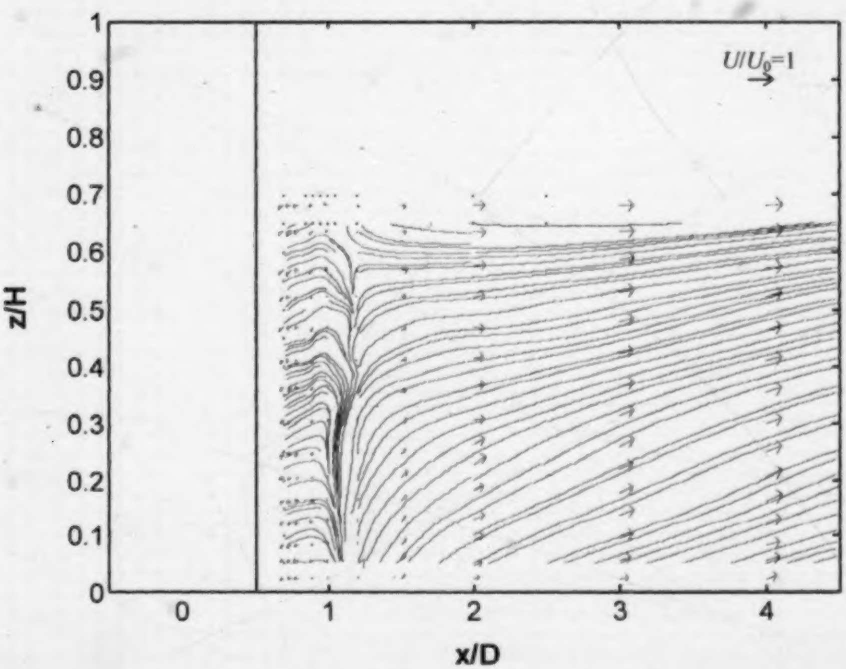

Fig. 6.9 Near-wake streamlines with velocity vectors on POS: Smooth bed/Regime-4

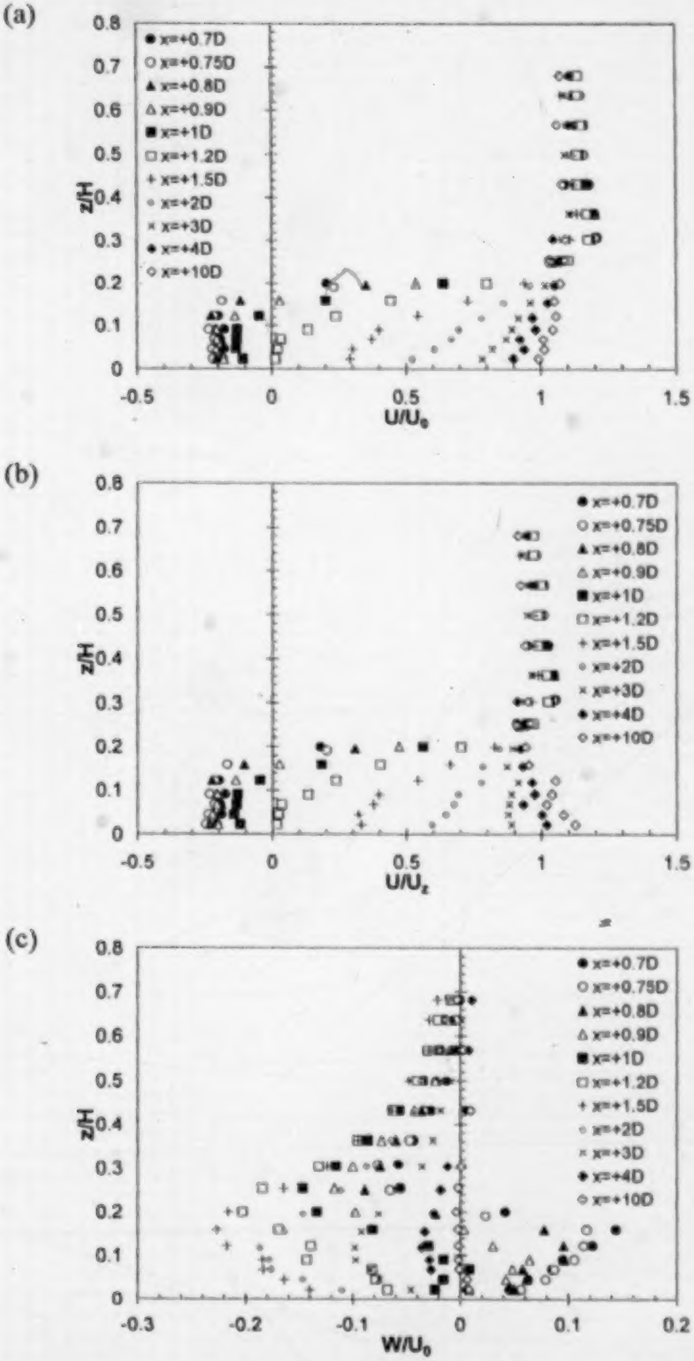

Fig. 6.10 Normalized mean velocity profiles on downstream POS: Smooth bed/Regime-1; (a) longitudinal mean velocity (U/U_0), (b) speed up factor (U/U_z), and (c) vertical mean velocity (W/U_0)

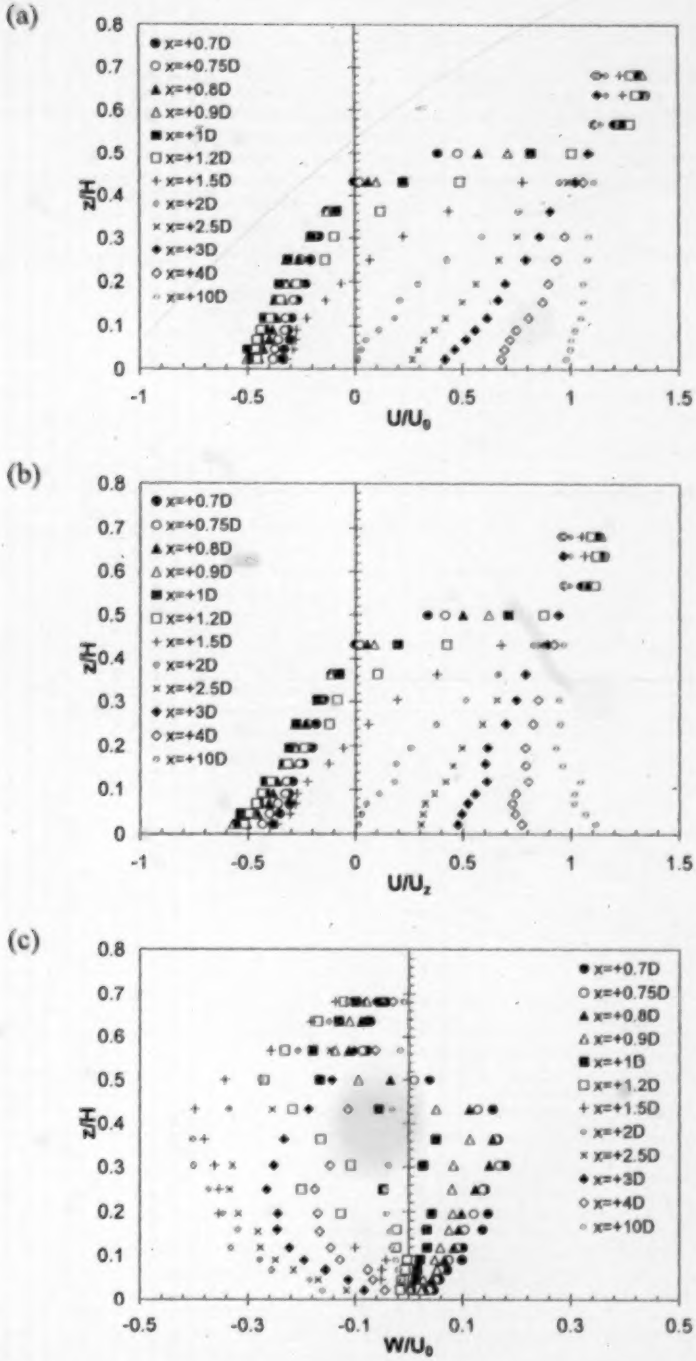

Fig. 6.11 Normalized mean velocity profiles on downstream POS: Smooth bed/Regime-2; (a) longitudinal mean velocity (U/U_0), (b) speed up factor (U/U_z), and (c) vertical mean velocity (W/U_0)

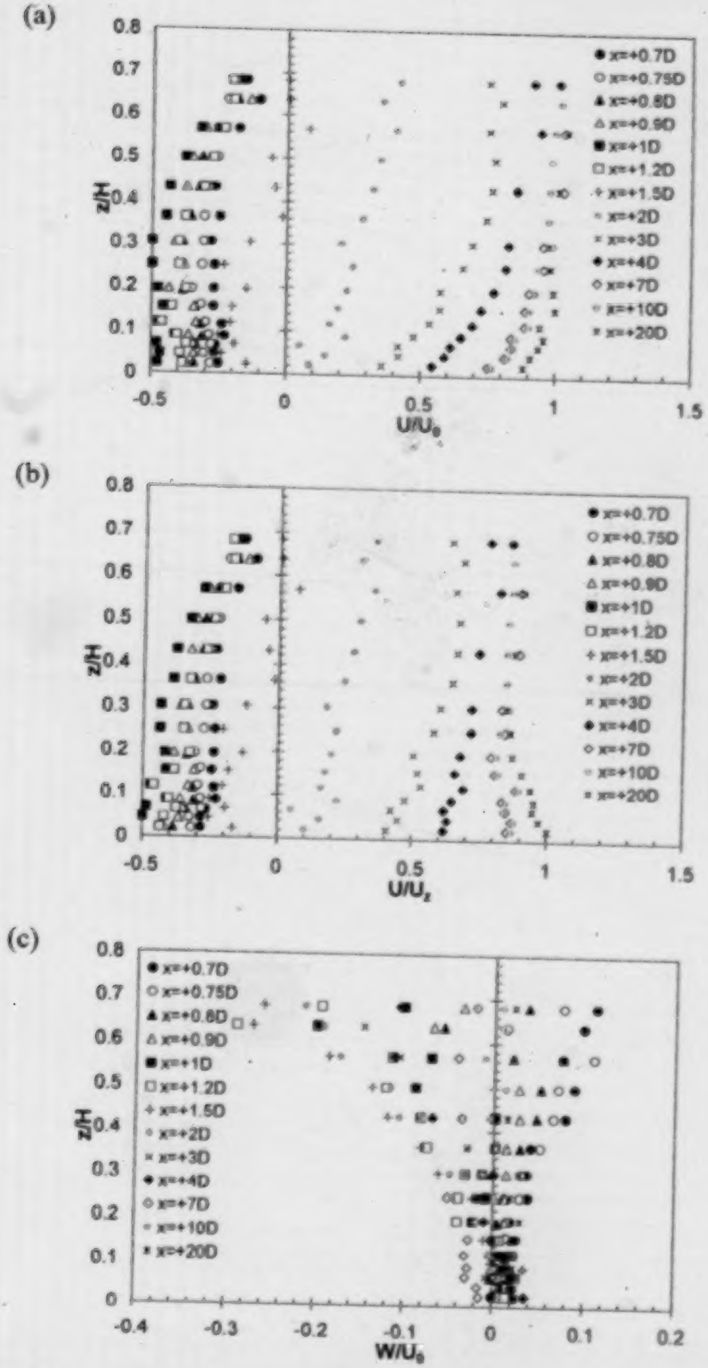

Fig. 6.12 Normalized mean velocity profiles on downstream POS: Smooth bed/Regime-3; (a) longitudinal mean velocity (U/U_0), (b) speed up factor (U/U_z), and (c) vertical mean velocity (W/U_0)

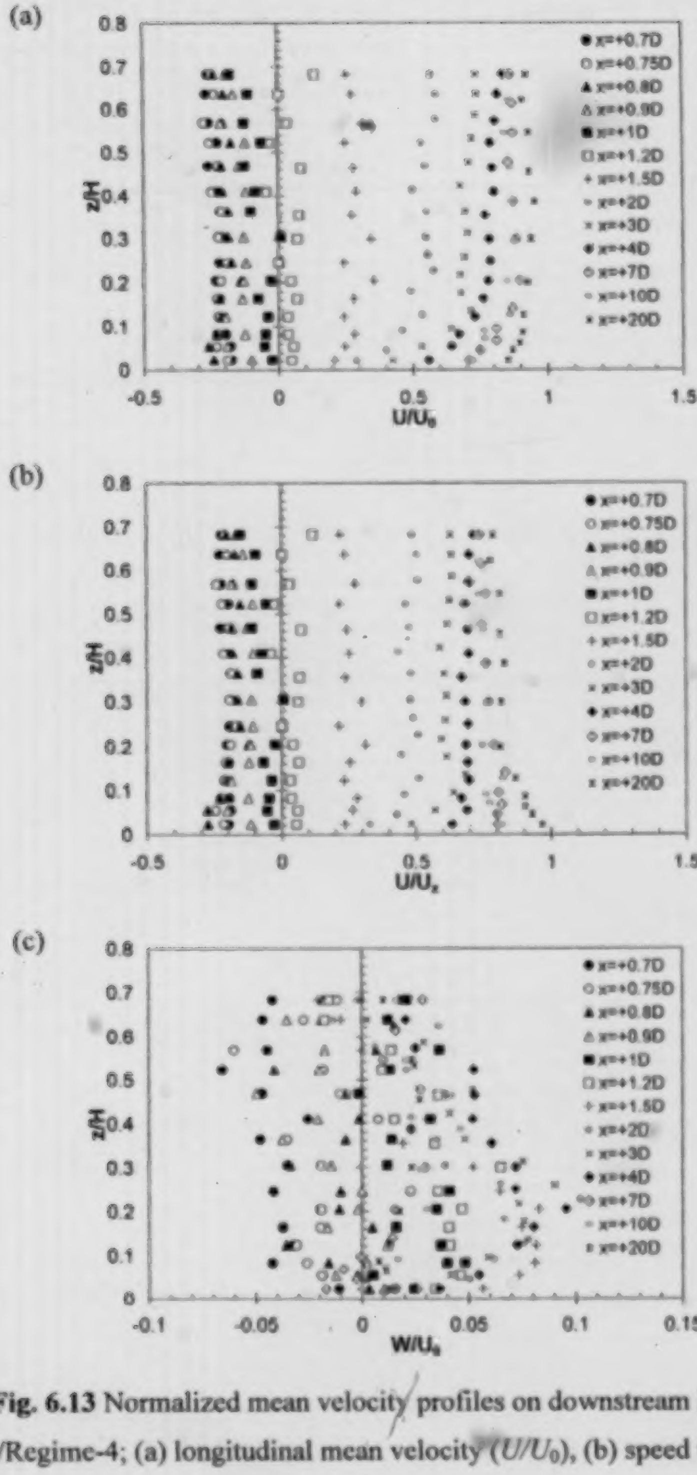

Fig. 6.13 Normalized mean velocity profiles on downstream POS: Smooth bed/Regime-4; (a) longitudinal mean velocity (U/U_0), (b) speed up factor (U/U_z), and (c) vertical mean velocity (W/U_0)

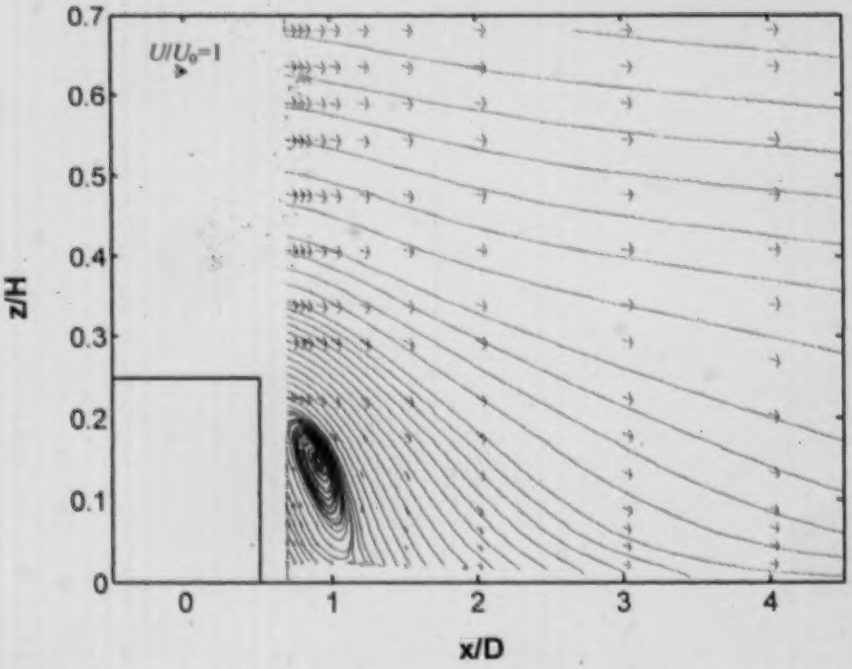

Fig. 6.14 Near-wake streamlines with velocity vectors on POS: Rough bed/Regime-1

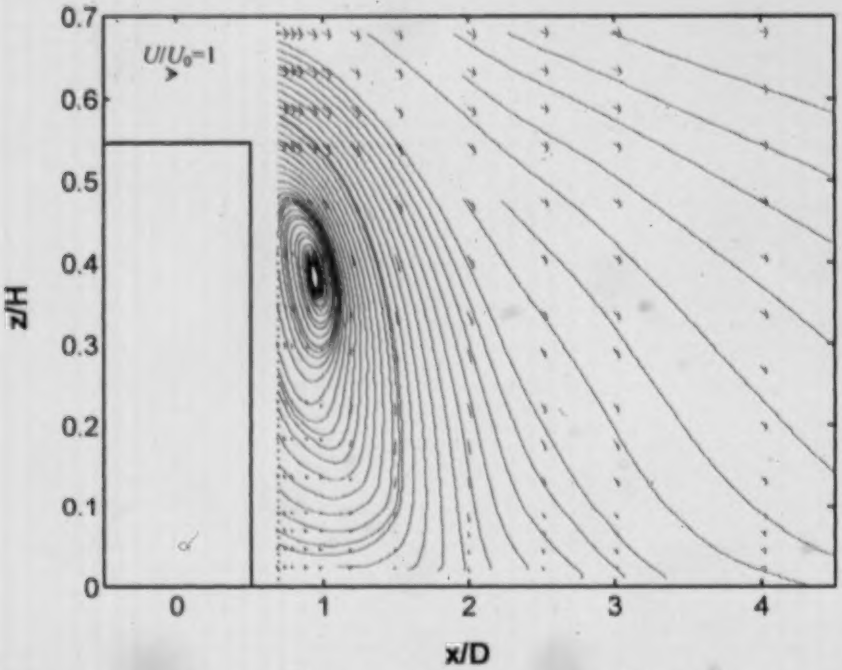

Fig. 6.15 Near-wake streamlines with velocity vectors on POS: Rough bed/Regime-2

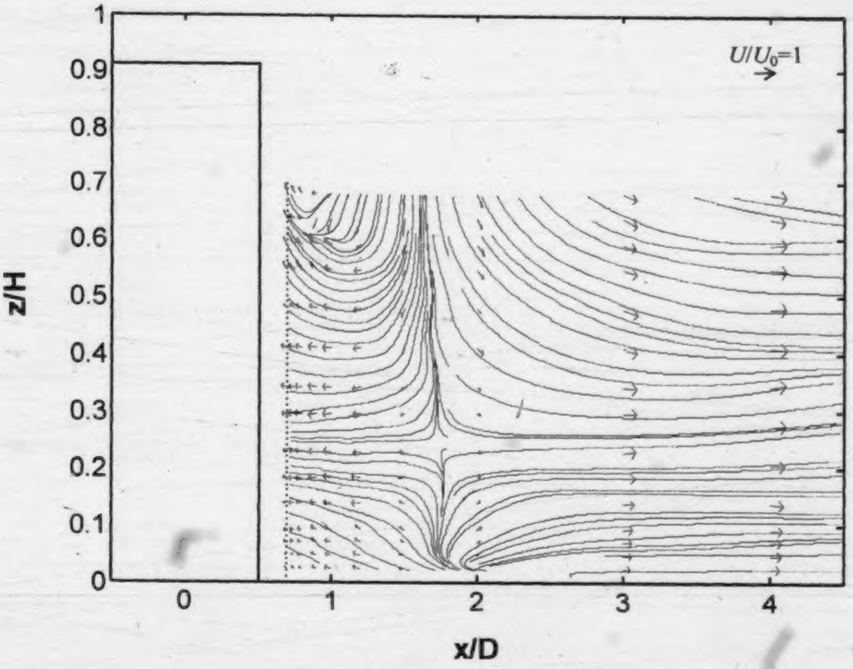

Fig. 6.16 Near-wake streamlines with velocity vectors on POS: Rough bed/Regime-3

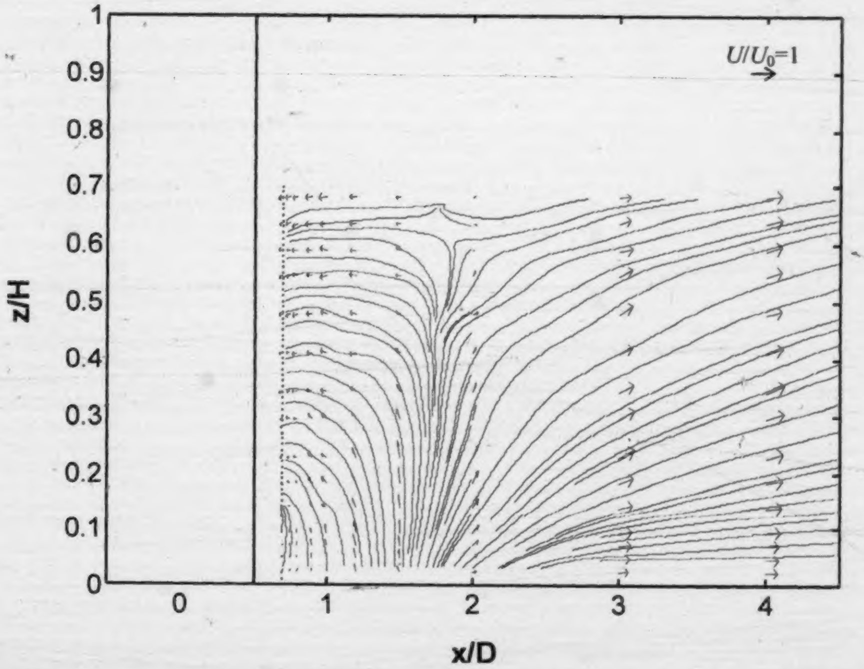

Fig. 6.17 Near-wake streamlines with velocity vectors on POS: Rough bed/Regime-4

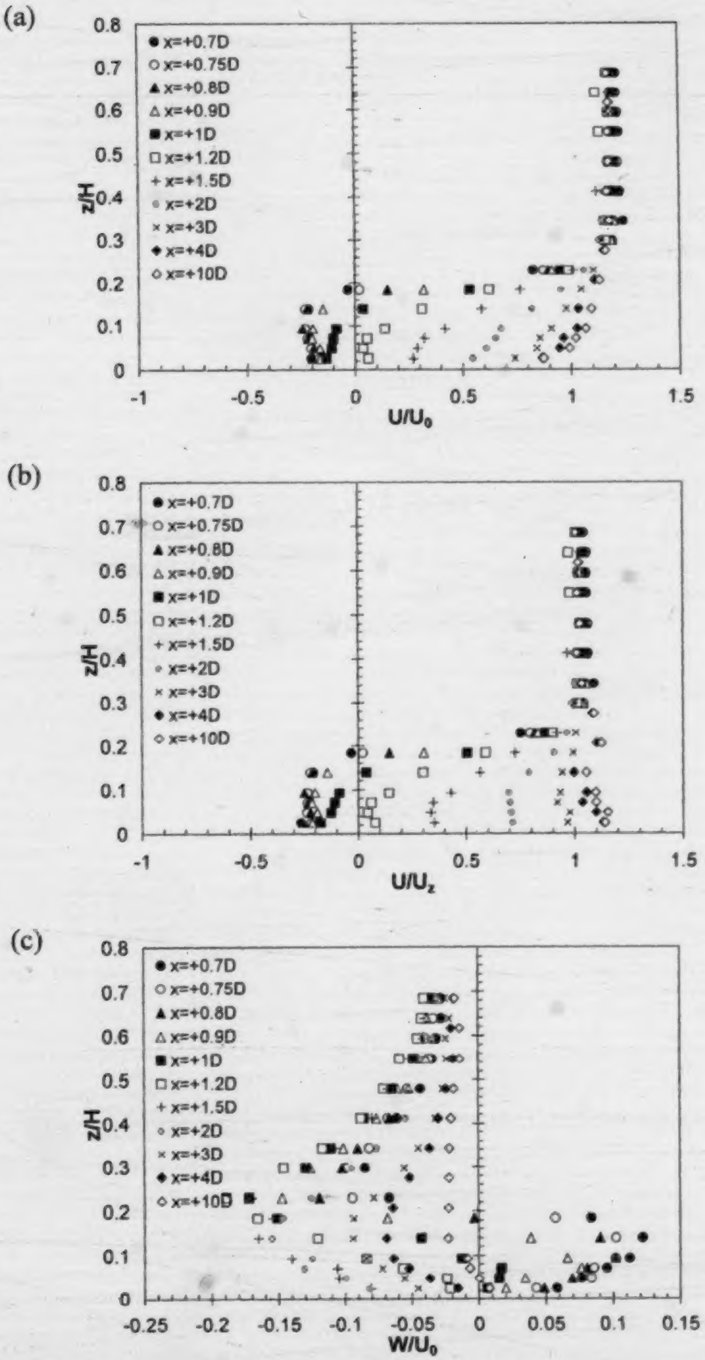

Fig. 6.18 Normalized mean velocity profiles on downstream POS: Rough bed/Regime-1; (a) longitudinal mean velocity (U/U_0), (b) speed up factor (U/U_z), and (c) vertical mean velocity (W/U_0)

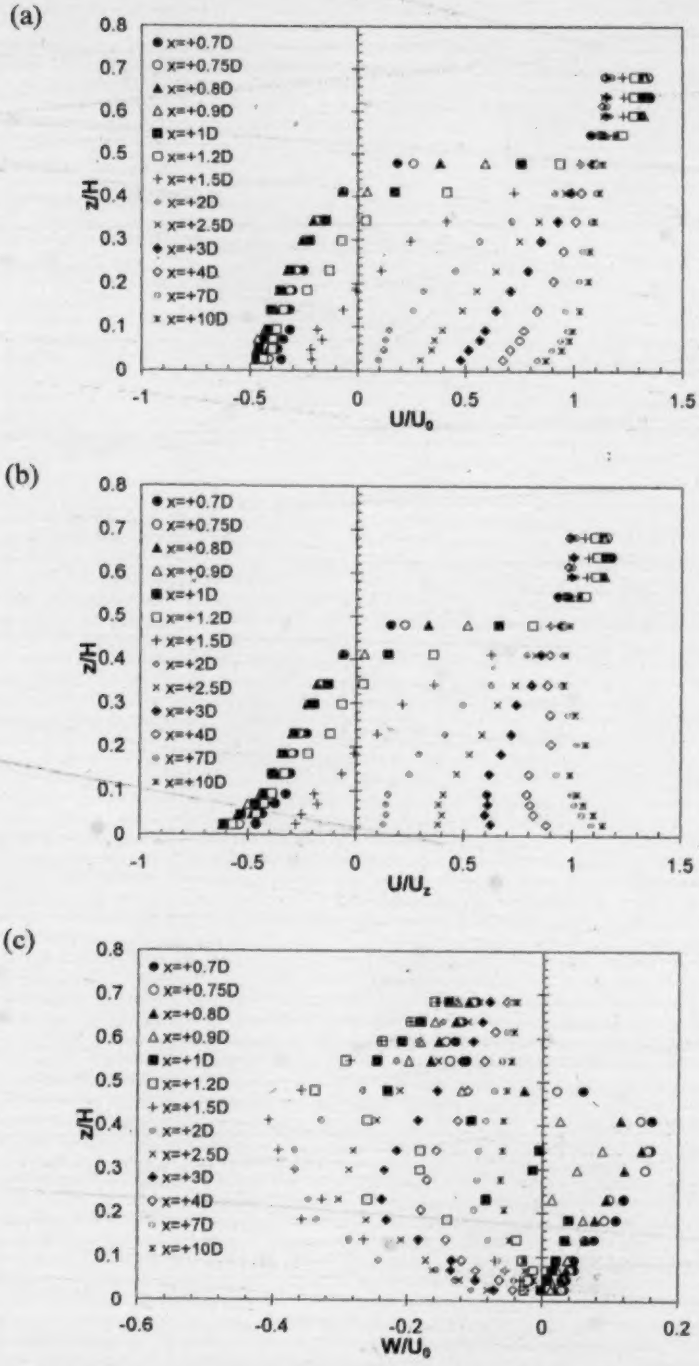

Fig. 6.19 Normalized mean velocity profiles on downstream POS:
Rough bed/Regime-2; (a) longitudinal mean velocity (U/U_0), (b) speed up factor (U/U_z),
and (c) vertical mean velocity (W/U_0)

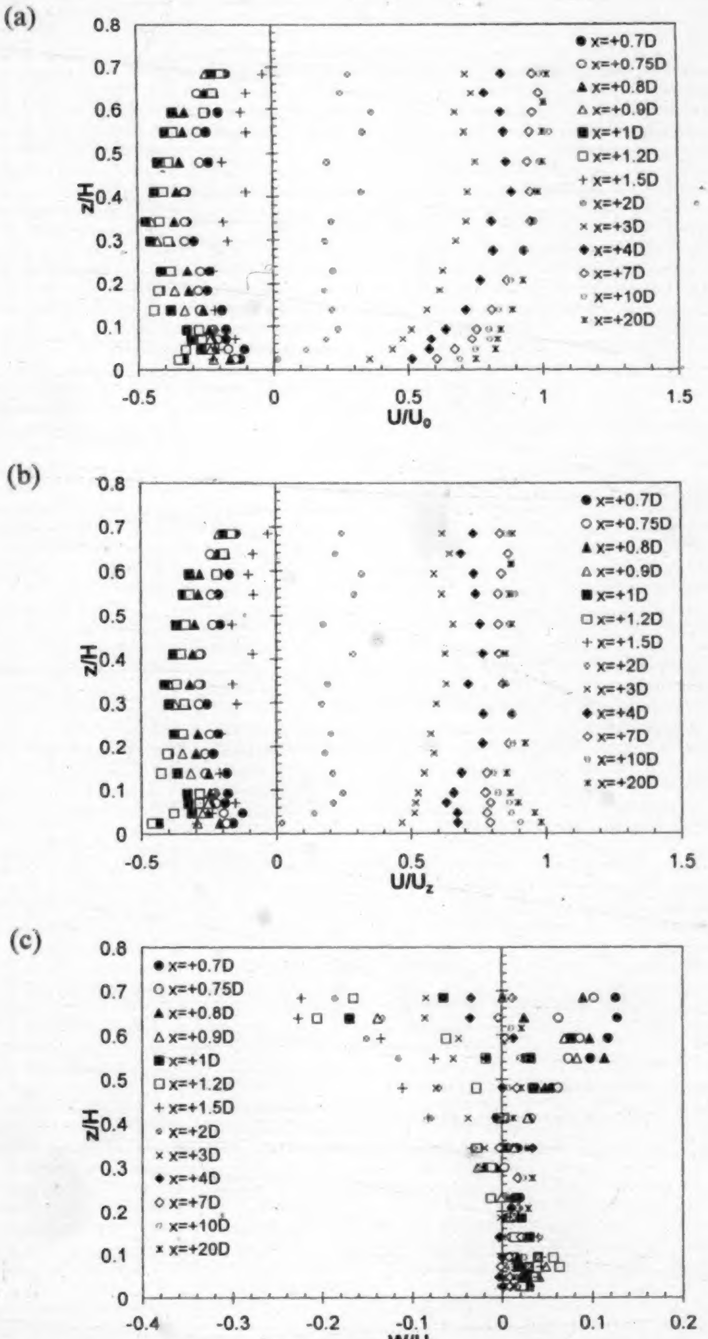

Fig. 6.20 Normalized mean velocity profiles on downstream POS: Rough bed/Regime-3; (a) longitudinal mean velocity (U/U_0), (b) speed up factor (U/U_z), and (c) vertical mean velocity (W/U_0)

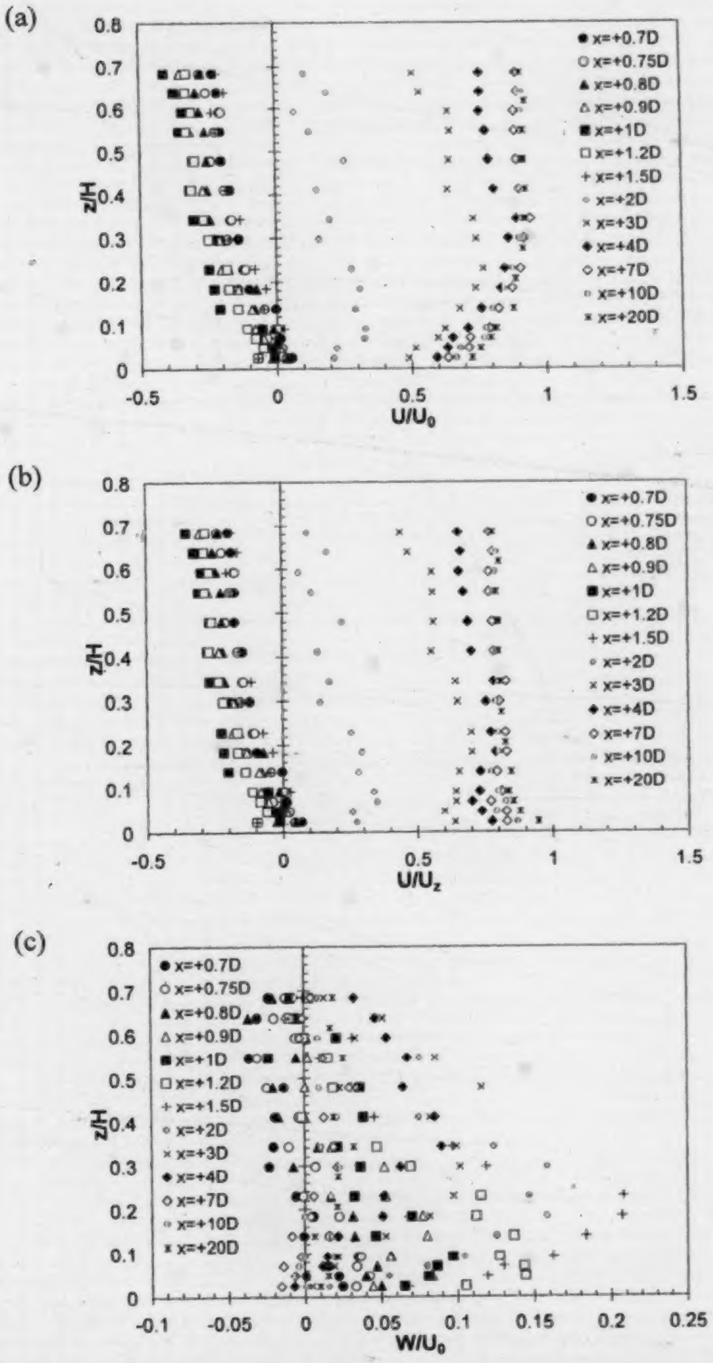

Fig. 6.21 Normalized mean velocity profiles on downstream POS: Rough bed/Regime-4; (a) longitudinal mean velocity (U/U_0), (b) speed up factor (U/U_z), and (c) vertical mean velocity (W/U_0)

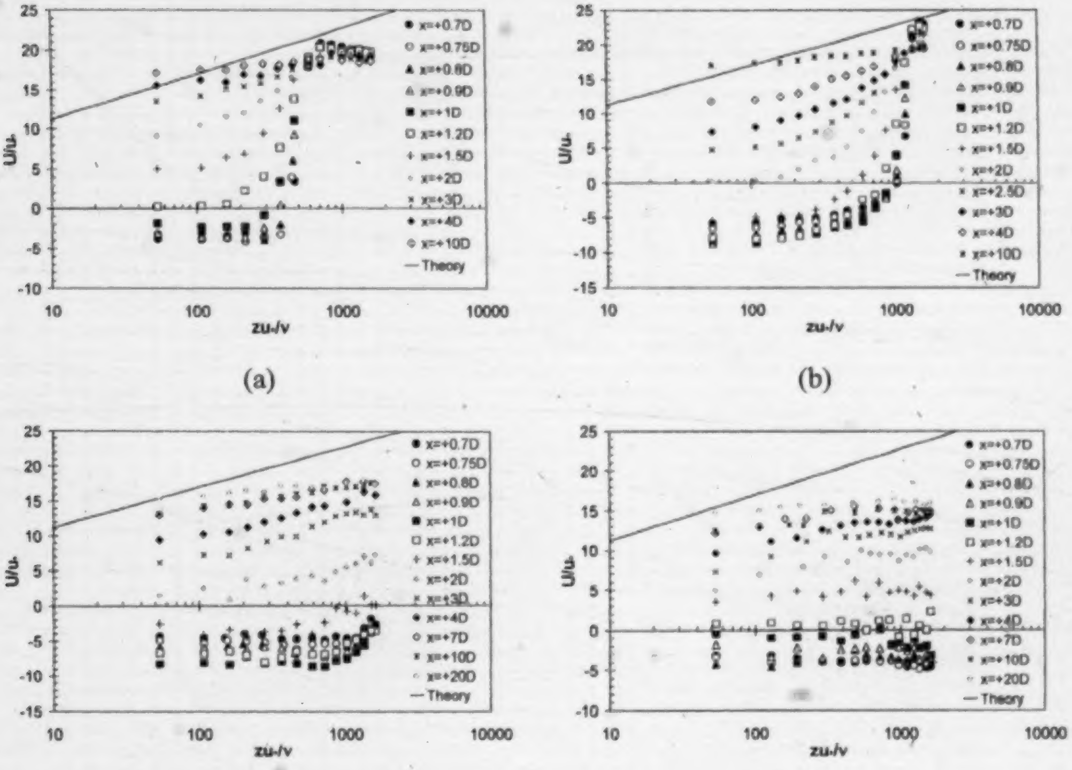

(a) (b)

(c) (d)

Fig. 6.22 Logarithmic velocity profiles on downstream POS: Smooth bed; (a) Regime-1, (b) Regime-2, (c) Regime-3, and (d) Regime-4

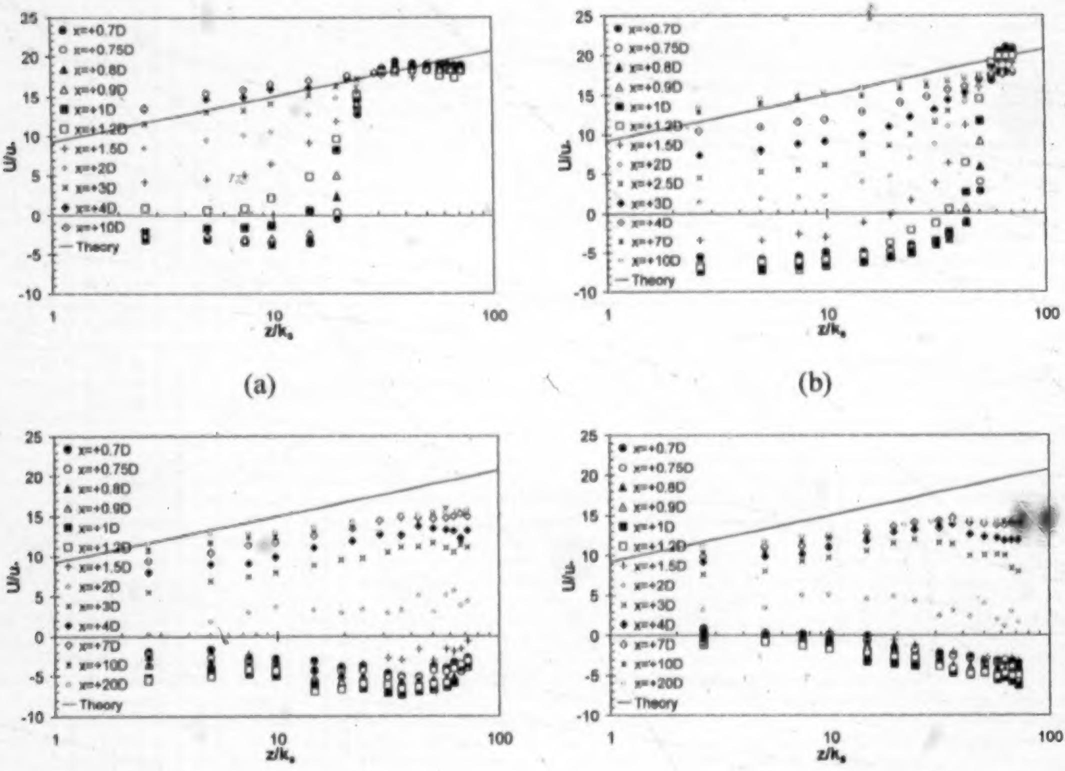

(a) (b)

(c) (d)

Fig. 6.23 Logarithmic velocity profiles on downstream POS: Rough bed; (a) Regime-1, (b) Regime-2, (c) Regime-3, and (d) Regime-4

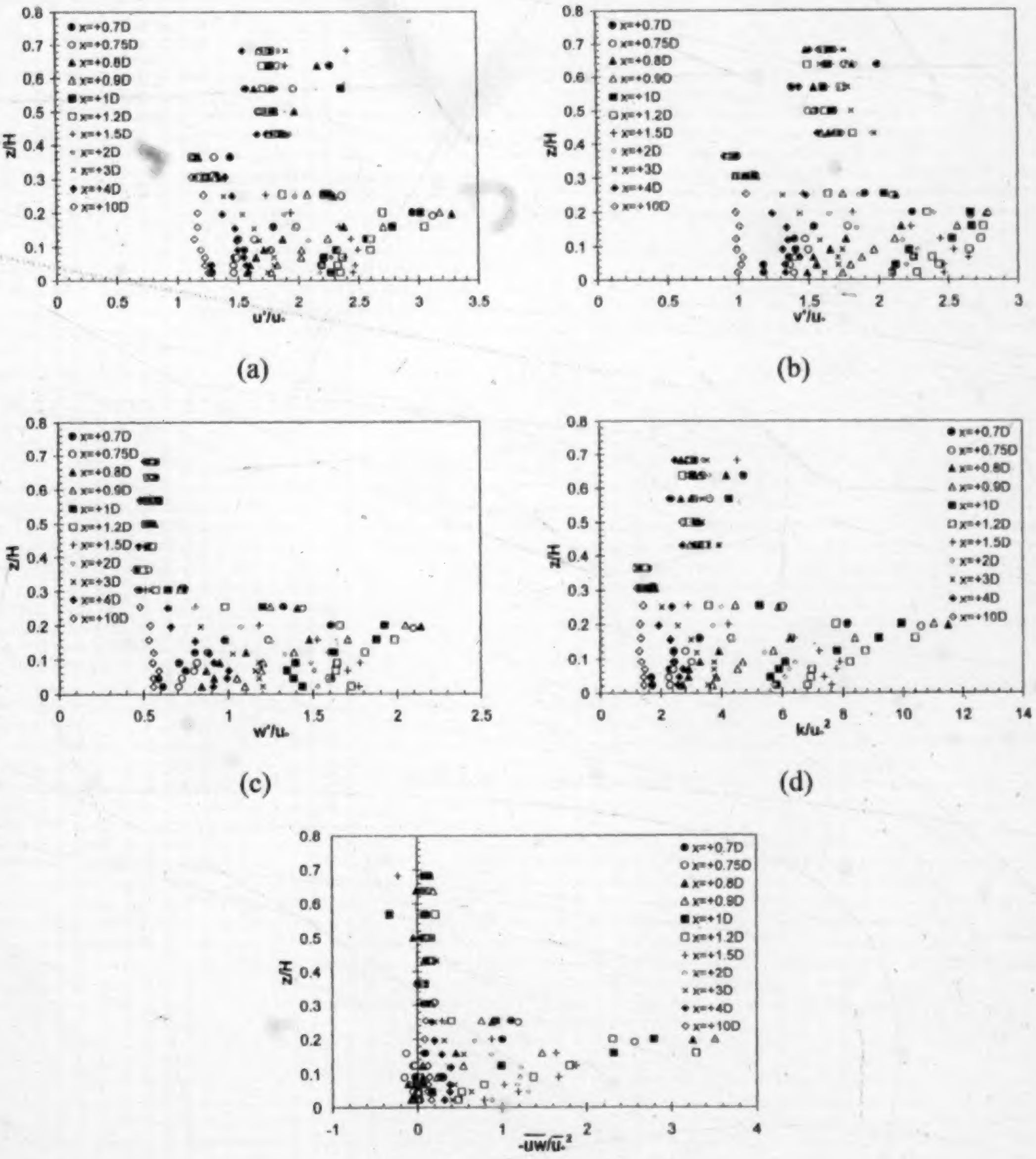

(a)

(b)

(c)

(d)

(e)

Fig. 6.24 Normalized profiles of turbulence quantities (a) longitudinal r.m.s. velocity, (b) transverse r.m.s. velocity, (c) vertical r.m.s. velocity, (d) turbulent kinetic energy, and (e) primary Reynolds stress on downstream POS: Smooth bed/Regime-1

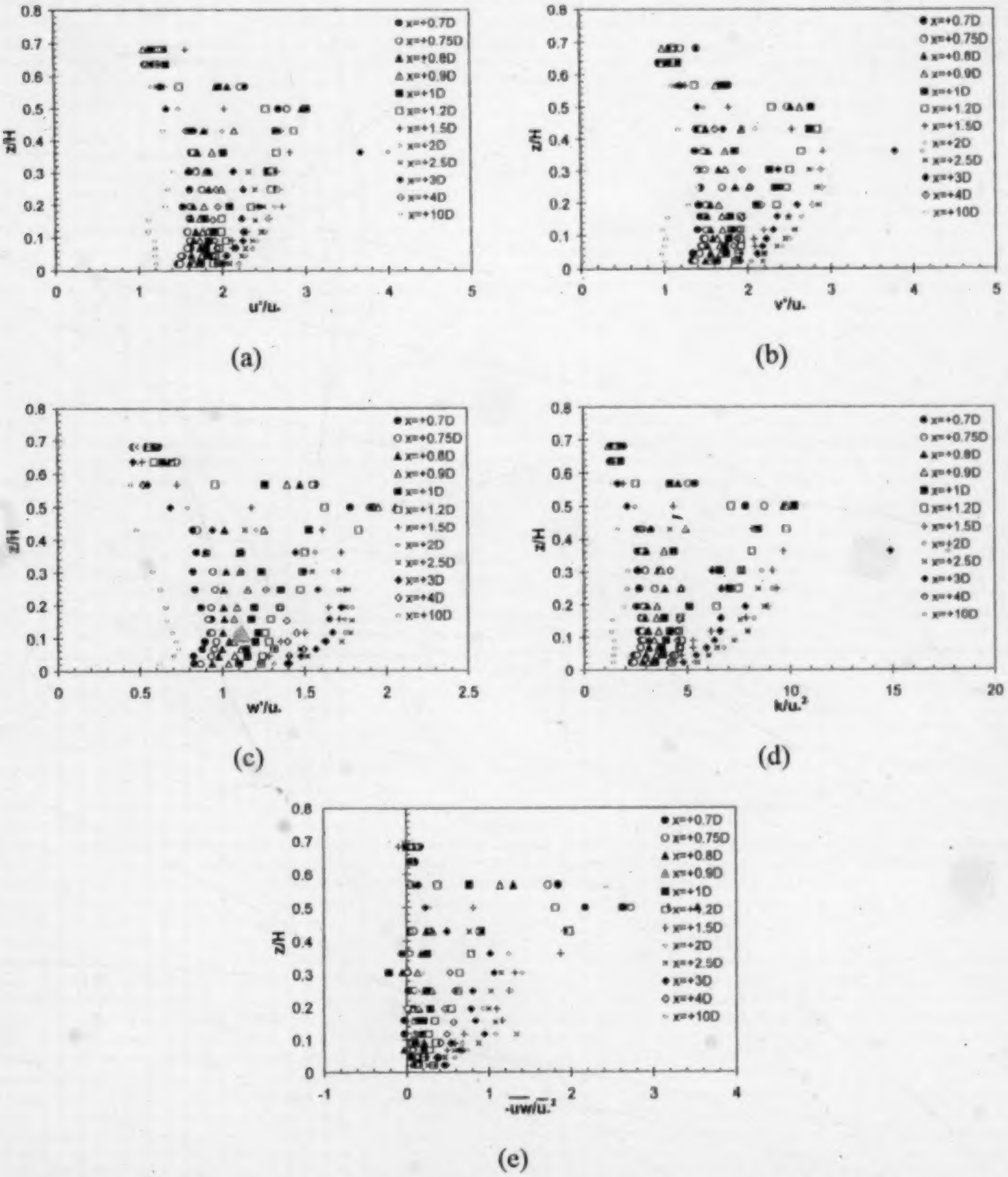

Fig. 6.25 Normalized profiles of turbulence quantities (a) longitudinal r.m.s. velocity, (b) transverse r.m.s. velocity, (c) vertical r.m.s. velocity, (d) turbulent kinetic energy, and (e) primary Reynolds stress on downstream POS: Smooth bed/Regime-2

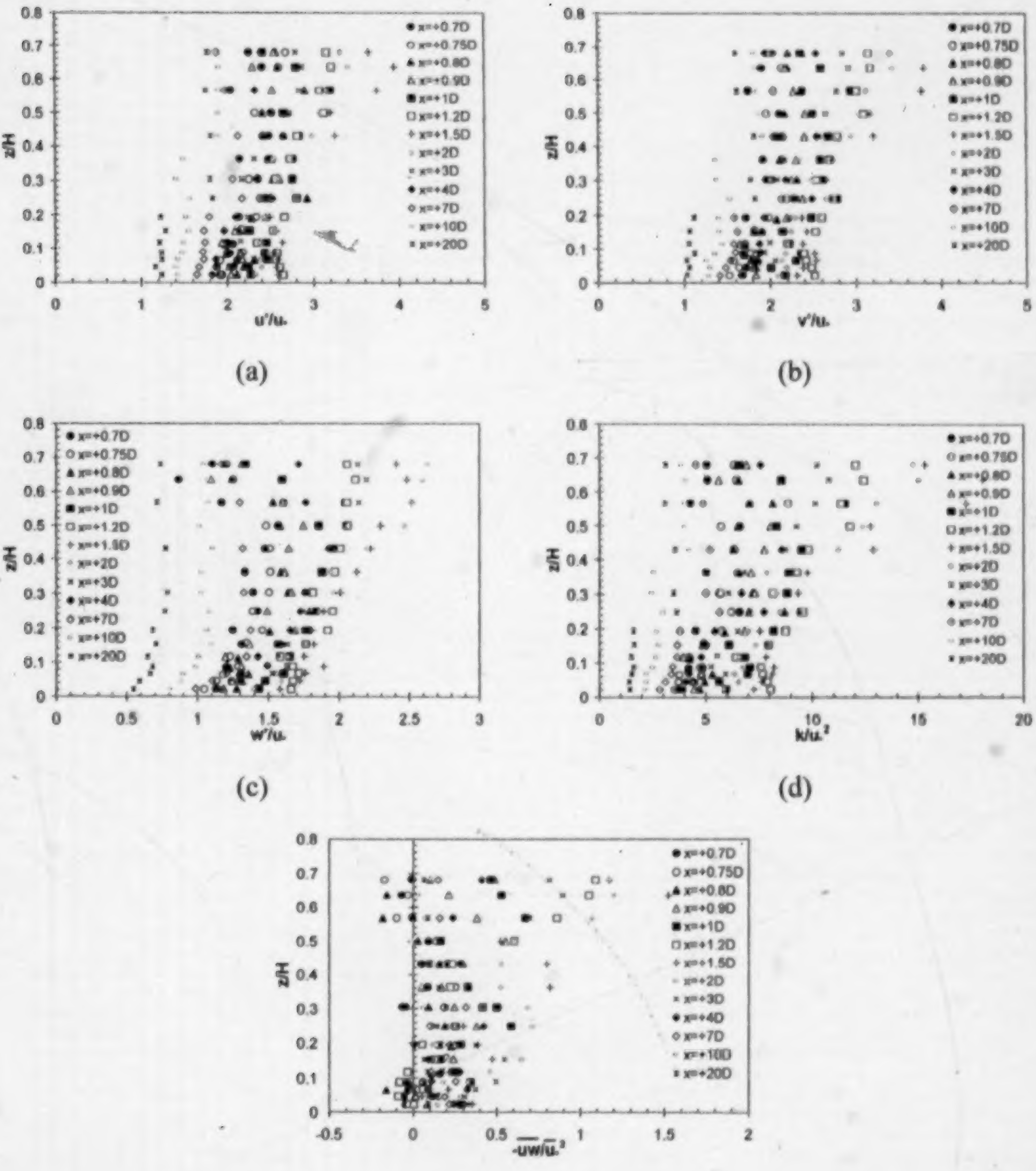

(a) (b)

(c) (d)

(e)

Fig. 6.26 Normalized profiles of turbulence quantities (a) longitudinal r.m.s. velocity, (b) transverse r.m.s. velocity, (c) vertical r.m.s. velocity, (d) turbulent kinetic energy, and (e) primary Reynolds stress on downstream POS: Smooth bed/Regime-3

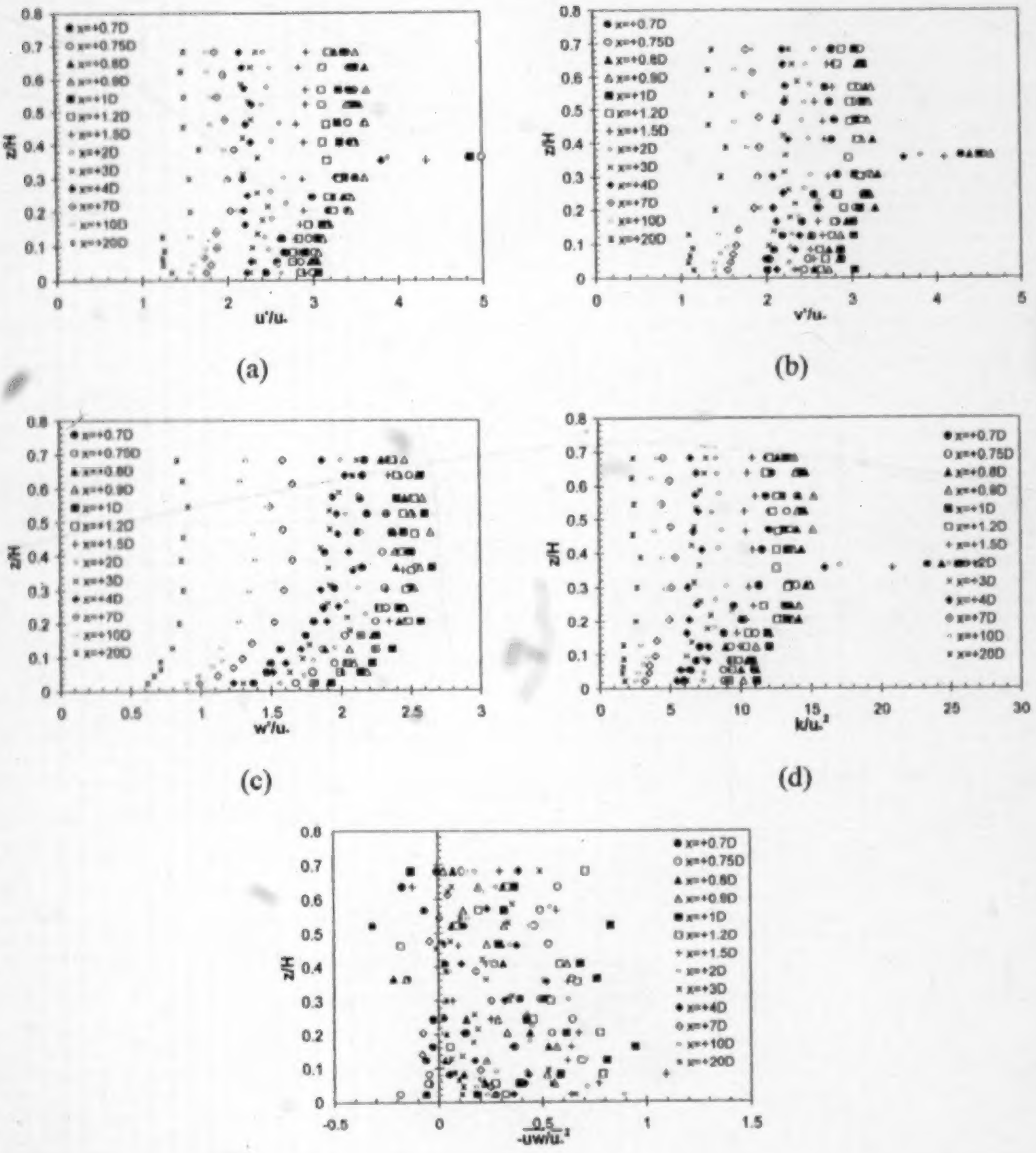

(a) (b) (c) (d) (e)

Fig. 6.27 Normalized profiles of turbulence quantities (a) longitudinal r.m.s. velocity, (b) transverse r.m.s. velocity, (c) vertical r.m.s. velocity, (d) turbulent kinetic energy, and (e) primary Reynolds stress on downstream POS: Smooth bed/Regime-4

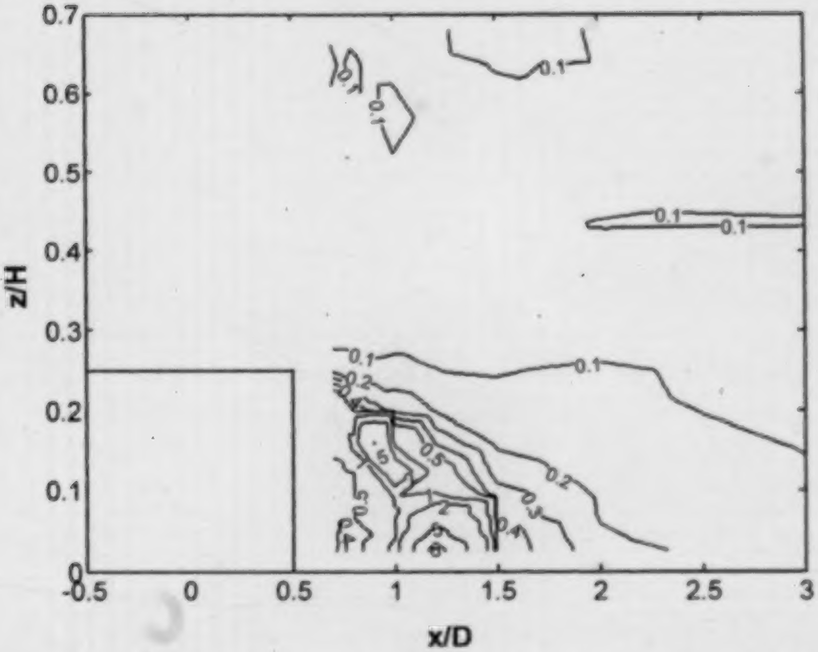

Fig. 6.28(a) Longitudinal turbulent intensity contour on DPOS: Smooth bed/Regime-1

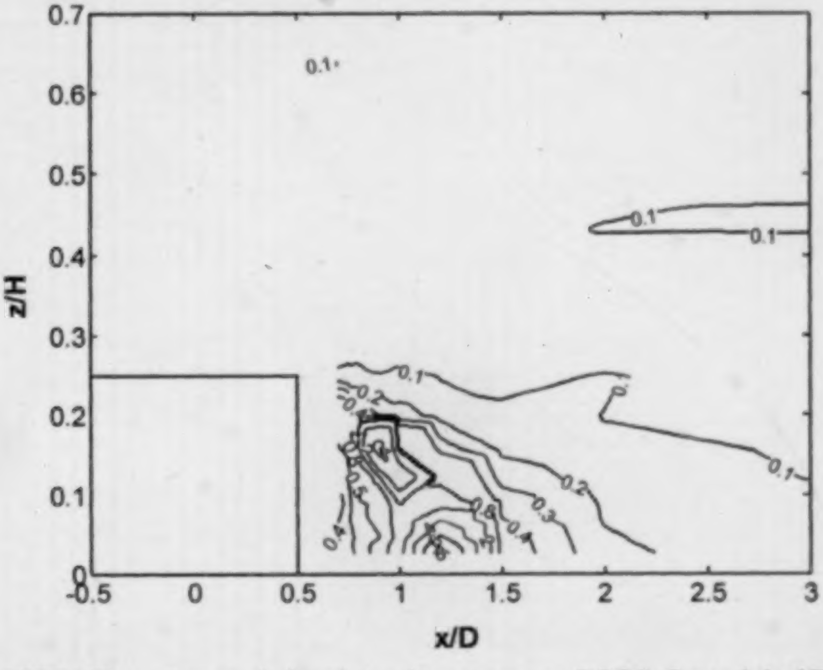

Fig. 6.28(b) Transverse turbulent intensity contour on DPOS: Smooth bed/Regime-1

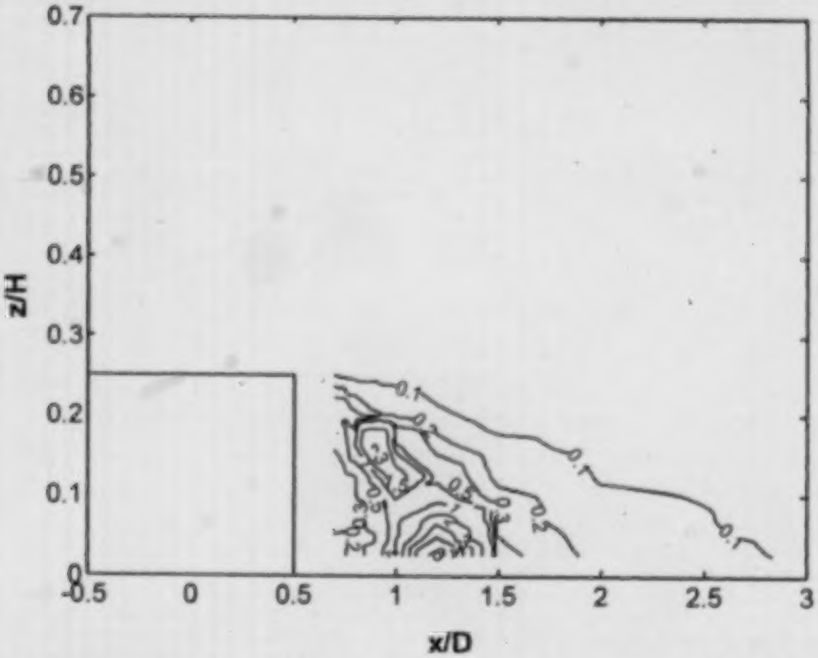

Fig. 6.28(c) Vertical turbulent intensity contour on DPOS: Smooth bed/Regime-1

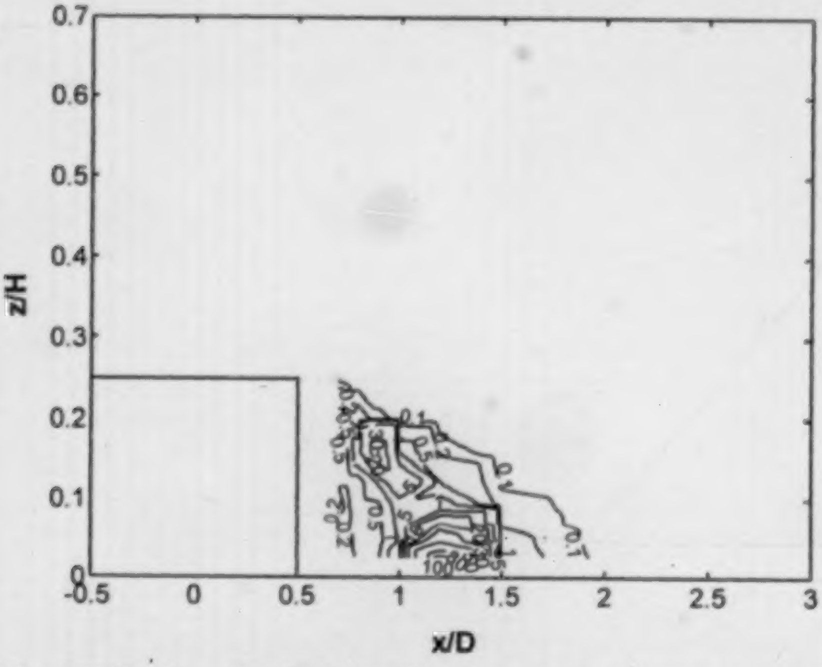

Fig. 6.28(d) Normalized turbulent kinetic energy (k/U^2) contour on DPOS:

Smooth bed/Regime-1

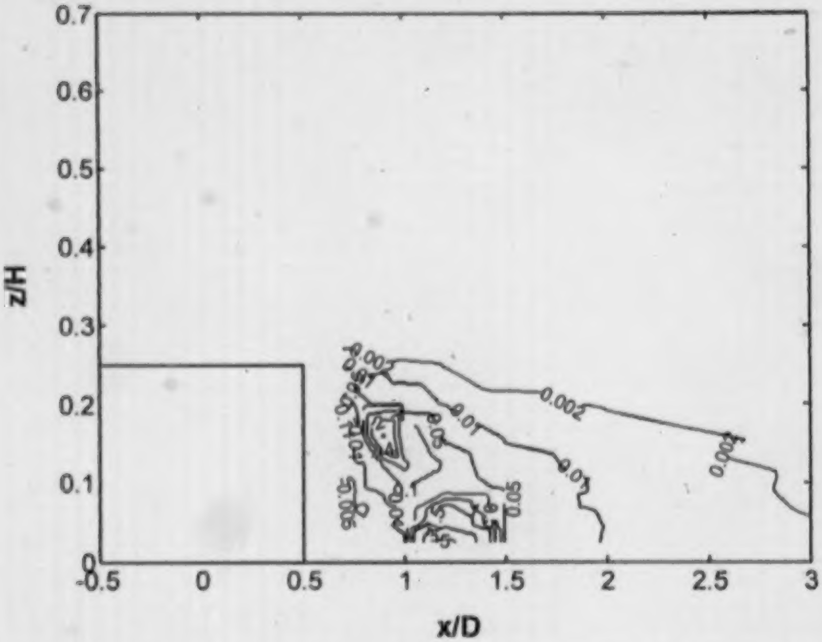

Fig. 6.28(e) Normalized primary Reynolds stress ($-\overline{uw}/U^2$) contour on DPOS: Smooth bed/Regime-1

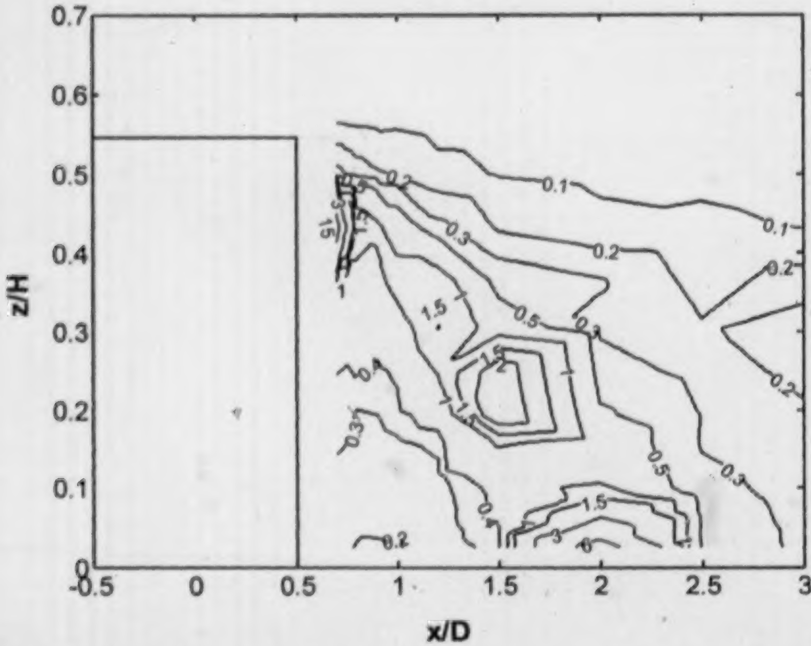

Fig. 6.29(a) Longitudinal turbulent intensity contour on DPOS: Smooth bed/Regime-2

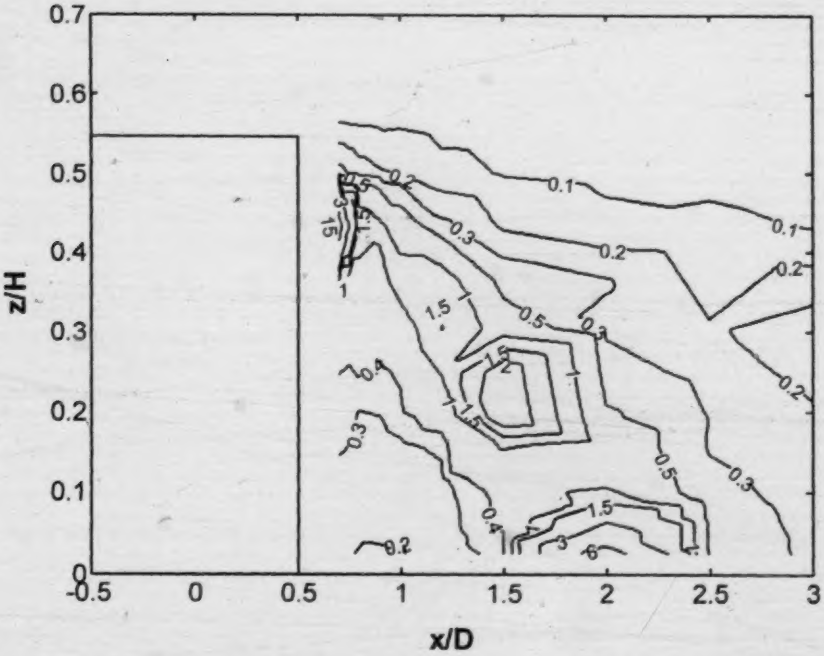

Fig. 6.29(b) Transverse turbulent intensity contour on DPOS: Smooth bed/Regime-2

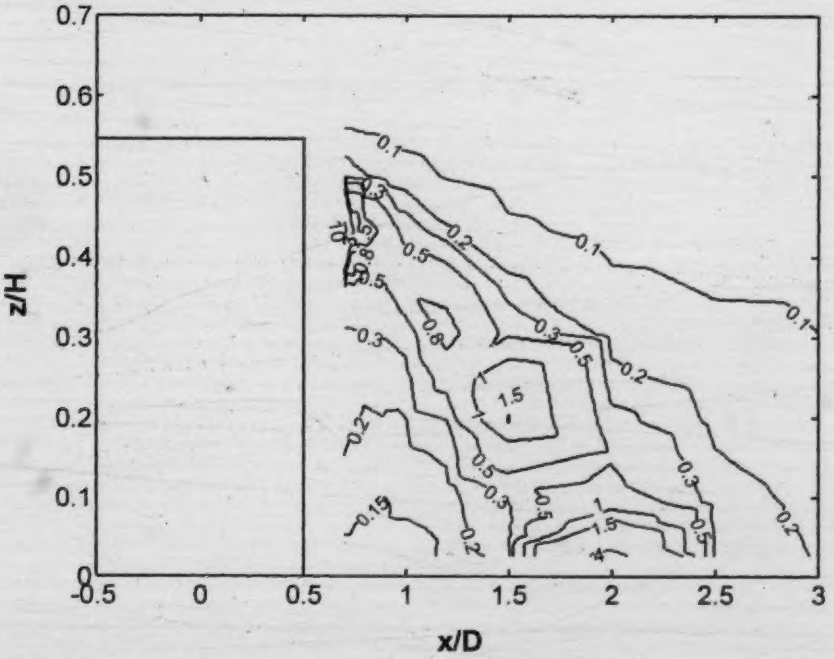

Fig. 6.29(c) Vertical turbulent intensity contour on DPOS: Smooth bed/Regime-2

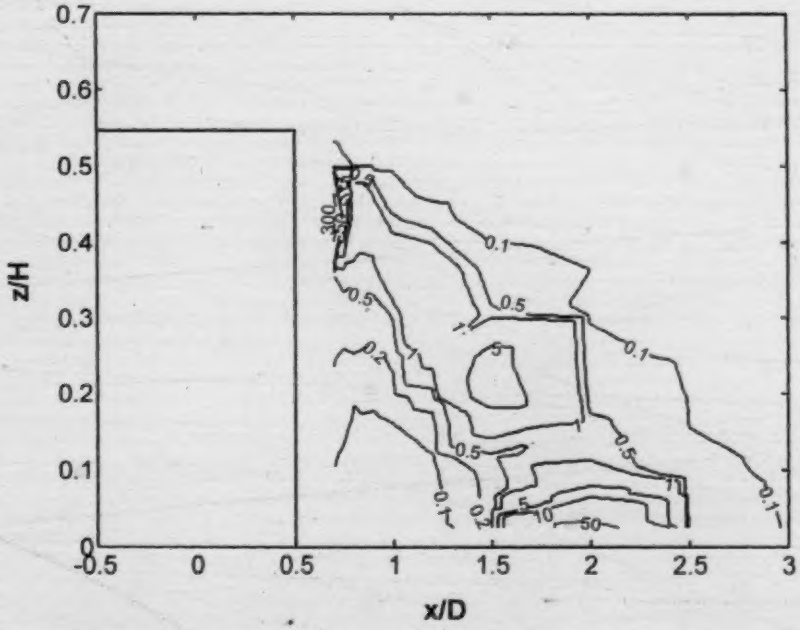

Fig. 6.29(d) Normalized turbulent kinetic energy (k/U^2) contour on DPOS:

Smooth bed/Regime-2

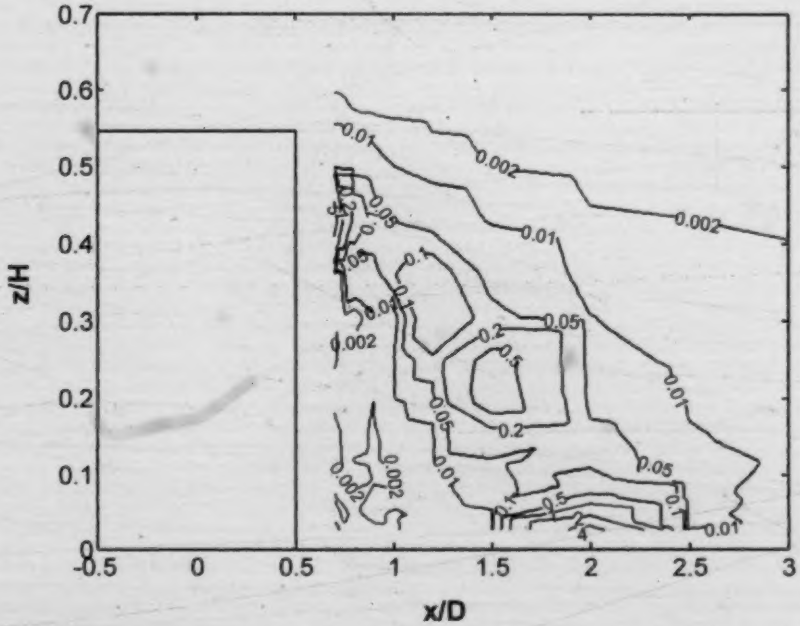

Fig. 6.29(e) Normalized primary Reynolds stress ($-\overline{uw}/U^2$) contour on DPOS:

Smooth bed/Regime-2

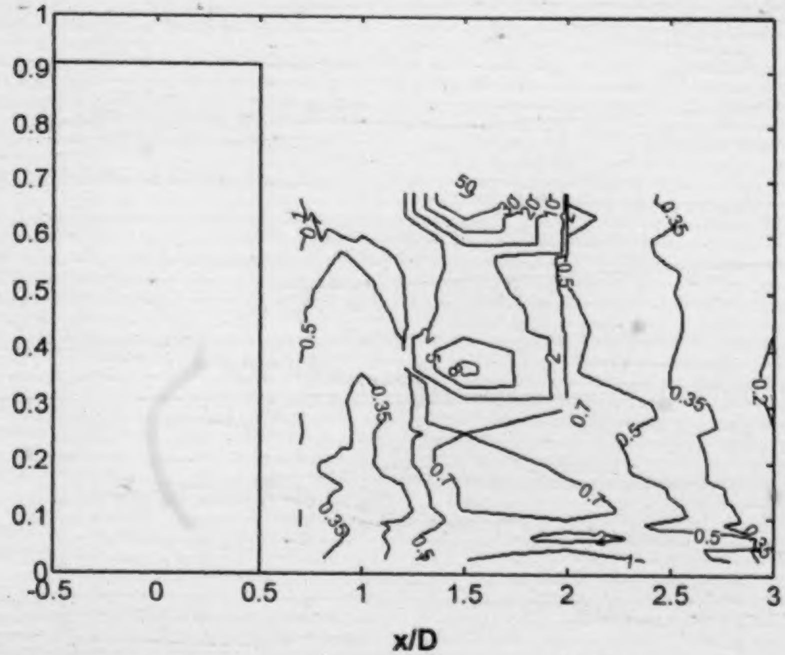

Fig. 6.30(a) Longitudinal turbulent intensity contour on DPOS: Smooth bed/Regime-3

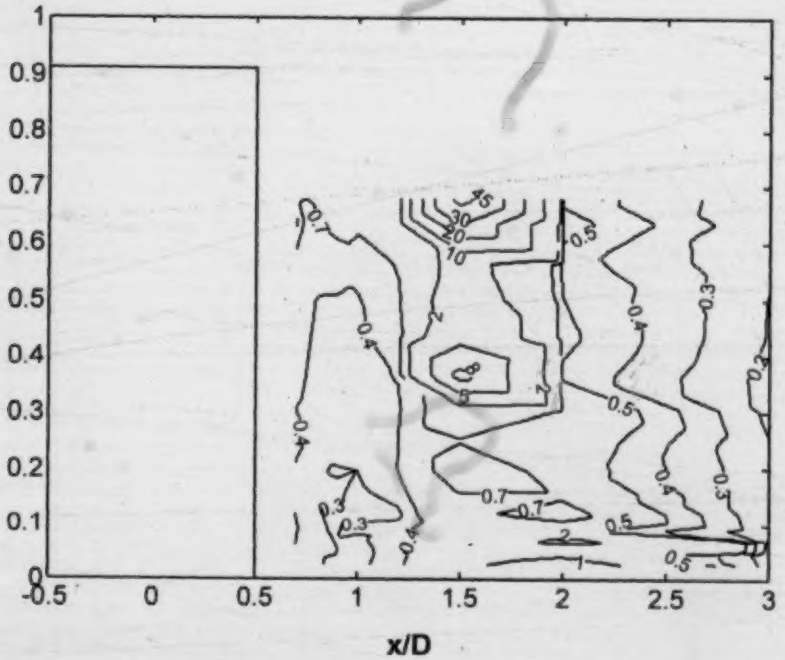

Fig. 6.30(b) Transverse turbulent intensity contour on DPOS: Smooth bed/Regime-3

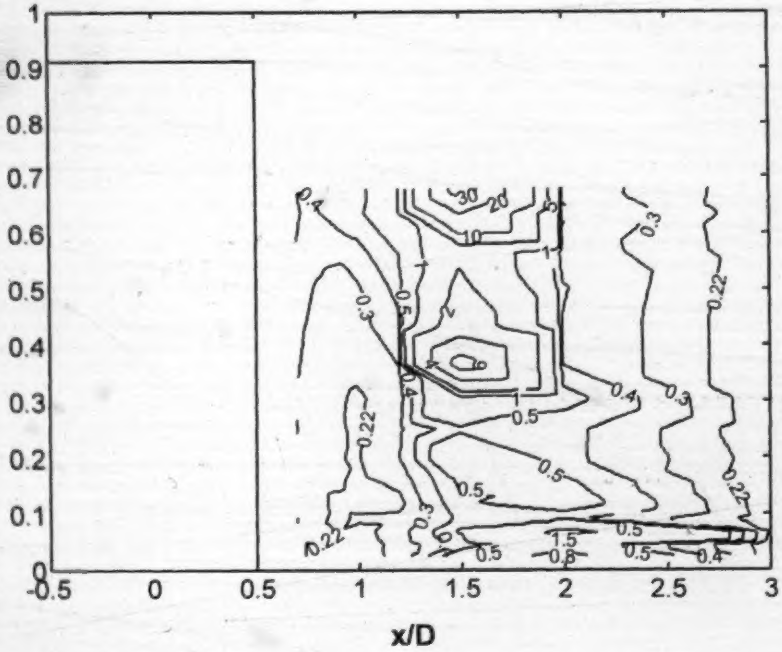

Fig. 6.30(c) Vertical turbulent intensity contour on DPOS: Smooth bed/Regime-3

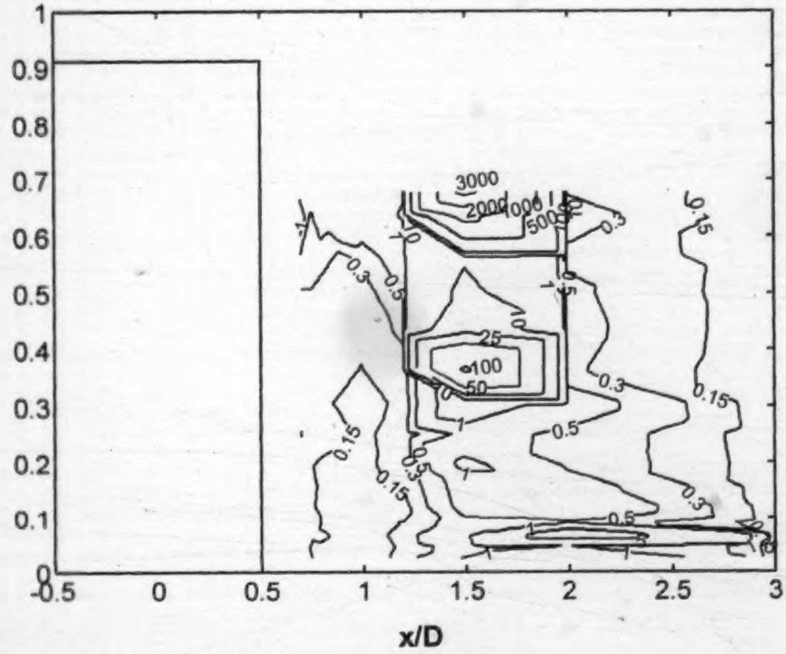

Fig. 6.30(d) Normalized turbulent kinetic energy (k/U^2) contour on DPOS:

Smooth bed/Regime-3

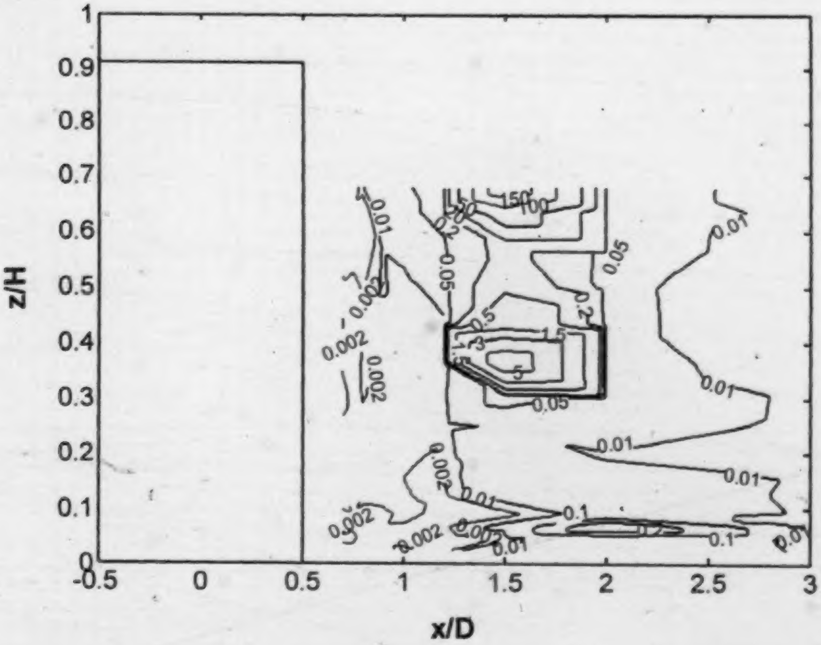

Fig. 6.30(e) Normalized primary Reynolds stress ($-\overline{uw}/U^2$) contour on DPOS: Smooth bed/Regime-3

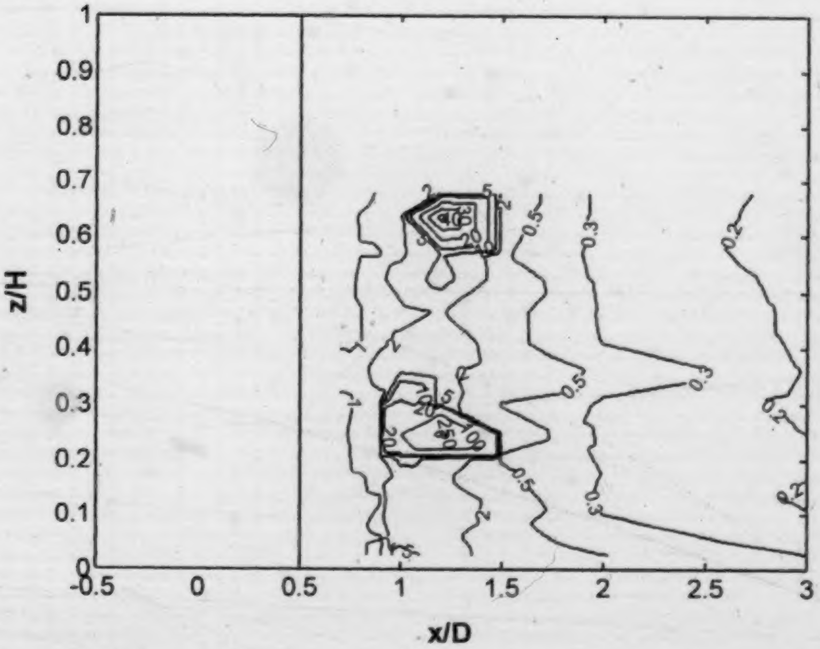

Fig. 6.31(a) Longitudinal turbulent intensity contour on DPOS: Smooth bed/Regime-4

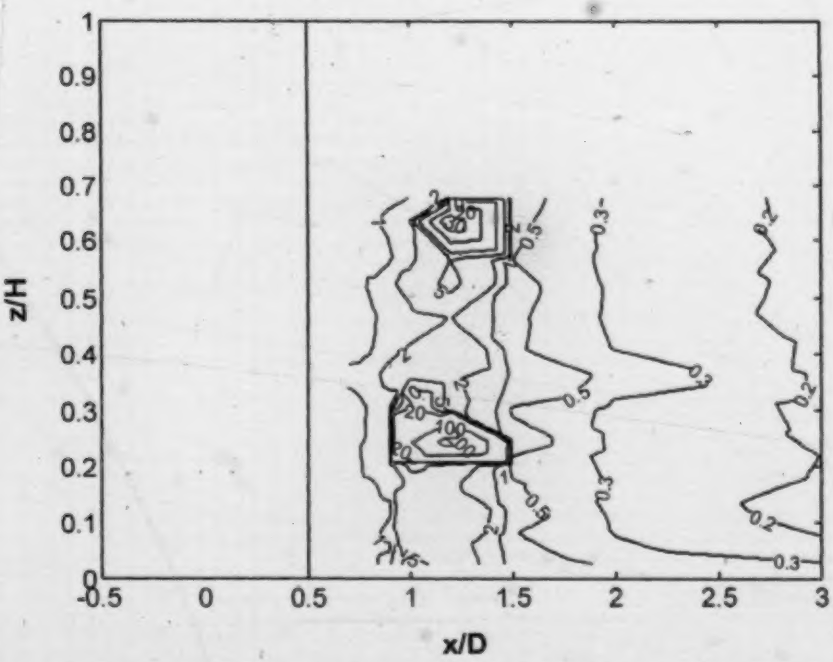

Fig. 6.31(b) Transverse turbulent intensity contour on DPOS: Smooth bed/Regime-4

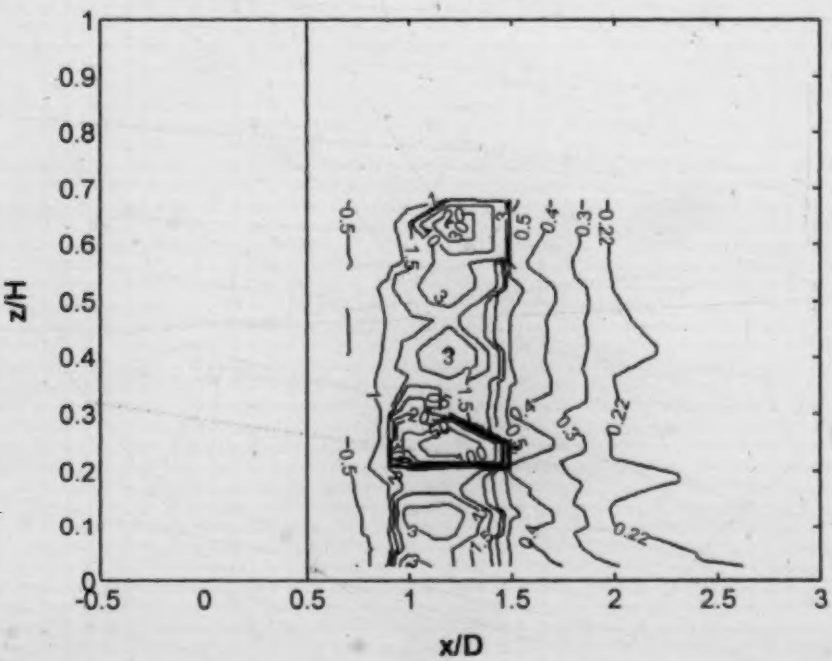

Fig. 6.31(c) Vertical turbulent intensity contour on DPOS: Smooth bed/Regime-4

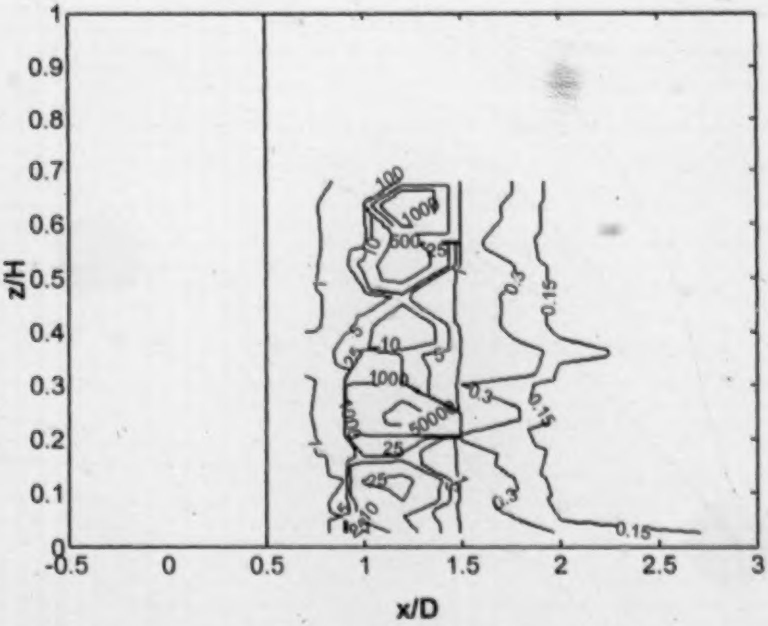

Fig. 6.31(d) Normalized turbulent kinetic energy (k/U^2) contour on DPOS: Smooth bed/Regime-4

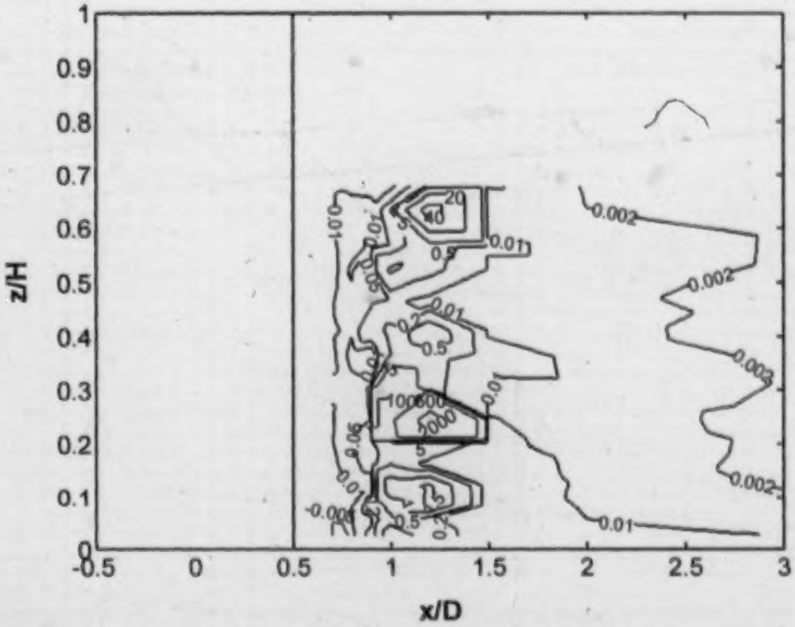

Fig. 6.31(e) Normalized primary Reynolds stress ($-\overline{uw}/U^2$) contour on DPOS: Smooth bed/Regime-4

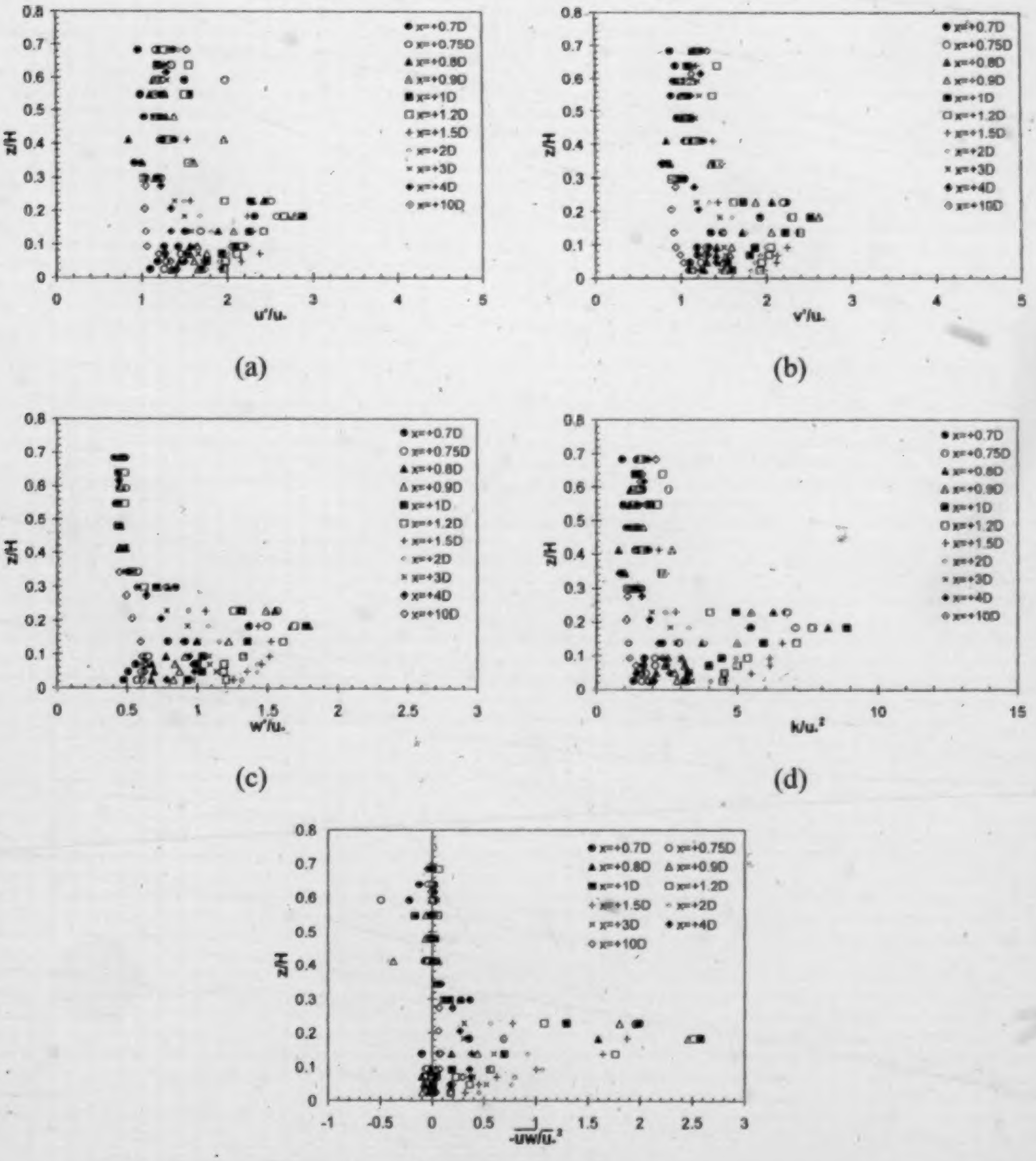

(a) (b)

(c) (d)

(e)

Fig. 6.32 Normalized profiles of turbulence quantities (a) longitudinal r.m.s. velocity, (b) transverse r.m.s. velocity, (c) vertical r.m.s. velocity, (d) turbulent kinetic energy, and (e) primary Reynolds stress on downstream POS: Rough bed/Regime-1

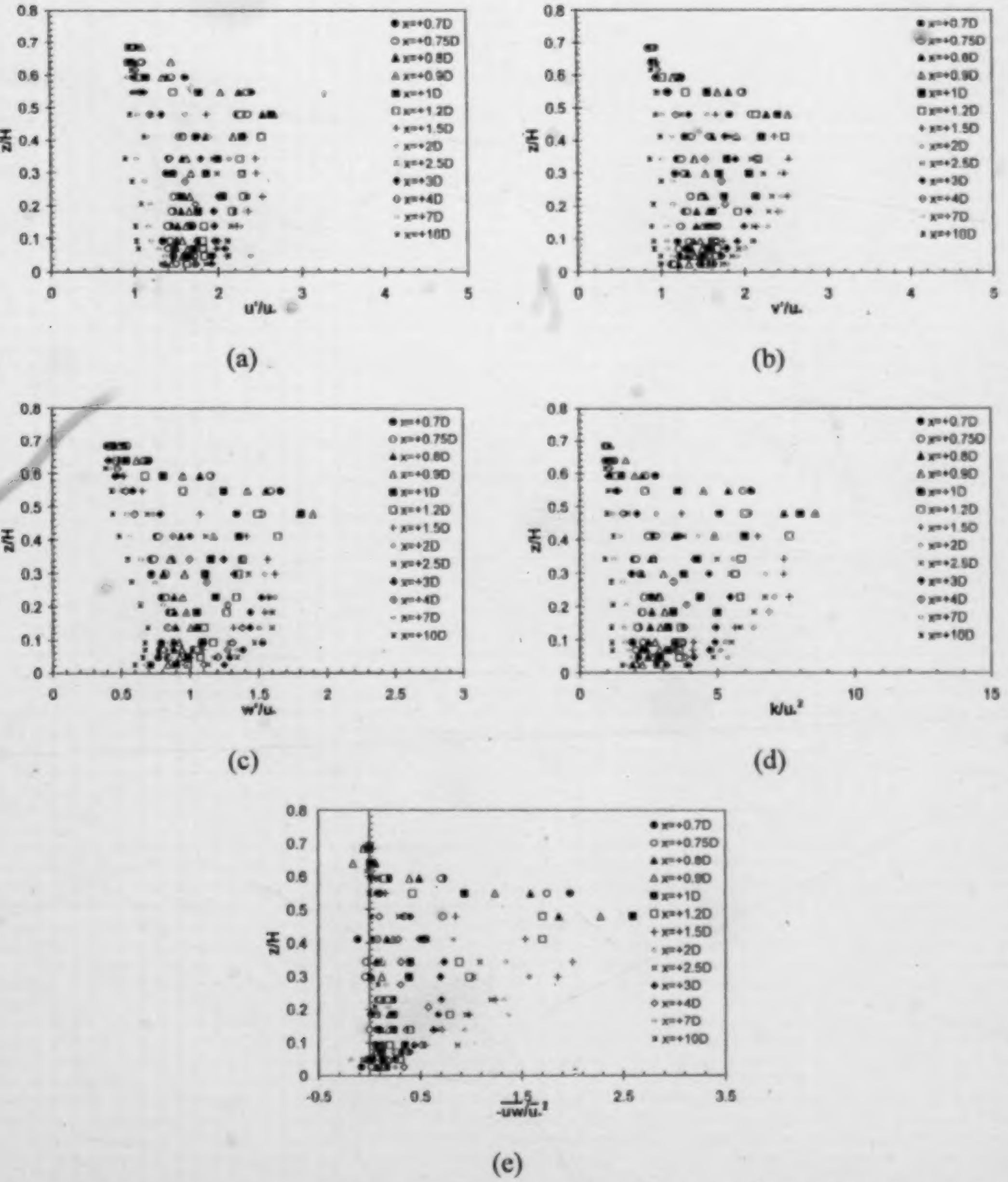

(a) (b)

(c) (d)

(e)

Fig. 6.33 Normalized profiles of turbulence quantities (a) longitudinal r.m.s. velocity, (b) transverse r.m.s. velocity, (c) vertical r.m.s. velocity, (d) turbulent kinetic energy, and (e) primary Reynolds stress on downstream POS: Rough bed/Regime-2

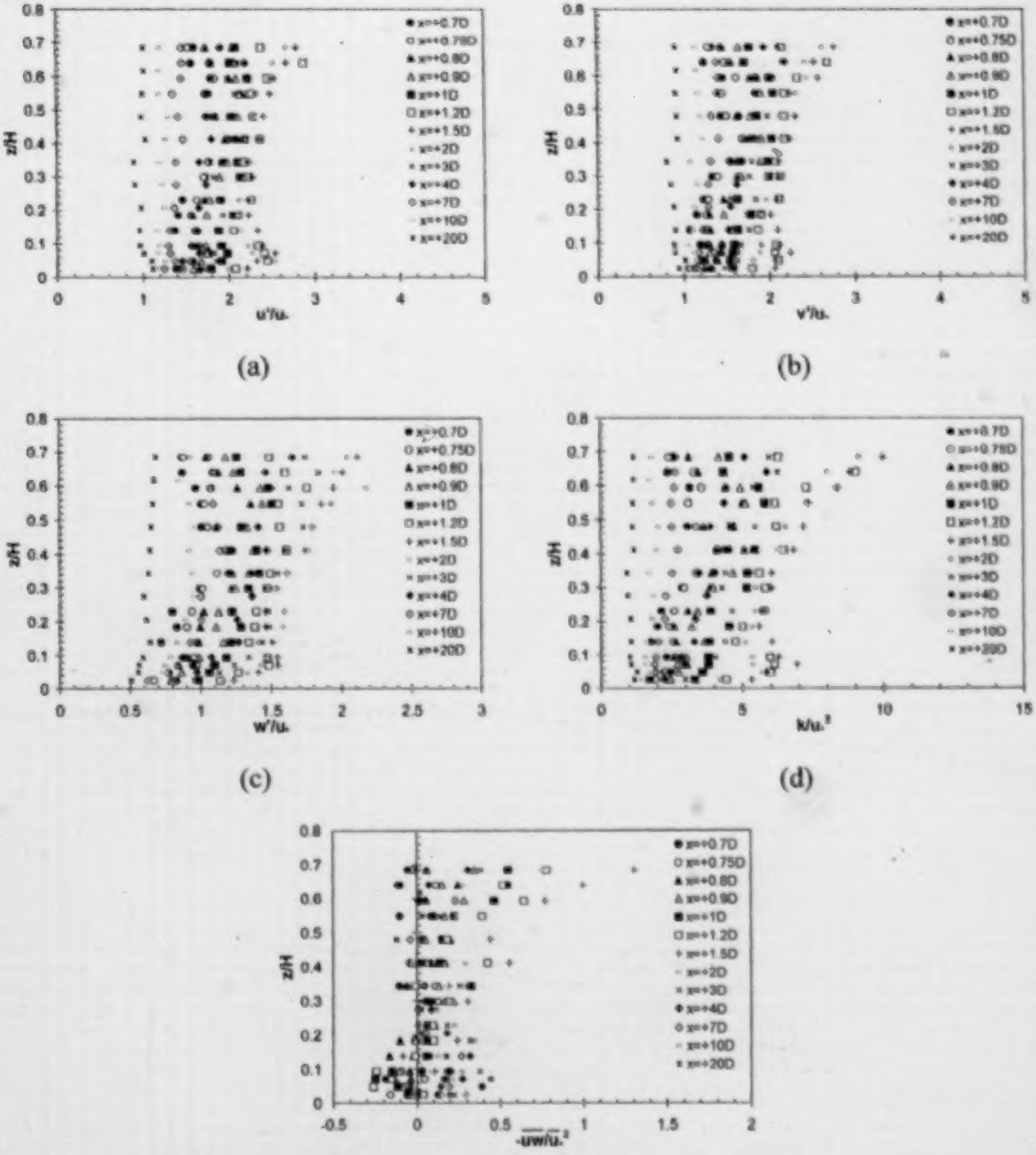

(a) (b)

(c) (d)

(e)

Fig. 6.34 Normalized profiles of turbulence quantities (a) longitudinal r.m.s. velocity, (b) transverse r.m.s. velocity, (c) vertical r.m.s. velocity, (d) turbulent kinetic energy, and (e) primary Reynolds stress on downstream POS: Rough bed/Regime-3

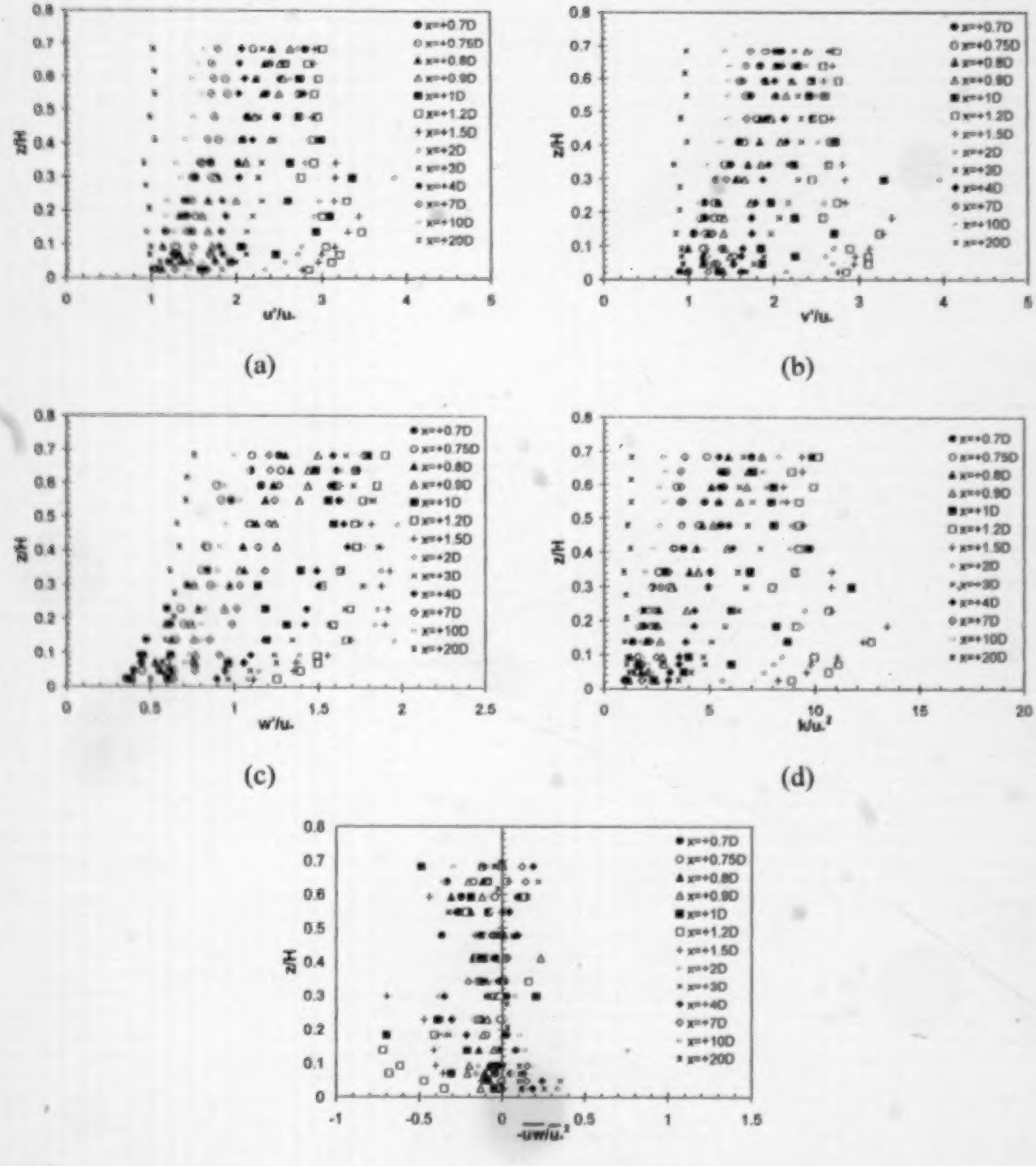

(a) (b) (c) (d) (e)

Fig. 6.35 Normalized profiles of turbulence quantities (a) longitudinal r.m.s. velocity, (b) transverse r.m.s. velocity, (c) vertical r.m.s. velocity, (d) turbulent kinetic energy, and (e) primary Reynolds stress on downstream POS: Rough bed/Regime-4

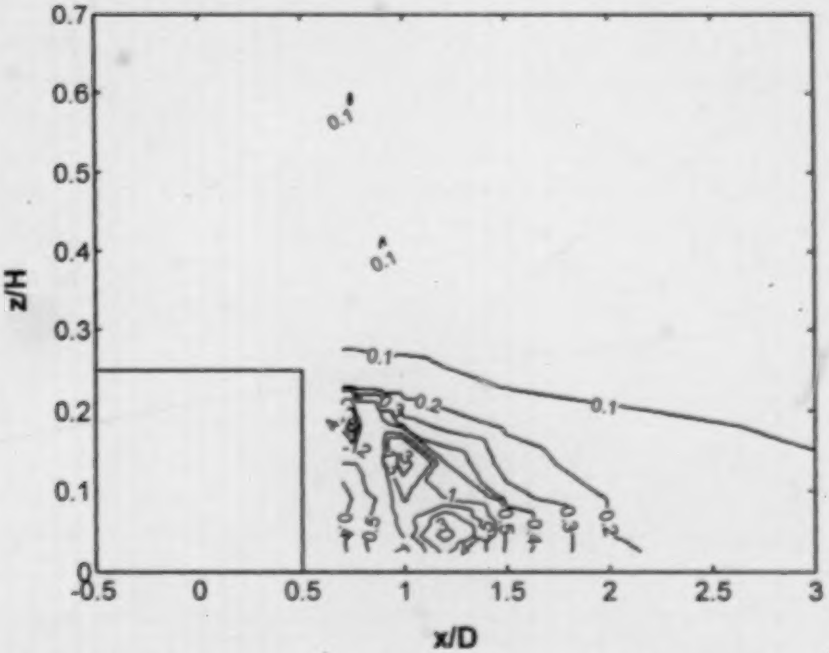

Fig. 6.36(a) Longitudinal turbulent intensity contour on DPOS: Rough bed/Regime-1

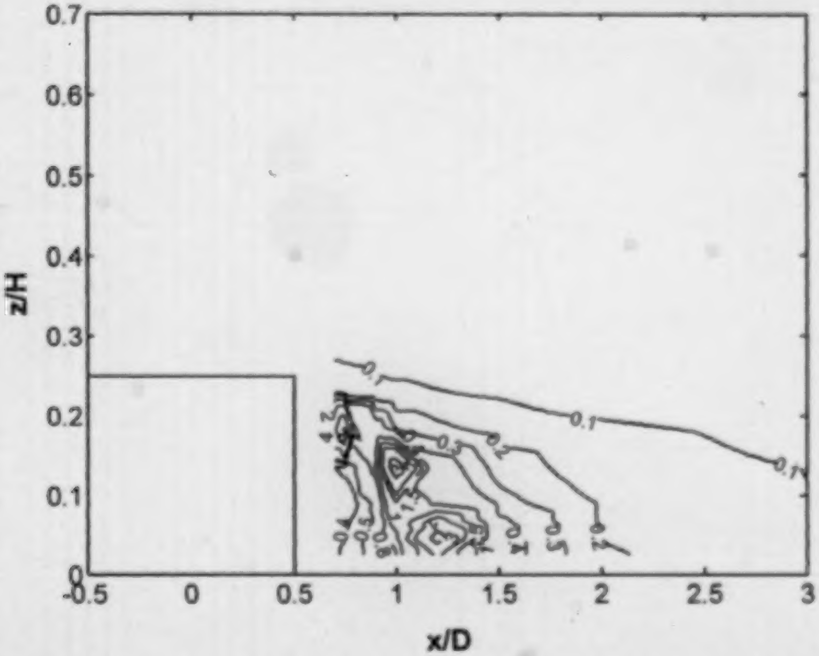

Fig. 6.36(b) Transverse turbulent intensity contour on DPOS: Rough bed/Regime-1

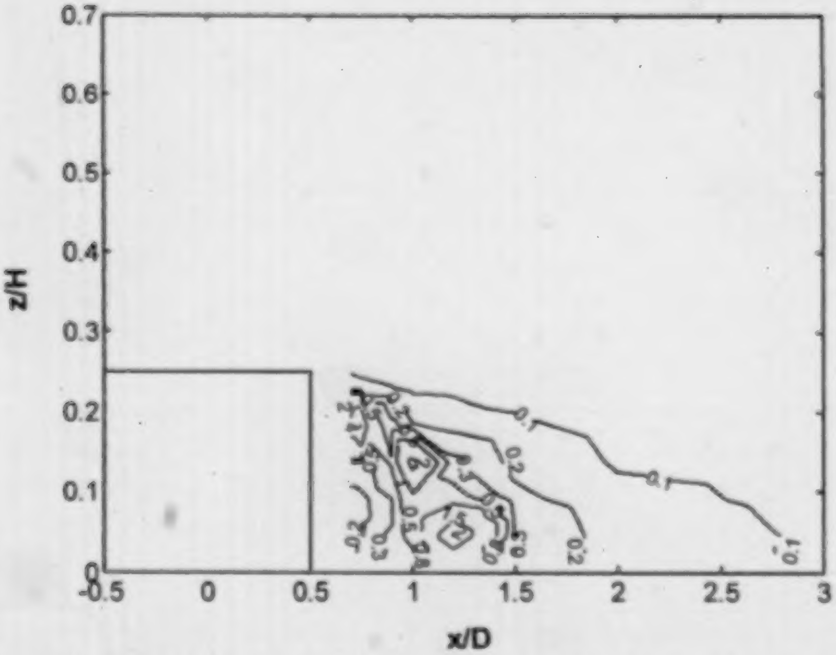

Fig. 6.36(c) Vertical turbulent intensity contour on DPOS: Rough bed/Regime-1

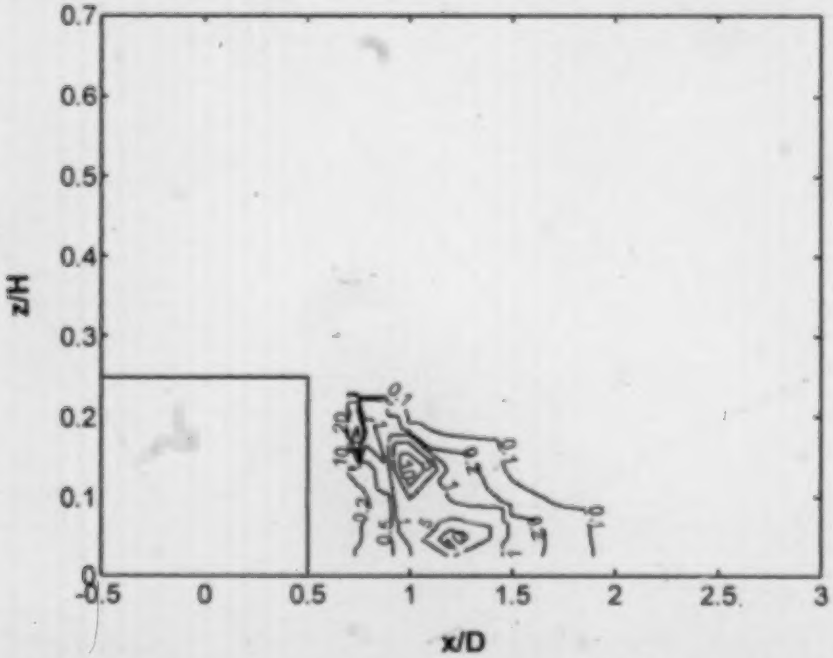

Fig. 6.36(d) Normalized turbulent kinetic energy (k/U^2) contour on DPOS: Rough bed/Regime-1

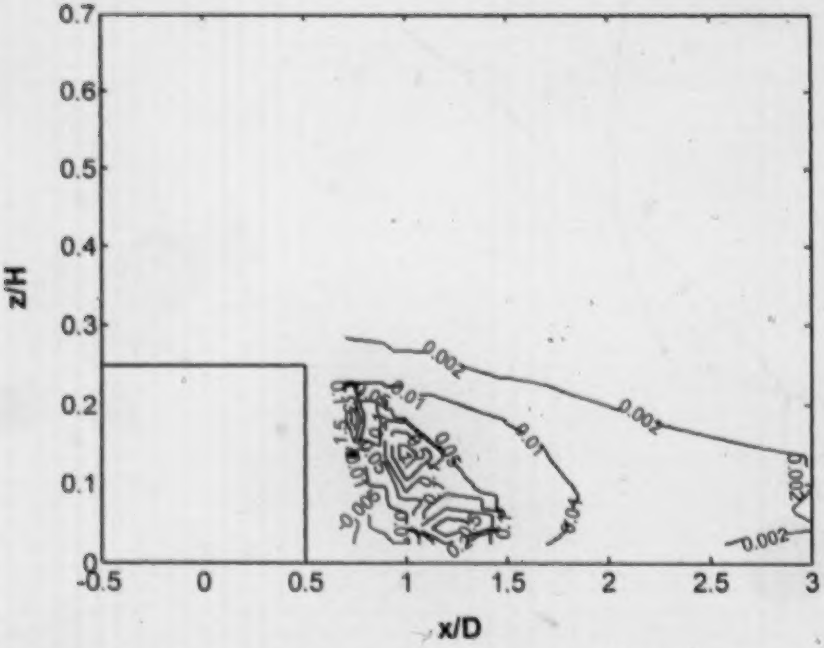

Fig. 6.36(e) Normalized primary Reynolds stress ($-\overline{uw}/U^2$) contour on DPOS: Rough bed/Regime-1

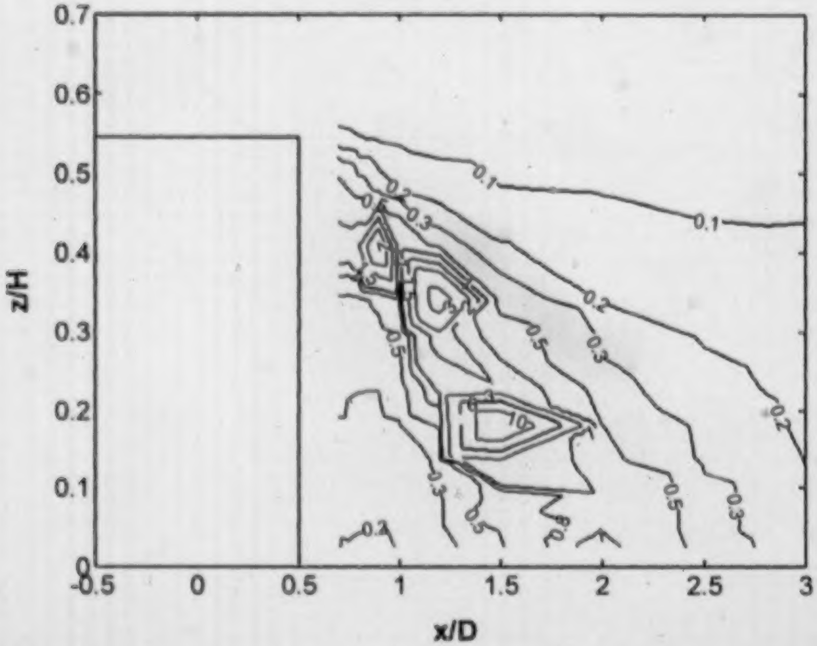

Fig. 6.37(a) Longitudinal turbulent intensity contour on DPOS: Rough bed/Regime-2

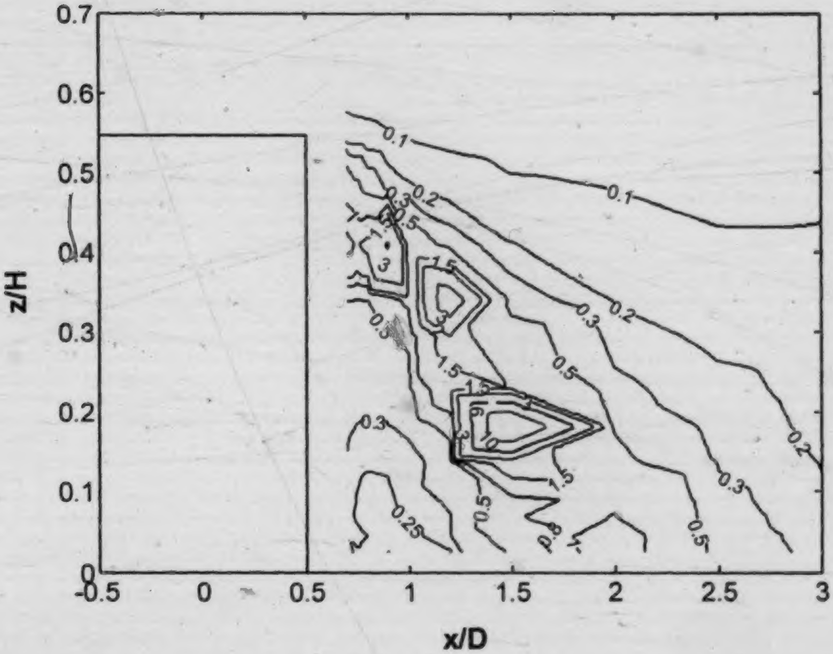

Fig. 6.37(b) Transverse turbulent intensity contour on DPOS: Rough bed/Regime-2

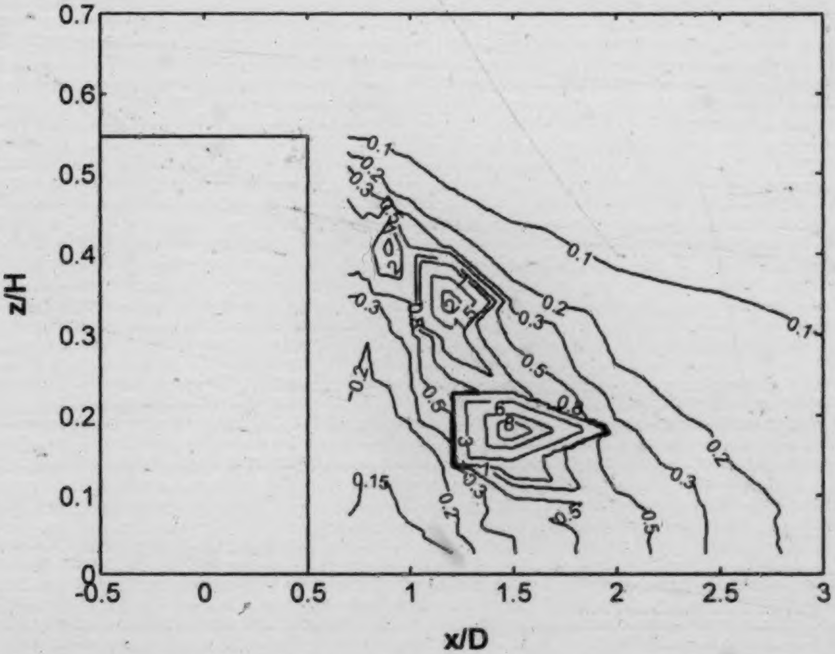

Fig. 6.37(c) Vertical turbulent intensity contour on DPOS: Rough bed/Regime-2

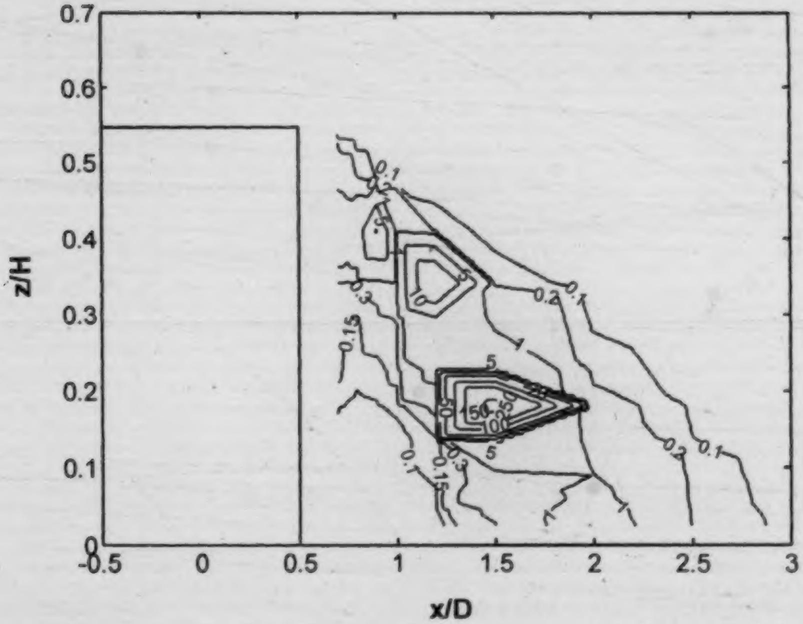

Fig. 6.37(d) Normalized turbulent kinetic energy (k/U^2) contour on DPOS: Rough bed/Regime-2

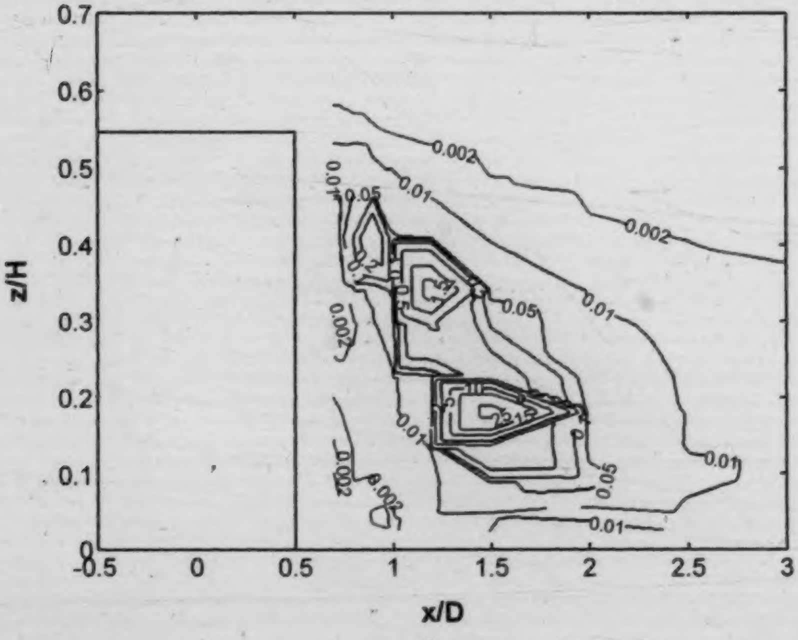

Fig. 6.37(e) Normalized primary Reynolds stress ($-\overline{uw}/U^2$) contour on DPOS: Rough bed/Regime-2

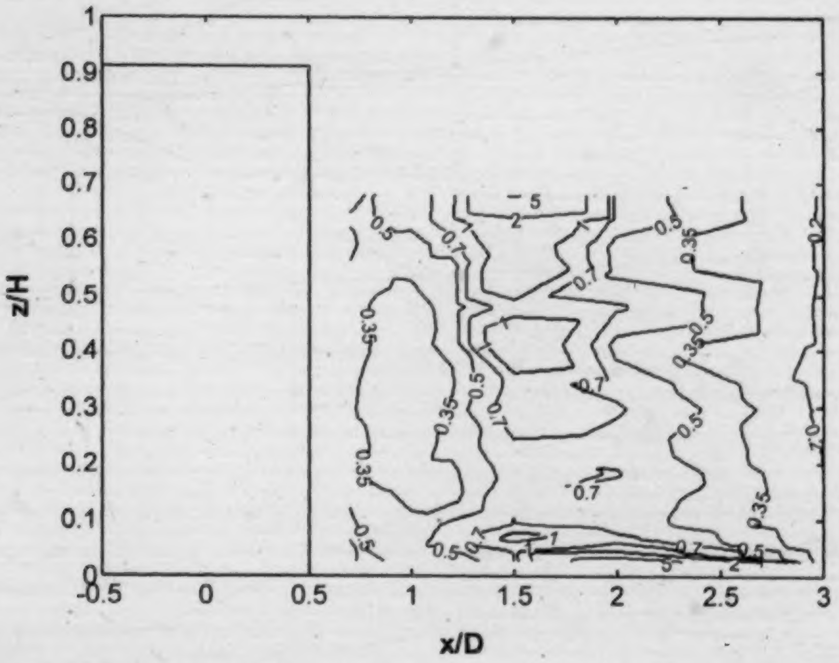

Fig. 6.38(a) Longitudinal turbulent intensity contour on DPOS: Rough bed/Regime-3

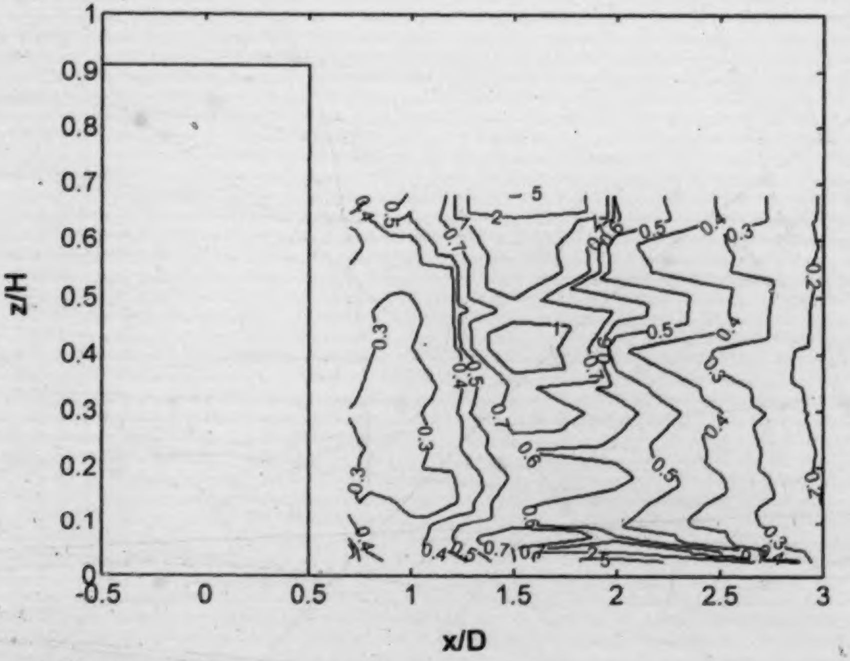

Fig. 6.38(b) Transverse turbulent intensity contour on DPOS: Rough bed/Regime-3

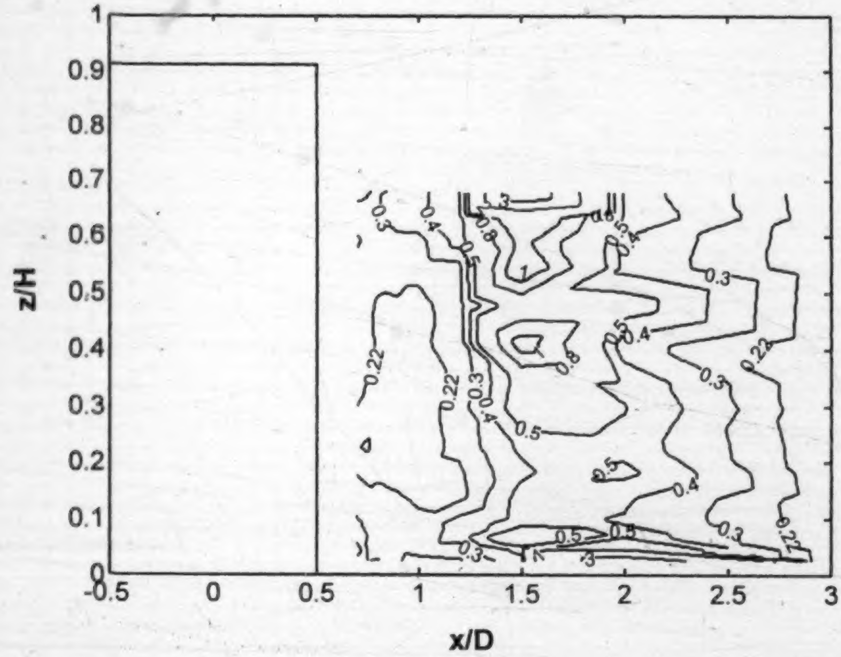

Fig. 6.38(c) Vertical turbulent intensity contour on DPOS: Rough bed/Regime-3

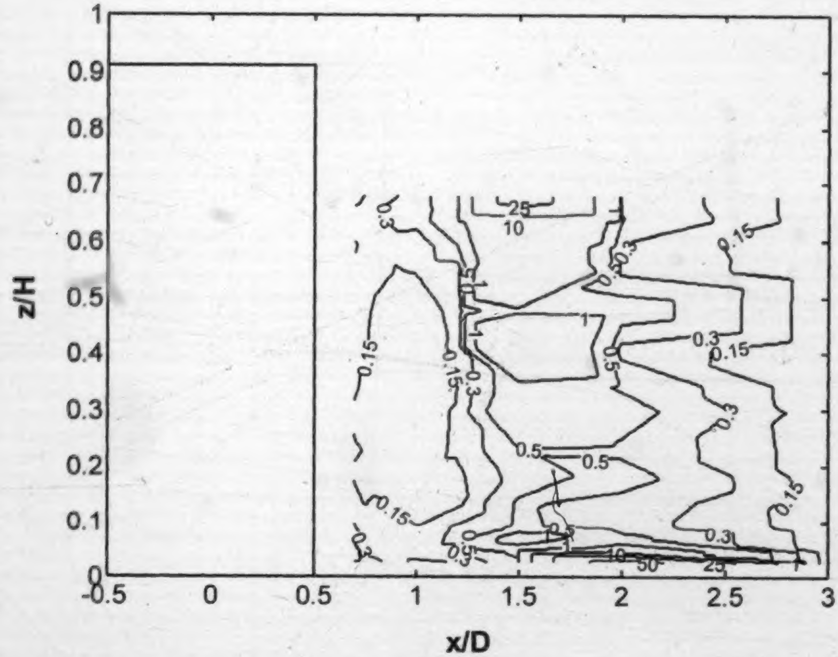

Fig. 6.38(d) Normalized turbulent kinetic energy (k/U^2) contour on DPOS: Rough bed/Regime-3

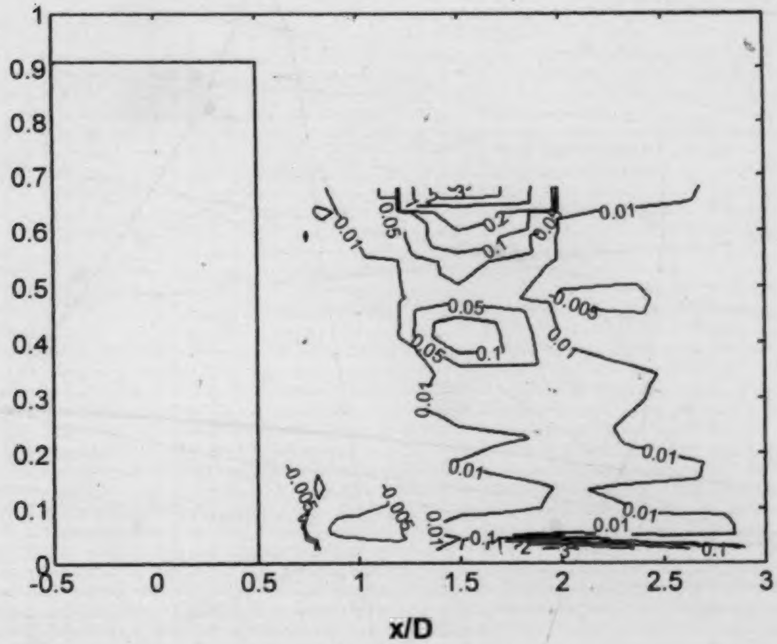

Fig. 6.38(e) Normalized primary Reynolds stress $(-\overline{uw}/U^2)$ contour on DPOS: Rough bed/Regime-3

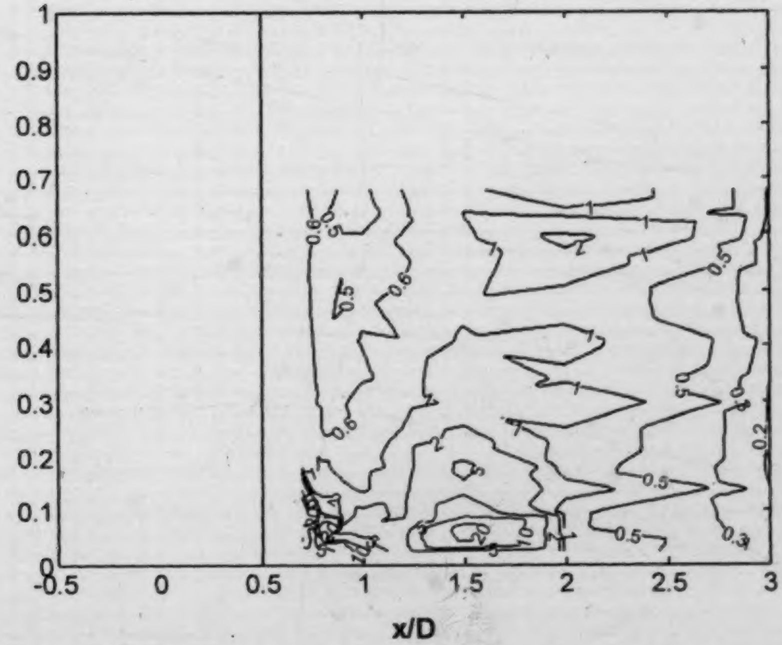

Fig. 6.39(a) Longitudinal turbulent intensity contour on DPOS: Rough bed/Regime-4

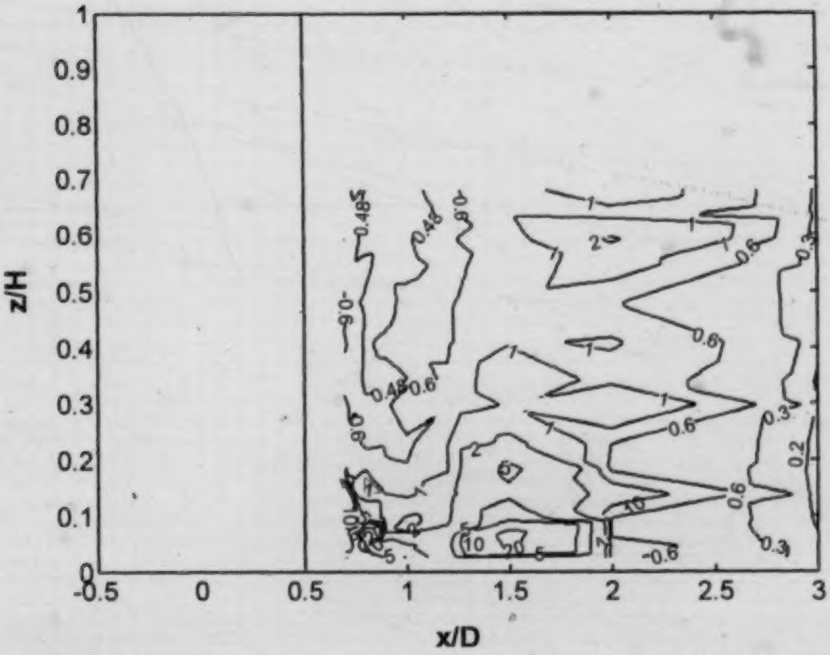

Fig. 6.39(b) Transverse turbulent intensity contour on DPOS: Rough bed/Regime-4

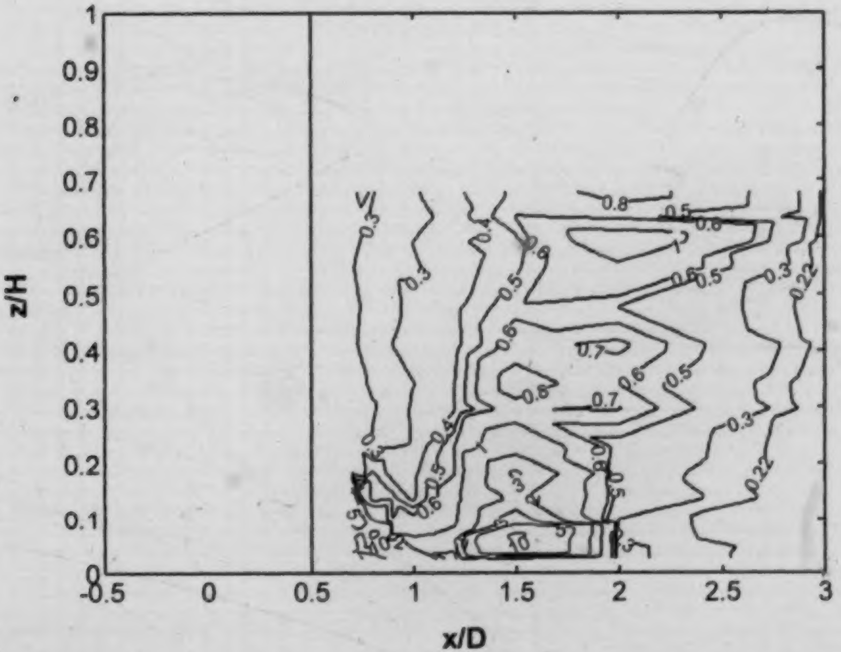

Fig. 6.39(c) Vertical turbulent intensity contour on DPOS: Rough bed/Regime-4

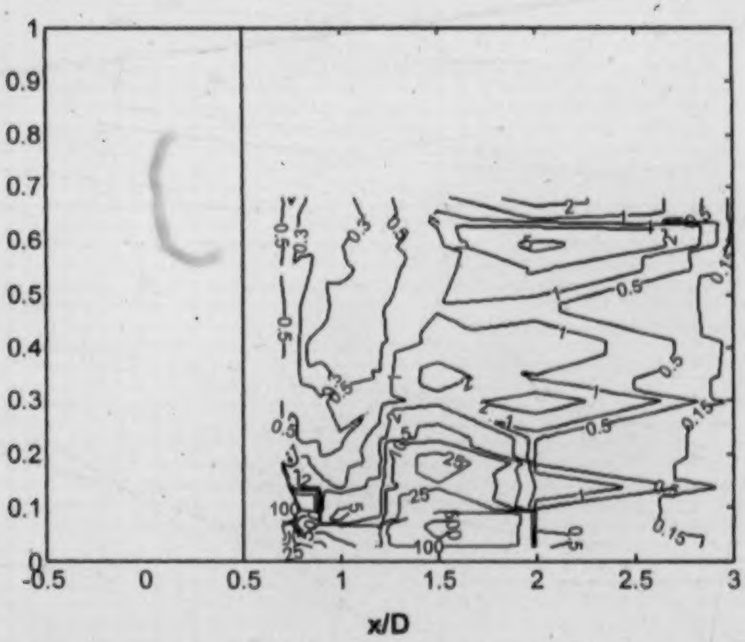

Fig. 6.39(d) Normalized turbulent kinetic energy (k/U^2) contour on DPOS: Rough bed/Regime-4

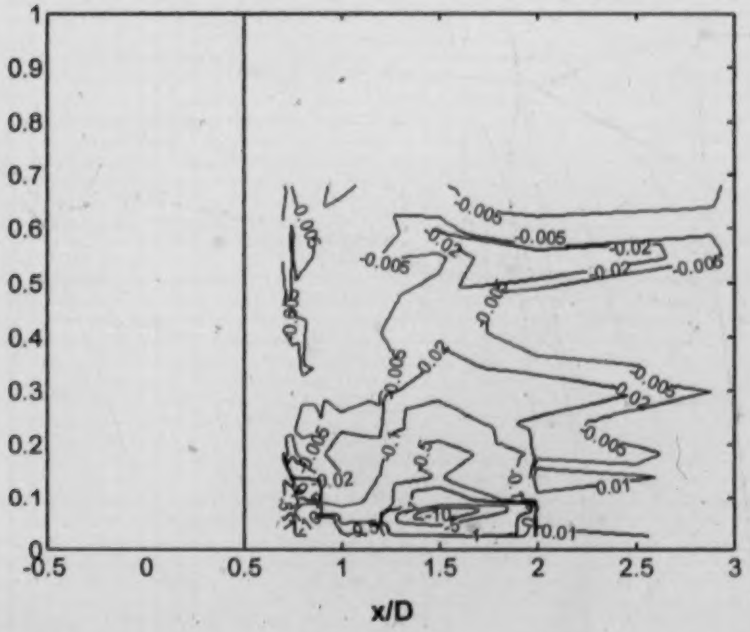

Fig. 6.39(e) Normalized primary Reynolds stress ($-\overline{uw}/U^2$) contour on DPOS: Rough bed/Regime-4

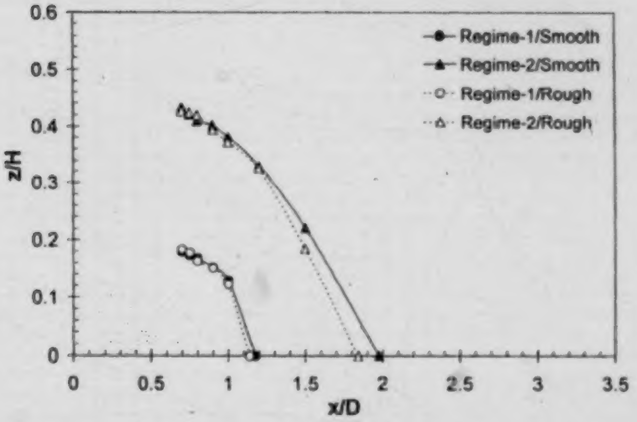

Fig. 6.40(a) Zero velocity (i.e. $U=0$) envelope of the closed recirculating zone

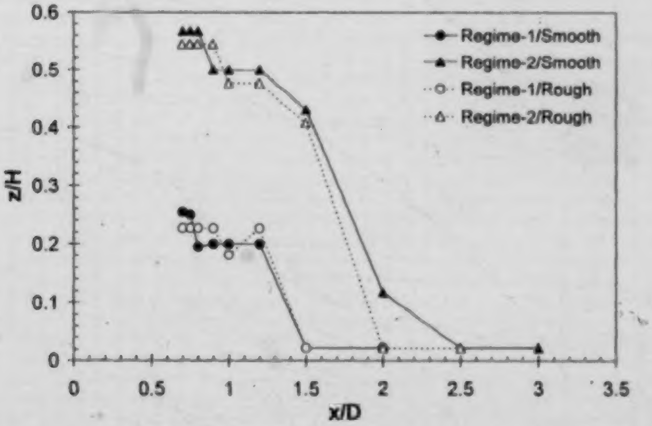

Fig. 6.40(b) Free shear (i.e. $\partial^2 U/\partial z^2=0$) envelope of the closed recirculating zone

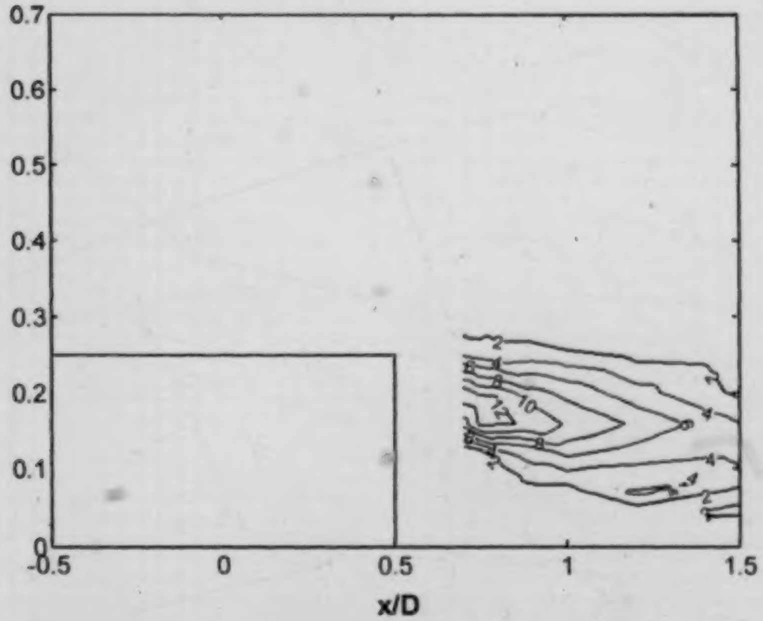

Fig. 6.41(a) Vorticity (ω_y) contour in the closed recirculating zone: Smooth bed/Regime-1

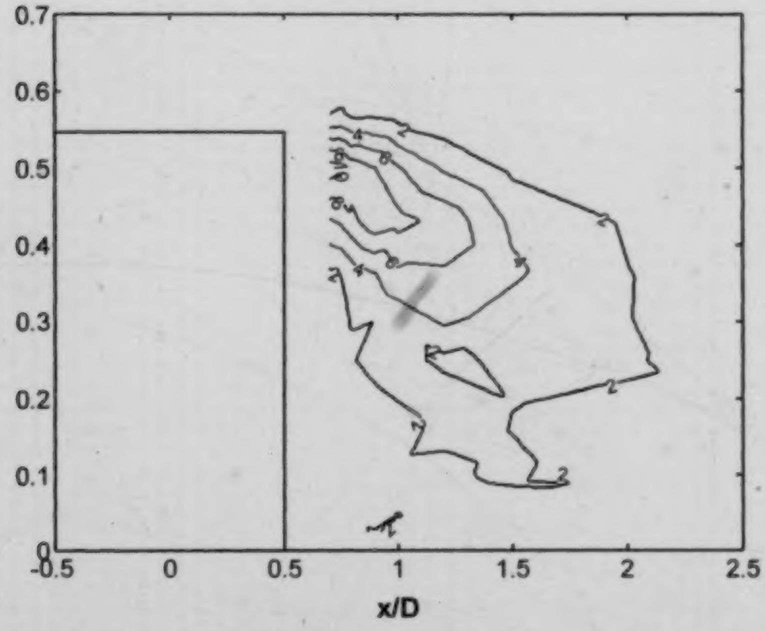

Fig. 6.41(b) Vorticity (ω_y) contour in the closed recirculating zone: Smooth bed/Regime-2

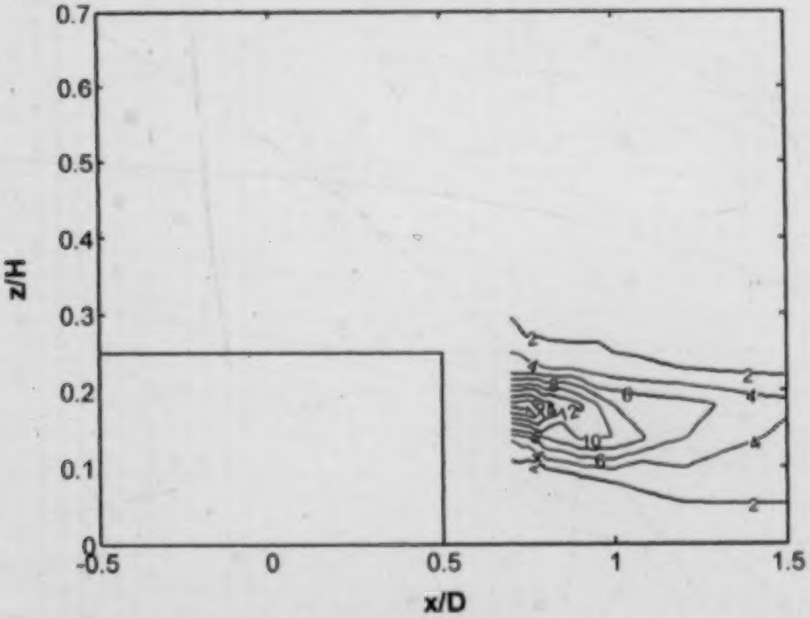

Fig. 6.41(c) Vorticity (ω_y) contour in the closed recirculating zone: Rough bed/Regime-1

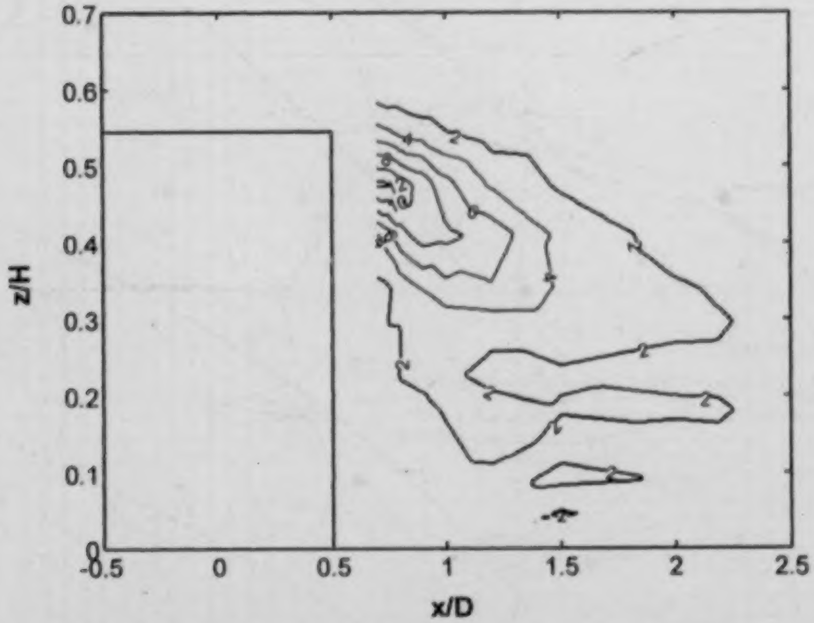

Fig. 6.41(d) Vorticity (ω_y) contour in the closed recirculating zone: Rough bed/Regime-2

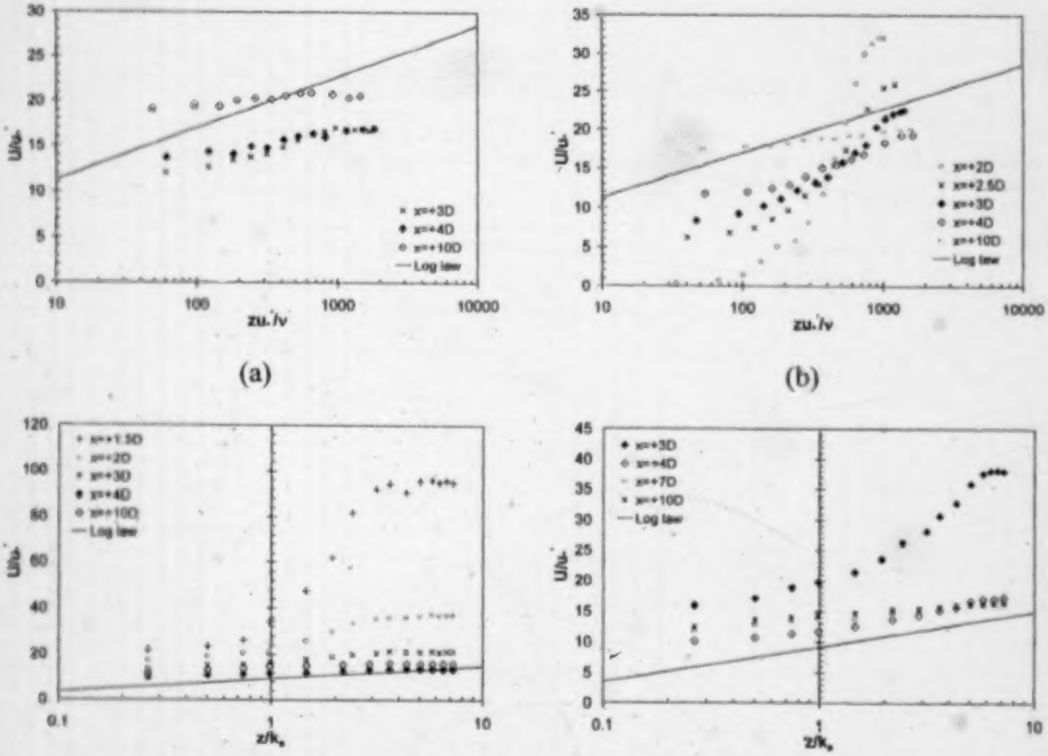

(a) (b)

(c) (d)

Fig. 6.42 Inner region similarity with logarithmic law in wall wake; (a) Smooth bed/Regime-1, (b) Smooth bed/Regime-2, (c) Rough bed/Regime-1, and (d) Rough bed/Regime-2

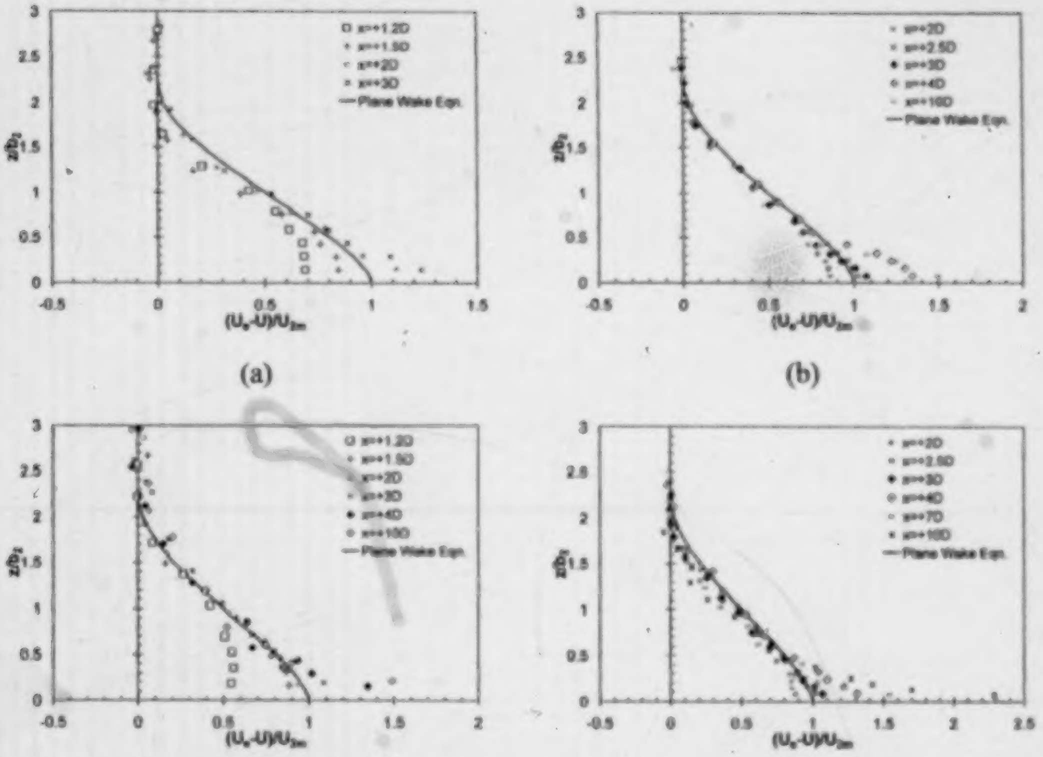

(a) (b)

(c) (d)

Fig. 6.43 Wall wake similarity in the outer region with plane wake equation; (a) Smooth bed/Regime-1, (b) Smooth bed/Regime-2, (c) Rough bed/Regime-1, and (d) Rough bed/Regime-2

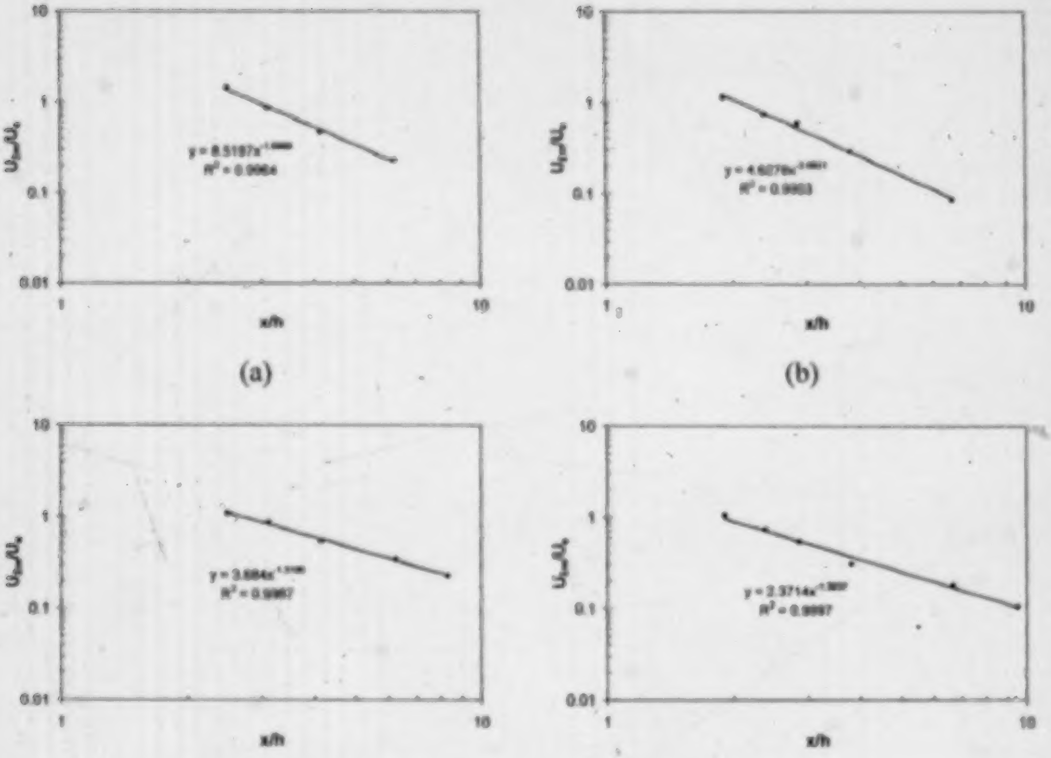

(a) (b)

(c) (d)

Fig. 6.44 Variation of the velocity scale (U_{2m}/U_e) with distance x/h; (a) Smooth bed/Regime-1, (b) Smooth bed/Regime-2, (c) Rough bed/Regime-1, and (d) Rough bed/Regime-2

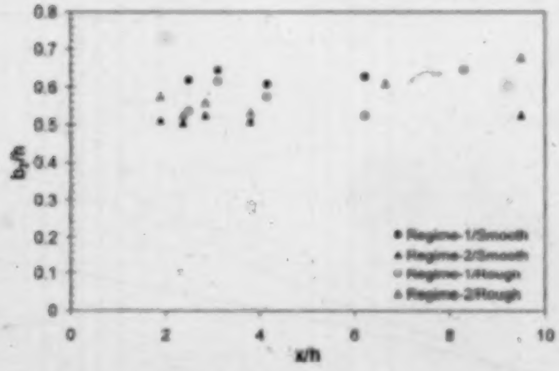

Fig. 6.45 Variation of the length scale (b_2/h) with distance x/h

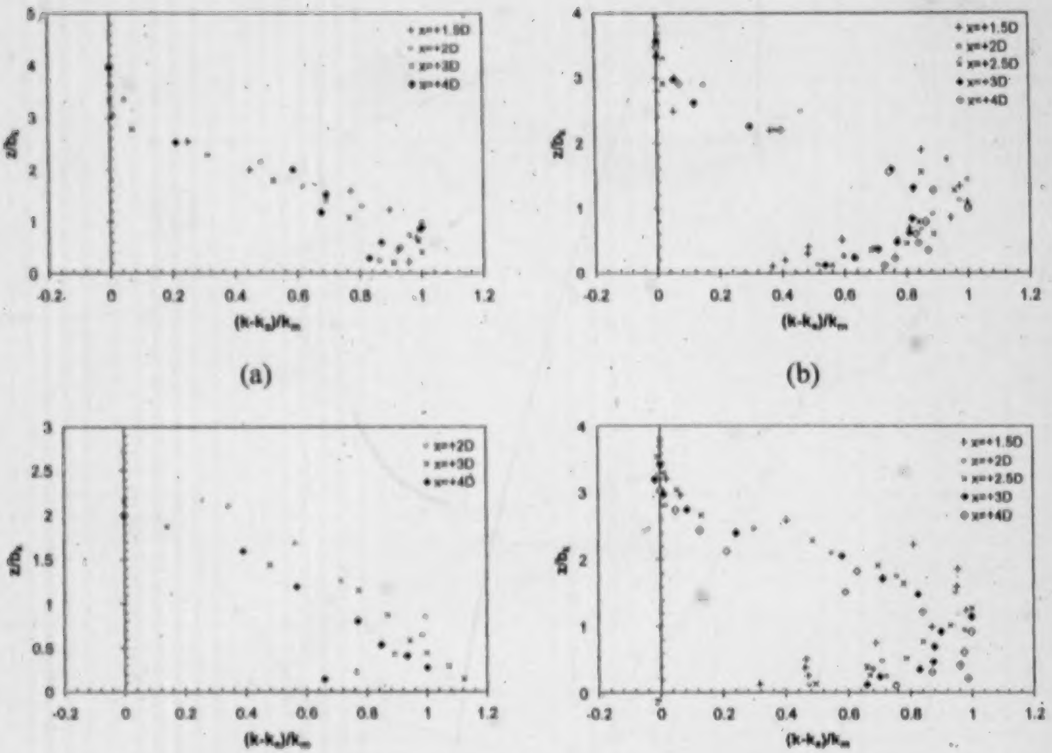

(a) (b)

(c) (d)

Fig. 6.46 Similarity profiles for turbulent kinetic energy $(k-k_e)/k_m$ vs z/b_k;

(a) Smooth bed/Regime-1, (b) Smooth bed/Regime-2,

(c) Rough bed/Regime-1, and (d) Rough bed/Regime-2

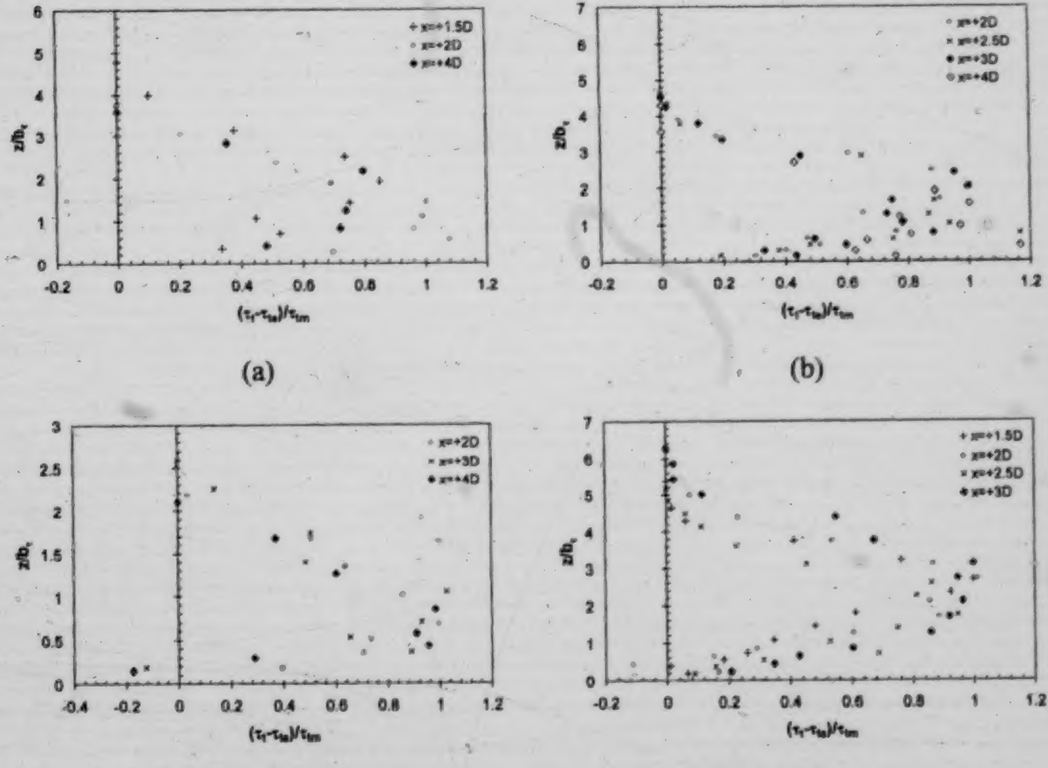

(a) (b)

(c) (d)

Fig. 6.47 Similarity profiles for turbulent shear stress $(\tau_t - \tau_{tc})/\tau_{tm}$ vs z/b_τ;
(a) Smooth bed/Regime-1, (b) Smooth bed/Regime-2,
(c) Rough bed/Regime-1, and (d) Rough bed/Regime-2

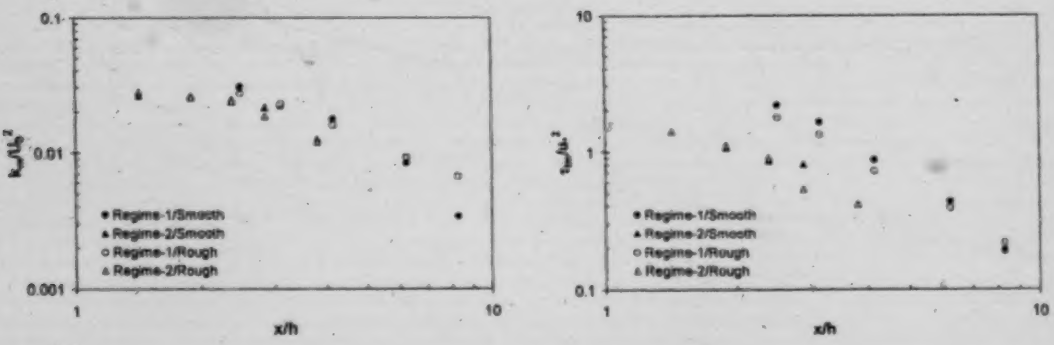

(a) (b)

Fig. 6.48 Variation of (a) turbulent kinetic energy scale (k_m/U_0^2), and (b) turbulent shear stress scale (τ_{tm}/u_*^2) with distance x/h

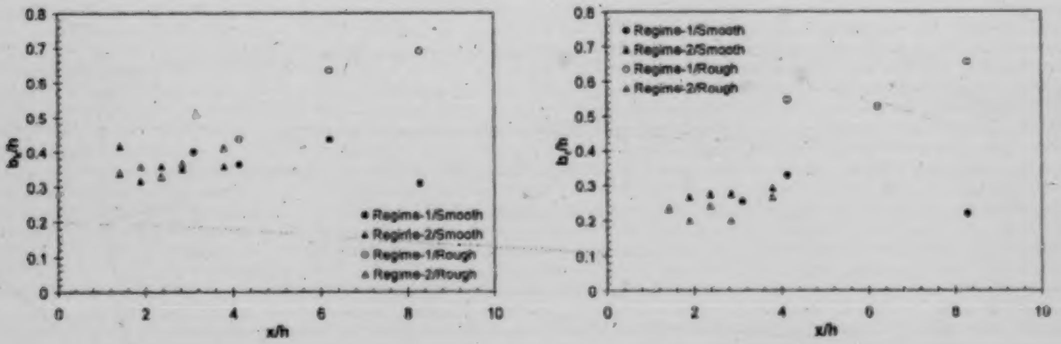

(a) (b)

Fig. 6.49 Variation of the length scale of (a) turbulent kinetic energy (b_k/h), and (b) turbulent shear stress (b_τ/h) with distance x/h

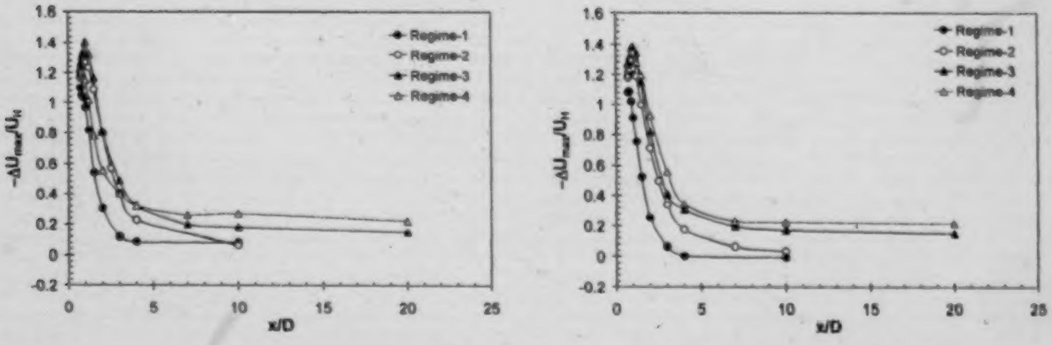

(a) (b)

Fig. 6.50 Variation of maximum defect in mean velocity ($-\Delta U_{max}/U_H$) with distance x/D; (a) Smooth bed, and (b) Rough bed

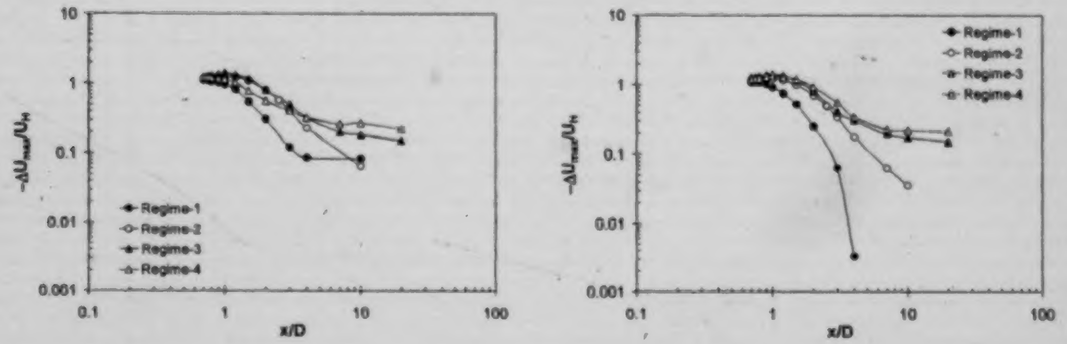

(a) (b)

Fig. 6.51 Variation of maximum defect in mean velocity ($-\Delta U_{max}/U_H$) in logarithmic scale with distance x/D; (a) Smooth bed, and (b) Rough bed

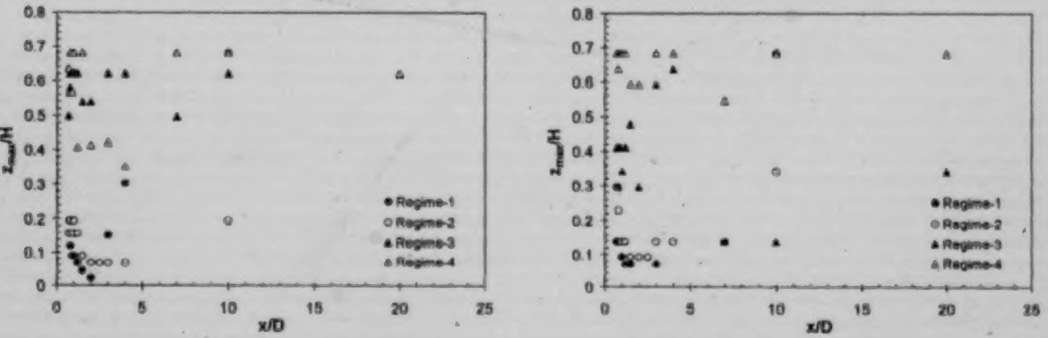

(a) (b)

Fig. 6.52 Variation of the height of maximum velocity defect z_{max}/H with distance x/D; (a) Smooth bed, and (b) Rough bed

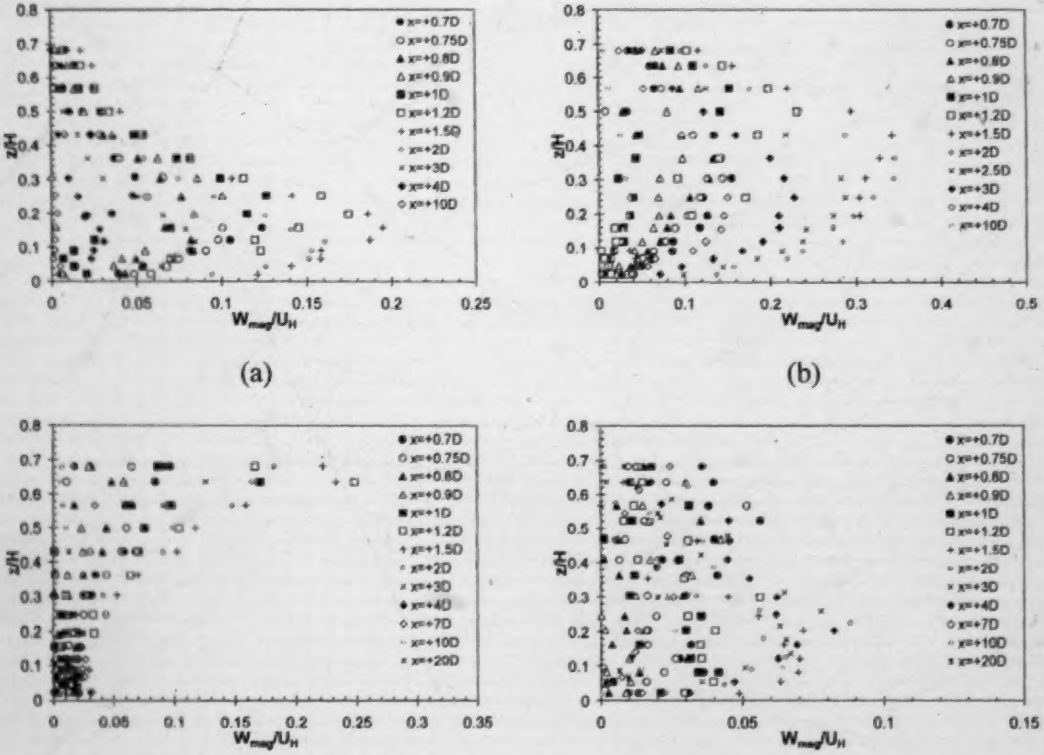

(a) (b)

(c) (d)

Fig. 6.53 Normalized vertical mean velocity magnitudes profile on downstream POS on Smooth bed; (a) Regime-1, (b) Regime-2, (c) Regime-3, and (d) Regime-4

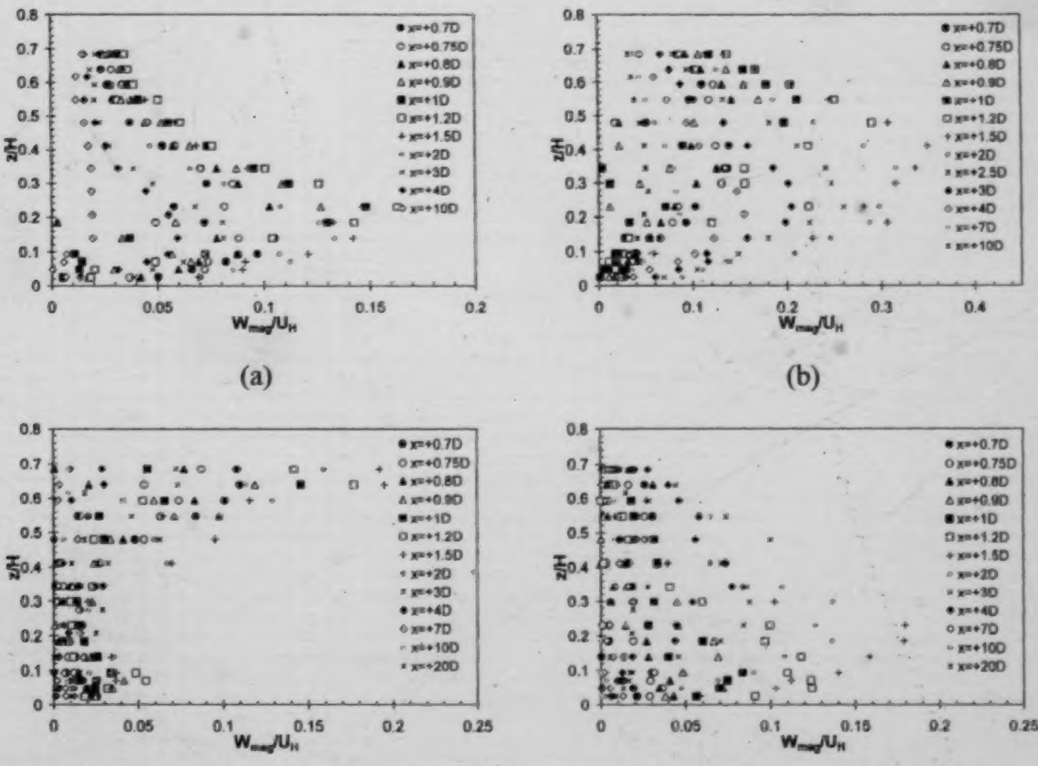

(a) (b)

(c) (d)

Fig. 6.54 Normalized vertical mean velocity magnitudes profile on downstream POS on Rough bed; (a) Regime-1, (b) Regime-2, (c) Regime-3, and (d) Regime-4

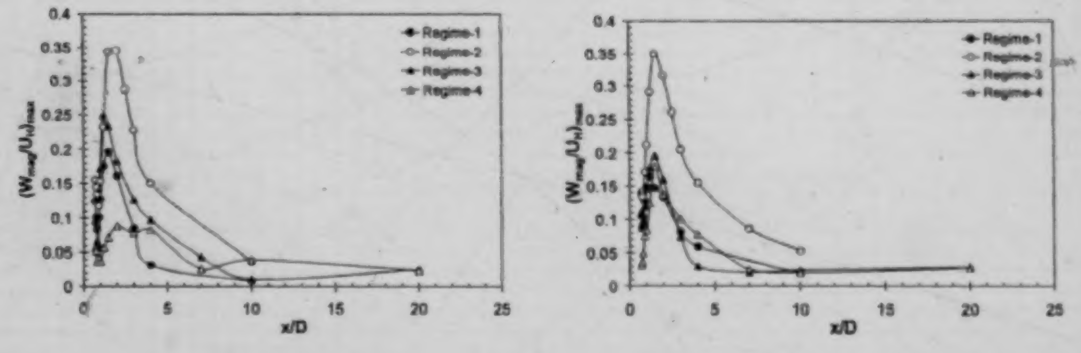

(a) (b)

Fig. 6.55 Variation of the maximum normalized vertical mean velocity with distance *x/D*; (a) Smooth bed, and (b) Rough bed

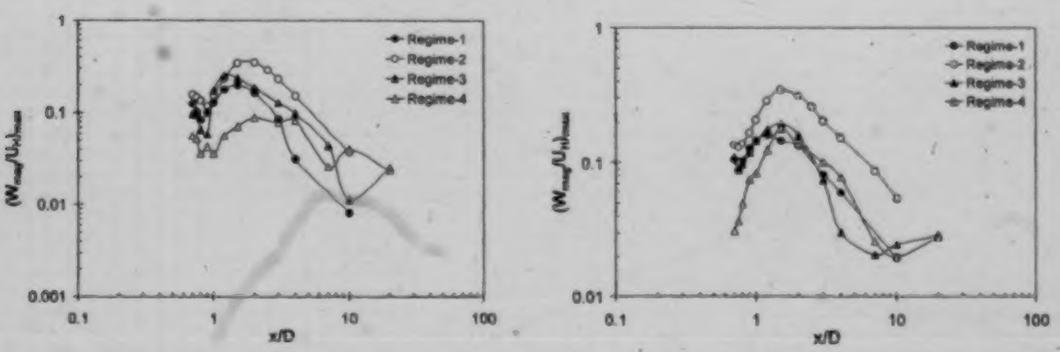

(a) (b)

Fig. 6.56 Variation of the maximum normalized vertical mean velocity with distance *x/D* in logarithmic scale; (a) Smooth bed, and (b) Rough bed

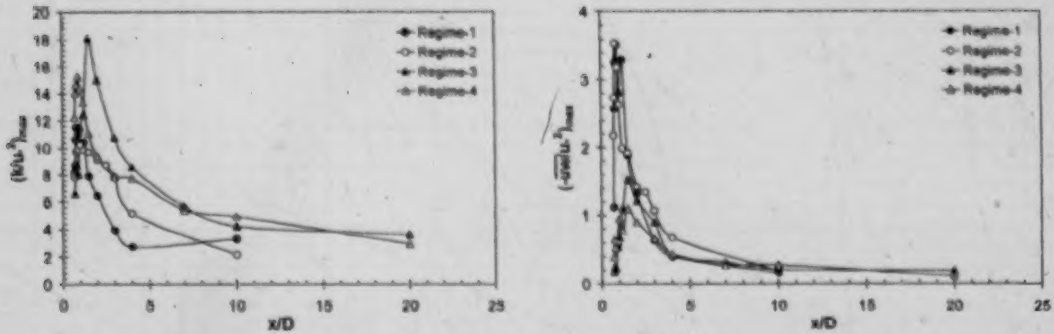

(a) (b)

Fig. 6.57 Variation of the maximum values of normalized (a) turbulent kinetic energy $(k/u_*^2)_{max}$, and (b) turbulent shear stress $(-\overline{uw}/u_*^2)_{max}$ with distance x/D on Smooth bed

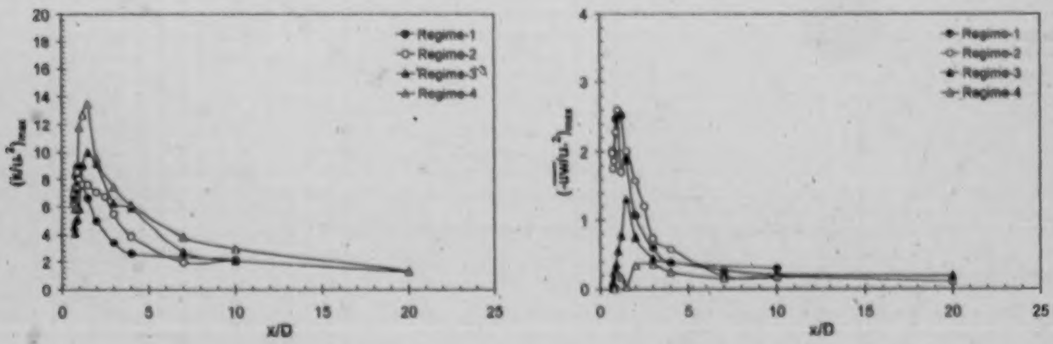

(a) (b)

Fig. 6.58 Variation of the maximum values of normalized (a) turbulent kinetic energy $(k/u_*^2)_{max}$, and (b) turbulent shear stress $(-\overline{uw}/u_*^2)_{max}$ with distance x/D on Rough bed

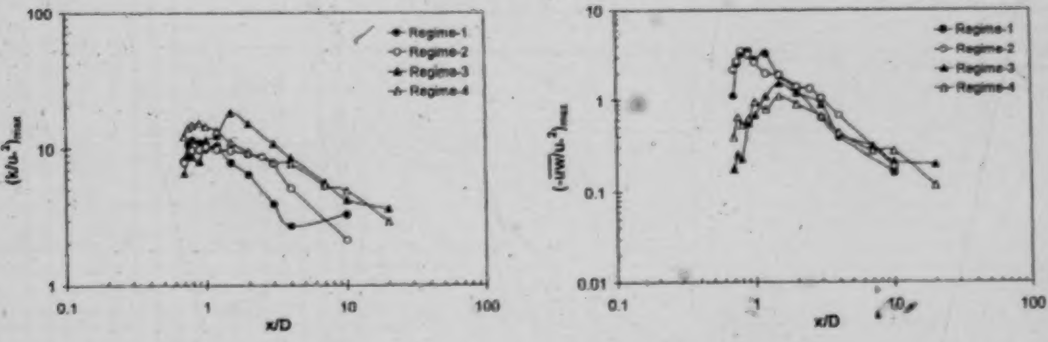

(a) (b)

Fig. 6.59 Variation of the maximum values of normalized (a) turbulent kinetic energy $(k/u_{*}^{2})_{max}$, and (b) turbulent shear stress $(-\overline{uw}/u_{*}^{2})_{max}$ with distance x/D in logarithmic scale on Smooth bed

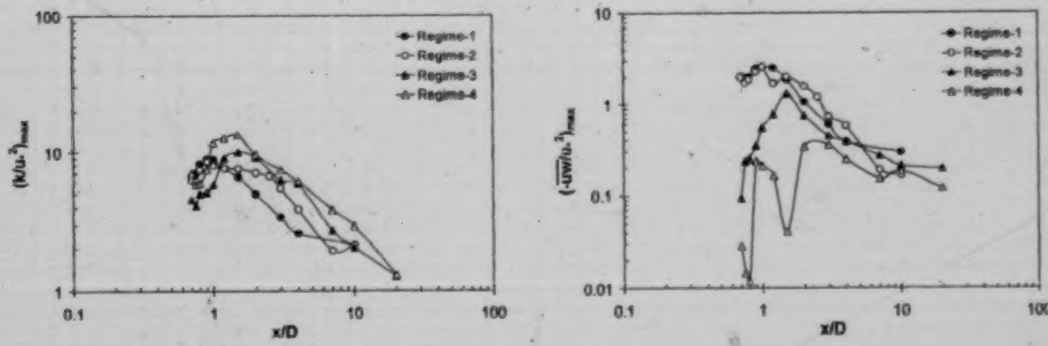

(a) (b)

Fig. 6.60 Variation of the maximum values of normalized (a) turbulent kinetic energy $(k/u_{*}^{2})_{max}$, and (b) turbulent shear stress $(-\overline{uw}/u_{*}^{2})_{max}$ with distance x/D in logarithmic scale on Rough bed

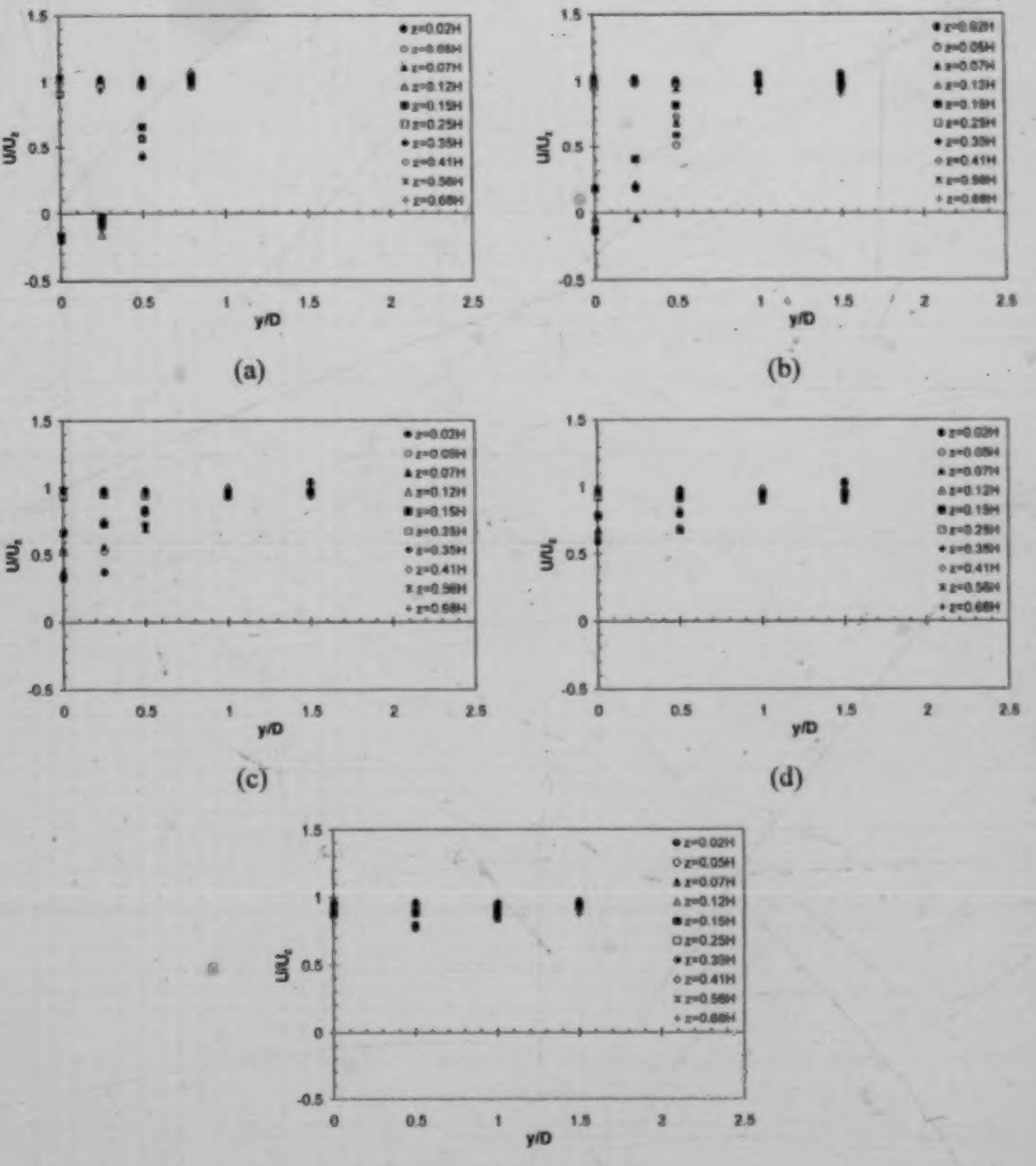

(a)

(b)

(c)

(d)

(e)

Fig. 6.61 Normalized mean velocity profile across the wake at (a) *x/D*=+0.7, (b) *x/D*=+1, (c) *x/D*=+1.5, (d) *x/D*=+2, and (e) *x/D*=+3: Smooth bed/Regime-1

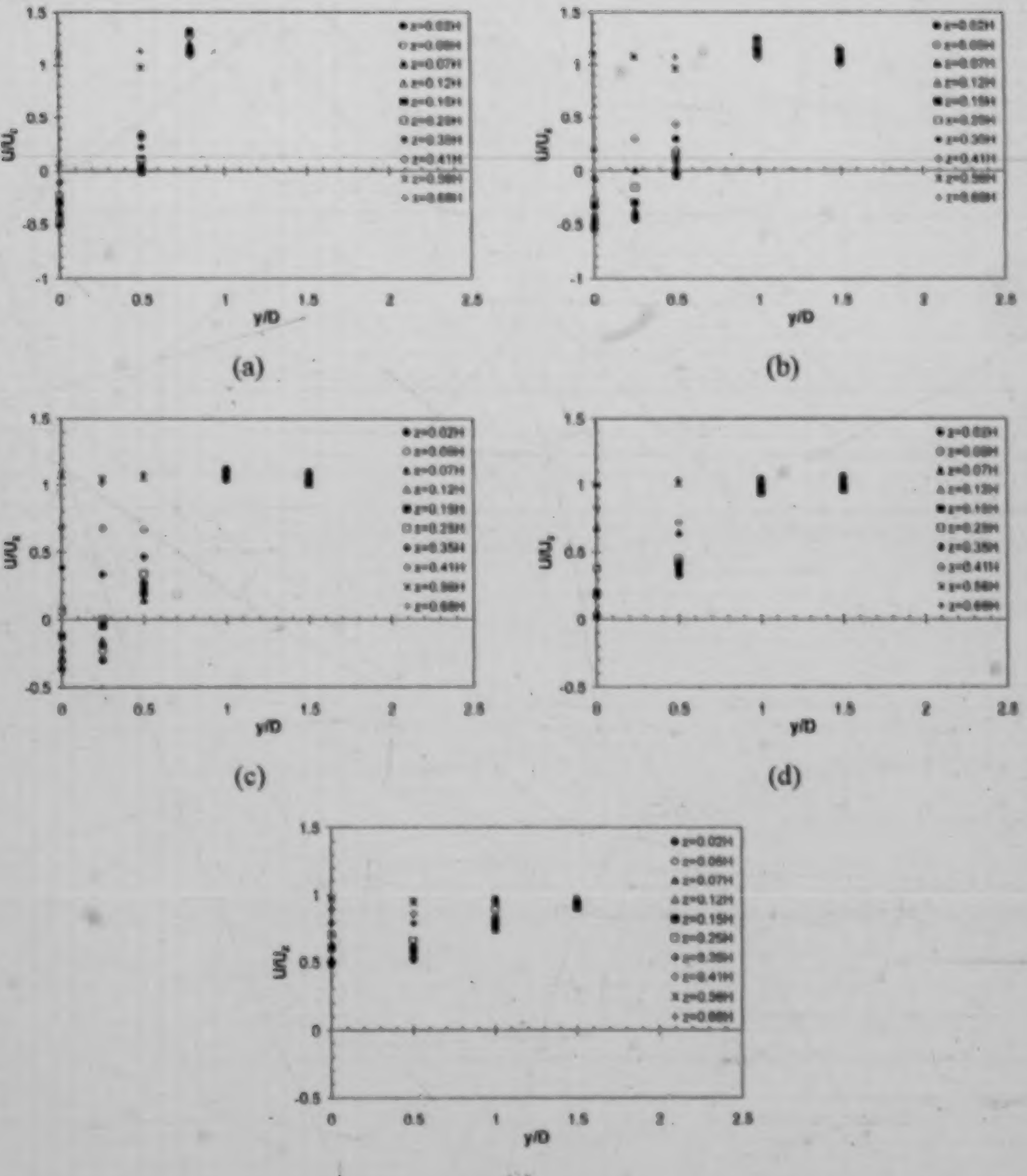

(a)

(b)

(c)

(d)

(e)

Fig. 6.62 Normalized mean velocity profile across the wake at (a) *x/D*=+0.8, (b) *x/D*=+1, (c) *x/D*=+1.5, (d) *x/D*=+2, and (e) *x/D*=+3: Smooth bed/Regime-2

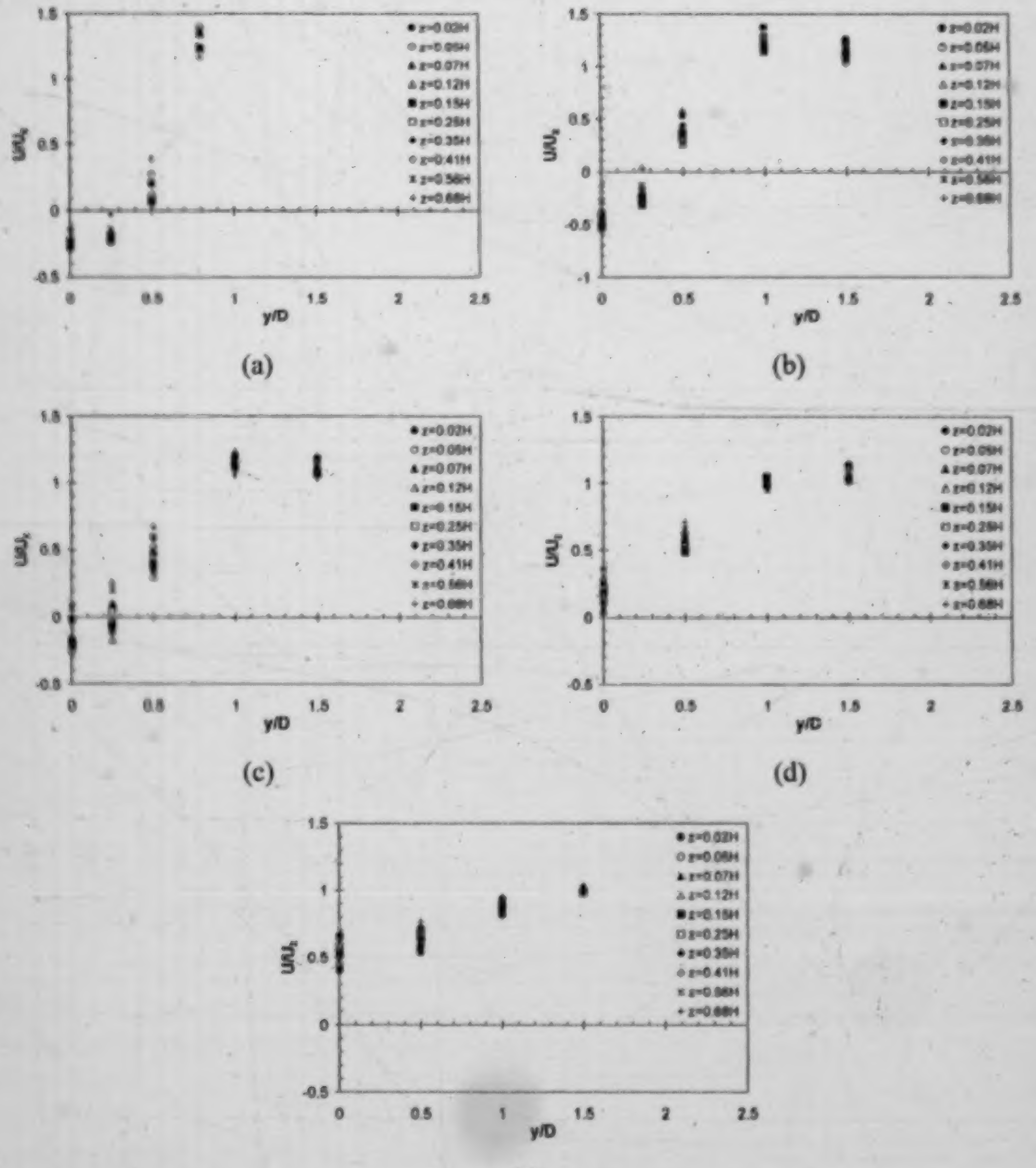

(a) (b)

(c) (d)

(e)

Fig. 6.63 Normalized mean velocity profile across the wake at (a) *x/D*=+0.7, (b) *x/D*=+1, (c) *x/D*=+1.5, (d) *x/D*=+2, and (e) *x/D*=+3: Smooth bed/Regime-3

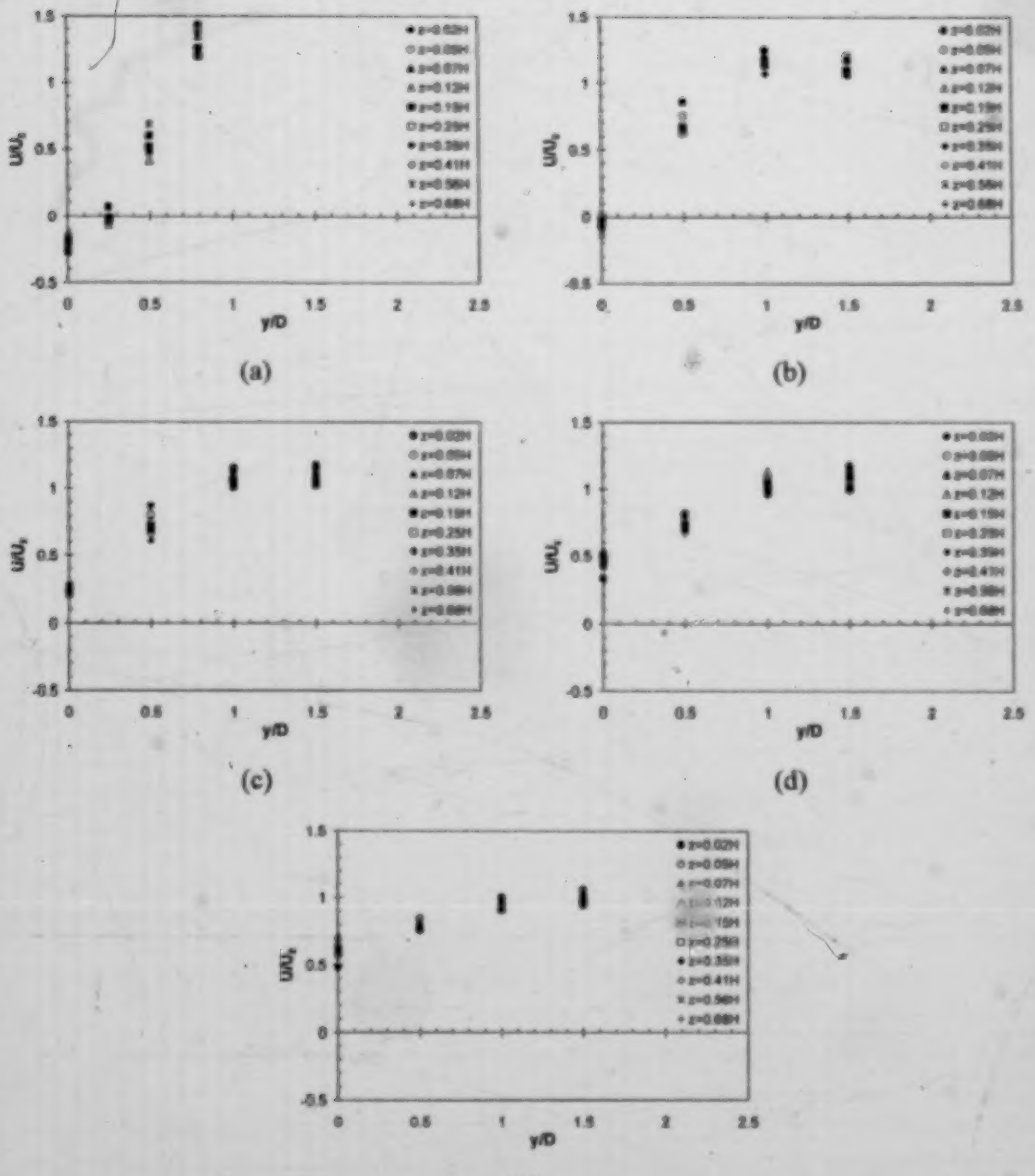

(a) (b)

(c) (d)

(e)

Fig. 6.64 Normalized mean velocity profile across the wake at (a) x/D=+0.8, (b) x/D=+1, (c) x/D=+1.5, (d) x/D=+2, and (e) x/D=+3: Smooth bed/Regime-4

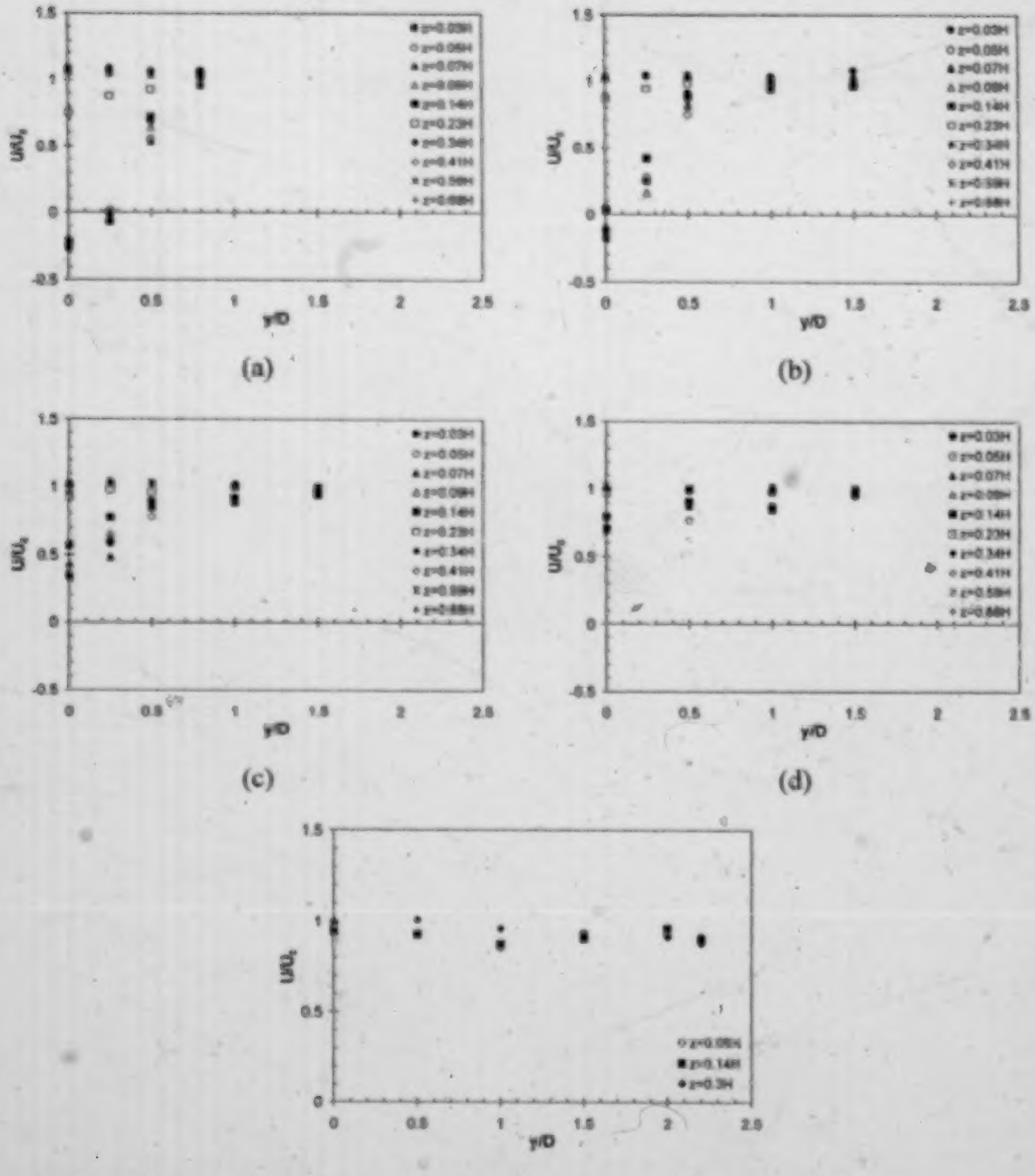

(a) (b)

(c) (d)

(e)

Fig. 6.65 Normalized mean velocity profile across the wake at (a) *x/D*=+0.7, (b) *x/D*=+1, (c) *x/D*=+1.5, (d) *x/D*=+2, and (e) *x/D*=+3: Rough bed/Regime-1

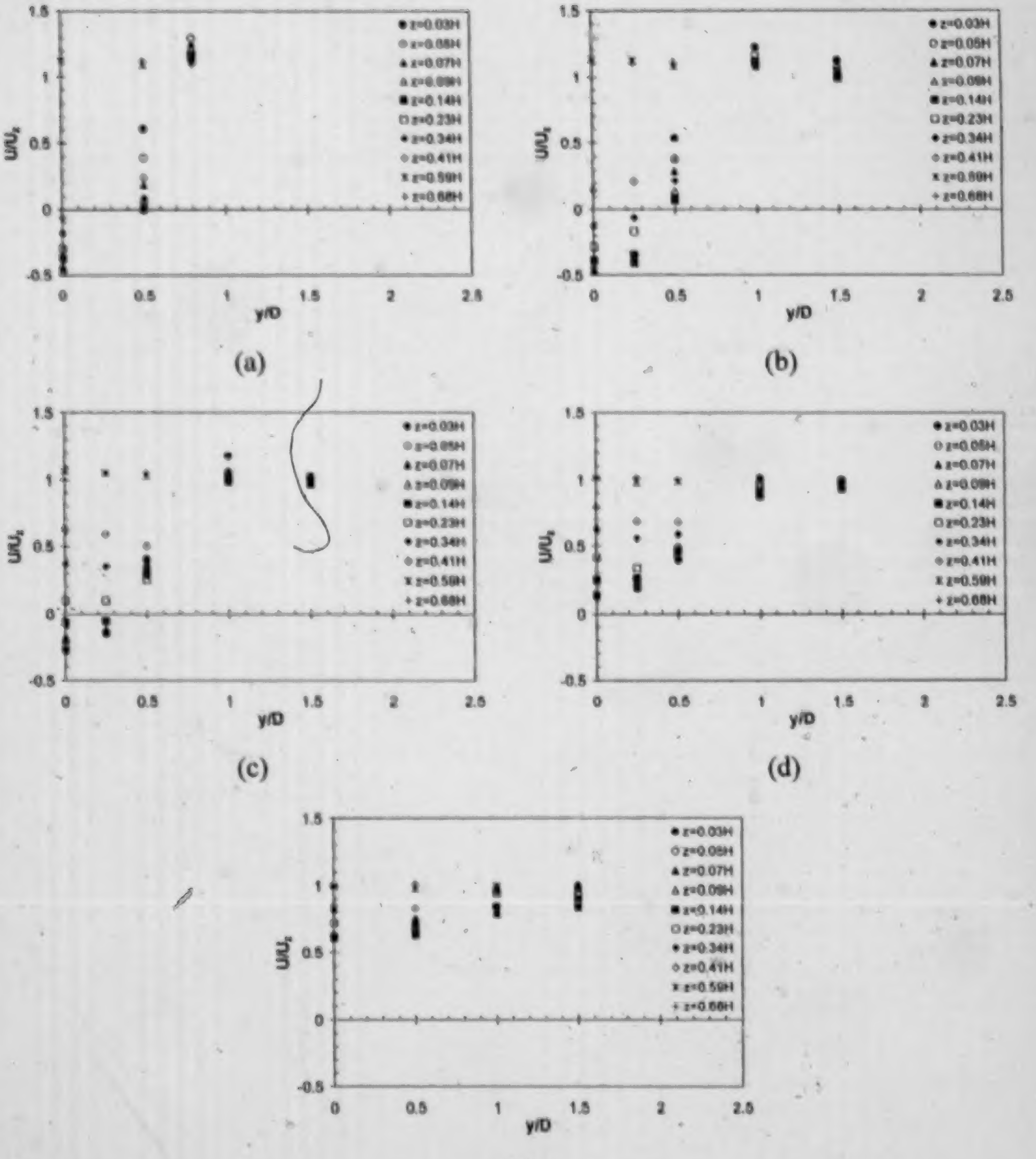

(a)

(b)

(c)

(d)

(e)

Fig. 6.66 Normalized mean velocity profile across the wake at (a) *x/D*=+0.8, (b) *x/D*=+1, (c) *x/D*=+1.5, (d) *x/D*=+2, and (e) *x/D*=+3: Rough bed/Regime-2

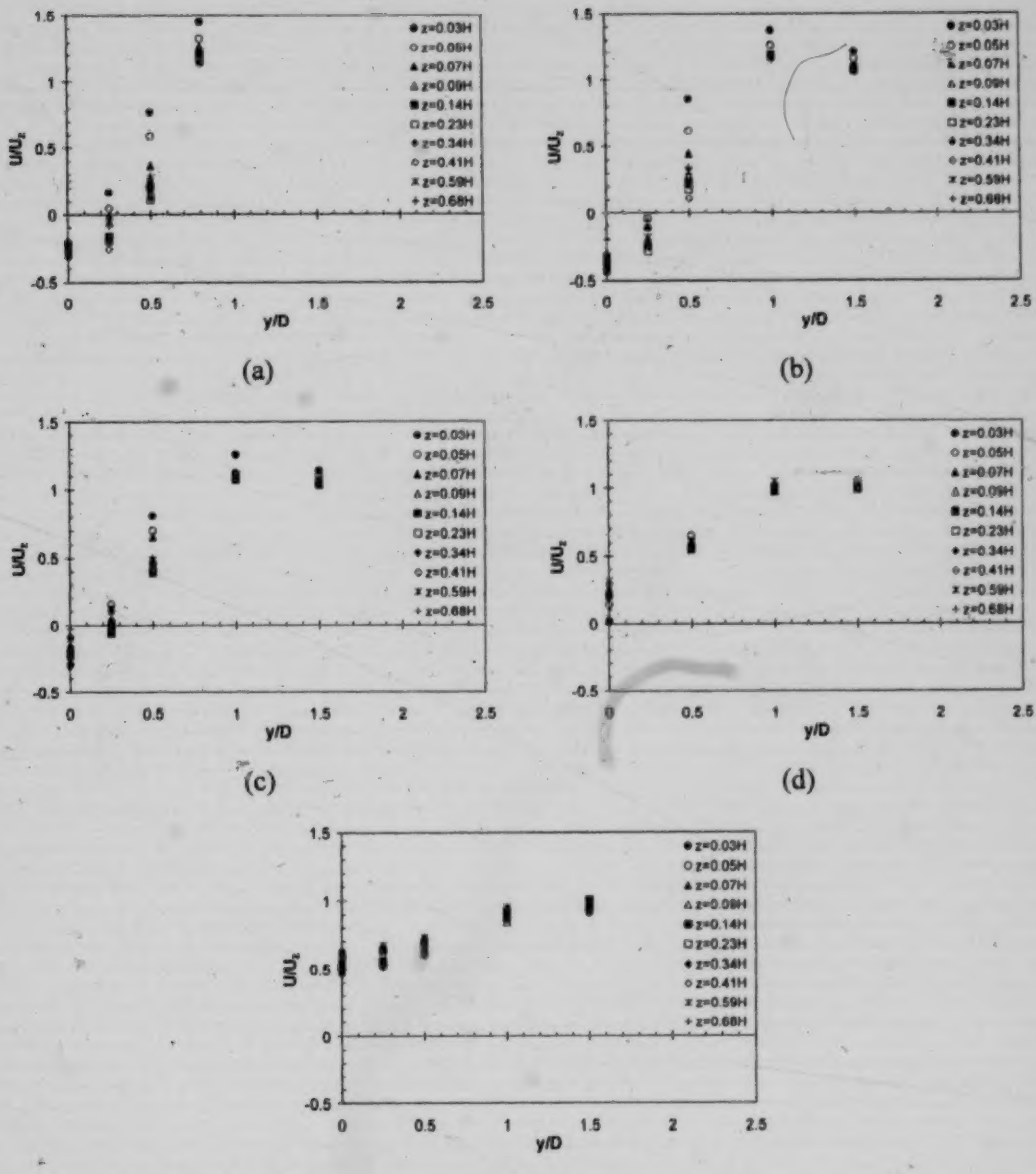

(a)

(b)

(c)

(d)

(e)

Fig. 6.67 Normalized mean velocity profile across the wake at (a) *x/D*=+0.8, (b) *x/D*=+1, (c) *x/D*=+1.5, (d) *x/D*=+2, and (e) *x/D*=+3: Rough bed/Regime-3

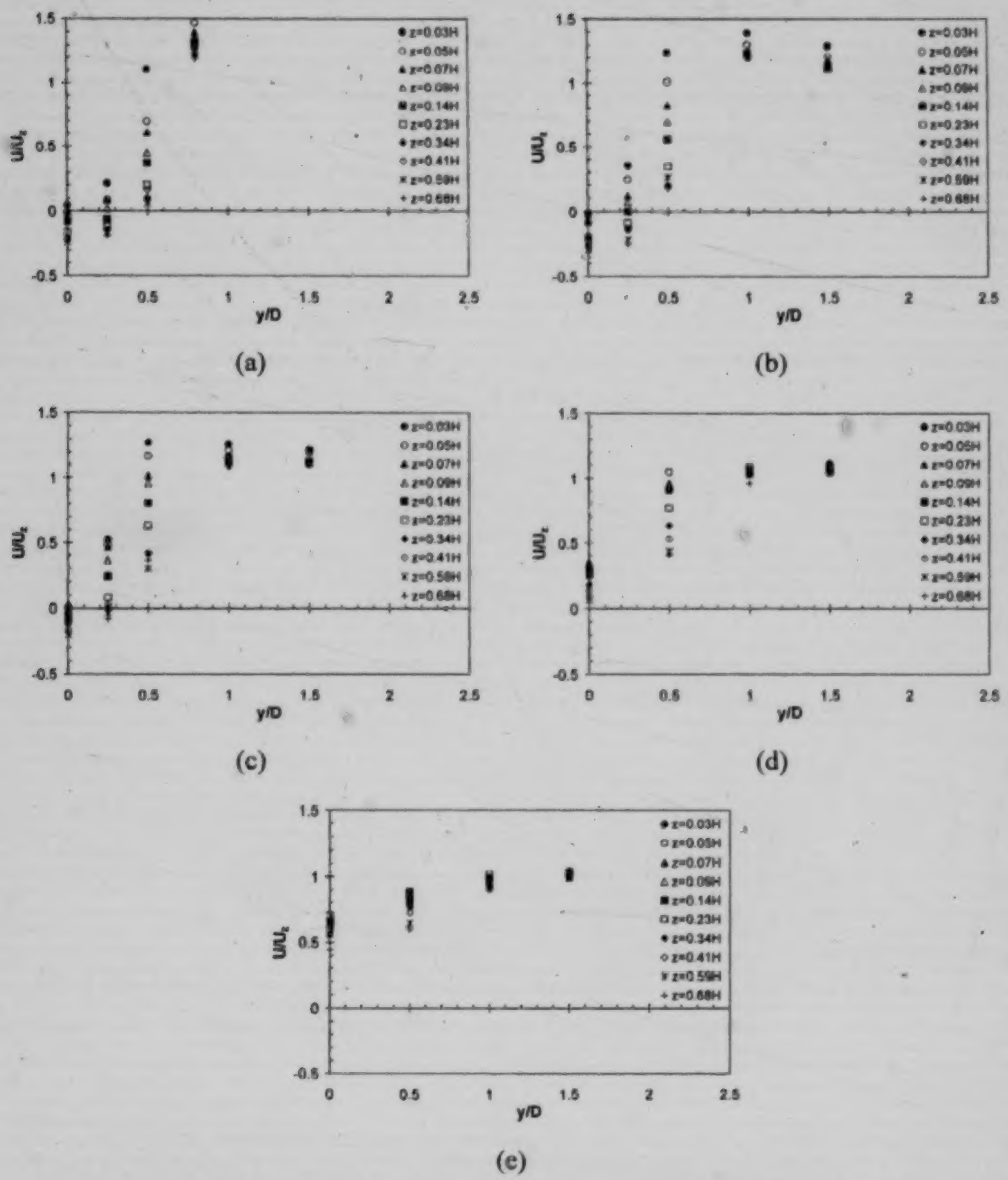

(a) (b) (c) (d) (e)

Fig. 6.68 Normalized mean velocity profile across the wake at (a) *x/D*=+0.8, (b) *x/D*=+1, (c) *x/D*=+1.5, (d) *x/D*=+2, and (e) *x/D*=+3: Rough bed/Regime-4

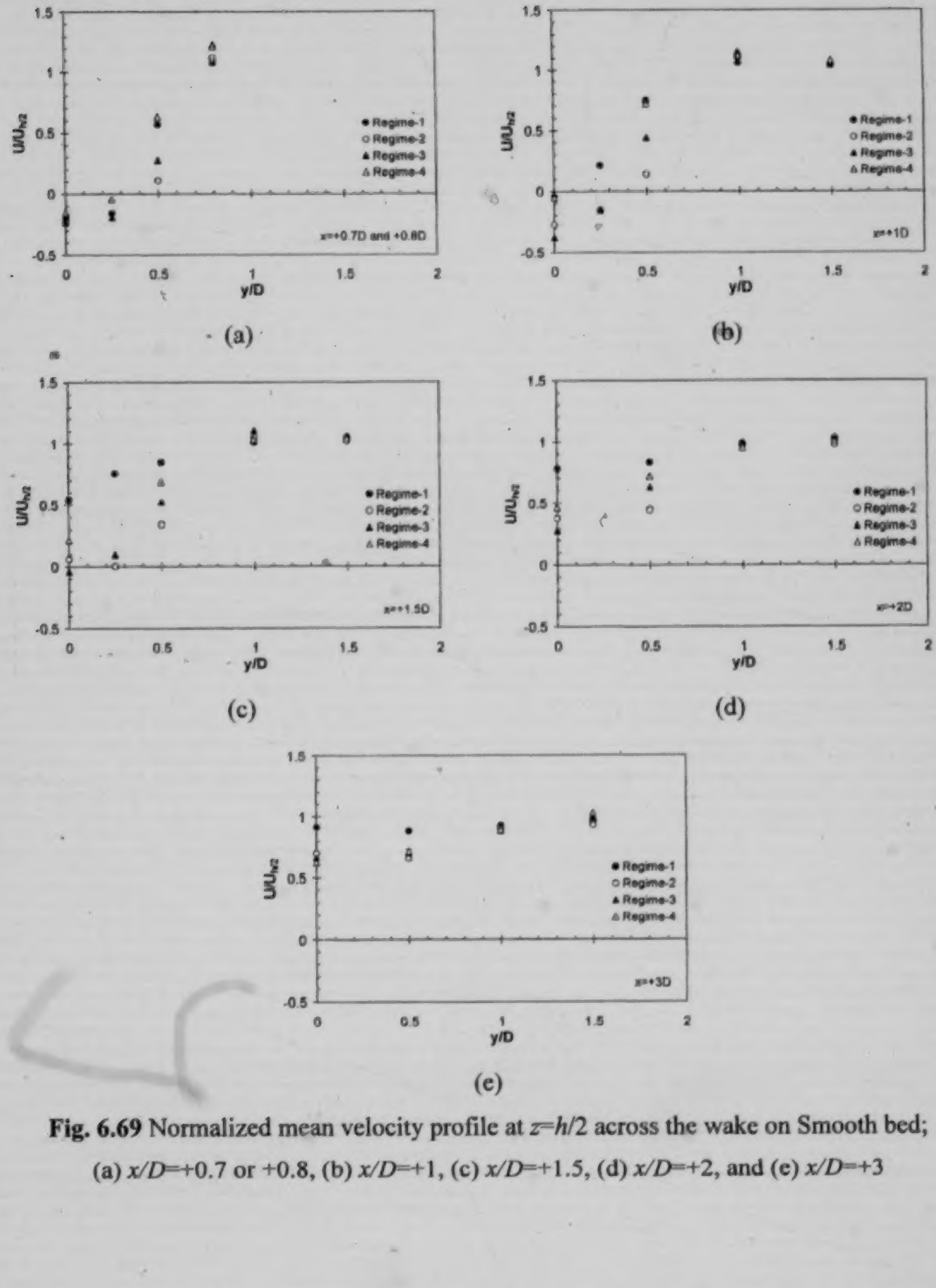

(a) (b)

(c) (d)

(e)

Fig. 6.69 Normalized mean velocity profile at *z*=*h*/2 across the wake on Smooth bed; (a) *x/D*=+0.7 or +0.8, (b) *x/D*=+1, (c) *x/D*=+1.5, (d) *x/D*=+2, and (e) *x/D*=+3

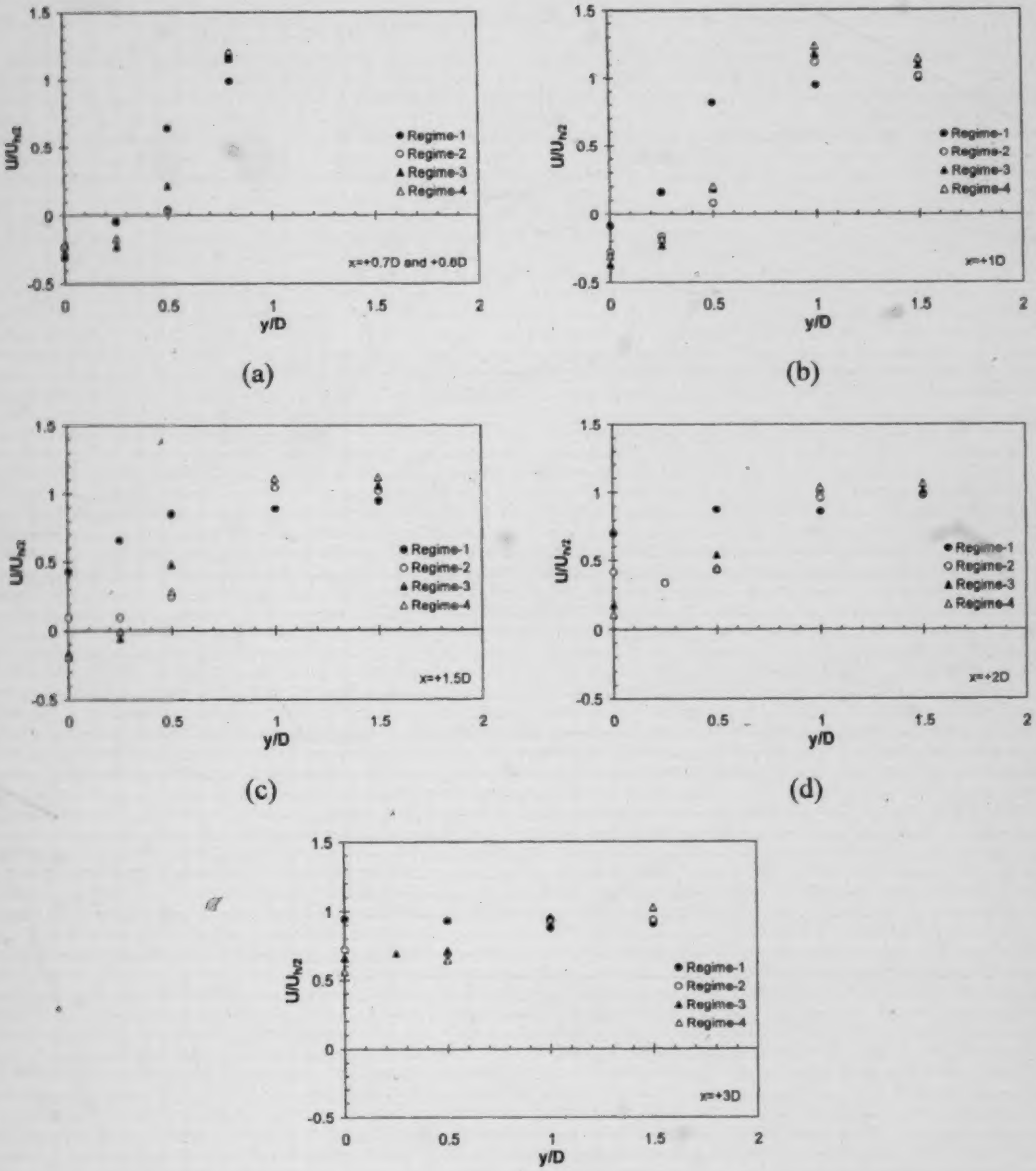

(a) (b)

(c) (d)

(e)

Fig. 6.70 Normalized mean velocity profile at $z=h/2$ across the wake on Rough bed; (a) x/D=+0.7 or +0.8, (b) x/D=+1, (c) x/D=+1.5, (d) x/D=+2, and (e) x/D=+3

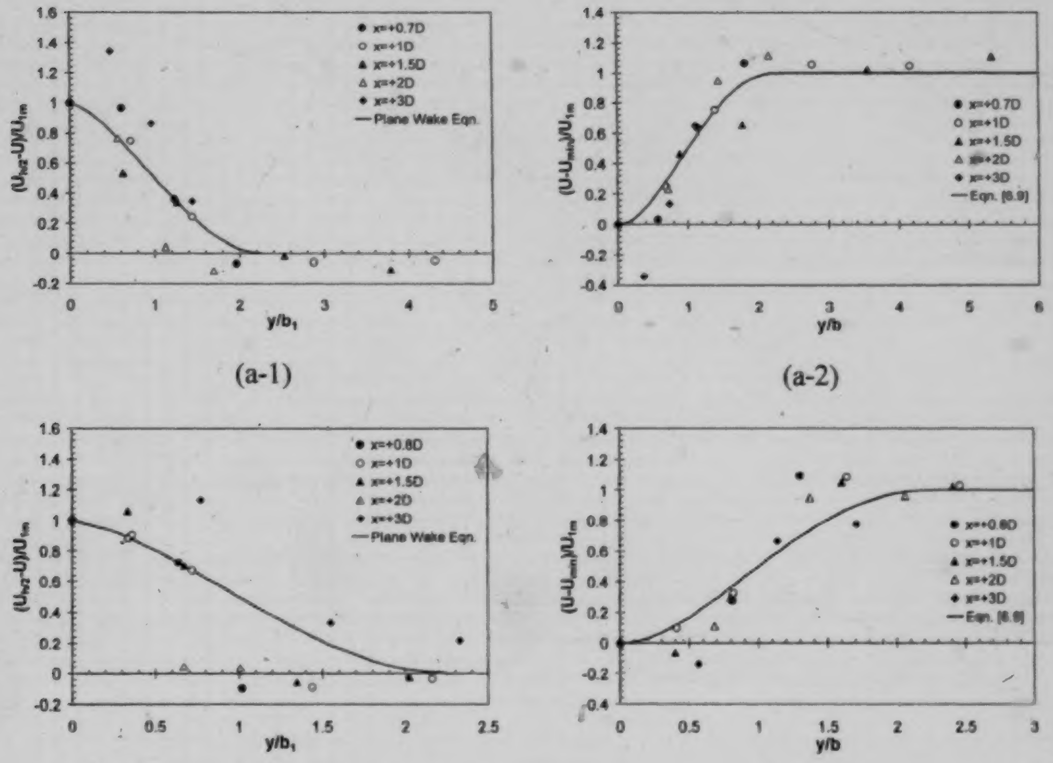

(a-1) (a-2)

(b-1) (b-2)

Fig. 6.71 Wake similarity profile at $z=h/2$ on Smooth bed;

(a) Regime-1, and (b) Regime-2

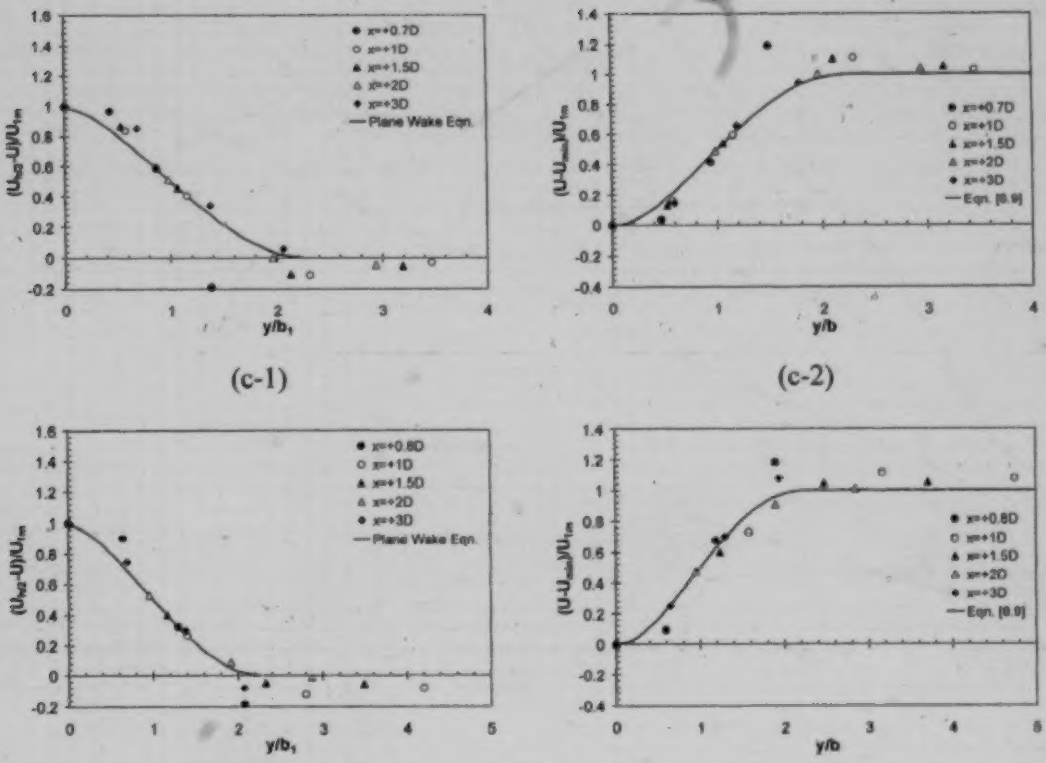

(c-1) (c-2)

(d-1) (d-2)

Fig. 6.71 (Contd.) Wake similarity profile at $z=h/2$ on Smooth bed; (c) Regime-3, and (d) Regime-4

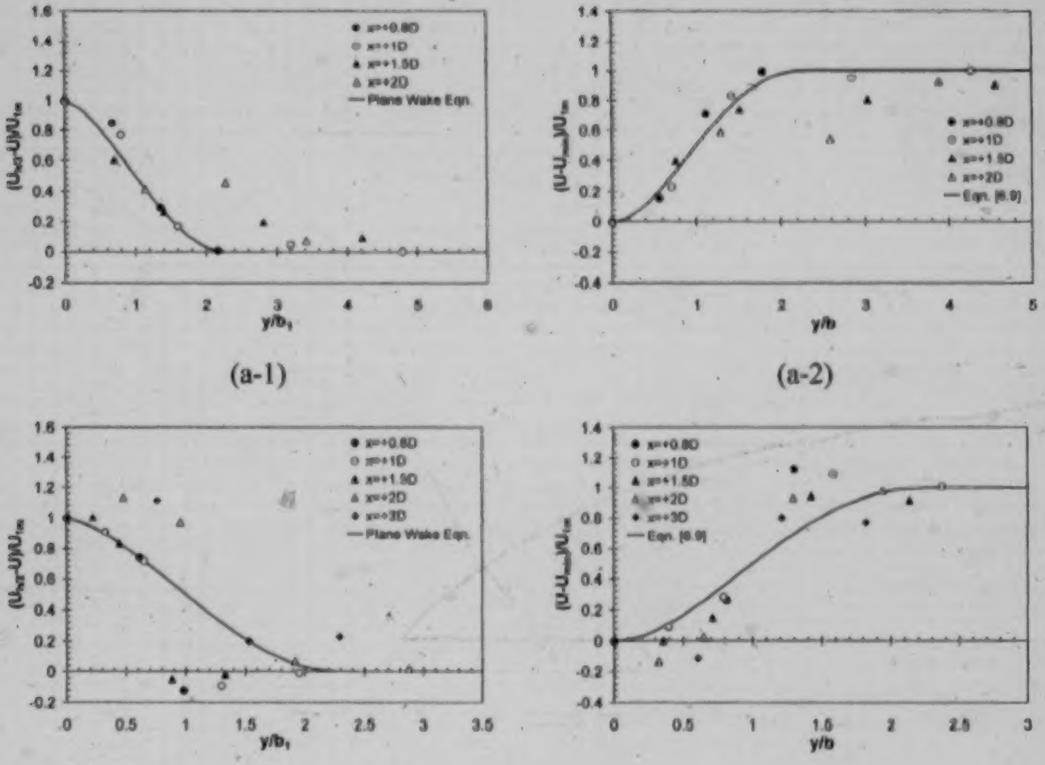

(a-1) (a-2)

(b-1) (b-2)

Fig. 6.72 Wake similarity profile at $z=h/2$ on Rough bed;

(a) Regime-1, and (b) Regime-2

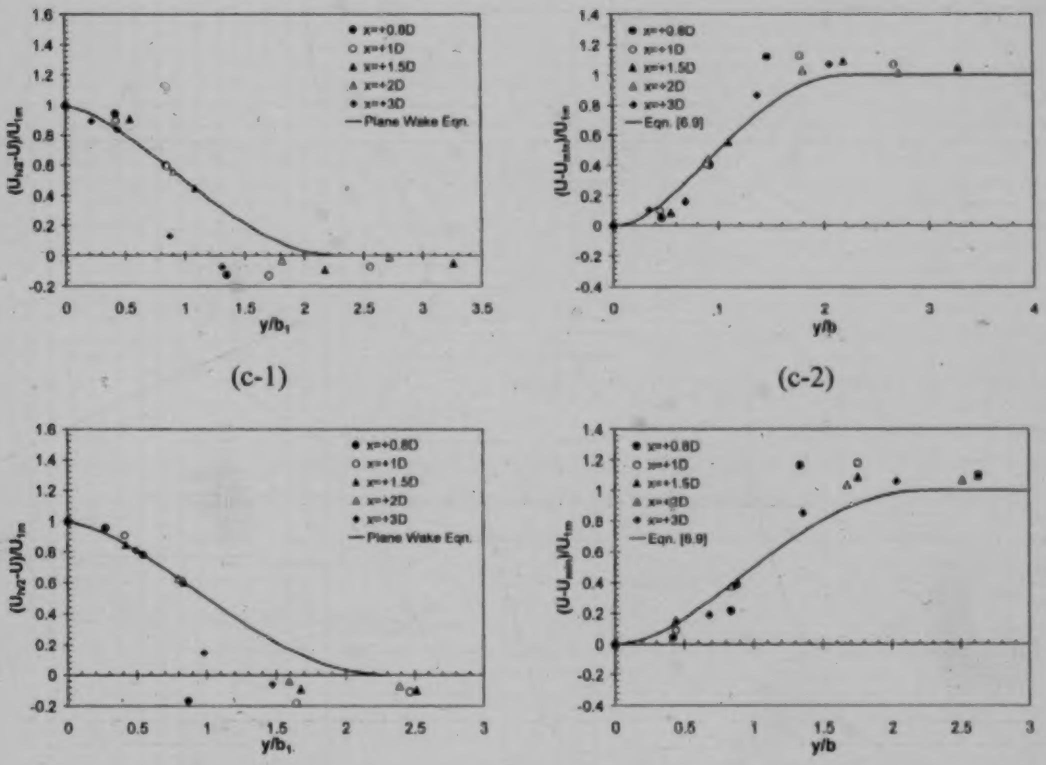

(c-1) (c-2)

(d-1) (d-2)

Fig. 6.72 (Contd.) Wake similarity profile at $z=h/2$ on Rough bed;

(c) Regime-3, and (d) Regime-4

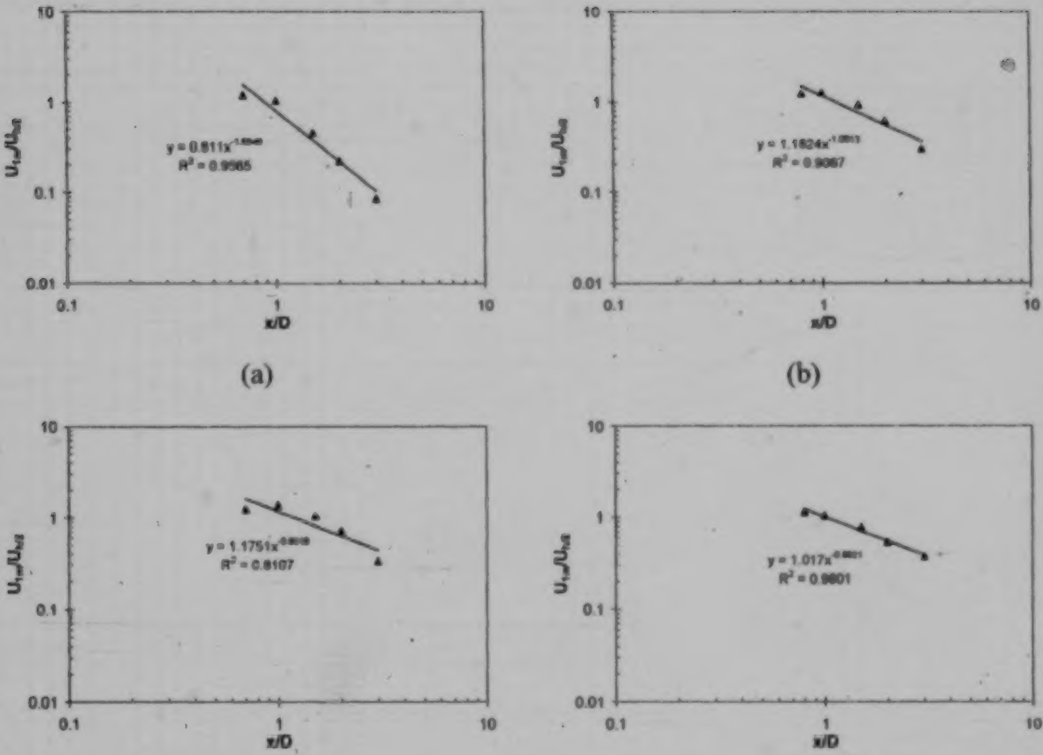

(a) (b)

(c) (d)

Fig. 6.73 Variation of the velocity scale ($U_{1m}/U_{h/2}$) with distance x/D on Smooth bed; (a) Regime-1, and (b) Regime-2, (c) Regime-3, and (d) Regime-4

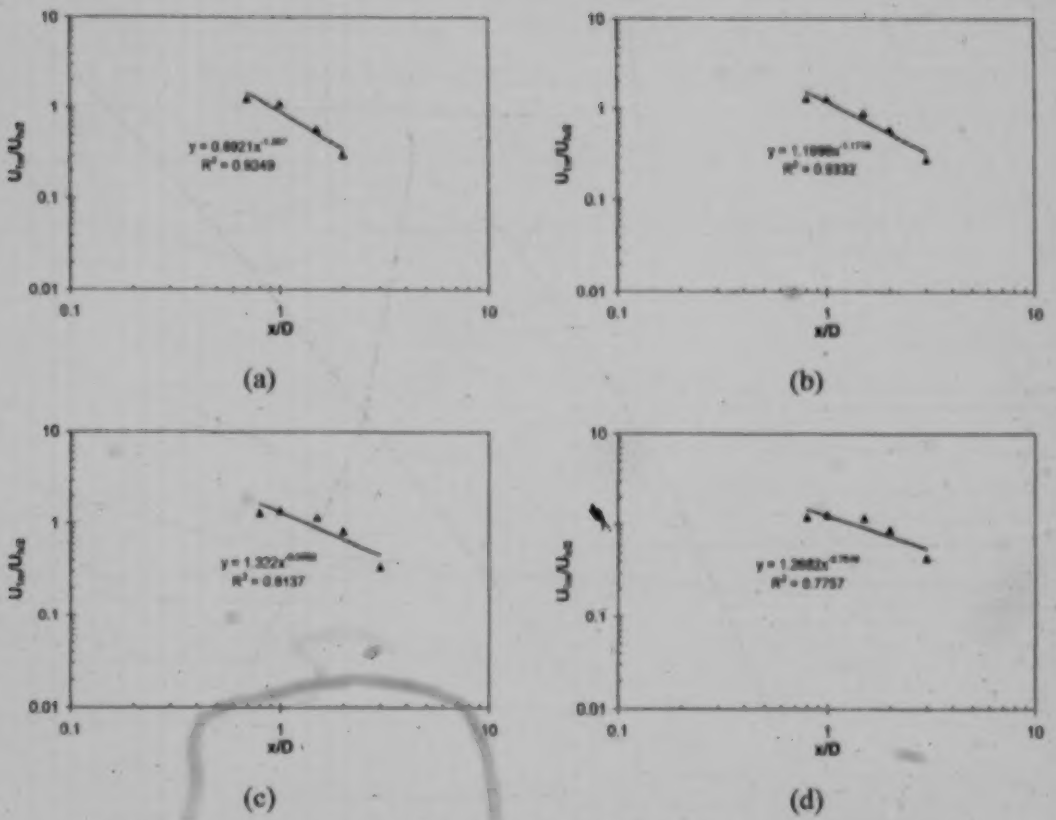

(a) (b)

(c) (d)

Fig. 6.74 Variation of the velocity scale ($U_{1m}/U_{h/2}$) with distance x/D on Rough bed; (a) Regime-1, and (b) Regime-2, (c) Regime-3, and (d) Regime-4

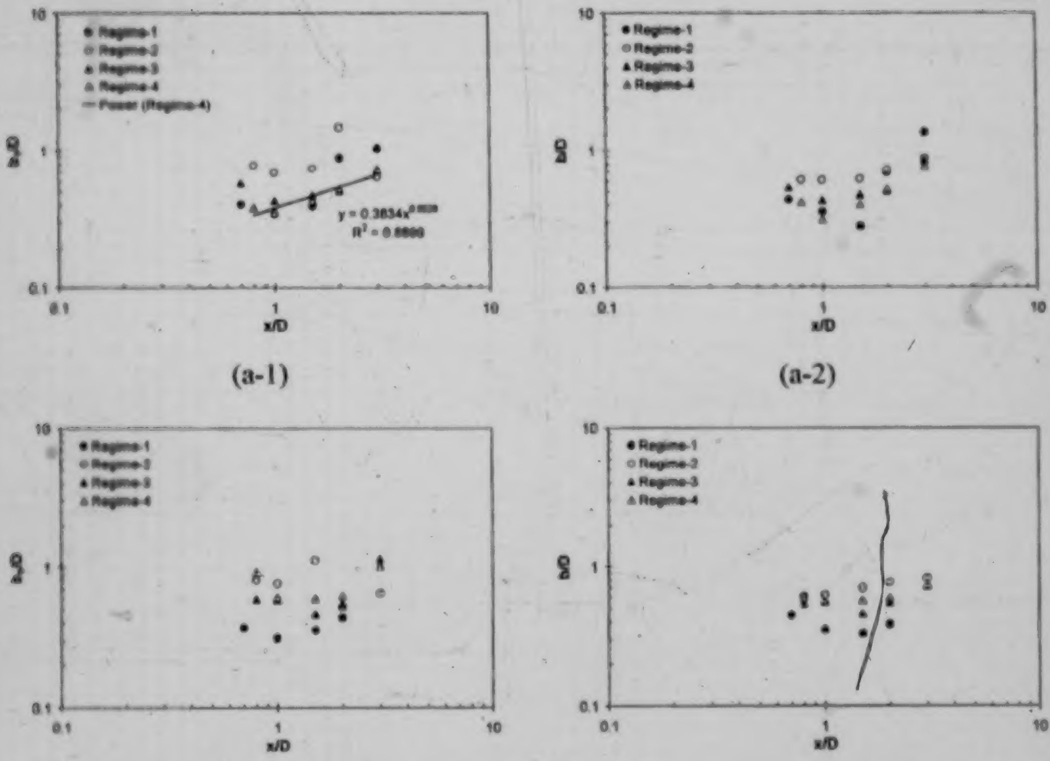

(a-1) (a-2)

(b-1) (b-2)

Fig. 6.75 Variation of the length scale ($b_1/\overline{D}$ and b/D) with distance x/D on (a) Smooth bed, and (b) Rough bed

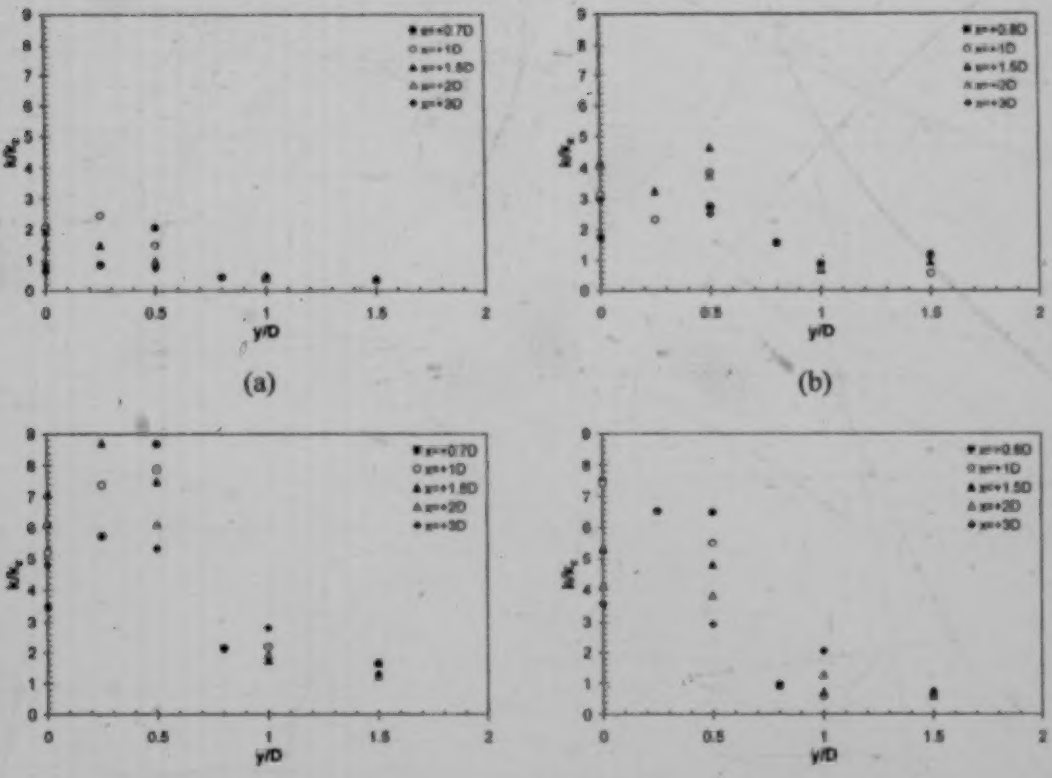

(a) (b)

(c) (d)

Fig. 6.76 Normalized turbulent kinetic energy profile across the wake at $z=h/2$ on Smooth bed; (a) Regime-1, (b) Regime-2, (c) Regime-3, and (d) Regime-4

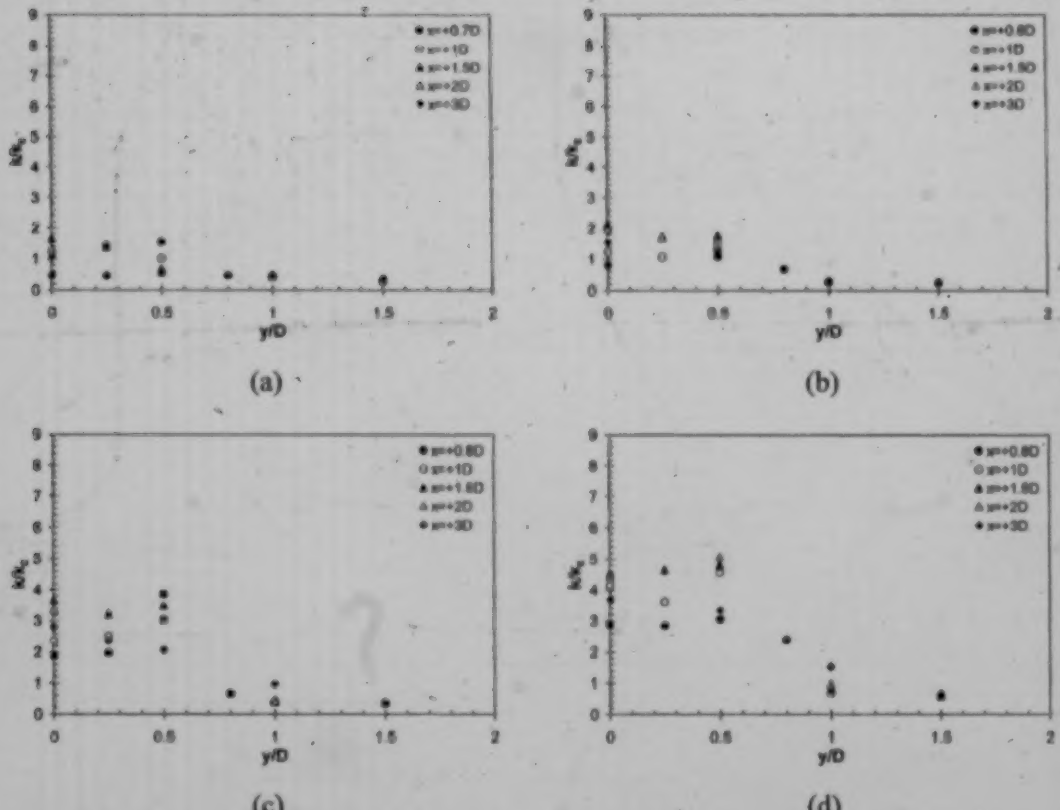

(a)

(b)

(c)

(d)

Fig. 6.77 Normalized turbulent kinetic energy profile across the wake at $z=h/2$ on Rough bed; (a) Regime-1, (b) Regime-2, (c) Regime-3, and (d) Regime-4

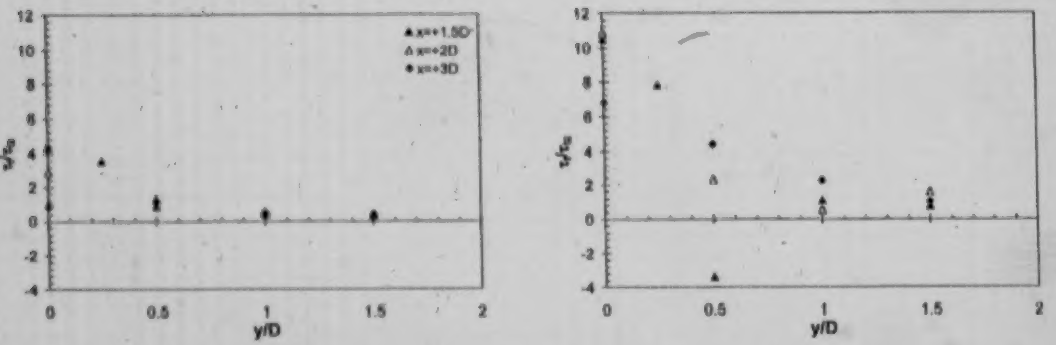

(a) (b)

Fig. 6.78 Normalized turbulent shear stress profile across the wake at z=h/2 on Smooth bed; (a) Regime-1, and (b) Regime-2

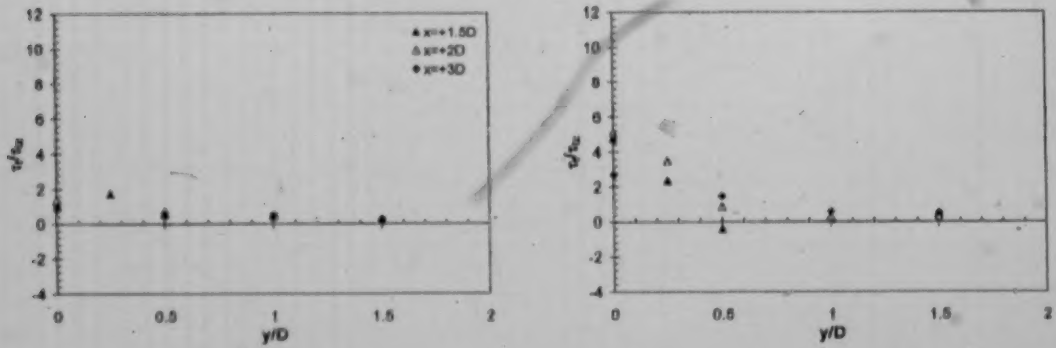

(a) (b)

Fig. 6.79 Normalized turbulent shear stress profile across the wake at z=h/2 on Rough bed; (a) Regime-1, and (b) Regime-2

6.6 References

Akilli, H., and Rockwell, D. (2002). "Vortex formation from a cylinder in shallow water." *Physics of Fluids*, 14(9), 2957-2967.

Antonia, R. A. (1991). "Organization in a turbulent near wake." *Fluid Dynamics Research*, 7, 139-149.

Arya, S. P. S., and Gadiyaram, P. S. (1986). "An experimental study of flow and dispersion in the wakes of three-dimensional low hills." *Atmospheric Environment*, 20(4), 729-740.

Arya, S. P. S., and Shipman, M. S. (1981). "An experimental investigation of flow and diffusion in the disturbed boundary layer over a ridge- I. Mean flow and turbulence structure." *Atmospheric Environment*, 15(7), 1173-1184.

Balachandar, R., Ramachandran, S., and Tachie, M. F. (2000). "Characteristics of shallow turbulent near wakes at low Reynolds numbers." *Journal of Fluids Engineering*, 122, 302-308.

Balachandar, R., Tachie, M. F., and Chu, V. H. (1999). "Concentration profiles in shallow turbulent wakes." *Journal of Fluids Engineering*, 121, 34-43.

Castro, I. P., and Snyder, W. H. (1982). "A wind tunnel study of dispersion from sources downwind of three-dimensional hills." *Atmospheric Environment*, 16(8), 1869-1887.

Chang, P. K. (1970). *Separation of flow*, Pergamon Press, New York, NY, USA.

Chen, D., and Jirka, G. H. (1995). "Experimental study of plane turbulent wakes in a shallow water layer." *Fluid Dynamics Research*, 16, 11-41.

Ingram, R. G., and Chu, V. H. (1987). "Flow around islands in Rupert bay: An investigation of the bottom friction effect." *Journal of Geophysical Research*, 92(C13), 14521-14533.

Kahraman, A., Sahin, B., and Rockwell, D. (2002). "Control of vortex formation from a vertical cylinder in shallow water: Effect of localized roughness elements." *Experiments in Fluids*, 33, 54-65.

Lloyd, P. M., and Stansby, P. K. (1997a). "Shallow-water flow around model conical islands of small side slope. I: Surface piercing." *Journal of Hydraulic Engineering*, 123(12), 1057-1067.

Lloyd, P. M., and Stansby, P. K. (1997b). "Shallow-water flow around model conical islands of small side slope. II: Submerged." *J. of Hydraulic Eng.*, 123(12), 1068-1077.

Perrin, R., Braza, M., Cid, E., Cazin, S., Moradei, F., Barthet, A., Sevrain, A., and Hoarau, Y. (2006). "Near-wake turbulence properties in the high Reynolds number incompressible flow around a circular cylinder measured by two and three component PIV." *Flow Turbulence Combust*, 77, 185-204.

Pingree, R. D., and Maddock, L. (1979). "The tidal physics of headland flows and offshore tidal bank formation." *Marine Geology*, 32, 269-289.

Rajaratnam, N., and Rai, S. P. (1979). "Plane turbulent wall wakes." *Journal of the Engineering Mechanics Division*, 105(EM5), 779-794.

Roshko, A. (1961). "Experiments on the flow past a circular cylinder at very high Reynolds number." *Journal of Fluid Mechanics*, 10(3), 345-356.

Schlichting, H. (1968). *Boundary-layer theory*, 6th Edition, McGraw-Hill Book Company, NY, USA.

Sforza, P. M., and Mons, R. F. (1970). "Wall-wake: Flow behind a leading edge obstacle." *American Institute of Aeronautics and Astronautics Journal*, 8(2), 2162-2167.

Shamloo, H., Rajaratnam, N., and Katopodis, C. (2001). "Hydraulics of simple habitat structures." *Journal of Hydraulic Research*, 39(4), 351-366.

Smith, H. D., and Foster, D. L. (2007). "Three-dimensional flow around a bottom-mounted short cylinder." *Journal of Hydraulic Engineering*, 133(5), 534-544.

Tachie, M. F., and Balachandar, R. (2001). "Shallow wakes generated on smooth and rough surfaces." *Experiments in Fluids*, 30, 467-474.

Townsend, A. A. (1976). *The structure of turbulent shear flow*, Cambridge University Press, London, UK.

Wolanski, E., Imberger, J., and Heron, M. L. (1984). "Island wakes in shallow coastal waters." *Journal of Geophysical Research*, 89(C6), 10553-10569.

Yakhot, A., Anor, T., Liu, H., and Nikitin, N. (2006). "Direct numerical simulation of turbulent flow around a wall-mounted cube: spatio-temporal evolution of large-scale vortices." *Journal of Fluid Mechanics*, 566, 1-9.

Zdravkovich, M. M. (1997). *Flow around circular cylinders*, Oxford University Press, New York, NY, USA.

Chapter 7: Conclusions and Recommendations

7.1 Summary

The results of a systematic experimental investigation of flow around bed-mounted cylinders in open channels were presented in this thesis. The quality of experimental data was demonstrated with repeated measurements. The results of an investigation of the undisturbed approach flow structure are presented in order to provide for better understanding of the changes in flow caused by the cylindrical objects. The changes in approach flow were subsequently studied in the upstream region surrounding the cylinders. Deflected velocities were also studied in terms of existing three-dimensional turbulent boundary layer theories. Flow visualization and direct measurements of bed shear stress around the cylinders have enhanced our understanding of the complex structure of these flows. This study also provided a detailed study of the three-dimensional shallow turbulent near-wake flows behind bed-mounted cylinders with different levels of submergence in an open channel. Mean and turbulent flow fields in the near-wake region were examined using reliable ADV measurements.

7.2 Conclusions of the Study

Conclusions of the study were presented in previous chapters according to the focus of study region. The general conclusions of the entire study are summarized in the following paragraphs.

A fully developed and symmetric approach flow was confirmed by the study of the undisturbed flow. The channel aspect ratio was chosen to be 5.5 because of unavoidable physical limitations of the experimental setup, as explained in Chapter 2. The impact of the small channel aspect ratio was that the straight approach flow experiences turbulence driven secondary currents. The effect of these secondary currents on the mean flow structure is minor, since the secondary flow velocities were only a few percent of the main stream velocity. However, these secondary currents were found to alter the turbulence characteristics of the open channel flow significantly compared to 2D wide channel. The study shows that the major difference in turbulence characteristics occur in the primary Reynolds stress. The turbulent shear stress profiles do not agree with linear stress profile and the measured values of turbulent shear stress near the bed at the channel center are 1.5-2 times smaller than the bed shear stress (τ_0). Bed roughness was found to suppress the development of turbulence driven secondary currents.

Flow visualizations revealed that when the cylinders became more deeply submerged the upstream boundary layer separation point moved closer to the object, and as a result the size of the horse-shoe vortex system became smaller. However, bed resistance to the backward flow upstream of the cylinders held the separation point with the short region between -1*D* to -1.2*D* irrespective of the level of submergence. It was also observed that the horse-shoe vortex trails were relatively wider (~0.4D) and further away from the cylinder surface on a rough bed. Wake vortices were found to shed in alternate fashion with *S*~0.2 for the slightly submerged and non-submerged cylinders. The width of the wake, however, was less for the non-submerged cylinder. A closed recirculating wake was found to be a characteristic feature of the flows around moderate to deeply submerged objects. Bed roughness has been found to interrupt wake vortices and their interaction with the horse-shoe vortex system near the bed. Dye plume was found to spread away from the cylinder near the bed (at $z<0.2H$) without forming wake vortices.

Bed shear stress amplification near the shoulder of the cylinders occurred in all flow regimes. However, the relative increase in bed shear stress was found to be inversely related to the level of submergence of the cylinders. The maximum amplification of bed shear stress (i.e. τ_{0max}/τ_{00}) for a deeply submerged cylinder was 3.5, while it is approximately 5.5 for a surface piercing cylinder on smooth bed. In general, the ratios of τ_{0max}/τ_{00} were approximately twice as large on a rough bed compared to a smooth bed for similar flow conditions. Bed shear stress results presented in this study provide qualitative information on the scour potential of the flow around submerged cylinders in natural rough bed streams.

Skewed 3D flow around cylindrical objects on smooth and rough beds were explained with the help of Prandtl and Johnston's cross-flow models. The existence of the collateral and skewed zones in the boundary layer was observed at stations upstream of the cylinders on smooth bed. Bed roughness is found to inhibit the effect of the lateral pressure gradient that causes skewing in the boundary layer. As a result, theoretical models did not agree well with the rough bed measurements. This study showed that Perry and Joubert's velocity defect function can be a useful tool for predicting the deflected flow around submerged objects on smooth and rough beds. Specifically the theory can be used to predict the magnitudes of velocity in the deflected flow around fish habitat structures, water intake or outfall structures and submerged islands.

The study of flow in the upstream region surrounding the cylinder showed that in spite of deceleration of the approach flow on the plane of symmetry, the mean longitudinal velocity profiles plotted in terms of Clauser's scheme collapsed in a narrow band in all flow regimes on both smooth and rough beds. These results indicate that an approximate relationship can be determined to describe the approach flow profiles subjected to an adverse pressure gradient. Flow deflections in the transverse as well as vertical direction in the upstream region surrounding the cylinders were enormous irrespective of the level of submergence. The influence of bed roughness on the flow deflection patterns and the lateral spread of increased turbulence were nominal for different flow regimes. Increased turbulence region on $x=0$ plane spread up to $y=1.2D$. In the upstream region surrounding the cylinders, the near-bed turbulent kinetic energy and turbulent shear stress were increased as much as 2-3 times compared to the values observed relatively far away from the cylinders. Near-bed turbulent kinetic energy at $x=0$ was found to be approximately 2.5% of the mean kinetic energy for all flow regimes on smooth and rough beds. Near-bed observations of increased turbulence surrounding the cylinders and velocity amplification at $x=0$ could be indicators of local scour. Future studies of similar flows on erodible beds could enhance our knowledge regarding the influence of flow structure on local scour.

Study of the shallow turbulent wake on the downstream plane of symmetry revealed the general flow patterns in the shallow near-wake region for different levels of submergence. The size of the closed recirculation zone and the point of reattachment for moderate to deeply submerged cylinders; and the length of the wake-bubble or recirculation zone for slightly submerged and surface piercing cylinders were observed. It was found that the deeply submerged object (Regime-1) creates stronger vorticity compared to moderately submerged object (Regime-2); and bed roughness enhances the strength of the vorticity in the closed wake region.

The mean velocity defect and wake turbulence were found to increase in the near-wake before decaying in the downstream direction. The rates of decay of the velocity defect and wake turbulence were found to be related to the level of submergence of the cylinders and bed roughness. Flows behind moderate to deeply submerged cylinders (Regime-1 and 2) were found to overcome the defects of mean velocity and turbulence faster than slightly submerged and surface piercing cylinders (Regime-3 and 4). However, bed roughness was found to promote the rates of decay of the mean and turbulent flow defects behind slightly submerged and surface piercing cylinders (Regime-3 and 4).

Wall wake analyses demonstrated that the flows in the region away from the bed are quite similar and can be described with the well-known plane wake equation. Wall wake similarity was also observed for the turbulence properties, such as the turbulent kinetic energy and primary Reynolds stress for moderate to deeply submerged cylinders (Regime-1 and 2). Wake analyses on the horizontal plane showed that the mean velocity profiles were similar across the flow in the near-wake region at all elevations for slightly submerged and surface piercing cylinders; and at all elevations below the object height very close to the moderate to deeply submerged cylinders. Normalized mean velocity profiles across the wake on the horizontal plane for slightly submerged and surface piercing cylinders (Regime-3 and 4) were in fair agreement with the well-known plane wake equation. However, the normalized mean velocity profiles were found to exhibit considerable similarity in all flow regimes when a slightly modified transverse length scale (i.e. half-width) was used.

Therefore, the present study provides valuable understanding of the flows around bed-mounted objects such as fish-rocks for different levels of submergence. Knowledge of hydraulics in terms of bed shear stress amplification, vortex structures, near-bed turbulence and high velocity around the cylinders will serve as qualitative indicators for local scour potential. Thus the observations of this study would be very useful for improving engineering judgment for the design and implementation of simple fish habitat structures. This study also provides valuable quantitative information for the design of simple fish habitat structures. More specifically, the results of wake similarity, the rates of decay of wake turbulence and velocity defect, and the applicability of Perry and Joubert's model for upstream deflected flow regions will serve as tools for computing the magnitudes and the area of reduced velocity and increased turbulence. The results of normalized bed shear stress distributions with respect to upstream bed shear stress would be useful for determining the variation in bed shear stress around a fish-rock. Assuming a scale model (i.e. geometric and Froude number similarity) the essential habitat conditions in the prototype (i.e. velocity, turbulence and shear stress) can be predicted from the observed conditions of the physical model used in this study. Unavailability of scour depth measurements will limit the results to provide information regarding the change in water depth. A future study on mobile bed with similar flow conditions can contribute to predict the variation in water depth caused by local scour and deposition in the surrounding regions of a fish-rock. The extensive and reliable database obtained from this study could be utilized for numerical studies to overcome the limitations of computational modeling applied for the design of habitat structures. All these achievements can lead us towards an improved habitat enhancement design in future.

7.3 Recommendations for Future Study

In order to enhance our understanding of flow around bed-mounted cylinders in open channels that will ultimately lead to effective design of simple fish habitat structures the following studies are recommended.

- Study of local scour around cylinders for similar flow conditions would be extremely valuable. Measurements of velocity and bed shear stress would be an asset.

- Numerical study of similar flow around cylinders is highly recommended. The present experiments provide a database for use in computational fluid dynamic (CFD) modeling.
- Further experimental studies of flow and scour can be conducted using different object shapes (e.g. cones). However, it would be more useful if the objects are used in different orientations in a cluster. The effect of object surface roughness can also be investigated, as the natural rocks are rough in texture.
- Future experiments can be conducted in different experimental flow conditions, especially with different Froude numbers. The influence of bed roughness can be further investigated by using different roughness elements.